BRNO UNIVERSITY OF TECHNOLOGY
VYSOKÉ UČENÍ TECHNICKÉ V BRNĚ

FACULTY OF CIVIL ENGINEERING
FAKULTA STAVEBNÍ

INSTITUTE OF STRUCTURAL MECHANICS
ÚSTAV STAVEBNÍ MECHANIKY

SMOOTHED PARTICLE HYDRODYNAMICS IN STRUCTURAL DYNAMICS
SMOOTHED PARTICLE HYDRODYNAMICS VE STRUKTURÁLNÍ DYNAMICE

DOCTORAL THESIS
DISERTAČNÍ PRÁCE

AUTHOR — Ing. Martin Hušek
AUTOR PRÁCE

SUPERVISOR — doc. Ing. Jiří Kala, Ph.D.
VEDOUCÍ PRÁCE

BRNO 2021

Abstract

The focus of the thesis is on the application of the Smoothed Particle Hydrodynamics (SPH) method in structural dynamics with an emphasis on usage of quasi-brittle materials. The thesis is divided into several parts to provide a comfortable transition between the theory and application. The first part is focused on the introduction, history, and theoretical background of SPH. Numerical examples in which strengths and weaknesses of SPH are shown follow. In addition to pure SPH models, several coupling approaches with the Finite Element Method (FEM) are also discussed.

After the introduction of SPH, the focus is on quasi-brittle materials and their reinforced variants. The numerical concept and mathematical background of the Continuous Surface Cap Model (CSCM) are outlined, several benchmarks are presented. Strain-rate effects and their impact on pure SPH and coupled SPH-FEM models are evaluated next. In this section, the author proposes a new approach for SPH models reinforcement with FEM beam elements while strengths of both methods are preserved. The coupling approach was named *sublayer coupling* and shows a potential in simulations while the SPH tensile instability is alleviated.

Since concrete is often associated with heterogeneity and very specific material structure, a unique *algorithm for concrete structure generation* in combination with SPH is proposed in the next chapter. The concept is based on utilization of coherent noise functions which can bring a variability to numerical models. It has been proved that the algorithm is robust, stable, and easy to implement into the SPH framework. With regard to that, the so-called *numerical heterogeneity*, a concept of parameters variability implementation, is introduced together with examples.

The last part of the thesis is dedicated to the application of SPH in real experiments, specially designed to test SPH to the full. The first experiment focuses on a high velocity impact (HVI) in which the functionality of the proposed approach of the sublayer reinforcement coupling is demonstrated. The second experiment deals with an explosion (blast load) in which the focus is on both the loaded specimen and charge. Since SPH simulates the explosive, detonation products, and the loaded specimen, it is in fact a fully coupled fluid-structure interaction (FSI) simulation. Furthermore, the SPH reinforcement with the sublayer coupling is tested again, yet for much higher load rate. The constitutive model strain-rate effects are also the subject of the study in both experiments.

Conclusions are discussed at the end of the thesis.

Keywords

Concrete; Explosion; Impact; Kernel; LS-DYNA; Smoothed Particle Hydrodynamics; Structural Dynamics.

Abstrakt

Disertační práce je zaměřena na aplikaci metody Smoothed Particle Hydrodynamics (SPH) ve strukturální dynamice s důrazem na použití kvazi-křehkých materiálů. Disertační práce je rozdělena do několika částí tak, aby došlo k plynulému navázání mezi teorií a aplikací. První část je zaměřena na úvod, historii a teoretické pozadí SPH. Numerické příklady, kde jsou ukázány silné a slabé stránky SPH, následují. Diskutovány jsou rovněž metody tvorby kombinovaných modelů s Finite Element Method (FEM).

Po úvodu do SPH se práce soustředí na kvazi-křehké materiály a jejich vyztužené varianty. Nastíněny jsou numerické koncepty a matematické pozadí Continuous Surface Cap Model (CSCM) spolu s několika benchmarky. Následuje rozbor vlivu rychlosti přetvoření na modely SPH a na kombinované modely SPH-FEM. V této sekci autor představuje nový způsob vyztužení modelů SPH s pomocí nosníkových prvků FEM, zatímco jsou silné stránky obou metod zachovány. Tento způsob spojení byl nazván *vazba podvrstvou* a ukazuje potenciál v simulacích, zatímco je tahová nestabilita SPH zmírněna.

Jelikož je beton často spojován s heterogenitou a velmi specifickou materiálovou strukturou, unikátní *algoritmus pro generaci struktury betonu* v kombinaci s SPH je představen v následující kapitole. Koncept je založen na využití koherentních funkcí šumu, které mohou přinést variabilitu do numerických modelů. Bylo prokázáno, že algoritmus je robustní, stabilní a jednoduchý na implementaci do SPH. S ohledem na to, takzvaná *numerická heterogenita*, koncept implementace parametrové variability, je představena spolu s příklady.

Poslední část práce je zaměřena na aplikaci SPH ve skutečných experimentech, speciálně navržených pro otestování SPH jak jen to lze. První experiment se soustředí na náraz ve vysoké rychlosti (HVI), kde je prokázána funkcionalita navrhovaného způsobu vyztužení s podvrstvou. Druhý experiment se zabývá výbuchem (zatížení tlakovou vlnou), kde zaměření je na zatěžovaný vzorek a nálož. Vzhledem k tomu, že SPH simuluje nálož, plyny výbuchu a zatěžovaný vzorek, jedná se ve skutečnosti o plně svázanou simulaci interakce tekutiny a struktury (FSI). Navrhovaný způsob vyztužení s podvrstvou je znovu testován, avšak pro mnohem vyšší rychlosti zatížení. Efekty vlivu rychlosti přetvoření implementovaného do konstitučního modelu jsou rovněž předmětem zkoumání v obou experimentech.

Závěry jsou diskutovány na konci práce.

Klíčová slova

Beton; Exploze; Náraz; Kernel; LS-DYNA; Smoothed Particle Hydrodynamics; Strukturální dynamika.

Bibliographic Citation

HUŠEK, Martin. *Smoothed Particle Hydrodynamics in Structural Dynamics*. Brno, 2021. 295 p. Doctoral thesis. Brno University of Technology, Faculty of Civil Engineering, Institute of Structural Mechanics. Supervised by doc. Ing. Jiří Kala, Ph.D.

Dedication

I would like to dedicate this work to Rachel Amber. You will never be forgotten.

Declaration of Originality

I declare that this doctoral thesis titled *Smoothed Particle Hydrodynamics in Structural Dynamics* was composed by myself, that the work contained herein is my own except where explicitly stated otherwise in the text, and that this work has not been submitted for any other degree or processional qualification except as specified.

Brno, 2021

Ing. Martin Hušek

Acknowledgements

I would like to thank my supervisor, doc. Ing. Jiří Kala, Ph.D., for professional guidance, given freedom in research, and given opportunities in applied mechanics.

My appreciations go to my family for being always there for me whenever I needed.

I would like to pay special regards to my friend and colleague Dr.-Ing. Stefan Eckardt for showing me what is possible.

Table of Contents

Chapter 1

Introduction

Since the thesis is divided into several parts, a brief introduction with outlines and goals of the thesis is presented first. An explanation why there is a need for meshfree or meshless methods is also discussed in the chapter. Meshfree methods are very popular in many fields of research and much can be written from a global perspective. But since the Faculty of Civil Engineering is the author's alma mater, an emphasis is on the application of Smoothed Particle Hydrodynamics (SPH) in structural mechanics.

1.1 Outline of the Thesis

In **Chapter 1** *Introduction*, the outline of the thesis is discussed. The outline should serve as a detailed table of contents in which a reader can find what is the focus of each chapter. The goals of the thesis are also summarized here. The reasons why the SPH method was chosen and why there is and should be a motivation to use meshfree methods are also discussed.

In **Chapter 2** *Smoothed Particle Hydrodynamics*, the SPH method is discussed in detail. In the first part of chapter, the early beginnings and development of SPH are reviewed. Since history goes together with the applied research, the most important mile stones of the SPH applications in various research fields are also included. The mathematical formulation of SPH follows. The essentials, derivations, and overall theory take place here. A detailed examination of kernel functions together with their comparison are part of the chapter. Derivations of the general continuum equations in the SPH framework are subsequently discussed. The implementation of SPH in simulations with material strength follows. As any other numerical method even SPH suffers with some numerical difficulties and artificial errors. Therefore, in the last section of the chapter the most important corrections and corrective schemes are summarized.

In **Chapter 3** *From Theory to Application*, the logic of SPH is demonstrated in several tests and benchmarks. The purpose of the chapter is to provide a transition from the mathematical definition to the real application. Since SPH is usually applied in fluid simulations and as such very often overlooked by the academic community in structural

mechanics, the focus is on quasi-static and dynamic applications in structural mechanics. Some numerical difficulties and their consequences are pointed out here. The last part of the chapter shows the performance of the Moving Least Square Particle Hydrodynamics (MLSPH) method.

In **Chapter 4** *Coupling SPH and FEM*, the most popular approaches for SPH and the Finite Element Method (FEM) coupling are reviewed. It is without a question that FEM is still one of the most used numerical methods and most likely will be in the near future. However, FEM fails in many applications in which SPH excels. Therefore, coupled SPH-FEM models might be the answer. Due to the Lagrangian nature of both methods it is possible to couple them together quite easily. The chapter serves as a groundwork for the following chapters where advanced approaches for the coupling are proposed and discussed.

In **Chapter 5** *Quasi-Brittle Materials*, the focus is on quasi-brittle materials in the SPH framework. Discussed is the Continuous Surface Cap Model (CSCM) which is one of the few models that supports strain-rate effects, kinematic hardening, moduli reduction, and strain softening with the damage formulation. The essentials of the material theory are outlined, strengths and weaknesses of the model are demonstrated. The performance of CSCM with SPH on real experiments is also shown in the chapter. In the first experiment, pure SPH models with CSCM are used to demonstrate the ability of a dynamic fracture propagation prediction on L-shaped structural members. In the second experiment, the adaptive transformation of FEM into SPH is demonstrated while CSCM is employed.

In **Chapter 6** *Reinforced Concrete*, approaches for quasi-brittle materials reinforcement in the SPH framework are described. It is usually not a problem to use standard numerical approaches to introduce a reinforcement into a model. However, in case of SPH it can be a problem. Since SPH suffers from the so-called tensile instability, it is in fact quite difficult to simulate a reinforcement in concrete. The tensile instability is a numerical error which leads to a false crack development in material. There are several ways to deal with the problem. The standard solution is to use special kernel functions. However, this usually means that the adaptive nature of SPH is lost. For that reason, the author proposes a new sublayer coupling approach with FEM elements which are not affected by the tensile instability. The coupling is demonstrated on examples.

In **Chapter 7** *Heterogeneity in Numerical Models*, a new approach for material heterogeneity implementation into numerical models is proposed. The motivation is to get closer to reality where concrete clearly exhibits signs of random behaviour with respect to its structure. Due to the Lagrangian nature of SPH, properties of particles might vary over domains and create fields of randomness. However, an uncorrelated random variation results into increased brittleness of the model. In contrast, a correlated variation is often too perfect. For that reason, the author proposes a new approach with which fractal-based noise functions are used to generate a structure of concrete on the mesolevel. The generated structure is further used for the material heterogeneity implementation. The idea of the algorithm together with examples are contents of the chapter. The noise functions together with an optimization process are described first. A demonstration on two examples in which sharp-edged and rounded aggregate are used follows. A basic application with SPH is shown at the end of the chapter.

In **Chapter 8** *Experiment – High Velocity Impact*, experimental measurements together with numerical simulations are presented. The chapter demonstrates strengths and weaknesses of SPH on a real experiment in which a high velocity impact (HVI) on concrete specimens was the subject of the study. The newly proposed reinforcement approach, performance of SPH with CSCM, and ability of SPH to predict a dynamic fracture propagation are discussed in the chapter. At the end of the chapter, the experimental measurements are compared to the simulations.

In **Chapter 9** *Experiment – Explosion*, experimental measurements together with numerical simulations are presented. The focus of the experiment was on responses of concrete slabs subjected to a blast load. The numerical simulations focused on the responses of the concrete slabs, yet, in addition, also on the detonation of the charge. For that reason, the chapter discusses not only the structural parts of the experiment but also the transformation of the explosive into detonation products, the fluid-structure interaction (FSI) between the gases and concrete, and again the performance of SPH with CSCM while using the proposed sublayer coupling approach. The last part of the chapter focuses on a sensitivity study in which the charge orientation was analysed in detail.

In **Chapter 10** *Conclusion*, the outcomes of the thesis are presented. Each chapter is summarized and reviewed. All the findings and conclusions of the thesis are discussed.

1.2 Goals of the Thesis

Since SPH is very well known in fluid simulations, it can be quite challenging demonstrating other possible applications in fields in which mesh-based methods are dominant. For example, structural mechanics problems are mostly solved with FEM and it can be difficult to prove that other methods can perform better. As a civil engineer, the author believes that meshfree methods should have a place in structural mechanics and especially in structural dynamics. To change the current state, a clear demonstration of the SPH abilities must be provided. Moreover, an emphasis should be on quasi-brittle materials as it is a fact that concrete and its reinforced variants are preferably used in civil engineering. With respect to that, a list of the goals of the thesis follows.

- Gather information about the SPH history, mathematical background, strengths and weaknesses, recent developments, and state of the art in real applications.
- Prove that SPH is able to pass basic patch tests with a focus on structural mechanics.
- Demonstrate the SPH functionality with plain and reinforced quasi-brittle materials subjected to a static and dynamic load.
- Demonstrate that SPH can be used as an enhancement to standard mesh-based methods.
- Develop a new approach for quasi-brittle materials reinforcement simulated with SPH, free of the tensile instability.

- Develop a new approach for material heterogeneity implementation into SPH models.
- Prove that SPH can represent real experiments in which reinforced concrete specimens are subjected to an impact load.
- Demonstrate the SPH functionality in FSI problems.
- Prove that SPH can represent real experiments in which reinforced concrete specimens are subjected to a blast load.

1.3 The Need for Meshfree Methods

Mesh-based, grid-based, or just mesh methods have a solid background in structural mechanics. Maybe the most popular method is the Galerkin FEM. In fact, it is quite popular across all fields of continuum mechanics, not only structural. Given the popularity, many modifications have been developed. For instance, the Extended Finite Element Method (XFEM), a subtype of the Generalized Finite Element Method (GFEM). Another examples could be the Finite Difference Method (FDM), the Finite Volume Method (FVM), and the Boundary Element Method (BEM); also used in many domains of continuum mechanics.

Why is there a need for meshfree methods if so many mesh-based methods are available? It is not an intention here to point out all the weaknesses of mesh-based methods but rather to discuss known obstacles which can be bypassed with meshfree methods. Since the Lagrangian FEM is the most popular, few examples of problematic areas can be mentioned.

Large deformations are and always will be a problem for mesh-based methods. Excessive deformations and distortions of elements lead to several issues.

- Highly distorted elements lose accuracy and lead to numerical errors. When an element loses its initial shape, e.g. aspect ratio, orthogonality, or skewness, its shape functions can no longer represent a correct solution. This is especially true when nonlinear material models are being used.
- Negative volume of an element can be a result of large deformations. There is nothing to prevent a passage of element faces (edges) except the stiffness of the element itself. Twisting, skewing, and other deformation shapes of an under-integrated element can simply result into negative volume, therefore, in a collapse of the calculation.
- In case of explicit integration schemes, the time step of the simulation is driven by shapes and sizes of elements. Therefore, if highly distorted elements are in the simulation, the time step can drop to zero. This results in a very long simulation time, i.e. the time which is needed to solve the simulated problem.

Penetration and perforation are very difficult tasks to simulate with mesh-based methods. At the beginning of the simulation, a mesh is generated. With the mesh a connection between nodes is given, therefore, something what could be termed a list of neighbours. Keeping remeshing techniques out of the equation, with the given mesh, the neighbouring elements never change. Therefore, how can be a penetration or perforation simulated and what are related problems?

- In impact simulations in which an impactor penetrates a target, elements of the target undergo large deformations. The reason for that is usually a constant motion of the impactor which is pushing elements of the target away from its trajectory. Therefore, problems related to highly distorted elements arise. The solution is to remove, deactivate, or erode the elements. However, this brings more problems than benefits. In general, there are two reasons for elements erosion.
- The erosion of elements, since they are no longer needed. If elements with a quasi-brittle material reach a residual strength, i.e. the material is completely damaged, there is no purpose for the elements to stay in the simulation. When the stiffness of the elements reaches a very small value, there can be only numerical problems. Since the elements with no stiffness can no longer carry any load, they can be removed from the simulation. When elements are eroded, a portion of mass is removed from the simulation, which is a violation of the conservation laws, however.
- The erosion of elements, since it is required. When a perforation is simulated, it is expected that an impactor perforate through a target. Since a mesh is strictly given from the point of its generation, without the element erosion the impactor cannot perforate through the target. At this point, the elements might not be fully damaged, i.e. the elements can still carry a load, yet they have to be eroded. Again, a portion of mass is removed from the simulation, and even worse, the stress state of the eroded elements is also dissipated, which is again a violation of the conservation laws.

The element size, orientation, and quality are another concern. It would be possible to write a thesis just about the problems related to the computational mesh. The following list is just a handful of all the issues.

- Choosing the element size is a double-sided coin. When the element size is too big, the discretization of a problem domain is usually not sufficient. Many important details, e.g. stress gradients, are not captured at all. Yet the simulation is faster and tends to be more robust due to the smaller number of elements. On the contrary, when the element size is too small, localization problems might occur. In other words, a plastic zone could be localized to a very small region, therefore, fracture energy must be normalized if used. In 3D, however, the normalization of fracture energy is something discussable. Yet, in many applications, with a smaller size of elements, the numerical solution converges to the analytical one. Furthermore, when an element is eroded, the size of the element plays significant role.

- As it is usually the case when a material is not linear and elastic, the mesh orientation is something which needs to be taken into account. When the subject of the simulation is a fracture growth and propagation, just a simple mesh reorientation might completely change the results. This artificial dependency is very well known to everyone who is interested in fracture mechanics. The mesh orientation goes hand in hand with the mesh size. Unfortunately, there is no general rule to say what is the correct settings. Therefore, mesh sensitivity studies are often needed. This is of course time-consuming.
- Shear locking, volume locking, hourglass effect, and other types of artificial issues. All is related to the element quality. Every element has a shape, size, and other properties which influence its quality. This is very important to keep in mind when a mesh is being generated. To have a good quality mesh is sometimes challenging. For a mesh of a better quality, the number of elements often increases. This again results in time-consuming simulations.

1.4 Side Notes

Please note the following list of additional information.

- Name of the thesis is composed of the numerical method name which is discussed and the application field. Since structural engineering has been associated with civil engineering, and dynamics refers to non-stationary events, the name of the thesis is simply *Smoothed Particle Hydrodynamics in Structural Dynamics*. Although the name is rather general, it must be noted that the focus of the thesis is strictly on the civil engineering application with an emphasis on quasi-brittle materials.
- Abbreviations are always written in expanded form the first time they occur in a chapter.
- All the discussed simulations and results in the thesis were calculated using Ansys solvers.
- Due to variety of topics in the thesis, the unit system is the base International System of Units (SI) except where explicitly stated otherwise in the text.
- In the thesis, a *fracture* refers to a mechanism of creating new surfaces within a domain, e.g. numerical fracture, and a *crack* refers to a discontinuity in the domain, e.g. crack pattern.

Chapter 2

Smoothed Particle Hydrodynamics

In this chapter the history, mathematical background, formulations, development, applications, and some latest improvements of Smoothed Particle Hydrodynamics (SPH) are discussed in detail. The purpose of the chapter is to offer a comprehensive description of SPH with a focus on structural dynamics. Since it is not always possible to draw a line between structural and fluid dynamics as they have many things in common, certain parts of the theory apply to both. Furthermore, since SPH was developed for very different purposes than structural dynamics, many other research fields intertwine as well.

2.1 History and Application

The first mention of SPH goes to 1977 when Lucy [1] proposed a numerical scheme for obtaining approximate solution of fission problems for optically thick protostars. The SPH as a name however, was not directly used by Lucy but Gingold and Monaghan in [2] in which polytropic stellar models were studied. Interestingly enough, the year was also 1977 when Gingold and Monaghan published their paper. It is always difficult to determine who was the first one with the idea, especially when several researchers develop the same method but use it in different fields or name it differently. In this case, acknowledgement taken from [2] points to the Lucy's original work.

> *In a lecture given at the Institute of Astronomy, Cambridge in 1976 Leon Lucy discussed the use of smoothing techniques for hydrodynamic codes. His ideas were adumbrated to us by our colleagues, but the mathematical development in this paper is independent of his work.* [2]

It is not a coincidence, however, that after SPH was successfully applied in astrophysical problems it was also applied in fluid dynamics (both liquid and gas phases) and high-speed structural dynamics. All three have in common that when particles move and represent either planets, cells of fluid or grains of sand, they can be described by the governing equations of the classical Newtonian hydrodynamics. It took many years to overcome all

the problems, however. The year 1977 was a milestone, yet there are many others in the history of SPH. The author collected the most significant ones in a chronological order.

- In 1982 Gingold and Monaghan [3] presented a comprehensive study in which different kernels were examined in fields of hydrodynamics. In the same year, Monaghan provided a proof that particle methods must work because they make use of interpolation methods [4]. In the same year, Zukas et al. pointed out that it is possible to use SPH for shock wave propagation problems [5].

- In 1983 Monaghan and Gingold proposed a new form of artificial viscosity, specially developed for shock simulations [6]. The paper focused on one-dimensional shock tube problems with incorporated artificial viscosity directly in the equations of motion.

- In 1985 Monaghan performed a comprehensive review in which particle methods for compressible flows were compared [7]. Both Particle in Cell (PIC) and SPH were discussed in detail. In the same year, Monaghan published another study in which B-splines were examined[8], clearly pointing to the possible application in SPH. Following that, Monaghan and Lattanzio presented an improved variant of SPH with increased efficiency, accuracy, and the B-splines [9]. Finally, in the same year Monaghan and Pongracic proved that the newly developed artificial viscosity in shock simulations eliminates spurious oscillations [10].

- In 1988 Benz first applied SPH in simulations of exchanging white-dwarf binaries and colliding planets [11]. In the same year, Monaghan proved that it is possible to use SPH in compressible gas flow simulations [12].

- In 1989 Monaghan proposed a corrected scheme of SPH preventing interpenetration of two interacting fluids [13]. The correction was named X Smoothed Particle Hydrodynamics (XSPH) and was introduced to improve accuracy when no artificial viscosity is used. The idea is based on the velocity field averaging which as a consequence also increases the stability of SPH. Benz first commented on issues concerning a variable smoothing length [14].

- In 1990 Benz further elaborated his study and published a review in which improvements on a variable smoothing length were proposed [15]. It must be noted, that the idea of the time dependent smoothing length scheme from [15] has been incorporated in many commercial codes and is still widely used. In the same year, Monaghan used SPH for the Universe modelling [16]. The same year, Libersky and Petscheck used SPH for high velocity impact (HVI) simulations with strength of materials [17]. Furthermore, Zukas proposed SPH as a suitable numerical method for colliding bodies which behave like fluids [18].

- In 1991 Monaghan and Lattanzio used SPH to simulate a collapse and fragmentation of cooling molecular clouds with respect to initial stability [19].

- In 1992 Monaghan collected the most relevant information about SPH and published a comprehensive review in which, among the others, gas dynamics, stellar collisions, magnetic phenomena, and nearly incompressible flow were discussed [20].

- In 1993 Libersky et al. published a study in which HVI experimental measurements were compared to SPH simulations with a great agreement [21]. In addition, Allahdadi et al. published a report with helpful comments on the SPH coding [22]. In the same year, Benz and Asphaug introduced a material damage as an additional material parameter in the SPH framework for HVI simulations [23]. Furthermore, Stellingwerf and Wingate published a study in which the difference between the fracture and fragmentation model within the SPH framework is discussed [24].

- In 1994 Monaghan extended SPH to deal with free surface incompressible flows [25]. A damn break and wave maker were successfully simulated, clearly showing the true potential of SPH. In the same year, Swegle et al. completed a comprehensive technical report in which the so-called tensile instability was addressed for the first time [26]. A new approach of dynamic fragmentation which explicitly reproduces growth of fractures was implemented into SPH framework by Benz and Asphaug the same year [27].

- In 1995 Benz and Asphaug further developed their concept of the fragmentation by nucleation of incipient shortcomings whose number density is given by the Weibull distribution [28]. Swegle et al. further examined the tensile instability and defined conditions for an artificial fracture growth [29]. Dyke and Ingel further evaluated the tensile instability, for the case in which stresses were calculated at points other than SPH particles [30]. Libersky et al. was able to improve HVI results with new kernel functions [31]. Since it was found that the tensile instability is correlated to the kernel, new formulations were also proposed. A new class of positive definite and compactly supported radial kernels were developed by Wendland [32]. In the same year, Fulbright et al. also proposed a new class of spheroidal kernels [33]. Monaghan and Kocharyan presented a concept of a multi-phase flow the same year [34].

- In 1996 Randles and Libersky further improved the stability of SPH and alleviated some issues related to boundary conditions [35]. Morris proposed a different approach in the question of the SPH stability by using higher order spline interpolants [36, 37]. In order to improve completeness conditions, reproducing conditions, and interpolant estimates, Liu et al. utilized a technique from the Reproducing Kernel Particle Method (RKPM) and implemented it into SPH [38]. More about RKPM techniques can be found in [39]. Belytschko et al. examined three approximations of meshless methods based on kernels, Moving Least Squares (MLS), and partitions of unity. It was proved that approximations constructed by kernels and moving least squares are identical once the requirement of consistency is imposed [40]. In the same year, Johnson performed a study in which known formulations of artificial viscosity were examined in HVI simulations [41]. It was proved, that artificial viscosity has a great impact on the results. This was followed by Johnson and Beissel in [42] in which a normalized smoothing function algorithm that can improve the accuracy of SPH was introduced. Johnson et al. further commented on some issues associated with kernels, free boundaries, material interfaces, and artificial viscosity in [43]. Fulk and Quinn performed a comprehensive study in which the quality and accuracy of kernels were discussed [44].

- In 1997 Dyka et al. further examined the tensile instability and made some observations on additional stress points evaluation and the critical time step [45]. In the same year, Morris and Monaghan introduced time-varying coefficients of viscosity [46]. Morris et al. proposed an additional treatment of the state equation, kernel interpolation, and boundary conditions [47]. Monaghan proved that it is possible to use the specific energy equation instead of the thermal energy equation in the SPH framework [48].

- In 1998 Belytschko et al. presented a comprehensive study on the SPH completeness in which reproducing conditions on the approximation and derivatives of the approximation were examined [49].

- In 1999 Moussa et al. defined conditions for the convergence of SPH for the Euler equations [50]. In the same year, Dilts developed a derivation of SPH in which a standard interpolant was replaced by the Lancaster and Saulkaskas MLS interpolant, and defined a new particle volume which ensures the thermodynamic compatibility. The method was named Moving Least Square Particle Hydrodynamics (MLSPH) [51]. Chen et al. proposed another modified variant of SPH by combining the kernel estimate with the Taylor series expansion. The derived method was named the Corrective Smoothed Particle Method (CSPM) and was first applied in boundary value problems in heat conduction simulations [52]. The artificial effect of the tensile instability was suppressed by CSPM. Vila further examined use of the variable smoothing length, renormalization, and use of the Godunov type finite difference fluxes in SPH [53]. Hicks and Liebrock presented two stabilization techniques in [54]. The techniques are know as the conservative smoothing and shape shifting. The same year, SPH was applied in new fields of research; Morris et al. used SPH for simulations of a pore-scale flow through porous media [55], Rasio and Lombardi simulated stellar interactions with a modified scheme of SPH in [56], Lee and Kluzniak used SPH for final stages of a black hole simulation with a soft Equation of State (EOS) [57]. Hultman and Pharasyn used SPH for an evaluation of a thermal instability of elliptical galaxies [58], and García-Senz et al. used SPH for a single and multiple detonations in white dwarfs [59]. Bonet and Lok presented a modified formulation of SPH in which the kernel and gradient corrections were introduced for an exact interpolation of a linear field. The Shepard's filters or interpolations for density and velocity fields were also implemented [60]. Monaghan and Kos presented a study in which solitary waves were of interest. Not only their simulations were able to replicate experimental measurements but a modified SPH was proposed. The method was named weakly compressible Smoothed Particle Hydrodynamics (WCSPH) [61]. Cummins and Rudman proposed a derivation of SPH for solving coupled incompressible fluid equations by solving the pressure Poisson equation [62]. The method is known as incompressible Smoothed Particle Hydrodynamics (ISPH).

- In 2000 Moussa and Vila further elaborated their convergence technique in which approximated Riemann solvers were used instead of artificial viscosity to stabilize the scheme [63]. Dilts implemented a geometric boundary detection technique into MLSPH and proved its functionality in HVI simulations [64]. In the same year, Monaghan proposed a new approach to remove the tensile instability by using

artificial stress or pressure [65]. Randles and Libersky extended SPH while using a companion set of interpolation points that carry stress, velocity gradient, and other derived field variables [66]. Belytschko et al. discussed usage of Eulerian and Lagrangian kernels and how they can improve the stability not only of SPH but meshless methods in general [67]. Vignjevic et al. examined zero-energy modes of SPH in detail [68]. Bonet and Kulasegaram developed the so-called corrected kernel within the SPH framework. The standard kernel function was corrected in such a way that the consistency condition is enforced, therefore, accuracy improved [69]. The method was named Corrected Smoothed Particle Hydrodynamics (CSPH). Chen and Beraun modified the standard SPH into generalized form to solve nonlinear dynamic problems by applying the kernel estimate into the Taylor series expansion [70]. Berczik incorporated a dynamical and chemical evolution of chemical enrichment of gas into SPH and formed a method today known as Chemo-Dynamical Smoothed Particle Hydrodynamics (CD-SPH) [71]. Morris proposed a new approach for simulating two-phase flows including a surface tension [72]. Lee presented simulations of final stages of a black hole with a stiff polytropic EOS [73].

- In 2001 Bonet and Kulasegaram further examined CSPH with Eulerian and Lagrangian kernels. It was proved that for some cases CSPH can be stable but a discretized domain can exhibit negative eigenvalues [74]. In the same year, Lanson and Vila introduced two new integration schemes into SPH to improve convergence and accuracy. The schemes are known as the strong renormalized meshless scheme and the weak renormalized meshless scheme which is conservative [75]. Gray et al. further elaborated Monaghan's work in which the artificial stress was considered but with respect to signs of principal stresses [76]. With this approach the tensile instability was fully suppressed. Furthermore, Thacker and Couchman successfully used SPH for the simulation of a galaxy formation in which the angular momentum from gas to dark matter was correctly transported [77].

- In 2002 Belytschko and Xiao proved that Lagrangian kernels eliminate the tensile instability [78]. In the same year, Li and Liu published a comprehensive review of meshfree and particle methods with their most common applications [79]. Inutsuka reformulated SPH by incorporating the artificial-viscosity free Riemann solver with consistent density estimate. The method is known as Godunov Smoothed Particle Hydrodynamics (GSPH) and is accurate for strong shocks problems [80].

- In 2003 Randles et al. proved that SPH with corrected derivatives is conditionally stable and accuracy can be increased with two-step integration scheme such as Predictor-Corrector [81]. In the same year, Liu et al. proposed several approaches for a kernel construction [82], followed by paper in which a new formulation of SPH for shock waves simulations based on the Taylor series expansion in piecewise continuous regions were discussed [83]. Rabczuk et al. performed a study in which SPH and MLSPH were compared in the application of high velocity fragmentation of concrete under a blast [84]. Liu and Liu published a book with a focus on SPH. A comprehensive mathematical background and useful programming techniques in FORTRAN were also included [85].

- In 2004 Rabczuk et al. developed the so-called Large Deformation Particle Method (LDPM) based on the Krongauz–Belytschko corrected-gradient meshfree method

with Lagrangian kernels. In this method, the gradient is corrected by a linear transformation so that the linear completeness is satisfied. It was proved that the method is robust and stable, free of the tensile instability [86]. It was outlined that a similar technique could be implemented in SPH as well. Li and Liu published a book with a focus on meshfree particle methods [87]. Compared methods were SPH, MLSPH, Element Free Galerkin (EFG), RKPM, Meshless Local Petrov-Galerkin (MLPG), and others.

- In 2005 Monaghan reviewed the theory and application of SPH since its inception in 1977 [88]. Vila developed the so-called hybrid SPH in which the renormalization and Godunov type schemes are combined. The method was successfully used for free surface flows [89]. Randles et al. proposed a new technique incorporating MLS for a field and boundary treatment together with a simple neighbour search algorithm [90].

- In 2006 Liu and Liu proposed a new technique to restore the particle consistency [91]. Moussa performed a study in which the SPH convergence was examined while taking into account nonlinear effects [92]. In the same year, Hu and Adams developed an angular-momentum conservative formulation of SPH for incompressible viscous flows [93]. Sigalotti et al. proposed a shock-capturing scheme which is based on adaptive density kernel estimation (ADKE) together with a variable smoothing length [94].

- In 2007 Cleary et al. applied SPH in new fields of research. Namely, in geophysical flows such as volcanic lava flows and tsunamis, several types of die casting, resin transfer moulding and flow in porous media, pyrometallurgy, and slurry flow in semi-autogenous grinding mills [95].

- In 2008 Cabezón et al. proposed a new family of smoothing kernels well suited to track discontinuities such as shock fronts and thermal waves [96].

- In 2009 Lacome et al. proposed a combined SPH formulation with adaptive Eulerian and Lagrangian kernels [97]. In the same year, Vignjevic and Campbell published a review of SPH developments in [98]. Lastiwka et al. proposed a new permeable boundary for flow simulations [99]. Xu et al. utilized the projection method for pressure and velocity coupling in ISPH [100].

- In 2010 Xu et al. developed a technique with which the tensile instability, therefore, numerical fractures would be eliminated. The idea was based on an add-in particle concept when a numerical fracture starts to form [101]. In the same year, Price published a study in which the magnetohydrodynamics (MHD) theory was incorporated into the SPH framework therefore called Smoothed Particle Magnetohydrodynamics (SPMHD). In the study, an excessive overview of the standard SPH techniques was provided [102]. Also, Liu and Lie published a review on SPH in which some latest improvements were discussed [103]. Antuono et al. proposed numerical diffusive terms in both the continuity and energy equations for smoothing pressure field [104]. Adami et al. proposed a new surface-tension formulation for a multi-phase SPH [105]. Hughes and Graham performed a study in which ISPH and WCSPH were compared in detail. Furthermore, some corrections which prevents particles from sticking to the boundary were proposed [106]. Liu

published a book in which the most common meshfree methods were compared [107]. Discussed methods were SPH, EFG, MLPG, and the Point Interpolation Method (PIM).

- In 2011 Jiang et al. combined the higher order SPH for exterior particles with the lower order SPH for interior particles. The technique was used in transient viscoelastic fluid flows [108]. In the same year, Jiang et al. proposed a first order symmetric Smoothed Particle Hydrodynamics (FO-SSPH) in which the first order kernel gradient was corrected based on a discretization of the gradient and the concept of the Taylor series [109]. Ren et al. also proposed an improved SPH. Improvements were achieved by deriving a corrected kernel gradient and density re-initialisation together with a new treatment of solid wall boundaries [110]. Marrone et al. further improved usage of numerical diffusive terms for impact flows simulations. The SPH with the diffusive terms was named δ-SPH [111].

- In 2012 Monaghan commented on SPH after 35 years from its creation. The incompressible and nearly incompressible flows were discussed in detail. Some comments on molecular dynamics and macroscopic continuum mechanics were also provided [112]. Adami et al. developed a new wall boundary condition for complex geometries [113]. Akinci et al. developed momentum-conserving two-way coupling techniques for fluids and arbitrary rigid objects based on hydrodynamic forces [114]. Federico et al. developed an open-channel flow boundary conditions [115].

- In 2013 Xu et al. applied SPH in simulations of non-Newtonian flows in which viscosity was modelled by using the Cross model [116]. In the same year, Prayogo and Naa used the improved SPH with the gradient kernel renormalization to simulate a dam break [117]. Adami et al. developed a transport velocity formulation (TVF) which ensures a uniform particle distribution by adding constant background pressure to the convective velocity [118]. Skillen et al. further improved ISPH which results in noise-free pressure field [119].

- In 2014 Yang et al. proposed a new kernel which combines two cosine functions and improves the accuracy of the kernel estimate. The application was presented on free surface flows problems [120]. Ihmsen et al. developed implicit incompressible Smoothed Particle Hydrodynamics (IISPH) with a significantly increased performance for a discretized form of the pressure Poisson equation (PE). It was proved that IISPH improves convergence of the solver and stability of the Predictor-Corrector time-integration scheme [121]. Puri and Ramachandran modified GSPH and developed the so-called approximate Riemann solver with Godunov Smoothed Particle Hydrodynamics (AGSPH) [122]. The method avoids the expensive solution of the nonlinear Riemann problem for every interacting particle pair which is required by GSPH.

- In 2015 Rosswog published two comprehensive studies. The first one focused on Newtonian fluid dynamics and special-relativistic tests [123], the second on compact object simulations [124]. *Both studies are exceptional work.*

- In 2016 Liu and Liu published another book on particle methods. Together with other particle methods, SPH was discussed in detail [125].

- In 2017 Bankole et al. developed a semi-implicit numerical scheme for SPH. The new scheme was applied in free surface flows [126]. In the same year, Frontiere et al. proposed a modified SPH formulation that utilizes the first order consistent reproducing kernel. The method is known as Conservative Reproducing Kernel Smoothed Particle Hydrodynamics (CRKSPH). The smoothing function of CRKSPH exactly interpolates linear fields with particle tracers [127]. Zhang et al. further improved and generalized TVF originally proposed by Adami et al. [118]. The formulation was named generalized transport velocity formulation (GTVF). It uses variable background pressure and supports solid mechanics [128].

- In 2018 Collé et al. developed a modified numerical scheme of SPH based on the Arbitrary Lagrangian-Eulerian (ALE) framework. The scheme was named γ-SPH-ALE and it improved the stability and accuracy of SPH and reduced computation time in general. The scheme was first used for a dynamic fragmentation modelling [129]. In the same year, Röthlin et al. provided an interesting benchmark on the most used meshless methods including SPH [130]. Tafuni et al. proposed a new open boundary algorithm for WCSPH [131].

- In 2019 Filho published a book in which the latest formulations, techniques, and corrections schemes of SPH were discussed [132]. Part of the book is a source code written in FORTRAN. Ramachandran et al. proposed a modified variant of WCSPH which solves for pressure using pseudo time iterations [133]. In the same year, Ramachandran and Puri developed a new scheme suitable for incompressible fluids in internal and external flows. With the proposed modifications, pressure distribution is smoother and without introducing artificial viscosity in the momentum equation [134]. Negi et al. developed an improved non-reflecting outlet boundary condition for WCSPH [135]. For the last three mentioned, an open source code written in Python is available.

- In 2020 Muta et al. proposed a new iterative variant of ISPH simply named simple itrative incompressible Smoothed Particle Hydrodynamics (SIISPH) [136]. The standard ISPH solves a sparse system of equations to obtain a solution to the pressure PE. In other words, a sparse matrix is solved. In contrast, SIISPH is matrix free while using an iterative formulation which makes it suitable for parallel processing implementation.

2.2 Insights

From the cross-section of the SPH history is obvious that SPH is quite popular in hydrodynamics. Needless to say, hydrodynamics does not mean only fluid simulations but rather fluid-like simulations. How does it fit into structural dynamics? It depends on how is the 'structural' understood. In the context of the thesis, structural represents *physical strength* of material. Such a material could be, e.g. concrete, steel, or their combination, i.e. a composite. Neither concrete nor steel behave like a fluid, however. Yet it really depends on the speed of the event. *When a material with physical strength undergoes deformation very fast, it behaves like a fluid.* A very good demonstration is the impact of the flying uranium alloy long rod projectile on the armour plate as described in the experiment from

1978 [137]. Here, without going into details, SPH was used to simulate both the alloy rod and armour plate. After the impact, both materials behave like fluids; splashing and mixing between each other as shown in Fig. 2.1. The reason for the fluid-like behaviour is simple; the striking velocity was more than 1200 m/s.

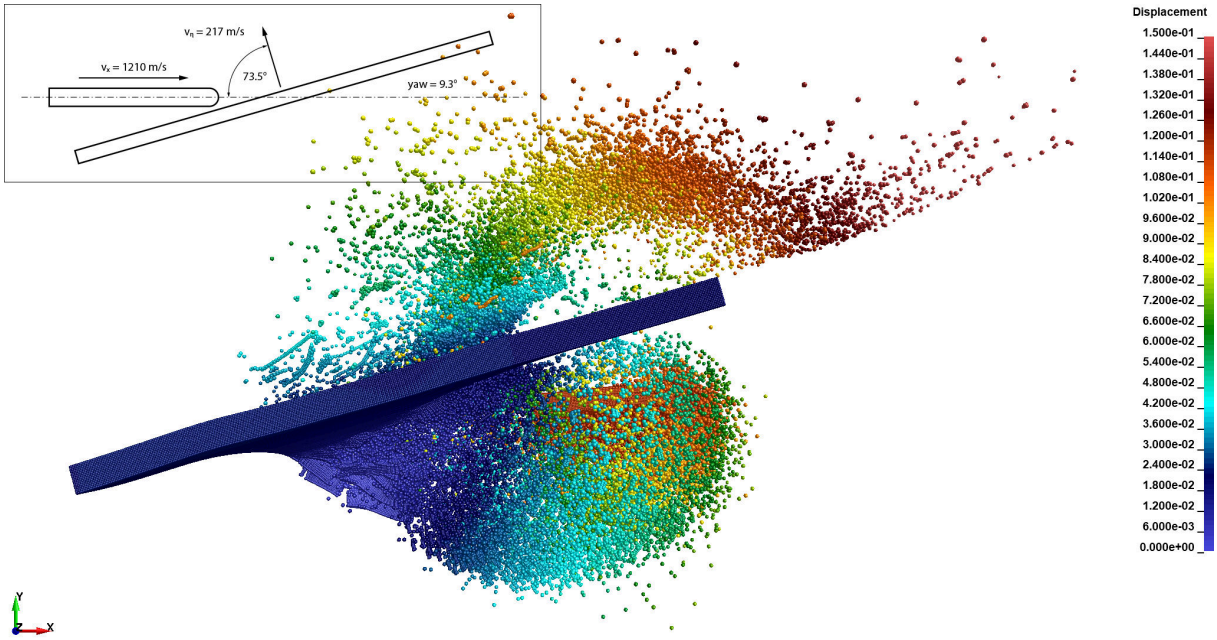

Fig. 2.1. HVI of the depleted uranium alloy long rod projectile into the oblique rolled homogeneous armour plate.

Before the mathematical description of SPH takes place, some insights are discussed first.

- SPH is a truly *meshfree* method. A predefined mesh is not required, neither for the integration nor for the particle interaction. In contrast, there are meshfree methods which are not truly meshfree. Such methods use background meshes or cells for the integration of the weak forms (EFG, MLPG, PIM) or for the calculation of spatial derivatives (PIC).
- SPH is a *particle* method. The solution domain is discretized into finite number of particles followed by the integral operation which is implemented in the stage of a function approximation. This could be considered the main difference between meshfree particle methods and meshfree weak form methods (EFG, MLPG, RKPM, or PIM). In the latter, the integration of the weak forms is done in the stage of the discrete system creation.
- SPH is a *Lagrangian* method. Each particle possesses individual material properties (mass, density, etc.) and moves according to the governing conservation equations, i.e. as a result of internal interactions, external forces applications, and boundary conditions.
- SPH is *adaptive*. The neighbouring particle search for internal and external interactions is performed at each time step. Based on the current set of arbitrarily distributed particles, a field variable approximation is calculated. This can be

considered the biggest advantage of SPH. Put simply, SPH can work on any set of arbitrarily distributed particles.

From the list it seems SPH has a lot in common with the Finite Element Method (FEM); except the mesh, of course. This is true, and thanks to the similarity, a coupling of both methods is done quite easily. The coupling itself is discussed in detail in **Chapter 4** *Coupling SPH and FEM*, however, some observations can be made at this point. As far as a real application is concerned, it might be that a pure SPH model would lead to a very long computational time. Therefore, a coupling with FEM might be of interest. In general, creating a coupled model might be difficult, but not for SPH. Due to the adaptive nature of SPH, particles might be arbitrarily distributed/generated. Which means, that an SPH model or a subpart of the model can be created directly from an existing mesh of a FEM model.

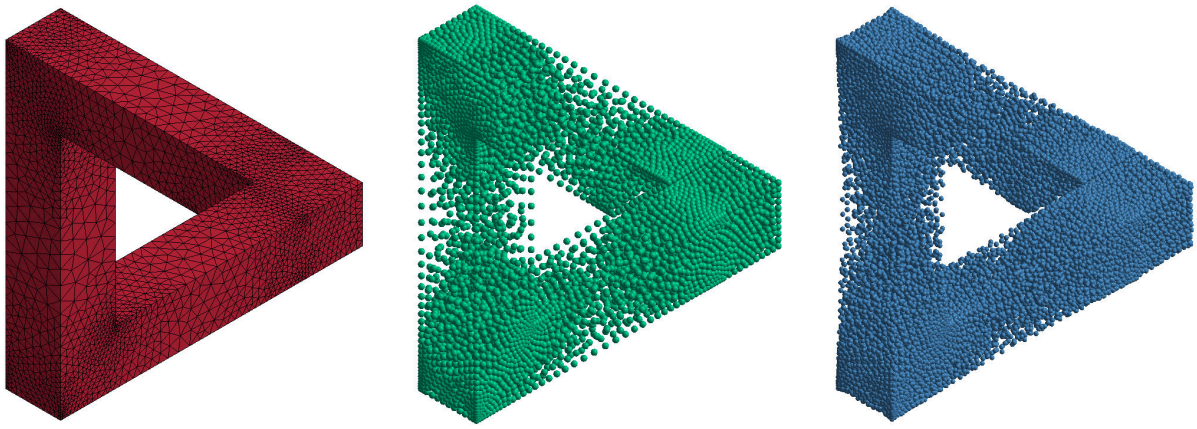

(a) FEM (b) SPH at nodes (c) SPH in elements

Fig. 2.2. Comparison of FEM and SPH numerical models.

As an example, three numerical models are shown in Fig. 2.2; a simple FEM model and two slightly different SPH models. The FEM model (a) was meshed with 4 nodes tetrahedral elements. The SPH model (b) was generated based on the nodes of the FEM model. In other words, the number of nodes and particles of the model (a) and (b) is the same. In contrast, the SPH model (c) was generated based on the elements of the FEM model. Therefore, the number of elements and particles of the model (a) and (c) is the same. Comparing (b) and (c) one could say the model (b) is more time-consuming since more particles mean more field variables. However, it is not that simple. When an explicit time integration scheme is used, the time step plays important role. In case of SPH, the time step is controlled by material properties and the so-called smoothing length h. The smoothing length can be related to the distance between two neighbouring particles. That said, the time step dt can be determined as

$$dt = C_{\mathrm{CFL}} \cdot \min_i \left(\frac{h_i}{c_i + |\boldsymbol{v}_i|} \right), \tag{2.2.1}$$

where c_i and $\boldsymbol{v}_i$ are the adiabatic sound speed (material property) and the velocity of particle i, respectively. The parameter C_{CFL} is a constant which refers to the Courant-Friedrichs-Lewy (CFL) condition [138]. In most cases, dt is found for every particle, then the minimum value from all particles is taken. It is clear from (2.2.1) that smaller the distance between particles, smaller the time step $\longrightarrow$ longer simulation time if other variables are constant. Satisfying the CFL condition does not necessary mean that convergence is guaranteed while solving partial differential equations (PDE) numerically, however. In some cases, dt must be even lower, e.g. when SPH is used to simulate an explosion the time step could drop to 10% of the CFL condition to prevent numerical instabilities. Although the simulation times are difficult to predict just from the number of particles, other observations can be made.

- **Shape of the model** – in case of the model (b), particles are placed at nodes of the model (a), i.e. also on external faces and edges. As far as the radius of the particles is not considered, the outer shape of both models is identical. The same cannot be said about the model (c) in which the particles are placed at centre of gravity (CG) of the elements of the model (a). This is the reason why the model (c) does not have straight faces and edges. However, if radius of the particles is taken into account, the model (b) represents an increased size of the model (a) while the model (c) is its exact representation, since the radius of each particle is related to the size of individual element. It can be however that for an interaction with other parts the radius is not considered. Then, the model (b) would be preferable, since its outer surface represents the model (a) better. It is up to the user to decide how is the SPH model generated. The decision leads to a different mass distribution.
- **Mass distribution** – in the model (a) all elements have volume and assigned density from which the mass of each element can be calculated. But how is the mass distributed to the nodes? Assuming a symmetric element, i.e. all sides of the element are the same, then the mass would be distributed equally between all nodes. If the element is deformed or randomly shaped however, a more complex technique based on the element's shape functions must be used. Yet the model (b) knows nothing about the shape functions. As a result, the total mass of the model (b) might be identical to the mass of the model (a) but the distribution could be slightly different. With a finer domain discretization, the mass distribution would not affect the solution significantly, however. In case of the model (c), the mass of each particle is well-defined. An element mass is equal to a particle mass, therefore, the mass distribution of the model (c) is identical to the model (a).

Usually, there are many requirements on numerical models. Therefore, it cannot be said that one generation approach is better than the other.

2.3 Mathematical Background

As many other numerical methods, SPH was developed to solve problems described by PDEs. The PDEs are not solved directly but after a domain discretization where the PDEs

are defined. For the discretized domain, a field approximation is constructed to obtain a set of ordinary differential equations (ODE). The set of ODEs is than solved with respect to time using some standard integration scheme. SPH uses the concept of shape functions to construct the field approximation. The shape functions, however, are not defined before the solution starts as in the case of FEM but during the solution. Moreover, in case of FEM the shape functions are constructed using individual elements in natural coordinate systems followed by a mapping into real coordinates. This means, the shape functions are identical for the same element type. In case of SPH, the shape functions are constructed based on the current particle distribution and position of evaluation.

There are several ways to construct shape functions for a field approximation. In terms of a classification; integral, differential, and series representation can be used, as also proposed in [107] and [139]. In the *integral representation*, the function is constructed as

$$f(x) = \int f(a)W(x-a)\,da, \tag{2.3.1}$$

where W is the smoothing function, and a are the points defined within its support. The consistency of (2.3.1) is achieved by properly chosen W. Methods belonging to the integral representation class are, e.g. SPH, RKPM, or the General Kernel Reproduction (GKR) method [139]. In the *differential representation*, the function is constructed as

$$f(x) = f(a) + f'(a)(x-a) + \frac{f''(a)}{2!}(x-a)^2 + \dots\,, \tag{2.3.2}$$

where a is the point where f is differentiable. Methods belonging to the differential representation class are, e.g. the Finite Difference Method (FDM) or the General Finite Difference Method (GFDM) [139]. The consistency in (2.3.2) is ensured by the theory of the Taylor series. In case of the *series representation*, the function is constructed as

$$f(x) = a_0 + a_1\hat{p}_1(x) + a_2\hat{p}_2(x) + \dots\,, \tag{2.3.3}$$

where $\hat{p}_i(x)$ are the basis functions and a_i are unknown coefficients to be determined. Methods belonging to the series representation class are, e.g. FEM, MLS, or PIM. The consistency in (2.3.3) is ensured by the completeness of the basis functions [139].

2.3.1 Kernel Approximation

In case of SPH, the integral representation is used. In literature, the so-called integral interpolant [37], kernel approximation [85], kernel estimation [15], or kernel estimate [35] can be also found. In the thesis, the *integral representation* is used for a rigorous form of the approximation and the *kernel approximation* otherwise. To derivate the kernel

approximation, identity where

$$f(\boldsymbol{x}) = \int_{\Omega} f(\boldsymbol{x}')\delta(\boldsymbol{x} - \boldsymbol{x}')\, d\boldsymbol{x}' \tag{2.3.4}$$

can be assumed first. Note that it is found to be useful to employ both tensor (superscripted) and vector (bold) notation within the thesis [21]. To not confuse readers, the tensor notation is also known as the index, indicial, or Einstein notation. In (2.3.4), f is the function of the position vector $\boldsymbol{x}$ and Ω is the volume of the integral that contains $\boldsymbol{x}$. The $\delta(\boldsymbol{x} - \boldsymbol{x}')$ is the Dirac delta function given as

$$\delta(\boldsymbol{x} - \boldsymbol{x}') = \begin{cases} \infty & \boldsymbol{x} = \boldsymbol{x}' \\ 0 & \boldsymbol{x} \neq \boldsymbol{x}', \end{cases} \tag{2.3.5}$$

with a normalization condition

$$\int_{\Omega} \delta(\boldsymbol{x} - \boldsymbol{x}')\, d\boldsymbol{x}' = 1. \tag{2.3.6}$$

Since the Dirac delta function is used in (2.3.4), the integral representation is exact as long as $f(\boldsymbol{x}')$ is continuous in Ω. The Dirac delta function cannot be used for establishing discrete numerical models since it has only a point support. Therefore, the Dirac delta $\delta(\boldsymbol{x} - \boldsymbol{x}')$ is replaced by a function $W(\boldsymbol{x} - \boldsymbol{x}', h)$ with a support of a finite spatial dimension h, therefore, (2.3.4) became

$$f(\boldsymbol{x}) \approx \int_{\Omega} f(\boldsymbol{x}')W(\boldsymbol{x} - \boldsymbol{x}', h)\, d\boldsymbol{x}', \tag{2.3.7}$$

where W is known as the smoothing function, smoothing kernel function, smoothing kernel, kernel function, or just kernel. The last mentioned, the *kernel*, is used in the thesis. In the kernel approximation definition, h is the so-called smoothing length or radius of influence defining the support or influence area of W. Equation (2.3.7) is only an approximation of the integral representation, however. In the SPH convention, (2.3.7) can be rewritten using the *kernel approximation operator*, marked by angle brackets $\langle\ \rangle$, and therefore

$$\langle f(\boldsymbol{x})\rangle = \int_{\Omega} f(\boldsymbol{x}')W(\boldsymbol{x} - \boldsymbol{x}', h)\, d\boldsymbol{x}'. \tag{2.3.8}$$

Such a notation can be found in many papers, e.g. [6, 15, 21] or [140] to name some. Since the kernel approximation operator is used, there is no approximation but equal sign in

(2.3.8). Clearly, if the integral of W is normalized to unity, then

$$\lim_{h \to 0} \langle f(\boldsymbol{x}) \rangle = f(\boldsymbol{x}) \tag{2.3.9}$$

and the kernel approximation is again exact. The kernel might be an arbitrary function, yet it must fulfil certain conditions. The list of conditions is discussed in section *Kernel* in detail. By considering the fact that W is a function strongly peaked at $\boldsymbol{x}' = \boldsymbol{x}$, it is possible to expand $f(\boldsymbol{x}')$ in a Taylor series in (2.3.8) about $\boldsymbol{x}$ and estimate the order of accuracy [15]. If W is chosen to be an even function of $\boldsymbol{x}$ only, e.g. a cubic spline as $W(\boldsymbol{x}, h) = W(|\boldsymbol{x}|, h)$, then it can be shown that

$$\begin{aligned} \langle f(\boldsymbol{x}) \rangle &= \int_{\Omega} [f(\boldsymbol{x}) + f'(\boldsymbol{x})(\boldsymbol{x}' - \boldsymbol{x}) + \mathcal{O}((\boldsymbol{x}' - \boldsymbol{x})^2)] W(\boldsymbol{x} - \boldsymbol{x}', h)\, d\boldsymbol{x}' \\ &= f(\boldsymbol{x}) \int_{\Omega} W(\boldsymbol{x} - \boldsymbol{x}', h)\, d\boldsymbol{x}' + f'(\boldsymbol{x}) \int_{\Omega} (\boldsymbol{x}' - \boldsymbol{x}) W(\boldsymbol{x} - \boldsymbol{x}', h)\, d\boldsymbol{x}' + \mathcal{O}(h^2), \end{aligned} \tag{2.3.10}$$

where $\mathcal{O}$ is the residual estimate. Since W was chosen to be an even function with respect to $\boldsymbol{x}$, therefore, $(\boldsymbol{x}' - \boldsymbol{x}) W(\boldsymbol{x} - \boldsymbol{x}', h)$ is an odd function for which

$$\int_{\Omega} (\boldsymbol{x}' - \boldsymbol{x}) W(\boldsymbol{x} - \boldsymbol{x}', h)\, d\boldsymbol{x}' = 0. \tag{2.3.11}$$

The integral in (2.3.11) is in the SPH terminology called the first moment of the kernel. Assuming W satisfies the normalization condition in (2.3.6), then (2.3.10) can be simplified as

$$\langle f(\boldsymbol{x}) \rangle = f(\boldsymbol{x}) + \mathcal{O}(h^2), \tag{2.3.12}$$

where (2.3.11) was also assumed. Hence, the approximation $f(\boldsymbol{x})$ by $\langle f(\boldsymbol{x}) \rangle$ is said to be second order accurate in h [15]. The kernel approximation is not necessarily of second order accuracy if the kernel is not an even function, or if it does not satisfy the normalization condition [85]. For example, in Fig. 2.3 a full and truncated kernel is shown. Both kernels are even functions, yet only the full kernel satisfies the normalization condition and its first moment is zero.

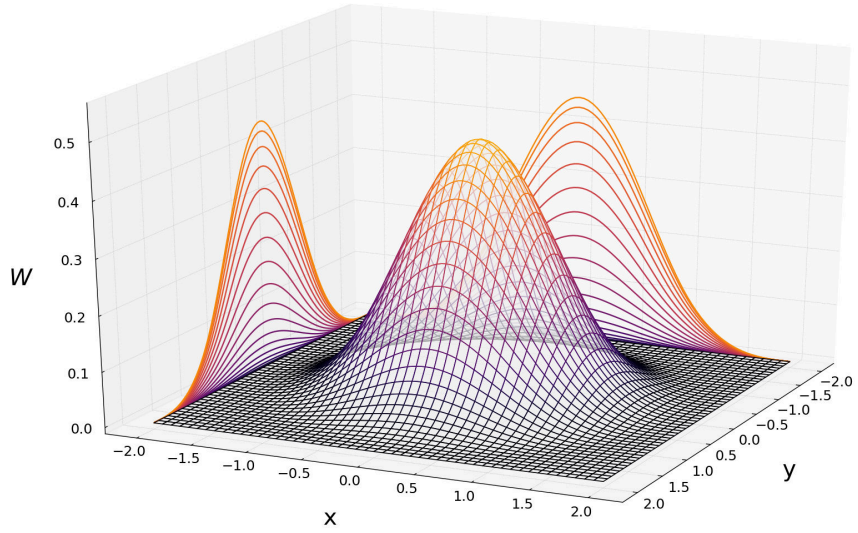

(a) full

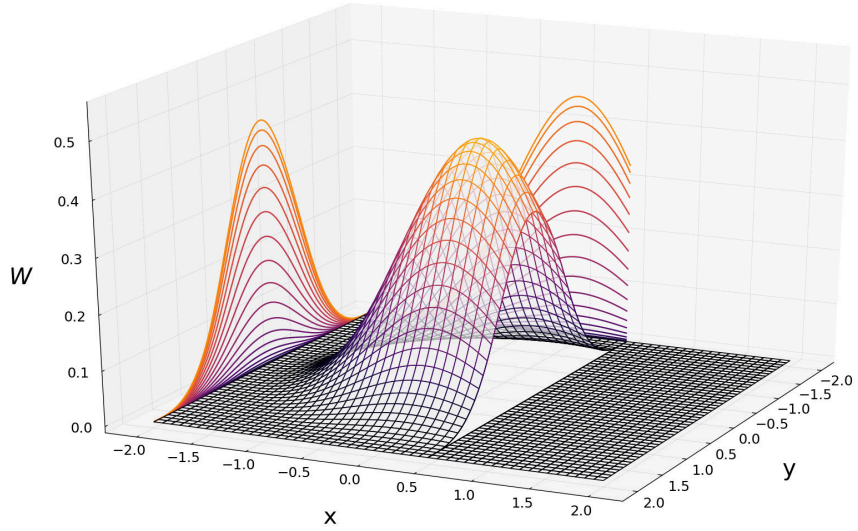

(b) truncated

Fig. 2.3. Comparison of a full and truncated kernel.

2.3.2 Kernel Approximation of Derivatives

The kernel approximation of a function derivatives can be derived by substituting $f(\boldsymbol{x})$ with $\nabla \cdot f(\boldsymbol{x})$ in (2.3.8), which gives

$$\langle \nabla \cdot f(\boldsymbol{x}) \rangle = \int_{\Omega} [\nabla \cdot f(\boldsymbol{x}')] W(\boldsymbol{x} - \boldsymbol{x}', h)\, d\boldsymbol{x}', \tag{2.3.13}$$

where the divergence in the integral is with respect to the primed coordinate [85]. Furthermore, by considering that

$$\begin{aligned}\big[\nabla \cdot f(\boldsymbol{x}')\big] W(\boldsymbol{x}-\boldsymbol{x}', h) = \nabla \cdot [f(\boldsymbol{x}') W(\boldsymbol{x}-\boldsymbol{x}', h)] \\ - f(\boldsymbol{x}') \cdot \nabla W(\boldsymbol{x}-\boldsymbol{x}', h),\end{aligned} \tag{2.3.14}$$

and therefore

$$\begin{aligned}\langle \nabla \cdot f(\boldsymbol{x}) \rangle = \int_{\Omega} \nabla \cdot [f(\boldsymbol{x}') W(\boldsymbol{x}-\boldsymbol{x}', h)]\, d\boldsymbol{x}' \\ - \int_{\Omega} f(\boldsymbol{x}') \cdot \nabla W(\boldsymbol{x}-\boldsymbol{x}', h)\, d\boldsymbol{x}',\end{aligned} \tag{2.3.15}$$

then using the divergence theorem [85], the first integral on the right-hand side of (2.3.15) can be converted into the integral over the surface S of the integration domain Ω as

$$\begin{aligned}\langle \nabla \cdot f(\boldsymbol{x}) \rangle = \int_{S} f(\boldsymbol{x}') W(\boldsymbol{x}-\boldsymbol{x}', h) \cdot \boldsymbol{n}\, dS \\ - \int_{\Omega} f(\boldsymbol{x}') \cdot \nabla W(\boldsymbol{x}-\boldsymbol{x}', h)\, d\boldsymbol{x}',\end{aligned} \tag{2.3.16}$$

where $\boldsymbol{n}$ is the unit vector normal to the surface S [85]. Kernels are usually defined with a compact support, which means their values go to zero outside their influence area. Therefore, if the support is fully located within a problem domain, it means the first integral on the right-hand side of (2.3.16), the surface integral, is zero. However, if the support is only partially within the problem domain, some special treatment must be applied to remedy the boundary effects if the surface integration is treated as zero in equation (2.3.16). That said, the kernel approximation of derivatives can be written as

$$\langle \nabla \cdot f(\boldsymbol{x}) \rangle = - \int_{\Omega} f(\boldsymbol{x}') \cdot \nabla W(\boldsymbol{x}-\boldsymbol{x}', h)\, d\boldsymbol{x}'. \tag{2.3.17}$$

From (2.3.17) perhaps the most important conclusion can be drawn. *The differential operation on a function is transformed into a differential operation on the kernel.* The kernel approximation of the derivative of a field function allows the spatial gradient to be determined from the values of the function and the derivatives of the smoothing function W, rather than from the derivatives of the function itself [125]. This feature is very similar to that in the weak form methods that reduce the consistency requirement on the assumed field functions and produce stable solutions for PDEs [107]. The kernel approximation

of higher order derivatives can be obtained in similar way by substituting $f(\boldsymbol{x})$ with the corresponding derivatives in (2.3.8) [85].

In addition, Fig. 2.3 can be discussed here again. Only the full kernel produces the surface integral in (2.3.16) equal to zero. This means that (2.3.17) is not valid for truncated kernels and special treatment must be applied if truncated kernels are used.

2.3.3 Particle Approximation

SPH is a representative of the collocation methods which means that a solution of PDEs or rather ODEs is found at collocation points – SPH particles. As already mentioned, particles can be arbitrary distributed and for the given set of particles the kernel approximation is discretized. The operation is known as *particle approximation*. This means in practice that (2.3.8) and (2.3.17) are defined in a discrete form. To replace the integral in (2.3.8) and (2.3.17), a summation over all the particles within the support domain is introduced. The particles within the support domain of particle i are called *neighbouring particles*, see Fig. 2.4.

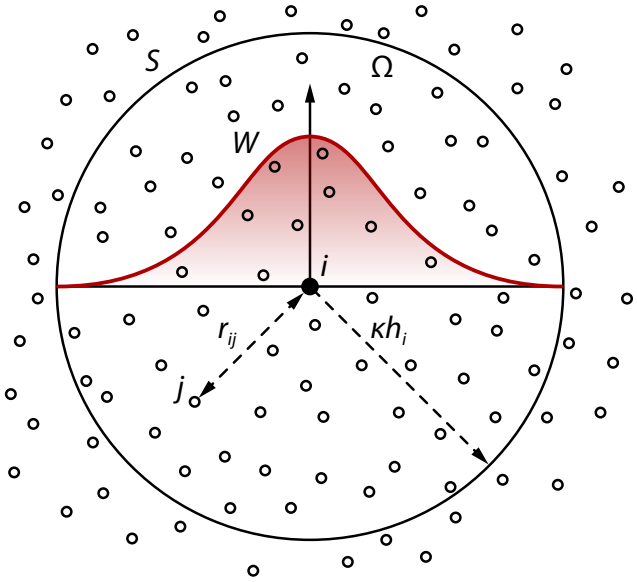

Fig. 2.4. Particle approximation.

Every particle in the problem domain has assigned volume and density. The volume of a particle comes from the model discretization and depends on the generation approach; briefly discussed in section *Insights*. Since volume and density of every particle are given, the mass of particle j can be found as

$$m_j = \Delta V_j \rho_j, \tag{2.3.18}$$

where ΔV_j and ρ_j are the volume and density, respectively. Equation (2.3.18) might seem trivial, yet it is the point where a very complex algorithm can be placed and creates the

so-called numerical heterogeneity (not related to the tensile instability). In **Chapter 7** *Heterogeneity in Numerical Models*, the heterogeneity implementation is discussed in detail.

The particle approximation is quite transparent process; starting with (2.3.8), replacing the integral with a particle summation in the second step, and followed by a density substitution in the next step. Since the density is directly placed in the particle approximation operation it has significant impact on the results. Therefore, choosing an appropriate approach for the density calculation can be considered a crucial decision. The operation can be summarized as

$$\begin{aligned}\langle f(\boldsymbol{x})\rangle &= \int_{\Omega} f(\boldsymbol{x}')W(\boldsymbol{x}-\boldsymbol{x}',h)\,d\boldsymbol{x}' \\ &= \sum_{j=1}^{N} f(\boldsymbol{x}_j)W(\boldsymbol{x}-\boldsymbol{x}_j,h)\Delta V_j \\ &= \sum_{j=1}^{N} f(\boldsymbol{x}_j)W(\boldsymbol{x}-\boldsymbol{x}_j,h)\frac{1}{\rho_j}(\rho_j\Delta V_j) \\ &= \sum_{j=1}^{N} f(\boldsymbol{x}_j)W(\boldsymbol{x}-\boldsymbol{x}_j,h)\frac{1}{\rho_j}(m_j),\end{aligned} \tag{2.3.19}$$

where N is the number of neighbouring particles, i.e. the particles within the support domain including the particle at $\boldsymbol{x}$. Although N is said to be the number of neighbouring particles, it should be noted, that in general N is the total number of particles. But since the support domain at $\boldsymbol{x}$ is compact, the total number of particles is reduced to a set of neighbours. Moreover, the number of neighbouring particles does not have to be constant. It can vary in time and space to improve accuracy and stability. That said, for the kernel approximation of a function, the particle approximation has the form of

$$\langle f(\boldsymbol{x})\rangle = \sum_{j=1}^{N} \frac{m_j}{\rho_j} f(\boldsymbol{x}_j)W(\boldsymbol{x}-\boldsymbol{x}_j,h), \tag{2.3.20}$$

and for derivatives of a function

$$\langle \nabla\cdot f(\boldsymbol{x})\rangle = -\sum_{j=1}^{N} \frac{m_j}{\rho_j} f(\boldsymbol{x}_j)\cdot\nabla W(\boldsymbol{x}-\boldsymbol{x}_j,h). \tag{2.3.21}$$

Finally, the approximation for particle i can be written as

$$\langle f(\boldsymbol{x}_i)\rangle = \sum_{j=1}^{N} \frac{m_j}{\rho_j} f(\boldsymbol{x}_j)W_{ij}, \tag{2.3.22}$$

and for derivatives as

$$\langle \nabla \cdot f(\boldsymbol{x}_i) \rangle = -\sum_{j=1}^{N} \frac{m_j}{\rho_j} f(\boldsymbol{x}_j) \cdot \nabla W_{ij}, \tag{2.3.23}$$

where

$$W_{ij} = W(\boldsymbol{x}_i - \boldsymbol{x}_j, h). \tag{2.3.24}$$

The particle approximation in (2.3.22) can be understood in the following way. The value of a function at particle i is approximated using the average of those values of the function at all the particles in the support domain (neighbouring particles) of particle i weighted by the kernel [85]. Same applies for derivatives of a function (2.3.23) with one difference, the values of neighbouring particles are weighted by the gradient of the kernel.

It is important to note that for the evaluation of $f(\boldsymbol{x})$, all the neighbouring particles including particle i itself are used [35]. Question might be, how can be $f(\boldsymbol{x})$ evaluated at particle i if $f(\boldsymbol{x}_i)$ is in the summation, therefore, unknown. There are two answers. First, the solution is calculated with time increments, therefore, field variables are frequently updated rather than completely recreated. Values from previous time steps are used to calculate the updated ones. Second, in continuum dynamics field variables are usually evaluated with respect to gradients, divergences. That is, a relative difference in a field function (between two interacting particles) is used rather than direct values (at the particles). This means, that the product of an interaction vanishes when a particle interacts with itself. In other words, in SPH there is no self-contribution [51]. Furthermore, the notation W_{ij} might be confusing. In the thesis however, W_{ij} strictly means the kernel (smoothing function) of particle i evaluated at particle j. A possible misinterpretation results in two different SPH concepts, the so-called *gather* and *scatter* concept. Both are explained in section *Gather and Scatter Concept* in detail.

In Fig. 2.4 a cross-section of a kernel is drawn, showing that it goes to zero at its boundary S. The size of the support domain Ω is given by the product of the smoothing length h and a constant κ. The κ is sometimes referred to as dimension constant and can serve many purposes. For example, if the smoothing length is driven by a flow equation, κ can additionally increase the size of the support domain to include more particles for the particle approximation, therefore, smeared out local spikes or singularities.

The particle approximation derivation in (2.3.19) is indeed an easy-to-follow process, however, if the truncated kernel as shown in Fig. 2.3 does not satisfy the normalization condition (among the others), can the particle approximation satisfy it? Simple answer is no, it cannot unless a special treatment is applied. There is a simple proof. In Fig. 2.5 the same kernel is shown again. In addition, arbitrary distributed particles are placed beneath the kernel with a given colour and size based on the kernel value (weight factor). If the particles are outside the support domain, their size is very small and colour is greyed out. Assuming the kernel is not truncated, then the sum of volumes of all the colourized

particles weighted by the kernel equals to one. However, if the kernel is truncated, the particles from the previous set can only disappear. Which means, the sum of the volumes of all colourized particles weighted by the kernel can be only lower than one.

Several complex techniques have been developed to fix the problem. Some are discussed in section *Consistency of the Kernel Approximation* and section *Consistency of the Particle Approximation*. However, one important finding can be pointed out which might simplify the problem with truncated kernels. If a discontinuity needs to be simulated with SPH, it is very easy to do so with massless particles, i.e. particles with mass equal to zero.

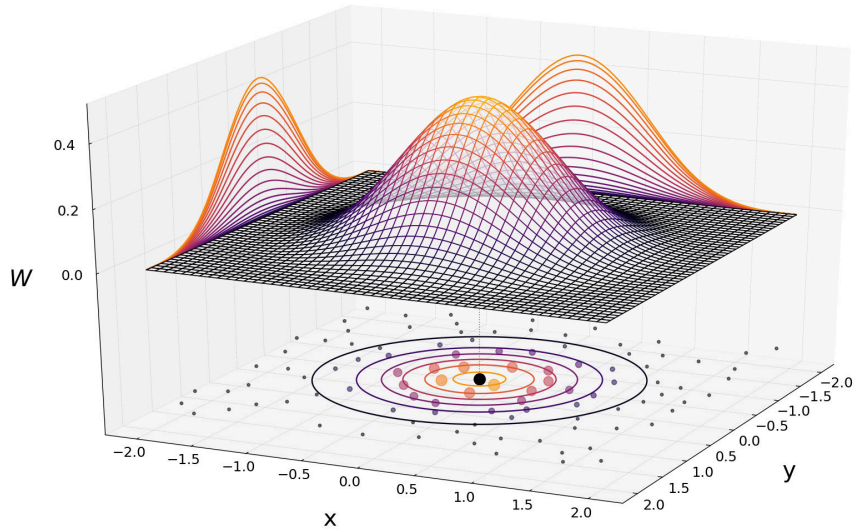

(a) full

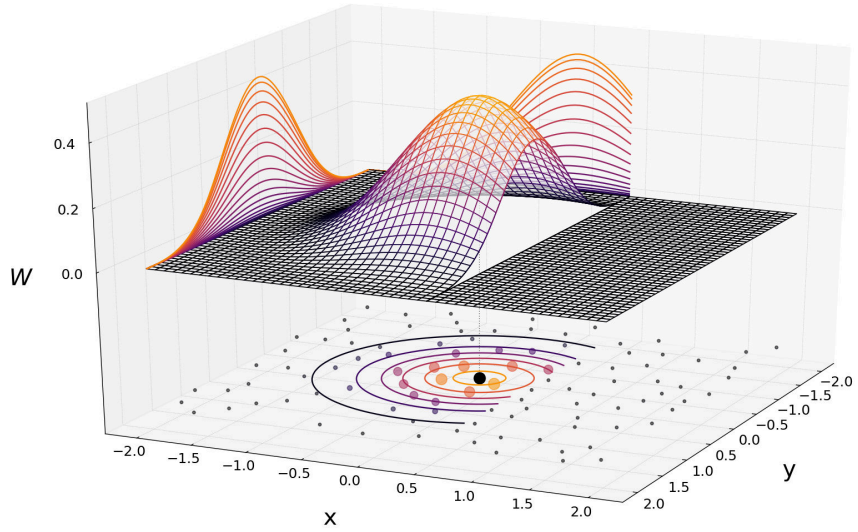

(b) truncated

Fig. 2.5. Comparison of a full and truncated kernel with distributed particles.

In (2.3.23) the gradient is taken with respect to the coordinates of particle j, therefore, ∇W_{ij} can be denoted as $\nabla_j W_{ij}$. Assuming again the kernel is an even function, i.e.

$W(\boldsymbol{x}_i - \boldsymbol{x}_j) = W(|\boldsymbol{x}_i - \boldsymbol{x}_j|, h)$, a useful property can be derived

$$\nabla_i W(|\boldsymbol{x}_i - \boldsymbol{x}_j|, h) = -\nabla_j W(|\boldsymbol{x}_i - \boldsymbol{x}_j|, h), \tag{2.3.25}$$

or just

$$\nabla_i W_{ij} = -\nabla_j W_{ij}, \tag{2.3.26}$$

which allows for a straight forward conservation of Nature's conservation laws [124] (also [15, 20]). Equation (2.3.23) can be therefore rewritten in a positive form by noting that ∇W_{ij} is taken with respect to the coordinates of particle i as

$$\langle \nabla \cdot f(\boldsymbol{x}_i) \rangle = \sum_{j=1}^{N} \frac{m_j}{\rho_j} f(\boldsymbol{x}_j) \cdot \nabla_i W_{ij}, \tag{2.3.27}$$

where

$$\nabla_i W_{ij} = \frac{\boldsymbol{x}_i - \boldsymbol{x}_j}{r_{ij}} \frac{\partial W_{ij}}{\partial r_{ij}} = \frac{\boldsymbol{x}_{ij}}{r_{ij}} \frac{\partial W_{ij}}{\partial r_{ij}}. \tag{2.3.28}$$

In (2.3.28) the r_{ij} is the distance between particle i and j, given as

$$r_{ij} = |\boldsymbol{x}_{ij}| = |\boldsymbol{x}_i - \boldsymbol{x}_j|. \tag{2.3.29}$$

Changing the negative sign to positive is a common technique and can be found in many papers [15, 20, 65, 76, 87] or [124]. Furthermore, very often can be found that simplified form of (2.3.28) is preferred, especially when discretized equations are written in the tensor notation [17, 21, 22, 85, 125] or [29] so that

$$\nabla_i W_{ij} = \frac{\partial W_{ij}}{\partial x_i}. \tag{2.3.30}$$

2.3.4 Direct Density Calculation

There are many ways to calculate density. In this section, the density calculation from the continuum equation is not discussed, but the focus is on the evaluation of density directly from SPH particles. Perhaps the most common way is the *summation density approach*.

Density at particle i is simply

$$\rho_i = \sum_{j=1}^{N} m_j W_{ij}. \tag{2.3.31}$$

The advantage of using (2.3.31) is that the total mass is conserved since the number and masses of the particles remain constant [37]. Yet, (2.3.31) applies only for a special case. As discussed in section *Kernel*, the smoothing length h might differ per particle. Equation (2.3.31) is based on the idea that all the neighbouring particles of particle i have the same smoothing length. However, if it is not the case, the generalized formulation of (2.3.31) should be used instead [141]. Then (2.3.31) reads

$$\rho_i = \sum_{j=1}^{N} m_j \frac{1}{2}\left[W(\boldsymbol{x}_i - \boldsymbol{x}_j, h_i) + W(\boldsymbol{x}_i - \boldsymbol{x}_j, h_j)\right]. \tag{2.3.32}$$

Interestingly enough, W_{ij} in (2.3.31) has a unit of inverse volume. The summation density approach conserves mass exactly, but suffers from a serious boundary deficiency due to the particle inconsistency [125]. Interestingly enough, Benz in [15] referred to (2.3.31) as the reason for the name of SPH.

> *Every particle of mass m_j is smoothed in space according to W which can be regarded as its density distribution in space. The density at any point in space is then obtained by summing up the contributions from all particles at that point. In fact, the name of the method, Smoothed Particle Hydrodynamics, actually derives from this interpretation.* [15]

There are other approaches for direct density calculation based on the Shepard filter or MLS. But since they only improve (2.3.31), they are discussed in section *Density Correction* in detail.

2.3.5 Other Formulations

There are other useful formulations to know about when PDEs are approximated with SPH. In [20] Monaghan mentioned something he called golden rules. The first golden rule suggests using the Gaussian kernel to better understand the physical interpretation of SPH equations. The first golden rule is discussed in section *Kernel* in detail, yet his second rule is briefly discussed here. The second golden rule is to place density inside operators. His proposal for higher accuracy was to define (2.3.13) in an asymmetric formulation as

$$\nabla \cdot f(\boldsymbol{x}) = [\nabla \cdot (\rho f(\boldsymbol{x})) - f(\boldsymbol{x}) \cdot \nabla \rho]/\rho, \tag{2.3.33}$$

which for the particle approximation yields

$$\langle \nabla \cdot f(\boldsymbol{x}_i) \rangle = \frac{1}{\rho_i} \sum_{j=1}^{N} m_j (f(\boldsymbol{x}_j) - f(\boldsymbol{x}_i)) \cdot \nabla_i W_{ij}. \tag{2.3.34}$$

Such a gradient definition is very useful since it has the advantage that the product vanishes exactly when values in the problem domain are constant. However, it has the disadvantage that linear and angular momentum are not conserved exactly, and it is difficult to construct a consistent energy equation [20].

Therefore, Monaghan proposed a symmetric or symmetrized formulation in which (2.3.13) is defined as

$$\nabla \cdot f(\boldsymbol{x}) = \rho \left[\nabla \cdot \left(\frac{f(\boldsymbol{x})}{\rho} \right) + \frac{f(\boldsymbol{x})}{\rho^2} \cdot \nabla \rho \right], \tag{2.3.35}$$

which for the particle approximation yields

$$\langle \nabla \cdot f(\boldsymbol{x}_i) \rangle = \rho_i \sum_{j=1}^{N} m_j \left(\frac{f(\boldsymbol{x}_i)}{\rho_i^2} + \frac{f(\boldsymbol{x}_j)}{\rho_j^2} \right) \cdot \nabla_i W_{ij}. \tag{2.3.36}$$

The advantage of the symmetric formulation in (2.3.36) is that it produces a symmetric central force between pairs of particles. As a result, linear and angular momentum are conserved exactly [20]. The symmetric formulation in (2.3.36) is not the only one, and as Monaghan said [20], there are infinite many symmetric formulations which can be derived from

$$\nabla \cdot f(\boldsymbol{x}) = \rho \left[\frac{1}{\rho^{2-\eta}} \nabla \cdot \left(\frac{f(\boldsymbol{x})}{\rho^{\eta-1}} \right) + \frac{f(\boldsymbol{x})}{\rho^{\eta}} \cdot \nabla \left(\frac{1}{\rho^{1-\eta}} \right) \right], \tag{2.3.37}$$

which leads to the generalized formulation where

$$\langle \nabla \cdot f(\boldsymbol{x}_i) \rangle = \rho_i \sum_{j=1}^{N} m_j \left(\frac{f(\boldsymbol{x}_i)}{\rho_i^{\eta} \rho_j^{2-\eta}} + \frac{f(\boldsymbol{x}_j)}{\rho_j^{\eta} \rho_i^{2-\eta}} \right) \cdot \nabla_i W_{ij}. \tag{2.3.38}$$

Letting $\eta = 2$, the formulation in (2.3.36) is obtained, and for $\eta = 1$ the particle approximation yields

$$\langle \nabla \cdot f(\boldsymbol{x}_i) \rangle = \rho_i \sum_{j=1}^{N} m_j \left(\frac{f(\boldsymbol{x}_i) + f(\boldsymbol{x}_j)}{\rho_i \rho_j} \right) \cdot \nabla_i W_{ij}. \tag{2.3.39}$$

Another symmetric formulation was proposed in [4, 141] and further examined in [37]. The formulation conserves momentum and avoids getting negative internal energy when integrating the energy equation [15]. The particle approximation is derived from the following identity

$$\nabla \cdot f(\boldsymbol{x}) = 2\sqrt{f(\boldsymbol{x})}\ (\nabla \cdot \sqrt{f(\boldsymbol{x})}), \tag{2.3.40}$$

which can be divided by density

$$\nabla \cdot f(\boldsymbol{x}) = \rho\Big[2\sqrt{f(\boldsymbol{x})}\ (\nabla \cdot \sqrt{f(\boldsymbol{x})})/\rho\Big], \tag{2.3.41}$$

and therefore for the particle approximation

$$\langle \nabla \cdot f(\boldsymbol{x}_i)\rangle = \rho_i \sum_{j=1}^{N} m_j \frac{2\sqrt{f(\boldsymbol{x}_i)}\sqrt{f(\boldsymbol{x}_j)}}{\rho_i \rho_j} \cdot \nabla_i W_{ij}. \tag{2.3.42}$$

When (2.3.36) and (2.3.42) are compared, some observations can be made. Both particle approximations represent a mean/averaging. In (2.3.36) the arithmetic mean is used, yet in (2.3.42) the geometric mean is used instead. Therefore, (2.3.42) can be directly derived from (2.3.36) by letting

$$\frac{1}{2}\left(\frac{f(\boldsymbol{x}_i)}{\rho_i^2} + \frac{f(\boldsymbol{x}_j)}{\rho_j^2}\right) \longrightarrow \frac{\sqrt{f(\boldsymbol{x}_i)}\sqrt{f(\boldsymbol{x}_j)}}{\rho_i \rho_j}. \tag{2.3.43}$$

Furthermore, in (2.3.42) the term $2\,\nabla_i W_{ij}$ was derived from the following identity

$$2\,\nabla_i W_{ij} = \nabla_i W(\boldsymbol{x}_i - \boldsymbol{x}_j, h_i) + \nabla_i W(\boldsymbol{x}_i - \boldsymbol{x}_j, h_j), \tag{2.3.44}$$

where $h_i = h_j$. This points to the fact, that each particle can have a different smoothing length h in general. The same idea was used in the direct density calculation in (2.3.32). The smoothing length and size of the support domain are discussed in section *Kernel* in detail. It can be said however, that the truly symmetric formulation must satisfy $h_i = h_j$ or other averaging must be employed. Other symmetric and asymmetric formulations can be found in many papers, e.g. in [15, 26, 85] or [125].

2.3.6 Approximation Properties

In [85] and [125] some useful SPH approximation properties were collected. Since the approximation properties are used in the following sections, they are also defined here.

The summation of functions

$$\langle f(\boldsymbol{x}) + g(\boldsymbol{x})\rangle = \langle f(\boldsymbol{x})\rangle + \langle g(\boldsymbol{x})\rangle, \tag{2.3.45}$$

their multiplication

$$\langle f(\boldsymbol{x})g(\boldsymbol{x})\rangle = \langle f(\boldsymbol{x})\rangle\langle g(\boldsymbol{x})\rangle, \tag{2.3.46}$$

and the multiplication with a constant

$$\langle \eta f(\boldsymbol{x})\rangle = \eta\langle f(\boldsymbol{x})\rangle. \tag{2.3.47}$$

The commutative property of a summation

$$\langle f(\boldsymbol{x}) + g(\boldsymbol{x})\rangle = \langle g(\boldsymbol{x}) + f(\boldsymbol{x})\rangle, \tag{2.3.48}$$

and the commutative property of a multiplication

$$\langle f(\boldsymbol{x})g(\boldsymbol{x})\rangle = \langle g(\boldsymbol{x})f(\boldsymbol{x})\rangle. \tag{2.3.49}$$

Derivatives can be placed within the kernel approximation operator as

$$\frac{d}{dt}\langle f(\boldsymbol{x})\rangle = \langle \frac{d}{dt} f(\boldsymbol{x})\rangle, \tag{2.3.50}$$

as well as divergence operator

$$\nabla \cdot \langle f(\boldsymbol{x})\rangle = \langle \nabla \cdot f(\boldsymbol{x})\rangle. \tag{2.3.51}$$

2.4 Kernel

It is often said that the kernel is the most important element of SPH. After all, it is the 'kernel'. From the author's experience with particle methods, the smoothing function itself is just one piece of the puzzle. Strictly speaking of SPH, the kernel determines the consistency therefore the accuracy of both the kernel and particle approximations. Yet when inappropriate time integration scheme or material model is used, the fact that the kernel is smooth up to tenth derivative is irrelevant. Of course, it does not mean that any

function can be used. A list of requirements and conditions together with the most used kernels are discussed here in detail.

The concept of the *integral representation* was used to derivate the *kernel approximation*. In the integral representation (2.3.4) the Dirac delta was used. As shown in (2.3.6), the Dirac delta is normalized. This is, in fact, the first kernel condition, the so-called *normalization condition* or *unity condition*

$$\int_{\Omega} W(\boldsymbol{x} - \boldsymbol{x}', h)\, d\boldsymbol{x}' = 1. \tag{2.4.1}$$

As shown in (2.3.9), when the smoothing length approaches to zero, the approximation is again exact and the kernel becomes the Dirac delta. This is often referred to as *Dirac delta condition* or just *Delta condition*, therefore, the second condition reads

$$\lim_{h \to 0} W(\boldsymbol{x} - \boldsymbol{x}', h) = \delta(\boldsymbol{x} - \boldsymbol{x}'). \tag{2.4.2}$$

The support domain cannot be infinitesimal and it cannot be infinite either. The reason why the support domain cannot be infinitesimal is clear – particles must influence each other. If not, there is no SPH. Yet, it might not be that obvious why the support domain cannot be infinite. Assuming that each particle has all particles as the neighbouring particles, then a localized change in a field function would be smeared over the whole problem domain – over all particles. Therefore, the third condition is the so-called *compact support condition*

$$W(\boldsymbol{x} - \boldsymbol{x}', h) = 0 \quad \text{if} \quad |\boldsymbol{x} - \boldsymbol{x}'| > \kappa h, \tag{2.4.3}$$

where again h is the smoothing length, κ is the dimension constant and together define the support domain Ω of a particle, see Fig. 2.4. This in other words means, that the kernel is defined for $|\boldsymbol{x} - \boldsymbol{x}'| \leq \kappa h$. As will be shown, 99.9% of all kernels examined in the thesis has the value at boundary S equal to zero, yet defined, and therefore (2.3.17) is satisfied. Which leads to the fourth condition, the so-called *positivity condition*

$$W(\boldsymbol{x} - \boldsymbol{x}', h) \geq 0 \quad \text{if} \quad |\boldsymbol{x} - \boldsymbol{x}'| \leq \kappa h. \tag{2.4.4}$$

The next condition can be understood as a complement to the previously mentioned localized change in a field function. As outlined, a localized change in a field function should not be smeared over all particles, yet it should have an influence on close neighbouring particles. This leads to the fifth condition, the so-called *decay condition*

$$W(\boldsymbol{x} - \boldsymbol{x}', h) \longrightarrow 0 \iff |\boldsymbol{x} - \boldsymbol{x}'| \longrightarrow \kappa h. \tag{2.4.5}$$

Equation (2.4.5) can be interpreted in the following way. The kernel value for a neighbouring particle should be monotonically decreasing with increasing distance from the particle for which the kernel is constructed [85]. The next condition was already assumed in (2.3.10), (2.3.11), and (2.3.25) so that the kernel should be an even function. Therefore, the sixth condition is the so-called *symmetry condition*

$$W(\boldsymbol{x}-\boldsymbol{x}',h)=W(|\boldsymbol{x}-\boldsymbol{x}'|,h), \tag{2.4.6}$$

or defined with the integral form directly with (2.3.11) as

$$\int_{\Omega}(\boldsymbol{x}'-\boldsymbol{x})W(\boldsymbol{x}-\boldsymbol{x}',h)\,d\boldsymbol{x}'=0. \tag{2.4.7}$$

Of course, if the kernel is truncated as shown in Fig. 2.5 (b), the sixth condition is not satisfied in general. The last seventh condition is the so-called *smoothness condition*. The smoothness of the kernel is given by the number of continuous derivatives it has over the support domain Ω, therefore

$$W(\boldsymbol{x}-\boldsymbol{x}',h)\in C^n(\Omega), \tag{2.4.8}$$

where n is a non-negative integer. Taking into account the third condition, the *compact support*, the notation $C^n(\Omega)$ can be simplified to C^n. The smoothness can be related to the consistency concept C^n in the traditional FEM. Essentially, the consistency refers to a polynomial reproducibility of up to nth order and the smoothness to the number of continuous derivatives. However, it can be that a kernel with smoothness of C^∞ has only C^0 consistency, e.g. when the kernel is truncated. Interestingly enough, (2.4.1) ensures C^0 order consistency of the integral representation of a continuum function.

2.4.1 Overview

Over decades many kernels were formulated. Properties of each kernel differ since they are usually tailored for a very specific application. In order to unify formulations of all kernels discussed in the thesis, the kernels are written in the form of

$$W(\boldsymbol{x}-\boldsymbol{x}',h)=W(q,h)=\frac{\sigma_{\kappa h}}{h^d}w(q), \tag{2.4.9}$$

where q is the relative distance between two points defined as

$$q=\frac{r}{h}=\frac{|\boldsymbol{x}-\boldsymbol{x}'|}{h}, \tag{2.4.10}$$

and r is the distance between the two points (particles in practice). In (2.4.9), d is the number of spatial dimensions and $\sigma_{\kappa h}$ is the normalization constant which is obtained from

$$\sigma_{\kappa h}^{-1} = \begin{cases} 2\int_0^{\kappa} w(q)\,dq & \text{in 1D} \\ 2\pi\int_0^{\kappa} w(q)q\,dq & \text{in 2D} \\ 4\pi\int_0^{\kappa} w(q)q^2\,dq & \text{in 3D} \end{cases} \tag{2.4.11}$$

where w is the kernel before the normalization or just non-normalized kernel, since W refers to the normalized one.

In the following overview, individual kernels are always defined with the support size as usually found in literature, i.e. as recommended by the authors. This means that κ is not the same for all kernels, yet it always defines the 'boundary' of the non-normalized kernel w. Later in the chapter, the kernels are compared all together. For fair comparison, $\kappa = 2$ is used for all, despite their previous definition. The conversion of the normalization constant $\sigma_{\kappa h}$ between two different supports is done in the following way. If kernel has a normalization $\sigma_{\eta h}$ for a support of ηh, it has a normalization of $\sigma_{\kappa h} = (\eta/\kappa)^d \sigma_{\eta h}$ if it is stretch to a support of κh.

For each kernel, first three derivatives are shown, and again for comparison purposes, the cubic spline (marked as M_4) is also placed in the graphs. The kernel values are calculated for 1D and plotted on the primary (left-hand side) vertical axis. The values of kernel derivatives are plotted on the secondary (right-hand side) axis as their range is quite different from the range of the kernel values.

The most commonly used kernels in SPH are based on the Schoenberg's B-spline functions [142]; M_n in Schoenberg's notation [143]. The B-splines are generated as Fourier transforms

$$M_n(x,h) = \frac{1}{2\pi}\int_{-\infty}^{\infty}\left[\frac{\sin(kh/2)}{kh/2}\right]^n \cos(kx)\,dk, \tag{2.4.12}$$

and algebraic forms are given by Schoenberg [142, 143] and Monaghan [8, 7, 9]. The smoothness of B-splines increase with n [9] (are of order n, i.e. degree $n-1$ [8]). For example, the kernel M_2 leads to an ordinary interpolation formula, but higher order M_n give smoothing interpolation formulae [8]. The higher order functions M_n and their first $n-2$ derivatives are continuous [8].

In practice, however, B-splines are rather defined as piece-wise continuous functions with a compact support having derivatives up to $n-2$ continuous [8, 123, 124]. Therefore, B-spline kernels are referred to as splines.

For easier differentiation in the following overview, the kernels based on the Schoenberg's B-splines are marked $M(q)$ instead of $W(q)$.

Linear Spline Kernel

The linear spline, M_2 in Schoenberg's notation, has a little purpose in SPH, since SPH requires at least continuity in the first and second derivative. Although M_2 gives linear interpolation, its first derivative is discontinuous. In its product form it gives what is called the equal area interpolation [88, 144]. The linear spline kernel is defined as

$$w_2(q) = \begin{cases} 1-q & 0 \leq q \leq 1 \\ 0 & \text{else,} \end{cases} \tag{2.4.13}$$

with the normalization constants given below.

	$\sigma_{\kappa h}$
1D	1
2D	$3/\pi$
3D	$3/\pi$

The kernel is plotted in Fig. 2.6 together with the cubic spline M_4.

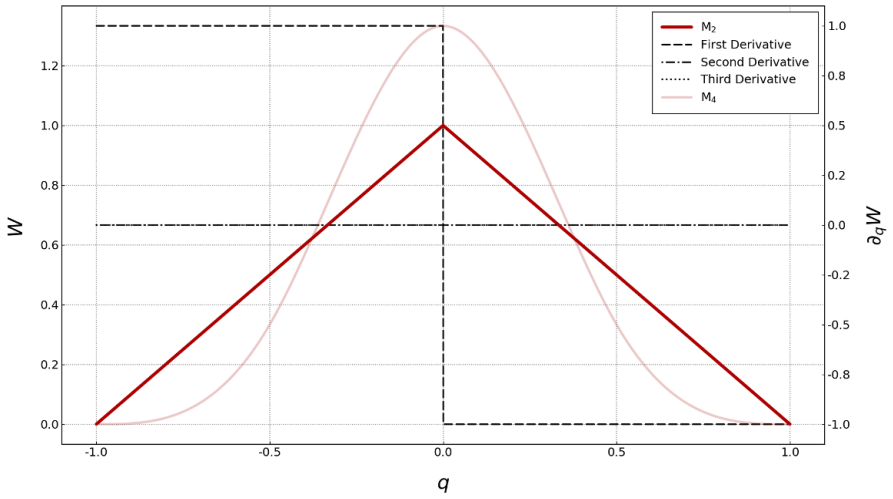

Fig. 2.6. Linear spline kernel, $\kappa = 1$.

Quadratic Spline Kernel

More interesting is perhaps the quadratic spline M_3 which was used in [43] for HVI simulations. Unlike other smoothing functions, values of its first derivative always increases as the particles move closer, and always decreases as they move apart. This was regarded by the authors as an important improvement over the cubic spline function, and it was reported to relieve the problem of compressive instability [85, 125]. The compressive instability is in essence the same as the tensile instability and results in formation of particle clusters which leads to numerical instability. Furthermore, in [144] is M_3 recommended for calculation of

grid density directly from the particles [9]. The quadratic spline kernel is defined as

$$w_3(q) = \begin{cases} \frac{3}{4} - \frac{3}{4}q + \frac{3}{16}q^2 & 0 \leq q \leq 2 \\ 0 & \text{else,} \end{cases} \tag{2.4.14}$$

with the normalization constants given below.

	$\sigma_{\kappa h}$
1D	1
2D	$2/\pi$
3D	$5/(4\pi)$

The kernel is plotted in Fig. 2.7 together with the cubic spline M_4.

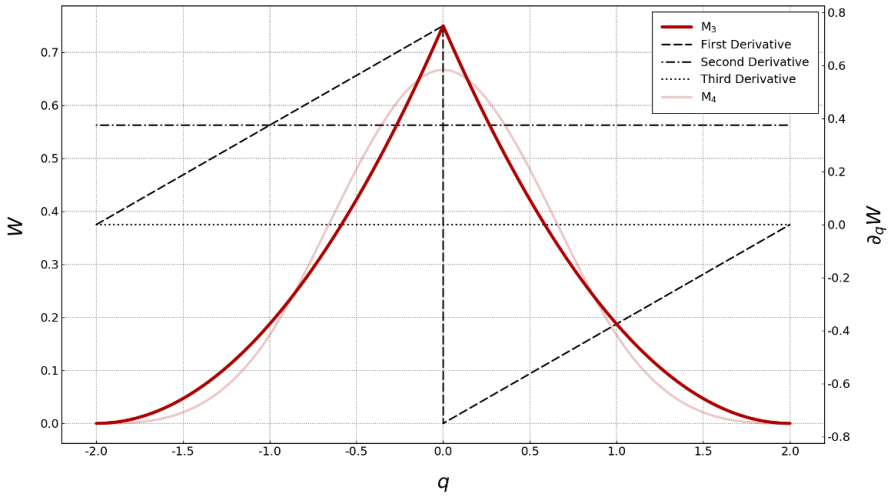

Fig. 2.7. Quadratic spline kernel, $\kappa = 2$.

Cubic Spline Kernel

Since SPH requires at the very least continuity in the first and second derivative, the cubic spline M_4 is the most popular kernel. It is often considered the *standard choice* in SPH [9]. However, the second derivative of the cubic spline is piecewise linear function, and accordingly, the stability properties can be inferior to those of smoother kernels. In addition, the smoothing function is in pieces, which makes it slightly more difficult to use it compared to one piece smoothing functions [87]. The cubic spline kernel is defined as

$$w_4(q) = \begin{cases} (2-q)^3 - 4(1-q)^3 & 0 \leq q < 1 \\ (2-q)^3 & 1 \leq q \leq 2 \\ 0 & \text{else,} \end{cases} \tag{2.4.15}$$

with the normalization constants given below.

	$\sigma_{\kappa h}$
1D	$1/6$
2D	$15/(14\pi)$
3D	$1/(4\pi)$

The kernel is plotted in Fig. 2.8.

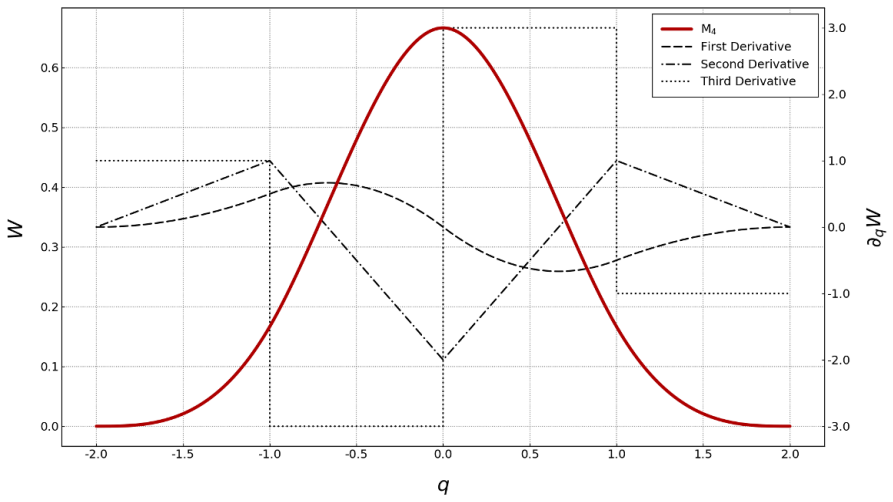

Fig. 2.8. Cubic spline kernel, $\kappa = 2$.

Quartic Spline Kernel

Higher order B-splines [142] were examined by Morris [37, 36]. It was proved that they more closely approximate the Gaussian kernel, are more accurate and stable. The quartic spline kernel is defined as

$$w_5(q) = \begin{cases} (2.5-q)^4 - 5(1.5-q)^4 + 10(0.5-q)^4 & 0 \le q < 0.5 \\ (2.5-q)^4 - 5(1.5-q)^4 & 0.5 \le q < 1.5 \\ (2.5-q)^4 & 1.5 \le q \le 2.5 \\ 0 & \text{else,} \end{cases} \tag{2.4.16}$$

with the normalization constants given below.

	$\sigma_{\kappa h}$
1D	$1/24$
2D	$96/(1199\pi)$
3D	$1/(20\pi)$

The kernel is plotted in Fig. 2.9 together with the cubic spline M_4.

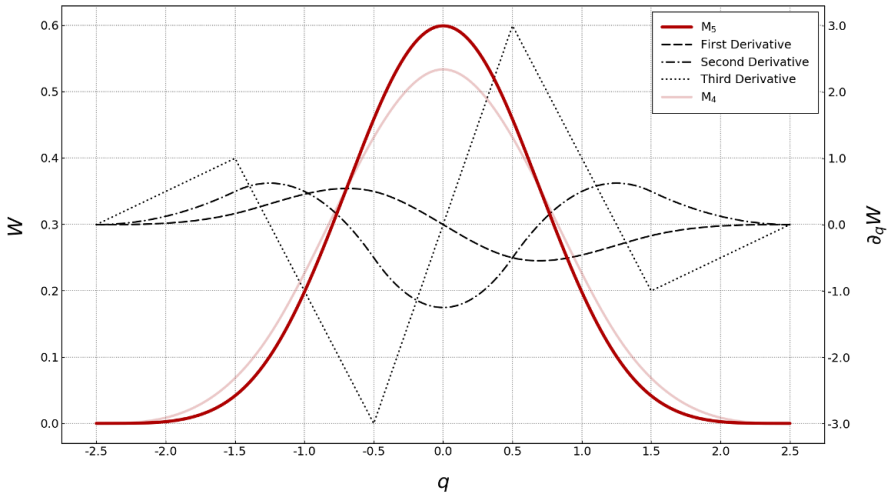

Fig. 2.9. Quartic spline kernel, $\kappa = 2.5$.

New Quartic Spline Kernel

In [82] a modified variant of the quartic kernel was proposed. The improvements consist of higher accuracy due to the smaller second moment (discussed later), smoother second derivative, therefore, more stable, and in addition it is defined in only one piece. The new quartic spline kernel is defined as

$$w_{5,new}(q) = \begin{cases} \frac{2}{3} - \frac{9}{8}q^2 + \frac{19}{24}q^3 - \frac{5}{32}q^4 & 0 \leq q \leq 2 \\ 0 & \text{else,} \end{cases} \tag{2.4.17}$$

with the normalization constants given below.

	$\sigma_{\kappa h}$
1D	1
2D	$15/(7\pi)$
3D	$315/(208\pi)$

The kernel is plotted in Fig. 2.10 together with the cubic spline M_4. It is obvious that there is almost no difference between the new quartic and the cubic kernel.

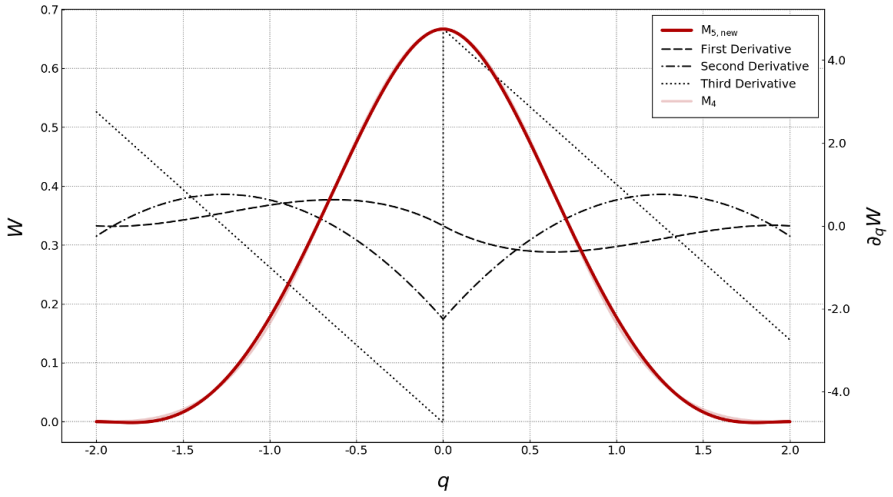

Fig. 2.10. New quartic spline kernel, $\kappa = 2$.

Quintic Spline Kernel

The quintic spline M_6 was also examined by Morris [37, 36]. Again, it was proved that higher order splines provide better accuracy and are generally more stable. The quintic spline kernel is defined as

$$w_6(q) = \begin{cases} (3-q)^5 - 6(2-q)^5 + 15(1-q)^5 & 0 \leq q < 1 \\ (3-q)^5 - 6(2-q)^5 & 1 \leq q < 2 \\ (3-q)^5 & 2 \leq q \leq 3 \\ 0 & \text{else,} \end{cases} \tag{2.4.18}$$

with the normalization constants given below.

	$\sigma_{\kappa h}$
1D	$1/120$
2D	$7/(478\pi)$
3D	$1/(120\pi)$

The kernel is plotted in Fig. 2.11 together with the cubic spline M_4.

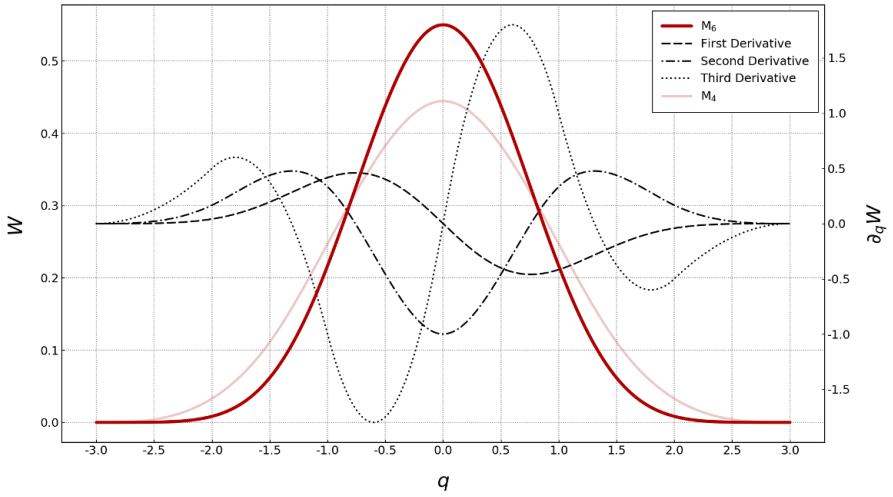

Fig. 2.11. Quintic spline kernel, $\kappa = 3$.

Bell-Shaped Kernel

When Lucy [1] started with SPH in 1977, he used the so-called bell-shaped kernel, which is a quartic function. The bell-shaped kernel is not part of the Schoenberg's B-splines and therefore is marked by its name in the graphs. The bell-shaped kernel is defined as

$$w(q) = \begin{cases} (1+3q)(1-q)^3 & 0 \leq q \leq 1 \\ 0 & \text{else,} \end{cases} \tag{2.4.19}$$

with the normalization constants given below.

	$\sigma_{\kappa h}$
1D	$5/4$
2D	$5/\pi$
3D	$105/(16\pi)$

The kernel is plotted in Fig. 2.12 together with the cubic spline M_4.

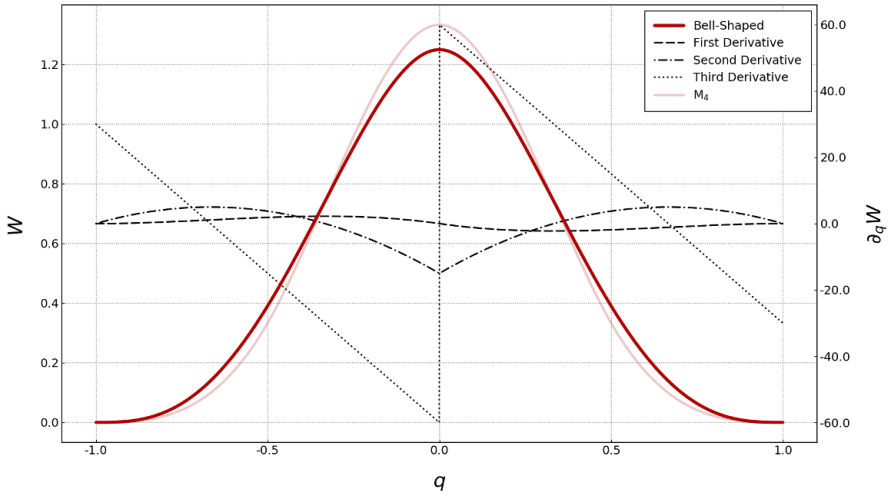

Fig. 2.12. Bell-shaped kernel, $\kappa = 1$.

Dome-Shaped Kernel

There is also the so-called dome-shaped kernel, elaborated in detail in [85, 125]. In contrast to the bell-shaped kernel, the dome-shaped kernel is only a quadratic function and is defined as

$$w(q) = \begin{cases} 1 - q^2 & 0 \leq q \leq 1 \\ 0 & \text{else,} \end{cases} \tag{2.4.20}$$

with the normalization constants given below.

	$\sigma_{\kappa h}$
1D	$3/4$
2D	$2/\pi$
3D	$15/(8\pi)$

The kernel is plotted in Fig. 2.13 together with the cubic spline M_4.

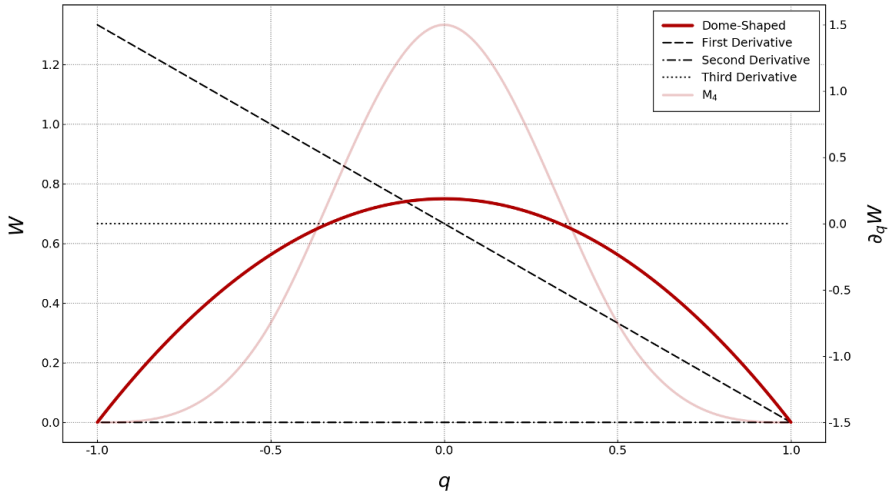

Fig. 2.13. Dome-shaped kernel, $\kappa = 1$.

Gaussian Kernel

As already discussed, in [20] Monaghan mentioned something he called golden rules. At this point the first rule applies. It was suggested to use the Gaussian kernel to better understand the physical interpretation of SPH equations. The Gaussian kernel was also used in the original work of Gingold and Monaghan [2]. The kernel is sufficiently smooth even for higher order derivatives, and is regarded as a golden selection since it is very stable and accurate especially for disordered particles [85]. It is, however, not really compact, as it never goes to zero theoretically, unless q approaches to infinity [85]. Because it approaches zero numerically very fast, it is practically compact [125], however. The Gaussian kernel is defined as

$$w(q) = \begin{cases} e^{-q^2} & 0 \leq q \leq 3 \\ 0 & \text{else.} \end{cases} \tag{2.4.21}$$

The kernel is manually truncated at $q = 3$ for computational purposes. However, it means that the surface integral in (2.3.16) is not zero and thus (2.3.17) is not exactly satisfied. Yet for $q = 3$ the surface integral in (2.3.16) yields value less than 0.1‰. The normalization constants are given below.

	$\sigma_{\kappa h}$
1D	$1/\pi^{1/2}$
2D	$1/\pi$
3D	$1/\pi^{3/2}$

The kernel is plotted in Fig. 2.14 together with the cubic spline M_4.

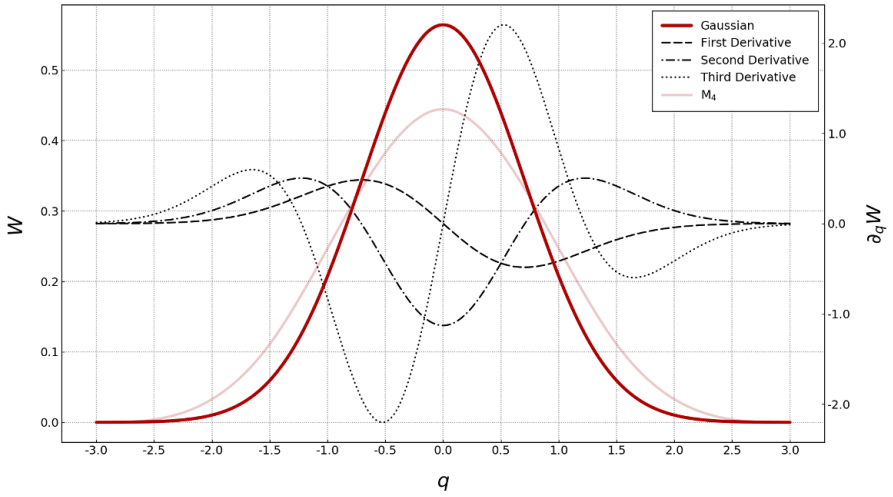

Fig. 2.14. Gaussian kernel, $\kappa = 3$.

Super Gaussian Kernel

A higher order Gaussian kernel was proposed by Monaghan and Lattanzio in [9] and studied in detail by Monaghan in [20]. The kernel was named super Gaussian and is defined with respect to the dimension d as

$$w(q) = \begin{cases} \left(1 + 0.5d - q^2\right) e^{-q^2} & 0 \leq q \leq 3 \\ 0 & \text{else.} \end{cases} \tag{2.4.22}$$

Here again, the kernel is manually truncated at $q = 3$ for computational purposes. And again, (2.3.17) is not exactly satisfied. As in the case with the Gaussian kernel, even for the super Gaussian kernel the values approaches zero very fast. One disadvantage of the higher order smoothing function is that the kernel is negative in some regions of its support domain [85]. This may lead to unphysical results for hydrodynamic problems [140]. The normalization constants are given below.

	$\sigma_{\kappa h}$
1D	$1/\pi^{1/2}$
2D	$1/\pi$
3D	$1/\pi^{3/2}$

The kernel is plotted in Fig. 2.15 together with the cubic spline M_4.

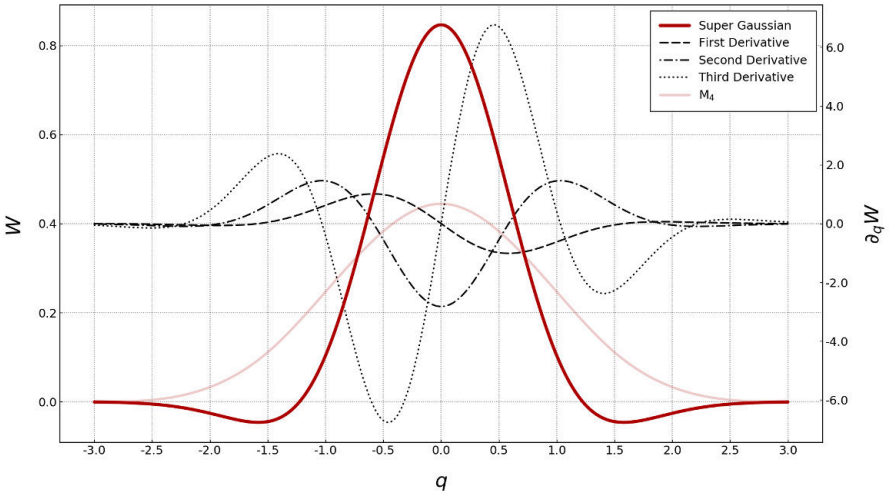

Fig. 2.15. Super Gaussian kernel, $\kappa = 3$.

Double Cosine Kernel

In 2014 the so-called double cosine kernel was proposed in [120]. As the name says, it combines two cosine functions into one kernel which means the kernel is sufficiently smooth. The second moment is minimized thus it has better accuracy. In addition, it is defined with respect to κ which means it has adjustable support which is very convenient. The double cosine kernel is defined as

$$w(q) = \begin{cases} 4\cos\left(\frac{\pi}{\kappa}q\right) + \cos\left(\frac{2\pi}{\kappa}q\right) + 3 & 0 \leq q \leq \kappa \\ 0 & \text{else,} \end{cases} \tag{2.4.23}$$

with the normalization constants given below.

	$\sigma_{\kappa h}$
1D	$1/(6\kappa)$
2D	$\pi/[(3\pi^2 - 16)\kappa^2]$
3D	$\pi/[(4\pi^2 - 30)\kappa^3]$

The kernel is plotted in Fig. 2.16 together with the cubic spline M_4. It is obvious that there is almost no difference between the double cosine kernel and the cubic kernel.

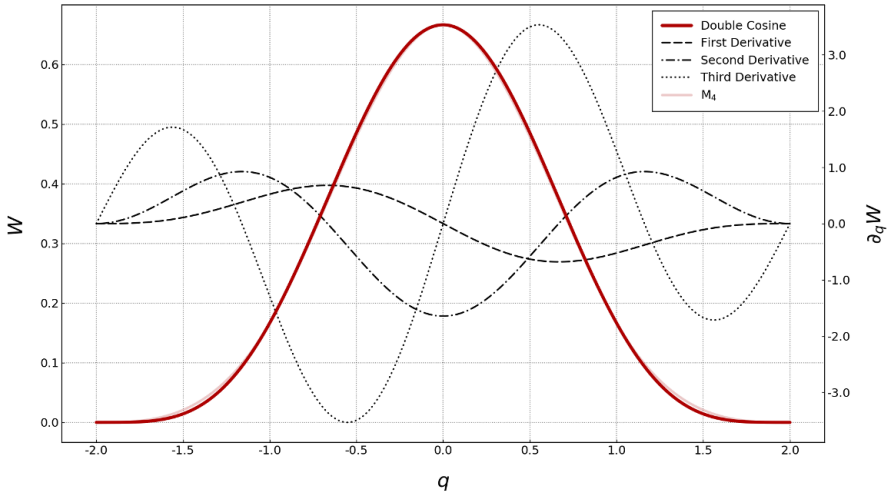

Fig. 2.16. Double cosine kernel, $\kappa = 2$.

One Parameter Family of Kernels

Another class of kernels is the so-called one parameter family of kernels. The idea is based on utilization of a harmonic function with a free exponent n. The advantage is that the exponent can be changed on 'fly' when strong gradients appear in field functions. The one parameter family of kernels is discussed in detail in [96]. For convenience, the kernels are marked $W_{\mathrm{H}n}$ where n is the exponent. The definition is as

$$w_{\mathrm{H}n}(q) = \begin{cases} 1 & q = 0 \\ \left[\dfrac{\sin\left(\frac{\pi}{2}q\right)}{\frac{\pi}{2}q}\right]^n & 0 < q \leq 2 \\ 0 & \text{else,} \end{cases} \tag{2.4.24}$$

with the normalization constants and plotted kernels for n up to 10 given below.

	$\sigma_{\kappa h,\mathrm{H1}}$	$\sigma_{\kappa h,\mathrm{H2}}$	$\sigma_{\kappa h,\mathrm{H3}}$	$\sigma_{\kappa h,\mathrm{H4}}$	$\sigma_{\kappa h,\mathrm{H5}}$
1D	0.424095	0.553818	0.660203	0.752215	0.834354
2D	0.196350	0.322194	0.450733	0.580312	0.710379
3D	0.098175	0.196350	0.317878	0.458918	0.617013

	$\sigma_{\kappa h,\mathrm{H6}}$	$\sigma_{\kappa h,\mathrm{H7}}$	$\sigma_{\kappa h,\mathrm{H8}}$	$\sigma_{\kappa h,\mathrm{H9}}$	$\sigma_{\kappa h,\mathrm{H10}}$
1D	0.909205	0.978402	1.043052	1.103944	1.161662
2D	0.840710	0.971197	1.101785	1.232440	1.363143
3D	0.790450	0.977949	1.178511	1.391322	1.615708

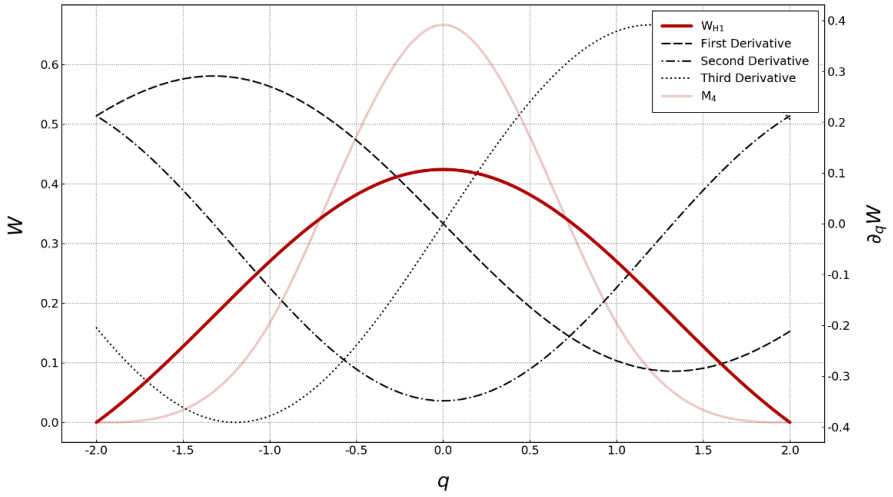

Fig. 2.17. Harmonic H1 kernel, $\kappa = 2$.

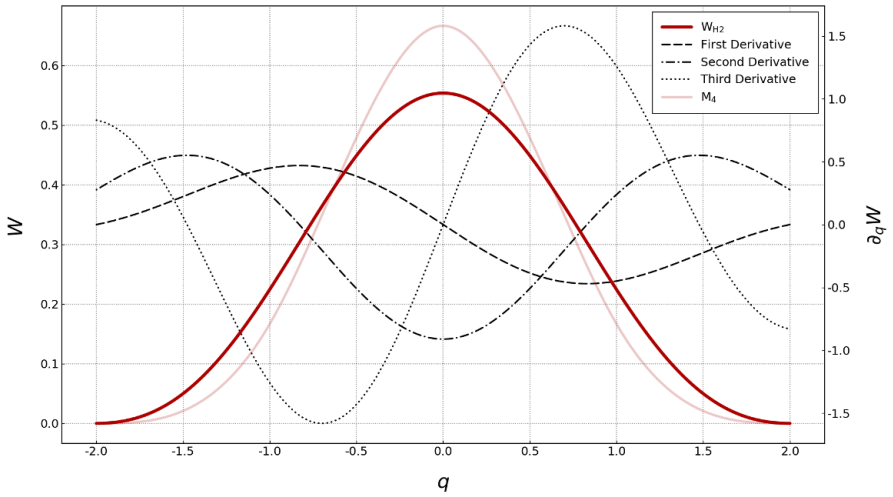

Fig. 2.18. Harmonic H2 kernel, $\kappa = 2$.

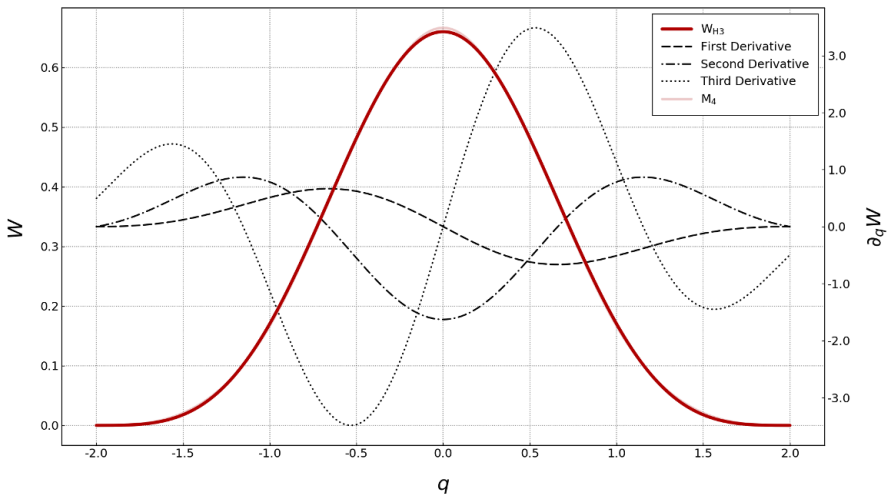

Fig. 2.19. Harmonic H3 kernel, $\kappa = 2$.

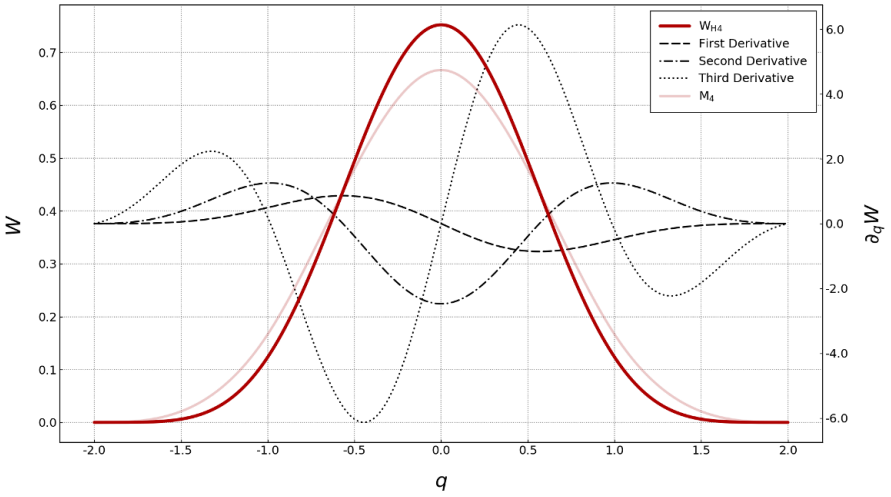

Fig. 2.20. Harmonic H4 kernel, $\kappa = 2$.

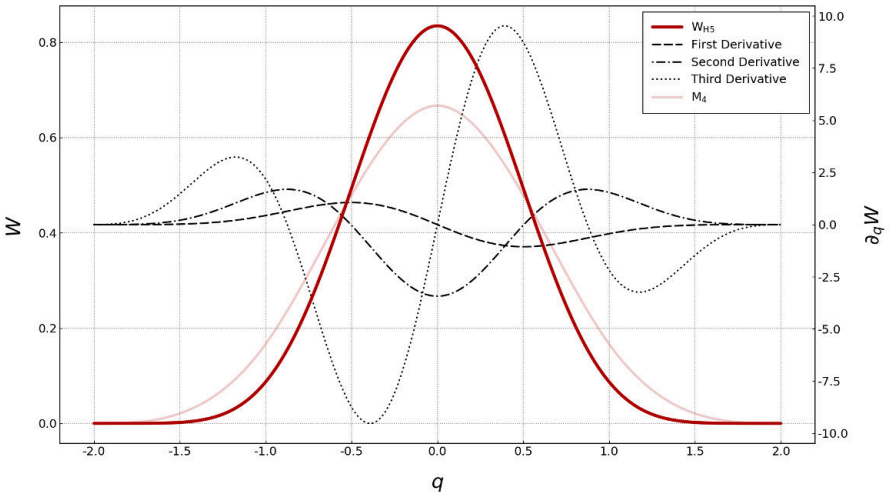

Fig. 2.21. Harmonic H5 kernel, $\kappa = 2$.

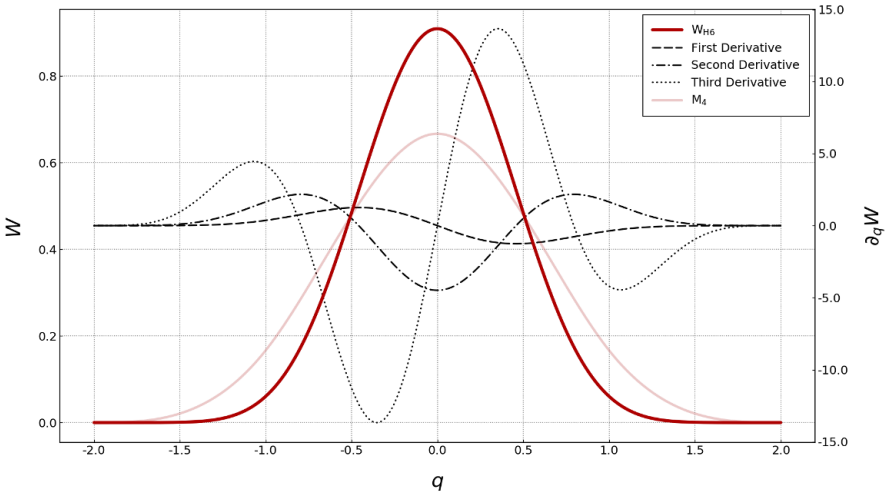

Fig. 2.22. Harmonic H6 kernel, $\kappa = 2$.

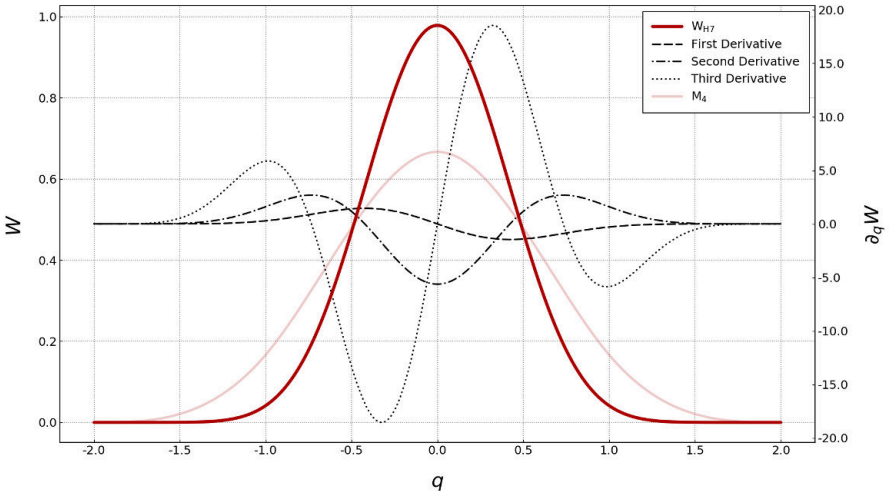

Fig. 2.23. Harmonic H7 kernel, $\kappa = 2$.

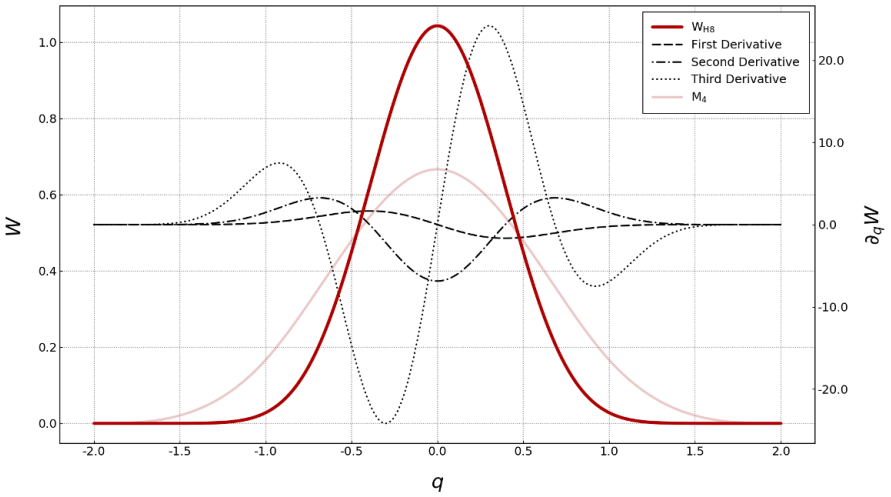

Fig. 2.24. Harmonic H8 kernel, $\kappa = 2$.

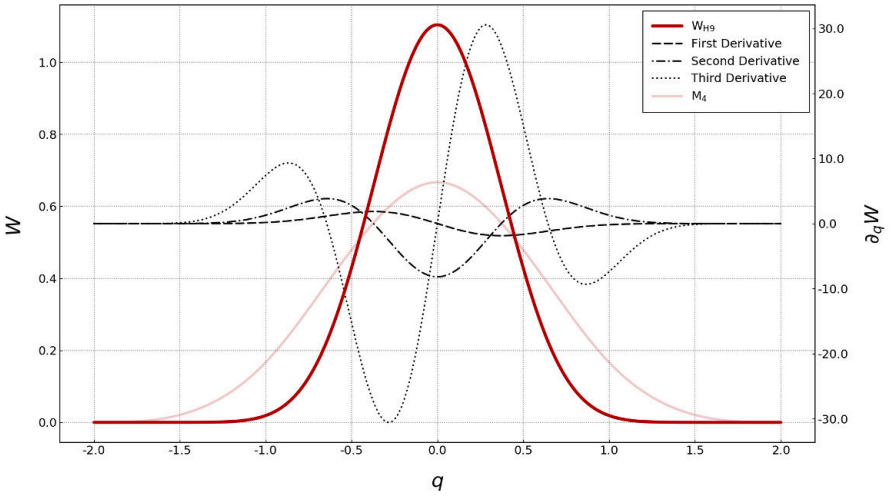

Fig. 2.25. Harmonic H9 kernel, $\kappa = 2$.

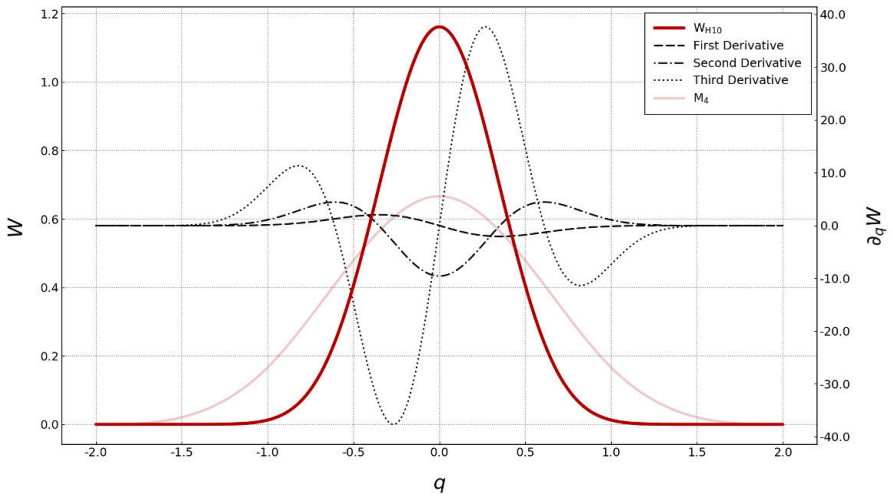

Fig. 2.26. Harmonic H10 kernel, $\kappa = 2$.

Interestingly enough, with a relatively low exponent the W_{H3} kernel Fig. 2.19 is very similar to the cubic spline M_4, while the W_{H5} kernel Fig. 2.21 is a close approximation of the quintic spline M_6 (for the same support, of course).

Wendland Kernels

Another interesting class of kernels with a compact support and positive Fourier transforms are the Wendland functions [32, 145]. The Wendland functions have been well appreciated for their good interpolation properties, and especially for one particular reason. When using the Wendland functions, a particle distribution remains highly ordered even in dynamical simulations and only allows for very little noise [124]. Study in [146] proved that these kernels are not prone to the pairing instability despite having a vanishing central derivative, see also [123]. The Wendland functions have been defined for dimensions up to 5 and smoothness up to C^6. For convenience, the kernels are marked $W_{\mathrm{C}n}$ where n is the smoothness number.

They are defined for 1D as

$$w_{\mathrm{C2}}(q) = \begin{cases} \left(1 - \frac{1}{2}q\right)^3 \left(1 + \frac{3}{2}q\right) & 0 \le q \le 2 \\ 0 & \text{else,} \end{cases} \tag{2.4.25}$$

$$w_{\mathrm{C4}}(q) = \begin{cases} \left(1 - \frac{1}{2}q\right)^5 \left(1 + \frac{5}{2}q + 2q^2\right) & 0 \le q \le 2 \\ 0 & \text{else,} \end{cases} \tag{2.4.26}$$

$$w_{\mathrm{C6}}(q) = \begin{cases} \left(1 - \frac{1}{2}q\right)^7 \left(1 + \frac{7}{2}q + \frac{19}{4}q^2 + \frac{21}{8}q^3\right) & 0 \le q \le 2 \\ 0 & \text{else,} \end{cases} \tag{2.4.27}$$

and for 2D and 3D as

$$w_{\mathrm{C2}}(q) = \begin{cases} \left(1-\frac{1}{2}q\right)^4 (1+2q) & 0 \le q \le 2 \\ 0 & \text{else,} \end{cases} \tag{2.4.28}$$

$$w_{\mathrm{C4}}(q) = \begin{cases} \left(1-\frac{1}{2}q\right)^6 \left(1+3q+\frac{35}{12}q^2\right) & 0 \le q \le 2 \\ 0 & \text{else,} \end{cases} \tag{2.4.29}$$

$$w_{\mathrm{C6}}(q) = \begin{cases} \left(1-\frac{1}{2}q\right)^8 \left(1+4q+\frac{25}{4}q^2+4q^3\right) & 0 \le q \le 2 \\ 0 & \text{else,} \end{cases} \tag{2.4.30}$$

with the normalization constants given below.

	$\sigma_{\kappa h,\mathrm{C2}}$	$\sigma_{\kappa h,\mathrm{C4}}$	$\sigma_{\kappa h,\mathrm{C6}}$
1D	$5/8$	$3/4$	$55/64$
2D	$7/(4\pi)$	$9/(4\pi)$	$78/(28\pi)$
3D	$21/(16\pi)$	$495/(256\pi)$	$1365/(512\pi)$

The kernels are plotted in Fig. 2.27, Fig. 2.28, and Fig. 2.29 for W_{C2}, W_{C4}, and W_{C6}, respectively. When compared to other kernels, the W_{C2} is relatively similar to the $M_{5,new}$, including derivatives.

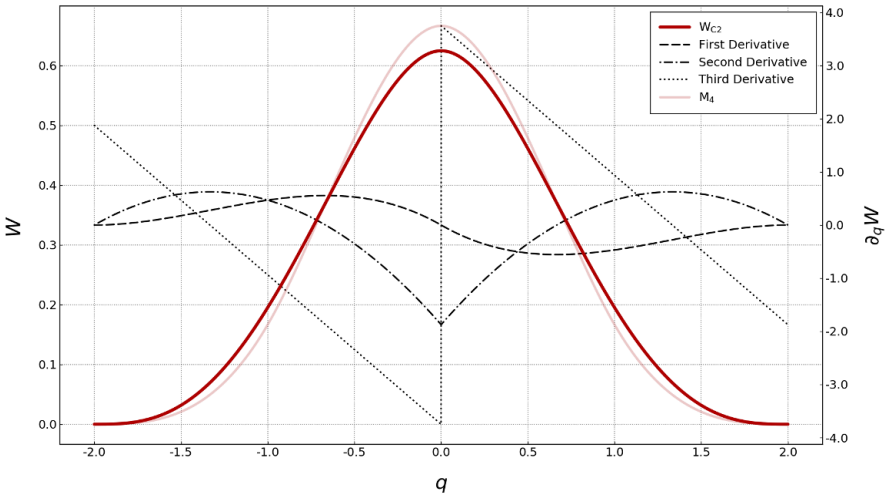

Fig. 2.27. Wendland C2 kernel, $\kappa = 2$.

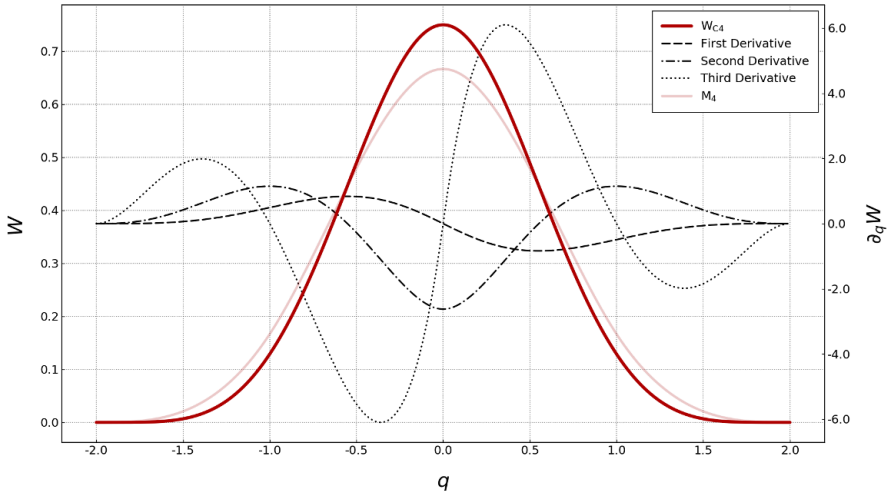

Fig. 2.28. Wendland C4 kernel, $\kappa = 2$.

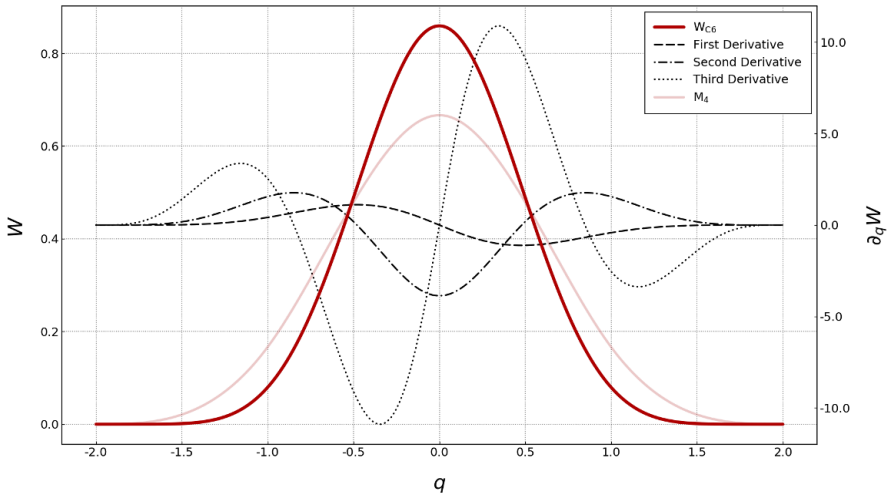

Fig. 2.29. Wendland C6 kernel, $\kappa = 2$.

Linear Quartic Kernel

Another class is formed by the kernels which possess non-vanishing central derivatives. In other words, their derivatives remain finite in the centre so that the repulsive forces between particles never vanish [123, 124]. The major motivation behind such kernels is to achieve a very regular particle distribution and in particular to avoid the pairing instability [124]. The first example of the kernel with non-vanishing central derivatives is the so-called linear quartic kernel W_{LIQ} proposed in [147]. The kernel is defined with free parameter x_s determining the connection point of the polynomial and linear functions [147]. The linear quartic kernel is definition as

$$w_{\mathrm{LIQ}}(q) = \begin{cases} F - q & 0 \leq q < x_s \\ Aq^4 + Bq^3 + Cq^2 + Dq + E & x_s \leq q \leq 1 \\ 0 & \text{else,} \end{cases} \tag{2.4.31}$$

where x_s is chosen by the user, and the unknown parameters are calculated as

$$\begin{aligned}
\alpha &= \frac{1}{x_s^3 - 3x_s^2 + 3x_s - 1}, \\
A &= \frac{\alpha}{2}, \\
B &= -\alpha(1 + x_s), \\
C &= 3\alpha x_s, \\
D &= -\alpha(-1 + 3x_s), \\
E &= \frac{\alpha(2x_s - 1)}{2}, \\
F &= Ax_s^4 + Bx_s^3 + Cx_s^2 + Dx_s + E + x_s.
\end{aligned} \tag{2.4.32}$$

For example, for $x_s = 0.3$ the kernel parameters are

	$x_s = 0.3$
A	$-500/343$
B	$1300/343$
C	$-900/343$
D	$-100/343$
E	$200/343$
F	$13/20$

with the normalization constants given below.

	$\sigma_{\kappa h}$
1D	$1000/447$
2D	$3750/(403\pi)$
3D	$30000/(2419\pi)$

The kernel is plotted in Fig. 2.30 together with the cubic spline M_4.

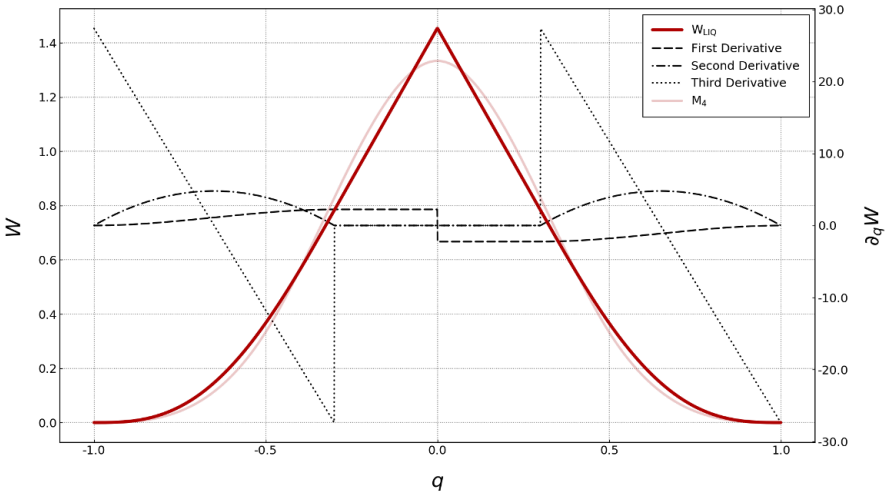

Fig. 2.30. Linear quartic kernel, $x_s = 0.3$, $\kappa = 1$.

Quartic Core Kernel

Another example of the kernel with non-vanishing central derivatives is a modified M_6 kernel [123, 124]. The idea behind the modification is that the core part of the M_6 kernel is replaced by a parabola. Therefore, it is named quartic core M_6 kernel or just QCM_6. The core part is bounded with a parameter q_c which is calculated from condition $d^2 w_6 / dq^2(q_c) = 0$. From (2.4.18) the $q_c = 0.75929848$. The quartic core kernel is defined as

$$w_{\mathrm{QCM}_6}(q) = \begin{cases} Aq^4 + Bq^2 + Cq + D & 0 \leq q < q_c \\ (3-q)^5 - 6(2-q)^5 + 15(1-q)^5 & q_c \leq q < 1 \\ (3-q)^5 - 6(2-q)^5 & 1 \leq q < 2 \\ (3-q)^5 & 2 \leq q \leq 3 \\ 0 & \text{else.} \end{cases} \tag{2.4.33}$$

The kernel parameters are calculated from conditions

$$\begin{aligned} w_{\mathrm{QCM}_6}(q_c) &= w_6(q_c), \\ w'_{\mathrm{QCM}_6}(q_c) &= w'_6(q_c), \\ w''_{\mathrm{QCM}_6}(q_c) &= w''_6(q_c), \\ w'''_{\mathrm{QCM}_6}(q_c) &= w'''_6(q_c), \end{aligned} \tag{2.4.34}$$

where the primes indicate the derivatives with respect to q [124]. For $q_c = 0.75929848$ the kernel parameters are

	$q_c = 0.75929848$
A	11.01753798
B	−38.11192354
C	−16.61958320
D	69.78576728

with the normalization constants given below.

	$\sigma_{\kappa h}$
1D	$8.24554795 \times 10^{-3}$
2D	$4.64964683 \times 10^{-3}$
3D	$2.65083908 \times 10^{-3}$

The kernel is plotted in Fig. 2.31 together with the cubic spline M_4.

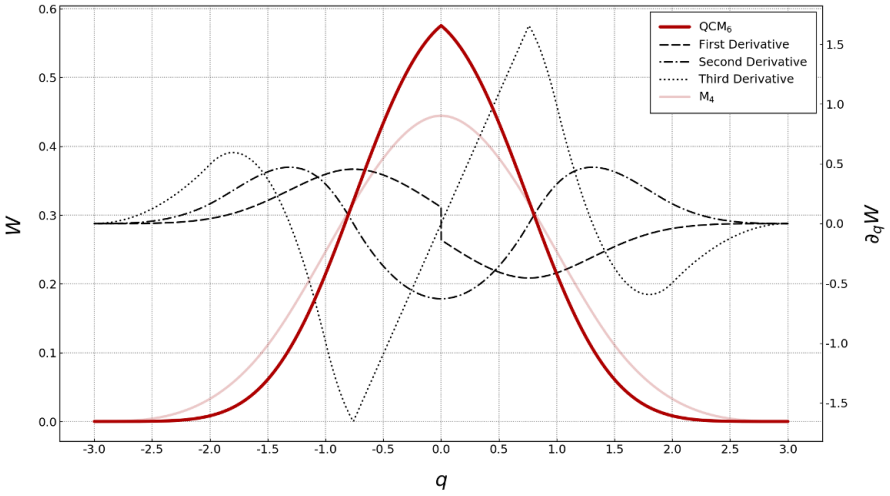

Fig. 2.31. Quartic core M6 kernel, $q_c = 0.75929848$, $\kappa = 3$.

The QCM_6 kernel is continuous everywhere up to the third derivative. In [123] was found, that the QCM_6 kernel has the property of producing very little noise. As shown in the 'noise box' experiment in [124], particles placed initially on a quadratic or hexagonal lattice in a pressure equilibrium remained on the lattice configuration even after an artificial noise was triggered.

Comparison

Although there are many other kernels, the selection in the thesis gathered the most common ones. It is very often difficult to choose a proper kernel for a given task, since there are many kernels to choose from. In structural dynamics, the cubic spline M_4 is a very good start. It can be that higher order kernels might improve a solution. Yet, when explicit solvers are used, higher order kernels tend to be very sensitive to the time step and thus the improvement might not be that pronounced. Furthermore, when artificial viscosity is introduced, usage of higher order kernels is also discussable.

In Fig. 2.32 kernels are compared for $\kappa = 2$. Since not all the discussed kernels were defined for the support size of $2h$, their normalization factors $\sigma_{\kappa h}$ were recalculated to satisfy the normalization condition in (2.4.1). As the number of the compared kernels is 26, Fig. 2.32 is quite full. From the graph is obvious however which space is occupied by the compared kernels the most. Interestingly enough, the cubic spline M_4 represents some kind of average of all. This might be yet another reason why the cubic spline is so popular as it provides a good compromise.

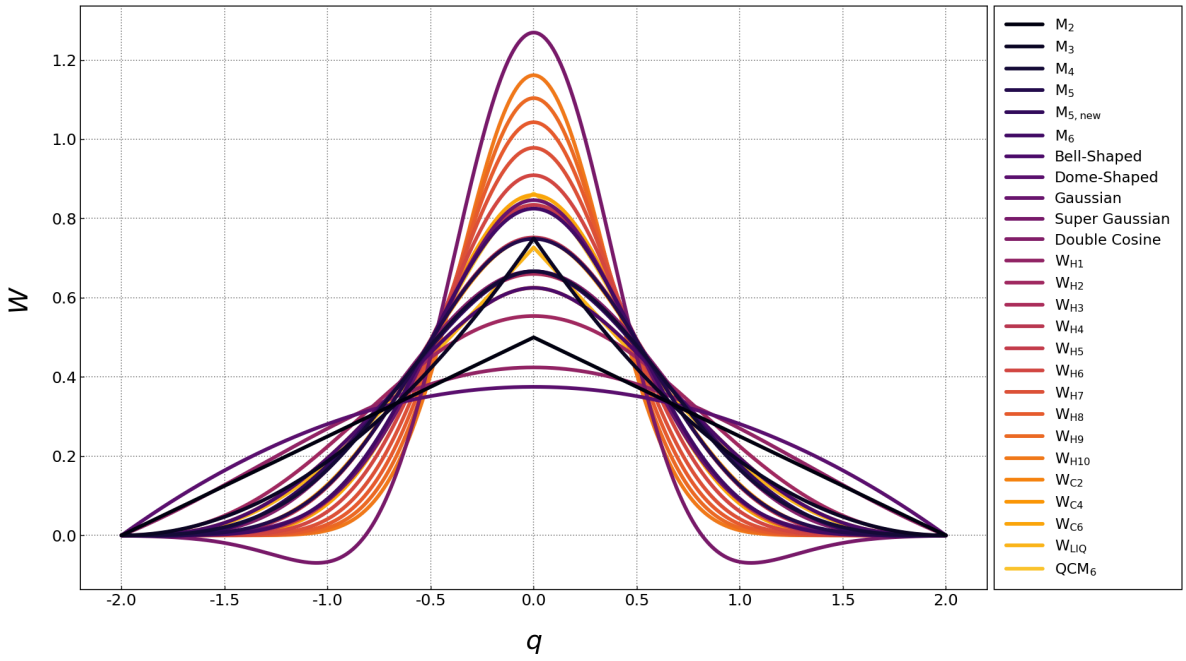

Fig. 2.32. Comparison of kernels, $\kappa = 2$.

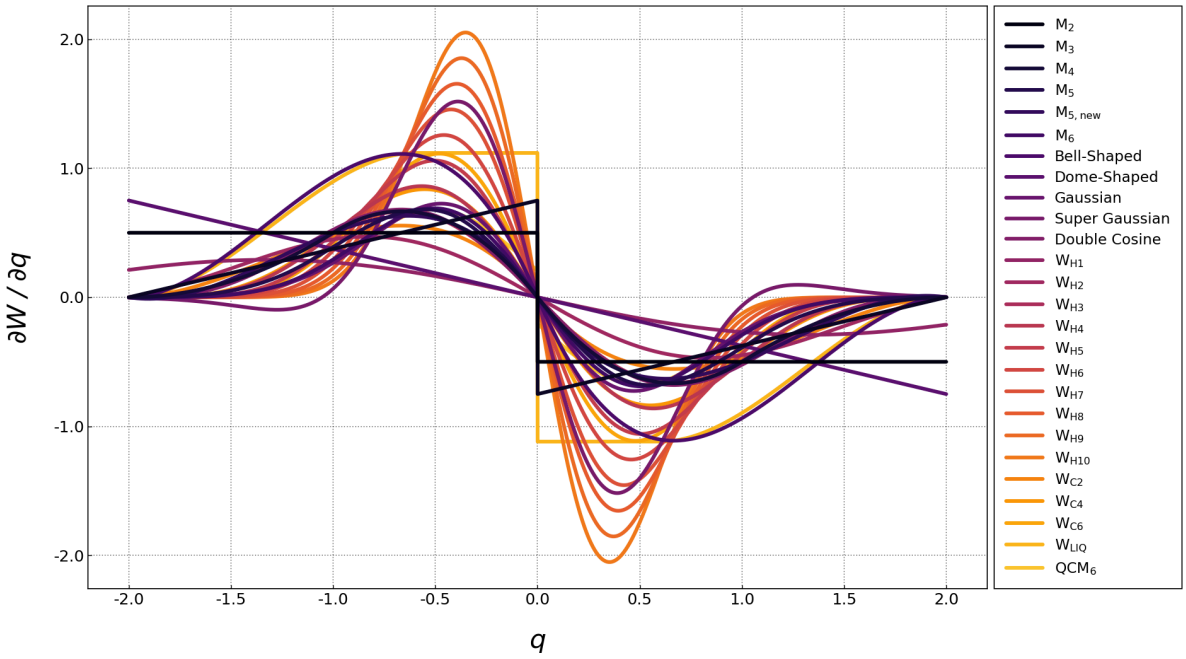

Fig. 2.33. Comparison of first derivatives of kernels, $\kappa = 2$.

The comparison continues in Fig. 2.33 for the first derivatives. It must be pointed out, that only in case of the quadratic spline M_3 the values increases as particles move closer, and decreases as they move apart. This means that only one of the simpler kernels can prevent the compressive instability. However, the compressive instability is in most cases not a problem since material yielding is usually reached before.

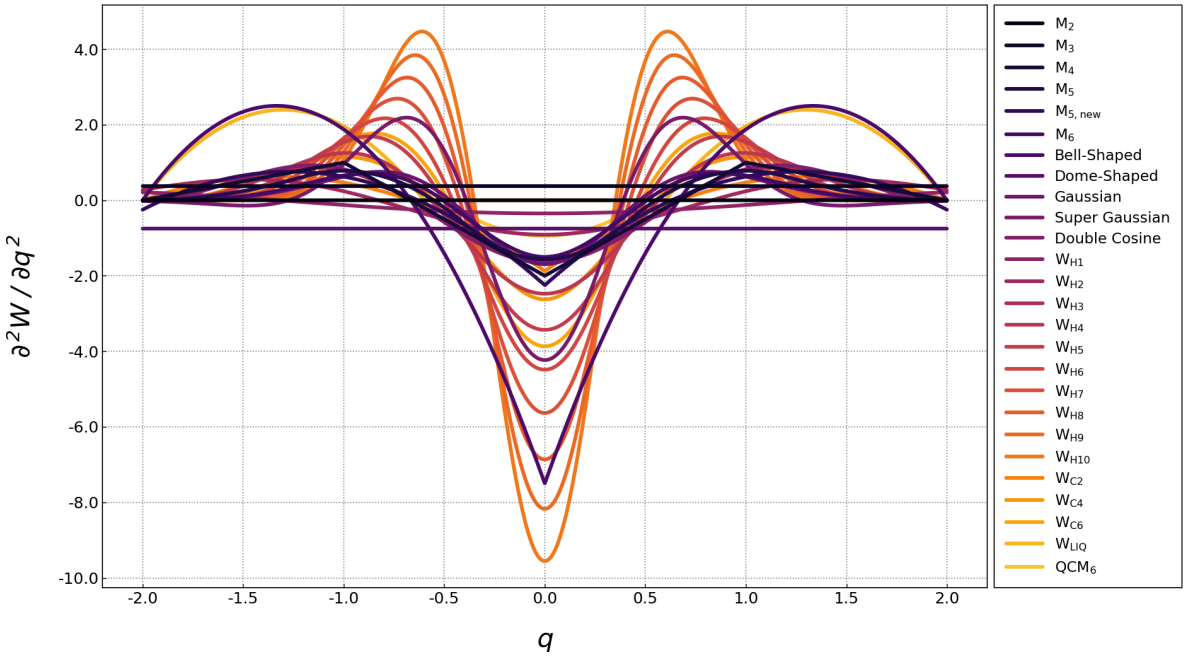

Fig. 2.34. Comparison of second derivatives of kernels, $\kappa = 2$.

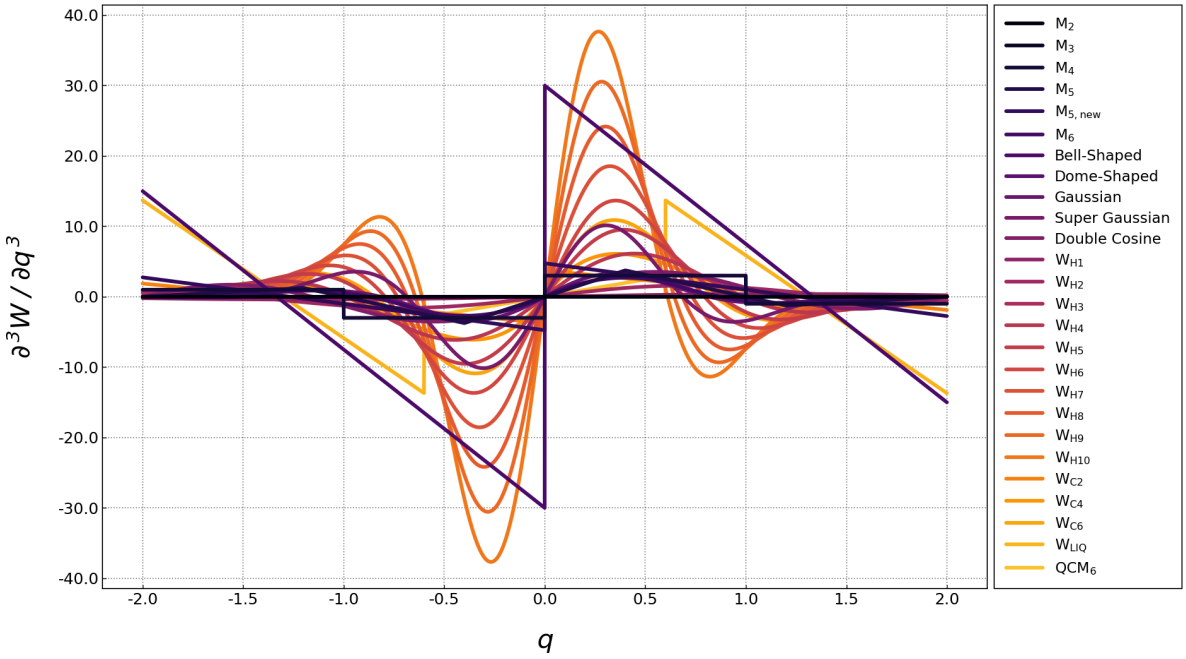

Fig. 2.35. Comparison of third derivatives of kernels, $\kappa = 2$.

The second derivative of a kernel is very important in structural mechanics, especially when ductile failure is simulated, e.g. steel reinforcement in tension. It is not directly related to PDEs but as will be shown in section *Tensile Instability*, the values of the second derivative are important indicator of numerical fractures. The comparison of the second derivatives is shown in Fig. 2.34. The third derivatives are not directly used in structural mechanics, yet the smoothness is one of the indicators for general accuracy. As obvious in Fig. 2.35 the harmonic kernels, e.g. W_{H3}, is rather a smooth function compared to the cubic spline M_4 which is only a piece-wise constant function. Yet they are both very similar when it comes to the base function.

2.4.2 Eulerian and Lagrangian Kernel

The shape of the support domain does not have to be spherical. However, spherical shapes are used the most in the SPH community. There are two kernel types which are closely related to the shape definition; the so-called Eulerian and Lagrangian kernels. The concept here is somehow similar to the Eulerian and Lagrangian meshes used in FEM. In FEM, if the mesh is fixed in space and material flows through it, the mesh is so-called Eulerian. In contrast, if the mesh is fixed to material, moves and deforms with it, the mesh is so-called Lagrangian. Since there is no mesh in SPH the definition is different yet as said related.

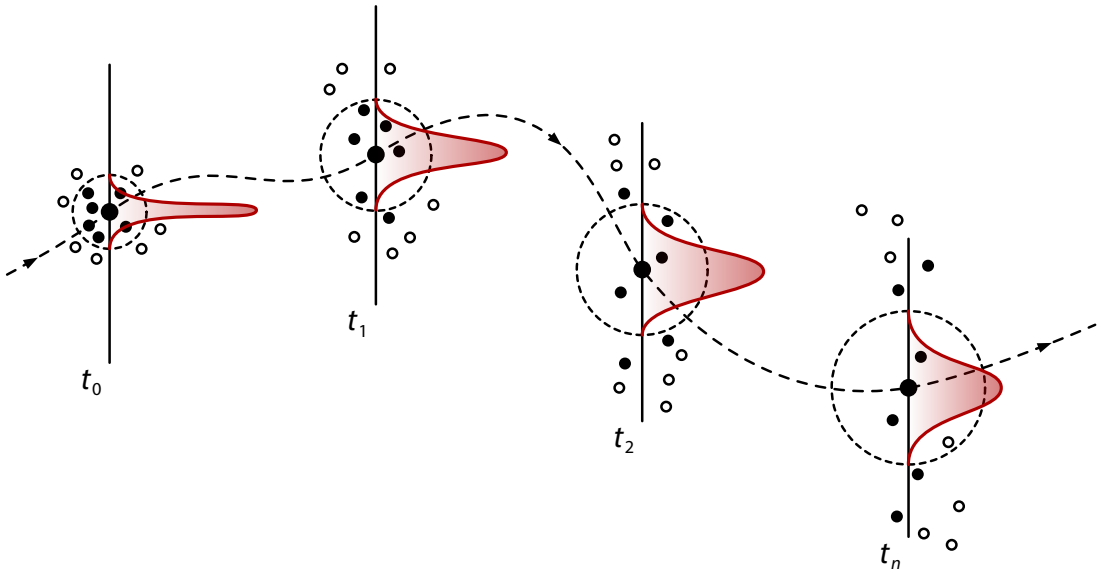

Fig. 2.36. Isotropic Eulerian kernel.

In SPH, each particle has its own support domain, the support is fixed to the particle. If neighbouring particles can enter and exit the support domain, the kernel is so-called Eulerian. This is similar to the FEM concept, since the support domain is fixed and material flows through it. In contrast, if neighbouring particles are fixed to the support domain, which means they cannot exit or change their initially assigned support domain, the kernel is so-called Lagrangian. In other words, the support domain of the Lagrangian kernel deforms as the particles move in the problem domain.

The size of the support domain does not have to be constant in time or space. The size adaptivity is discussed in section *Variable Smoothing Length* in detail. At this point, it is simply assumed that the size of the support varies to keep the number of neighbouring particles constant. In Fig. 2.36, an example of a development in time of the isotropic Eulerian kernel is shown. At time t_0 the initialization starts with the neighbouring particles search. The particles within the support domain are black and represent the initial neighbouring particles. As particles start to move, the size of the support domain increases. However, nothing exists to prevent particles from entering and exiting the support domain, therefore, the number of neighbouring particles is not constant in time. This is especially true when deformation is not isotropic.

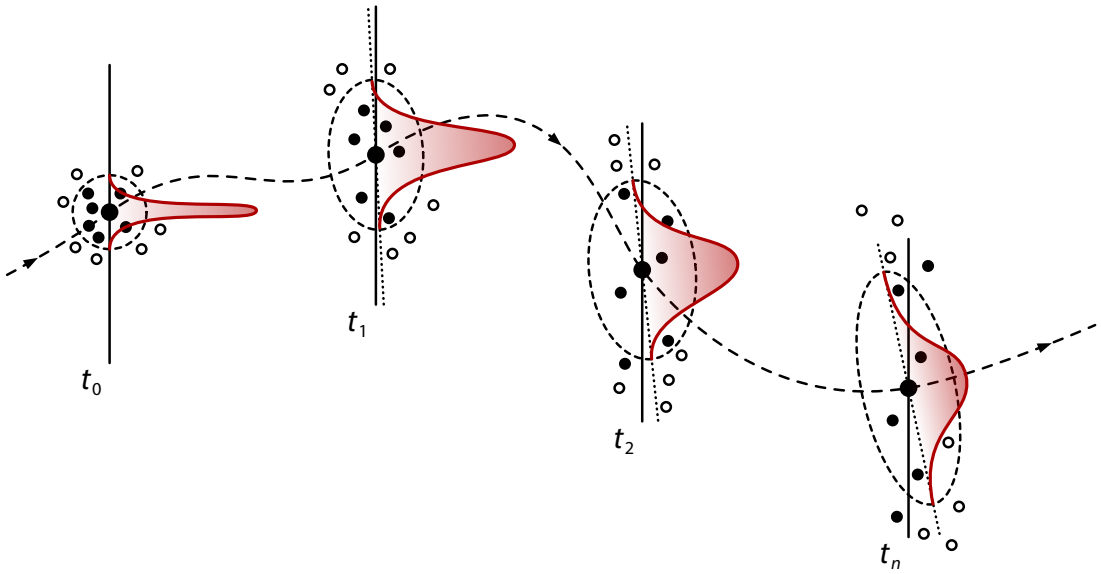

Fig. 2.37. Anisotropic Eulerian kernel.

Majority of problems in structural dynamics are nonlinear, however. This means, that deformations are anisotropic and the motion of particles might be dominant in only one direction. In order to improve the accuracy of SPH, the anisotropic Eulerian kernel was proposed in [148]. The idea is that the kernel is no longer spherical but rather ellipsoidal. This concept leads to adaptive Smoothed Particle Hydrodynamics (ASPH), which is discussed in section *ASPH* in detail. In 2D, the support is an ellipse. In 3D, the support is an ellipsoid. The major axis of the ellipse or ellipsoid is oriented in the direction of material flow. In Fig. 2.37, an example of a development in time of the anisotropic Eulerian kernel is shown. Compared to the isotropic Eulerian kernel, the number of particles within the support domain might be constant, yet it is not a rule.

The Lagrangian kernel is based on a different concept. In the first step, at time t_0, neighbouring particles are found for each particle. The list of the neighbouring particles is not updated during the simulation, however. This means that the support domain follows its initial neighbouring particles and deforms. An example is shown in Fig. 2.38. As the particles start to move the support starts to deform. The number of particles within the support is constant, however. Since every particle has sufficient number of neighbours, accuracy is improved. Furthermore, the concept of the Lagrangian kernel prevents the tensile instability since particle clustering is alleviated. Disadvantage is that SPH is no

longer adaptive, since the list of the neighbouring particles is not updated. If the condition that the neighbouring particle list cannot be updated is rigorous, the Lagrangian kernel is said to be total Lagrangian.

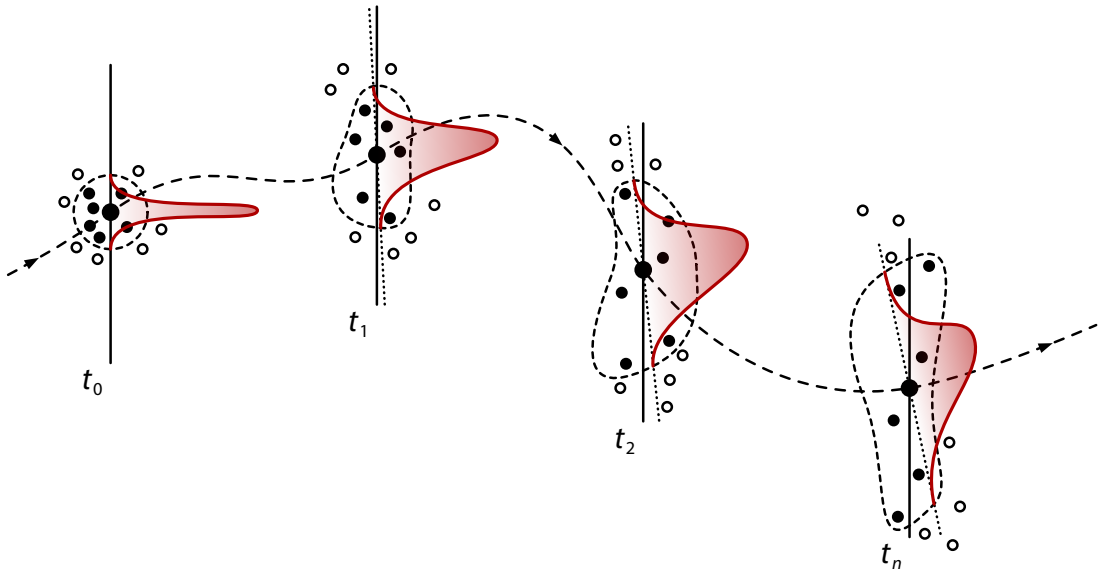

Fig. 2.38. Total Lagrangian kernel.

Again, with analogy to FEM, if there is the total Lagrangian kernel, is there an updated Lagrangian kernel? Yes, there is. But the concept of the updated Lagrangian somehow overlaps with the anisotropic Eulerian kernel. The updated Lagrangian kernel updates neighbouring particles, i.e. it is allowed to particles to enter and exit the support, but the update is not necessary every time step.

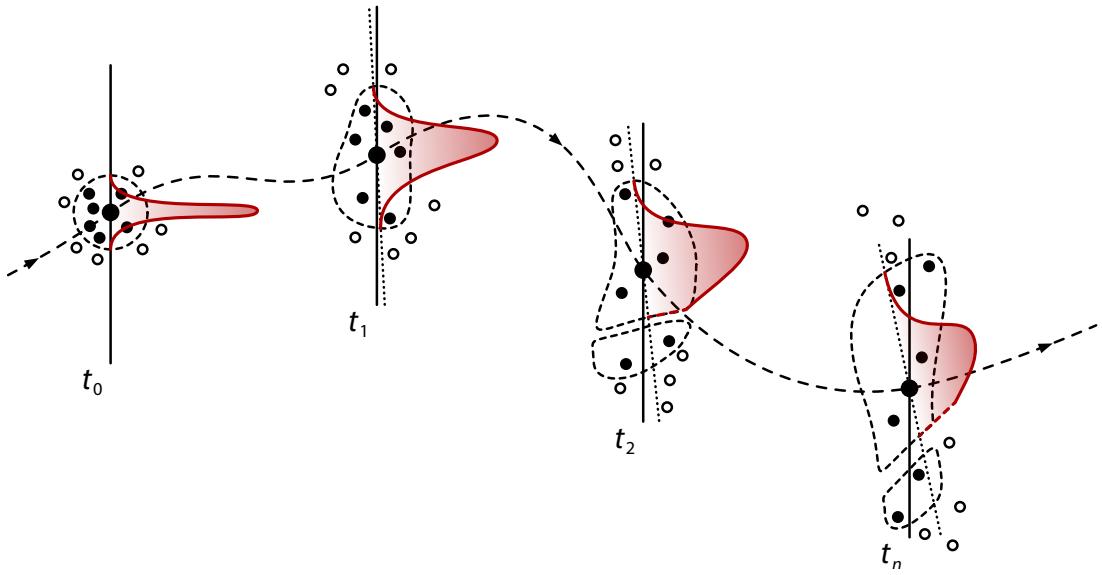

Fig. 2.39. Pseudo Lagrangian kernel.

The author's opinion is, that if particles can enter and exit the support domain, the kernel should be referred to as Eulerian. Interestingly enough, there is the so-called pseudo

Lagrangian kernel which is used when the support domain is truncated. For example, in solid mechanics, when a crack starts to propagate through material in such a way that the support domain is truncated, the initial neighbouring particle list is updated so that the particles separated by the discontinuity are no longer taken into the consideration. By definition, the pseudo Lagrangian kernel acts as a combined Eulerian-Lagrangian kernel. An example of the pseudo Lagrangian kernel development in time is shown in Fig. 2.39 in which a crack appears at time t_2 and truncates the support domain.

2.4.3 Gather and Scatter Concept

So far it was said that the value of a field function at particle i is averaged from values at neighbouring particles. This idea corresponds to the *gather* concept. In other words, only particles within the support domain of particle i have an influence on it. However, there is another concept which uses the so-called *influence domain* rather than the *support domain*. In the *scatter* concept, the logic of neighbouring particles selection is understood in the opposite way. Neighbouring particles of particle i are not those in its support domain. Particle j is neighbouring only if particle i is within its influence domain. The value of a field function at particle i is again averaged from its neighbouring particles, which are, however, defined differently.

- In the **gather** concept, particle i gathers the contributions from all particles which centres fall within the smoothing volume of particle i, i.e. $W(|\boldsymbol{x}_i - \boldsymbol{x}_j|, h_i)$ in the summation.
- In the **scatter** concept, particle i collects the contributions from all other particles j which smoothing volumes scatter onto location of particle i, i.e. $W(|\boldsymbol{x}_i - \boldsymbol{x}_j|, h_j)$ in the summation.

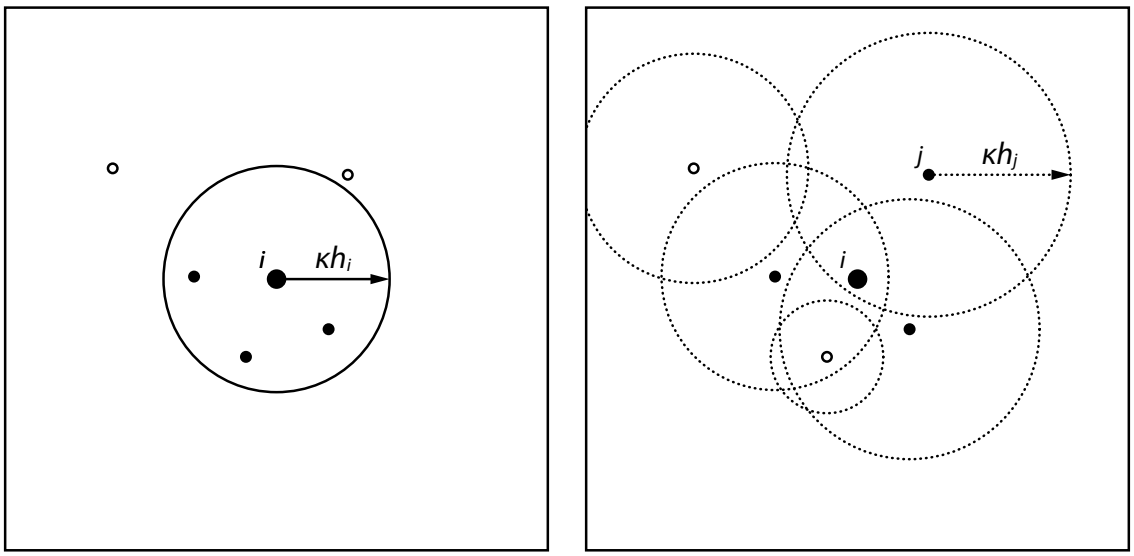

(a) gather concept (support domain) (b) scatter concept (influence domain)

Fig. 2.40. Comparison of the gather and scatter concept.

A visual demonstration can be seen in Fig. 2.40 in which particle i is placed in the centre of the problem domain, visualized with its support domain as a solid circle in case of the gather concept. The rest of the particles are particles j. In case of the scatter concept, all particles j have drawn their influence domain as a dotted circle.

In the case of the gather concept, three black particles are within the support domain of particle i. The top two particles j are outside the support and therefore without fill because they do not contribute to particle i. The size of the support domain is defined as κh_i.

In the case of the scatter concept, three particles j are black filled again. However, the neighbouring particles are defined with the influence domain and whether particle i is within their reach or not. The influence domain is defined as κh_j. In contrast to the gather concept, the bottom particle j no longer contributes to particle i, yet the top right particle j does.

In practice, the gather concept is used rather than the scatter concept. The reason for this is that in the gather concept the neighbouring particle search is done in easier way. Yet to fulfil the Newton's third law it cannot happen that in a pair of particles only one influences the other. That would mean the interaction forces are transferred in only one direction. The solution is to average the smoothing length of both which can result in either i) particles interact or ii) particles do not interact. If $h_i = h_j$ is taken, the support and influence domains are of the same size, therefore, the gather and scatter concepts are no different. Both concepts are discussed in detail in [141, 148] or [85].

2.4.4 Variable Smoothing Length

As outlined, the accuracy of SPH depends not only on the kernel but also on the number of neighbouring particles within the support domain. In optimal case, the number of neighbouring particles should remain constant. That means, if particles move from each other, the support domain should expand and if particles move closer to each other, the support domain should contract. This is not always possible since the stress state is not always hydrostatic. In structural dynamics, the stress field is usually anisotropic, therefore, deformation is anisotropic as well. For that reason, it is quite difficult to keep the number of neighbouring particles constant.

There are many ways to define the smoothing length h as a function of time and space. In early applications of SPH, a global smoothing length was used. It was based on initial average density of the system [85]. Since the global smoothing length was not able to capture local expansions or contractions of particle distributions, an individual smoothing length of each particle based on local density was introduced [12, 20]. The concept worked for isotropic deformations stable in time, but was not sufficient for anisotropic problems like a propagation of a shock wave. Therefore, some concepts of a fully dynamic development of the support domain were introduced for the isotropic Eulerian kernel [141, 149, 150].

Varying the size of the support domain in space and time proved to be a very promising approach. After all, the accuracy of SPH increased. The same technique was also applied to the anisotropic Eulerian kernel for which a smoothing length tensor rather than a

constant was used [148, 151]. The concept of the anisotropic Eulerian kernel was based on an ellipsoidal kernel rather than the traditional spherical kernel, and is closely related to ASPH.

The question is, what is the correct number of neighbouring particles? The author's opinion is, there is no general answer. Yet after decades of working with SPH, a quote from Morris seems to be still the best answer so far.

> *In one dimension, the number of neighbours (including the "home" particle itself) should be about 5. In two dimensions, it should be about 21 and in three dimensions, about 57. These numbers all correspond to the number of neighbours on a cubic lattice with a smoothing length of 1.2 times the particle spacing, and a kernel which extends to 2h (such as the cubic spline).* [37]

From what Morris had written, the optimal smoothing length is $h = 1.2\,\Delta x$ and $\kappa = 2$, where Δx is the particle spacing in a cubic lattice. This can be seen in Fig. 2.41 in which such a support domain is shown in 2D.

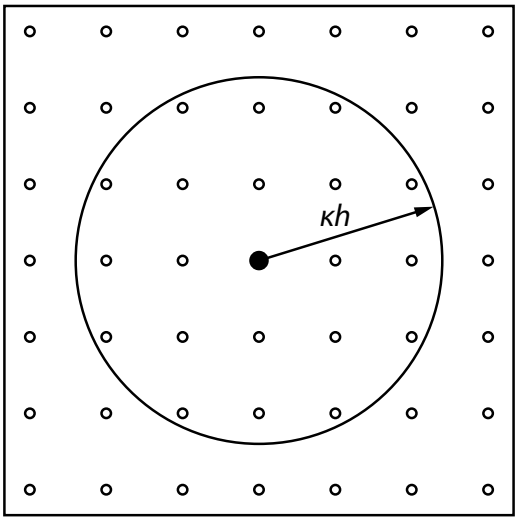

Fig. 2.41. Recommended size of the support domain in 2D for a cubic lattice particle distribution, $h = 1.2\,\Delta x$ and $\kappa = 2$.

There are many ways to dynamically change the size of the support domain, or just the smoothing length if κ is considered to be a constant throughout the simulation. The simplest approach proposed in [37] is to let

$$h = h_0 \left(\frac{\rho_0}{\rho} \right)^{1/d}, \tag{2.4.35}$$

where h_0 and ρ_0 are the initial smoothing length and initial density, respectively. The h and ρ are the current smoothing length and current density, respectively. The number

of dimensions is introduced with the constant d. The approach in (2.4.35) is sufficient if masses of particles are equal. To be able to calculate h, density ρ must be known, however. This is of course a problem, since only known density is from the previous step. As a consequence, the update of the smoothing length is too slow and thus not applicable to a shock wave propagations.

Benz [14] proposed an alternative approach, based on derivative of (2.4.35) and the continuity equation. The formulation which is nowadays implemented in almost every commercial solver was defined as

$$\frac{dh}{dt} = -\frac{1}{d}\frac{h}{\rho}\frac{d\rho}{dt} = \frac{1}{d}h\nabla \cdot \boldsymbol{v}, \tag{2.4.36}$$

where $\nabla \cdot \boldsymbol{v}$ is the divergence of the velocity field. In practice, (2.4.36) is added to the system of equations to be solved at each time step [15]. In some cases $\nabla \cdot \boldsymbol{v}$ has to be computed anyway so that no additional time is necessary [15]. To decrease the rate of the smoothing function change, modified formulation in [152] was proposed so that

$$\frac{dh}{dt} = -\frac{1}{d}\frac{h}{\rho}\frac{d\rho}{dt} = \frac{1}{d}h(\nabla \cdot \boldsymbol{v})^{1/3}. \tag{2.4.37}$$

Using dynamic smoothing lengths might result in a completely random number of neighbouring particles per particle. Therefore, it could happen that in a pair of particles, only one particle influences the other, yet not otherwise around since the smoothing length of both might not be equal. However, that would be (again) a violation of the Newton's third law. If momentum should be conserved exactly, the symmetry of particle interactions must be established. This can be done by modifying (2.3.24) as

$$W_{ij} = W(\boldsymbol{x}_i - \boldsymbol{x}_j, h_{ij}), \tag{2.4.38}$$

where h_{ij} can be found as

$$h_{ij} = \frac{1}{2}(h_i + h_j), \tag{2.4.39}$$

which represents the arithmetic mean. However, if for some reason $h_i \gg h_j$ and therefore $h_{ij} \approx 1/2h_i$, then it can overly smooth out interactions with surrounding particles. The geometric mean can be taken instead so that

$$h_{ij} = \frac{2h_i h_j}{h_i + h_j}. \tag{2.4.40}$$

The geometric mean might be a better choice in some cases, however, if again $h_i \gg h_j$ and therefore $h_{ij} \approx 2h_j$, then it could be that there is not enough neighbouring particles to capture global behaviour. Another possible solution is to use maximum of the smoothing lengths as

$$h_{ij} = \max(h_i, h_j), \tag{2.4.41}$$

or minimum of the smoothing lengths as

$$h_{ij} = \min(h_i, h_j). \tag{2.4.42}$$

In case of the maximum (2.4.41), the same as for the arithmetic mean applies. The support domain can be too big and smeared out local spikes. In case of the minimum (2.4.42), the same as for the geometric mean applies again. The resulting support domain might be too small to capture global behaviour.

Another approach would be to use an average of the kernel values as also used in (2.3.32). The idea was first introduced in [141] and it was suggested that averaged should be directly the kernel values as

$$W_{ij} = \frac{1}{2}\big[W(\boldsymbol{x}_i - \boldsymbol{x}_j, h_i) + W(\boldsymbol{x}_i - \boldsymbol{x}_j, h_j)\big], \tag{2.4.43}$$

to preserve the symmetry of the particle interaction. It must be pointed out, that even though the averaging of the smoothing lengths or the kernel values is introduced, it is not entirely consistent to allow h to vary in space and time. The original SPH equations of motion were derived assuming h was a constant [37]. To utilize the introduced in the best possible way, limits based on the problem should be defined. For example, the limit case based on the initial smoothing length as

$$h_0\,\eta_{min} < h < h_0\,\eta_{max}, \tag{2.4.44}$$

where η_{min} and η_{max} are the multipliers of the initial smoothing length h_0. With (2.4.44), at least some development limits in time and space of h are defined. This technique is used in [152].

2.5 Kernel Accuracy

Lower, mid, and higher order kernels were discussed, yet it would be misleading to assume that with higher order kernels more accurate results can be expected. Every kernel has its own advantage which goes hand in hand with the size of the support domain and number

of neighbouring particles. To be able to determine if a specific kernel is a good choice, general conditions of the kernel construction should be discussed first.

As shown in [85] and [125], if a function should be reproduced to nth order accuracy with a kernel, then the following conditions should be satisfied.

$$\begin{aligned}
\mu_0 &= \int_\Omega W(\boldsymbol{x}-\boldsymbol{x}',h)\,d\boldsymbol{x}' = 1 \\
\mu_1 &= \int_\Omega (\boldsymbol{x}-\boldsymbol{x}')W(\boldsymbol{x}-\boldsymbol{x}',h)\,d\boldsymbol{x}' = 0 \\
\mu_2 &= \int_\Omega (\boldsymbol{x}-\boldsymbol{x}')^2 W(\boldsymbol{x}-\boldsymbol{x}',h)\,d\boldsymbol{x}' = 0 \\
&\vdots \\
\mu_n &= \int_\Omega (\boldsymbol{x}-\boldsymbol{x}')^n W(\boldsymbol{x}-\boldsymbol{x}',h)\,d\boldsymbol{x}' = 0
\end{aligned} \tag{2.5.1}$$

Expressions in (2.5.1) are nothing else than moments of a function. Interestingly enough, the first expression is the first kernel condition, the normalization condition (2.4.1). The second expression in (2.5.1) was also already discussed when the error of the kernel approximation was derived in (2.3.11) and when the sixth kernel condition was defined (2.4.7). It was said, that a kernel should be an even (symmetric) function to have its first moment zero. In other words, the second expression in (2.5.1) is an odd function. Satisfying the moments of the kernel up to nth order, the function approximation is said to be of nth order accurate.

To approximate derivatives of a function, derivatives of the kernel must vanish at its boundary as also discussed in [85, 125]. Following the idea in (2.5.1), the surface integrals must satisfy

$$\begin{aligned}
&\int_S W(\boldsymbol{x}-\boldsymbol{x}',h)\cdot\boldsymbol{n}\,dS = 0 \\
&\int_S W'(\boldsymbol{x}-\boldsymbol{x}',h)\cdot\boldsymbol{n}\,dS = 0 \\
&\vdots \\
&\int_S W^{k-1}(\boldsymbol{x}-\boldsymbol{x}',h)\cdot\boldsymbol{n}\,dS = 0
\end{aligned} \tag{2.5.2}$$

where $\boldsymbol{n}$ is the unit vector normal to the surface S, see also (2.3.16). The expressions in (2.5.2) can be understood in the following way. For the first derivative of a function to be exactly reproduced, the kernel should have a compact support. For the second derivative of a function to be exactly reproduced, the first derivative of the kernel should also be

compactly supported over the same support domain [85, 125]. The same applies for higher derivatives as well.

In general, satisfying conditions in (2.5.1) leads to nth order approximation accuracy of a function. And satisfying conditions in (2.5.2) leads to nth order approximation accuracy of kth derivative of a function. Yet the question again, which kernel to choose? From the expressions in (2.5.1) and (2.5.2) it is clear that more conditions kernel satisfies, more accurate results can be expected. In a special case, when two kernels are compared and both do not satisfy a condition, e.g. their second moment is not exactly zero, then the kernel with a lower value should have better accuracy, therefore, be a better choice.

2.6 Consistency of the Kernel Approximation

The equations in (2.5.1) can be further used for the consistency of the kernel approximation derivation. The consistency concept was briefly discussed in section *Kernel* in which the most important kernel conditions were defined. It was said that the smoothness can be related to the consistency concept C^n in the traditional FEM. To exactly reproduce a function, the kernel should satisfy some conditions, which can be represented by the polynomial reproducibility of the kernel approximation [85].

That said, for a constant (zero order polynomial) field function $f(\boldsymbol{x}) = a$ to be exactly reproduced by the SPH kernel approximation [85], the following condition should be satisfied

$$\langle f(\boldsymbol{x})\rangle = \int_{\Omega} a\, W(\boldsymbol{x}-\boldsymbol{x}', h)\, d\boldsymbol{x}' = a, \tag{2.6.1}$$

which can be modified into the form of the normalization condition as

$$\int_{\Omega} W(\boldsymbol{x}-\boldsymbol{x}', h)\, d\boldsymbol{x}' = 1. \tag{2.6.2}$$

This in other words means, that if the kernel satisfies the normalization condition, the kernel approximation is zeroth order consistent, C^0. If a linear function $f(\boldsymbol{x}) = a_0 + a_1\boldsymbol{x}$ should be reproduced, the condition is defined as

$$\langle f(\boldsymbol{x})\rangle = \int_{\Omega} (a_0 + a_1\boldsymbol{x}')W(\boldsymbol{x}-\boldsymbol{x}', h)\, d\boldsymbol{x}' = a_0 + a_1\boldsymbol{x}, \tag{2.6.3}$$

which can be simplified into the form of

$$\int_{\Omega} \boldsymbol{x}' W(\boldsymbol{x} - \boldsymbol{x}', h)\, d\boldsymbol{x}' = \boldsymbol{x}. \tag{2.6.4}$$

If both sides of (2.6.2) are multiplied by $\boldsymbol{x}$ so that

$$\int_{\Omega} \boldsymbol{x} W(\boldsymbol{x} - \boldsymbol{x}', h)\, d\boldsymbol{x}' = \boldsymbol{x}, \tag{2.6.5}$$

and (2.6.4) is subtracted, then the condition for the linear function reproducibility yields

$$\int_{\Omega} (\boldsymbol{x} - \boldsymbol{x}') W(\boldsymbol{x} - \boldsymbol{x}', h)\, d\boldsymbol{x}' = 0. \tag{2.6.6}$$

The condition for the linear function reproducibility is nothing else than the first moment of the kernel μ_1. Therefore, if the kernel is symmetric, its first moment vanishes and the kernel approximation is C^1 consistent. It can be shown [85, 125], that for higher order polynomials reproducibility, the following condition must be satisfied

$$\int_{\Omega} (\boldsymbol{x} - \boldsymbol{x}')^n W(\boldsymbol{x} - \boldsymbol{x}', h)\, d\boldsymbol{x}' = 0, \tag{2.6.7}$$

which is nothing else than a higher order moment condition. In other words, if nth order moment of a kernel vanishes, the kernel approximation is C^n consistent.

2.7 Consistency of the Particle Approximation

In practice, to verify the consistency of the particle approximation, the continuous forms of the kernel approximation are converted into discrete. In order to do so, the integral becomes a summation over neighbouring particles. It must be pointed out, that if a kernel satisfies the conditions in (2.6.2) for C^0 and in (2.6.7) for higher order C^n, it does not necessarily mean that the same applies for the discrete forms. As an example, the conditions for C^0 and C^1 consistency are discussed. For C^0 consistency, the discrete formulation reads

$$\sum_{j=1}^{N} W(\boldsymbol{x} - \boldsymbol{x}_j, h) \Delta V_j = 1, \tag{2.7.1}$$

where N is the number of particles within the support domain (including particle i), and ΔV_j is the volume of particle j. For the linear consistency condition, the discrete form is defined as

$$\sum_{j=1}^{N}(\boldsymbol{x}-\boldsymbol{x}_j)W(\boldsymbol{x}-\boldsymbol{x}_j,h)\Delta V_j = 0. \tag{2.7.2}$$

To satisfy the consistency conditions, not only the kernel is important, but also the number of neighbouring particles within the support domain and their distribution. A typical example is shown in Fig. 2.42 in which particles have a uniform distribution, non-uniform distribution, and uniform distribution but within a truncated kernel.

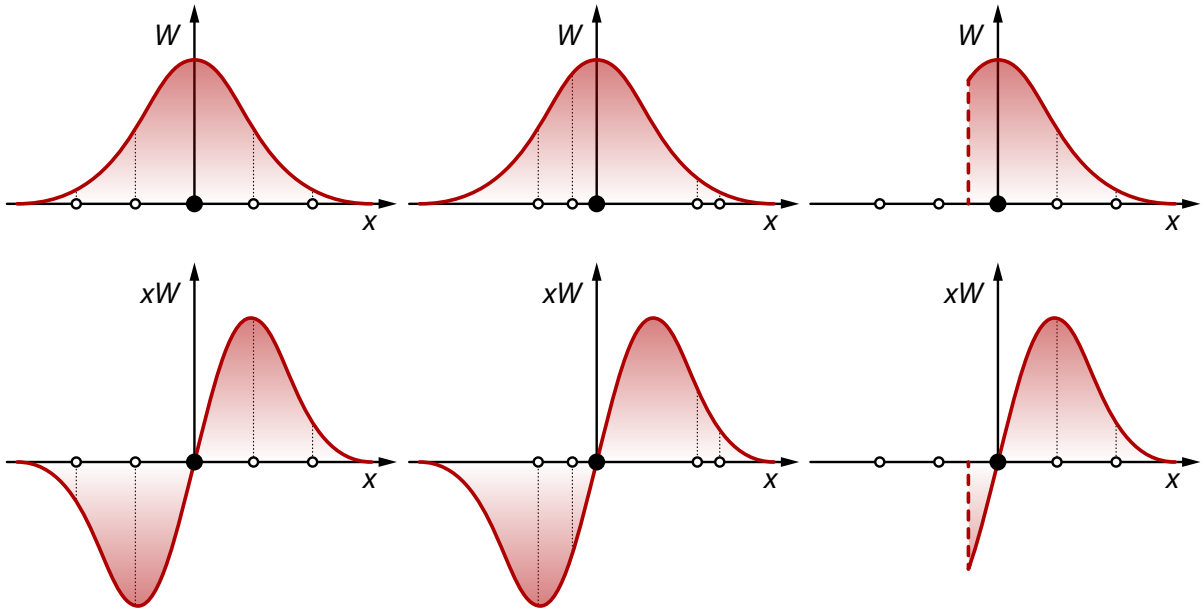

(a) uniform distribution (b) non-uniform distribution (c) truncated kernel

Fig. 2.42. Particle distribution within a support domain.

Starting with the uniform distribution in Fig. 2.42; to be C^0 consistent the number of neighbouring particles must be large enough to minimize the discretization error. To satisfy the C^0 condition exactly, $N \longrightarrow \infty$, see [153, 154]. If the distribution is uniform and symmetric, the C^1 condition is satisfied. In case of the non-uniform distribution, both conditions are satisfied only if $N \longrightarrow \infty$, which means that the non-uniform particle distribution becomes uniform again. In case of the truncated kernel, neither condition is satisfied.

That said, SPH is not even C^0 consistent in the particle approximation without a special treatment. The described problem is often referred to as *particle inconsistency* [37, 40, 85, 107]. Some techniques for improving the particle consistency are discussed in section *SPH Corrections*.

2.8 Conservation Laws

Since the idea of the thesis is to present the application of SPH in very specific part of structural dynamics, the focus of the section is on the conservation equations of continuum mechanics with an emphasis on material strength (with physical strength as previously discussed). In the following equations it was assumed that there is no body force, no mass and heat sources, no chemical potentials, no diffusion process, and no heat conduction involved [87]. That said, the conservation equations of continuum mechanics are the continuity equation

$$\frac{d\rho}{dt} = -\rho \nabla \cdot \boldsymbol{v}, \tag{2.8.1}$$

the momentum equation

$$\frac{d\boldsymbol{v}}{dt} = -\frac{1}{\rho} \nabla \cdot \boldsymbol{\sigma}, \tag{2.8.2}$$

the energy equation

$$\frac{de}{dt} = -\frac{1}{\rho} \boldsymbol{\sigma} : \nabla \otimes \boldsymbol{v}, \tag{2.8.3}$$

where

$$\frac{d\boldsymbol{x}}{dt} = \boldsymbol{v}. \tag{2.8.4}$$

In the equations $\boldsymbol{v}$ is the velocity vector, e is the specific internal energy, and $\boldsymbol{\sigma}$ is the total or Cauchy stress tensor with a minus sign (negative Cauchy stress), which has been a convention in SPH literature [87] (symbol $\boldsymbol{\sigma}^{+}$ is used for the standard Cauchy stress without a minus sign; discussed in section *Constitutive Modelling* in detail). The energy equation (2.8.3) was obtained by subtracting the mechanical energy balance law from the general energy equation [87].

As it might be preferable, the conservation equations follow also in terms of the tensor (superscripted) notation in which (assuming summation on repeated indices) $\boldsymbol{a} = (a^{\alpha\beta\cdots})$ denotes vector and tensor quantities; $\boldsymbol{a} \cdot \boldsymbol{b} = (a^{\alpha\cdots\beta}\, b^{\beta\cdots\gamma})$ the single inner (dot) product; $\boldsymbol{a} : \boldsymbol{b} = (a^{\alpha\cdots\beta\gamma}\, b^{\beta\gamma\cdots\mu})$ the double inner product; and $\boldsymbol{a} \otimes \boldsymbol{b} = (a^{\alpha\cdots\beta}\, b^{\gamma\cdots\mu})$ the tensor (outer) product. The 'del' operator is $\nabla = (\partial/\partial x^{\alpha})$. Then again, the conservation equations of continuum mechanics are the continuity equation

$$\frac{d\rho}{dt} = -\rho \frac{\partial v^{\beta}}{\partial x^{\beta}}, \tag{2.8.5}$$

the momentum equation

$$\frac{dv^{\alpha}}{dt} = -\frac{1}{\rho}\frac{\partial \sigma^{\alpha\beta}}{\partial x^{\beta}}, \tag{2.8.6}$$

the energy equation

$$\frac{de}{dt} = -\frac{\sigma^{\alpha\beta}}{\rho}\frac{\partial v^{\alpha}}{\partial x^{\beta}}, \tag{2.8.7}$$

where

$$\frac{dx^{\alpha}}{dt} = v^{\alpha}. \tag{2.8.8}$$

Dependent variables are the scalar density ρ, the specific internal energy e, the velocity vector v^{α}, and the total stress tensor $\sigma^{\alpha\beta}$. The independent variables are the spatial coordinates x and the time t. The total time derivative d/dt (or substantial derivative, material derivative, global derivative) is taken in the moving Lagrangian frame [21, 22]. The Greek superscripts $\alpha, \beta, \ldots$ are used to denote the coordinate directions, while the summation in the equations is taken over repeated indices.

There are many ways to transform the conservation equations into the SPH approximation. In section *Mathematical Background* several formulations were derived. The formulations can be understood as approximation rules. For example, derivatives of field functions are needed to create the particle approximation of the continuity equation in (2.8.1). The approximation in (2.3.27) can be used for such a purpose. However, the asymmetric approximation in (2.3.34) or the symmetric formulation in (2.3.36) and (2.3.39) can be used instead. Nevertheless, the direct density calculation as described in section *Direct Density Calculation* might be preferred in some cases. Of course, it always depends on the application, there is no general rule. To improve legibility, the approximation equations are written without the SPH kernel approximation operator $\langle\ \rangle$.

2.8.1 The Continuity Equation

Starting with the continuity equation; when the SPH approximation is applied only to the velocity divergence while the density is evaluated on the particle at which the gradient is calculated, then the SPH approximation reads

$$\frac{d\rho_i}{dt} = -\rho_i \sum_{j=1}^{N} \frac{m_j}{\rho_j} v_j^{\beta} \frac{\partial W_{ij}}{\partial x_i^{\beta}}. \tag{2.8.9}$$

Under some circumstances, such as nearly incompressible flow [25], it is advantageous to use the approximation in (2.3.34), however [37]. Then the SPH approximation of the continuity equation reads

$$\frac{d\rho_i}{dt} = \sum_{j=1}^{N} m_j v_{ij}^{\beta} \frac{\partial W_{ij}}{\partial x_i^{\beta}}. \tag{2.8.10}$$

Normally the density must be obtained first by a sum over all the particles before other quantities may be interpolated (involving a second pass over the particles) [37]. Having a differential equation for ρ means that it can be updated at the same time as other particle quantities and only one pass over the particles is required to obtain all the required information [37]. The main disadvantage is that (2.8.10) does not conserve mass exactly, but this does not cause problems in many applications [37]. It can be computationally advantageous to use (2.8.10) for several time steps and then correct the density by using (2.3.31) or (2.3.32) [37]. Note that the sign in (2.8.10) was changed since

$$v_{ij}^{\beta} = v_i^{\beta} - v_j^{\beta}, \tag{2.8.11}$$

which has the opposite logic to (2.3.34). Interestingly enough, as pointed out in [85], when the integral of the kernel gradient is taken as

$$\int_{\Omega} \nabla W(\boldsymbol{x} - \boldsymbol{x}', h)\, d\boldsymbol{x}' \approx \sum_{j=1}^{N} \frac{m_j}{\rho_j} \frac{\partial W_{ij}}{\partial x_i^{\beta}} = 0, \tag{2.8.12}$$

and rewritten into the form of

$$\rho_i \sum_{j=1}^{N} \frac{m_j}{\rho_j} v_i^{\beta} \frac{\partial W_{ij}}{\partial x_i^{\beta}} = \rho_i v_i^{\beta} \sum_{j=1}^{N} \frac{m_j}{\rho_j} \frac{\partial W_{ij}}{\partial x_i^{\beta}}, \tag{2.8.13}$$

which is zero, then added to (2.8.9), another formulation of the density approximation is derived as

$$\frac{d\rho_i}{dt} = \rho_i \sum_{j=1}^{N} \frac{m_j}{\rho_j} v_{ij}^{\beta} \frac{\partial W_{ij}}{\partial x_i^{\beta}}. \tag{2.8.14}$$

Furthermore, as discussed in [21, 22], when the differentiation is carried out directly on (2.3.31), the SPH approximation leads to

$$\frac{d\rho_i}{dt} = \rho_i \sum_{j=1}^{N} \frac{m_j}{\rho_i} v_{ij}^{\beta} \frac{\partial W_{ij}}{\partial x_i^{\beta}}, \tag{2.8.15}$$

which differs from (2.8.14) only in that ρ_i appears in the denominator rather than ρ_j, therefore, is in fact (2.8.10) if the density does not change over the time step significantly. The effect of using (2.8.15) instead of (2.8.14) was not yet examined [21, 22]. In general, introducing the velocity difference into the discrete particle approximation results in an error reduction arising from the particle inconsistency problem, see [4, 7, 12] and [85].

2.8.2 The Momentum Equation

The momentum equation can be approximated in the same way as the continuity equation. Using the simplest assumption, (2.8.6) is taken and approximated with (2.3.27). Then the momentum equation in the SPH approximation reads

$$\frac{dv_i^{\alpha}}{dt} = -\frac{1}{\rho_i} \sum_{j=1}^{N} m_j \frac{\sigma_j^{\alpha\beta}}{\rho_j} \frac{\partial W_{ij}}{\partial x_i^{\beta}}. \tag{2.8.16}$$

As discussed in section *Other Formulations*, more accurate approximations can be obtained when the density is placed inside operators as suggested in [20], further discussed in [37], and most importantly used in [35] for the derivation of the stress gradient renormalization. The renormalization is discussed in section *SPH Corrections* in detail. In practice, the approximation in (2.3.34) is taken and applied to the momentum equation so that

$$\frac{dv_i^{\alpha}}{dt} = -\sum_{j=1}^{N} \frac{m_j}{\rho_i \rho_j} (\sigma_j^{\alpha\beta} - \sigma_i^{\alpha\beta}) \frac{\partial W_{ij}}{\partial x_i^{\beta}}, \tag{2.8.17}$$

where the inner force between particles is zero for a constant stress field. However, linear and angular momentum are not conserved exactly [37]. A symmetric formulation can be derived by using (2.3.36), then

$$\frac{dv_i^{\alpha}}{dt} = -\sum_{j=1}^{N} m_j \left(\frac{\sigma_i^{\alpha\beta}}{\rho_i^2} + \frac{\sigma_j^{\alpha\beta}}{\rho_j^2} \right) \frac{\partial W_{ij}}{\partial x_i^{\beta}}. \tag{2.8.18}$$

The advantage of the symmetric formulation is that linear and angular momentum are conserved exactly, since particle forces are equal and opposite and act along the line joining

their centres (provided that the kernel is symmetric) [37]. This form is also preferable because it is quite straightforward to obtain a consistent energy equation [37], and it reduces errors arising from the particle inconsistency [4, 7, 12] and [85]. Of course, many other variants can be derived taking into account the generalized formulation (2.3.38) proposed by Monaghan [20]. Therefore, when (2.3.39) is used, the formulation of the momentum equation reads

$$\frac{dv_i^\alpha}{dt} = -\sum_{j=1}^{N} m_j \left(\frac{\sigma_i^{\alpha\beta} + \sigma_j^{\alpha\beta}}{\rho_i \rho_j} \right) \frac{\partial W_{ij}}{\partial x_i^\beta}. \tag{2.8.19}$$

Interestingly enough, as pointed out in [85], when the same procedure as shown in (2.8.12) is applied to the momentum equation so that

$$\sum_{j=1}^{N} m_j \frac{\sigma_i^{\alpha\beta}}{\rho_i \rho_j} \frac{\partial W_{ij}}{\partial x_i^\beta} = \frac{\sigma_i^{\alpha\beta}}{\rho_i} \sum_{j=1}^{N} \frac{m_j}{\rho_j} \frac{\partial W_{ij}}{\partial x_i^\beta}, \tag{2.8.20}$$

which can be subtracted from (2.8.16) since it is zero, then the formulation in (2.8.19) is obtained. In addition, if the geometric mean is used rather than the arithmetic as described in (2.3.42), then the approximated momentum equation in (2.8.18) reads

$$\frac{dv_i^\alpha}{dt} = -\sum_{j=1}^{N} m_j \frac{2\sqrt{\sigma_i^{\alpha\beta}}\sqrt{\sigma_j^{\alpha\beta}}}{\rho_i \rho_j} \frac{\partial W_{ij}}{\partial x_i^\beta}, \tag{2.8.21}$$

as also discussed in [37]. Other formulations can be found in [87] or [152]. In structural dynamics, the momentum equation plays the most important role. There is no general rule which formulation should be used, however.

2.8.3 The Energy Equation

In some applications, e.g. a detonation of an explosive, internal energy of particles is perhaps more important than their momentum. The idea of the SPH approximation of the energy equation (2.8.7) can again follow what was implied in the continuity and momentum equation. In practice, five variants of the energy equation in the SPH framework are used. Using (2.3.34) the energy equation reads

$$\frac{de_i}{dt} = \frac{\sigma_i^{\alpha\beta}}{\rho_i^2} \sum_{j=1}^{N} m_j v_{ij}^\alpha \frac{\partial W_{ij}}{\partial x_i^\beta}, \tag{2.8.22}$$

which is considered to be the asymmetric formulation [20, 21, 22]. The opposite sign in (2.8.22) was introduced as implied in (2.8.11). The energy equation can be expressed in rather different way, however [20, 37, 87]. By noting that

$$\frac{de}{dt} = -\nabla \cdot \left(\frac{\boldsymbol{\sigma} \cdot \boldsymbol{v}}{\rho} \right) + \boldsymbol{v} \cdot \left(\nabla \cdot \left(\frac{\boldsymbol{\sigma}}{\rho} \right) \right), \tag{2.8.23}$$

the approximation of the energy equation reads

$$\frac{de_i}{dt} = \sum_{j=1}^{N} m_j \frac{\sigma_j^{\alpha\beta}}{\rho_j^2} v_{ij}^{\alpha} \frac{\partial W_{ij}}{\partial x_i^{\beta}}. \tag{2.8.24}$$

Taking into account that the size of the support can differ in an interaction pair, a modified formulation based on (2.8.22) and (2.8.24) can be derived as

$$\frac{de_i}{dt} = \sum_{j=1}^{N} m_j \frac{\sigma_i^{\alpha\beta}}{\rho_i \rho_j} v_{ij}^{\alpha} \frac{\partial W_{ij}}{\partial x_i^{\beta}}. \tag{2.8.25}$$

Equation (2.8.25) was used in [35] for the derivation of the stress gradient renormalization and numerical validations of HVI experiments. The renormalization is discussed in detail in section *SPH Corrections*. The formulation is often used in simulations in which a material behaves like a fluid. However, neither of the equations above conserve energy exactly [20, 79]. To achieve energy conservation, an average of (2.8.22) and (2.8.24) can be taken [20] so that

$$\frac{de_i}{dt} = \frac{1}{2} \sum_{j=1}^{N} m_j \left(\frac{\sigma_i^{\alpha\beta}}{\rho_i^2} + \frac{\sigma_j^{\alpha\beta}}{\rho_j^2} \right) v_{ij}^{\alpha} \frac{\partial W_{ij}}{\partial x_i^{\beta}}. \tag{2.8.26}$$

Using (2.8.26) energy of the discrete system is conserved exactly [20, 37, 79]. Note that the formulation can be also derived using (2.3.36) approximation scheme. As pointed out in [85], another formulation can be simple derived when the product within the parenthesis in (2.8.26) is replaced by the formulation in (2.3.39). Then the SPH approximation reads

$$\frac{de_i}{dt} = \frac{1}{2} \sum_{j=1}^{N} m_j \left(\frac{\sigma_i^{\alpha\beta} + \sigma_j^{\alpha\beta}}{\rho_i \rho_j} \right) v_{ij}^{\alpha} \frac{\partial W_{ij}}{\partial x_i^{\beta}}. \tag{2.8.27}$$

It is important to note that the listed equations are not unique and other formulations can be derived, see [152].

2.9 Artificial Viscosity

When a shock wave propagates through a continuum, thickness of the shock front might be only few molecules. Such a transition layer is often considered to be a discontinuity in physical domain. Without proper treatment, large unphysical oscillations are generated downstream of shocks [37]. In the original formulation of SPH there was no mechanism built in that allows for the dissipation of kinetic energy into heat [15]. Such a mechanism is always present in nature due to the intrinsic viscosity. No matter how small the viscosity is, it will always be sufficient to dissipate kinetic energy in a shock since the gradient of the variables across the shock will adjust itself so as to allow for it [15].

In numerical methods like the Finite Volume Method (FVM), FDM, or FEM, two standard formulations are used to introduce a dissipation into the system. The first one is known as *bulk viscosity*, defined as

$$\Pi_l = \begin{cases} -\alpha_l \rho \Delta x c \nabla \cdot \boldsymbol{v} & \nabla \cdot \boldsymbol{v} < 0 \\ 0 & \text{else,} \end{cases} \tag{2.9.1}$$

and the second is known as *von Neumann-Richtmyer viscosity* [155], defined as

$$\Pi_q = \begin{cases} \beta_q \rho \Delta x^2 (\nabla \cdot \boldsymbol{v})^2 & \nabla \cdot \boldsymbol{v} < 0 \\ 0 & \text{else,} \end{cases} \tag{2.9.2}$$

where α_l and β_q are free parameters, Δx is the typical length scale over which the shock is spread (usually the element size in mesh-based methods and the particle spacing in SPH), and c is the adiabatic sound speed. Note that the bulk viscosity Π_l is linear term and the von Neumann-Richtmyer viscosity Π_q is quadratic. Both terms are necessary only when material is in compression. Since Π_q smooths out discontinuities in quadratic sense of the velocity divergence, not all oscillations are necessarily dampened. For that reason, both terms are very often combined [152]. The artificial viscosity terms are usually added to the physical pressure term, and help to diffuse sharp variations in the flow and to dissipate energy of high frequency term [85, 125].

Strictly speaking of SPH, using (2.9.1) and (2.9.2) does not necessary damp velocity fluctuations on scales smaller than Δx, where usually $\Delta x \approx h$ [15]. To avoid this, Monaghan and Gingold [6] proposed a formulation which provides the necessary dissipation to convert kinetic energy into heat at the shock front, but also prevent unphysical penetration for particles approaching each other [156, 13, 85]. The formulation is known as *Monaghan type artificial viscosity* and is defined as

$$\Pi_{ij} = \begin{cases} \dfrac{-\alpha_l c_{ij} \mu_{ij} + \beta_q \mu_{ij}^2}{\rho_{ij}} & \boldsymbol{v}_{ij} \cdot \boldsymbol{x}_{ij} < 0 \\ 0 & \text{else,} \end{cases} \tag{2.9.3}$$

where

$$\mu_{ij} = \frac{h_{ij}\boldsymbol{v}_{ij} \cdot \boldsymbol{x}_{ij}}{|\boldsymbol{x}_{ij}|^2 + \epsilon h_{ij}^2}, \tag{2.9.4}$$

is the first estimate of the velocity divergence at particle i due to the presence of particle j [15], and

$$c_{ij} = \frac{1}{2}(c_i + c_j), \tag{2.9.5}$$

$$\rho_{ij} = \frac{1}{2}(\rho_i + \rho_j), \tag{2.9.6}$$

$$h_{ij} = \frac{1}{2}(h_i + h_j), \tag{2.9.7}$$

are the averaged values of neighbouring particle pairs, but

$$\boldsymbol{v}_{ij} = \boldsymbol{v}_i - \boldsymbol{v}_j, \tag{2.9.8}$$

$$\boldsymbol{x}_{ij} = \boldsymbol{x}_i - \boldsymbol{x}_j, \tag{2.9.9}$$

are their differences. The term ϵh_{ij}^2 in (2.9.4) is the so-called clipping function [12] and has been added to keep the viscosity bounded for particles as they approach, for small $|\boldsymbol{x}_{ij}|$. It is recommended that $0 < \epsilon \ll 1$ [6], but in practice $\epsilon \lesssim 0.1$. For example, if the clipping function equals $0.01h_{ij}^2$, then the velocity smoothing will only take place if the particle spacing is $< 0.1h$ [20]. The values of α_l and β_q are not critical, but they should be near $\alpha_l = 1$ and $\beta_q = 2$ [20]. However, in literature can be found that $\alpha_l \sim 1$ and $\beta_q \sim 1$ [152], yet $\alpha_l \sim 0.5$ and $\beta_q \sim 1$ in [21, 22].

The term involving $(\boldsymbol{v}_{ij} \cdot \boldsymbol{x}_{ij})^2$ in (2.9.3) was constructed to prevent penetrations in high Mach number collisions by producing an artificial pressure roughly proportional to ρv^2 . The viscosity vanishes for rigid rotations and is Galilean invariant [20, 37].

A modified formulation of (2.9.3) was proposed by Hernquist and Katz [141] to eliminate the presence of artificial viscosity farther away from the shock front. The formulation is defined as

$$\Pi_{ij} = \frac{q_i}{\rho_i^2} + \frac{q_j}{\rho_j^2}, \tag{2.9.10}$$

where

$$q_i = \begin{cases} \alpha_l \rho_i h_i c_i |\nabla \cdot \boldsymbol{v}_i| + \beta_q \rho_i h_i^2 |\nabla \cdot \boldsymbol{v}_i|^2 & \nabla \cdot \boldsymbol{v} < 0 \\ 0 & \text{else,} \end{cases} \tag{2.9.11}$$

and $\nabla \cdot \boldsymbol{v}_i$ can be estimated as

$$\nabla \cdot \boldsymbol{v}_i = -\frac{1}{\rho_i} \sum_{j=1}^{N} m_j \boldsymbol{v}_{ij} \cdot \frac{1}{2} \left[\nabla_i W(\boldsymbol{x}_i - \boldsymbol{x}_j, h_i) + \nabla_i W(\boldsymbol{x}_i - \boldsymbol{x}_j, h_j) \right], \tag{2.9.12}$$

if not directly taken from the momentum equation approximation as pointed out in [141] and [15]. Other formulations can be found in [46] and [152]. The application of the artificial viscosity is discussed further in the next section.

2.10 Material Strength

All the discussed equations so far were general equations which can be applied in fluid dynamics, magnetohydrodynamics, or structural dynamics. To capture the essence of structural behaviour however, material strength must be introduced into the SPH equations. Consequently, SPH becomes indeed a multifunctional tool.

The beauty of SPH in structural dynamic applications comes from the fact, that a steady state behaviour can be captured due to nested constitutive equations within the SPH framework as well as the ability to describe a fluid-like behaviour of a material under high-speed deformation due to the SPH adaptivity. It can be difficult to imagine a material like steel to behave like a fluid, however. When 'events' happen very fast, the standard interpretation of constitutive equations in structural dynamics should not be taken seriously. Materials with structural strength behave like fluids when they undergo deformation fast enough so that inertia becomes the driving parameter. An example was already shown in Fig. 2.1 in which the uranium alloy rod impacted the armour plate at striking velocity more than 1200 m/s [137]. Since SPH has no problem with either quasi-static or hyper-speed deformations, it should be naturally the method of the first choice.

2.10.1 Constitutive Modelling

To implement material strength into SPH, constitutive laws must be considered in equations derived in section *Conservation Laws*. The first step is to take the total stress tensor $\sigma^{\alpha\beta}$ and expand it into the form of

$$\sigma^{\alpha\beta} = p\delta^{\alpha\beta} - \tau^{\alpha\beta}, \tag{2.10.1}$$

where p is the isotropic pressure, $\delta^{\alpha\beta}$ is the Kronecker delta, and $\tau^{\alpha\beta}$ is the shear (traceless symmetric deviatoric) stress tensor. Note that the negative sign was used in (2.8.2) and (2.8.3), therefore, the total stress tensor here refers to the negative counterpart of the Cauchy stress. Yet still applies that positive pressure implies a compressive force pushing the system inward, but positive stress means a force acting outward to pull the system apart. The isotropic pressure p can be calculated in many ways. For elastic materials under slow to moderate deformation Hooke's law can be used as

$$p = -K\varepsilon_v = \rho_0 c_0^2 \left(1 - \frac{\rho_0}{\rho}\right), \tag{2.10.2}$$

where $K = \rho_0 c_0^2$ is the bulk modulus [29, 76], ρ_0 and ρ are the initial and current density, respectively; c_0 is the adiabatic sound speed, and ε_v is the volumetric strain defined as

$$\varepsilon_v = \frac{\Delta V}{V_0} = \frac{\rho_0}{\rho} - 1. \tag{2.10.3}$$

Equation (2.10.2) represents the change in pressure resulting from the change in density. That is, when a material is under hydrostatic pressure and the volume decreases, the current density ρ is greater than the initial ρ_0, therefore, the volumetric strain decreases. Placing negative ε_v into (2.10.2) results in positive pressure. Substituting (2.10.2) into (2.10.1) with respect to (2.8.2) and (2.8.3), i.e. the Cauchy stress tensor with a minus sign, the product is negative hydrostatic stress when pressure is positive, $\sigma^+ = -p$, yet the negative counterpart reads $\sigma = p$.

In fact, many material models are defined with the same sign convention. That is, when the first invariant of the stress tensor $I_1 > 0$, then the material is in compaction, since $I_1 = 3p$, see *CSCM Material Model*. For structural analysts, it might be confusing a little. However, when hydrodynamics is combined with structural dynamics, concessions must be made. For that reason, all stress-strain diagrams have the convention always clarified.

When a material undergoes deformation very fast, formulation in (2.10.2) is not sufficient and state variables must be considered. For this purpose, EOS relations are used, since they represent pressure-volume-energy dependencies. For example, in [21, 22] the Mie-Grüneisen equation for solids was used in HVI simulations. However, the formulation can be used in other applications in which a shock front needs to be considered. The Mie-Grüneisen EOS is defined as

$$p_{\text{EOS}} = \Gamma\rho e + p_{\text{H}} \left(1 - \frac{1}{2}\Gamma\eta\right), \tag{2.10.4}$$

where the subscript H in p_{H} refers to the Hugoniot curve [152], Γ is the Grüneisen parameter (function), η is closely related to the volumetric strain, yet defined with respect to the

current configuration rather than the initial as

$$\eta = \frac{\rho}{\rho_0} - 1, \tag{2.10.5}$$

together with

$$p_{\mathrm{H}} = \begin{cases} a_1\eta + a_2\eta^2 + a_3\eta^3 & \eta > 0 \\ a_1\eta & \text{else,} \end{cases} \tag{2.10.6}$$

where a_1, a_2, and a_3 are the Hugoniot polynomial coefficients [152] which can be computed from the linear shock velocity relation [85, 35]. Equation (2.10.4) is useful in fluid mechanics and a shock wave physics in which the conservation equations involve pressure, volume, internal energy, but not explicitly temperature [157]. Since this form does not give access to temperature and entropy it is often termed *incomplete* [158], therefore, $p_{\mathrm{EOS}} = p(\rho, e)$. When an interaction between a gas and structure is simulated, other EOS formulations might be preferred. The first estimate could be found with EOS of the ideal gas if there are no better assumptions. For the ideal gas, the equation reads

$$p_{\mathrm{EOS}} = (\gamma - 1)\rho e, \tag{2.10.7}$$

where γ is the adiabatic index or heat capacity ratio which is calculated as a ratio of the heat capacity at constant pressure C_p to the heat capacity at constant volume C_v so that

$$\gamma = \frac{C_p}{C_v}, \tag{2.10.8}$$

although still $p_{\mathrm{EOS}} = p(\rho, e)$. Furthermore, in solid mechanics, stress can be a function of strain and strain rate. For an anisotropic shear stress, if displacements are assumed to be small, stress rate is proportional to strain rate through the shear modulus G (Lamé's second parameter). Written in tensor notation as

$$\dot{\tau}^{\alpha\beta} = 2G\bar{\dot{\varepsilon}}^{\alpha\beta} = 2G\left(\dot{\varepsilon}^{\alpha\beta} - \frac{1}{3}\delta^{\alpha\beta}\dot{\varepsilon}^{\gamma\gamma}\right), \tag{2.10.9}$$

where $\dot{\tau}^{\alpha\beta}$ is the shear stress rate tensor, $\bar{\dot{\varepsilon}}^{\alpha\beta}$ is the traceless part of $\dot{\varepsilon}^{\alpha\beta}$ which is the strain-rate tensor. The superimposed dot on the stress and strain tensor refers to the material time derivative. However, for finite displacements this equation is not material frame indifferent, i.e. the material response will depend on rotations (and possibly translations) of the material in unphysical way [21, 22]. A variety of frame-indifferent stress rates have been formulated. The Jaumann derivative, also called the Jaumann stress rate, or simply the Jaumann rate is the most widely used in hydrocodes [21, 22, 51]. For

the Jaumann rate the constitutive equation reads

$$\begin{aligned}\dot{\tau}^{\alpha\beta} &= 2G\bar{\dot{\varepsilon}}^{\alpha\beta} + \tau^{\alpha\gamma}\dot{\omega}^{\gamma\beta} + \dot{\omega}^{\alpha\gamma}\tau^{\gamma\beta} \\ &= 2G\left(\dot{\varepsilon}^{\alpha\beta} - \frac{1}{3}\delta^{\alpha\beta}\dot{\varepsilon}^{\gamma\gamma}\right) + \tau^{\alpha\gamma}\dot{\omega}^{\gamma\beta} + \dot{\omega}^{\alpha\gamma}\tau^{\gamma\beta},\end{aligned} \tag{2.10.10}$$

where the strain-rate tensor $\dot{\varepsilon}^{\alpha\beta}$ is defined as

$$\dot{\varepsilon}^{\alpha\beta} = \frac{1}{2}\left(\frac{\partial v^{\alpha}}{\partial x^{\beta}} + \frac{\partial v^{\beta}}{\partial x^{\alpha}}\right), \tag{2.10.11}$$

and the rotation-rate (spin-rate) tensor $\dot{\omega}^{\alpha\beta}$ is defined as

$$\dot{\omega}^{\alpha\beta} = \frac{1}{2}\left(\frac{\partial v^{\alpha}}{\partial x^{\beta}} - \frac{\partial v^{\beta}}{\partial x^{\alpha}}\right). \tag{2.10.12}$$

As pointed out in [17], the difference between the strain rate and rotation rate is that only the off-diagonal component of $\dot{\omega}$ are non-zero since the velocity gradients are subtracted and not added. Computing $\dot{\omega}$ is therefore only trivially different from computing the shear strain.

For the particle approximated solution, (2.10.11) and (2.10.12) must be discretized as well so that

$$\dot{\varepsilon}_i^{\alpha\beta} = \frac{1}{2}\sum_{j=1}^{N}\left(\frac{m_j}{\rho_j}\, v_{ji}^{\alpha}\frac{\partial W_{ij}}{\partial x_i^{\beta}} + \frac{m_j}{\rho_j}\, v_{ji}^{\beta}\frac{\partial W_{ij}}{\partial x_i^{\alpha}}\right), \tag{2.10.13}$$

$$\dot{\omega}_i^{\alpha\beta} = \frac{1}{2}\sum_{j=1}^{N}\left(\frac{m_j}{\rho_j}\, v_{ji}^{\alpha}\frac{\partial W_{ij}}{\partial x_i^{\beta}} - \frac{m_j}{\rho_j}\, v_{ji}^{\beta}\frac{\partial W_{ij}}{\partial x_i^{\alpha}}\right), \tag{2.10.14}$$

where $v_{ji}^{\alpha} = v_j^{\alpha} - v_i^{\beta}$. Since the strain-rate tensor $\dot{\varepsilon}_i^{\alpha\beta}$ and the rotation-rate tensor $\dot{\omega}_i^{\alpha\beta}$ can be calculated for every interacting pair, stress rates and stresses can be evaluated. The implementation of the above equations results in a modification of the approximated conservation laws. To make the equations complete, the artificial viscosity in (2.9.3) is added to the total stress tensor so that $\sigma^{\alpha\beta} = \sigma_{real}^{\alpha\beta} + \sigma_{viscous}^{\alpha\beta}$. For convenience, the most popular formulations in continuum mechanics follow. That would be the asymmetric

formulation defined in (2.3.34) for the continuity equation

$$\frac{d\rho_i}{dt} = \sum_{j=1}^{N} m_j v_{ij}^{\beta} \frac{\partial W_{ij}}{\partial x_i^{\beta}}, \tag{2.10.15}$$

and for the momentum and energy equation that would be the symmetric formulation defined in (2.3.36), for which

$$\frac{dv_i^{\alpha}}{dt} = -\sum_{j=1}^{N} m_j \left(\frac{\sigma_i^{\alpha\beta}}{\rho_i^2} + \frac{\sigma_j^{\alpha\beta}}{\rho_j^2} + \Pi_{ij} \right) \frac{\partial W_{ij}}{\partial x_i^{\beta}}, \tag{2.10.16}$$

$$\frac{de_i}{dt} = \frac{1}{2} \sum_{j=1}^{N} m_j \left(\frac{\sigma_i^{\alpha\beta}}{\rho_i^2} + \frac{\sigma_j^{\alpha\beta}}{\rho_j^2} + \Pi_{ij} \right) v_{ij}^{\alpha} \frac{\partial W_{ij}}{\partial x_i^{\beta}}. \tag{2.10.17}$$

2.10.2 Tensile Instability

As any other numerical method, also SPH has shortcomings. In this section, the focus is on the so-called tensile instability which can be, however, observed also in compression (sometimes called the compressive instability). Quite a bit of attention has been paid to the tensile instability [29, 159, 30, 45, 67, 65, 74, 78, 81, 160] or [161], and many solutions were proposed to eliminate the problem. To briefly introduce the elephant in the room, the tensile instability is a numerical defect which is closely related to the kernel and stress state. As the name says, the problem was first observed in tensile regions and very often can make an impression of material fracture. However, the fracture is not an outcome of the material model as it is likely to see it even for elastic materials. Simulation examples are discussed in **Chapter 3** *From Theory to Application*, but for purpose of clarity, illustrations of the instability in tension and compression are also shown in Fig. 2.43.

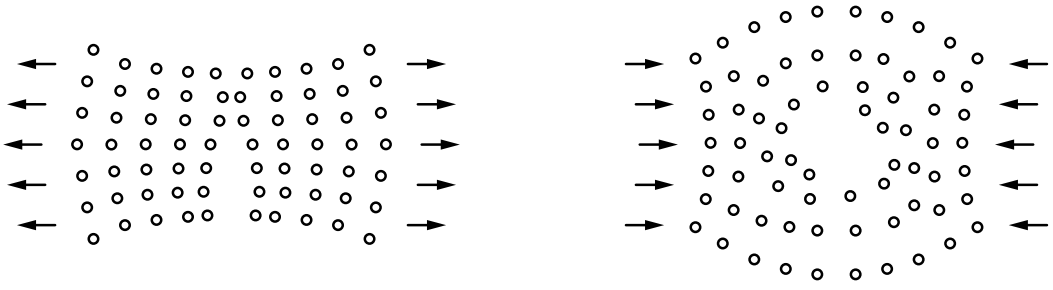

(a) tension (b) compression

Fig. 2.43. Illustration of the SPH instability.

In Fig. 2.43 two different particle distributions are shown after stress fields (imposing tension and compression) were applied to them. Although the results in tension and compression differ, they have the same important sign with which the instability can be identified – *particle clustering* or *particle clumping*. Before the numerical fracture is visible, it is in fact the particle clustering which gives the first indication of the instability. For instance, in Fig. 2.43 (a) particles start to move in the direction of the principal stress, which means, that in the second direction the particles start to move closer to each other. Assuming the kernel is isotropic (spherical) and not expanding in time, the particles start to lose their neighbours in the direction of the larger deformation, but gain more neighbours in the direction of the compact deformation. Naturally, this leads to a weaker bond along the principal stress. The particles start to separate, consequently form clusters with respect to dominant inner forces. The clustering resembles fracture and fragmentation, but is in fact a numerical artifact [29].

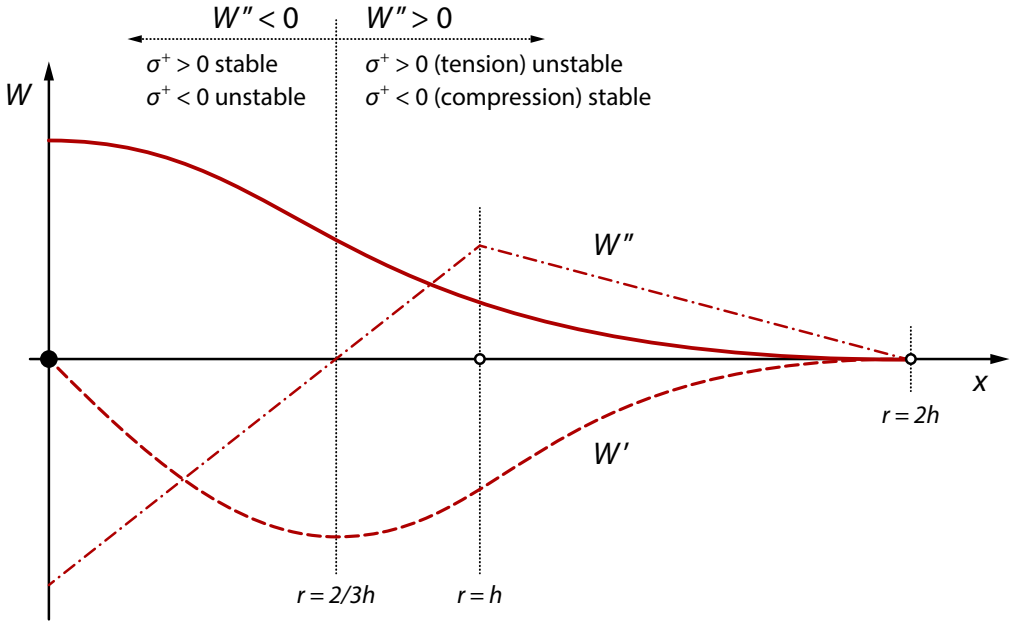

Fig. 2.44. Stable and unstable regions of the cubic spline kernel.

In [29], the von Neumann stability analysis [162] was performed to identify conditions which result in the tensile instability. It was proved that the kernel and stress field conditions are the driving parameters. According to [29], the tensile instability depends neither on the artificial viscosity nor on the time integration scheme. The condition or criterion for being stable or unstable was defined in terms of the stress state and the second derivative of the kernel as

$$W''_{\alpha\alpha}\sigma^{+\alpha\alpha} > 0, \tag{2.10.18}$$

where $W''_{\alpha\alpha}$ is the second derivative of the kernel with respect to its argument. The convention is that the stress component $\sigma^{+\alpha\alpha}$ is negative in compression and positive in tension. There are no stress or strain thresholds for the onset of the instability [29].

The condition involves only the sign of the product of the total stress times the second derivative of the kernel [29]. A graphical interpretation of (2.10.18) is shown in Fig. 2.44 in which the cubic spline kernel W is plotted together with its first two derivatives W' and W''. Assuming 1D particle array with a particle spacing $\Delta x = h$ and $\kappa = 2$, then for $r = 2/3h$ the second derivative of the kernel is zero, for $r < 2/3h$ negative, and for $r > 2/3h$ positive. Since the first neighbouring particle is placed at $r/h = 1$ and the second at $r/h = 2$, it is expected that the behaviour will be unstable under tension however stable under compression. Note that r/h stands for the relative distance q for which the kernel is derived, see (2.4.10).

Along the mathematical condition, [29] provided also a physical understanding of the tensile instability. The explanation would be following. Taking the momentum equation in 1D (see generalized form (2.8.2)), stating that $\sigma^+ = -p$ and not considering viscous stresses, therefore, for the effective stress can be written

$$\frac{dv}{dt} = \frac{1}{\rho}\frac{\partial \sigma^+}{\partial x}, \tag{2.10.19}$$

then due to the discretization can be assumed that

$$\frac{dv}{dt} \approx \frac{\Delta v}{\Delta t} = \frac{\Delta \sigma^+}{\rho \Delta x}, \tag{2.10.20}$$

and since mass can be calculated as $m = \rho \Delta x$, therefore

$$\frac{dv}{dt} \approx \frac{\Delta \sigma^+}{m} \propto \Delta \sigma^+. \tag{2.10.21}$$

However, in section *The Momentum Equation* was shown that

$$\frac{dv}{dt} \propto \Delta(-\sigma^+ W'), \tag{2.10.22}$$

where $W' = \nabla_j W$ so the logic of signs is not changed, see Fig. 2.44. Comparing the solution in (2.10.21) with the SPH approximation in (2.10.22) it is obvious that the effective stress in case of the SPH approximation is proportional to $-\sigma^+ W'$, but not directly to σ^+. This leads to a strange behaviour even with elastic material. When particles separate from each other and strain is monotonically increasing, stress starts to decrease from a certain point. Ultimately stress goes to zero as particles further separate. A graphical interpretation is shown in Fig. 2.45. Such a behaviour can be only explained by a negative modulus (imaginary sound speed). The stress-strain relation is clearly unstable in such a region, since changes in stress act to amplify, rather than reduce, changes in strain [29].

But why the particle clustering, why not just the numerical fracture? A very good explanation was given in [51]. When particles start to separate and stress increases, it

would be assumed that the stress field became constant if particles keep a constant relative distance. Unfortunately, not in SPH since particles *cannot see* the constant stress field, it is not that simple. In Fig. 2.46 a sum of two cubic spline kernels multiplied by -1 is shown at increasing separations. Both kernels have a smoothing length $h = 1$ and $\kappa = 2$. It represents the pressure profile that particle i would see in a tensile region from two neighbouring particles. The contribution from the particle itself is not taken into account since the value of the kernel derivative at the location of particle i is zero – *in SPH there is no self-contribution* [51]. As obvious from Fig. 2.46, when the distance of two neighbouring particles is 4/3, a bump in the pressure profile starts to form. As particles further separate the bump is more evident. When the particle separation is greater than 4/3, particle i is attracted to one or the other neighbouring particle. As a result, the particle clustering starts to form and numerical fracture is evident.

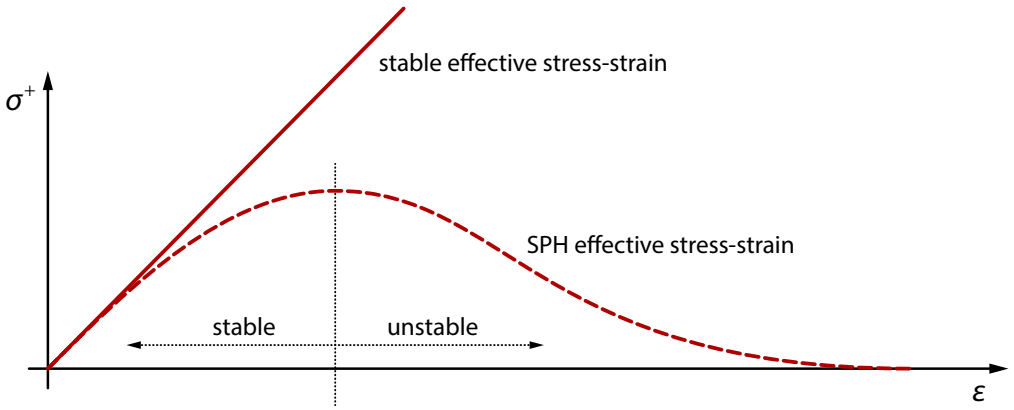

Fig. 2.45. Stable stress-strain diagram compared to the SPH approximation.

The tensile instability is not necessarily a problem in all fields of the SPH application. For example, astrophysical applications and non-viscous fluid simulations seem to be free of the tensile instability. However, it is indeed a problem in solid mechanics especially when a ductile behaviour or material softening is simulated. In the first case, it is not possible to simulate a material under tension at all, in the later one never knows if cracks in a quasi-brittle material are real or not. However, in case of a high-speed loading and when a material undergoes deformations very fast, constitutive equations are perhaps of second importance since the material behaves like a fluid, see section *Material Strength*.

Over the years, several techniques were proposed to eliminate or at least to alleviate the instability. Morris suggested using special kernels to suppress the instability [37], however, the solution is not general [85, 125]. The CSPM minimizes the tensile instability by using the kernel estimate with the Taylor series expansion [52]. Using artificial viscosity to overcome the problem was proposed by Monaghan et al. [65, 76], however, the solution works only if particles move with an average velocity [65], i.e. using XSPH [13]. As was aptly pointed out in [125] and [125], the problem of the tensile instability is rooted in the particle approximation which is conducted only over the particles that represent the entire system, therefore the collocation method. In other words, additional stress points, integration, or sampling points can be used to eliminate the tensile instability. The concept was first applied in [30, 45], and later generalized in [66, 81, 90]. The generalized formulation uses

two types of particles – velocity and stress particles. The velocity particles carry only information about the velocity field and the stress particles carry the rest of the field variables except the velocity. However, computational demands increase significantly.

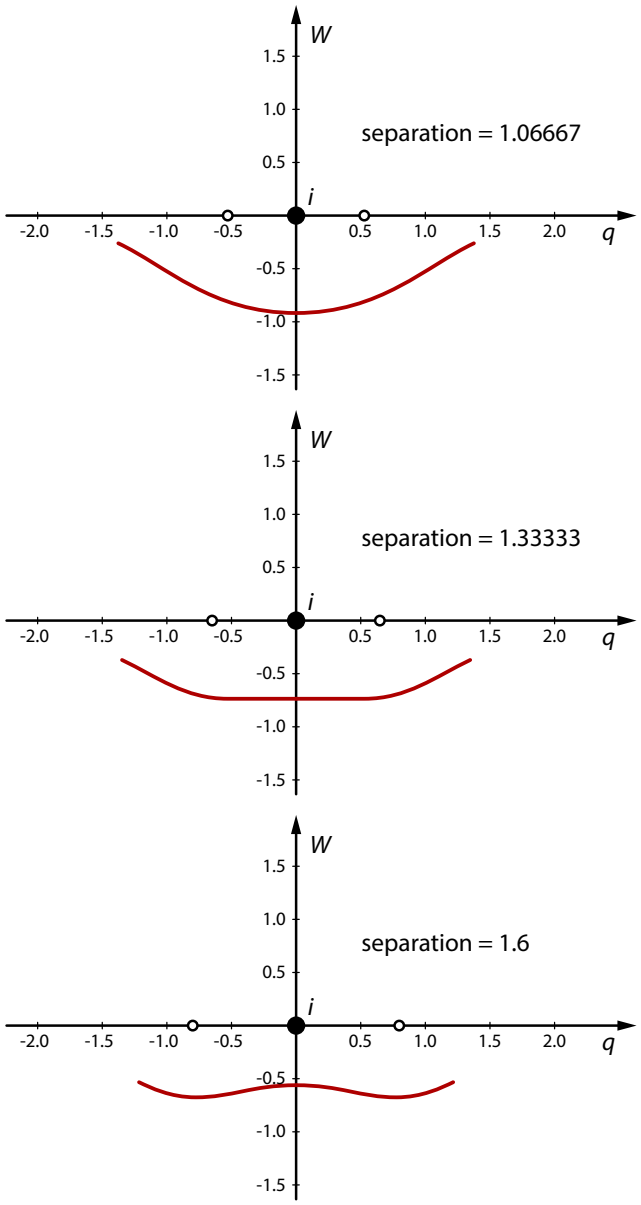

Fig. 2.46. Pressure profile in the proximity of a particle in a tensile region.

Interestingly enough, a lower order kernel with its second derivative everywhere equal to zero is stable in all stress regimes [29]. As proved in [43], the quadratic spline kernel M_3 eliminates instability in compression Fig. 2.7. However, lower order kernels are usually not smooth enough and therefore not accurate in field gradients. A solution from a different perspective would be to keep particles in a regular distribution. In order to do so, kernels with non-vanishing central derivatives can be used, e.g. the linear quartic kernel Fig. 2.30 or the quartic core M_6 kernel Fig. 2.31.

The ultimate solution would be to keep the initial set of neighbouring particles unchanged, therefore, the particle clustering would not result into unbalance forces. In such a case, even

if particle clusters are formed, it does not necessarily mean that the particles in the cluster are from the same neighbouring set. In practice, the Lagrangian kernel must be used as discussed in section *Eulerian and Lagrangian Kernel*, see Fig. 2.38. If the solution with the Lagrangian kernel is extreme and large deformations are being simulated, an acceptable compromise could be using ASPH with the anisotropic Eulerian kernel Fig. 2.37.

2.11 Boundary Treatment

As discussed in section *Mathematical Background* and section *Consistency of the Particle Approximation*, the SPH requirements are not exactly met when dealing with truncated kernels, see Fig. 2.3, Fig. 2.5, and Fig. 2.42. Yet, it does not have to be a truncated kernel to observe other problems in the proximity of boundaries, e.g. a free surface simulation. In that case a problem arise due to the *particle deficiency*. Since the consistency of the particle approximation depends not only on the kernel but also on the number of particles within the support domain, conditions in (2.7.1) and (2.7.2) are no longer satisfied due to the particle deficiency, i.e. just a few particles are placed on one side of the support domain.

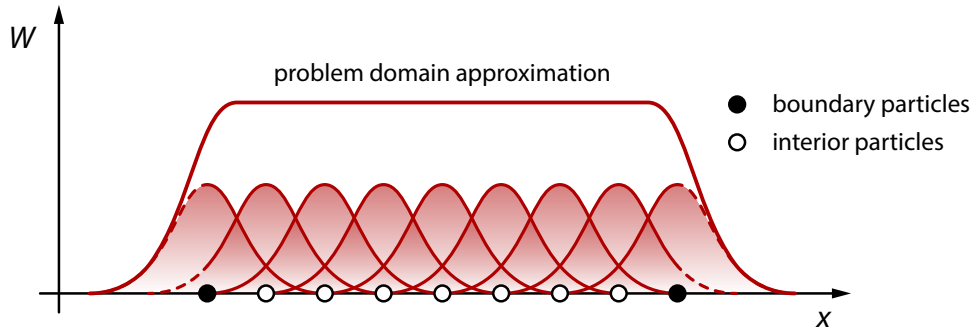

Fig. 2.47. SPH boundary approximation.

The particle deficiency results in decreased accuracy at the boundaries and state variables are usually smoothed out as can be seen in Fig. 2.47. There are some techniques however with which accuracy at boundaries can be restored. Perhaps the most important technique is to use the so-called *ghost particles*. Ghost particles are virtual particles placed outside the discretization domain. Their properties differ with respect to the simulated boundary condition. If the condition is reflective, which simulates a rigid wall, the ghost particles would have identical properties to the real particles except that the sign of the normal velocity component is reversed. If the condition is transmissive, which simulates an open boundary, the ghost particles would have identical properties to the real particles.

For example, in [17] ghost particles were used as a rigid wall in HVI simulations with material strength. They were placed in more than one layer with spacing of the real particles. In [25], ghost particles were used in free surface flow simulations, again as a rigid wall. Particles were placed in one layer, directly at the boundary, preventing from unphysical penetrations through the boundary. Interestingly, to increase accuracy repulsive

forces were calculated with respect to known forces between molecules. For a boundary and fluid particle separated by a distance r_{ij}, the force per unit mass $f(r_{ij})$ had the Lennard-Jones form

$$f(r_{ij}) = \begin{cases} \eta_0 \left[\left(\frac{r_0}{r_{ij}} \right)^{\eta_1} - \left(\frac{r_0}{r_{ij}} \right)^{\eta_2} \right] \frac{\boldsymbol{x}_{ij}}{r_{ij}^2} & r_{ij} \leq r_0 \\ 0 & \text{else,} \end{cases} \tag{2.11.1}$$

where the parameter η_0 is a problem dependent parameter and should be chosen to be in the same scale as the square of the largest velocity, and $\eta_1 > \eta_2$. In [25] values $\eta_1 = 4$ and $\eta_2 = 2$ were used. Similar results were found with $\eta_1 = 12$ and $\eta_2 = 6$, however. The parameter η_0 was chosen to be 5 times the force of the water slope. The length scale r_0 is the cut-off distance. When the distance between particles is greater than r_0, the repulsive force is not applied. If r_0 is too large, some particles may feel the repulsive force from the virtual particles in the initial distribution, thus leads to an initial disturbance and even blow-up of particle positions [85]. If it is too small, the real particles may have already penetrated the boundary before feeling the influence of the repulsive force [85]. Good results are obtained when r_0 is approximately the initial particle spacing.

In practice, there are two types of ghost particles. They can be distinguished by their location with respect to real particles. A schema of the boundary treatment with ghost particles is shown in Fig. 2.48. The first type is known as *ghost boundary particles* and the second type as *ghost exterior particles*. The first type was used in [25] and as the name suggest, they are placed directly at the boundary in one layer. They take part in the kernel approximation and the particle approximation for the real particles. The position and physical variables do not evolve in the simulation process, however.

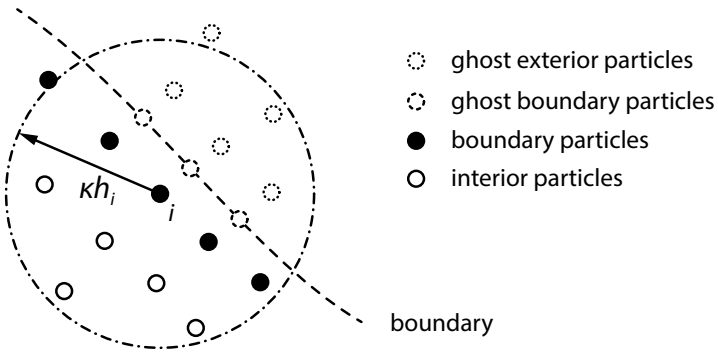

Fig. 2.48. SPH boundary treatment with ghost particles.

The second type, the ghost exterior particles are placed in more than one layer and fill close region of the boundary. The generation of the exterior ghost particles can be automized in such a way that if a real particle i is located within the distance of κh_i from the boundary, a virtual particle is placed symmetrically on the outside of the boundary. The generation should be done in each step. This approach was used in [17]. The ghost exterior particles

have the same density and pressure as the corresponding real particles but as previously mentioned, the sign of the normal velocity component is reversed if the reflective condition is simulated. When only the ghost exterior particles are used, the boundary penetration is not completely eliminated. However, they can be used for both the solid and free surface boundary treatment. As will be discussed in section *SPH Corrections*, the ghost exterior particles are useful for a renormalization in the proximity of general boundaries. For reasons mentioned, a combination of both ghost particle types is usually used.

Even today, dealing with the boundary treatment in SPH is very often frustrating, especially in structural mechanics. As found in Randles and Libersky's paper [35], it was also the case 15 years ago, which is quite amusing.

> *Boundary conditions in SPH have been both a sore point and a neglected subject.* [35]

2.12 SPH Corrections

From the presented essentials of the SPH theory it might seem there are many shortcomings and the method is not suitable for structural dynamic applications. During the last several years however, most of the issues were eliminated or alleviated enough so that SPH can be used as a general tool for structural and fluid mechanics. The following sections discuss the most important SPH corrections relative to structural dynamic applications.

2.12.1 Density Correction

Density corrections can be divided into two classes. In the first class, there would be the corrections dealing with the boundary treatment. In the second, there would be so-called domain filters. Using a density correction at free surfaces, properties of only few particles or particle layers would be modified. Applying filters however, properties of all particles within the problem domain would be changed.

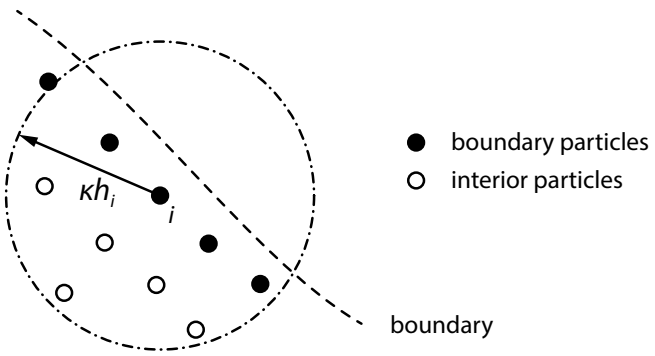

Fig. 2.49. SPH renormalization at a boundary using real particles only.

The first density correction discussed here deals with the particle inconsistency at boundaries. As already outlined in section *Boundary Treatment*, the particle approximation conditions are not generally satisfied at boundaries. Therefore, a consistency error at vicinity of free surfaces is inevitable. In [35] a very useful density correction (sometimes density renormalization) was proposed. The correction is based on the idea of the ghost particles as shown in Fig. 2.48, yet not directly employing them. Nevertheless, particles are also separated into two subsets as outlined in the previous section – interior and boundary particles, see Fig. 2.49.

The idea is that the density of the interior particles is calculated in the standard way, e.g. using (2.3.31), but for the boundary particles the density is calculated as

$$\rho_i = \frac{\sum_{j=1}^{I} m_j W_{ij}}{\sum_{j=1}^{I} \frac{m_j}{\rho_j} W_{ij}}, \tag{2.12.1}$$

where particles j are the interior particles $j \in I \subseteq N$ and ρ_j is the density before the density correction is applied. Note that the interior particles are a subset of the neighbouring particles N, therefore, for the particles close to boundary only $I \subset N$ since $I \neq N$. Equation (2.12.1) not only takes care of the density deficiency at free boundaries, it also solves the contact boundary problem with the density discontinuity if neighbours of a particle are taken only from the same material and not from different materials [35, 85].

As proposed in [128], a similar technique can be used in weakly-compressible or incompressible fluid dynamics. The formulation is similar to (2.12.1) but with a small change. The expression reads

$$\rho_i = \frac{\sum_{j=1}^{N} m_j W_{ij}}{\min\left(1, \sum_{j=1}^{N} \frac{m_j}{\rho_j} W_{ij}\right)}, \tag{2.12.2}$$

where ρ_j is the density before the density correction is applied and the limitation of the denominator is introduced due to the unity condition, see (2.4.1). Note that the full set of N neighbouring particles is taken instead of the subset I. When the density correction is applied over all particles within the problem domain, however, the correction is usually considered to be a filter rather than a correction. The result of (2.12.2) is a smoother density field. This technique is rarely used in pure structural dynamics, however, it is useful when it comes to fluid-structure interaction (FSI) problems.

The following two density corrections are indeed density filters. Their purpose is to smooth out the density field and eliminate steep gradients and oscillations. When a density filter

is used, the pressure field is smoothed out as a consequence. Therefore, their application takes place mostly in fluid simulations or when a material behaves like a fluid, e.g. HVI simulations. The first introduced filter is the so-called Shepard filter, also known as Shepard interpolant, or Shepard functions [163], an approximation widely used in fitting data [49]. It is a zeroth order filter (constant completeness) [49, 164] and it is sufficient to apply it every nth step (20 – 50). The smoothed density is defined as

$$\rho_i = \sum_{j=1}^{N} \rho_j \tilde{W}_{ij} \frac{m_j}{\rho_j} = \sum_{j=1}^{N} m_j \tilde{W}_{ij}, \tag{2.12.3}$$

where ρ_j is the density before the density filter is applied, and the kernel $\tilde{W}_{ij}$ is zeroth order corrected as

$$\tilde{W}_{ij} = \frac{W_{ij}}{\sum_{k=1}^{N} \frac{m_k}{\rho_k} W_{ik}}. \tag{2.12.4}$$

The second density filter uses the kernel MLS correction introduced in [165], further discussed in [49]. It is important to note, that applying the MLS correction to the kernel in order to obtain a density filter will not produce the same result as in the case of directly using MLSPH. In MLSPH the kernel is created with a specific level of completeness [166]. However, an approximation equivalent to MLS can be constructed by correcting the kernel [40]. To create a first order density filter (linear completeness), the smoothed density is defined as

$$\rho_i = \sum_{j=1}^{N} \rho_j W_{ij}^{\mathrm{MLS}} \frac{m_j}{\rho_j} = \sum_{j=1}^{N} m_j W_{ij}^{\mathrm{MLS}}, \tag{2.12.5}$$

where ρ_j is the density before the density filter is applied, and the kernel W_{ij}^{MLS} is first order corrected as

$$W_{ij}^{\mathrm{MLS}} = \boldsymbol{\beta}(\boldsymbol{x}_i) \cdot (\boldsymbol{x}_i - \boldsymbol{x}_j) W_{ij}, \tag{2.12.6}$$

where the correction vector $\boldsymbol{\beta}(\boldsymbol{x}_i)$ is given as

$$\boldsymbol{\beta}(\boldsymbol{x}_i) = \boldsymbol{A}(\boldsymbol{x}_i)^{-1} [1, 0, \ldots, 0]^{\mathsf{T}}, \tag{2.12.7}$$

where

$$\boldsymbol{A}(\boldsymbol{x}_i) = \sum_{j=1}^{N} \hat{\boldsymbol{p}}_j \hat{\boldsymbol{p}}_j^{\mathsf{T}} W_{ij} \frac{m_j}{\rho_j}, \tag{2.12.8}$$

where $\hat{\boldsymbol{p}}$ are the monomial basis functions or just basis. For example, in 2D if the vector of monomials is defined as

$$\hat{\boldsymbol{p}}^{\mathsf{T}} = \left[\; 1, \quad x, \quad y \; \right], \tag{2.12.9}$$

therefore

$$\hat{\boldsymbol{p}}\hat{\boldsymbol{p}}^{\mathsf{T}} = \begin{bmatrix} 1 & x & y \\ x & x^2 & xy \\ y & xy & y^2 \end{bmatrix}, \tag{2.12.10}$$

then W_{ij}^{MLS} is said to be first order corrected. Note that simplified notation was used in (2.12.9) and (2.12.10) to improve legibility. The monomial basis functions $\hat{\boldsymbol{p}}^{\mathsf{T}} = [1, x, y]$ are treated in local manner, i.e. $\hat{\boldsymbol{p}}^{\mathsf{T}} = [1, x_i - x_j, y_i - y_j]$. The MLS derivation is discussed in section *MLSPH* in detail.

The MLS density filter can be also applied only every nth time step. The MLS filter is computationally more expensive than the Shepard filter, yet it does not lead to volume increase. The product of a density filter application is a reinitialized density field. For that reason, the application of density filters is often referred to as density reinitialization [128, 164, 167] or [168]. Note that the Shepard filter can be used or applied for any scalar of field function.

2.12.2 Gradient Correction

To preserve linear and angular momentum, internal energy must be invariant with respect to rigid body motions [60]. The invariance with respect to translations is usually satisfied by most SPH schemes and generally linear momentum is preserved. The rotational invariance, however, requires a correct evaluation of gradients of a linear velocity field and is more difficult to achieve. Bonet and Lok [60] proved that satisfying

$$\sum_{j=1}^{N} \frac{m_j}{\rho_j} (\boldsymbol{x}_j - \boldsymbol{x}_i) \otimes \nabla_i W_{ij} = \boldsymbol{I}, \tag{2.12.11}$$

ensures that the gradient of any linear velocity distribution is correctly evaluated. There are different techniques with which (2.12.11) can be satisfied. For example, either the kernel gradient or the kernel itself can be corrected. In case of the kernel gradient correction, a correction matrix $\boldsymbol{L}$ was proposed in [60] so that

$$\tilde{\nabla}_i W_{ij} = \boldsymbol{L}_i \nabla_i W_{ij}. \tag{2.12.12}$$

Using $\boldsymbol{L}$, the velocity gradient is evaluated as

$$\begin{aligned} \nabla \boldsymbol{v}_i &= \sum_{j=1}^{N} \frac{m_j}{\rho_j} (\boldsymbol{v}_j - \boldsymbol{v}_i) \otimes \tilde{\nabla}_i W_{ij} \\ &= \sum_{j=1}^{N} \frac{m_j}{\rho_j} (\boldsymbol{v}_j - \boldsymbol{v}_i) \otimes \boldsymbol{L}_i \nabla_i W_{ij}. \end{aligned} \tag{2.12.13}$$

The correction matrix $\boldsymbol{L}$ is obtained at each particle by enforcing that (2.12.11) is satisfied by the corrected kernel gradient [60]. That gives

$$\sum_{j=1}^{N} \frac{m_j}{\rho_j} (\boldsymbol{x}_j - \boldsymbol{x}_i) \otimes \tilde{\nabla}_i W_{ij} = \left(\sum_{j=1}^{N} \frac{m_j}{\rho_j} (\boldsymbol{x}_j - \boldsymbol{x}_i) \otimes \nabla_i W_{ij} \right) \boldsymbol{L}_i^{\mathsf{T}} = \boldsymbol{I}, \tag{2.12.14}$$

from which

$$\boldsymbol{L}_i = \left(\sum_{j=1}^{N} \frac{m_j}{\rho_j} \nabla_i W_{ij} \otimes (\boldsymbol{x}_j - \boldsymbol{x}_i) \right)^{-1}. \tag{2.12.15}$$

The use of the gradient correction technique ensures that the gradient of any linear velocity field is exactly evaluated [60]. In addition, angular momentum will be preserved provided that the internal forces are derived from a variational principle [60].

2.12.3 Kernel Correction

The second common technique used to satisfy (2.12.11) is to correct the kernel itself. As proposed in [169, 170], the kernel is modified to ensure that polynomial functions up to a given degree are exactly interpolated [60]. This is achieved by interpolating with corrected kernel $\tilde{W}_{ij}$ as

$$\boldsymbol{v}_i = \sum_{j=1}^{N} \frac{m_j}{\rho_j} \boldsymbol{v}_j \tilde{W}_{ij}, \tag{2.12.16}$$

where for the first degree correction $\tilde{W}_{ij}$ would be defined as

$$\tilde{W}_{ij} = W_{ij}\alpha_i[1 + \boldsymbol{\beta}_i \cdot (\boldsymbol{x}_i - \boldsymbol{x}_j)]. \tag{2.12.17}$$

In (2.12.17) the parameters α and $\boldsymbol{\beta}$ are given by the assumption that any linear velocity distribution is exactly interpolated as

$$\boldsymbol{v}_0 + \boldsymbol{v}_1 \cdot \boldsymbol{x}_i = \sum_{j=1}^{N} \frac{m_j}{\rho_j}(\boldsymbol{v}_0 + \boldsymbol{v}_1 \cdot \boldsymbol{x}_j)\tilde{W}_{ij}, \tag{2.12.18}$$

where $\boldsymbol{v}_0$ and $\boldsymbol{v}_1$ are arbitrary vectors, therefore, consistency conditions

$$\sum_{j=1}^{N} \frac{m_j}{\rho_j}\tilde{W}_{ij} = 1, \tag{2.12.19}$$

and

$$\sum_{j=1}^{N} \frac{m_j}{\rho_j}(\boldsymbol{x}_i - \boldsymbol{x}_j)\tilde{W}_{ij} = \boldsymbol{0}, \tag{2.12.20}$$

must be satisfied by the corrected kernel itself. To do so, substituting (2.12.17) into (2.12.20) gives the parameter $\boldsymbol{\beta}$ as

$$\boldsymbol{\beta}_i = \left[\sum_{j=1}^{N} \frac{m_j}{\rho_j}(\boldsymbol{x}_i - \boldsymbol{x}_j) \otimes (\boldsymbol{x}_i - \boldsymbol{x}_j)W_{ij}\right]^{-1} \sum_{j=1}^{N} \frac{m_j}{\rho_j}(\boldsymbol{x}_j - \boldsymbol{x}_i)W_{ij}. \tag{2.12.21}$$

When the parameter $\boldsymbol{\beta}$ is known, the scalar parameter α can be evaluated from

$$\alpha_i = \frac{1}{\sum_{j=1}^{N} \frac{m_j}{\rho_j}[1 + \boldsymbol{\beta}_i \cdot (\boldsymbol{x}_i - \boldsymbol{x}_j)]W_{ij}}, \tag{2.12.22}$$

which was introduced by substituting (2.12.17) into (2.12.19). Using (2.12.16) ensures that linear functions are perfectly interpolated and their gradients are exactly obtained. As pointed out in [60], the use of the above formulations is not suitable for calculations with explicit time integration schemes since the evaluation of the gradient is computationally expensive. To decrease the level of complexity, the correction vector can be taken as $\boldsymbol{\beta} = \boldsymbol{0}$

so that

$$\boldsymbol{v}_i = \frac{\sum_{j=1}^{N} \frac{m_j}{\rho_j} \boldsymbol{v}_j W_{ij}}{\sum_{j=1}^{N} \frac{m_j}{\rho_j} W_{ij}}, \tag{2.12.23}$$

where the denominator is indeed the parameter α [60]. In essence, (2.12.23) is a weighted average. It is also known as the Shepard filter which was discussed in (2.12.4) [163].

2.12.4 Mixed Kernel and Gradient Correction

Following the idea of the gradient correction in (2.12.12) together with the kernel correction in (2.12.23), a mixed correction scheme was proposed in [60]. The mixed correction starts with an assumption of a velocity field approximated as

$$\boldsymbol{v}_i = \sum_{j=1}^{N} \frac{m_j}{\rho_j} \boldsymbol{v}_j \tilde{W}_{ij}, \tag{2.12.24}$$

where the corrected kernel with the Shepard filter is defined as

$$\tilde{W}_{ij} = \frac{W_{ij}}{\sum_{j=1}^{N} \frac{m_j}{\rho_j} W_{ij}}, \tag{2.12.25}$$

and the velocity gradient is evaluated as

$$\nabla \boldsymbol{v}_i = \sum_{j=1}^{N} \frac{m_j}{\rho_j} \boldsymbol{v}_j \otimes \tilde{\nabla}_i \tilde{W}_{ij}, \tag{2.12.26}$$

where the corrected gradient of the corrected kernel is given as

$$\tilde{\nabla}_i \tilde{W}_{ij} = \boldsymbol{L}_i \nabla_i \tilde{W}_{ij}. \tag{2.12.27}$$

Note that the term $-\boldsymbol{v}_i$ is not used in (2.12.26) compared to (2.12.13) since the constant kernel correction ensures that the gradient of a constant function will vanish [60]. The

gradient of the corrected kernel can be evaluated as

$$\nabla_i \tilde{W}_{ij} = \frac{\nabla_i W_{ij} - \eta_i}{\sum_{j=1}^{N} \frac{m_j}{\rho_j} W_{ij}}, \tag{2.12.28}$$

where

$$\eta_i = \frac{\sum_{j=1}^{N} \frac{m_j}{\rho_j} \nabla_i W_{ij}}{\sum_{j=1}^{N} \frac{m_j}{\rho_j} W_{ij}}. \tag{2.12.29}$$

And to satisfy (2.12.11), the correction matrix $\boldsymbol{L}$ is given as

$$\boldsymbol{L}_i = \left(\sum_{j=1}^{N} \frac{m_j}{\rho_j} \nabla_i \tilde{W}_{ij} \otimes \boldsymbol{x}_j \right)^{-1}. \tag{2.12.30}$$

2.12.5 The Renormalization

In 1996 Randles and Libersky [35] proposed a normalization for the divergence of the stress tensor $\boldsymbol{\sigma}$. Although the density correction (2.12.1) was described in the same paper, the normalization for the divergence of the stress tensor was the part which became quite popular and is today referred to as *the renormalization*. The renormalization deals with the particle inconsistency while using the idea of the ghost exterior particles, yet not directly employing them in the calculation, see Fig. 2.50.

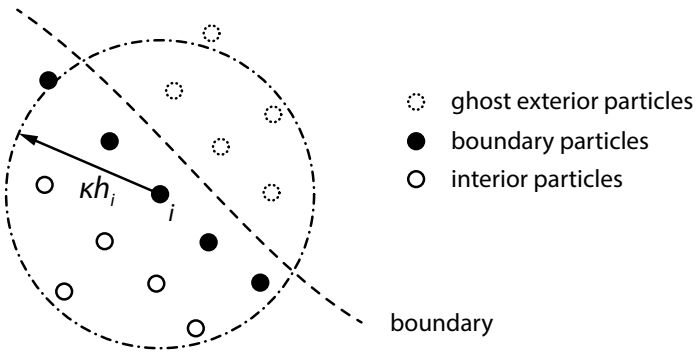

Fig. 2.50. SPH renormalization at a boundary.

Note that the following derivation of the renormalization uses the same momentum and energy equations as in the original paper [35], i.e. (2.8.17) and (2.8.25), respectively. However, any formulation listed in section *Conservation Laws* can be used. To renormalize the divergence of the linear stress tensor in the form of $\boldsymbol{\sigma} = \boldsymbol{a} + \boldsymbol{b} \cdot \boldsymbol{x}$, where $\boldsymbol{a}$ and $\boldsymbol{b}$ are the constant second and third rank tensors symmetric in the first two indices [35], the formulation

$$(\nabla \cdot \boldsymbol{\sigma})_i = \left(-\sum_{j=1}^{N} \frac{m_j}{\rho_j} (\boldsymbol{\sigma}_j - \boldsymbol{\sigma}_i) \otimes \nabla_i W_{ij} \right) : \boldsymbol{B}, \tag{2.12.31}$$

was proposed to get the exact result for $\nabla \cdot \boldsymbol{\sigma}$. Note that the formulation derived in (2.8.17) was used although in the vector notation to improve legibility. Evaluating (2.12.31) for the linear $\boldsymbol{\sigma}$ gives

$$\boldsymbol{b} : \boldsymbol{I} = \boldsymbol{b} : \left[\left(-\sum_{j=1}^{N} \frac{m_j}{\rho_j} (\boldsymbol{x}_j - \boldsymbol{x}_i) \otimes \nabla_i W_{ij} \right) \cdot \boldsymbol{B} \right]. \tag{2.12.32}$$

Equation (2.12.32) will be satisfied for an arbitrary $\boldsymbol{b}$ only if

$$\boldsymbol{B} = \left(-\sum_{j=1}^{N} \frac{m_j}{\rho_j} (\boldsymbol{x}_j - \boldsymbol{x}_i) \otimes \nabla_i W_{ij} \right)^{-1}, \tag{2.12.33}$$

where $\boldsymbol{B}$ is the second rank tensor [35]. Therefore, the momentum equation in (2.8.17) can be rewritten in the renormalized form as

$$\frac{d\boldsymbol{v}_i}{dt} = \left(-\sum_{j=1}^{N} \frac{m_j}{\rho_i \rho_j} (\boldsymbol{\sigma}_j - \boldsymbol{\sigma}_i) \otimes \nabla_i W_{ij} \right) : \boldsymbol{B}, \tag{2.12.34}$$

and the energy equation in (2.8.25) as

$$\frac{de_i}{dt} = \boldsymbol{\sigma}_i : \left[\left(-\sum_{j=1}^{N} \frac{m_j}{\rho_i \rho_j} (\boldsymbol{v}_j - \boldsymbol{v}_i) \otimes \nabla_i W_{ij} \right) \cdot \boldsymbol{B} \right]. \tag{2.12.35}$$

Using (2.12.34) and (2.12.35) any linear stress field can be reproduced. Note that the renormalization might alleviate the tensile instability yet not fully eliminate it.

2.12.6 ASPH

In many applications the concept of the isometric Eulerian kernel as shown in Fig. 2.36 is not sufficient. Problems arise when deformation of a simulated domain is highly anisotropic and particles start to form clusters in the direction of the principal flow. Since the particle clustering is closely related to the tensile instability, numerical fractures are usually consequence of an anisotropic deformation. Furthermore, the usage of the isometric Eulerian kernel often leads to a decrease in accuracy when deformations are rather anisotropic. However, when the anisotropic Eulerian kernel is used instead, as shown in Fig. 2.37, accuracy is often improved. The anisotropic Eulerian kernel alleviate the negative impact of the tensile instability, but never fully eliminates it. When the anisotropic kernel with an adaptive development in time and space is used, SPH is referred to as ASPH.

ASPH was first used in [171] in which effects of a black hole on stellar material approximated with SPH particles were examined. The stellar material was squeezed in one direction as it approached the orbit of the black hole. From the logic of the deformation, the usage of the isometric kernel was unfounded. The anisotropic kernel was introduced instead. The concept of ASPH was generalized in [148] and further studied in [151] in which the local, linear coordinates transformation was proposed.

The main idea of ASPH is that in 3D the kernel is of ellipsoidal shape which can be arbitrarily oriented in addition. The scalar smoothing length h is replaced by a tensor $\boldsymbol{H}$ to characterize the support domain of the kernel.

$$\boldsymbol{H} = \begin{bmatrix} h_{xx} & h_{yx} & h_{zx} \\ h_{xy} & h_{yy} & h_{zy} \\ h_{xz} & h_{yz} & h_{zz} \end{bmatrix} \tag{2.12.36}$$

The tensor $\boldsymbol{H}$ is second order, real, and symmetric; i.e. $h_{yx} = h_{xy}$, $h_{zx} = h_{xz}$, $h_{yz} = h_{zy}$. The eigenvectors of $\boldsymbol{H}$ are the directions along the three axes of the ellipsoid and the corresponding eigenvalues are the dimensions of the ellipsoid along each axis. The tensor $\boldsymbol{H}$ for each particle is dynamically evolved by using the components of the deformation tensor $\partial v_i/\partial x_j$ to follow the local deformation and vorticity of the flow [148].

The concept of ASPH is schematically shown in Fig. 2.51. Three principal axes based on the principal direction of the deformation tensor are defined for the ellipsoidal support domain. Three principal vector values $(\boldsymbol{h}_x, \boldsymbol{h}_y, \boldsymbol{h}_z)$ are updated based on the principal values of the deformation tensor. The tensor $\boldsymbol{H}$ can be transformed through a local, linear transformation of coordinates into those where the underlying anisotropic volume changes appear to be isotropic [151]. It should be noted that ASPH improves the approximation accuracy, but it does not eliminate the tensile instability problem. Furthermore, a disadvantage of ASPH is that the time step might be much smaller compared to the standard SPH due to the reduced smoothing length in the compressed direction [85]. More about ASPH can be found in [148, 151] or [85].

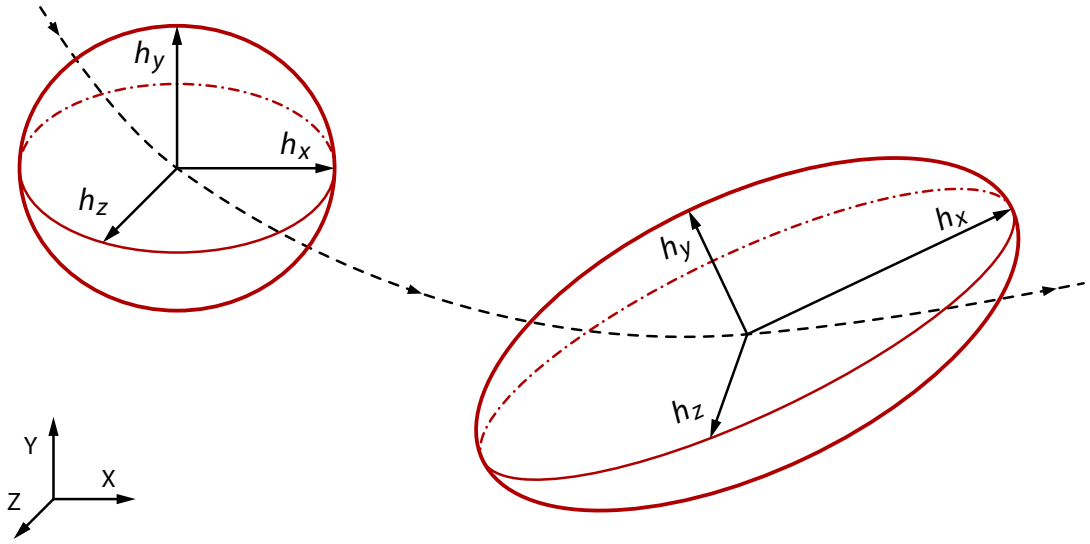

Fig. 2.51. ASPH kernel development.

2.12.7 MLSPH

In 1999 Dilts pointed out that pathologies (undesirable features appearing in special circumstances) of SPH have a single root cause: the inability of SPH to accurately interpolate when the particles are unevenly spaced and sized [51]. In mathematical terms, the SPH equations are not consistent in that the derivative approximations do not necessarily converge to the continuum values as the (non-uniform) particle size and spacing go to zero [40, 51]. In order to improve the stability and accuracy of SPH, Dilts proposed the so-called MLSPH in which the standard kernel is replaced by MLS interpolants introduced in [172] and applied to mechanics in [173] and [174]. As discussed in [51], MLSPH shows improvements due to the linear consistency of its gradients on three canonical difficulties of the standard SPH: i) spurious boundary effects, ii) erroneous rates of strain and rotation, and iii) tensile instability.

As in section *Kernel Approximation* in which the angle brackets $\langle\ \rangle$ were used to define the kernel approximation operator, here $\langle\ \rangle^{\text{MLS}}$ operator is used to distinguish the MLS and the standard kernel approximation. As in the standard SPH formulation, also in MLSPH the value of a function $f(\boldsymbol{x})$ at a location defined with $\boldsymbol{x}$ can be approximated using

$$\langle f(\boldsymbol{x})\rangle^{\text{MLS}} = \sum_{j=1}^{N} f(\boldsymbol{x}_j)\phi_j(\boldsymbol{x}), \tag{2.12.37}$$

where ϕ_j was used to replace the standard SPH kernel and associated volume of particles, which were defined with respect to (2.3.20) as

$$\phi_j = \frac{m_j}{\rho_j} W(\boldsymbol{x} - \boldsymbol{x}_j, h). \tag{2.12.38}$$

In MLSPH, however, the function ϕ_j is found in different way. The principle property of MLS interpolants is to exactly reproduce an arbitrary given set of functions known as monomial basis functions or just basis. These can be in 2D, e.g. linear

$$\hat{\boldsymbol{p}}^{\mathsf{T}} = \left[\ 1,\quad x,\quad y\ \right], \tag{2.12.39}$$

or quadratic set of functions

$$\hat{\boldsymbol{p}}^{\mathsf{T}} = \left[\ 1,\quad x,\quad y,\quad x^2,\quad xy,\quad y^2\ \right]. \tag{2.12.40}$$

Of course, it is also possible to use other functions in the basis. In problems with singular solutions, singular functions can be included in the basis [40]. Using $\hat{\boldsymbol{p}}$, the approximation in (2.12.37) can be rewritten in the form of

$$\langle f(\boldsymbol{x})\rangle^{\mathrm{MLS}} = \sum_{j=1}^{N} \hat{p}_j(\boldsymbol{x}) a_j(\boldsymbol{x}) \equiv \hat{\boldsymbol{p}}^{\mathsf{T}}(\boldsymbol{x})\boldsymbol{a}(\boldsymbol{x}), \tag{2.12.41}$$

with $\boldsymbol{a}(\boldsymbol{x})$ chosen to minimize a weighted, discrete L_2 error norm [174] as

$$\mathcal{O}(\boldsymbol{x}) = \sum_{j=1}^{N} \left[\hat{\boldsymbol{p}}^{\mathsf{T}}(\boldsymbol{x}_j)\boldsymbol{a}(\boldsymbol{x}) - f(\boldsymbol{x}_j)\right]^2 W(\boldsymbol{x}-\boldsymbol{x}_j, h). \tag{2.12.42}$$

The fact that $\boldsymbol{a}$ is not a constant but depends on $\boldsymbol{x}$ accounts for the *moving* part of the name [51]. The solution for $\boldsymbol{a}(\boldsymbol{x})$ can be found and gives an interpolant of the form

$$\phi_j(\boldsymbol{x}) = \hat{\boldsymbol{p}}^{\mathsf{T}}(\boldsymbol{x}) \cdot \boldsymbol{A}(\boldsymbol{x})^{-1} \cdot \hat{\boldsymbol{p}}(\boldsymbol{x}_j)\, W(\boldsymbol{x}-\boldsymbol{x}_j, h), \tag{2.12.43}$$

where

$$\boldsymbol{A}(\boldsymbol{x}) = \sum_{j=1}^{N} \hat{\boldsymbol{p}}(\boldsymbol{x}_j)\hat{\boldsymbol{p}}^{\mathsf{T}}(\boldsymbol{x}_j) W(\boldsymbol{x}-\boldsymbol{x}_j, h). \tag{2.12.44}$$

Finally, for particle i (using simplified notation $\hat{\boldsymbol{p}}_i = \hat{\boldsymbol{p}}(\boldsymbol{x}_i)$, $\phi_{ij} = \phi_j(\boldsymbol{x}_i)$) can be written

$$\langle f(\boldsymbol{x}_i)\rangle^{\mathrm{MLS}} = \sum_{j=1}^{N} f(\boldsymbol{x}_j)\phi_{ij}, \tag{2.12.45}$$

where

$$\phi_{ij} = \hat{\boldsymbol{p}}_i^{\mathsf{T}} \cdot \boldsymbol{A}_{ij}^{-1} \cdot \hat{\boldsymbol{p}}_j \, W_{ij}, \tag{2.12.46}$$

and

$$\boldsymbol{A}_{ij} = \sum_{j=1}^{N} \hat{\boldsymbol{p}}_j \hat{\boldsymbol{p}}_j^{\mathsf{T}} \, W_{ij}. \tag{2.12.47}$$

Gradients of the MLS approximation are treated in the same way as in the standard SPH formulation, i.e. the differential operation on a function is transformed into a differential operation on the MLS interpolant. Therefore, the gradient is given by

$$\nabla\phi_{ij} = [\nabla(\hat{\boldsymbol{p}}_i^{\mathsf{T}}) \cdot \boldsymbol{A}_{ij}^{-1} \cdot \hat{\boldsymbol{p}}_j - \hat{\boldsymbol{p}}_i^{\mathsf{T}} \cdot \boldsymbol{A}_{ij}^{-1} \cdot \nabla \boldsymbol{A}_{ij} \cdot \boldsymbol{A}_{ij}^{-1} \cdot \hat{\boldsymbol{p}}_j] \, W_{ij} + \hat{\boldsymbol{p}}_i^{\mathsf{T}} \cdot \boldsymbol{A}_{ij}^{-1} \cdot \hat{\boldsymbol{p}}_j \cdot \nabla W_{ij}. \tag{2.12.48}$$

For certain applications linear or quadratic basis functions cannot guarantee sufficient accuracy. The reason for that is usually insufficient number of neighbouring particles. In such situations the matrix $\boldsymbol{A}$ can become singular and use of the original MLS interpolants becomes problematic [51]. However, since basis functions can be chosen freely, order of interpolants can be increased in terms of the completeness of the polynomial basis, the concept known from FEM. In the same way Dilts [51] proposed the concept of a variable-rank MLS in which the basis are formed as

$$\hat{\boldsymbol{p}}\hat{\boldsymbol{p}}^{\mathsf{T}} = \begin{bmatrix} \overset{0}{\boxed{1}} & \overset{1}{x} & y & x^2 & xy & y^2 \\ x & x^2 & xy & x^3 & x^2y & xy^2 \\ y & xy & y^2 & x^2y & xy^2 & y^3 \\ x^2 & x^3 & x^2y & x^4 & x^3y & x^2y^2 \\ xy & x^2y & xy^2 & x^3y & x^2y^2 & xy^3 \\ y^2 & xy^2 & y^3 & x^2y^2 & xy^3 & y^4 \end{bmatrix}, \tag{2.12.49}$$

where the rank is chosen in order to have the full-$\hat{\boldsymbol{p}}$ matrix $\boldsymbol{A}$ formed by (2.12.44). Interestingly enough, if the rank drops to zero, i.e. $\hat{\boldsymbol{p}}^{(0)} = [\,1\,]^{\mathsf{T}}$, then (2.12.44) always yields an invertible $\boldsymbol{A}$, corresponding to Shepard functions [163] so that

$$\phi_{ij} = \frac{W_{ij}}{\sum_{j=1}^{N} W_{ij}}, \tag{2.12.50}$$

which was already discussed in section *Density Correction*. Note that simplified notation was used for the basis functions to improve legibility. The monomial basis functions $\hat{\boldsymbol{p}}^{\mathsf{T}} = [\,1, x, y\,]$ are treated in local manner, i.e. $\hat{\boldsymbol{p}}^{\mathsf{T}} = [\,1, x_i - x_j, y_i - y_j\,]$.

As shown in section *Accuracy with MLS Interpolant* in which the rank $\hat{\boldsymbol{p}}^{(1)} = [\,1, x, y\,]^{\mathsf{T}}$ was used, MLSPH gives a correct solution for randomly distributed particles as shown in Fig. 2.52 in which $h = \Delta x$ and $\kappa = 2$. The unity approximation for a variable particle distribution is not the only positive side effect. The tensile instability is alleviated as well, and a shock front is preserved in case of resonance, i.e. when a shock front is multiplied by itself.

MLSPH is discussed in detail in [51, 64] in which Dilts discussed not only the concept but proved the stability and increased accuracy of the method. The MLS approximation itself is further studied in [174, 165, 40, 166, 49]. Applications of MLSPH in HVI simulations are covered in [84]. A combination of MLSPH together with the stabilized and nodally integrated weak-form [175] was proposed in [176] and implemented into LS-DYNA [177]. From the author's experience, MLSPH proved to be very stable, accurate, and useful when materials with structural strength are used.

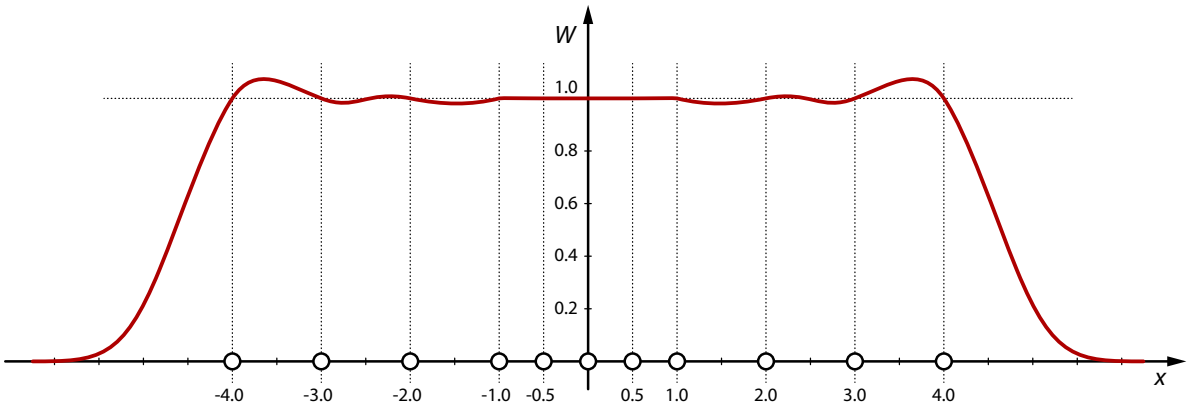

(a) SPH

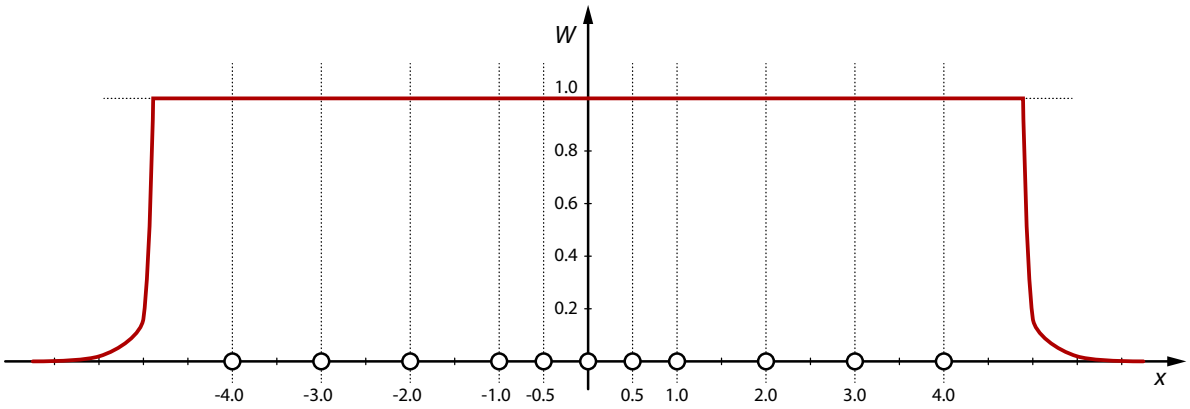

(b) MLSPH

Fig. 2.52. Comparison of the SPH and MLSPH interpolation of unity for a non-uniform particle distribution.

2.12.8 XSPH

In 1989 Monaghan observed that particles can stream through each other unless the viscosity of the system is large [13]. When an artificial viscosity is applied to the system, however, local gradients might be suppressed. To minimize the particle passage, XSPH was proposed. In XSPH, particles are moved with a smoothed velocity but the acceleration equation is unchanged. The X in the name stands for an unknown factor, and the method itself is a correction in essence. Therefore, XSPH is sometimes termed *correction position stepping* SPH. The idea starts with the motion equation of particle i where

$$\frac{d\boldsymbol{x}_i}{dt} = \boldsymbol{v}_i. \tag{2.12.51}$$

To create a smoothed velocity field, the velocity of particle $\boldsymbol{v}_i$ is replaced by the averaged one

$$\hat{\boldsymbol{v}}_i = \boldsymbol{v}_i - \tilde{\epsilon} \sum_{j=1}^{N} \frac{m_j}{\rho_{ij}} \boldsymbol{v}_{ij} \hat{W}_{ij}, \tag{2.12.52}$$

where ρ_{ij} is the average density symmetric with respect to i and j defined as

$$\rho_{ij} = \frac{1}{2}(\rho_i + \rho_j), \tag{2.12.53}$$

or it can be defined as an inverted average as used in [178], then

$$\frac{1}{\rho_{ij}} = \frac{1}{2}\left(\frac{1}{\rho_i} + \frac{1}{\rho_j}\right), \tag{2.12.54}$$

and $\hat{W}_{ij}$ is the smoothing kernel which can be different from the kernel used in other SPH equations, e.g. as

$$\hat{W}_{ij} = \frac{1}{2}\left[W(\boldsymbol{x}_i - \boldsymbol{x}_j, h_i) + W(\boldsymbol{x}_i - \boldsymbol{x}_j, h_j)\right]. \tag{2.12.55}$$

In (2.12.52), $\tilde{\epsilon}$ is the unknown (stepping) factor for which $0 \leq \tilde{\epsilon} \leq 1$ [20]. XSPH moves a particle with velocity that is closer to the average velocity in its neighbourhood. The average velocity differs from the actual velocity by terms of order $\mathcal{O}(h^2)$, which is consistent with the errors in the other SPH equations [76].

Moving the particles with $\hat{\boldsymbol{v}}$ does not affect the conservation of linear and angular momentum (by ensuring appropriate symmetry for the terms in (2.12.55) [178]). It can be

seen from (2.12.52) that reversing the velocity reverses the trajectory in the absence of viscosity in the acceleration equation. Consequently, if $\hat{\boldsymbol{v}}$ is used, it is expected there is an invariant equivalent to the usual energy [76]. Moving the particles with $\hat{\boldsymbol{v}}$ means that advection is defined by

$$\frac{d}{dt} = \frac{\partial}{\partial t} + \hat{\boldsymbol{v}} \cdot \nabla. \tag{2.12.56}$$

Then the density can be calculated by solving the continuity equation, or, in principle, by the direct summation over the particles. As recommended in [76], when only one material is used in the simulation, the SPH continuity equation is defined as

$$\frac{d\rho_i}{dt} = \sum_{j=1}^{N} m_j \hat{v}_{ij}^{\beta} \frac{\partial W_{ij}}{\partial x_i^{\beta}}, \tag{2.12.57}$$

which was already introduced in (2.8.10). However, if more than one material is used and the densities differ more than a factor ~ 2, it is recommended to use

$$\frac{d\rho_i}{dt} = \rho_i \sum_{j=1}^{N} \frac{m_j}{\rho_j} \hat{v}_{ij}^{\beta} \frac{\partial W_{ij}}{\partial x_i^{\beta}}, \tag{2.12.58}$$

as previously defined in (2.8.14). XSPH was proved to be useful in simulations of nearly incompressible fluids such as water, in which it keeps the particles orderly in the absence of viscosity [20], in simulations of a compressible turbulence in which linear and angular momentum are conserved [178], and of course in solid mechanics simulations in which decay of shear is noticeable when an excessive amount of artificial viscosity is used [65]. Another positive side effect observed when XSPH is used, is that the tensile instability is alleviated [76].

2.13 Time Integration

After the approximation of the conservation laws is chosen, the SPH equations can be integrated in time with a numerical integration algorithm for PDEs (integration scheme), to obtain positions and velocities. Because the SPH algorithm reduces the original continuum PDEs to sets of ODEs, any stable time stepping algorithm for ODEs can be used [88]. There are many integration schemes to choose from. For example, the Euler integration, Runge-Kutta integration, Verlet integration, Leapfrog integration, or Predictor-Corrector integration to name some. By using the standard Leapfrog or the Predictor-Corrector integration, second order accuracy in time is achieved without requiring an excessive number of sweeps over the particles [37]. The time step for the simulation should be chosen according to the CFL condition [138] so the time-integration is stable. In some applications,

however, the time step must be significantly smaller to capture a propagating shock wave or shock front, e.g. close-in detonations.

The author finds the Predictor-Corrector integration scheme to be very stable and fast in the most structural dynamic applications, therefore, the Predict-Evaluate-Correct (PEC) algorithm is discussed further. In PEC, velocities and positions are predicted first in the middle of the time step

$$\tilde{\boldsymbol{v}}_i^{n+\frac{1}{2}} = \boldsymbol{v}_i^n + \frac{dt}{2}\boldsymbol{f}_i^n, \tag{2.13.1}$$

$$\tilde{\boldsymbol{x}}_i^{n+\frac{1}{2}} = \boldsymbol{x}_i^n + \frac{dt}{2}\boldsymbol{v}_i^n, \tag{2.13.2}$$

necessary variables are then evaluated

$$\rho_i^{n+\frac{1}{2}} = \rho(\tilde{\boldsymbol{x}}_i^{n+\frac{1}{2}}), \tag{2.13.3}$$

$$\boldsymbol{f}_i^{n+\frac{1}{2}} = \boldsymbol{f}(\tilde{\boldsymbol{x}}_i^{n+\frac{1}{2}}, \tilde{\boldsymbol{v}}_i^{n+\frac{1}{2}}, \rho_i^{n+\frac{1}{2}}, \ldots), \tag{2.13.4}$$

$$\boldsymbol{v}_i^{n+\frac{1}{2}} = \boldsymbol{v}_i^n + \frac{dt}{2}\boldsymbol{f}_i^{n+\frac{1}{2}}, \tag{2.13.5}$$

$$\boldsymbol{x}_i^{n+\frac{1}{2}} = \boldsymbol{x}_i^n + \frac{dt}{2}\boldsymbol{v}_i^{n+\frac{1}{2}}, \tag{2.13.6}$$

and after the correction, velocities and positions are calculated at the end of the time step

$$\boldsymbol{v}_i^{n+1} = 2\boldsymbol{v}_i^{n+\frac{1}{2}} - \boldsymbol{v}_i^n, \tag{2.13.7}$$

$$\boldsymbol{x}_i^{n+1} = 2\boldsymbol{x}_i^{n+\frac{1}{2}} - \boldsymbol{x}_i^n, \tag{2.13.8}$$

where $\boldsymbol{f}_i$ is the force per unit mass (acceleration), and superscripts n refer to the time step index. As pointed out in [37], in practice some simplifications are made to make the integration faster, e.g. the force $\boldsymbol{f}_i^n \approx \boldsymbol{f}_i^{n-1/2}$. As already mentioned in section *Insights*, for explicit time integration schemes, the time step dt can be taken as

$$dt = C_{\mathrm{CFL}} \cdot \min_i \left(\frac{h_i}{c_i + |\boldsymbol{v}_i|} \right), \tag{2.13.9}$$

where c_i and $\boldsymbol{v}_i$ are the adiabatic sound speed and the velocity of particle i, respectively. The factor C_{CFL} is chosen to satisfy the CFL condition. There are other ways to calculate the time step [37, 85] or [87]. However, from the author's experience, (2.13.9) is sufficient in

most cases. At the end, it does not matter how the time step is chosen, but one condition must be always fulfilled. Morris expressed it quite fittingly:

> *...the maximum rate of propagation of information numerically must exceed the physical rate.* [37]

A graphical representation of the SPH calculation cycle is shown in Fig. 2.53.

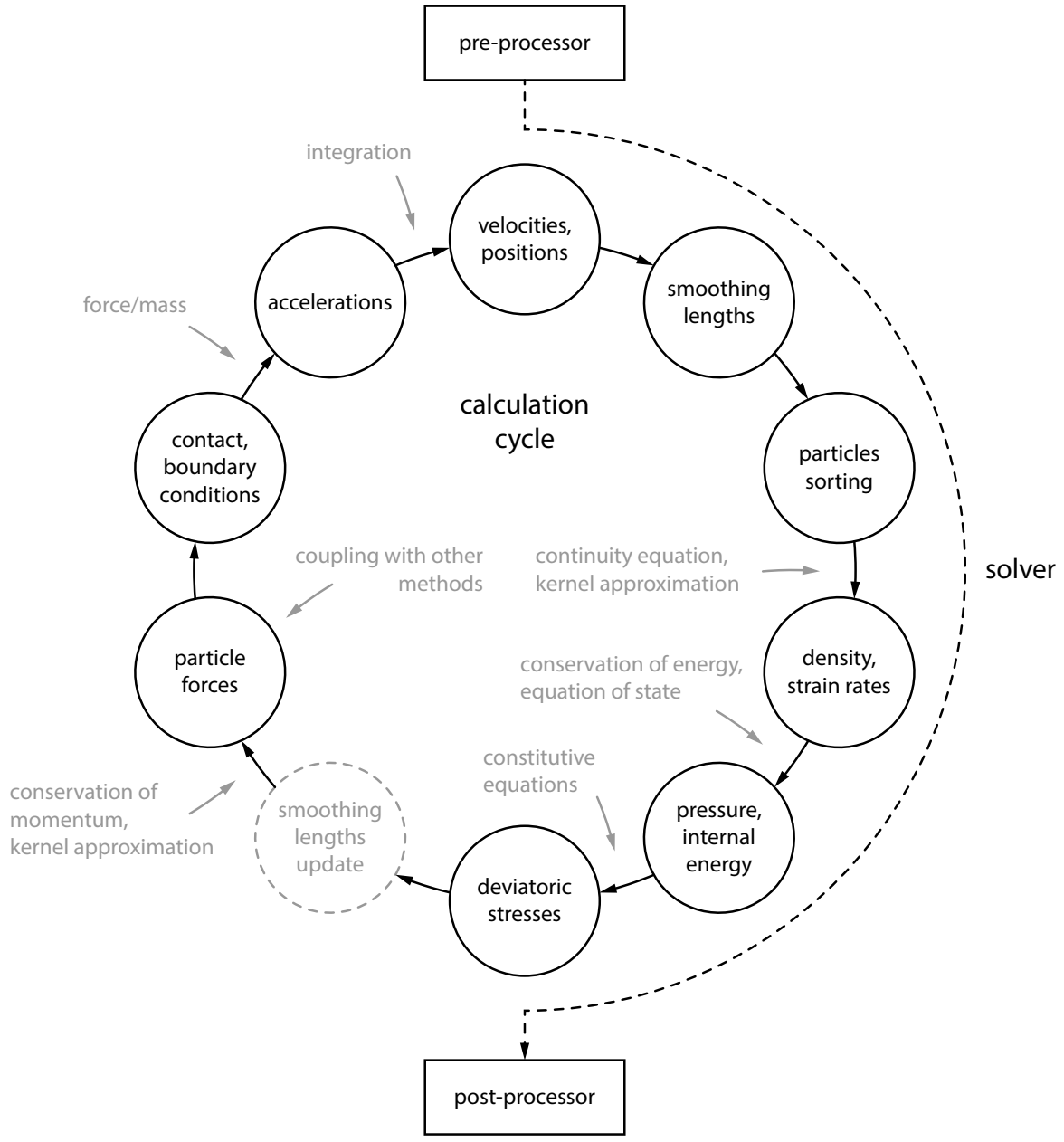

Fig. 2.53. SPH calculation cycle.

Chapter 3

From Theory to Application

The chapter serves as a 'bridge' between the theoretical background and numerical modelling. Discussed are the aspects of Smoothed Particle Hydrodynamics (SPH) which might not be obvious from the presented theory. The focus is on the number of neighbouring particles over time, drawbacks of the standard SPH formulation, the impact of the kernel type, the tensile instability, and the interaction between particles. At this point, the mathematical formulations are substituted with numerical examples to make the previous statements visual.

3.1 Number of Neighbouring Particles

The size of the support domain might be constant during the simulation, however, that would be a very special case. The main reason why the support contracts and expands in time is to keep the number of neighbouring particles more or less constant. Of course, this applies to the Eulerian kernels only as previously discussed in section *Eulerian and Lagrangian Kernel*. But what does it mean in practice and how to find out if the concept of SPH works?

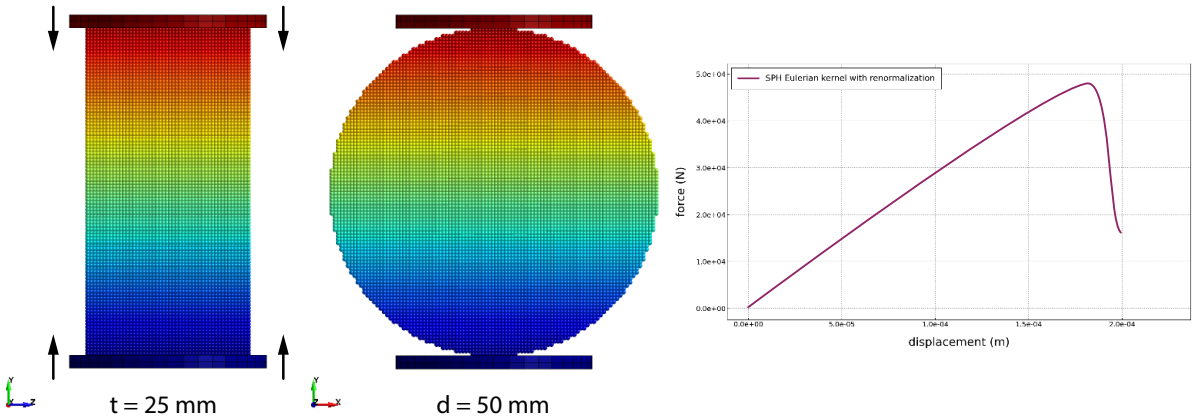

Fig. 3.1. Brazilian splitting test example.

To understand the adaptive nature of SPH, a simple example is discussed first. In Fig. 3.1, a schema of the Brazilian splitting (tensile) test, also known as the indirect tensile test, is shown. Put simply, the test is used in rock mechanics for determining tensile strength of a rock. More about the experiment itself can be found in [179, 180]. Here, SPH was used to simulate the rock disk (specimen), and the Finite Element Method (FEM) to simulate the rigid platens. In the simulation as well as in the real experiments, the steel platens move towards each other and crush the specimen in between them. Although the experiment seems like a compressive test, the actual failure of the specimen is in tension, therefore, the indirect tensile test.

For the purpose of simplicity the standard Mohr-Coulomb material model was used. Since the focus of the example is not on the material modelling but SPH, the material model itself is not discussed here in detail, only the material parameters are given. The rock specimen had assigned density of 2750 kg/m^3, shear modulus of 18 GPa, Poisson's ratio of 0.2, inner friction angle φ of 45°, and cohesion c of 30 MPa. Since no tension cutoff or additional yield surfaces were used, the Mohr-Coulomb failure surface was defined as

$$\tau_{max} = c + \sigma_n \tan\varphi, \tag{3.1.1}$$

where τ_{max} is the maximum shear stress (on any plane), and σ_n is the normal stress (on that plane). As discussed in section *Material Strength*, σ_n is positive in compression, which is consistent with the graphical interpretation in Fig. 3.2. The reason why the *planes* are mentioned is that the Mohr-Coulomb model can be easily enhanced into a jointed model. However, in this case only the standard Mohr-Coulomb was used.

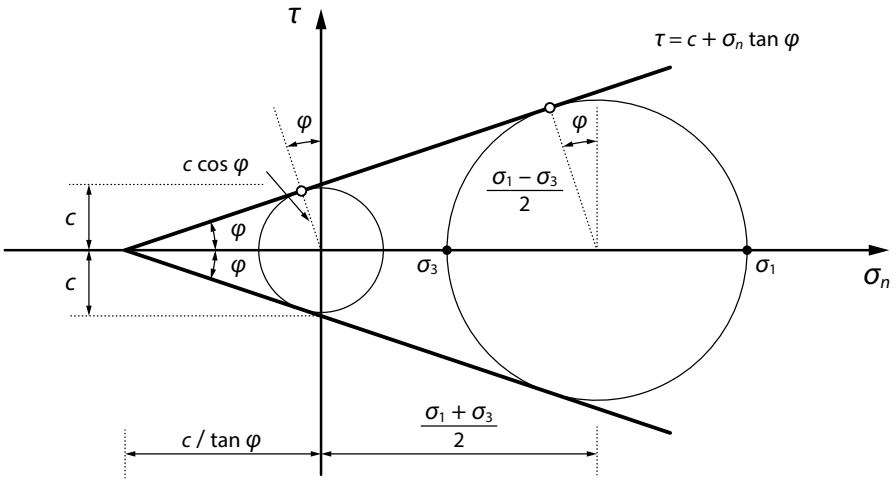

Fig. 3.2. Mohr-Coulomb criterion with a straight-line failure envelope.

With respect to (3.1.1), the uniaxial tensile strength f_t can be calculated as

$$f_t = c\,\frac{2\cos\varphi}{1+\sin\varphi} = 2c\tan\left(45 - \frac{\varphi}{2}\right), \tag{3.1.2}$$

which in terms of a vertical force F gives

$$f_t = \frac{2F}{\pi t d} = 0.637\,\frac{F}{td}, \tag{3.1.3}$$

where t and d are the thickness and diameter of the disk, respectively. Taking the material parameters and the size of the disk into account, i.e. thickness $t = 25\,\text{mm}$ and diameter $d = 50\,\text{mm}$ as shown in Fig. 3.1, the maximum force F should be close to 48.8 kN. Indeed, this is the case as can be seen in the graph in Fig. 3.1. Since the measured resistance of the specimen is within an acceptable range, it is considered to be a proof that the SPH approximation worked as expected. Yet, the SPH behaviour should be discussed in detail.

The simulation was calculated in 3D using the isotropic Eulerian kernel with the renormalization introduced in section *The Renormalization*. The particles were distributed in a cubic lattice with a spacing $\Delta x = 0.5\,\text{mm}$ in all three directions, therefore, the cross-section is not perfectly circular but polygonal. The initial support was defined with recommended $h = 1.2\,\Delta x$ and $\kappa = 2$, as discussed in section *Variable Smoothing Length*. The cubic spline defined in (2.4.15) was used as the kernel, yet no special treatment was applied to alleviate the tensile instability, since the material failure was observed before any particle clustering. The smoothing length was updated in time as defined in (2.4.36). The top and bottom platens were simulated with rigid FEM, therefore, a contact between the particles and the elements was defined. The contact algorithms are discussed in **Chapter 4** *Coupling SPH and FEM* in detail.

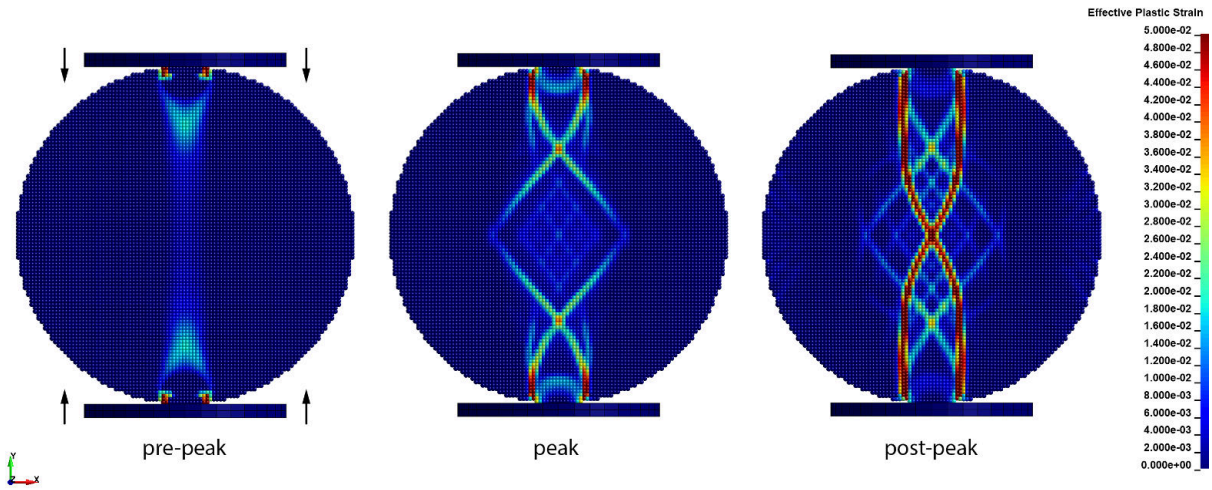

Fig. 3.3. Brazilian splitting test – effective plastic strain over time.

To understand what the particles 'did' during the simulation, the plastic deformation should be evaluated first. In Fig. 3.3, three states of the specimen's deformation are shown. The pre-peak corresponds to the loading point in which cracks start to develop. The peak shows the deformation at the point of the maximal force, and the post-peak shows the deformation at the end of the softening. The pre-peak damage shows a formation of a main vertical crack which is one of the expected failure modes. At the peak, the specimen loses resistance and additional cracks are formed. The post-peak shows a complete specimen failure; multiple vertical cracks are formed.

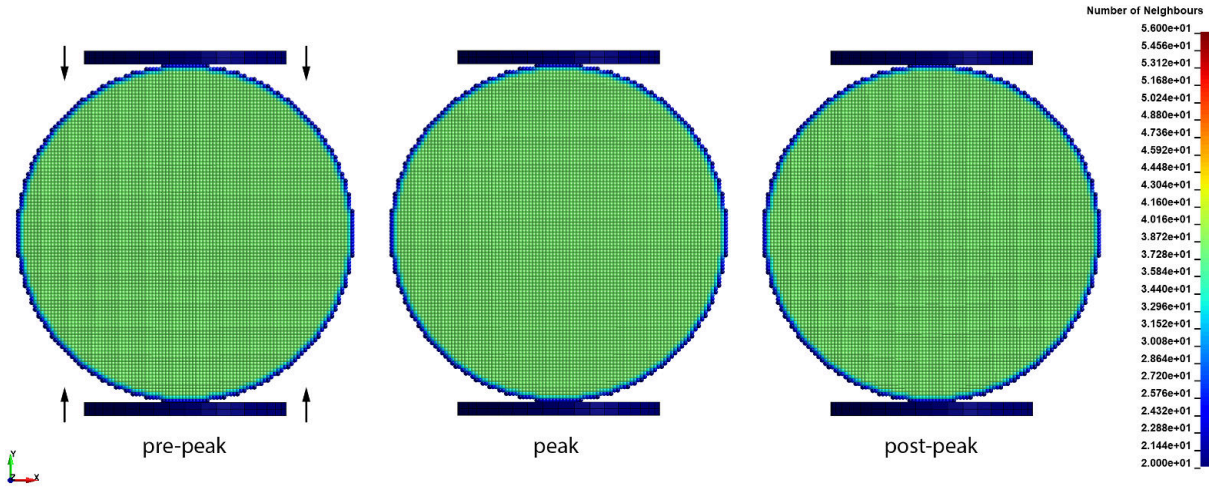

Fig. 3.4. Brazilian splitting test – number of neighbours over time.

The results make complete sense. But why was the solution stable? The cracks opened, the particles moved from each other, the consistency was not preserved, yet the solution was stable. Looking at the number of neighbours per each particle in Fig. 3.4 it seems that nothing interesting happened. The plots are basically identical. From the moment of the initialization till the end the number of neighbours is constant (per particle). Well, this is the answer. This is the reason why was the solution stable. Since every particle had sufficient number of neighbours, the accuracy was sufficient. This is the adaptivity of SPH. The 'development' algorithm in (2.4.36) expanded/contracted the support domains in such a way the number of neighbours was constant.

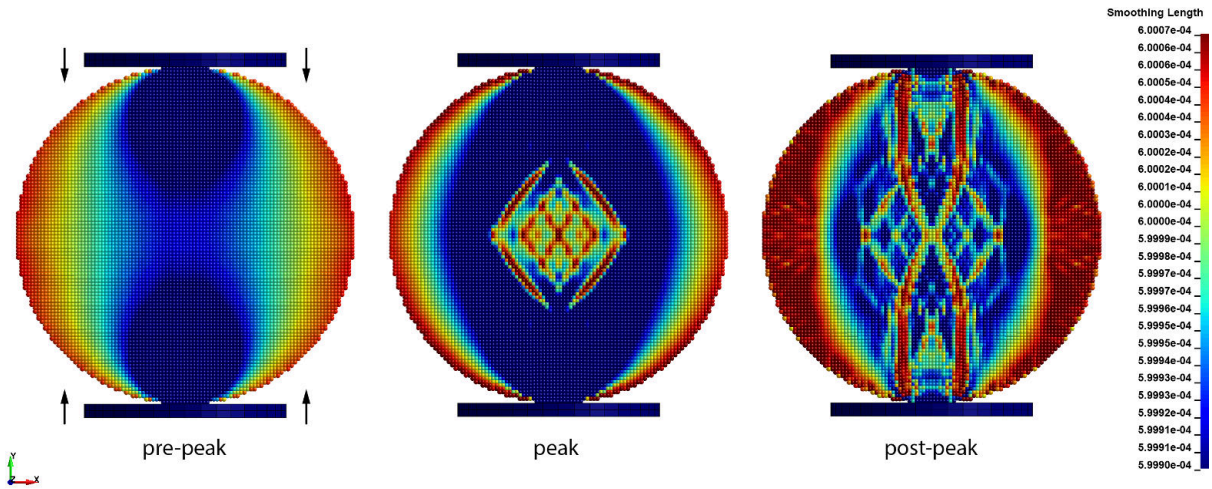

Fig. 3.5. Brazilian splitting test – smoothing length over time.

A closer look at the development of the smoothing lengths gives the full story. As shown in Fig. 3.5, the smoothing lengths were constantly updated from the beginning. Since the particles in the column between the platens were in compression, their relative motion were towards each other. Therefore, the smoothing lengths decreased (blue) from the initial value of 0.6 mm. In contrast, the tension on the outer surface caused a separation of the particles, therefore, the smoothing lengths increased (red). At the peak, when the main

cracks were already opened, the particles in their proximity had increased support, yet the rest of the domain was in compression with smaller support domains. The post-peak shows quite complex situation. Almost every particle had a different size of the support. The pattern is far more complex than the strain itself. The smoothing lengths show not only the current state in time but provide a very good estimate to what will happen next.

The mechanics of SPH is very complex compared to the classical FEM. For that reason, SPH results might give an impression that something does not work. However, if the number of neighbouring particles is sufficient and the tensile instability is not amplified, the problem is most likely somewhere else. SPH is a complex tool which can simulate either the Universe expansion or indirect tensile test. Yet there are another aspects which should be kept in mind.

3.2 Particle Interaction

Another important aspect of SPH simulations is the particle interaction. Strictly speaking of the standard SPH, i.e. the formulation with the isotropic Eulerian kernel without corrections, no additional mechanism is needed for the particle interaction between two separate parts. No contact algorithm or coupling is necessary; particles interact between each other when their support domains overlap. However, this built-in mechanism might cause difficulties.

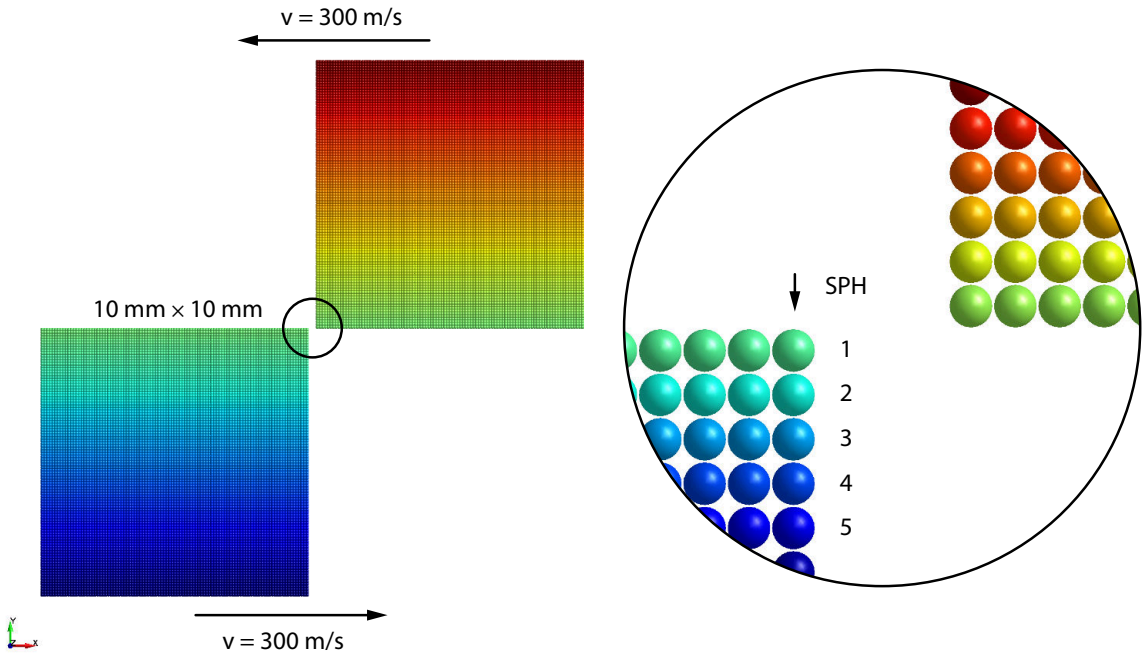

Fig. 3.6. Two flying boxes example.

An example in which two flying boxes pass each other as shown in Fig. 3.6 can be discussed. A very simple 2D model in which two identical 10 mm × 10 mm boxes with a particle spacing of 0.1 mm fly 300 m/s in opposite directions with a 'distance' between them.

The simulations were calculated with the isotropic Eulerian kernel with recommended $h = 1.2\,\Delta x$ and $\kappa = 2$, as discussed in section *Variable Smoothing Length*. No special treatment was applied to alleviate the tensile instability, no technique to update the smoothing length was used. Furthermore, a linear elastic material model was used with assumptions of steel mechanical properties, i.e. density of 7850 kg/m^3, Young's modulus of 210 GPa, and Poisson's ratio of 0.3. If the same simulation was calculated with FEM event with a contact specified, there would be no interaction. But with SPH?

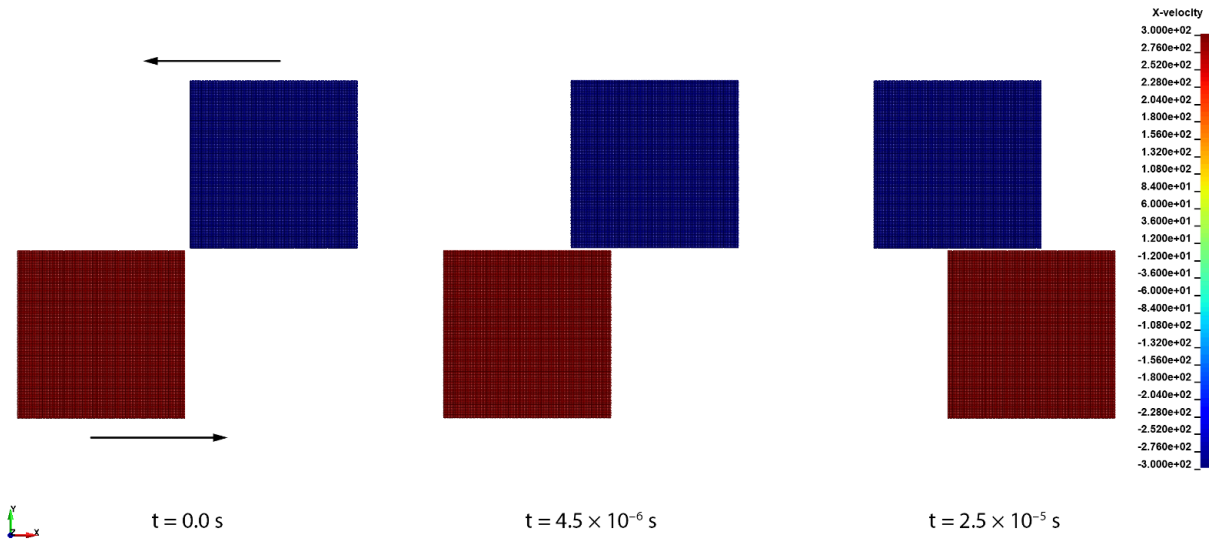

Fig. 3.7. Two flying boxes interaction – distance between the boxes 0.24 mm (support size 0.24 mm).

Assuming the distance between the two boxes is 0.24 mm, no interaction would be expected. The reason for this is that the support domain of the particles is exactly 0.24 mm. Put simply, at the distance of 0.24 mm the value of the kernel is zero. As shown in Fig. 3.7 it is indeed the case. The boxes were just flying with initial velocities with no interaction.

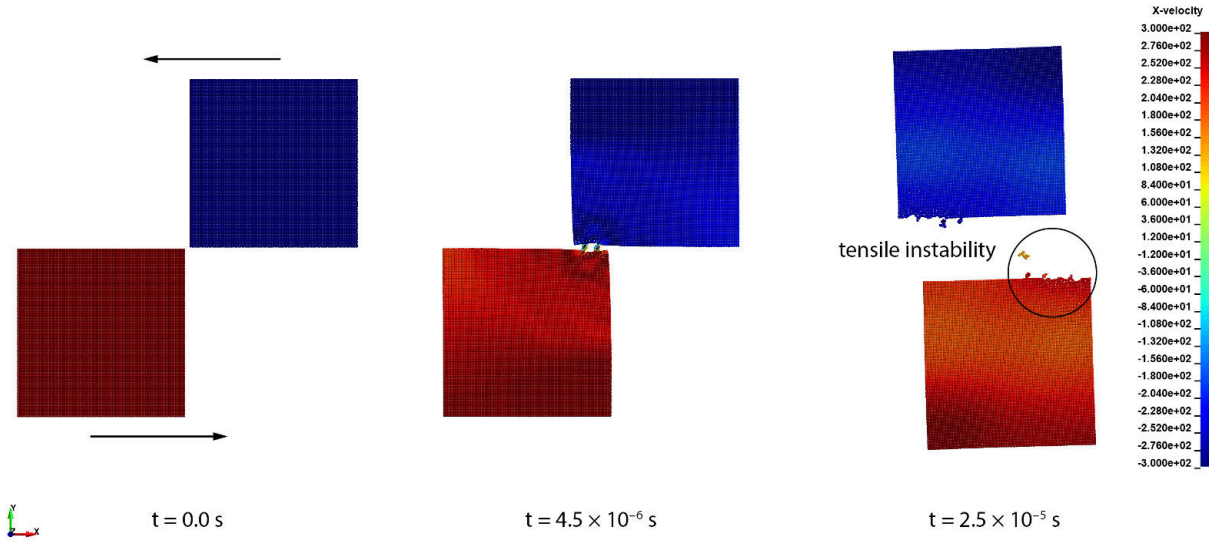

Fig. 3.8. Two flying boxes interaction – distance between the boxes 0.2 mm (support size 0.24 mm).

However, when the distance is only 0.2 mm, which means the boundary particles are also neighbouring particles, the interaction is more than just noticeable as shown in Fig. 3.8. From the results it is obvious, that when neighbouring particles of the boxes were in a proximity, a region of an artificial interaction was formed. It almost seems that a joint connection was created. Since the relative momentum of the boxes was quite high, the joint was broken and the boxes just bounced from each other. As obvious from Fig. 3.8, the boundary particles were ripped out and the initial shapes of the boxes were distorted. The interaction could be described as a side impact rather than a front impact, however.

When the distance between the boxes is equal to the particle spacing, i.e. 0.1 mm, the result is even more questionable. As shown in Fig. 3.9, the corner particles literally glued two independent parts together, formed a joint, and completely changed the physics. Due to the temporary joint creation, the velocity component in the X-direction was transformed into a velocity component in the Y-direction. In other words, the horizontal motion was transformed into a rotation and then into a vertical motion.

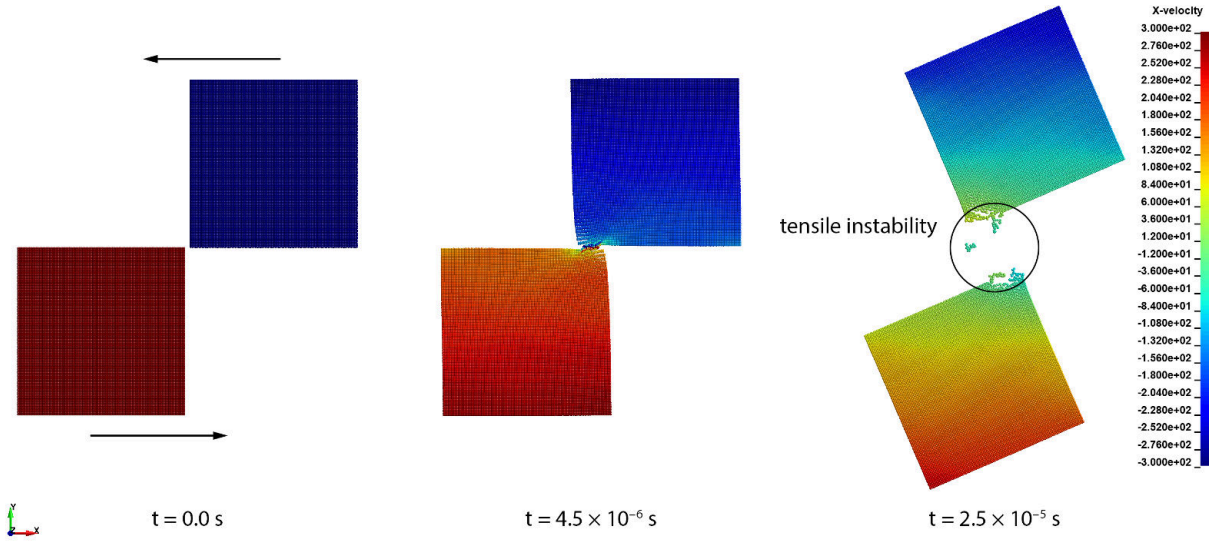

Fig. 3.9. Two flying boxes interaction – distance between the boxes 0.1 mm (support size 0.24 mm).

The results can be discussed in more detail to better understand the theory of SPH. For this purpose, the stress component in the X-direction, density, and number of neighbouring particles were extracted for the first five SPH particles in different layers of the bottom box as shown in Fig. 3.6. The results are collected in Fig. 3.10, Fig. 3.11, and Fig. 3.12 for the distance between the boxes of 0.24 mm, 0.2 mm, and 0.1 mm, respectively.

Starting with the distance of 0.24 mm, there should be no change compared to the initial state. In Fig. 3.10, however, some oscillations in the stress are noticeable. Yet, the peak value is only -5×10^{-7} Pa which is rather numerical zero. Oscillations are also visible in the number of neighbouring particles. The reason for that is of course a numerical noise, since the support of particle 1 was *touching* the particles in the first layer of the top box. The density is constant, no issue there.

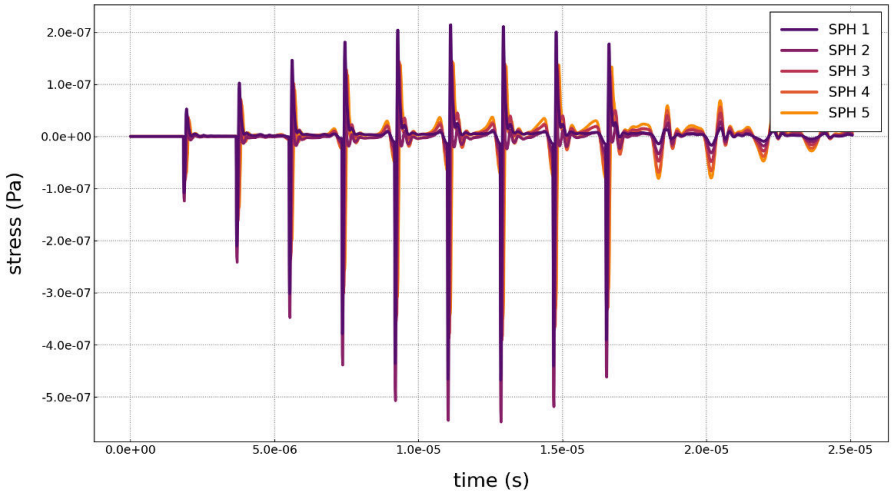

(a) stress component in the X-direction

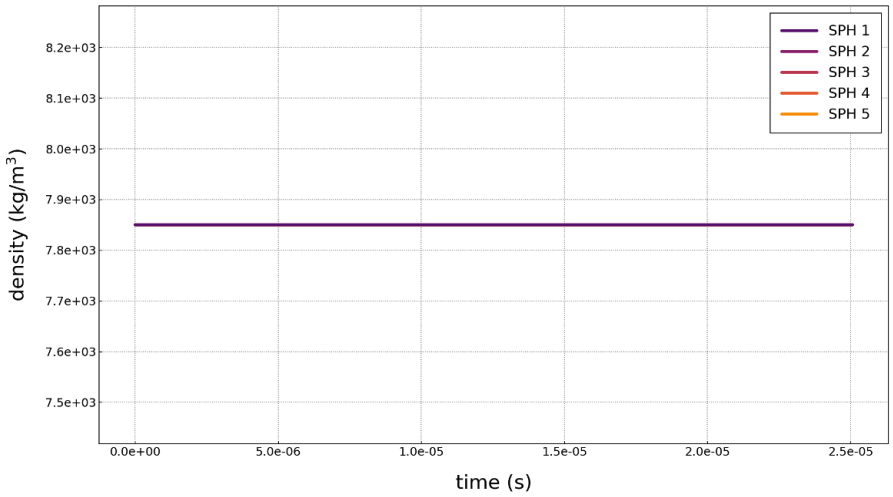

(b) density

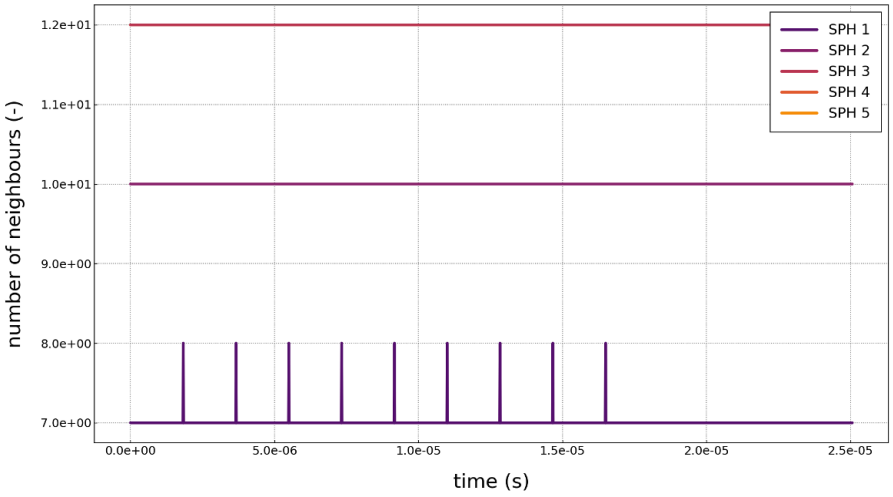

(c) number of neighbours

Fig. 3.10. Two flying boxes interaction – distance between the boxes 0.24 mm (support size 0.24 mm).

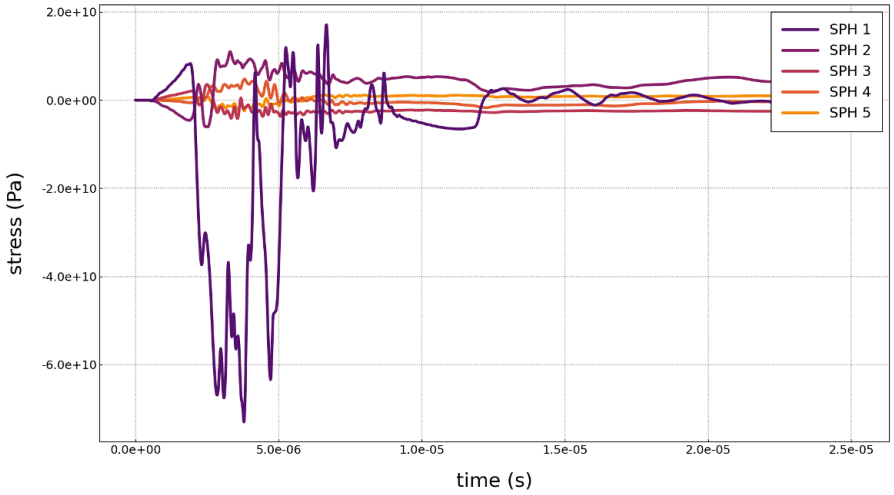

(a) stress component in the X-direction

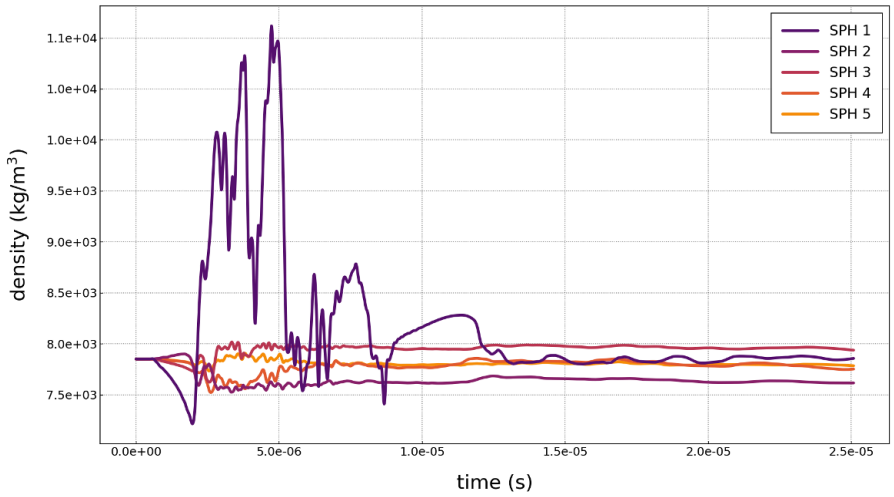

(b) density

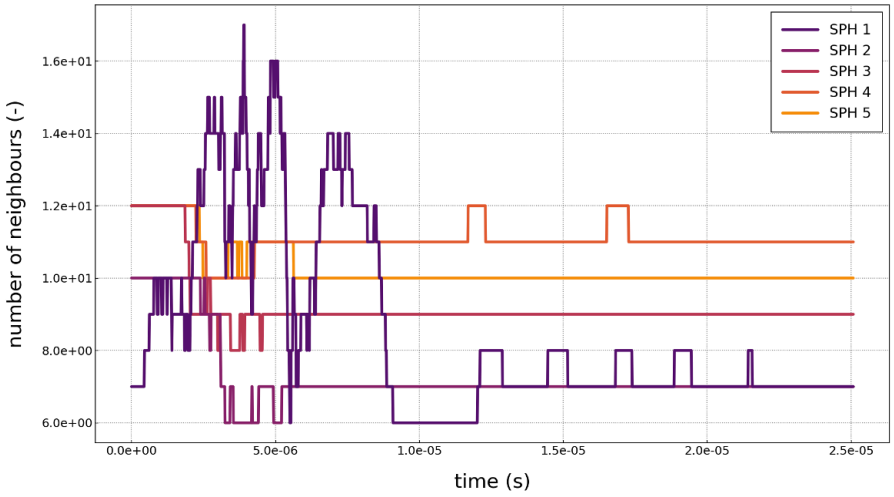

(c) number of neighbours

Fig. 3.11. Two flying boxes interaction – distance between the boxes 0.2 mm (support size 0.24 mm).

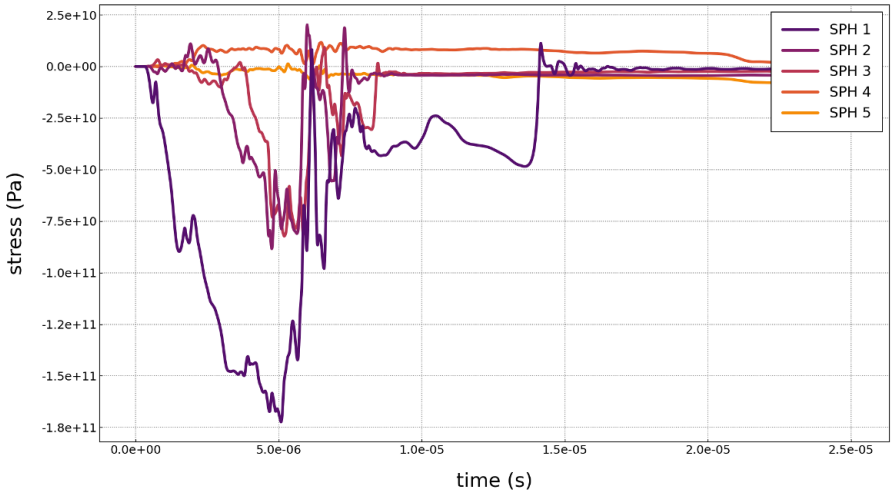

(a) stress component in the X-direction

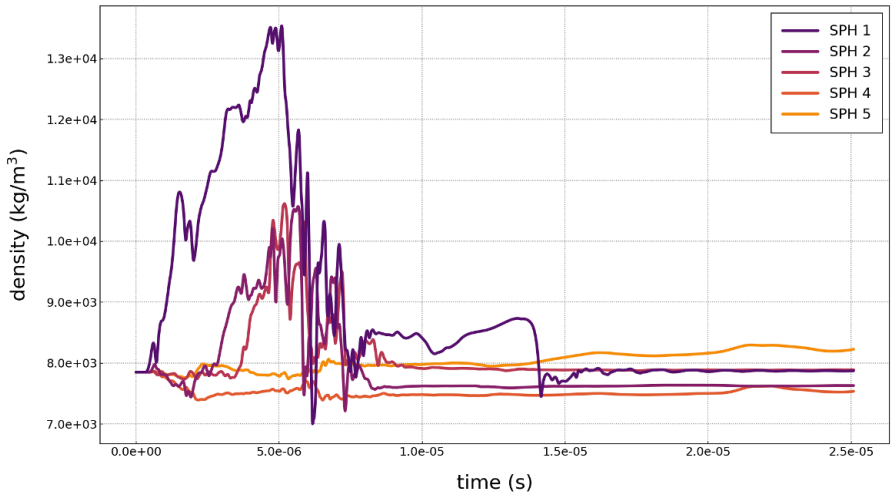

(b) density

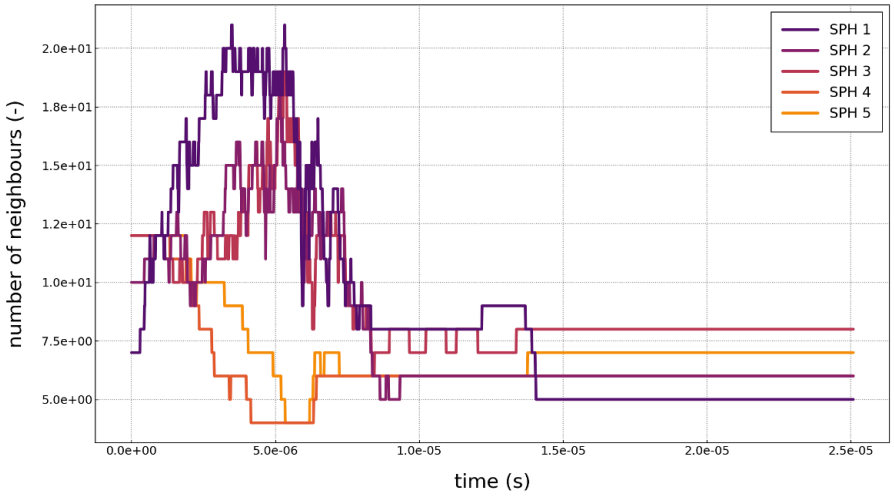

(c) number of neighbours

Fig. 3.12. Two flying boxes interaction – distance between the boxes 0.1 mm (support size 0.24 mm).

For the distance of 0.2 mm it is clear from Fig. 3.11 that some stress changes were developed. Yet, from all the graphs in Fig. 3.11 it seems that only particle 1 was exposed to the full impact force; peak stress -7×10^{10} Pa (compression in the X-direction). The density graph shows an expansion at the beginning. This is due to the development of a friction force. In other words, the top box was dragging the boundary particles with it which resulted in a momentary expansion. However, after the joint was formed, a significant increase in compaction can be seen at 4.5×10^{-6} s. Interestingly enough, the number of neighbouring particles of particle 1 almost doubled compared to the initialization.

For the distance of 0.1 mm the mechanics is again different from the two previous cases. For particle 1 there was no expansion in volume or tension in the X-direction. The stress and density graphs of particle 1 clearly show a result of an impact, see Fig. 3.12. The stress peak of -1.8×10^{11} Pa together with the compaction up to double of the initial density prove that something went wrong. Yet, it can be seen again that the number of neighbouring particles doubled compared to the initialization. This proves that the concept of the Eulerian kernel works correctly, yet with side effects. To eliminate the issue with the particle interaction, the Lagrangian kernel can be used instead. As discussed in the following sections, changing to the Lagrangian kernel does not have to be a good trade-off, however.

3.3 Tensile Instability Trade-off

The tensile instability was introduced in section *Tensile Instability*, yet only an illustrative example was provided in Fig. 2.43. In this section, the impact of the tensile instability is shown on a real example. Discussed is quite famous experiment in which two rubber rings, here elastic, bounce from each other in high speed. A schema of the example is shown in Fig. 3.13. Note that similar simulations and experimental results are given in many papers [181, 182] or [26, 76, 183, 184, 128, 130]. Despite the available results, to understand the influence of the tensile instability, such a simple stability test should be always performed when possible.

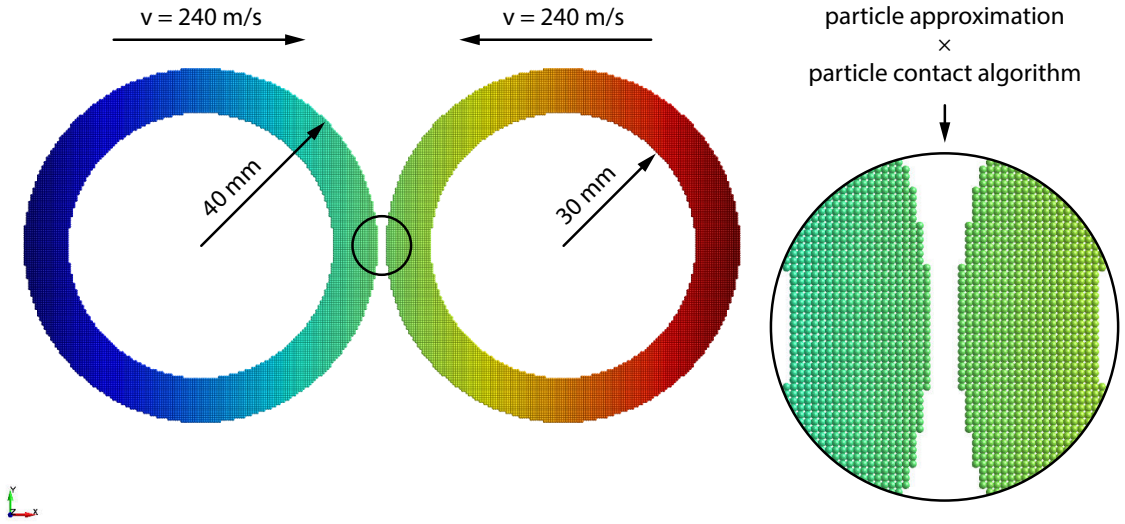

Fig. 3.13. Two elastic rings impact example.

The example consists of two flying elastic rings in a collision course. Both rings are identical, i.e. inner radius of 30 mm and outer radius of 40 mm. Only their velocity vector is opposite, i.e. velocity of $\pm 240\,\mathrm{m/s}$. In this particular case the material was linear elastic, with density of $1000\,\mathrm{kg/m^3}$, Young's modulus of 10 MPa, and Poisson's ratio of 0.39. The simulations were calculated in 2D, using a particle distribution in a cubic lattice with a particle spacing of 0.5 mm. As shown in [181], the cubic lattice distribution is the most sensitive when it comes to the tensile instability. The standard smoothing length $h = 1.2\,\Delta x$ and $\kappa = 2$ were used.

With regard to the standard SPH, i.e. the formulation with the isotropic Eulerian kernel, even with the renormalization, any interaction between two separate parts is handled naturally. This is again due to the adaptive nature of SPH. Yet, in the standard SPH the tensile instability is not treated. Therefore, after the impact, both rings fell apart as can be seen in Fig. 3.14. Why? In the initial state, all the particles have the same velocity, therefore, the stress is constant (zero). After the impact, however, regions of compression (red) and tension (blue) are formed. That can be seen at time $1 \times 10^{-4}\,\mathrm{s}$. The instabilities are formed in both regions, yet in tension they are more visible since the particles separate. Although the particles move from each other in the tensile region, the stress does not increase, as explained in Fig. 2.45. As a result, the solution is not stable and cracks propagate through the elastic material.

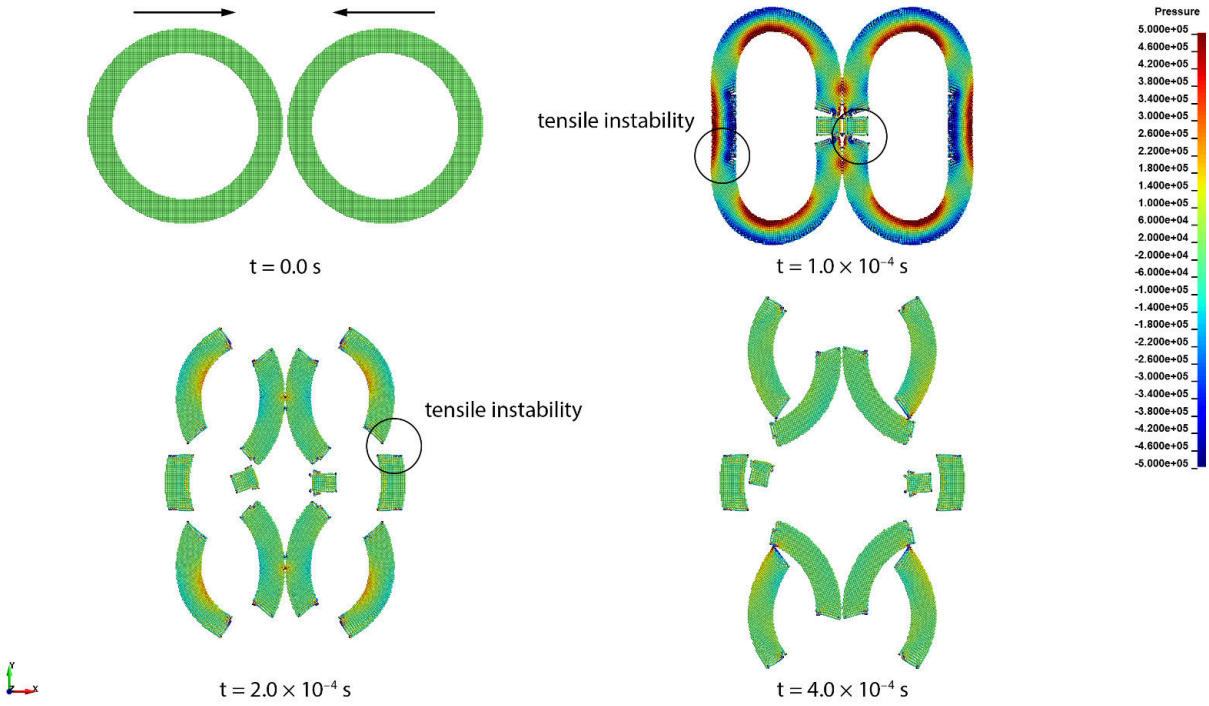

Fig. 3.14. Two elastic rings impact – isotropic Eulerian kernel with renormalization.

There are many ways to deal with the tensile instability. The easiest solution is to use the total Lagrangian kernel Fig. 2.38. The list of the neighbouring particles is defined during the initialization and never updated. Therefore, the kernel deforms and follows the neighbouring particles as they move. However, SPH is no longer adaptive, there is no update in the neighbouring list. Therefore, the interaction between separate parts must

be treated differently. A possible solution is to introduce a particle contact algorithm, discussed in detail in [183]. The particle contact algorithms are often very complex and sensitive. In other words, what works in one case, most likely will not work in other. Losing the adaptivity of SPH in order to suppress the tensile instability is a bad trade-off.

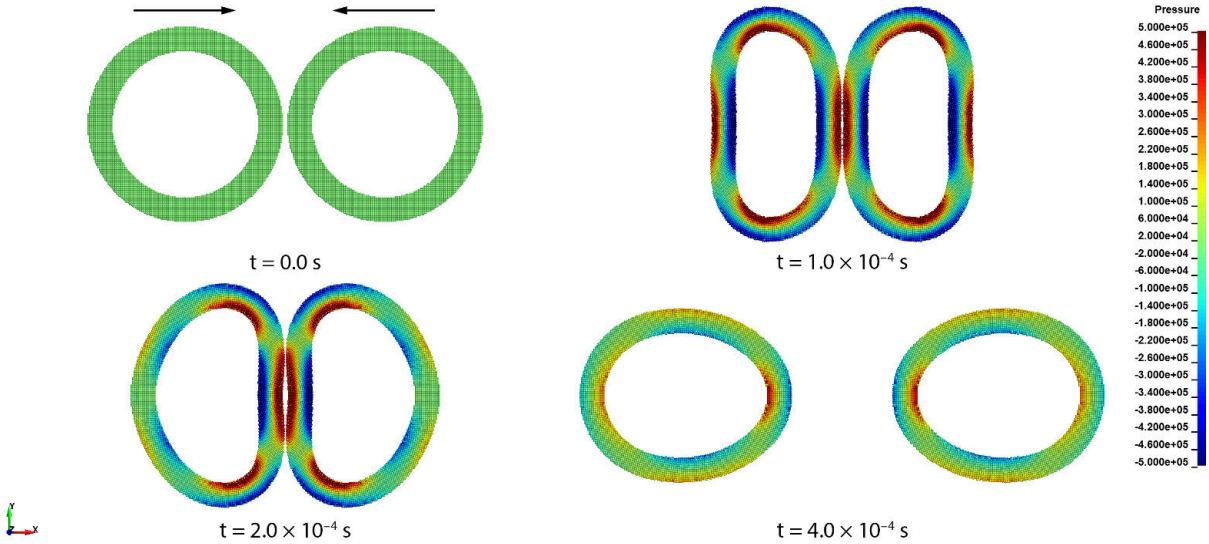

Fig. 3.15. Two elastic rings impact – total Lagrangian kernel with renormalization.

As shown in Fig. 3.15, using the total Lagrangian kernel indeed solves the tensile instability problem. The regions of compression (red) and tension (blue) are formed again, yet there is no stability issue. Without further details, the contact was set up to mimic the results of the particle interaction in the standard SPH. Therefore, after the impact at time 1×10^{-4} s, the elastic rings bounce from each other and fly in opposite directions.

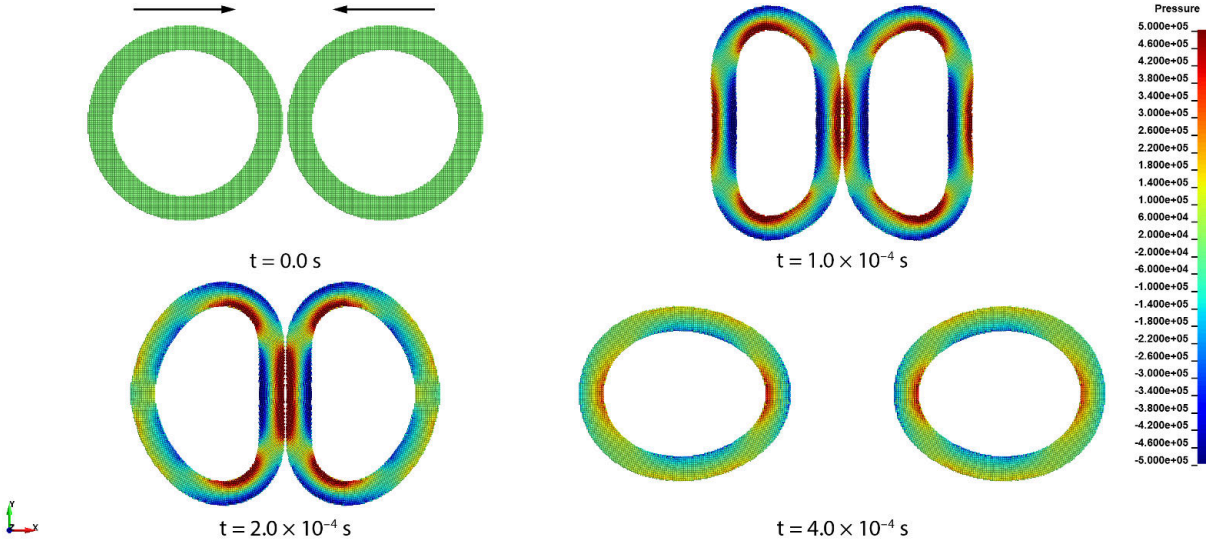

Fig. 3.16. Two elastic rings impact – MLSPH.

Of course, there is another solution. Using Moving Least Square Particle Hydrodynamics (MLSPH) the tensile instability is alleviated enough to be hardly noticeable. The adaptivity

of SPH is preserved, the boundary treatment improved, and the stability and accuracy of the solution increased. Of course, the solution time can be rather expensive, discussed in detail in the following section. Results of MLSPH can be seen in Fig. 3.16. Comparing the total Lagrangian kernel and MLSPH results, one can find no difference.

3.4 Accuracy with MLS Interpolant

As previously discussed in section *SPH Corrections*, the standard SPH formulation suffers from some numerical problems such as the boundary inaccuracy and the tensile instability. Furthermore, under some circumstances the standard SPH might produce results with errors larger than those obtained using other methods tailored for specific problems [85]. There is a simple example in which all the shortcomings can be shown – a wave propagation through a rod. There are other variants of the test, e.g. the well known Taylor impact test, yet the wave propagation will do just fine. In any case, all the tests are considered to be benchmarks of numerical methods. There is a good reason for that.

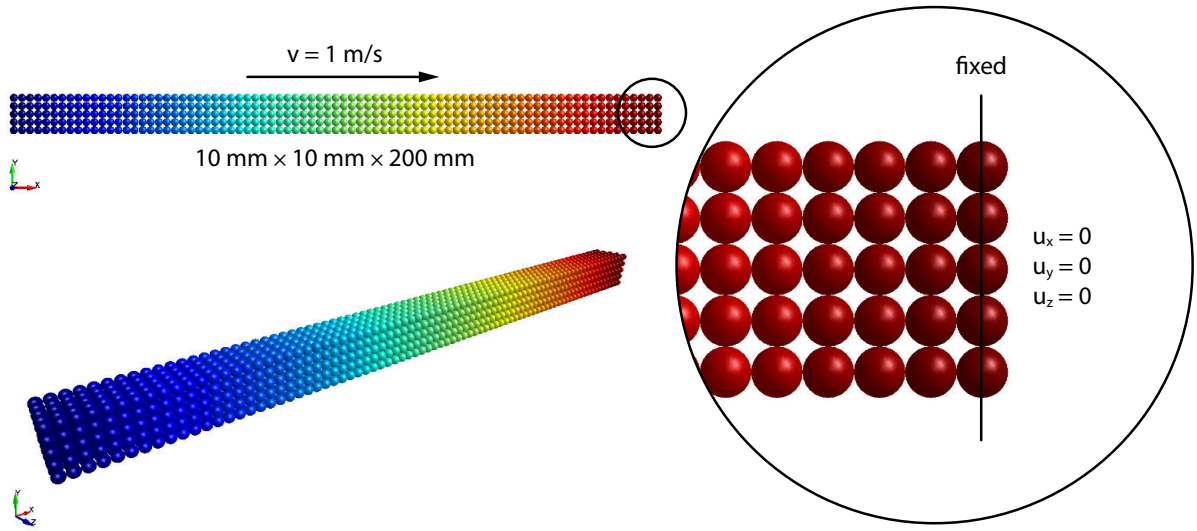

Fig. 3.17. Wave propagation example.

In the wave propagation test, a shock front propagates through a rod which is fixed on one side and free on the other. The shock front cannot escape from the rod unless there is a damping or other dissipative mechanism. If there is no damping, the shock front should bounce from the ends of the rod and create two stress zones in which one is in compression and the second in tension.

In the following example, three numerical models were calculated in order to find out which one captures longitudinal displacements of a rod without energy dissipation or stability issues over time. The numerical solutions are also compared with the analytical solution, which is the 'correct solution'. Since the longitudinal dimension of a rod is larger than its other dimensions, 1D simplified assumptions can be used for the analytical solution. Then

the longitudinal displacement in time is given as

$$u(x,t) = \sum_{k=1}^{\infty} \frac{8(-1)^{k+1}}{\pi^2(2k-1)^2} \frac{v_0 l}{c} \sin\left((2k-1)\frac{c\pi}{2l}t\right) \cos\left((2k-1)\frac{\pi}{2l}x\right), \tag{3.4.1}$$

where v_0 and l are the initial velocity and length of the rod, respectively; c is the adiabatic sound speed which is a material property, x is the location of the unknown displacement, and t is the time. The adiabatic sound speed in 1D can be taken as $c = \sqrt{E/\rho}$, where E and ρ are the Young's modulus and density, respectively.

In this particular example, also discussed in [176, 177], an elastic rod with a rectangular cross-section of 10 mm × 10 mm and length of 200 mm was used. The free end of the rod was at $x = 0$, and the fixed end at $x = l$. The initial velocity of the rod was 1 m/s, density of 2000 kg/m^3, Young's modulus of 10 MPa, and Poisson's ratio of 0 so the assumptions of 1D apply. The simulations were calculated in 3D, however. Again, the linear elastic material model was used. The recommended $h = 1.2\,\Delta x$ and $\kappa = 2$ were used as discussed in section *Variable Smoothing Length*. The particle spacing was constant, uniform $\Delta x = 2.5$ mm in all three dimensions. A schema of the example is shown in Fig. 3.17 in which the free end is on the left-hand side and the fixed end on the right-hand side.

The material parameters, initial conditions, and solver settings were the same for all three models. The only difference was the type of the kernel – the isotropic Eulerian kernel, the isotropic Eulerian kernel with the renormalization, see section *The Renormalization*, and the Moving Least Squares (MLS) based kernel with linear monomial basis functions, see section *MLSPH*. The first model with the isotropic Eulerian kernel is considered to be the standard SPH formulation. Applying the renormalization second rank tensor $\boldsymbol{B}$, improvements in stress gradients are expected [35]. Using MLSPH not only improvements in stresses but in accuracy as well are expected.

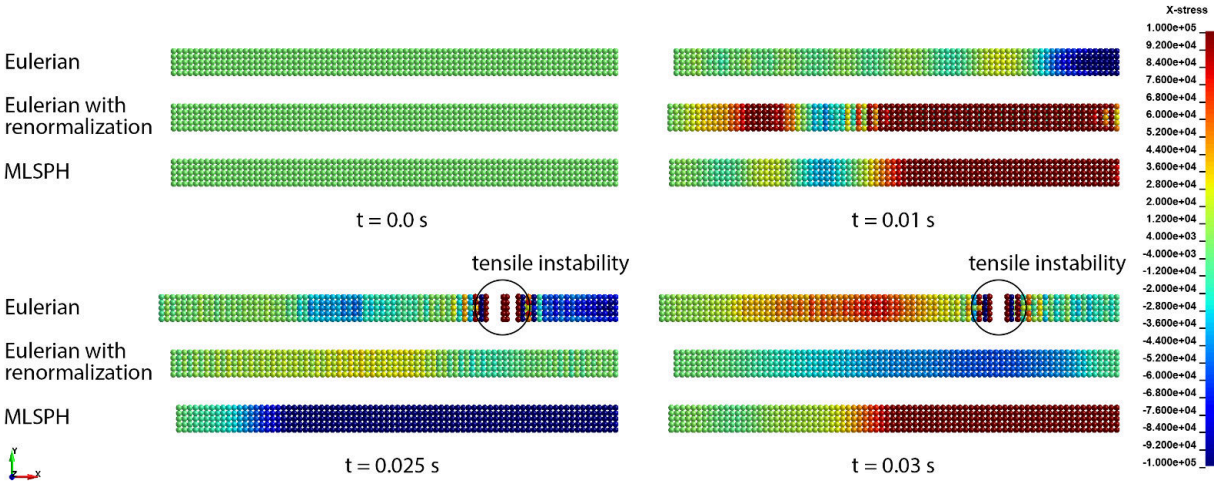

Fig. 3.18. Wave propagation over time.

The shock front propagation over time is shown in Fig. 3.18. Starting at time 0 s, all the particles have the same velocity, therefore, the stress distribution is constant (stress

component in the X-direction); the colour is green. In other words, at this point the rod is about to impact a 'rigid' surface, yet simulated with the fixed particles on the right-hand side. After the impact, the shock front starts to propagate from the fixed end through the rod and bounce back from the free end. This can be seen through time 0.01 to 0.03 s. The differences in the stress distribution for each model are obvious. Starting with the isotropic Eulerian kernel, it seems that the shock front is a bit behind compared to the other two models. At the time when the stress is in compression, the other two models show tension. Furthermore, at time 0.025 s, the tensile instability is fully developed. It is obvious that after the numerical crack is fully grown through the cross-section, the rod is split into two parts.

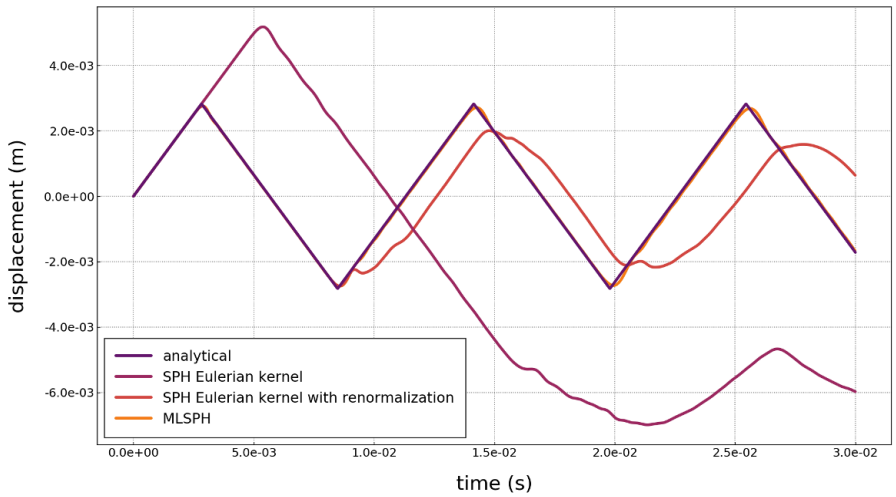

(a) displacement at $x = 0$

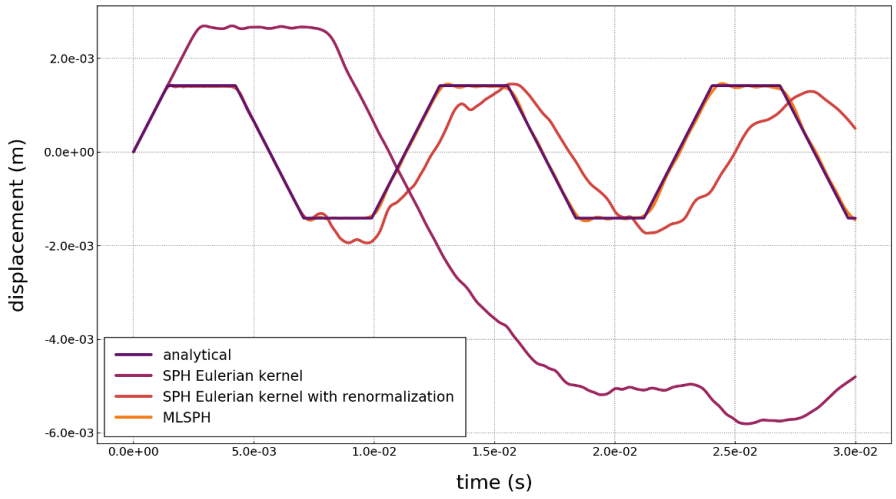

(b) displacement at $x = l/2$

Fig. 3.19. Longitudinal displacement over time.

The second model, the one with the isotropic Eulerian kernel and the renormalization, seems to alleviate the tensile instability. Yet something is wrong with the stress distribution. At time 0.01 s it seems that two shock fronts were formed. This would be possible only if the strain rates were burdened with an error. Moreover, at time 0.025 s and also 0.03 s it

seems the stress intensity drops significantly. This is usually the case when a damping or other form of energy dissipation is present.

The last model, the MLSPH based kernel shows stable results over time. It is obvious that only one shock front propagates through the rod and the stress state changes from tension to compression periodically. Of course, the stress is not the only compared variable. In Fig. 3.19 two graphs of longitudinal displacements can be discussed further.

Starting with the graph for $x = 0$ (free end); as already mentioned, the first model is a bit behind when it comes to the timing. This is supported by the shown displacement in time. It seems that the first shock front reflection resulted into an excessive amplitude. It is also evident that the tensile instability broke the solution when the second reflection was about to happen. The isotropic Eulerian kernel with the renormalization is not too far from the analytical solution. However, the mentioned damping effect and the second shock front brought a noise into the results; the error is increasing in time. The MLSPH solution is more than sufficient when it comes to the comparison with the analytical solution. The curves of the analytical solution and the MLSPH solution overlap, therefore, it is difficult to see two curves. Yet the peak of the MLSPH curve is slightly reduced. This can be addressed to the discretization error, however.

The second graph in Fig. 3.19 shows again a longitudinal displacement, yet in the middle of the rod, i.e. $x = l/2$. What was already said about the three models can be said again. The MLSPH solution is without a doubt the most accurate one. Should be mentioned, however, the solution time of the MLSPH took almost twice as much compared to the standard Eulerian kernel solution.

Chapter 4

Coupling SPH and FEM

Without a doubt the Finite Element Method (FEM) is still the most popular numerical method, not only in the academic circles but in the commercial spheres as well. For that reason the author decided to include FEM as a counterpart mesh-based method to Smoothed Particle Hydrodynamics (SPH) and discuss some useful coupling approaches and techniques. Since SPH is not as popular as FEM in structural dynamics, even though there are many advantages of using it, small steps are usually the best way to convince other researchers that SPH can be beneficial. Here, the first step would be to show that interaction between both methods is quite easy to do.

Since both methods are Lagrangian (can be defined as Eulerian, however), the coupling can be done in many ways. There is no general rule which approach is better. The decision should be made with respect to the simulated problem. In essence, there are three approaches.

- **Penalty-based approach** in which common techniques known from FEM are employed. That would be, e.g. the penalty-based contact algorithm with the nodal penetration detection in which the nodes would be represented by SPH particles.
- **Constraint-based approach** in which one or more degrees of freedom (DOF) are tied. That could be, e.g. when velocities and accelerations of FEM nodes and SPH particles are coupled.
- **Transition layer-based approach** in which the *hybrid* FEM elements are used. The idea is that the hybrid elements contain SPH particles placed inside them, e.g. at locations of the integration (material) points. The motion of FEM elements and SPH particles is again coupled, yet the transition between the hybrid elements and other SPH particles is done with the kernel approximation.

Important to note, in FEM two contact classes are usually recognized – penalty-based and constraint-based class. The difference is not only in the contact formulation but also in the application. The penalty-based contact uses penalty forces imposing certain conditions, e.g. no penetrations. The constraint-based contact uses kinematic constraints rather than the penalty forces. Both contacts can transmit compression and tension, however. Both

contact classes can also have strength limits, i.e. when the initially bonded region fails under stress conditions and can further transmit compressive load only. The region where FEM elements/nodes and SPH particles are coupled is referred to as *interface* in the following text.

4.1 Penalty-Based Approach

As previously mentioned, both FEM and SPH are or could be defined in the Lagrangian framework. That is, the elements and particles represent a certain amount of volume which is moving with the mesh or particles. As a result, the nodes and particles carry lumped mass and the problem domain is said to be discretized with them. In the FEM terminology, a contact can be defined between nodes, nodes and element faces, or directly between element faces regardless the nodes. Clearly, in the SPH analogy, FEM nodes would be replaced by SPH particles. The rest remains the same, however.

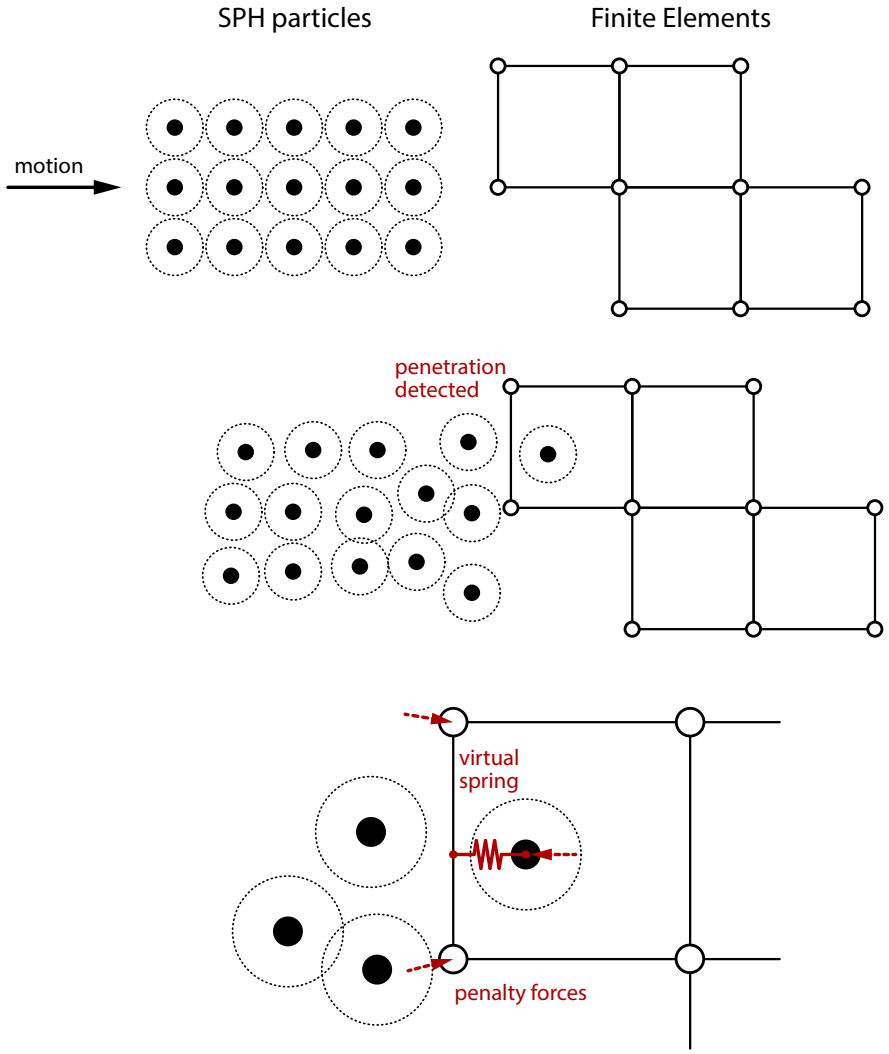

Fig. 4.1. SPH-FEM coupling with the penalty-based contact.

The logic of the penalty-based contact is quite simple. When a node or particle penetrates a FEM element, a penalty force is applied to the penetrating node or particle and to the element's nodes in order to minimize the penetration. The penalty force can be understood as an outcome of a virtual spring which was created between the penetrating entities. This can be seen in Fig. 4.1 in which SPH particles impact FEM elements. Note that the dotted circles around the SPH particles represent lumped volumes. Clearly from the Fig. 4.1 the lumped volumes between the particles can overlap. Why? The lumped volume is not treated with the contact itself, it is just an information for the particle approximation. If there is no artificial viscosity or correction, it can be that the particles stream through each other [13]. Furthermore, the lumped volume does not define the size or location of the virtual spring. The spring goes from the point of the penetration to the centre of the SPH particle. The contact can work in compression as well as in tension. The naming and logic are the same, yet it can be sometimes confusing since a negative penetration defines an opening (when a particle moves from an element).

The most important question is how to define the stiffness k_s of the virtual spring, since it controls the magnitude of the penalty force F_p as

$$F_p = k_s \delta_{pen}, \tag{4.1.1}$$

where δ_{pen} would be the penetration of either a node or particle. When it comes to FEM, two approaches for k_s calculation are recommended [152, 185]. The first one is based on material properties of the interacting entities and for solid elements the stiffness is defined as

$$k_s = \frac{\eta K A^2}{V}, \tag{4.1.2}$$

and for shell elements as

$$k_s = \frac{\eta K A}{\max(\text{shell diagonal})}, \tag{4.1.3}$$

where η is the scale factor for the interface stiffness, K is the bulk modulus, A is the area of the element face where the penetration occurs, and V is the element volume. Both (4.1.2) and (4.1.3) work fine until materials with very different properties interact, e.g. steel and foam. The resulting K would be most likely an average of both bulk moduli or their min/max value. Therefore, it could be that the spring stiffness is overestimated for the foam and underestimated for the steel. Another issue could be that the time step of the explicit scheme is not taken into account. Therefore, the formulation

$$k_s = \frac{1}{2} \eta \frac{m}{dt^2}, \tag{4.1.4}$$

where η is again the scale factor for the interface stiffness, m is the mass of the nodes and particles in the interaction, and dt is the current or initial time step. There is no general rule which time step should be used, however. It must be pointed out that the penalty-based contact can never fully prevent penetrations. If the penetrations should be zero, then the stiffness k_s must be infinite, which is numerically impossible.

Since the penalty-based contact is preferred in compression only scenarios, i.e. tensile stresses are not transmitted with the interface, a list of possible applications includes

- structure to soil interactions,
- structure to fluid interactions,
- debris simulations,
- blast simulations (SPH as an explosive),
- mold filling simulations,
- wading simulations,
- phase change simulations,
- element erosion with mass conservation interactions.

Furthermore, most of the commercial codes do not directly support the contact between the beam/link FEM elements and nodes or SPH particles. There are other approaches to define a connection between them, however. The topic is discussed in **Chapter 6** *Reinforced Concrete* in detail.

4.2 Constraint-Based Approach

The logic of the second approach is completely different. No penalty forces are applied but rather kinematic constraints are imposed. As a result, no penetrations occur. The approach can be very useful when two independent FEM and SPH parts should be 'glued' together. The constraint-based contact ensures the deformation at the interface is continuous, i.e. deformations of FEM elements/nodes are the same as deformations of SPH particles.

For example, in Fig. 4.2 SPH particles are attached to the top-left element. For convenience, all the FEM elements are rigid and only the SPH part is allowed to deform. If the SPH particles are set in motion, the FEM elements will simply follow, and the deformation at the interface will be continuous with respect to the rigid elements. This means, that the SPH particles initially attached to the FEM elements cannot move relatively to them.

A disadvantage of the constraint-based contact is that it is quite difficult to establish the interface during the simulation (not impossible, however). To prescribe constraints during the initialization phase is not a problem. The problem domain is known, the interface is usually prepared so that SPH particles are 'touching' or are in a proximity of FEM

elements. Yet during the simulation when the problem domain might be deformed and the initial interface is most likely lost, it is very difficult to connect two independent parts.

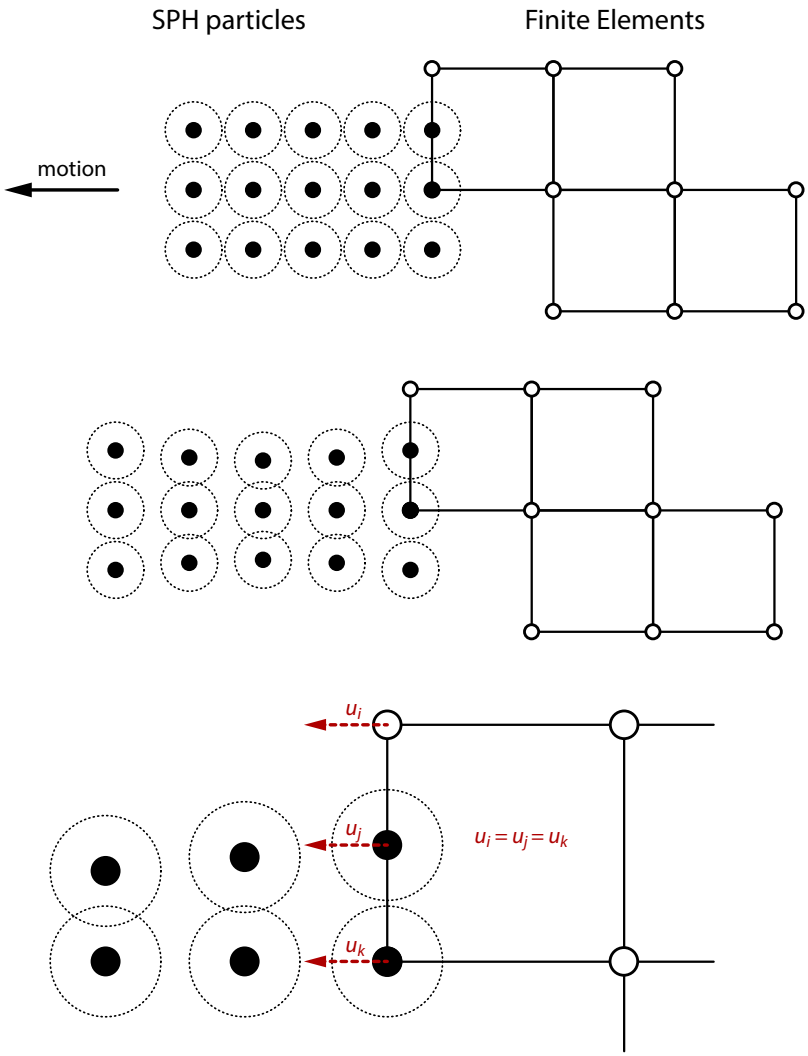

Fig. 4.2. SPH-FEM coupling with the constraint-based contact.

Since the constraint-based contact is less expensive in terms of a computational effort, yet it is rather difficult to establish the interface during the simulation, it is very often combined with the first discussed contact, the penalty-based. Then the constraints are used to create a bond between two independent parts at the beginning, but the penalty forces are used for the interaction during the simulation. The concept is following. During the initialization, the contact is constraint, two separate parts are fully connected. During the simulation, if a limit state is reached, the contact is broken and deactivated. That means, tensile stresses are no longer transmitted and the contact interface might open. However, if the stresses are compressive and both parts are again in contact, the stresses are transmitted but with penalty forces. Therefore, penetrations might not be exactly zero.

The application range for the constraint-based contact would preferably include

- flexible to flexible initial coupling,

- rigid to flexible initial coupling,
- reinforcement simulations,
- submodel simulations,
- wear simulations,
- rivet simulations.

4.3 Transition Layer-Based Approach

The last approach combines the idea of SPH, the penalty-based contact, and the constraint-based contact. In essence, an SPH particle can be placed inside a FEM element, e.g. at location of its integration (material) point. The SPH particle is constraint within the element, i.e. it always follows the element. The particle inherits all kinematic variables, constitutive properties, and if needed also stress state from the element. This is the concept of the hybrid elements. The communication with other SPH particles which are outside FEM elements, e.g. with a completely independent SPH part, is done in the standard way with the kernel approximation. No special SPH formulation is needed, no special treatment is necessary. The particles start to interact the moment their support domains start to overlap. The result of the particle interaction is transmitted into FEM elements with interaction forces which are applied to the nodes. Of course, the interaction forces are applied only to the hybrid elements, not to all elements.

This quite unique concept is very robust, stable, and easy to implement. Of course, the interaction can be established only if the Eulerian or pseudo Lagrangian kernel is used. There is no general rule for the number of SPH particles inside FEM elements. Therefore, it always depends on the SPH discretization level, application, and if the hybrid elements might be eroded or not; discussed in **Chapter 5** *Quasi-Brittle Materials* in detail.

An example can be considered again. Starting with the same distribution as in Fig. 4.2, yet without constraints at the interface but directly at the integration points. From Fig. 4.3 can be seen that three hybrid elements have been defined, always with one SPH particle per FEM element. The hybrid elements are usually used only on the outer surfaces of FEM parts, since there is no interaction expected with the inner elements (except when the element erosion is considered). The interface becomes active when any external SPH particle enters the support domain of the hybrid elements. As shown in Fig. 4.3, when the external particles are set in motion, the sorting algorithm finds if there is an interaction with the hybrid elements. Since two external SPH particles are within the support of the hybrid element, interaction forces between the particles start to develop. Subsequently, the interaction forces are applied to the nodes of the FEM element. The sum of the interaction forces applied to the FEM nodes is in fact the force which was developed during the kernel approximation. Although the example shows an initial coupling with FEM elements, the logic works also the other way around. That is, initially the SPH and FEM parts might be far from each other, yet after the contact, the hybrid elements serve as the interface.

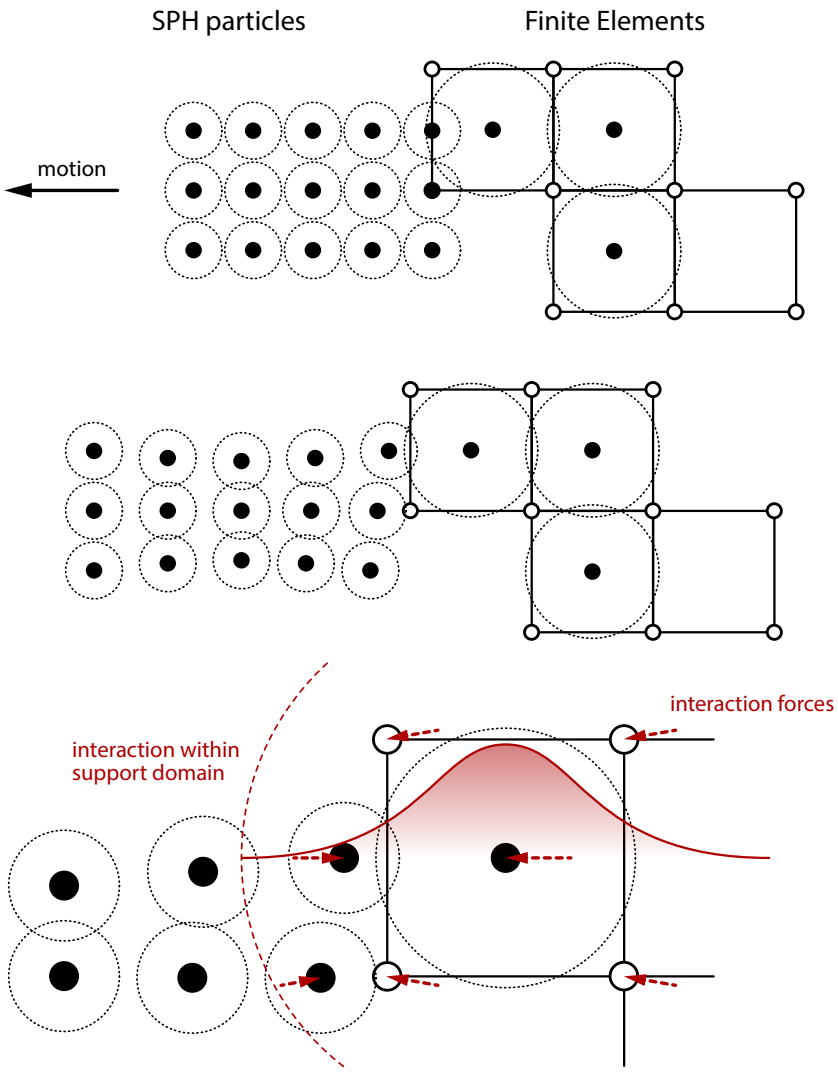

Fig. 4.3. SPH-FEM coupling with the transition layer made of the hybrid elements.

Using the transition layer with the hybrid elements, the application is limitless, i.e. both previously discussed lists of applications can be considered. One should be kept in mind, however. As shown in section *Particle Interaction*, the interface in case of the hybrid elements extends the size of FEM elements. Put simply, any SPH particle which enters the support domain of the hybrid elements would have an impact on the FEM elements.

4.4 Comparison of the Coupling Approaches

To see how the coupling approaches perform, an example of a structural deformation is discussed next. As can be seen in Fig. 4.4, a beam of length 5 m with a rectangular cross-section of 0.25 m × 0.25 m was fixed on the left-hand side while moved down 0.5 m on the right-hand side. For comparison purposes, the example was simulated with pure FEM, coupled SPH-FEM with the penalty-based contact, constraint-based contact, and with the transition layer made of the hybrid elements. Since only translational DOFs at

nodes/particles were assumed, the tangents at location of the supports were not exactly zero since only one layer of FEM nodes was with the prescribed boundary conditions. The pure FEM model is understood as a reference. It is expected that the coupled models result in the same deformation, stress state, and force resistance (force reaction).

The coupled models, as shown in Fig. 4.4, were split into three regions FEM-SPH-FEM. The middle part which was discretized with SPH particles was 2 m long, the rest of the model was pure FEM. The element size was constant 0.05 m in all three directions. The SPH part of the model was generated from the original FEM part, i.e. each element was replaced by one SPH particle placed at the centre of gravity (CG) of the original element. This however resulted into initial offset from the interface as shown in Fig. 4.4. In other words, SPH particles were not directly placed on the faces of the elements. An initial offset can be taken into account, however. It can be subtracted from the actual penetration/gap and treated as there is no offset at all. That means, only (4.1.1) needs to be modified as

$$F_p = k_s(\delta_{pen} - \delta_{ini}), \tag{4.4.1}$$

where δ_{ini} is the initial gap in this case. The SPH part of the model can be generated from FEM nodes, however. In that case, there would be no initial gap/penetration, and the SPH particles would be directly touching the FEM elements. Of course, radii of the particles cannot be taken into account. In either case, the cross-section should remain constant 0.25 m × 0.25 m. More about a model generation was discussed in section *Insights*.

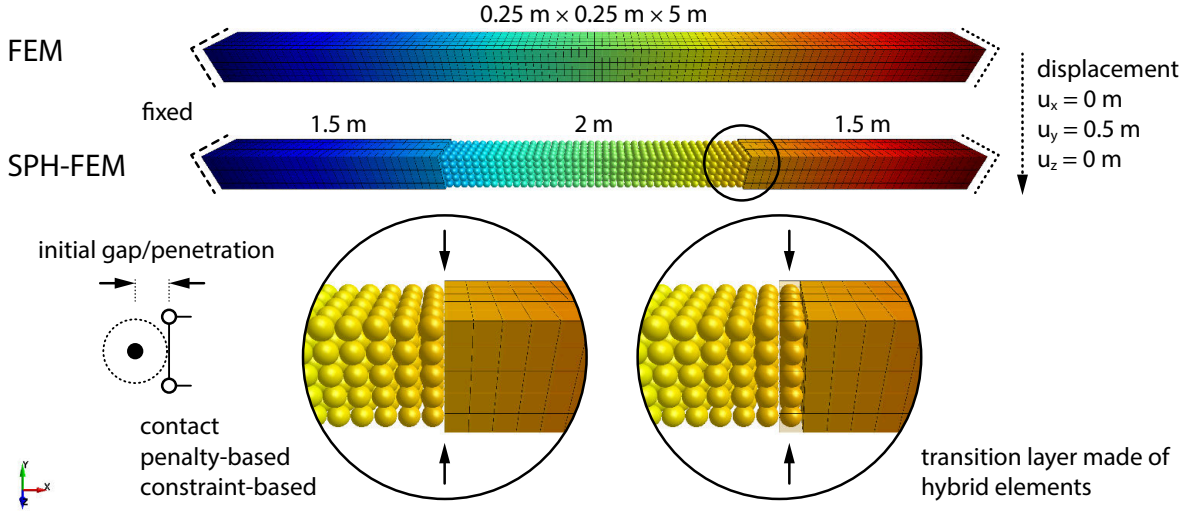

Fig. 4.4. SPH-FEM coupling example.

In case of the transition layer-based approach or just with the hybrid elements, the SPH part of the model was again 2 m long. The first neighbouring FEM elements were used as the hybrid ones as can be seen in detail in Fig. 4.4. Since the elements size was constant 0.05 m, the transition layer of thickness 0.05 m was used.

A linear elastic material model was used with assumptions of steel mechanical properties, i.e. density of 7850 kg/m^3, Young's modulus of 210 GPa, and Poisson's ratio of 0.3. For

the SPH part of the model the isotropic Eulerian kernel was used with the recommended $h = 1.2\,\Delta x$ and $\kappa = 2$, as discussed in section *Variable Smoothing Length*. Note that Δx corresponds to the elements size of 0.05 m. The smoothing length was updated with respect to (2.4.36), and the renormalization discussed in section *The Renormalization* was used to improve accuracy of the stress gradients. Furthermore, the Monaghan type artificial viscosity (2.9.3) with parameters $\alpha_l = 1$ and $\beta_q = 1$ was used.

Starting with the results in terms of displacements, shapes of all models should be more or less the same. This is indeed true as can be seen in Fig. 4.5. The fixed support on the left-hand side has zero displacement while the support on the right-hand side has resultant displacement 0.5 m, since only the vertical displacement of 0.05 m was prescribed. The shape along the beam is the same for all models, the inflection point is always in the middle.

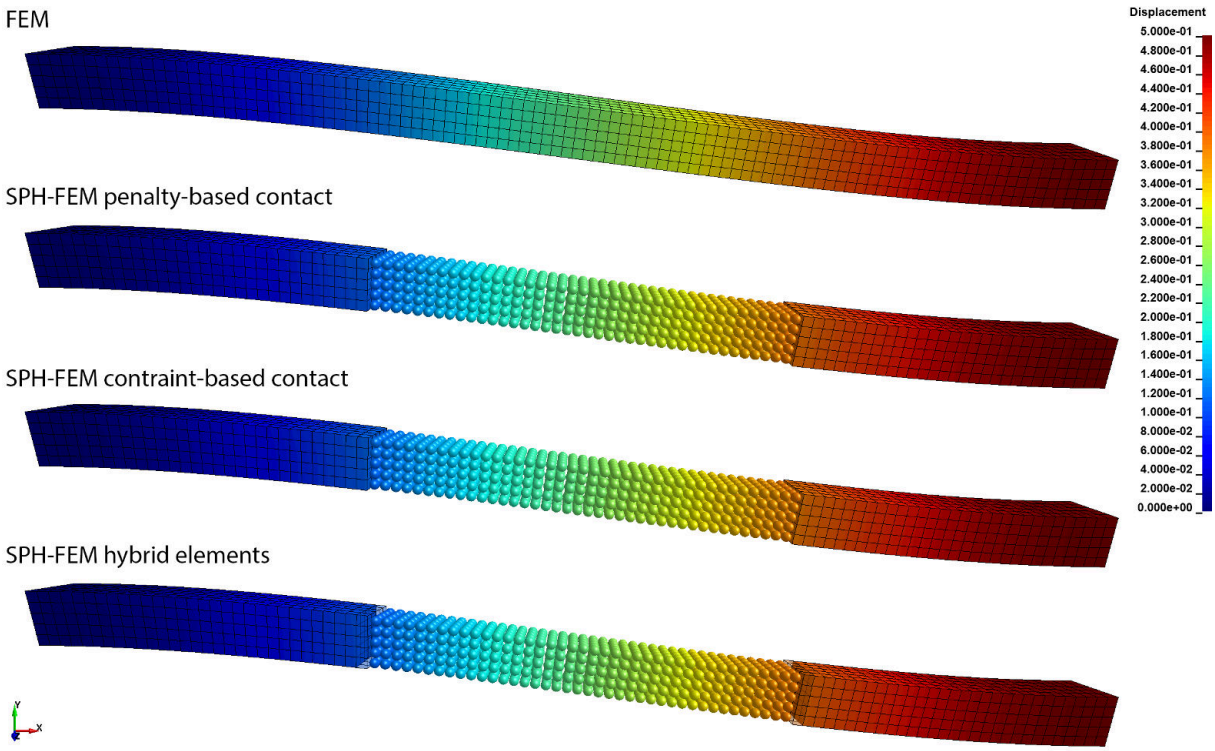

Fig. 4.5. SPH-FEM coupling comparison – displacement.

As shown in Fig. 4.6 in which stresses in the form of the von Mises effective stress are compared, the contour distributions are not the same for the compared models. Taking the pure FEM model as a reference in which the contours smoothly transmit along the beam, it is obvious that when the penalty and constraint-based contact is used in the interface, stress oscillations are visible. Oscillations in solutions are nothing new, however. They are well known from the Finite Difference Method (FDM) and FEM in which they are referred to as zero-energy modes in general, and in case of elements deformation as the Hourglass effect [85]. Similarly, in case of SPH when particles are uniformly distributed, it could happen that the sum of derivatives is zero since the kernel derivatives are equal in magnitude but opposite in the sign [85], therefore, a solution can be found although it makes no sense in terms of the physics. To completely remove the spurious zero-energy

modes, an approach in which additional stress points are used for field functions evaluation was proposed in [30, 45, 66, 68].

The stress oscillations are visible only when the penalty and constraint-based contacts are used for the interface treatment, however. When the stresses are evaluated in the proximity of the interface, it seems that a layer of SPH particles which is in contact suffers with a sudden stress drop. This is of course a singularity in the problem domain and as a consequence the stress field oscillates along the beam till the effect is dispersed. In contrast, in case of the hybrid elements the stress profile is smooth, yet some stress peaks are also visible in the proximity of the interface. In general, the proximity of coupled regions is always problematic since not all conditions of the continuity are enforced.

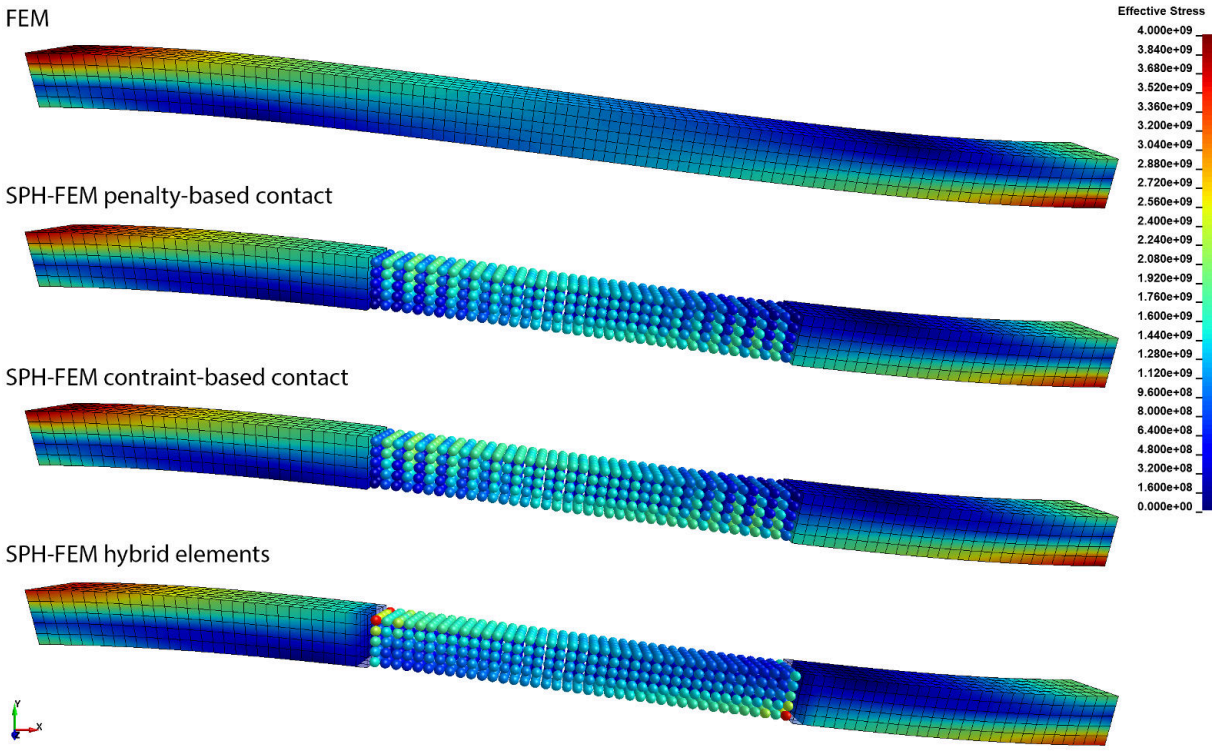

Fig. 4.6. SPH-FEM coupling comparison – effective stress.

It is important to understand what is the reason for the sudden stress drop when the contact formulations are used. Put simply, since the particles were not directly placed on the faces of the elements, the initial offset was maintained throughout the simulation. The enforced offset, however, behaves like a rigid entity in which stresses drop to zero. This is another reason why the stress drop is not visible when the hybrid elements are used. The direct consequence of the stress drop are the oscillations in the SPH domain.

A qualitative indicator of energy dissipation can be measured with the model resistance, e.g. with a vertical component of the reaction force over time. As shown in Fig. 4.7, all models are more or less comparable. However, it is so that the coupled models show a rather softer behaviour. Since the interface is a discontinuity in the problem domain which introduces energy dissipation among the others, the softer behaviour makes sense. It seems that the dissipation is pronounced the most in the model with the hybrid elements. It could very well be, however, that with more than one particle per hybrid element the effect

would be alleviated. Overall, the coupled SPH-FEM models return the same response as the pure FEM model, therefore, all the methods are considered interchangeable and combinable in the discussed extend.

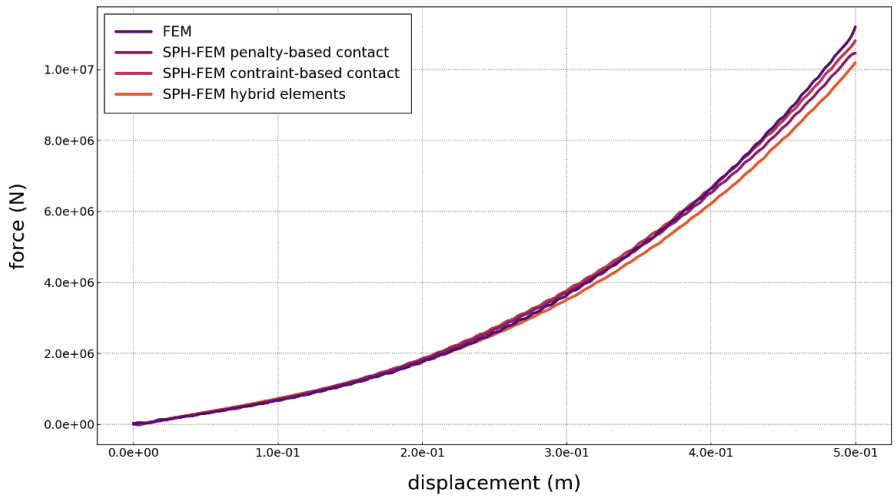

Fig. 4.7. SPH-FEM coupling comparison – reaction force.

Yet it must be pointed out, that there might be cases in which differences in results of the discussed coupling approaches might be significant. There is no general answer which approach is better, it always depends on the application. From the discussed results it is clear that if the coupling should serve only in domains of lower importance, the penalty or constraint-based approach will do just fine in general. However, if stresses in the proximity of the interface are important, the transition layer with the hybrid elements would be more appropriate. What should be also considered is the fact, that when the penalty-based contact algorithm is used, the time step of the explicit integration scheme might be reduced as shown in (4.1.4). This is usually not the case for the constraint-based contact algorithm or for the hybrid elements.

Chapter 5

Quasi-Brittle Materials

In this chapter, quasi-brittle materials are discussed in terms of the Smoothed Particle Hydrodynamics (SPH) framework. Since the majority of constructions in civil engineering are made of concrete or reinforced variants of concrete, it is natural that the performance of SPH with quasi-brittle materials should be subjected to a thorough investigation. Since it is not the subject of the thesis to benchmark all the available material models, only a representative model is chosen and discussed in detail. Given the variability of load types in structural dynamics, the Continuous Surface Cap Model (CSCM) as the most versatile material model was chosen. In the first part of the chapter, the mathematical definition together with practical applications are given. In the second part, two experiments in which SPH is used with CSCM are discussed. Some advanced coupling techniques between SPH and the Finite Element Method (FEM) are shown at the end of the chapter. The concept of the FEM element erosion with transformation of the eroded mass into SPH particles is also outlined.

5.1 Materials with Softening

There are many advanced materials, yet in civil engineering the *good old* concrete seems to be always the first choice. As a matter of fact, there are advanced types of concrete with some special properties, e.g. self-compacting concrete, fiber-reinforced concrete, or lightweight concrete. For numerical simulations, various material models have been developed in order to capture complex responses of concrete. What should a material model of concrete be able to represent? Uniaxial and multi-axial strength, material hardening and softening, stiffness and strength degradation, dilation and shear enhanced compaction, strain-rate effects, and creep should be captured or at least considered in the material model. That said, it is indeed a very difficult task to develop a user-friendly model and still reflect behaviour of concrete. As shown in Fig. 5.1 in which four concrete classes are compared in the uniaxial compressive stress test, each class represents a change not only in the peak strength, but also in the stiffness, ductility, brittleness, and overall nonlinearity.

In addition, a concrete specimen might undergo load cycles. The reason for that does not have to be an excited load. In case of a high velocity impact (HVI), stress waves

propagate through the specimen, bounce back and forth, and result in some kind of cyclic load inside the material. In practice, cracks open and close, the stiffness changes, and the concrete strength degrades. Yet it is even more complicated. When a crack is opened and the stress state is in tension, the global stiffness is usually decreased. However, if the stress state is in compression, therefore, the crack is closed, the stiffness is said to be recovered. Furthermore, when a concrete is beyond its peak strength and cracks are already formed, the average slope of the loading/unloading curves decreases with increased straining which indicates a progressive degradation of the elastic moduli as shown in Fig. 5.2.

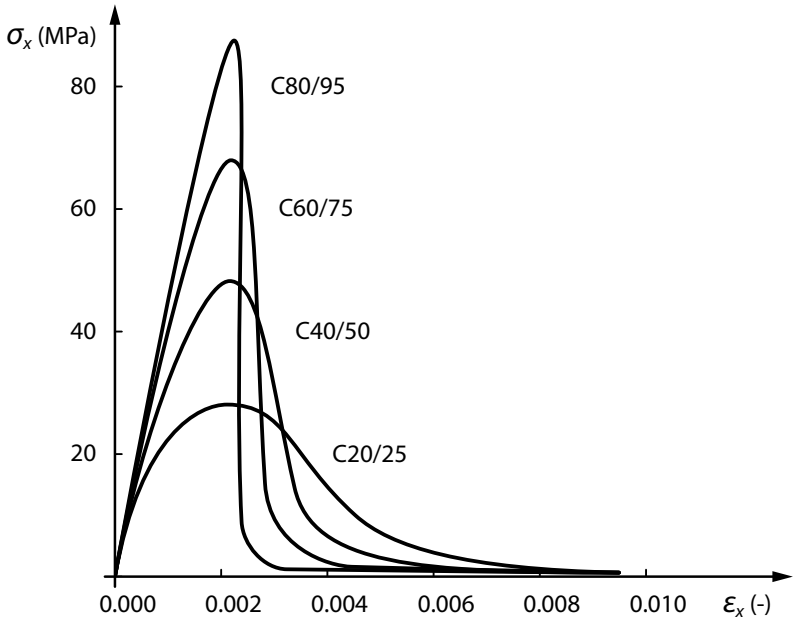

Fig. 5.1. Example of the uniaxial compressive stress test for different concrete classes; source [186].

Even if the peak strength and stiffness are captured with the material model under a quasi-static load, it does not necessary mean the responses are valid with increased load rate. The so-called strain-rate effects can be understood as an increase in strength, yet not necessarily in stiffness, with increasing strain over time. This behaviour is observed in compression as well as in tension. As pointed out in [187], the rate dependent response of concrete is controlled through three different effects:

- through the rate dependency of the growing microcracks (influence of inertia at the micro level),
- through the viscous behaviour of the bulk material between the cracks (viscosity due to the water content),
- through the influence of inertia, which comes from different sources.

For quasi-brittle materials, such as concrete, the first two effects are important for relatively low and medium strain rates [187, 188, 189, 190]. For higher strain rates the influence of

inertia dominates, however, the rate dependency cannot be neglected [187, 191]. In [187], sources of inertia which need to be considered were defined as

- structural inertia, which is present even in case of an elastic analysis,
- inertia activated due to the material softening or hardening,
- inertia at the crack tip that is responsible for crack branching.

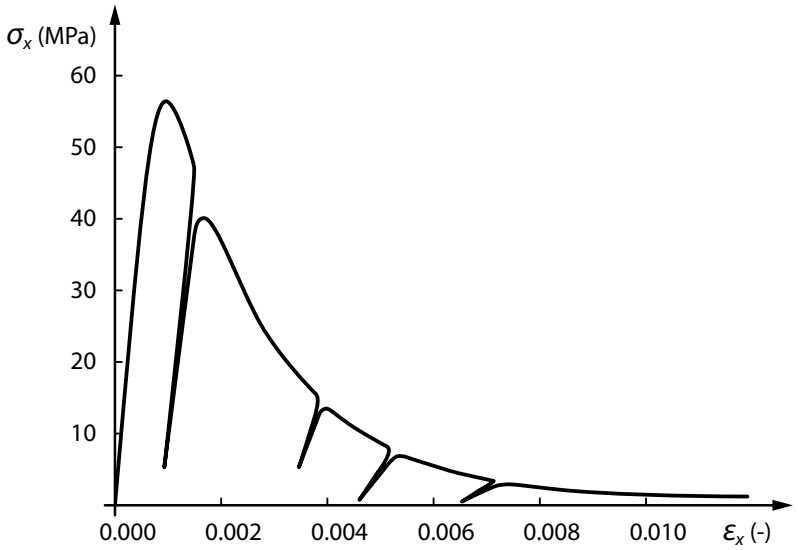

Fig. 5.2. Example of the uniaxial compressive stress test showing softening and degradation of the elastic moduli with increased straining; source [192].

The first point in the list does not have to be discussed as it is naturally taken into account by the model itself, i.e. the numerical SPH model despite the material model. The second point in the list is discussed in this chapter, yet it must be noted that there is a difference between the *inertial confinement* and *constitutive model strain-rate effects* (e.g. strain-rate hardening of a shear failure surface). It was found that even material models without rate effects implemented can return reasonable responses in dynamic simulations [193]. That is, with increasing strain rate, increase in strength can be observed. As explained in detail in [193, 194, 195], this effect is related to the inertial confinement. However, when constitutive model strain-rate effects are omitted and the inertial confinement is the only driving mechanism in the model, it can be that responses of concrete are over- or under-estimated. For that reason, material models used in dynamics should consider rate effects by their internal algorithm. The third point in the list does not have to be discussed either as it is an outcome of increased strain rate, therefore, an indicator if the physics in the numerical model is correct.

It is known fact that a standard concrete has a low tensile strength compared to its compressive strength. The unconfined tensile strength f_t is typically 8 to 15% of the unconfined compressive strength f_c [186]. However, with increasing strain rate, the dynamic tensile strength is increased intensively more than in case of the dynamic compressive

strength. This behaviour is shown in Fig. 5.3 in which the factor for the dynamic strength f_d based on the quasi-static strength f_s is plotted [196]. For example, strain rates in range of 1 to 10 per second will result into the peak strength increase of about 20 to 50% in compression and well more than 100% in tension [186]. The initial elastic modulus does not change significantly with strain rate, however [197].

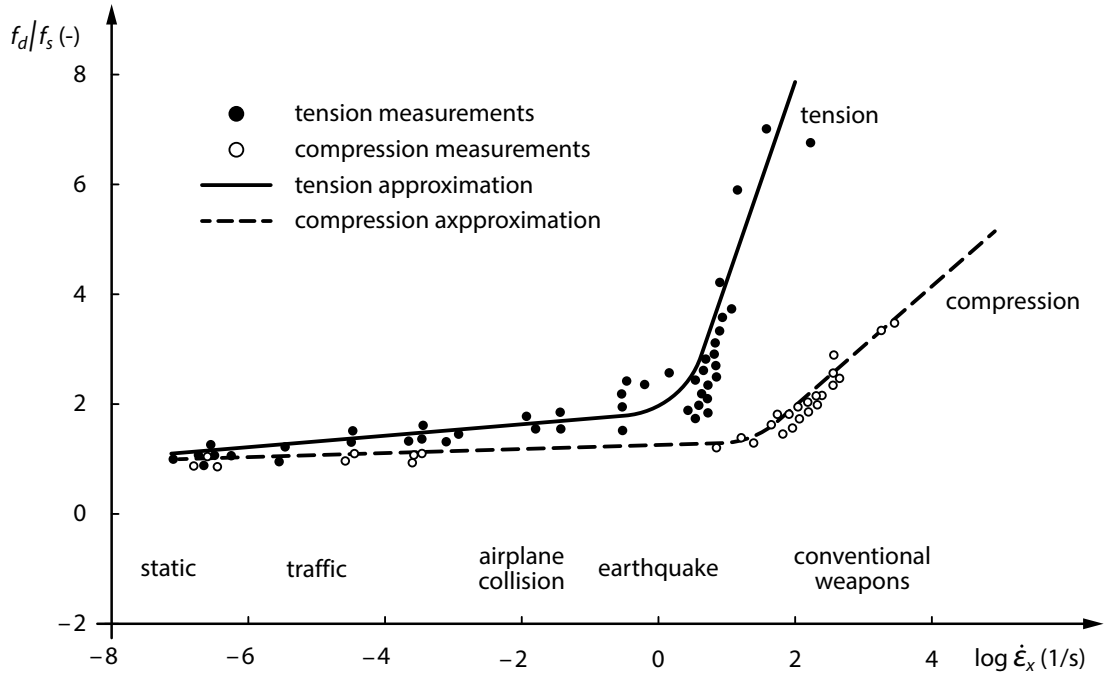

Fig. 5.3. Rate effects of concrete in tension and compression; source [196].

That said, it might seem there is no material model capable of providing all the needed 'features'. By the author's experience, there is one material model which is more than suitable for civil engineering applications, especially for structural dynamics. The model is called CSCM, and will be discussed in the following section.

5.2 CSCM Material Model

CSCM is a three-invariant-based material model, specifically designed for use in roadside safety simulations. Since roadside safety is a part of structural dynamics, the author was always able to make of use of it in SPH simulations. The reasons why is CSCM so popular in the structural dynamics community are summarized below.

- Captures responses of standard concrete classes.
- Simulates hardening, softening, strength and stiffness degradation, shear enhanced compaction, pore collapse, and dilatancy of concrete.
- Supports full or partial modulus recovery in compression (stiffness recovery with crack closing).

- The softening rate can be specified with the fracture energy separately for compression, tension, and shear.
- The fracture energy is regularized with respect to the discretization size, e.g. the element size or particle spacing.
- Supports strain-rate effects implemented with the viscoplastic formulation.
- The yield surface is a combination of the shear failure surface and hardening cap with a smooth transition.
- Combines the elastoplastic and damage formulation.
- Supports pre-existing damage modelling.
- Input parameters can be easily obtained from standard experiments, i.e. the triaxial compression (TXC) test, the triaxial extension (TXE) test, and the torsion (TOR) test.
- The yield surface cross-section in the deviatoric plane can be controlled, e.g. can be changed into the irregular hexagon-like shape of Willam-Warnke [198].
- Can be easily converted into a two-invariant model.
- The return algorithm employs a subincrementation rather than an iteration to ensure accurate return of the stress state to the yield surface.

The list collects the most important highlights of CSCM, yet there are some more. Those, however, are closely related to the framework implementation. Since LS-DYNA was used for the simulations within the thesis, it is worth to mention some other features which can be beneficial for structural dynamics simulations. The implementation of CSCM in LS-DYNA additionally offers following.

- Supports the input parameters generation for concrete strength between about 20 and 58 MPa (2901 to 8412 psi).
- When the parameter generation is used, the aggregate size scales the fracture energy.
- The internal parameters are available to the user, i.e. the brittle and ductile damage, the intersection of the cap with the shear surface, the intersection of the cap with the pressure axis, and plastic volumetric strain.
- Maximum strain increment over the time step can be controlled.

Based on a framework implementation features might differ. The mathematical definition should be the same, however. Since it is not the goal of the thesis to dive into a material modelling but to examine the SPH performance with quasi-brittle materials, only essential formulations are discussed further. The comprehensive material definition and development can be found in original papers [199, 200, 192] or in LS-DYNA related literature [201, 202, 203, 186].

Note that CSCM uses rather large number of variables. For that reason, some previously defined variables are redefined for this chapter. Meaning of some general symbols remain the same, e.g. stress invariants I_1, J_2, J_3 or pressure p. However, the number of Greek letters is limited, therefore, α, β, γ, or even κ are used again. For that reason, CSCM variables are collected separately in *Symbols in CSCM*.

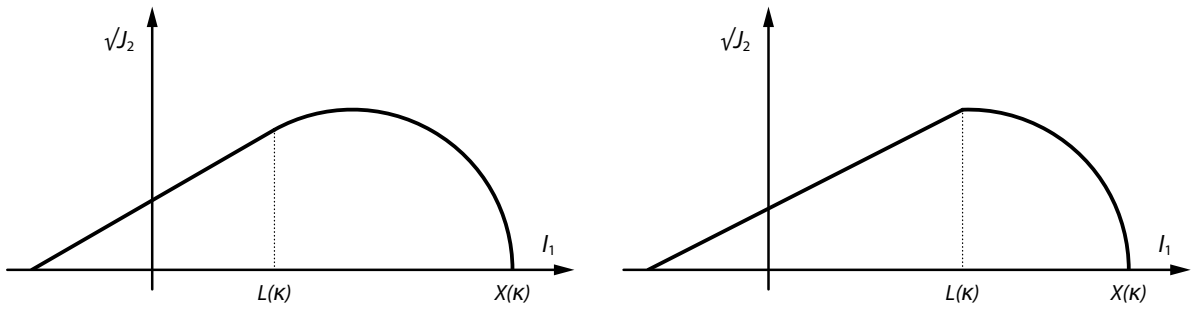

(a) smooth cap (b) non-smooth cap

Fig. 5.4. Comparison of the smooth cap yield surface and non-smooth cap yield surface; source [192].

As already mentioned, the CSCM yield surface is defined with respect to three stress invariants – the first invariant of the stress tensor I_1, the second invariant of the deviatoric stress tensor J_2, and the third invariant of the deviatoric stress tensor J_3. The invariants are defined in terms of the deviatoric stress tensor τ and pressure p as

$$I_1 = 3p = \sigma^{\alpha\alpha}, \tag{5.2.1}$$

$$J_2 = \frac{1}{2}\tau^{\alpha\beta}\tau^{\alpha\beta}, \tag{5.2.2}$$

$$J_3 = \frac{1}{3}\tau^{\alpha\beta}\tau^{\beta\gamma}\tau^{\gamma\alpha}. \tag{5.2.3}$$

To improve legibility in the following section, the Greek indices are not used, yet the logic from section *Conservation Laws* is preserved. The yield surface consists of two failure surfaces (multi-surface definition), yet the transition between them is smooth. The yield surface f is defined as

$$f(I_1, J_2, J_3, \kappa) = J_2 - \mathcal{R}^2 F_f^2 F_c, \tag{5.2.4}$$

where F_f is the shear failure surface, F_c is the hardening cap, and $\mathcal{R}$ is the Rubin three-invariant reduction factor [204]. Thanks to the multiplicative split, the slope between the shear surface and cap is smooth as can be seen in Fig. 5.4 (a). The strength of concrete is modelled by the shear surface F_f in the tensile and low confining pressure regimes, and by the cap F_c in the moderate to high confining pressure regimes [186]. More importantly,

the cap is used to model plastic volume change related to the pore collapse (although the pores are not explicitly modelled) [186]. Both failure surfaces are shown in Fig. 5.5 in which F_c is a non-dimensional function. The shear surface F_f is defined as

$$F_f(I_1) = \alpha - \lambda e^{-\beta I_1} + \theta I_1, \tag{5.2.5}$$

where α, λ, β, and θ are the model parameters used to match the laboratory material response data from TXC tests conducted on plain concrete cylinders [186].

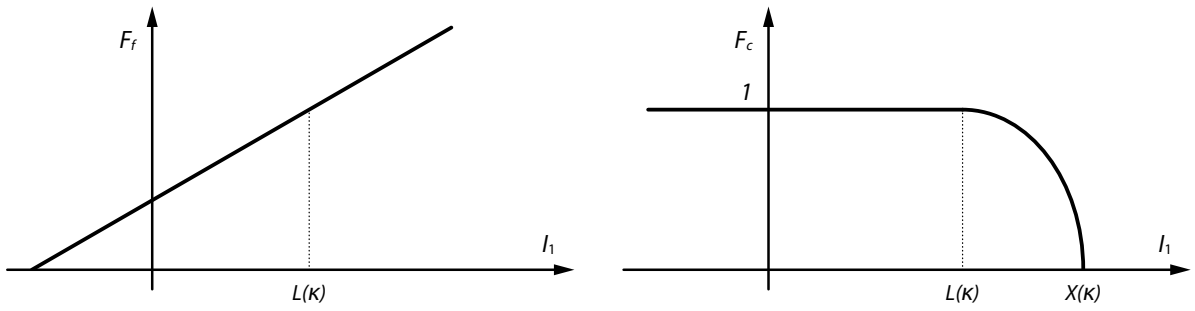

(a) shear surface (b) two-part cap function

Fig. 5.5. Shear and cap failure surfaces; source [192].

The isotropic hardening cap surface is based on a non-dimensional functional form given as

$$F_c(I_1, \kappa) = 1 - \frac{[I_1 - L(\kappa)][|I_1 - L(\kappa)| + I_1 - L(\kappa)]}{2[X(\kappa) - L(\kappa)]^2}, \tag{5.2.6}$$

where κ is the hardening parameter that controls motion of the cap, and $L(\kappa)$ and $X(\kappa)$ define the geometry of the cap [199]. The function F_c can be rewritten in more understandable form of

$$F_c(I_1, \kappa) = \begin{cases} 1 & I_1 \leq L(\kappa) \\ 1 - \dfrac{[I_1 - L(\kappa)]^2}{2[X(\kappa) - L(\kappa)]^2} & \text{else,} \end{cases} \tag{5.2.7}$$

which defines F_c as unity for I_1 less than $L(\kappa)$ and ellipse for $L(\kappa) \leq I_1 \leq X(\kappa)$ [199]. The ellipticity of the cap is determined by another parameter R that relates the geometric parameter $L(\kappa)$ to $X(\kappa)$ through the relation [199]

$$X(\kappa) = L(\kappa) + RF_f(L(\kappa)), \tag{5.2.8}$$

where $L(\kappa)$ is defined as

$$L(\kappa) = \begin{cases} \kappa & \kappa > \kappa_0 \\ \kappa_0 & \text{else,} \end{cases} \tag{5.2.9}$$

where κ_0 is the value of I_1 at the initial intersection of the shear and cap failure surfaces, see Fig. 5.5. The cap moves to simulate plastic volume change [186]. The cap expands ($X(\kappa)$ and κ increase) to simulate plastic volume compaction [186]. The cap contracts ($X(\kappa)$ and κ decrease) to simulate plastic volume expansion, called dilation [186]. The motion (expansion and contraction) of the cap is based on the hardening law defined as

$$\varepsilon_v^p = W(1 - e^{-D_1(X-X_0)-D_2(X-X_0)^2}), \tag{5.2.10}$$

where ε_v^p is the plastic volumetric strain, W is the maximum plastic volumetric strain (at hydrostatic compression 'lockup'), X_0 is the initial abscissa intercept of the cap, and D_1 and D_2 are the shape factors [199]. The parameters $L_0 = L(\kappa_0), X_0 = X(\kappa_0), W, R, D_1$, and D_2 are material parameters determined from laboratory material response data [199], usually fits to the pressure-volumetric strain curves in isotropic compression and uniaxial strain [186]. The parameter X_0 determines the pressure at which the compaction initiates in isotropic compression. Yet R combined with X_0 determines the pressure at which the compaction initiates in uniaxial strain. The parameters D_1 and D_2 determine the shape of the pressure-volumetric strain curves. And W determines the maximum plastic volume compaction [186].

It is well known that geologic materials fail at lower values of J_2 (principal stress difference) for the TXE and TOR tests than it does for the TXC test conducted at the same pressure. Typical failure curves from the tests are shown in Fig. 5.6, plotted as a stress difference quantity $\sqrt{J_2} = (\sigma_x - \sigma_r)/\sqrt{3}$ versus pressure $I_1/3$, where σ_x and σ_r are the axial and radial stresses, respectively. This in other words means, that the concrete strength depends on the third invariant of the deviatoric stress tensor J_3 [186]. When viewed in the deviatoric plane, a three-invariant yield surface is triangular or hexagonal. As shown in Fig. 5.7, a two-invariant formulation would have a circular shape (Drucker-Prager, von Mises), yet a three-invariant would have a shape of a hexagon (Mohr-Coulomb), or an irregular hexagon-like shape (Willam-Warnke) in which each of the six sides is quadratic (rather than linear) between the TXC and TXE states [199, 192, 186]. Note, the convention in Fig. 5.7 follows $\sigma_1 \geq \sigma_2 \geq \sigma_3$ and (5.2.1).

To capture the essence of Fig. 5.6, CSCM uses the Rubin scaling function $\mathcal{R}$ [204]. It determines the strength of concrete for any state of stress relative to the strength for TXC. The strengths for TXE and TOR are modelled by scaling back the TXC shear strength by the Rubin function $\mathcal{R}F_f$ [186]. The Rubin function $\mathcal{R}$ is a scaling function that changes the shape (radius) of the yield surface in the deviatoric plane as a function of angle $\hat{\beta}$ as shown in Fig. 5.8 [186].

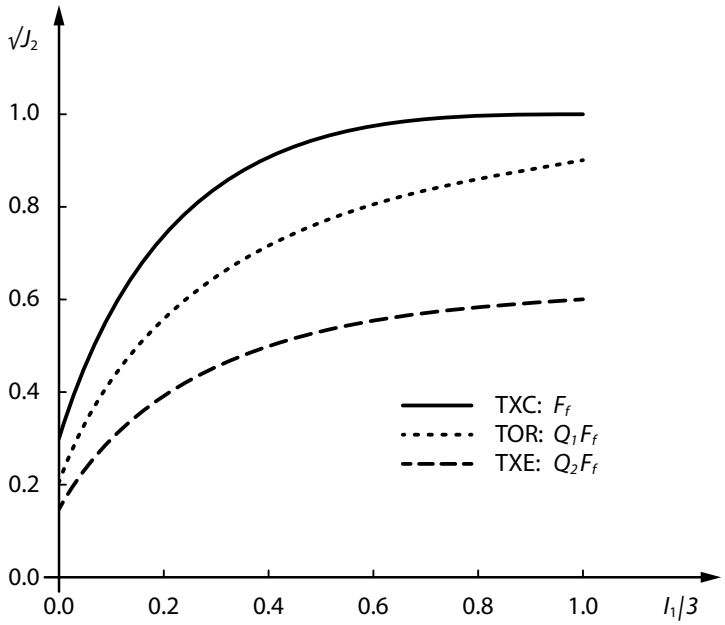

Fig. 5.6. Schematic failure curves for triaxial compression (TXC), a deviatoric state of torsion (TOR), and triaxial extension (TXE); source [192].

For example, if two-invariant formulation is required, the Rubin scaling function $\mathcal{R} = 1$, which means that TXC, TOR, and TXE strengths are modelled the same; shown as the circle in Fig. 5.8 [186]. The angle $\hat{\beta}$ is confined to the range $-\pi/6 \leq \hat{\beta} \leq \pi/6$, and is related to the invariants J_2 and J_3 as

$$\sin 3\hat{\beta} = \hat{J}_3 = \frac{3\sqrt{3}}{2}\frac{J_3}{J_2^{3/2}}, \tag{5.2.11}$$

where $\hat{J}_3$ is the normalized invariant which remains in the range $-1 \leq \hat{J}_3 \leq 1$. As shown in [204], for TXC, TOR, and TXE the values of $\hat{\beta}$ and $\hat{J}_3$ are related by

$$\begin{aligned} \hat{\beta} &= \frac{\pi}{6}, & \hat{J}_3 &= 1 & &\text{for TXC,} \\ \hat{\beta} &= 0, & \hat{J}_3 &= 0 & &\text{for TOR,} \\ \hat{\beta} &= -\frac{\pi}{6}, & \hat{J}_3 &= -1 & &\text{for TXE.} \end{aligned} \tag{5.2.12}$$

The full form of the Rubin scaling function is given in [204] (also in [199, 192, 186]), therefore, only the outcome for CSCM is discussed further. Rubin developed an analytical expression for $\mathcal{R}$ in terms of experimental values for Q_1 and Q_2 as functions of pressure. Giving that, three functions of pressure are indicated, denoted F_f, Q_1, and Q_2. The function F_f is fit to the failure curve measured from TXC test. The product of $Q_1 F_f$ and $Q_2 F_f$ are fit to failure curves measured from TOR and TXE tests, respectively.

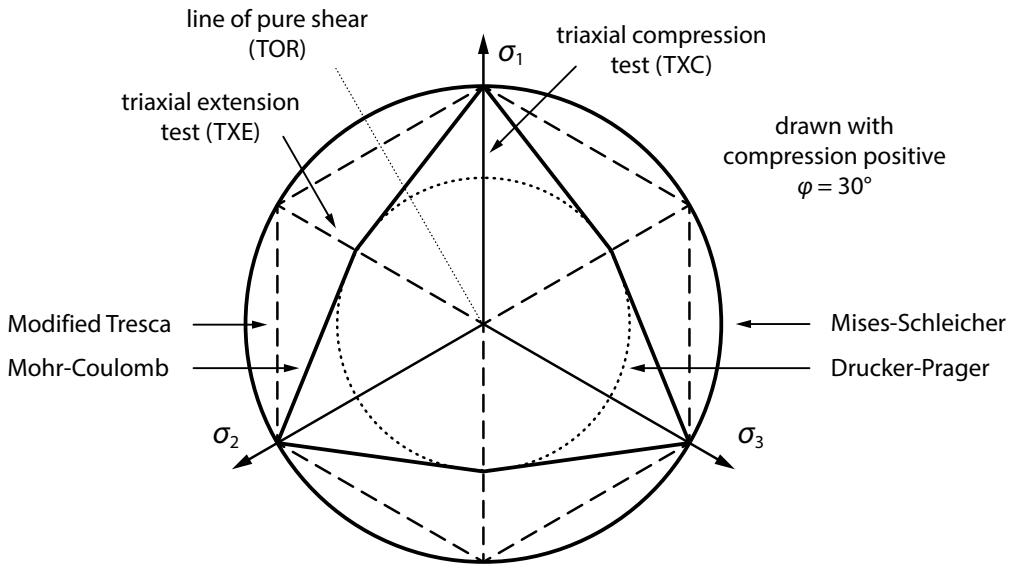

Fig. 5.7. Three common failure surfaces in the deviatoric plane.

Since $\mathcal{R}$ takes on positive values less than or equal to one, therefore, it scales the failure curve F_f for stress states other than TXC, a generalized formulation for Q_1 and Q_2 was proposed in [192] as

$$Q_1 = \alpha_1 - \lambda_1 e^{-\beta_1 I_1} + \theta_1 I_1, \tag{5.2.13}$$

$$Q_2 = \alpha_2 - \lambda_2 e^{-\beta_2 I_1} + \theta_2 I_1, \tag{5.2.14}$$

where $\alpha_1, \lambda_1, \beta_1, \theta_1$, and $\alpha_2, \lambda_2, \beta_2, \theta_2$ are evaluated by fitting experimental data from TOR and TXE tests. The shape of the yield surface in the deviatoric plane transitions with pressure from triangular, to irregular hexagonal, to circular, as schematically shown in Fig. 5.8. Other fits and formulations are available in [199, 192] and [186].

Using CSCM just with the defined yield surface, the model returns perfectly plastic behaviour. Of course, for the laboratory tests such as direct pull, unconfined compression, TXC, and TXE this behaviour is not realistic. Although the perfectly plastic response is typical for concrete at high confining pressures, it is not representative of concrete at lower confinement and in tension [186]. In CSCM both strain softening and modulus reduction are modelled with a damage formulation. The damage formulation is based on [205, 206] in which the stress tensor with damage σ_d is introduced as

$$\sigma_d = (1 - d)\sigma_{vp}, \tag{5.2.15}$$

where d is the scalar damage parameter that transforms the stress tensor without damage σ_{vp} (defined later, see (5.2.24)) into the stress tensor with damage σ_d. Note that the notation σ_{vp} refers to the stresses after they have been updated by the viscoplasticity

algorithm including possible rate effects. Clearly from (5.2.15), d ranges from 0 for no damage to 1 for complete damage. The implementation in CSCM works with accumulated damage which results in reduction of bulk and shear moduli isotropically (simultaneously and proportionally) [186]. For example, if Fig. 5.2 would be simulated with CSCM, limited to one unloading/reloading cycle, the damage parameter d would be applied as shown in Fig. 5.9.

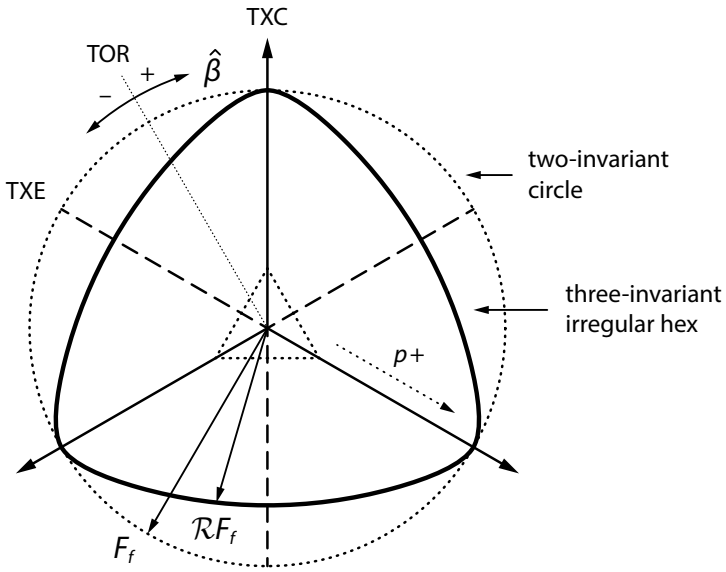

Fig. 5.8. Example of two- and three-invariant shapes of a concrete model in the deviatoric plane.

In CSCM two types of damage are employed – brittle and ductile damage. Damage initiates and accumulates when strain-based energy terms exceed the damage threshold. The logic is that the brittle damage accumulates when pressure is *tensile*, and the ductile damage accumulates when pressure is *compressive*. The strain-based energy terms or just simply accumulations are denoted for the brittle and ductile damage as r_b and r_d, respectively. In essence r_b is a function of the maximum principal strain ε_{max}, and r_d is a function of the total strain ε. They are expressed as

$$\text{brittle damage accumulation:} \quad r_b = \sqrt{E\varepsilon_{max}^2}, \tag{5.2.16}$$

$$\text{ductile damage accumulation:} \quad r_d = \sqrt{\frac{1}{2}\sigma^{\alpha\beta}\varepsilon^{\alpha\beta}}, \tag{5.2.17}$$

with initial thresholds r_{b_0} and r_{d_0}. Note that (5.2.17) uses elastoplastic stresses components (with kinematic hardening) calculated before the application of the damage and rate effects. Therefore, r_d does not represent the true strain energy in the concrete. The initial threshold is calculated from the initial yield surface since the initial damage surface is coincident with the shear surface [186]. Damage increases only if the initial threshold values are exceeded, and since the damage accumulations r_b and r_d are distinguished, the

scalar parameter d is distinguished as well. Taking into account the initial thresholds and the accumulations, CSCM defines

$$\text{brittle damage:} \quad d(r_b) = \frac{d_{max}}{D}\left[\frac{1+D}{1+De^{-C(r_b - r_{b_0})}} - 1\right], \tag{5.2.18}$$

$$\text{ductile damage:} \quad d(r_d) = \frac{d_{max}}{B}\left[\frac{1+B}{1+Be^{-A(r_d - r_{d_0})}} - 1\right], \tag{5.2.19}$$

where parameters A, B, C, and D set the shape of the softening curve plotted as stress-displacement or stress-strain [203], and d_{max} is the maximum damage level that can be attained. For pure shear stress state, parameters C and D are taken [201].

For the brittle damage, d_{max} is set to 0.999 to avoid computational difficulties associated with zero stiffness at the value of 1 [186]. The value of 0.999 is generally used at low confining pressure regimes for the ductile damage. However, at moderate confining pressures, it is less than 0.999 (in agreement with TXC data with residual strength [186]) and driven by

$$d_{max} = \begin{cases} \left(\dfrac{\sqrt{3J_2}}{I_1}\right)^{1.5} & \dfrac{\sqrt{3J_2}}{I_1} < 1 \\ 0.999 & \text{else.} \end{cases} \tag{5.2.20}$$

The problem with (5.2.18) and (5.2.19) is that the parameters A and B or C and D specify the energy release rate, also known as the fracture energy G_f, yet do not take into account the discretization resolution. In other words, the solution is depended on the size of FEM elements or SPH particles.

Since G_f is a material property rather than a model parameter, CSCM uses an automatic regularization technique based on the discretization level. As a result, only softening parameters B and D are required, and parameters A and C are recalculated from the fracture energy G_f. The fracture energy renormalization is discussed in [186, 203] and [202] in detail. The fracture energy G_f is differentiated again for the brittle and ductile damage as G_{fb} and G_{fd}, respectively. Both are calculated from the provided fracture energies in uniaxial tensile stress G_{ft}, pure shear stress G_{fs}, and uniaxial compressive stress G_{fc}. They are defined as

$$\text{tensile pressure:} \quad G_{fb} = G_{fs} + \overbrace{\left(\frac{-I_1}{\sqrt{3J_2}}\right)^{v}}^{k_b} \cdot (G_{ft} - G_{fs}), \tag{5.2.21}$$

$$\text{compressive pressure:} \quad G_{fd} = G_{fs} + \overbrace{\left(\frac{I_1}{\sqrt{3J_2}}\right)^{\mu}}^{k_d} \cdot (G_{fc} - G_{fs}), \tag{5.2.22}$$

where the internal parameters k_b and k_d are restricted to the interval $[0, 1]$, and can be controlled with υ for the shear-to-tension transition, and μ for the shear-to-compression transition. Value of 0 is for pure shear stress, value of 1 is for uniaxial tensile or compressive stress. More about their derivation can be found in [186, 203].

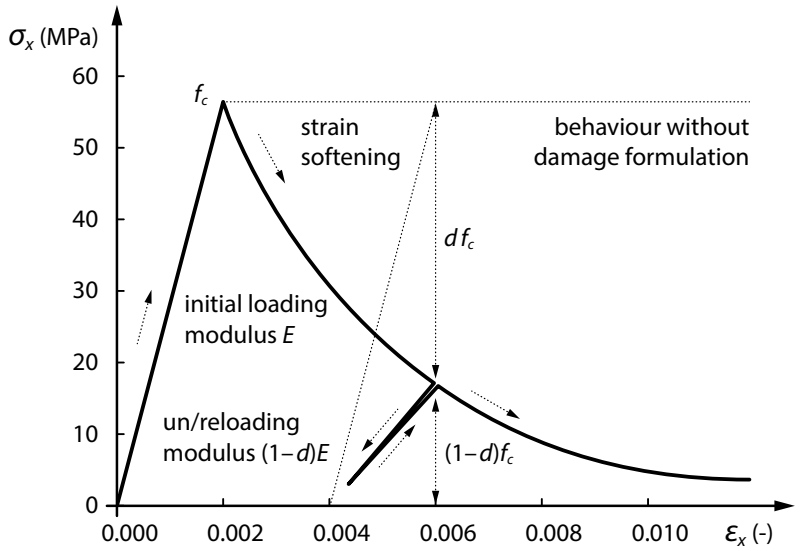

Fig. 5.9. Compressive stress test showing softening and degradation of the elastic moduli with increased straining using the damage formulation.

In addition to the reduction of the maximum damage level with confinement (pressure), the compressive softening parameter A might be reduced with confinement as

$$A = A(d_{max} + 0.001)^{\xi}, \tag{5.2.23}$$

where positive value of ξ reduces A when the maximum damage is less than 0.999, otherwise A is unaffected by ξ [186]. Since ξ is only active at moderate confinement levels, it is known as moderate pressure softening parameter [201].

Since the yield surface, the damage surface, and the fracture energy are defined, *rate effects* can be discussed next. The rate effects are implemented with the viscoplastic formulation based on [207], and require only one parameter called fluidity parameter η. The logic of the algorithm is following. At each time step dt, the algorithm interpolates between the elastic trial stress σ_t and inviscid stress σ_p (without rate effects) to set the viscoplastic stress σ_{vp} (with rate effects) [186] as

$$\sigma_{vp} = (1 - \gamma)\sigma_t + \gamma\sigma_p, \tag{5.2.24}$$

where

$$\gamma = \frac{dt/\eta}{1 + dt/\eta}. \tag{5.2.25}$$

When η is set to zero, the inviscid stress σ_p is attained so that the solution is independent of strain rate. When $\eta \longrightarrow \infty$, the elastic trial stress σ_t is attained at each and every time step which corresponds to the absence of the plastic flow. At each time step, the viscoplastic stress is bounded between the current rate-independent stress and elastic trial stress [186]. The viscoplastic algorithm allows the viscoplastic stress state to lie outside the yield surface [186]. However, using constant fluidity parameter might be problematic when more than one strain-rate data are to be fitted. For that reason, the implementation in CSCM offers additional parameters η_0 and $\bar{\eta}$ with which

$$\eta = \frac{\eta_0}{\dot{\varepsilon}^{\bar{\eta}}}, \tag{5.2.26}$$

where $\dot{\varepsilon}$ is the effective strain rate. Then, the strengths with strain-rate effects, here denoted as f_{dt} and f_{dc}, are calculated as

$$f_{dt} = f_t + E\dot{\varepsilon}\eta, \tag{5.2.27}$$

$$f_{dc} = f_c + E\dot{\varepsilon}\eta, \tag{5.2.28}$$

where f_t and f_c are the strengths without strain-rate effects, i.e. taken usually from a quasi-static load rate range. The term $E\dot{\varepsilon}\eta$ is known as *dynamic overstress*, and can be bounded with overstress limits δ_c and δ_t as

$$\text{if} \quad E\dot{\varepsilon}\eta > \delta \quad \text{then} \quad \eta = \frac{\delta}{E\dot{\varepsilon}}, \tag{5.2.29}$$

where $\delta = \delta_c$ when pressure is compressive, and $\delta = \delta_t$ when pressure is tensile [186]. Again, with CSCM it is possible to fit data in brittle and ductile mode independently. The logic here follows (5.2.21) and (5.2.22) so that

$$\text{tensile pressure:} \quad \eta_b = \eta_s + \overbrace{\left(\frac{-I_1}{\sqrt{3J_2}}\right)^{v}}^{k_b} \cdot (\eta_t - \eta_s), \tag{5.2.30}$$

$$\text{compressive pressure:} \quad \eta_d = \eta_s + \overbrace{\left(\frac{I_1}{\sqrt{3J_2}}\right)^{\mu}}^{k_d} \cdot (\eta_c - \eta_s), \tag{5.2.31}$$

where the internal parameters k_b and k_d are restricted to the interval $[0, 1]$, and can be controlled with υ for the shear-to-tension transition, and μ for the shear-to-compression transition. The parameters η_t, η_c, and η_s are the fluidity parameters for uniaxial tensile stress, uniaxial compressive stress, and shear stress given by

$$\eta_t = \frac{\eta_{t_0}}{\dot{\varepsilon}^{\bar{\eta}_t}}, \tag{5.2.32}$$

$$\eta_c = \frac{\eta_{c_0}}{\dot{\varepsilon}^{\bar{\eta}_c}}, \tag{5.2.33}$$

$$\eta_s = \psi\eta_t, \tag{5.2.34}$$

where ψ is the scaling factor of the tensile fluidity parameter η_t with which η_s is defined. When viscoplastic formulation is used, some previously defined parameters must be reformulated. The initial threshold for the damage accumulation when considering rate effects is denoted as r_0^{vp}, i.e. either $r_{b_0}^{vp}$ or $r_{d_0}^{vp}$, and is shifted (delayed) as

$$r_0^{vp} = r_s\left(1 + \frac{E\dot{\varepsilon}\eta}{r_s\sqrt{E}}\right), \tag{5.2.35}$$

where r_s is the damage threshold before the application of the rate effects, i.e. either r_{b_0} or r_{d_0} [186]. The maximum damage level also changes with the rate effects as

$$d_{max} = d_{max} \cdot \max\left[1.0, \left(1 + \frac{E\dot{\varepsilon}\eta}{r_s\sqrt{E}}\right)^{1.5}\right], \tag{5.2.36}$$

where d_{max} on the right-hand side of the equation is either 0.999 or defined by (5.2.20). Finally, the fracture energy scales as

$$G_f^{vp} = G_f\left(1 + \frac{E\dot{\varepsilon}\eta}{r_s\sqrt{E}}\right)^{\omega}, \tag{5.2.37}$$

where G_f on the right-hand side of the equation is either G_{fb} or G_{fc}, and the parameter ω can increase the fracture energy as a function of the rate effects. With value of $\omega = 1$, the increase in the fracture energy with the rate effects is approximately proportional to the increase in the strength with the rate effects. With value of $\omega = 0$, constant fracture energy is maintained independent of the rate effects [186]. For HVI simulations, values of ω between 0.5 and 1 are recommended [203].

In unconfined compression, the stress-strain behaviour of concrete typically exhibits nonlinearity and dilation prior to the peak [192, 186, 203], see Fig. 5.1. Yet, the pre-peak nonlinearity is more pronounced in compression than in tension or shear. To capture this

nonlinear pre-peak behaviour, a *kinematic hardening* is implemented in CSCM. Since the softening is treated with specified fracture energies, the hardening can be defined independently. In other words, the pre-peak nonlinearity can be controlled without changing the softening of the material. The hardening starts when the initial shear yield surface is reached. The initial yield surface is defined as $N_h F_f$, where the parameter N_h is a fraction of the final yield surface. Parameter N_h must be greater than zero and less or equal to one. In practice, however, reasonable values are $0.7 < N_h \leq 1$. To control the rate of the hardening, parameter C_h is introduced. Growth of the initial yield surface is controlled with back stress for which a stress-based hardening law is defined. The inviscid stress σ_p has the form of

$$\sigma_p^{n+1} = \sigma_h^{n+1} + \sigma_b^{n+1} \tag{5.2.38}$$

where σ_h is the initial yield stress, and σ_b is the back stress. The back stress is a state variable that defines the translation of the yield surface and is defined as

$$\sigma_b^{n+1} = \sigma_b^n + \Delta\sigma_b, \tag{5.2.39}$$

where $\Delta\sigma_b$ is the incremental back stress of the current time step. Note that σ_b is zero upon initial yielding and reaches the maximum value at ultimate yield [186]. The incremental back stress is defined as

$$\Delta\sigma_b = C_h G_b(\sigma_p - \sigma_b)\Delta\dot{\varepsilon}\, dt, \tag{5.2.40}$$

where C_h is the aforementioned rate controlling parameter, G_b is the limiting function for the incremental back stress, and $\Delta\dot{\varepsilon}$ is the effective strain-rate increment. The function G_b restricts the motion of the yield surface so that it cannot translate outside the ultimate surface [208, 186]. The hardening definition together with examples are collected in [186, 203] and discussed in detail in [208]. When the kinematic hardening is used, the shear surface definition is given as

$$F_f(I_1) = N_h(\alpha - \lambda e^{-\beta I_1} + \theta I_1), \tag{5.2.41}$$

which is just scaled (5.2.5). Since the yield surface is well-defined, an illustration of the CSCM in principal stress space can be rendered. Using positive stresses as compression, i.e. when the hydrostatic axis for which $\sigma_1 = \sigma_2 = \sigma_3$ is increasing in value, compaction and therefore the ductile damage is simulated. A full shape of CSCM yield surface can be seen in Fig. 5.10. The shape of the yield surface in the deviatoric plane transitions with pressure from triangular to irregular hexagonal. It does not go fully to circular shape since the cap is used. In Fig. 5.11 a cut through the yield surface and the meridian plane which is passing through $\sigma_1 = \sigma_2 = \sigma_3$, is shown. All stress states which are inside the yield surface are in elastic state. For different strength classes the yield surface expands or contracts as shown in Fig. 5.12. The expansion and contraction is more pronounced in

compression. More about CSCM and about the mechanisms used in CSCM can be found in [186, 199, 200, 192, 202, 203] and [204, 207, 208, 205, 206], respectively.

To better understand how CSCM behaves with different material parameters, simple uniaxial tests are discussed in the following section. All the tests were calculated using LS-DYNA with the explicit time integration scheme. It is very convenient that implementation of CSCM in LS-DYNA offers the generation of the material parameters. Therefore, there is no need to define all the parameters listed in *Symbols in CSCM*. Ultimately, only the unconfined or uniaxial compressive strength (UCS) together with density must be specified. Based on the UCS, the rest of the parameters are generated with respect to experimental measurements internally stored in CSCM. When the parameters are generated, it is possible to review them and modify them, however.

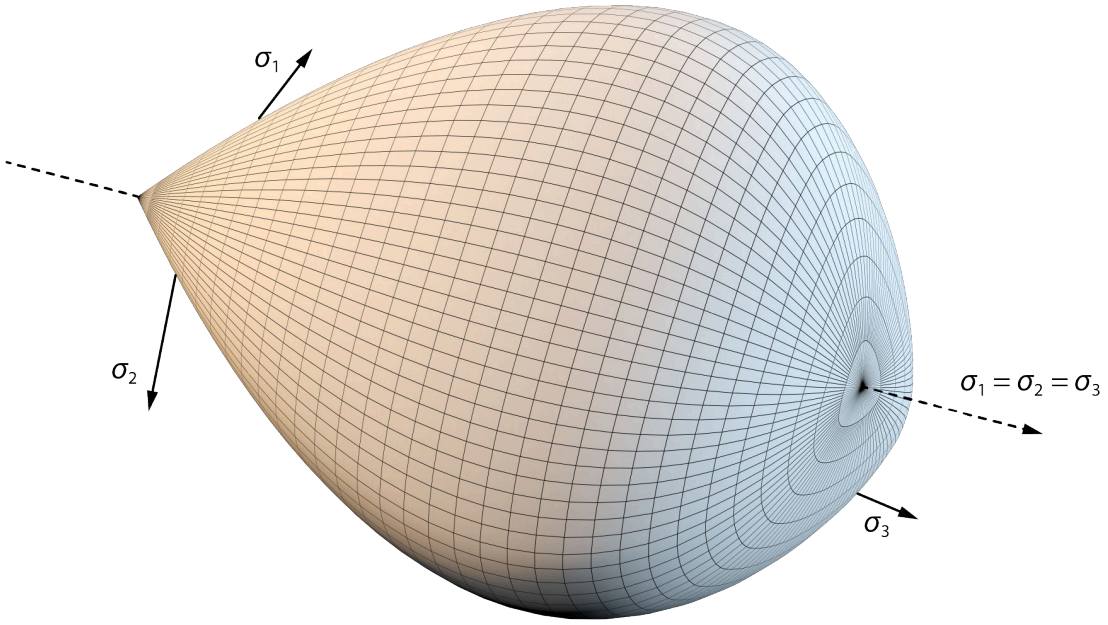

Fig. 5.10. Illustration of the CSCM yield surface in principal stress space.

5.2.1 'One Element' Test

In SPH there is no such thing as one element test known from FEM. Since particles must have neighbours (without neighbouring particles there is no SPH), the simplest SPH model for material testing would be $3 \times 3 \times 3$ particles distributed in a shape of a cube in 3D. In essence, it would be enough to have just $2 \times 2 \times 2$ particles. That would mean, however, there is no particle with all degrees of freedom (DOF) unconstrained, since the exterior particles on one side in each direction would be supported. The rest of the logic from the FEM one element test is the same, however. The 'cube' is fixed on one side in each direction, which means, a load in one direction leads to an uniaxial stress state in that direction, and the other two directions expand/contract based on the load.

In the following simulations, a cube of size $0.1\,\mathrm{m} \times 0.1\,\mathrm{m} \times 0.1\,\mathrm{m}$ was used with the discretization of $3 \times 3 \times 3$ particles. The simulations were calculated using the isotropic

Eulerian cubic spline kernel. The particles were distributed in a cubic lattice with a spacing $\Delta x = 0.05\,\mathrm{m}$ in all three directions. The initial support was defined with recommended $h = 1.2\,\Delta x$ and $\kappa = 2$, as discussed in section *Variable Smoothing Length*.

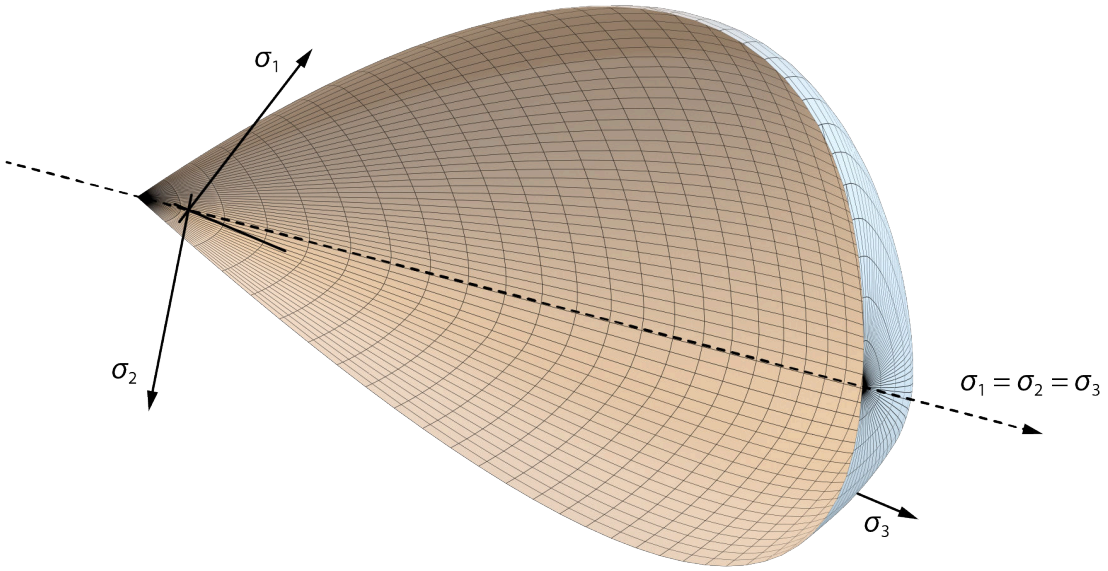

Fig. 5.11. Illustration of a cut through the CSCM yield surface in principal stress space.

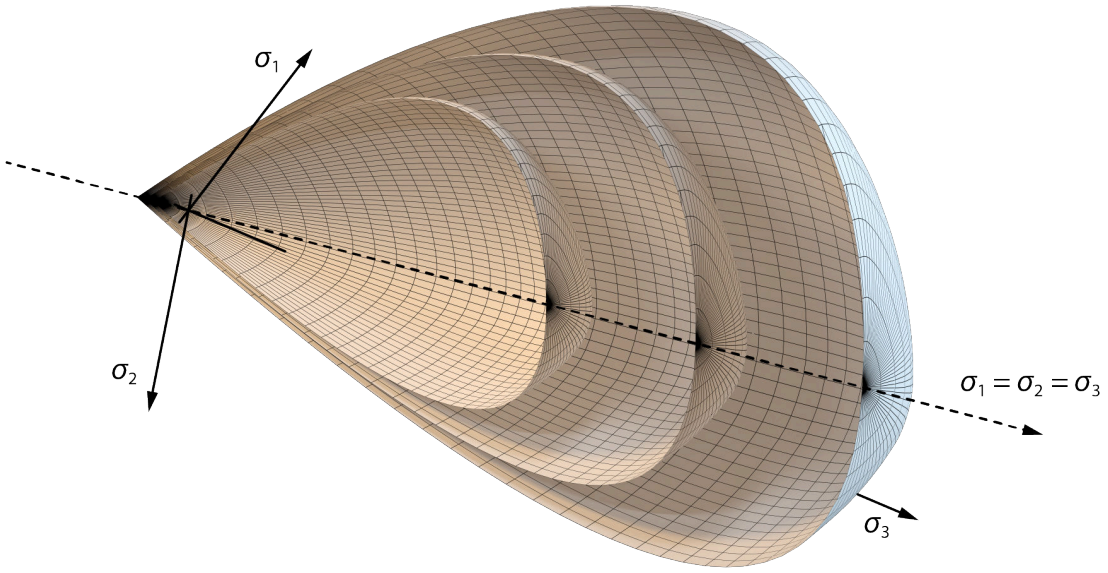

Fig. 5.12. Illustration of a cut through the CSCM yield surface for three different strength classes in principal stress space.

To improve stress gradients at boundaries, the renormalization introduced in section *The Renormalization* was used. In all cases, the loading was controlled with a prescribed

displacement, and the boundary conditions were specified to mimic an uniaxial stress state. As previously mentioned, only density of 2400 kg/m^3 and the UCS were defined since the internal algorithm of LS-DYNA offers generation of all the input parameters. Since the experiment is purely structural, the sign convention from structural engineering is used, i.e. compressive stress and strain are negative, tensile stress and strain are positive.

In the first test, standard concrete classes with respect to Eurocode 2 [209] are compared. The concrete classes in Eurocode 2 are marked with capital C and two numbers. The first number corresponds to $f_{ck,cyl}$ which is the characteristic compressive cylinder strength of concrete at 28 days, and the second to $f_{ck,cube}$ which is the characteristic compressive cube strength of concrete at 28 days. For example, C16/20 stands for the concrete class with the characteristic compressive cylinder strength of 16 MPa, and the characteristic compressive cube strength of 20 MPa. As shown in Fig. 5.13, six different strength classes are compared. Since the cube of 0.1 m × 0.1 m × 0.1 m was used in the simulations, the UCS value in CSCM corresponds to $f_{ck,cube}$. It is clear from Fig. 5.13, that with increasing UCS not only the peak strength in both tension and compression are increasing, but also the initial stiffness, the fracture energy, and the rate of the softening. These aspects of CSCM behaviour in LS-DYNA need to be kept in mind when a material calibration is being done.

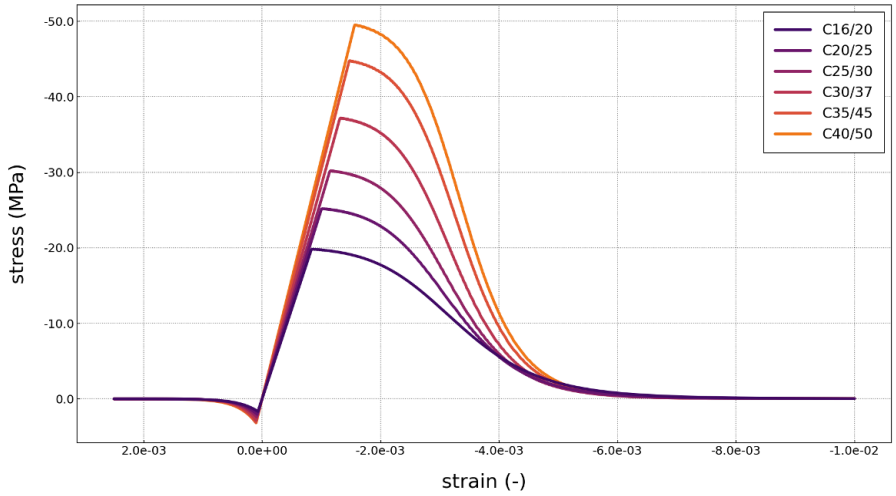

Fig. 5.13. Comparison of uniaxial compressive/tensile strengths of CSCM for different strength classes.

The second test shows the influence of the hardening parameters N_h and C_h for concrete class C25/30. As discussed in section *CSCM Material Model*, the nonlinear pre-peak behaviour of concrete can be either completely deactivated as shown in Fig. 5.13 or can be controlled with the initial size of the yield surface and the rate of the hardening. The parameter N_h is a fraction of the final yield surface, which can be also understood as a percentage of the UCS when the hardening starts. As shown in Fig. 5.14, N_h values in range of 0.7 to 1.0 were tested. Clearly, for $N_h = 1.0$ the stress-strain curve is the same as in Fig. 5.13. Yet, for values of 0.9, 0.8, and 0.7, the hardening starts approximately at 90%, 80%, and 70% of the UCS, respectively. Although the pre-peak nonlinearity is more pronounced in compression than in tension, or shear, the trend is the same. The parameter C_h was defined to have more or less parallel hardening curves. Note that the fracture

energy for the softening was the same for all models. And since the fracture energy is proportional to the area under the softening branch, all the softening branches are parallel.

The third test shows the influence of strain rate. Again, for concrete class C25/30, the comparison is shown in Fig. 5.15 for different load rates which resulted into different strain rates. All the material parameters which are not related to the viscoplastic formulation were kept the same. The rate dependent parameters were also kept the same except one. The fluidity parameter in compression η_c was slightly increased for higher strain rates (in range 1 to 100 per second), the reason is explained later. Important to note, the parameter ω was set to 1, which means, that the fracture energy was increased proportionally to the increase in strength as defined in (5.2.37). Therefore, the results in Fig. 5.15 are not showing increase in brittleness with the increasing dynamic strength. In Fig. 5.15, the $\log \dot{\varepsilon} = -6$ curve represents a quasi-static load since such a rate would roughly correspond to the beginning of the dynamic range, see Fig. 5.3. As discussed in section *Materials with Softening*, with increasing strain rate, the dynamic tensile strength is increased intensively more than in case of the dynamic compressive strength. This can be also seen in Fig. 5.15 in which for the highest strain rate the UCS is scaled by factor of 2, yet the unconfined or uniaxial tensile strength (UTS) is scaled maybe by factor of 8. This again corresponds to Fig. 5.3.

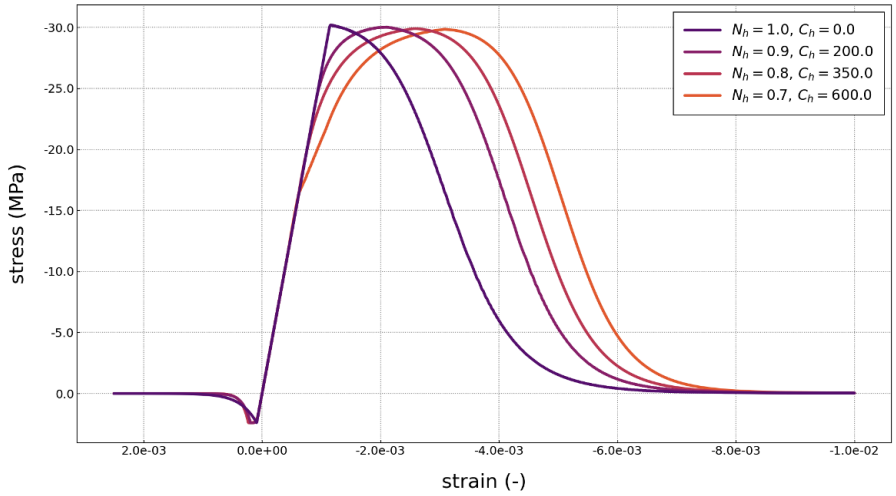

Fig. 5.14. Comparison of uniaxial compressive/tensile strengths of CSCM for different hardening parameters.

Note that in case of the higher strain rates the pre-peak hardening in both tension and compression is not a result of activated hardening but rather an effect of the fluidity parameter η. As shown in (5.2.24), the viscoplastic stress σ_{vp} is bounded between the current rate-independent stress σ_p and the elastic trial stress σ_t. The percentage contribution of each is controlled by γ which is a function of the fluidity parameter (5.2.25). Based on the value of η, the hardening, softening, even the residual strength are influenced. This can be seen in the compressive part of the diagram in Fig. 5.15 in which the higher strain rates have the hardening pronounced more, yet the residual value of the strength is not influenced by the 'viscosity'. In contrast, for the lower rates in compression (up to 1 per second), the fluidity parameter was the same which resulted into increased residual strength with increasing rate (viscosity is acting as a counter force when enough damage

is accumulated). This is not the case for tension, however, since the brittle damage results in a crack opening, therefore, stress drops to zero. Interestingly enough, the initial elastic modulus does not change significantly with strain rate as also previously discussed [197].

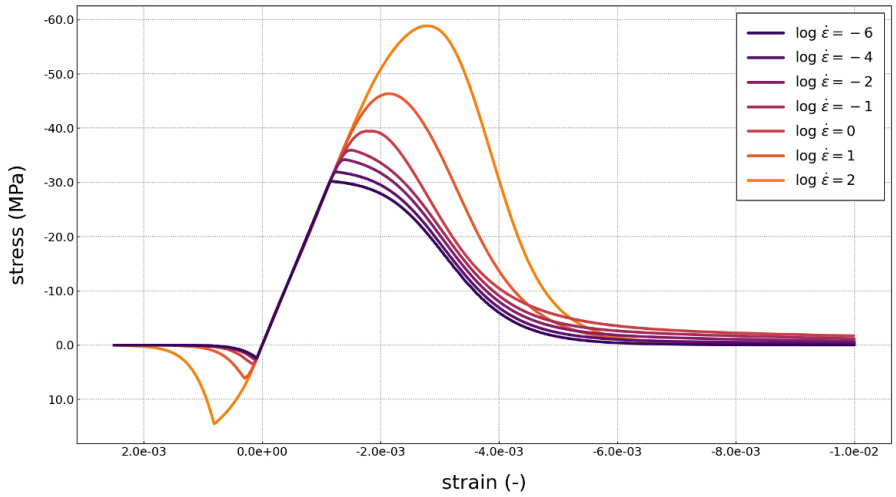

Fig. 5.15. Comparison of uniaxial compressive/tensile strengths of CSCM for different strain rates.

5.3 Experiment – L-Shaped Structural Members

To better understand how SPH behaves with quasi-brittle materials, experimental and numerical investigations of the so-called L-shaped structural member or just L-specimen are briefly discussed. The experiment was first introduced by Winkler et al. in [210] in which a constitutive model for concrete was studied. The experiment became quite popular and today serves as a benchmark for newly developed numerical methods and material models [211, 187]. As pointed out in [211], the L-specimen poses a very interesting problem from the point of view of crack propagation and fracture of concrete, and is often used to demonstrate the capabilities of material models as well as the phenomenon of mesh sensitivity. For SPH, especially when materials with softening are used, it is an excellent benchmark.

The experiment itself is quite simple, only the L-specimen made of plain concrete is needed. The L-specimen is fixed on one side and subjected to imposed loading on the other, therefore, the inner corner is 'opening' in time. A schema of the experiment is shown in Fig. 5.16. Since the SPH behaviour under a dynamic load is to be discussed, the experimental measurements from [187] are used for comparison. In [187], rate effects were examined with a controlled displacement. Rates of the displacement were varied from 0.25 mm/s up to 5000 mm/s resulting into three different crack patterns. Note that the rate of 5000 mm/s was the machine actuator displacement rate. When measurements were evaluated, it was found from displacement history curves that the maximum rate was only 2400 mm/s, however. The rate drop can be associated to many things which are not important at this point. From the experiment, crack patterns are given together with displacement rates, therefore, can be used for the comparison with SPH. The patterns

can be sorted by quasi-static, moderate, and high rates of displacement. The patterns are schematically shown in Fig. 5.17. For the quasi-static rates the crack is almost perpendicular to the loading direction. In contrast, for the moderate rates the crack is almost parallel to the loading direction. Interestingly enough, for the high rates the crack pattern is formed as a combination of both previously mentioned. Since the last crack pattern tends to be the most complex, the loading rate which is associated with it is used for the SPH evaluation; the rate of 2400 mm/s.

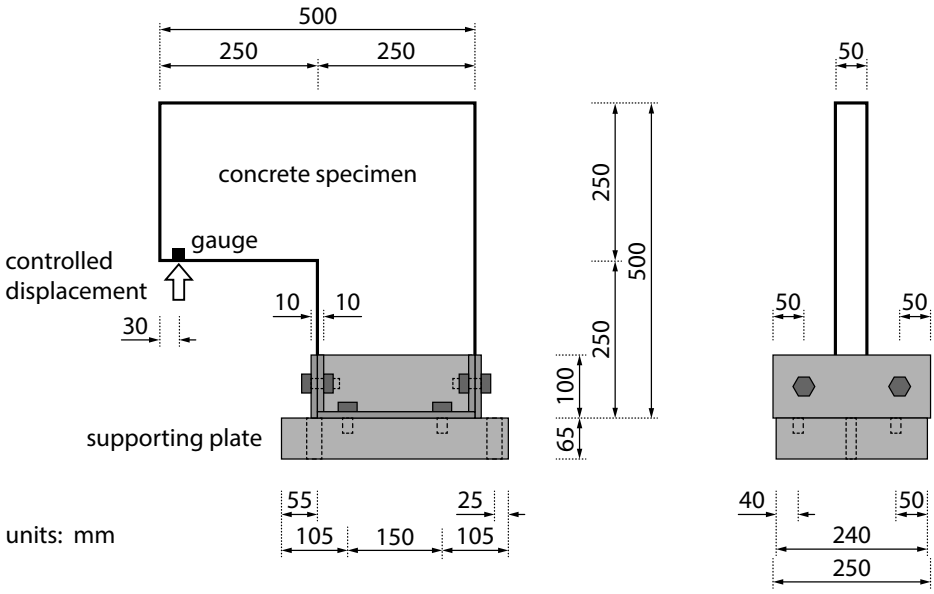

Fig. 5.16. Schema of the L-shaped structural member experiment setup; source [187].

To make the evaluation of SPH more interesting, simulations were divided into two subsections. In the first section, the influence of the particle discretization density was tested. In the second section, the influence of the support size when irregular zones are placed in the way of the propagating crack(s) was examined. As far as the terminology goes, *fracture* refers to a mechanism of creating new surfaces within a domain, and *crack* refers to a discontinuity in the domain.

5.3.1 Influence of the Particle Discretization Density

In essence, accuracy of numerical methods strongly depends on the level of discretization. If the discretization of a problem domain is too coarse, details such as steep gradients can be completely missed. If the problem domain is discretized with higher density, i.e. the discretization is fine, solution tends to converge to more accurate results. Yet it is not always that easy. When fracture mechanics is introduced into the numerical model, a finer discretization does not necessarily mean more accurate solution.

That said, the first part of the SPH evaluation with CSCM shows the influence of the particle discretization density. As shown in Fig. 5.16, the experiment is rather simple to simulate. Therefore, pure SPH models were used with three discretization densities. Taking into account the thickness of the L-specimen of 50 mm, the particle spacing of 16.67 mm, 10 mm, and 6.25 mm were tested. That would be the definition of the coarse, normal, and fine model.

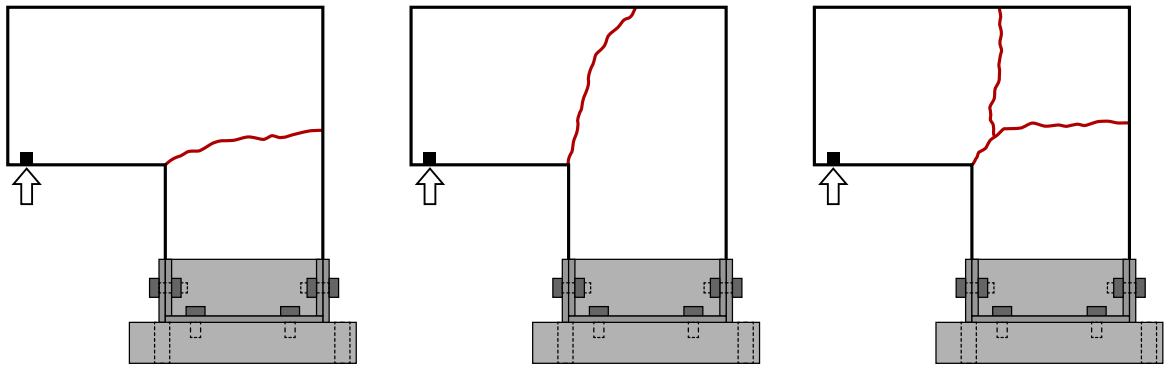

(a) quasi-static rates $< 0.25\,\mathrm{mm/s}$ (b) moderate rates $< 1100\,\mathrm{mm/s}$ (c) high rates $> 1100\,\mathrm{mm/s}$

Fig. 5.17. Schema of crack patterns of the L-shaped structural member experiment; source [187].

Following the setup of the experiment in Fig. 5.16, the particles on both sides of the L-specimen up to 100 mm from the bottom were fixed, and the particles on the free end of the L-specimen were with the prescribed displacement rate of 2400 mm/s in the vertical direction. The total Lagrangian kernel as shown in Fig. 2.38 was used together with the cubic spline and recommended $h = 1.2\,\Delta x$ and $\kappa = 2$. It was not necessary to apply any special treatment to alleviate the tensile instability since the total Lagrangian kernel was used. No techniques to update the smoothing length, no correction schemes or extensions were used. The material parameters of the concrete are collected in Tab. 5.1. The particles were distributed into a cubic lattice, therefore, referred here as the uniform distribution.

ρ	mass density ($\mathrm{kg/m^3}$)	2210.0
E	Young's modulus (GPa)	32.2
ν	Poisson's ratio (-)	0.18
f_c	compressive strength (MPa)	46.25
f_t	tensile strength (MPa)	3.12
G_f	fracture energy ($\mathrm{J/m^2}$)	58.56

Tab. 5.1. Material parameters of CSCM used in the L-shaped structural member simulations.

It is important to mention that the constitutive model strain-rate effects of CSCM were not active in this particular case. Yet, as discussed in section *Materials with Softening*, there are other sources which control rate dependent responses of concrete [187], e.g. structural inertia [193]. However, a comprehensive study was performed by the author in [212, 213] in which all the aspects are discussed, therefore, only the main observations from the simulations are presented here. There are several important responses when quasi-brittle materials are used in simulations – those related to the elastic state, e.g. reaction forces and the stiffness prior the peak strength, and those related to the plastic state, e.g. the damage distribution and post-peak behaviour.

To analyse responses of the first group, force-displacement diagrams can be used. As shown in Fig. 5.18, all three SPH models give reasonable responses. The initial stiffness of each model is comparable with the one measured in the experiment [187], and the peak forces are also relatively the same. The lack of the oscillations in the models can be explained with the introduced Monaghan type artificial viscosity (2.9.3) with parameters $\alpha_l = 1$ and $\beta_q = 1$. The post-peak behaviour is different, however. The SPH models tend to be more brittle than the real specimen in the experiment [187]. This seems to be promoted the most in the coarse model, yet with the finer discretization the post-peak behaviour closer approximates the experimental response. Since the post-peak behaviour is usually not that important, it can be said, that the responses of the SPH models are accurate enough.

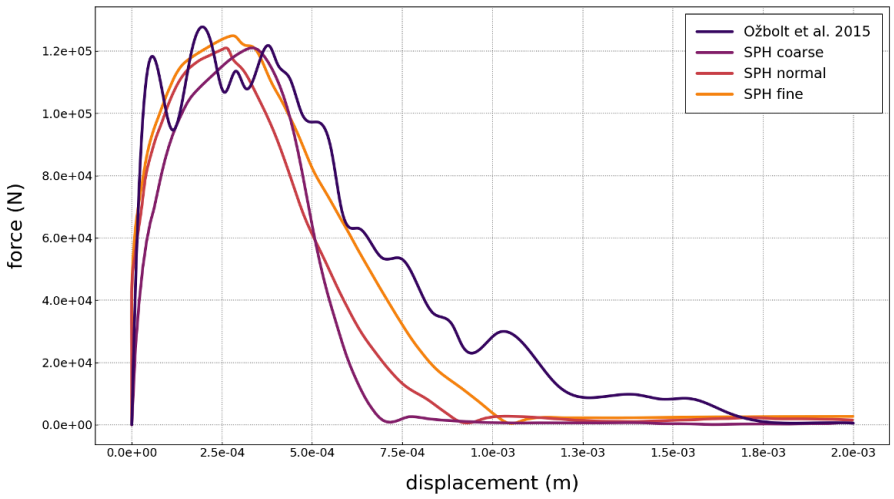

Fig. 5.18. Force-displacement diagrams comparison of different discretization densities; displacement rate 2400 mm/s.

The second group of responses can be analysed by comparing developed crack patterns. Since CSCM employs the damage formulation, crack patterns can be evaluated with either plastic strains or the damage directly. As discussed in section *CSCM Material Model*, the damage in terms of CSCM is a scalar parameter with values in range 0 to 1. In general, higher value of the damage parameter does not necessary mean that the crack opening is greater, yet in this particular case it does, since in all cases it is the brittle (tensile) damage mode which is developed. This can be seen very clearly in Fig. 5.19.

All three discretizations give the same crack pattern which means that the discretization density have just a minor impact on the results and the fracture energy normalization

implemented in CSCM works as expected. In numerical methods, the discretization density plays significant role in both space and time. With the results shown in Fig. 5.19 it was proved that SPH is stable when it comes to the qualitative comparison of discretization levels and that the brittle behaviour can be successfully simulated with it. The simulations are discussed in more detail in the author's [212, 213].

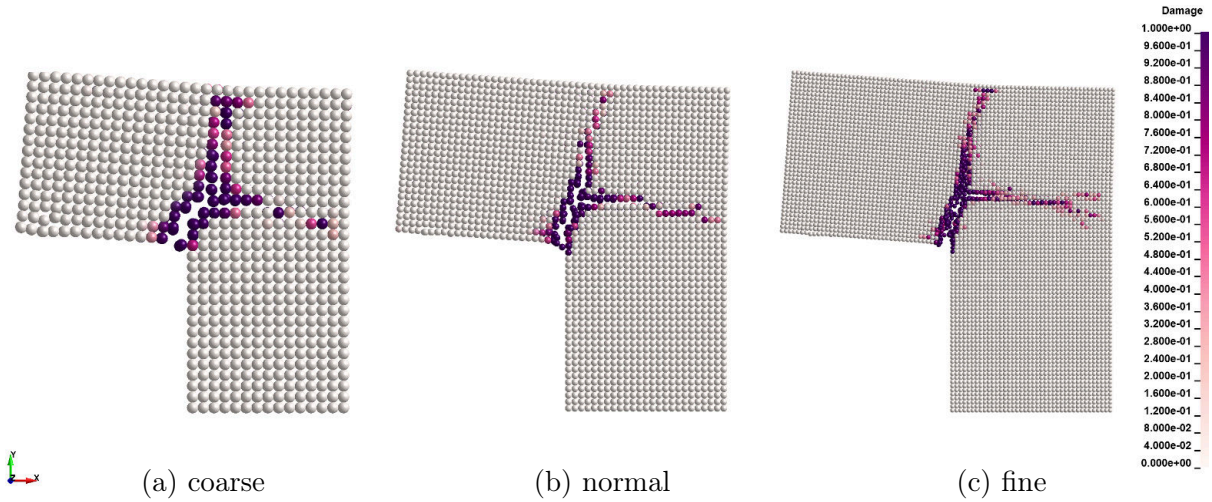

(a) coarse (b) normal (c) fine

Fig. 5.19. Crack patterns comparison for different discretization densities; displacement rate 2400 mm/s.

5.3.2 Influence of the Support Domain Size

The first test proved that SPH works quite well with brittle materials, naturally handles rate effects, and most importantly is not sensitive when it comes to different discretization densities. However, the particles were distributed uniformly. In other words, the number of particles used in the particle approximation was sufficient, therefore, the solution was accurate enough, see section *Consistency of the Particle Approximation*. To test SPH to its limits, an extreme case of a non-uniform particle distribution is discussed next.

In the second test, 'obstacles' were placed into the uniform model with the fine particle spacing of 6.25 mm as shown in Fig. 5.20. The obstacles were nothing else than zones with increased particle spacing up to 16.6 mm. With regard to this, an irregular zone of transition was also created and the particle distribution was no longer uniform. Put simply, the fine model was combined with the coarse one in such a way that zones with the increased particle spacing were placed in the way of the propagating cracks. Such forms of irregularities are not rigorous obstacles but rather soft numerical obstacles. The reason why is the topic discussed is following. In SPH simulations, the quality of the discretization matters. Yet it is not the same as in FEM or other mesh-based methods. In SPH, the regularity or uniformity is more important than the discretization density. Therefore, transition zones in which the discretization is highly non-uniform are or could be problematic. A propagating crack just simply 'goes around' these zones. A crack tends to propagate in the direction in which the number of particles is sufficient and distribution is uniform.

Keeping the same SPH settings as in the first study with the uniform distribution, i.e. the total Lagrangian kernel with the cubic spline, $h = 1.2\,\Delta x$ and $\kappa = 2$, the L-specimen was again loaded with the prescribed displacement rate of 2400 mm/s in the vertical direction. The results of the second study are collected in Fig. 5.21. Comparing the uniform and non-uniform distribution with $\kappa = 2$ in both models, the results are quite different. The crack pattern of the non-uniform distributed model shows the response predicted in Fig. 5.20 (b). Put simply, the crack 'went' around the zones of the non-uniform distribution. What is the explanation?

Every particle represents a mass and volume, although the particles are just points in space. Yet this lumped properties which particles carry with them are directly used in the conservations laws, therefore, the mass, volume, and density together form another weight parameter despite the kernel weighting. Put simply, a 'bigger' particle in the interaction returns a greater force than a 'smaller' particle. Therefore, a crack propagates towards smaller particles which are uniformly distributed, i.e. in the direction of a smaller resistance.

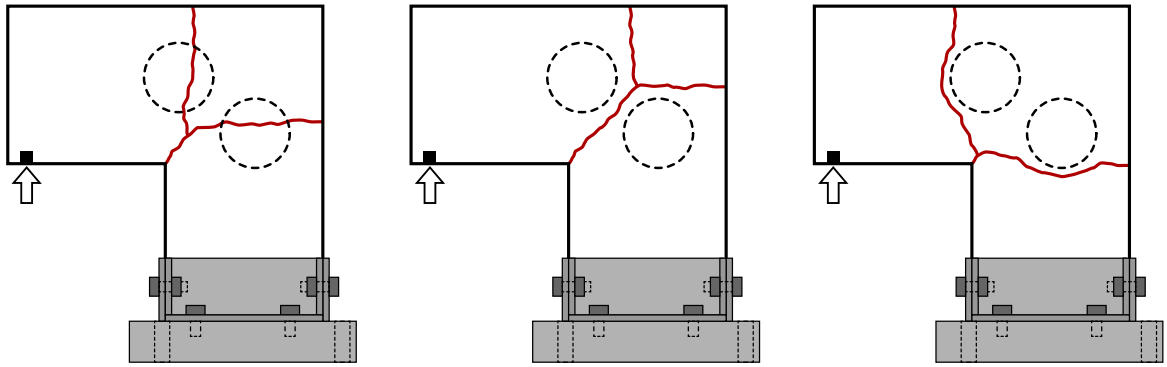

(a) crack pattern from the experiment

(b) expected pattern SPH variant 1

(c) expected pattern SPH variant 2

Fig. 5.20. Schema of expected crack patterns in SPH simulations of the L-shaped structural member experiment.

What could ultimately happen is shown in Fig. 5.20 in which the zones with the increased particle spacing are represented with the dashed circles. The propagating crack might completely bypass the non-uniform zones. In Fig. 5.20, the variant (a) would be the ideal case, the crack pattern would still correspond to the one from the experiment. Yet it can be that SPH simulations result into the pattern shown in (b) or even worse (c). The crack pattern in (c) is not likely to happen, yet it is still possible for certain displacement rates.

As shown in Fig. 5.21, with decreasing κ from the initial value of 2, the crack pattern converges to the correct solution. Why? The explanation is following. As previously mentioned, a bigger particle represents a greater resistance, therefore, if there are bigger particles in the support at the location of the crack tip, well, the resistance is greater and it is likely that the crack bypass the zone. But that means the support must be big enough since bigger particles are distributed farther from each other. Since the smoothing length $h = 1.2\,\Delta x$, it could be that with smaller κ only the particles with relatively same 'weight'

are taken into consideration in the kernel approximation. Which would mean that the crack propagation is again driven by the physics and not influenced by a discretization error. This is exactly shown in Fig. 5.21. With decreasing κ, only comparable particles are used in the support domain which results in more-or-less correct solution. It is important to understand, however, that with decreasing κ the accuracy of the kernel approximation decreases as well.

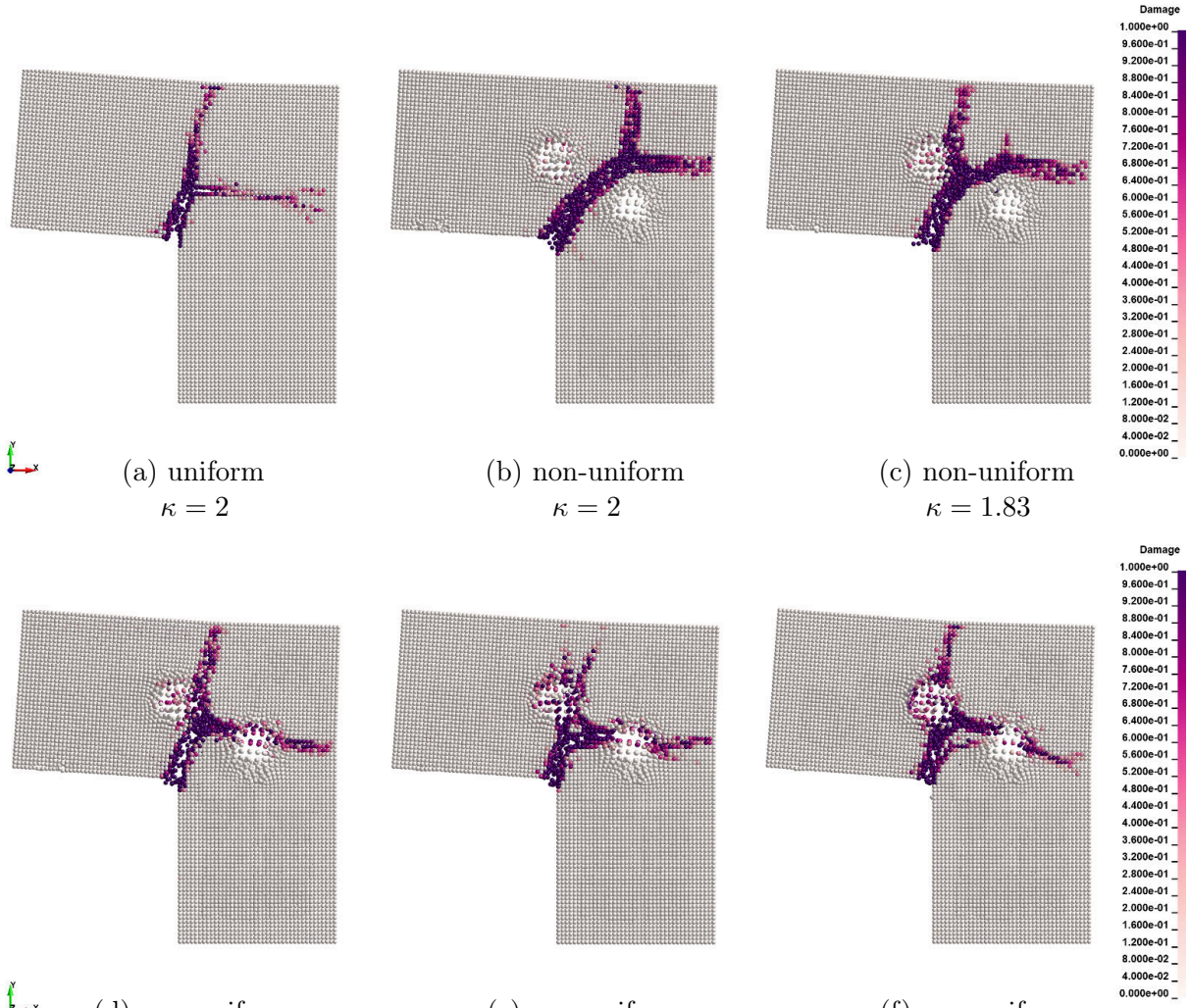

(a) uniform $\kappa = 2$ (b) non-uniform $\kappa = 2$ (c) non-uniform $\kappa = 1.83$

(d) non-uniform $\kappa = 1.67$ (e) non-uniform $\kappa = 1.33$ (f) non-uniform $\kappa = 1$

Fig. 5.21. Crack patterns comparison for different values of κ; displacement rate 2400 mm/s.

5.4 Experiment – Concrete Spalling

As discussed in **Chapter 4** *Coupling SPH and FEM*, it is not always necessary to use pure SPH models, especially when an existing model is already built and SPH is used just as an enhancement. Beauty of SPH is its adaptivity which can be used in many ways. For example, a FEM model can be a starting point for an HVI debris simulation. However, it is quite difficult to simulate spalling and scabbing of concrete with either Lagrangian

or Eulerian FEM. For SPH, on the other hand, it is not a problem at all. But how to transform FEM into SPH during the simulation? The concept and demonstration of the transformation is discussed in this section.

5.4.1 Element Erosion

The idea of the SPH and FEM coupling in HVI debris simulations is quite straightforward. At the beginning, there is only a FEM model with assigned brittle material, e.g. with CSCM. After the model is subjected to the impact and the load-carrying capacity of the FEM elements is reached, either in compression or tension, the elements have no stiffness, therefore, a little purpose to remain active. In other words, the elements can be eroded since they represent debris. Mass cannot just disappear, however. A possible solution is to transform the failed elements into SPH instead. The mass and energy (internal and kinetic) are preserved and the simulation can advance in time but as coupled SPH-FEM.

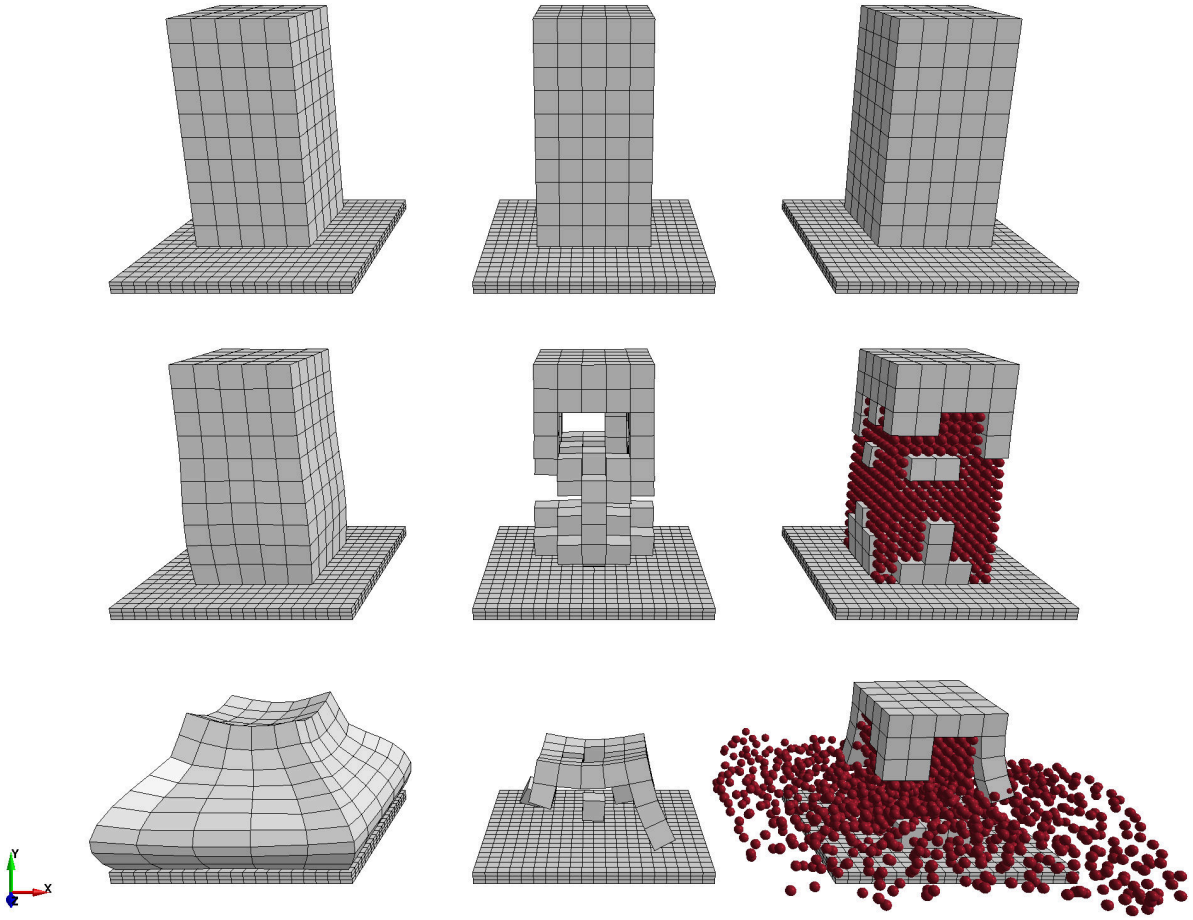

(a) no erosion (b) erosion (c) erosion into SPH

Fig. 5.22. Three models comparison in a simple HVI simulation with CSCM.

To better understand the concept, three models are compared in a simple HVI simulation in which a concrete block impacts a rigid surface as shown in Fig. 5.22. All three models

used the same CSCM material model with identical parameters (not important at this point). The models (a) and (b) were pure FEM models, with just one difference. Elements in the model (b) were eroded when the CSCM damage value of 1 was reached. The model (c) was similar to the model (b). However, when elements were eroded in the model (c) the mass was transformed into SPH. The particles further interacted with the rest of the FEM part of the model and between each other. The interaction between FEM and SPH can be done in different ways as discussed in **Chapter 4** *Coupling SPH and FEM*. In this case, the penalty-based contact was used.

As shown in Fig. 5.22, all three models impacted the rigid surface at the same time and since the models were identical prior the erosion, the acting force on the rigid surface was also the same. After the impact however, each model started to behave differently. The model with no erosion shows excessive deformation, a 'jelly' like behaviour. Since the elements in the lower part of the model reached the maximum possible value of the damage and thus had only the residual strength and stiffness, their behaviour reminds rather a flow of a fluid. The model response is completely valid, numerically stable, yet due to the excessive deformation of the elements, the simulation time step was significantly reduced. In contrast, the same elements were eroded in the model (b). As a result, the displacement of the top part of the model is exaggerated. Although the time step was constant throughout the simulation, the response of the model is inaccurate. The model with the transformation into SPH solves the problems of both models. The elements in the lower part were eroded, yet the mass was preserved. The newly generated particles interacted with the rest of the model, therefore, the displacement of the top part is closer to the one seen in the model (a). In contrast to the model (a), the time step was almost constant throughout the simulation since all the excessively deformed elements were eroded.

This rather simple example in Fig. 5.22 shows a complex technique with a potential in structural dynamic applications. The author used the described technique in simulations of an HVI experiment to further study the behaviour of coupled SPH-FEM models. A brief review of the results and findings from the author's [214, 215] follow.

5.4.2 Three Approaches, Three Results

In 2001 Buchar et al. [216] performed an experiment in which concrete blocks were impacted by steel projectiles accelerated to different velocities. Penetration depths and volumes of spalled concrete were subjects of the study. Results and observations from the experiment are collected in [216, 217]. For purpose of the thesis, only the experimentally measured penetration depths are discussed and compared with the results of the three previously outlined numerical models.

A schema of the experiment is shown in Fig. 5.23, and it must be pointed out, that boundary conditions of the concrete block are 'questionable'. The block was placed on a ground/table and fixed with a clamp. The pressing force exerted by the clamp is unknown, however. The back side of the block was supported by a wooden desk [217]; perhaps also attached to the clamp. Therefore, it is not possible to say if the concrete was initially confined or not. Nevertheless, in the simulations the back side of the block was fixed and the rest of the surfaces were free to expand; as it seems it would be the case in the real

experiment. A plane concrete with the UCS of 43.1 MPa was used for all tested blocks with dimensions of 0.1 m × 0.1 m × 0.1 m.

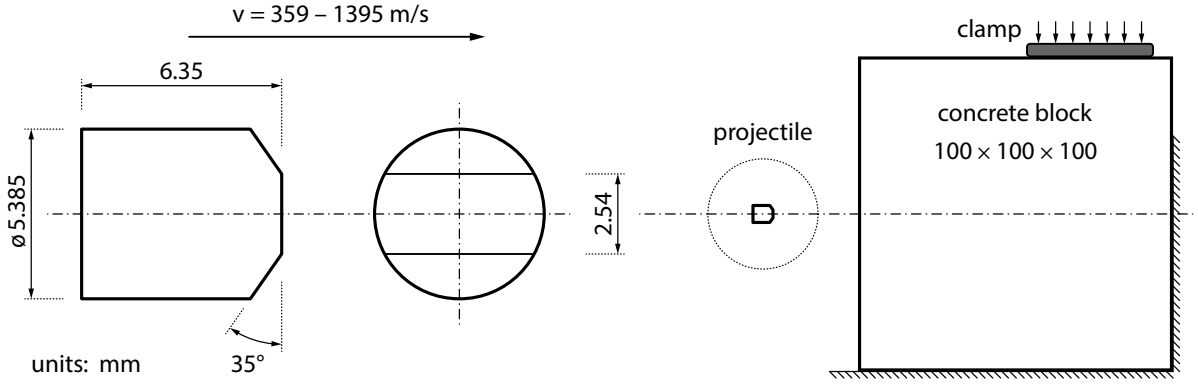

Fig. 5.23. Schema of the block HVI experiment; source [217].

The standardized projectile type 1 according to NATO Stanag 2920 [218] was used in all cases, i.e. for striking velocities between 359 and 1395 m/s. The projectile itself is meant to be used in fragment simulations and was specially developed to have a constant relation between its weight, diameter, and striking face. In other words, fragment penetrations were studied in [216] rather than penetrations of an armour-piercing shell. The projectile was only 1.102 g made of steel. The material parameters of the steel were taken from [219], and were used in the Johnson-Cook material model also described in the paper. In addition to that, the Equation of State (EOS) parameters of the steel from [220] were used in the Grüneisen EOS model; described in detail in [221].

ρ	mass density (kg/m^3)	2400.0
E	Young's modulus (GPa)	29.92
ν	Poisson's ratio (-)	0.15
f_c	compressive strength (MPa)	43.1
f_t	tensile strength (MPa)	3.09
G_f	fracture energy (J/m^2)	84.46

Tab. 5.2. Material parameters of CSCM used in the block HVI simulations.

CSCM with the constitutive model strain-rate effects was used in the numerical simulations. The initial value of UCS, i.e. without the rate effects, was as in the experiment 43.1 MPa. The rest of the material parameters were not calibrated but those from the automatic generation process implemented in CSCM in LS-DYNA [186, 203]. The most important parameters are collected in Tab. 5.2. The numerical models were identical except the element erosion handling. As outlined in Fig. 5.22, the first model was the standard FEM model without any element erosion. The second and the third model allowed the aforementioned element erosion when the CSCM damage value of 1 was reached. The third

model, however, transformed the eroded mass into SPH particles, therefore, the mass and energy were preserved.

To minimize possible errors during the transformation from FEM to SPH, the following concept was used. When a FEM model is generated, SPH particles are already placed in the model. Based on the discretization density, one or more particles are placed inside each element. The particles, however, are inactive. When the particles became active, i.e. after elements are eroded, they inherit all the Lagrangian nodal and integration point quantities of the elements. Only the damage value is set back to 0, since the activated particles simulate debris of finite sizes which are can exhibit a resistance. These properties are strictly assigned to the activated particles only. In this particular case, one SPH particle was used per FEM element since the mesh was fine enough. The isotropic Eulerian kernel was used together with the cubic spline for all particles. No technique to alleviate the tensile instability was used. For the interaction between FEM and SPH, the penalty-based contact with a viscous damping was used.

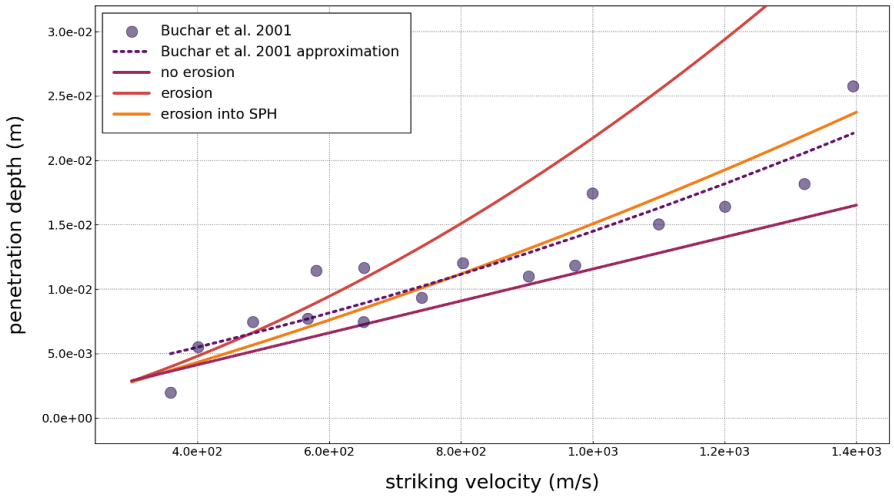

Fig. 5.24. Penetration depths over the range of striking velocities.

Starting with the comparison of the penetration depths in Fig. 5.24, the measurements from the experiment were reproduced quite well at least for two out of the three numerical models. For convenience, the measurements from the experiment are shown as discrete points as well as an approximation based on the Moving Least Squares (MLS) polynomial of second degree (dashed line). The responses of all three models are almost identical for striking velocities below 400 m/s. For moderate and high striking velocities, however, the simple model with the element erosion is inapplicable. The reason is simple; the erosion of the mass during the time when the shock wave is 'bouncing' in the concrete artificially increases the penetration depth. The model without the element erosion shows a good correlation with the experiment, maybe a rather stiffer behaviour. It must be noted, however, the model is inapplicable in practice, yet for a different reason than the model with the element erosion. Since the time step in the explicit integration scheme was driven by the Courant-Friedrichs-Lewy (CFL) condition [138], due to the presence of excessively distorted elements the time step was almost zero throughout the simulation. In addition, highly distorted elements might result in negative volume. When the volume is negative, the explicit solution fails. The results of the model with the SPH transformation are similar

to the pure FEM model without the element erosion for lower striking velocities. For higher striking velocities, however, the model with SPH shows a slow exponential growth which can be also observed in the experiment. In contrast, the FEM model without the element erosion shows a stiffer behaviour. The explanation could be that the distorted elements further act against the projectile.

The actual damage of the concrete block is shown in Fig. 5.25 for the model without the erosion, in Fig. 5.26 for the model with the erosion, and in Fig. 5.27 for the model with the erosion and transformation into SPH; all for striking velocity of 800 m/s. The crack patterns of all three models are similar, the trend of the main diagonal cracks is again in a good correlation with the experiment [217].

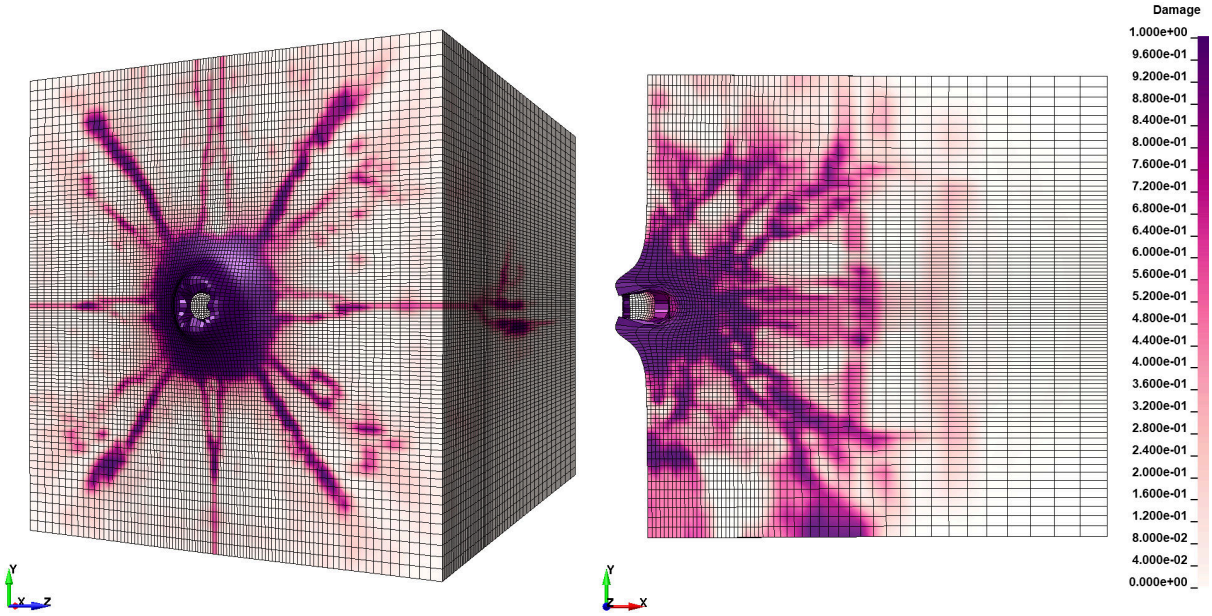

(a) iso view (b) cross-section

Fig. 5.25. Damage of the concrete block without the erosion; striking velocity 800 m/s.

Since the element erosion takes place when the damage reaches value of 1, it makes sense to see dark purple contours only in the first model. The crack patterns of the models with the erosion are similar, yet not identical. The reason for that is the mass dissipation. When the mass is just simply eroded and removed, therefore, dissipated, the dynamic response of the model is different. The problem is that a crack is represented by eroded elements (removed mass). Since there is no mass which can act against the closure of the crack, the model shows reduced stiffness. This leads to easier crack propagation in general. When the eroded mass is replaced by SPH particles however, the crack cannot simply close since the newly activated particles do not allow it. The particles represent debris, small pieces of concrete. Even a small piece of concrete under hydrostatic pressure cannot just simply disappear.

The consequence of the eroded mass is reduced confinement. When the projectile penetrates deeper into the concrete, the forces acting on the lateral surface of the projectile further

slow it down due to friction. When the confining mass is eroded however, the only acting force is on the striking face. This can be seen in Fig. 5.25 and Fig. 5.27. Both models, without the element erosion and with SPH simulate the confinement. The model with the element erosion does not, see Fig. 5.26.

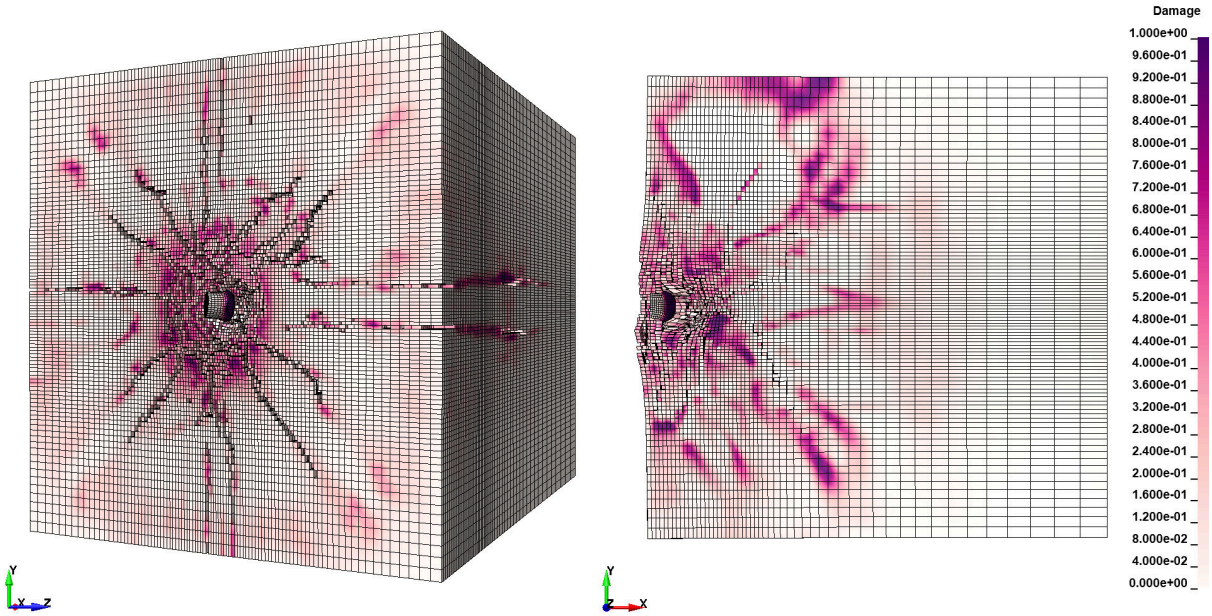

(a) iso view (b) cross-section

Fig. 5.26. Damage of the concrete block with the erosion; striking velocity 800 m/s.

The very same applies for a crack propagation into depth. The penetration depth is strongly influenced by the stiffness of the domain under the impacted surface. At the moment of the impact, the concrete deeper below the impacted region is suddenly compressed. After the cracking of the concrete begins, the previously compressed domain starts to expand. Since the expansion is anisotropic, many elements reach the limit of the brittle damage, therefore, are eroded. Once the erosion begins, it is promoted by the material oscillations. Yet it does not necessary mean that the kinetic energy of the projectile is already zero. It only means that deeper below the impacted region there are missing elements, therefore, the stiffness is reduced. However, if the material is not dissipated at all or the eroded elements are replaced by SPH, the domain/mass is still there, therefore, provides sufficient support. This can be clearly seen in Fig. 5.27. The cracks deeper in the concrete are filled with SPH particles and better simulate the response of the concrete.

As previously mentioned, SPH particles are in the numerical model from the beginning, yet not active. For that reason, the computational demands are almost the same as in the pure FEM models. When elements reach the limit value of the damage and are eroded, SPH particles are activated. In other words, for every deactivated element there is one particle activated. Therefore, the computation time increases only slightly due to the SPH sorting. The process of the SPH activation can be seen in Fig. 5.28. The value of 1 (dark purple) means that the particle is active. At the end of the simulation, the total mass of the active particles is equal to the eroded mass of the elements.

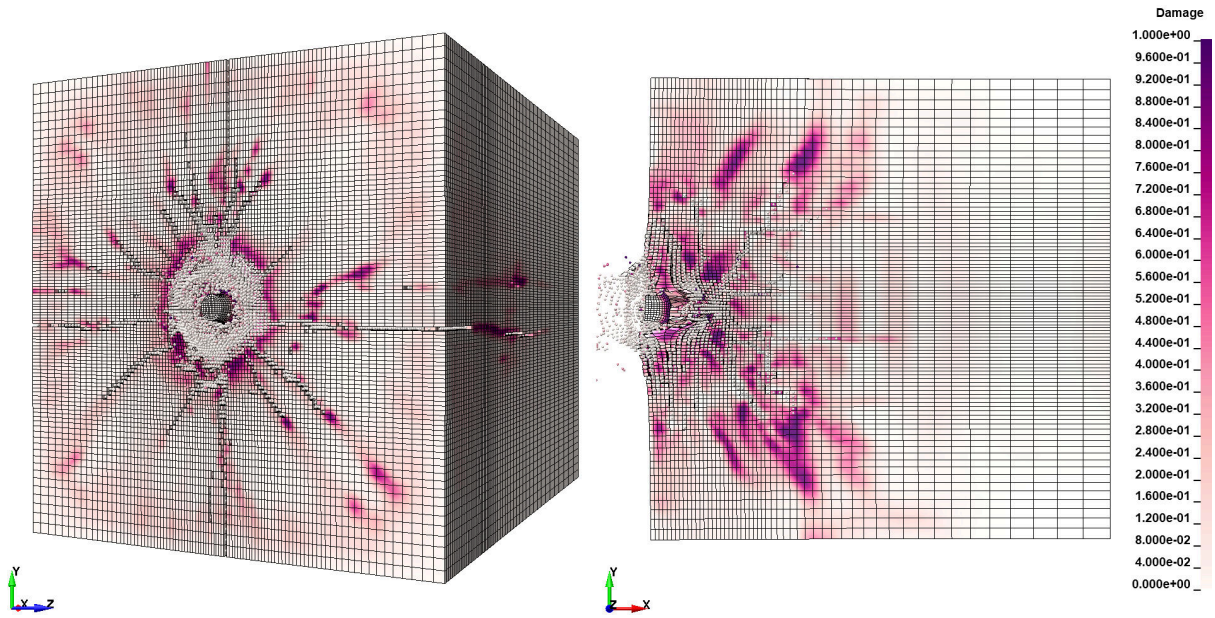

(a) iso view (b) cross-section

Fig. 5.27. Damage of the concrete block with the erosion into SPH; striking velocity 800 m/s.

Note that after the elements are eroded, the damage value of the newly activated particles is set back to 0, see Fig. 5.27. The idea behind that is to simulate debris as a small pieces of concrete and not as a dust. Even debris might exhibit a resistance under a load. For that reason, the damage value must be set back, otherwise, the SPH particles would have no stiffness in the interaction, see Fig. 5.9. A complex study can be found in the author's [214, 215] in which additional aspects are discussed, although with the Johnson-Holmquist concrete (JHC) material model.

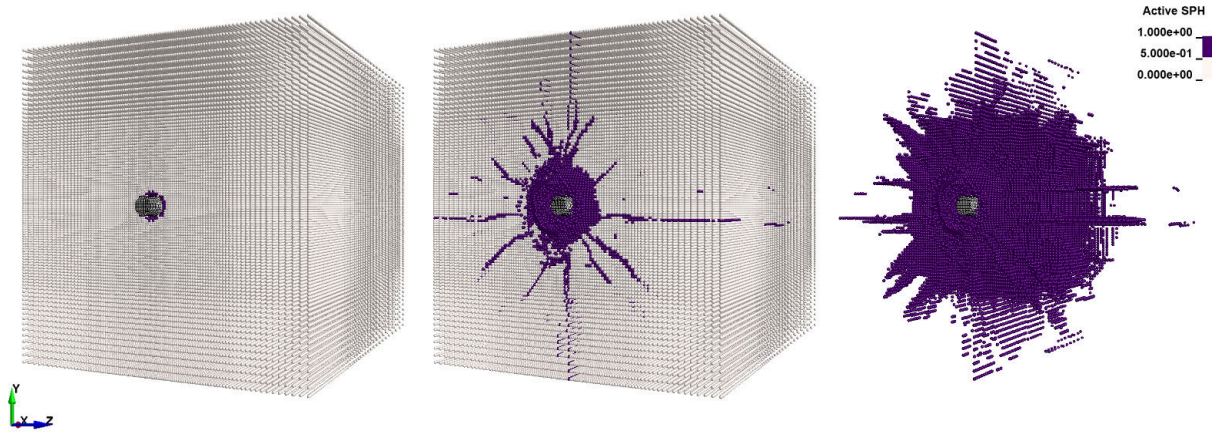

(a) impact (b) end of the simulation (c) end of the simulation, active SPH only

Fig. 5.28. Activation of SPH particles during the simulation; striking velocity 800 m/s.

Chapter 6

Reinforced Concrete

In terms of plain concrete, Smoothed Particle Hydrodynamics (SPH) can be very useful and offer much more than standard mesh-based methods. Reinforced concrete, however, might be a problem. Again, the tensile instability is to blame. The idea of having a tool generic enough to simulate material behaviour under a quasi-static load as well as under a high-speed load, or even a hyper-speed load with a fragmentation of a matter is of course appealing. SPH can be the tool. Sometimes might be useful however to borrow pieces from other methods and use them as an enhancement in SPH. In this chapter, the concept of a reinforced concrete modelling with SPH is discussed.

6.1 When FEM Excels

When it comes to reinforced concrete simulations, it is without a doubt that the Finite Element Method (FEM) should be used in preparation phases. Its simplicity and functionality, especially when it comes to 1D elements is quite surprising. Even today, when high-performance computing (HPC) is widely available, 1D FEM elements are still used for the reinforcement. As a matter of fact, even when reinforced concrete is simulated with SPH the author tends to use FEM for a verification. For that reason, the chapter starts with FEM, then moves to SPH.

What is reinforced concrete? Put simply, any combination of concrete and reinforcing element(s). The reinforcement can be made of steel, polymers, textile, and many other materials. In civil engineering, the most common form is a reinforcement with steel. For that reason, the chapter focuses on a steel reinforcement, however, what is discussed here applies to many other materials. From the numerical point of view, it does not matter which materials are combined. Yet, some special treatment is needed when densities of the coupled materials differ significantly, e.g. three orders of magnitude. In essence, there are two approaches to create a 'reinforcement' in FEM; using

- special elements with a smeared reinforcement,
- discrete elements connected to master elements.

There is no general rule when to use which, however, using discrete elements, i.e. using additional elements to those which represent the concrete, is more convenient. The question is, how can be the discrete reinforcing elements connected/attached to the concrete elements? There are three common approaches, two of them already discussed in **Chapter 4** *Coupling SPH and FEM*. The connection can be done by using

- shared nodes,
- penalty-based approach,
- constraint-based approach.

Using shared nodes would be considered the oldest approach. The model must be created in such a way that nodes of the concrete and reinforcing elements have identical locations, i.e. a node of a concrete element is used in a reinforcing element. This is, of course, a very difficult task especially when a complex reinforcement should be modelled. The advantage is that no special treatment is needed and the simulation time is not artificially increased. A disadvantage could be that only no-slip conditions can be simulated.

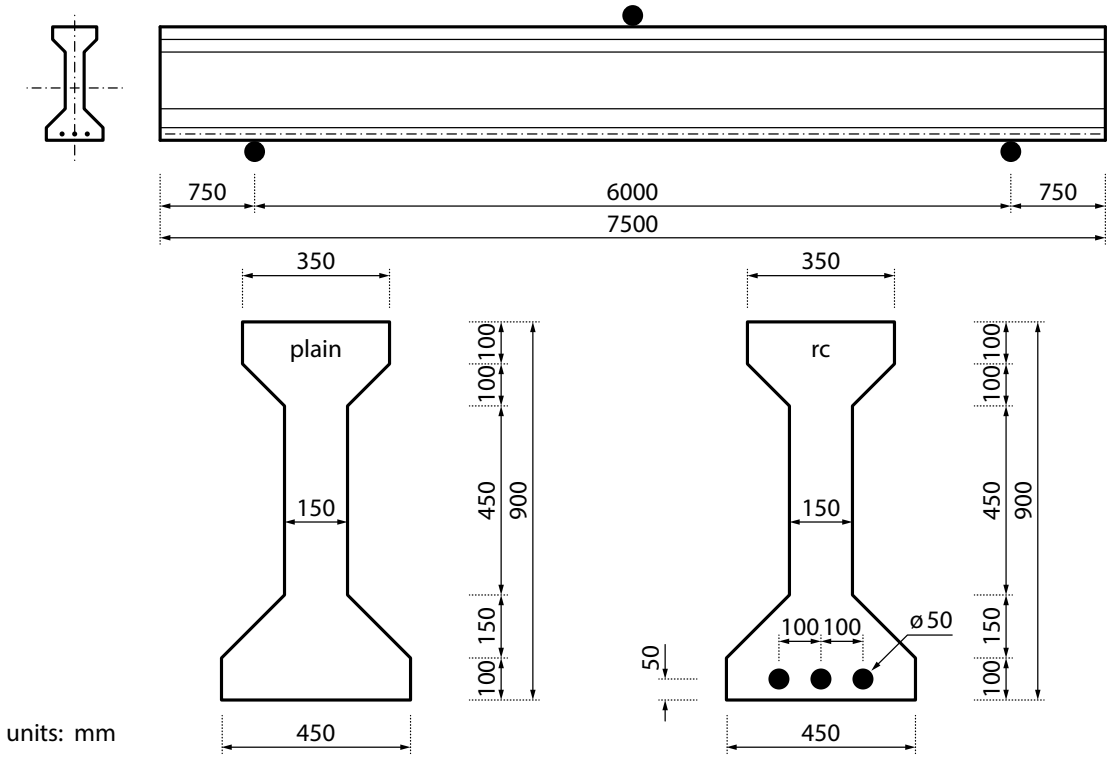

Fig. 6.1. Schema of the three-point flexural test of the plain and reinforced I-girder.

The penalty-based contact can be used instead. Although the contact takes place inside the concrete, not onto the outer surface, the logic of the contact is still the same. The only difference is that the 'penetration' is everywhere outside the initial coupling point.

Compared to the previous approach, the biggest advantage is the simplicity in usage. Only the definition of the contact is needed in addition; nodes of both entities can be independently placed within each other. Another advantage is a possible de-bonding in compression and tension. A slip between the reinforcement and concrete, however, is very often not possible since only the nodal locations are known, not the orientation of the reinforcement. The simulation time might be increased since the contact itself brings additional computation and might have an impact on the time step.

The constraint-based approach uses kinematic constraints rather than penalty forces. Usually, the coupling is applied to accelerations and velocities. Again, nodes of both entities might be distributed independently within each other, only the kinematic constraints must be defined. Compared to the penalty-based approach, additional coupling points might be added along the reinforcing elements. Due to that, the orientation of the reinforcement is known, therefore, a slip between the reinforcement and concrete can be modelled. However, de-bonding in compression and tension is usually not possible, both or neither can be simulated only.

ρ	mass density (kg/m^3)	2400.0
E	Young's modulus (GPa)	28.27
ν	Poisson's ratio (-)	0.15
f_c	compressive strength (MPa)	37.1
f_t	tensile strength (MPa)	2.84
G_f	fracture energy (J/m^2)	74.93

Tab. 6.1. Material parameters of CSCM used in the three-point flexural test simulations.

To better understand the influence of the reinforcement in concrete, a three-point flexural test of a plain and steel reinforced I-girder is discussed next. Since the focus of the chapter is not on an excessive comparison of all modelling approaches in FEM but rather the SPH performance, only the results of FEM with the constraint-based coupling are shown. A schema of the three-point flexural test is shown in Fig. 6.1. Compared are two pure FEM models – plain and reinforced. Both models are identical except the reinforcement. Standard brick elements with reduced integration were used for the concrete, beam elements for the reinforcement. The supports and the loading cylinder were defined as analytical entities.

ρ	mass density (kg/m^3)	7850.0
E	Young's modulus (GPa)	210.0
E_{tan}	tangent modulus (GPa)	21.0
ν	Poisson's ratio (-)	0.3
f_y	yield strength (MPa)	500.0

Tab. 6.2. Material parameters of the steel used in the three-point flexural test simulations.

The Continuous Surface Cap Model (CSCM) was used for the concrete, and a simplified elastoplastic model for the reinforcement. The material parameters of the concrete are collected in Tab. 6.1 and for the steel in Tab. 6.2. The supports, the two bottom cylinders, were fixed and the top cylinder had prescribed vertical motion with a smooth ramping defined with the sinus function (inflection point in the middle of the total displacement). Static friction coefficient of 0.1 was used between the cylinders and concrete.

Interesting enough, a special technique for the FEM model generation was used. The so-called voxelization was introduced in order to have identical FEM and SPH models. The voxelization is a meshing technique with which a problem domain is discretized with voxels (grid). It is very similar to the Eulerian FEM mesh generation but with one difference – empty voxels are subsequently removed. The voxelization is especially popular in 3D printing, yet it is very useful for SPH models generation as well. As discussed in section *Variable Smoothing Length* and section *Consistency of the Particle Approximation*, it is beneficial to use a cubic lattice particle distribution. Such a distribution is usually outcome of the voxelization.

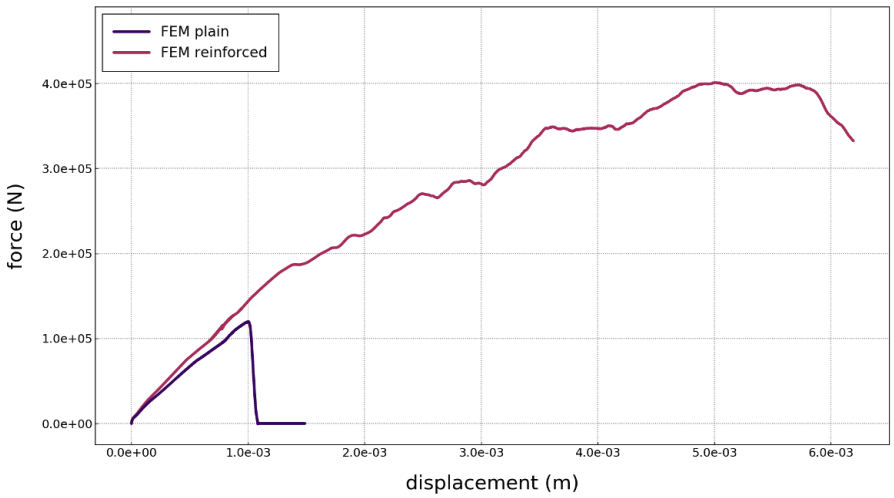

Fig. 6.2. Force-displacement diagrams comparison of the plain and reinforced I-girder FEM models.

When reinforced concrete is simulated, a special attention should be paid to two response classes. Those are stress and strain related responses. The stress related responses can be easily evaluated from force-displacement diagrams, e.g. the initial force gradients and peak force. The strain related responses are represented with plasticity or in case of CSCM with the damage.

Starting with the force-displacement diagrams in Fig. 6.2, the effect of the reinforcement is obvious. The initial stiffness is increased, yet only slightly, since the reinforcing elements are placed only at the bottom part of the I-girder. In addition to the increased stiffness, the peak force of the reinforced I-girder shows the true motivation behind reinforced concrete. Since tensile stresses are carried over by the steel and only compressive stresses by the concrete, the maximum load-carrying capacity of the reinforced I-girder is greatly increased.

The crack pattern (the damage distribution) again shows why is reinforced concrete so popular. Instead of one major crack as shown in the case of the plain concrete, the reinforced concrete shows series of micro-cracks located at the bottom part of the I-girder, the proximity of the reinforcement. As far as the numerical modelling goes, this is a proof that no-slip conditions were enforced. In other words, the model shows a perfect connection between the concrete and steel.

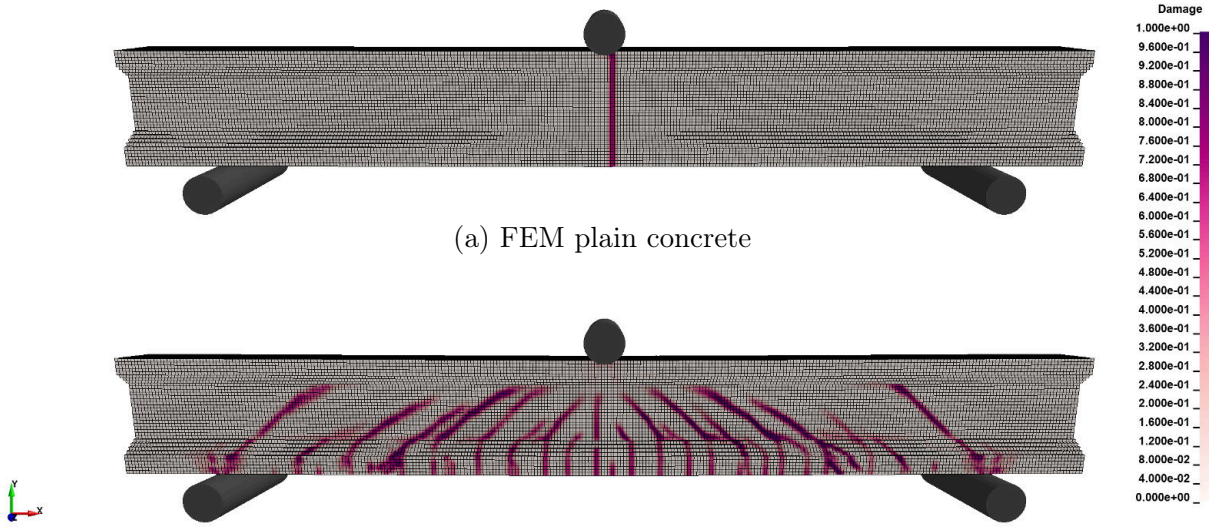

(a) FEM plain concrete

(b) FEM reinforced concrete

Fig. 6.3. Damage comparison of the plain and reinforced I-girder FEM models.

6.2 Pure SPH Models

In case of pure SPH models, however, the tensile instability might be a problem. Since the tensile instability is a numerical problem which has nothing to do with reality, simulating reinforced concrete might be difficult for two reasons. The first reason is related to concrete since it is quasi-brittle material. It is expected to see crack openings (brittle damage), however, it is difficult to say if it is a material or numerical fracture. The second reason is related to the reinforcement. It is not expected to see crack openings in the reinforcement at all (if designed correctly). However, it is expected to see yielding or ductile damage if the strength limit is reached.

There are many indicators which can tell if SPH models show numerical or real cracks. Most of them work with stress paths and require the history tracking. However, since FEM models are available, a simple comparison is just enough at this point. Of course, the Lagrangian kernel can be used, then no tensile instability occurs. Usually it is a good practice to compare both the Eulerian and Lagrangian kernel, however.

When working with pure SPH models, it is important to understand that the kernel is spatial and acts in all directions. In other words, when the reinforcement is as defined in Fig. 6.1, the behaviour of the FEM and SPH models might be identical in the longitudinal

direction, yet could be quite different in the transverse direction (perpendicular to the axial axis of the reinforcement in the plane of the reinforcement). The reason for this is that support domains of each rebar overlap, therefore, a connection is assumed not only in the longitudinal direction but also in the transverse direction. In contrast, FEM beam elements would act independently in the transverse direction, see Fig. 6.4. In flexural tests, however, the longitudinal deformation dominates, therefore, both models are comparable. Furthermore, the 'overlap' can be reduced with the anisotropic kernels.

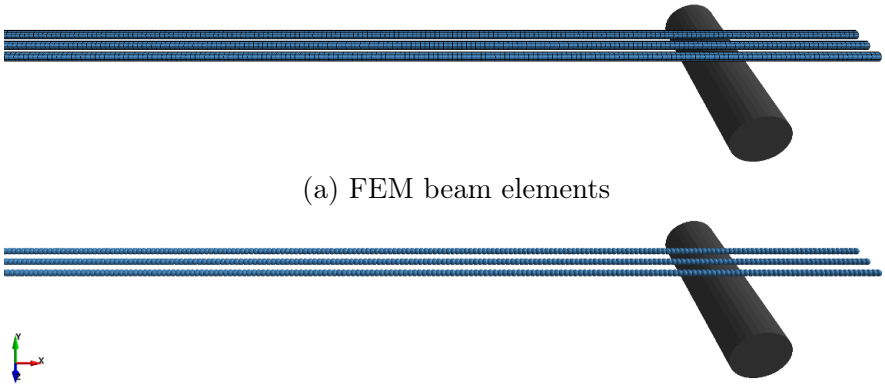

(a) FEM beam elements

(b) SPH particles

Fig. 6.4. FEM and SPH reinforcement comparison.

In Fig. 6.5, the comparison of the load-displacement diagrams of the FEM and pure SPH models are shown. Note that the abbreviations ER and LR stand for the isotropic Eulerian kernel with the renormalization and the total Lagrangian kernel with the renormalization, respectively. From the results it seems that the force responses of the plain concrete are captured quite well in both models. The reinforced models show again a good correlation with the FEM model, yet the LR model shows a rather stiffer behaviour which leads to a higher peak force. Overall, all three models are comparable.

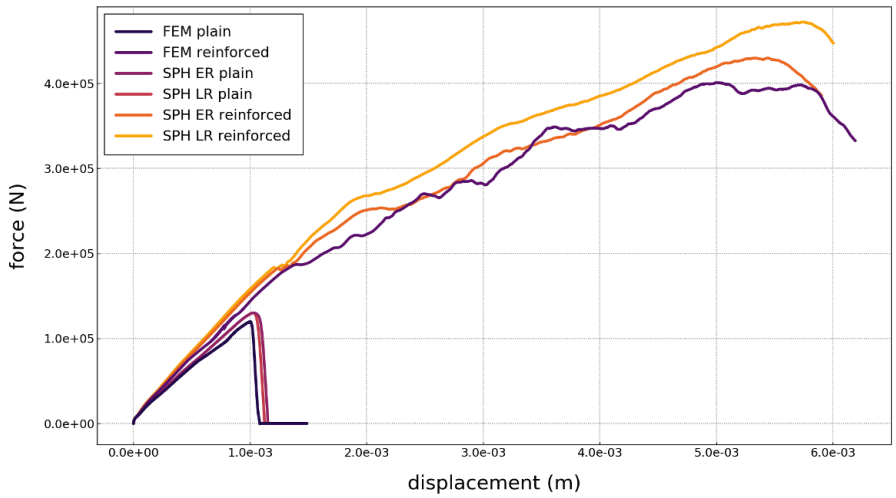

Fig. 6.5. Force-displacement diagrams comparison of the plain and reinforced I-girder SPH models.

Looking at the force-displacement diagrams in detail, the ER model shows no tensile instability. One explanation could be, that the ductile failure of the reinforcement takes place before numerical cracks start to form. For that reason, the peak force is reached prior the numerical instability. The crack pattern of the ER and LR models are again comparable with the one seen in the FEM model. In case of the plain concrete, only one major crack is formed in the middle of the I-girder as shown in Fig. 6.6.

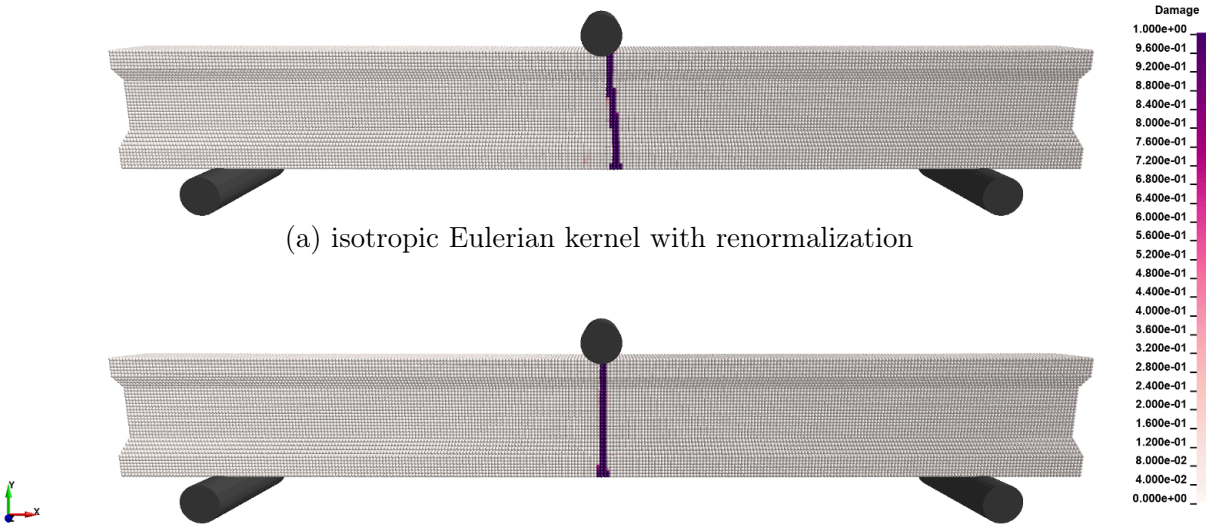

(a) isotropic Eulerian kernel with renormalization

(b) total Lagrangian kernel with renormalization

Fig. 6.6. Damage comparison of the plain I-girder SPH models.

Both reinforced SPH models show again a very similar crack pattern to the one from the FEM solution as shown in Fig. 6.7. Even more important, the ER and LR solutions are almost identical, which further supports the fact that the tensile instability was not amplified in this particular case.

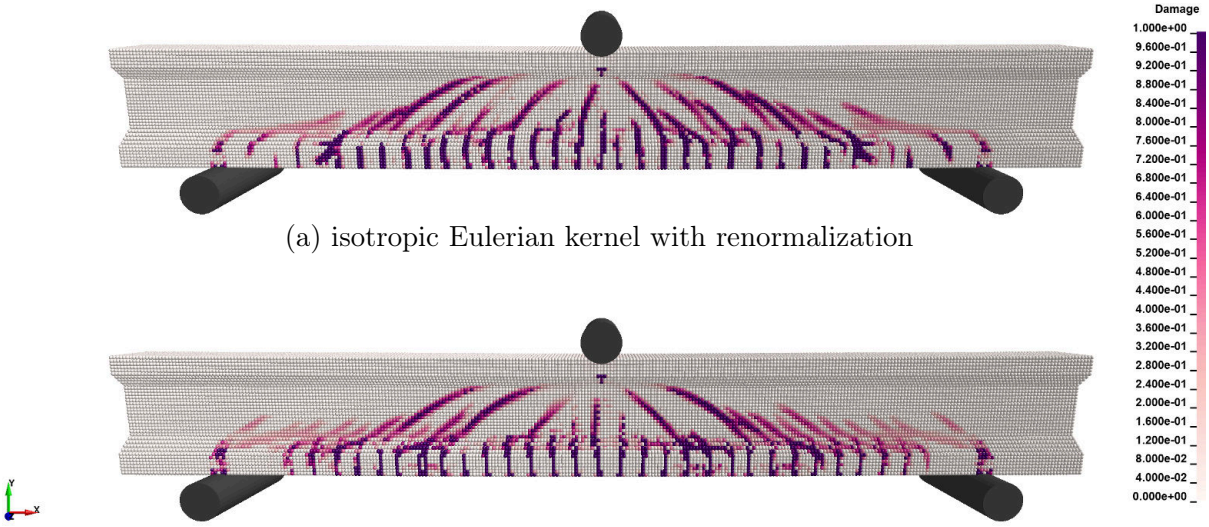

(a) isotropic Eulerian kernel with renormalization

(b) total Lagrangian kernel with renormalization

Fig. 6.7. Damage comparison of the reinforced I-girder SPH models.

6.3 Sublayer Coupling with FEM

As outlined, using pure SPH models with the total Lagrangian kernel might not be always optimal. When a high velocity impact (HVI) is being simulated, the behaviour of models with the total Lagrangian kernel is rather 'stiffer'. The reason for that is similar to the one in FEM simulations, already discussed in section *Experiment – Concrete Spalling*. In FEM, highly distorted yet not eroded elements might exhibit geometrical stiffening. Analogy in SPH can be found when the total Lagrangian kernel is used. When particles separate (move from each other), normally their support domains would stop overlap and the particles would no longer be in interaction. In case of the total Lagrangian kernel, this is not possible, the neighbouring list is simply not updated. Therefore, particles interact even when the model is excessively distorted. This leads to an increase in stiffness of the model. The second thing is, as already mentioned, the kernel acts in all directions. This can be a problem when a complex reinforcement is modelled. Reinforcing elements should act only in the longitudinal direction of each rebar or stirrup. When isotropic kernels are used, it is not always possible to satisfy this condition. Using anisotropic kernels can improve the logic, yet it is very time-consuming to define the kernel's orientation for each rebar.

As discussed in **Chapter 4** *Coupling SPH and FEM*, the best from both worlds can be taken. Instead of using SPH to enhance FEM, FEM can be used to enhance SPH. In other words, beam elements can be used in SPH as the reinforcement. The question is, how to couple them together. Using a contact for the beam to particle interaction is possible, yet rather unreliable – forces are usually not fully transferred which leads to a slip or de-bonding between the concrete and reinforcement.

The idea of the oldest coupling approach based on shared nodes might be taken and further improved. The author proposes the following approach as *sublayer coupling*. When two separate FEM parts are being coupled with shared nodes, the nodes of both parts must have identical locations. In SPH it is not necessary due to the adaptive nature of SPH. In other words, the particles representing the concrete can be arbitrary distributed and the beam elements can be freely placed within the particles. To create a connection between them, every FEM node must become also an SPH particle. Then the connection is done naturally since support domains of the concrete and steel particles overlap. The artificially generated SPH particles represent the *sublayer* for the coupling.

There are three important aspects which must be considered, however. As discussed in section *Time Integration*, in explicit schemes every node and particle must have a certain mass – it is numerically necessary. And clearly from (2.13.9), smaller the mass, smaller the time step. Therefore, not only that every node and particle must have assigned mass, but the mass itself must be reasonable enough to have a reasonable time step. For that reason, when SPH particles are generated from the FEM nodes, it is not possible to say that the nodes are massless from now on. Yet it is possible to say that the FEM nodes have 50% of the initial mass and the SPH particles the rest, which is again 50% of the initial mass. A model build in such a way has the same inertial properties as the pure FEM or SPH model.

The second aspect is again related to the mass, yet indirectly in FEM but directly in SPH. Assuming that both parts of the reinforcement have assigned independent material model, the ratio of masses can be controlled with density of each part. When the density is decreased for FEM elements it does not influence their cross-section, however. But since the axial stiffness is a product of the Young's modulus and the cross-section area of the reinforcement, the change must be introduced into the SPH part of the reinforcement. In other words, if the axial stiffness of the FEM beam elements remains unchanged, the axial stiffness of the SPH reinforcement should be zero. Obviously, when SPH particles have no stiffness, there are no inner forces. But since the inner forces are an outcome of the FEM beam elements, the stiffness of the reinforcement is still captured even when SPH particles have no stiffness, see also Fig. 2.53. In the following comparison, the FEM stiffness was kept and the SPH stiffness was reduced to numerical zero. Note that the infinitesimal stiffness in explicit schemes is not a problem since it results in an increased time step. This is in contrast to the infinitesimal mass.

The third aspect is related to what was discussed in section *Conservation Laws*. The mass and density of SPH particles are directly used in the continuity and momentum equation. Which means, that the coupling force is proportional to the mass of interacting SPH particles. In homogenous isotropic material, all particles have the same mass and density, therefore, forces in interactions are comparable in magnitude. However, if mass of a particle is only 0.001% of the neighbouring particle mass, it might be that particles stream through each other. That said, a study on the mass ratio should be always performed when the coupled SPH-FEM reinforcement is used.

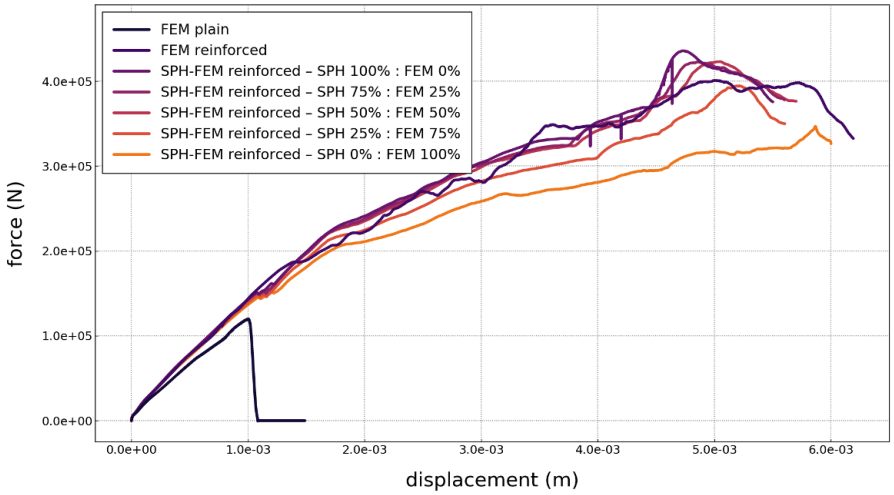

Fig. 6.8. Force-displacement diagrams comparison of the reinforced I-girder SPH-FEM models.

The comparison of the reinforced SPH models with FEM beam elements in which the ratio of masses was a variable follows. Note that the isotropic Eulerian kernel with the renormalization was used for the SPH part of the model. For testing purposes, two extreme cases were also simulated. Those are the models with either 0.001% mass of FEM nodes or SPH particles, which means the counterpart has 100% of the reinforcement mass. The time step of the extreme models was unbearably small, therefore, the models would not be applicable in practice.

In Fig. 6.8, the force-displacement diagrams are compared. Overall, the responses of all models are within the range of acceptable difference. The initial stiffness of all the models is more or less identical to the one from the pure FEM solution, the peak forces and softening show again the expected trend. As previously mentioned, with decreasing mass of SPH particles used in the reinforcement sublayer, it is expected that coupling forces might exhibit a slip or de-bonding between the concrete and steel. As shown in Fig. 6.8, it is indeed true. The model in which the SPH particles have the mass of the numerical zero shows reduced stiffness. In contrast, the model with the SPH particles with 100% of the reinforcement mass shows a rather stiffer behaviour, therefore, the peak force is slightly increased.

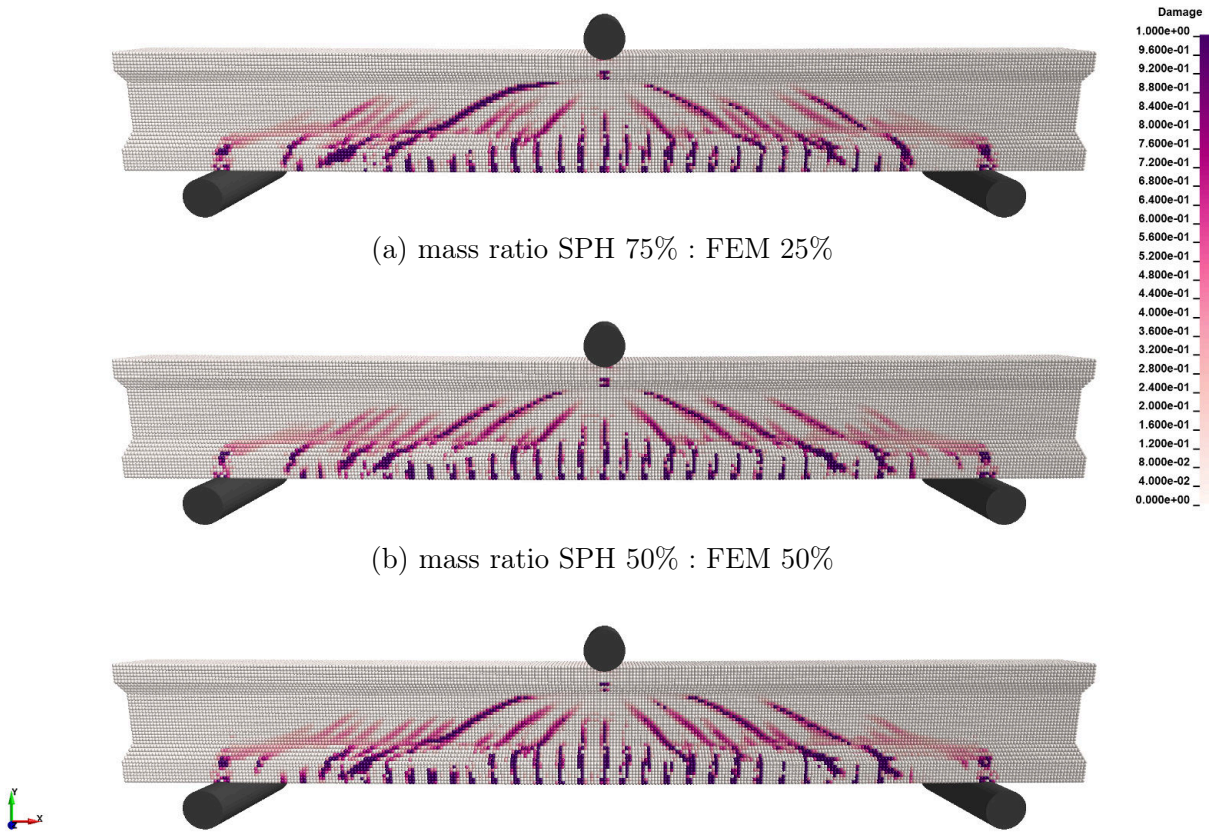

(a) mass ratio SPH 75% : FEM 25%

(b) mass ratio SPH 50% : FEM 50%

(c) mass ratio SPH 25% : FEM 75%

Fig. 6.9. Damage comparison of the reinforced I-girder SPH-FEM models.

The crack patterns of all models show comparable results with the pure FEM and pure SPH solutions, yet it seems the cracks in the pure FEM model have overall steeper angle. The tensile instability was not observed, all models were stable in solution. In Fig. 6.9 three coupled models are compared in which the SPH-FEM mass distribution varied between 25 and 75%. Those models would be recommended in practice, the results are more or less identical. Without seeing their force-displacement diagrams, it would be unlikely to tell the difference.

The findings that the coupled models with the sublayer approach are free of the tensile instability and are able to capture the behaviour of the reinforced I-girder are very important. Yet, only a verification with FEM models was performed. In **Chapter 8**

Experiment – High Velocity Impact and **Chapter 9** *Experiment – Explosion* validations on real experiments are discussed.

6.4 The Best of Both Worlds

When it comes to recommendations, it always depends on the application. If there is no need for a pure SPH model, the general recommendation would be to use SPH with the isotropic Eulerian kernel together with the coupled FEM reinforcement. As shown in Fig. 6.10, when the SPH model with the FEM reinforcement is used, equal mass distribution is a good first estimate. If de-bonding of the reinforcement is observed, increased mass of the SPH reinforcement particles improves the no-slip condition.

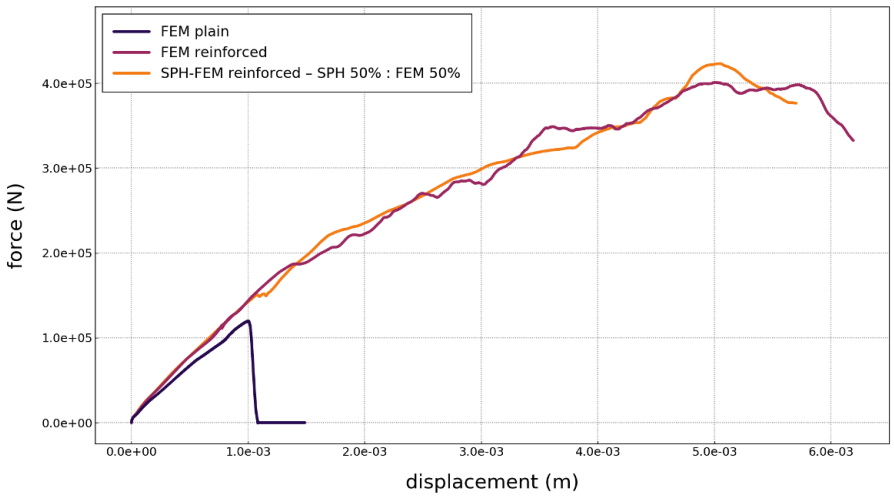

Fig. 6.10. Force-displacement diagrams comparison of selected models.

However, if a pure SPH model is needed, the first choice should be the total Lagrangian kernel in range of quasi-static and moderate speed deformations, and the isotropic or perhaps anisotropic Eulerian kernel for high speed deformations, e.g. HVI and other applications in which fragmentations might be expected. The reason for using the Eulerian kernel in some cases only was already outlined, i.e. when a material undergoes deformation fast enough, it behaves like a fluid. In most cases, the fluid-like behaviour is not controlled by constitutive laws but rather by momentum of the system. Due to that, even if the model is burdened with the tensile instability it should have no significant impact on the results. Yet the tensile instability should be expected as shown in section *Particle Interaction* and section *Tensile Instability Trade-off*.

Chapter 7

Heterogeneity in Numerical Models

In real life, in experiments, nothing is entirely perfect. Concrete specimens are not always straight, sometimes even pre-cracked, boundary conditions are never symmetric even when intended. This is the reason why experimental measurements exhibit differences. With every specimen, with every measurement, there is a deviation. Crack patterns are not always the same, peak forces very often vary, initial stiffness might be influenced by the testing device itself. As a result, statistics is always in the game, giving a window of variations. However, in simulations, everything can be 'perfect'. There is no deviation in geometry, material parameters are as defined, and when the model is symmetric, well, it is symmetric. But what if some variations should be in the model, what if the simulation results should exhibit a certain degree of randomness? In this chapter, the so-called *numerical heterogeneity* is discussed. The concept is based on utilization of coherent noise functions directly implemented into the model generation process. As a result, every generated Smoothed Particle Hydrodynamics (SPH) model has a variation in material properties which leads controlled randomness in results.

7.1 Randomness – Much Ado About Nothing?

When it comes to randomness, there are many ways to implement it into numerical models. For example, material strength can vary in the problem domain which results in a random failure. The question is, however, how to pass the information with the modified strength to SPH particles. The implementation can be done on the material model level. That would mean to create a function within the material model code directly. Yet, many material models are encrypted and locked to users, therefore, this is very often not possible. There is a simpler way. Since SPH particles are Lagrangian elements which carry (among the others) mass, density, therefore volume, the randomness implementation can be done directly here. As discussed in **Chapter 6** *Reinforced Concrete*, when particles have identical properties and have a uniform distribution, the behaviour of such SPH model is *homogeneous and isotropic*. When this is not true and some particles have rather different properties, e.g. much higher density, the behaviour of the same model is *heterogeneous and anisotropic*. Yet, if parameters in the model differ and it is not an outcome of a material model, the heterogeneity is just numerical, hence *numerical heterogeneity*.

To be more specific, an example of a numerical heterogeneity implementation into SPH models while using concrete is discussed next. Concrete is a composite material; composed of binders, fillers, water, additives, and admixtures. All the named have an influence on how concrete behaves under stress conditions. When it comes to the numerical modelling of concrete, a detail level should be chosen with respect to the simulated physical phenomena. In practice, four different levels are distinguished:

- macrolevel,
- mesolevel,
- microlevel,
- nanolevel.

So far the level detail was macrolevel, i.e. concrete was treated as a homogeneous continuum. For the heterogeneity implementation, however, the mesolevel must be used instead. On the mesolevel, concrete is understood as a composite consisting of aggregate, mortar-matrix, and the interfacial transition zone (ITZ) [222]. The microlevel and nanolevel can be used with SPH too, however, for problems simulated in structural dynamics it would be quite impractical. More about different modelling levels can be found in [222, 223].

In the SPH formulation discussed in the thesis, it was never strictly said that a particle represents a grain of aggregate but rather a lumped volume of continuum, which could, as a matter of fact, have the size of a grain of aggregate or a representative volume of concrete. That said, the simplest idea of the numerical heterogeneity implementation would be the one shown in Fig. 7.1, using the regions of aggregate and mortar-matrix.

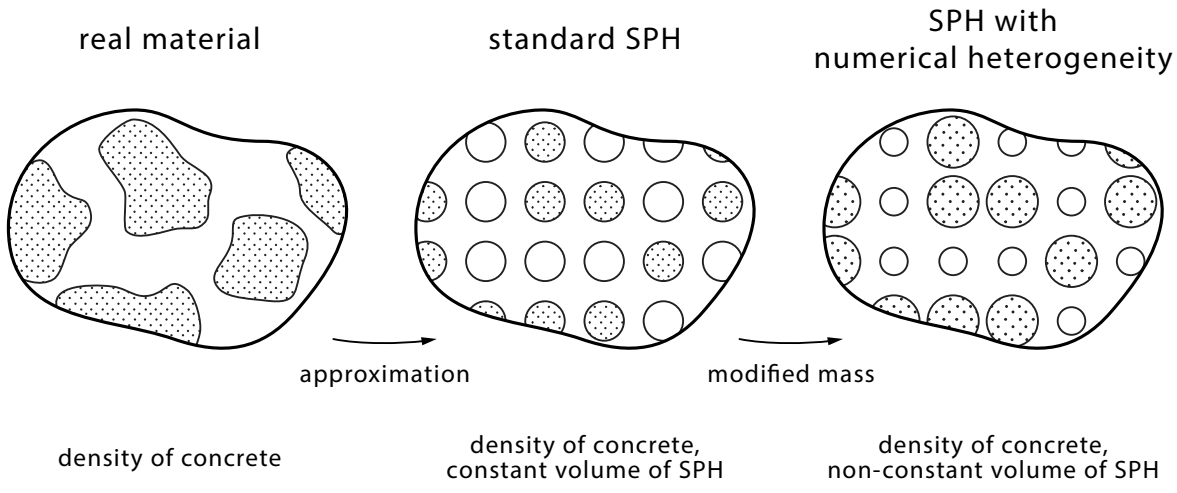

Fig. 7.1. Numerical heterogeneity implementation.

In the first step in Fig. 7.1, the concrete domain is approximated with SPH particles. Conveniently, the particle distribution is uniform, i.e. all particles possess the same volume. Preferably, only one material model is used. As a result, all particles have the same density, therefore, the same mass. In the second step, the particles are divided into two groups

based on the region they are in. Properties of the particles are then adjusted based on the assigned region, e.g. their density should be the density of the aggregate if they are within its region. However, in standard numerical models all particles usually have the same density, the one defined in the material model. Therefore, the particles representing the aggregate would have an increased mass rather than the density, and the particles representing the mortar-matrix would have a decreased mass. Naturally, this has a direct impact on the lumped volume as shown in Fig. 7.1.

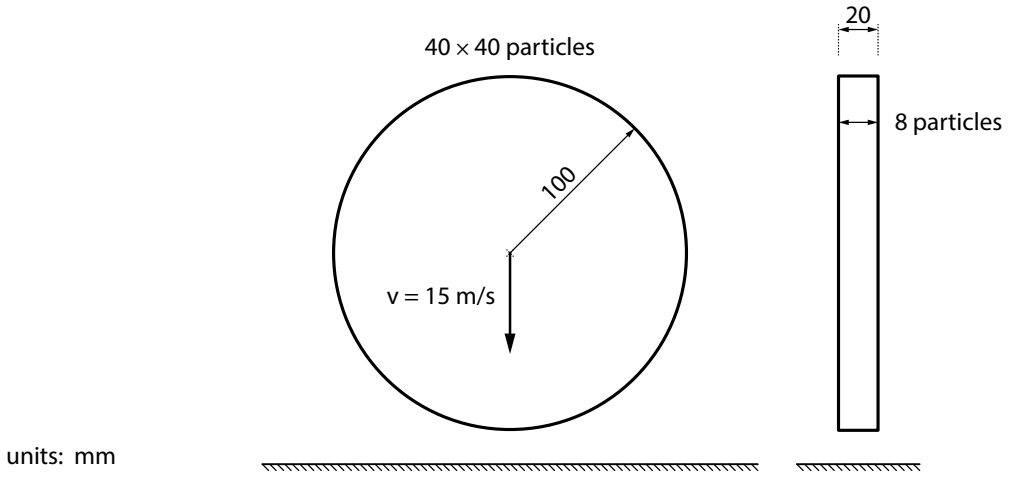

Fig. 7.2. Impact test example with implemented numerical heterogeneity.

The question is, how random results can be obtained with this approach and if it can represent reality. A simple example can be discussed as shown in Fig. 7.2 in which a concrete disk with initial velocity of 15 m/s impacts a rigid surface. The disk was simulated with SPH, the rigid surface was defined as an analytical entity. The only employed material was the Continuous Surface Cap Model (CSCM) with density of 2400 kg/m^3 and the unconfined or uniaxial compressive strength (UCS) of 43 MPa. The parameters were chosen so the disk breaks after the impact, yet they are not important at this point. The only important thing is that the CSCM parameters were the same for all particles.

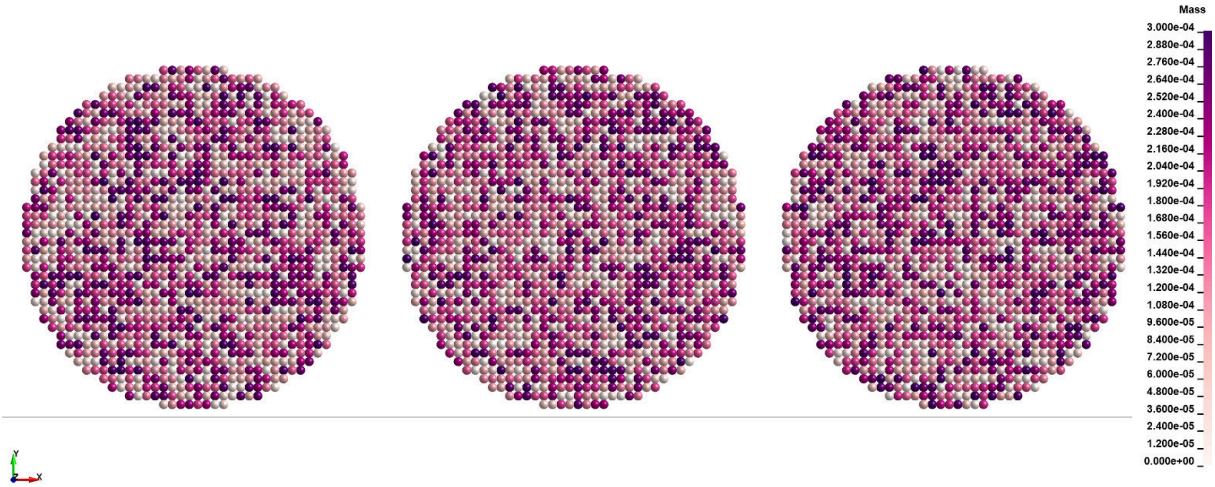

Fig. 7.3. Initial mass distribution comparison.

To test the randomness of the model, three random fields of masses were generated. Although the material model of a concrete was used, SPH particles had no information where the regions of aggregate and mortar-matrix are, therefore, their masses were randomly distributed as shown in Fig. 7.3. Since the SPH masses varied between 0 and 0.3 g and no control of the distribution was enforced, it is clear that the behaviour of each model might be random, yet uncontrolled. Importantly, the total mass of each disk was the same.

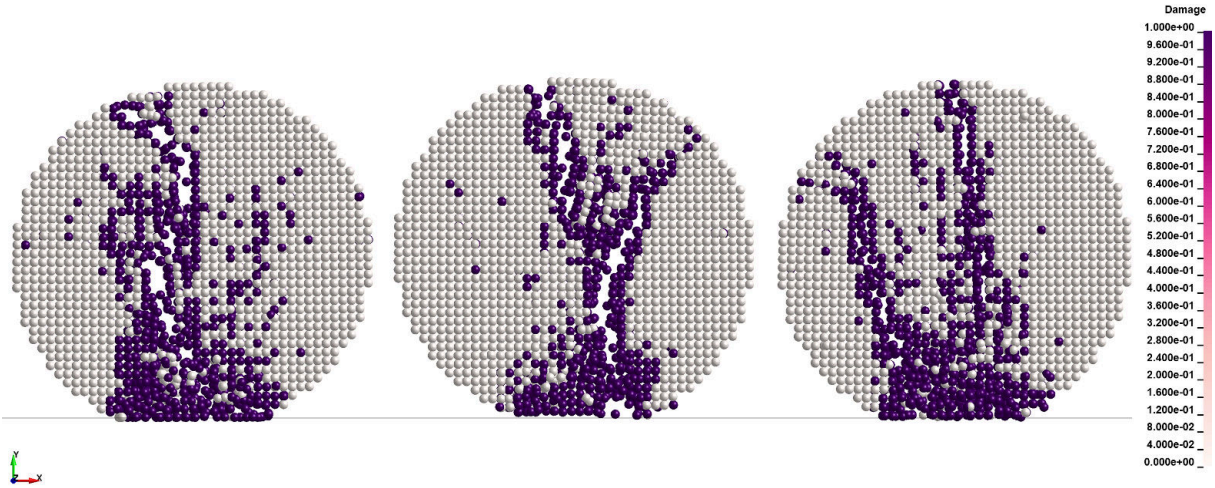

Fig. 7.4. Damage comparison after the impact.

The results after the impact are shown in Fig. 7.4. The behaviour is indeed random, each generated model has a unique crack pattern, failure mode. However, in practice, such a solution is unacceptable. When a random field is generated as a 'random', i.e. with no control of the randomness, the concrete behaves far more brittle. The SPH particles with very low masses represent a porous medium. In contrast, the particles with increased masses represent a skeleton. Clearly, the porous particles behave as a pre-cracked or pre-damaged material which might negatively influence the integrity of the structure. This was tested and proved by the author in [224] and further elaborated in [225] in which the effect of the support domain size was examined. The presented approach of the numerical heterogeneity implementation can be used in high velocity impact (HVI) simulations, however. The reason is quite simple. In HVI problems, the driving aspect is momentum, not material strength. Therefore, if inertial properties are represented correctly as shown in each model in Fig. 7.3, the approach might be used. This was proved by the author in [226]. For a general use, however, the approach for the numerical heterogeneity implementation must be improved.

7.2 Coherent Noise Function

The generated mass distributions in Fig. 7.3 were again too 'perfect'. However, perfect from the opposite end; they were too random with no control. Even in real material, not the numerical, random spatial fields can be observed where material properties differ. For example, in concrete during the imperfect process of formation and solidification, aggregate can be distributed better in certain fields, regions. Obviously, such fields with

higher aggregate concentration behave differently from those where the space is mostly filled with mortar-matrix.

There are many ways to create random fields where material properties would differ. Usually, those would be created with mathematical functions, e.g. spatially combined periodic functions. The majority of periodic functions are too perfect, however. The author's opinion is that there is a better way, there are better functions for exactly this purpose, yet very often overlooked. The so-called noise functions are far more 'random' and 'elegant' than the standard mathematical functions.

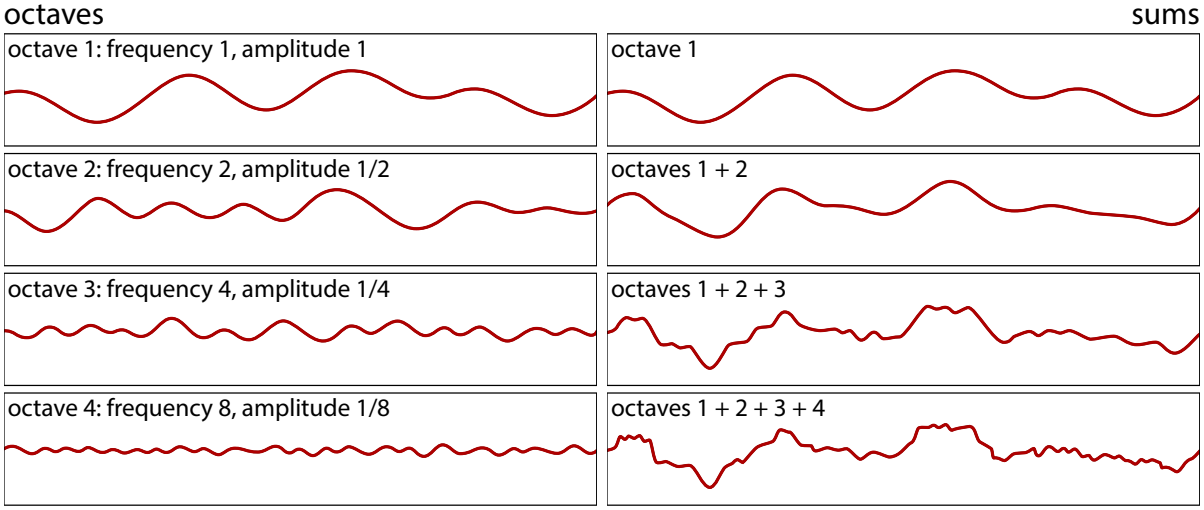

Fig. 7.5. Creation of higher order Perlin noise by summing the octaves of gradient-based coherent noises.

Yet again, there are many noise functions, so which one to choose? To make the decision, it must be known what should be the outcome. As previously mentioned, during the process of concrete creation, random fields might be formed. Yet it is so that the technology is being improved every day, therefore, it is unlikely that fields with a poor quality concrete would be formed on daily bases. Therefore, the outcome should be more or less uniform structure, random but consistent. Furthermore, it must be possible to recreate the structure whenever needed, therefore, it should be a pseudorandom function. The level of detail must be also controllable. It might be that the SPH discretization is finer, therefore, the level of detail must be increased.

The idea is to use coherent noise functions, a type of smooth pseudorandom noise. Coherent noise functions have very useful properties.

- Entering the same input value (seed) will always return the same output value.
- A small change in the input value (seed) will produce a small change in the output value.
- A large change in the input value (seed) will produce a random change in the output value.

A coherent noise function can be arbitrary and combinable in any way with other coherent functions, e.g. the Perlin noise [227]. As shown in Fig. 7.5, one of the options for the creation of a higher order coherent noise is to use the function itself repeatedly – due to its self-similar pattern it can be regarded as a *fractal*. Specifically, it is the Perlin noise; a type of coherent noise that is the sum of several coherent-noise functions of ever-increasing frequencies and ever-decreasing amplitudes. The omission of some octaves can result in the creation of a very different noise [228].

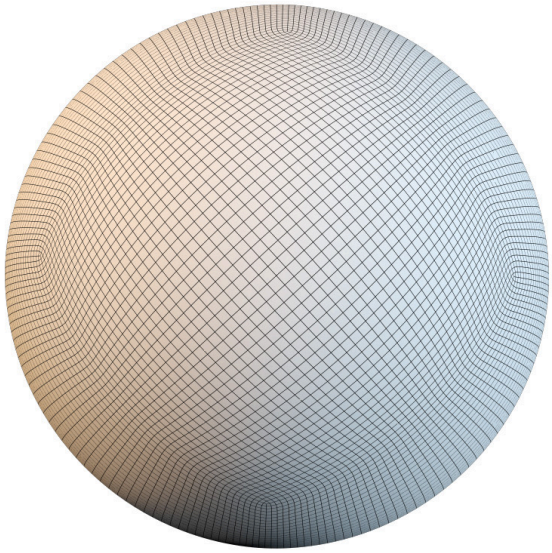

(a) initial geometry

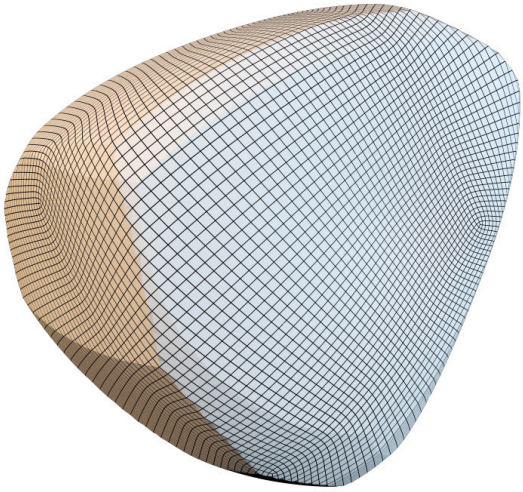

(b) octave 1

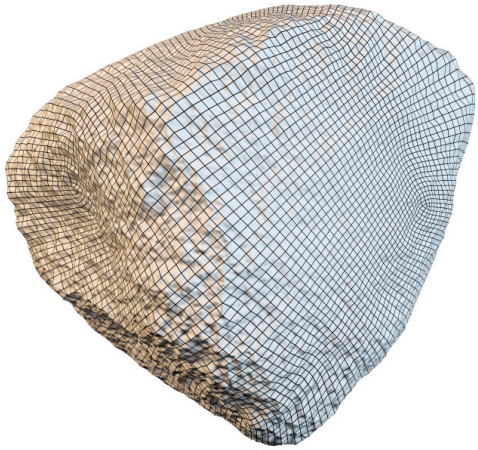

(c) octave 1 to 5

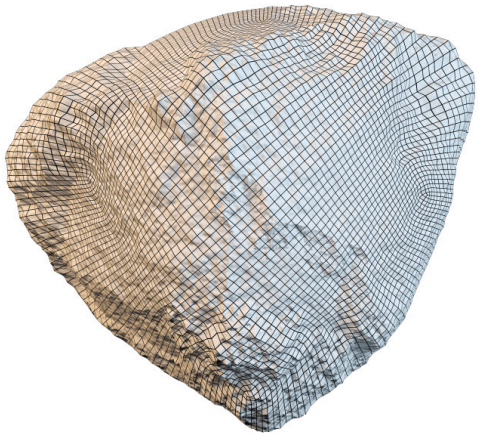

(d) imprint of another function

Fig. 7.6. Stone sculpting with coherent noise functions.

In practice, working with noise functions can be understood as a stone sculpting. At the beginning there is a domain which can be approximated with thousands SPH particles. However, a subdomain can be created with noise functions where SPH particles would have different properties. As shown in Fig. 7.6, a solid sphere can be taken as the initial

geometry. Then a noise function can be applied to it as a sculpting tool. The final domain is just an outcome of the applied noises. The final shape in Fig. 7.6 (d) is far away from a perfect sphere. Ken Perlin's comment on noise is quite fitting:

> *You can think of noise as "seasoning" for graphics. It often helps to add a little noise. A perfect model looks a little less perfect and, therefore, a little more realistic if some subtle noise effects are applied.* [229]

7.3 The Algorithm

The author found that coherent noise functions have the potential to reproduce concrete structure. Therefore, an improvement to the original idea of the numerical heterogeneity implementation is further proposed. In general, noise functions are spatial functions [228, 230], fairly complex to be visualized in 3D, therefore, often represented in 2D as a cut through their space. Such a cut usually shows clouds or gradients of grey tones. Interestingly enough, a photo of a concrete in a cross-section (cut through a specimen) is also a function. It can be understood as a 2D function in which aggregate is represented by value of 1 and mortar-matrix by value of 0. Since noise functions return similar binary responses, there is a good chance that visually comparable patterns can be generated. Put simply, it might be possible to recreate an input photo of a concrete in a cross-section with noise functions.

The outlined is the core idea of the proposed *algorithm for concrete structure generation*. Using an input photo of a concrete in which aggregate and mortar-matrix can be distinguished, followed by an optimization of a selected noise function is the key for the concrete structure recreation. The step-by-step schema of the algorithm is shown in Fig. 7.8. First three steps are done in a sequence, then the optimization of a 2D image starts. Since noise functions can be scaled, generated with different seed values, accumulated, inverted, projected into themselves, the optimization cycle can be fairly complex process, yet automized.

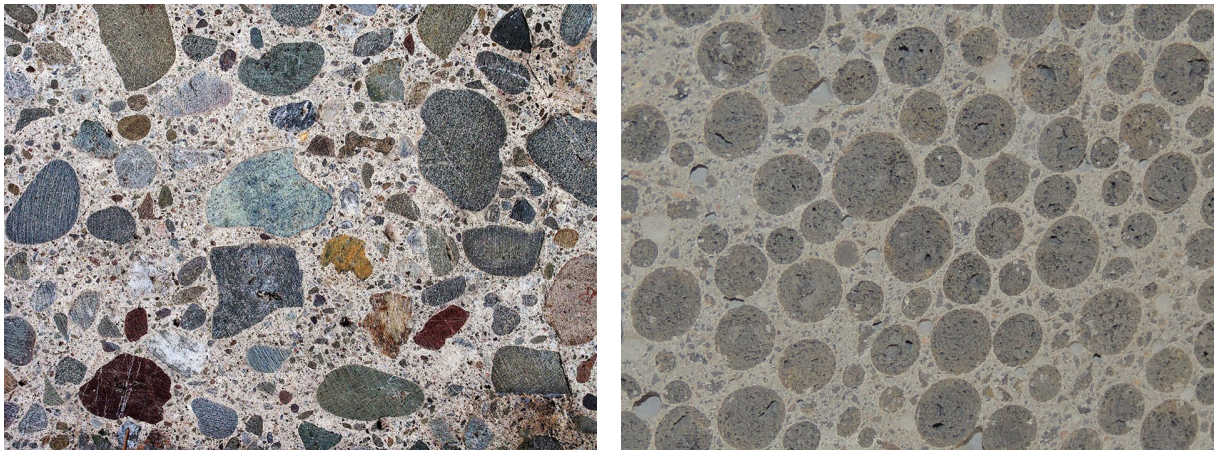

(a) sharp aggregate (b) rounded aggregate

Fig. 7.7. Comparison of two input photos of concrete cross-sections with differently shaped aggregate.

In the following sections, two examples of concrete structure generation are discussed in detail. The input photos are shown in Fig. 7.7. The algorithm is the same for both structure generations, the only difference is the input photo of a concrete which results in employment of different noise functions and their properties.

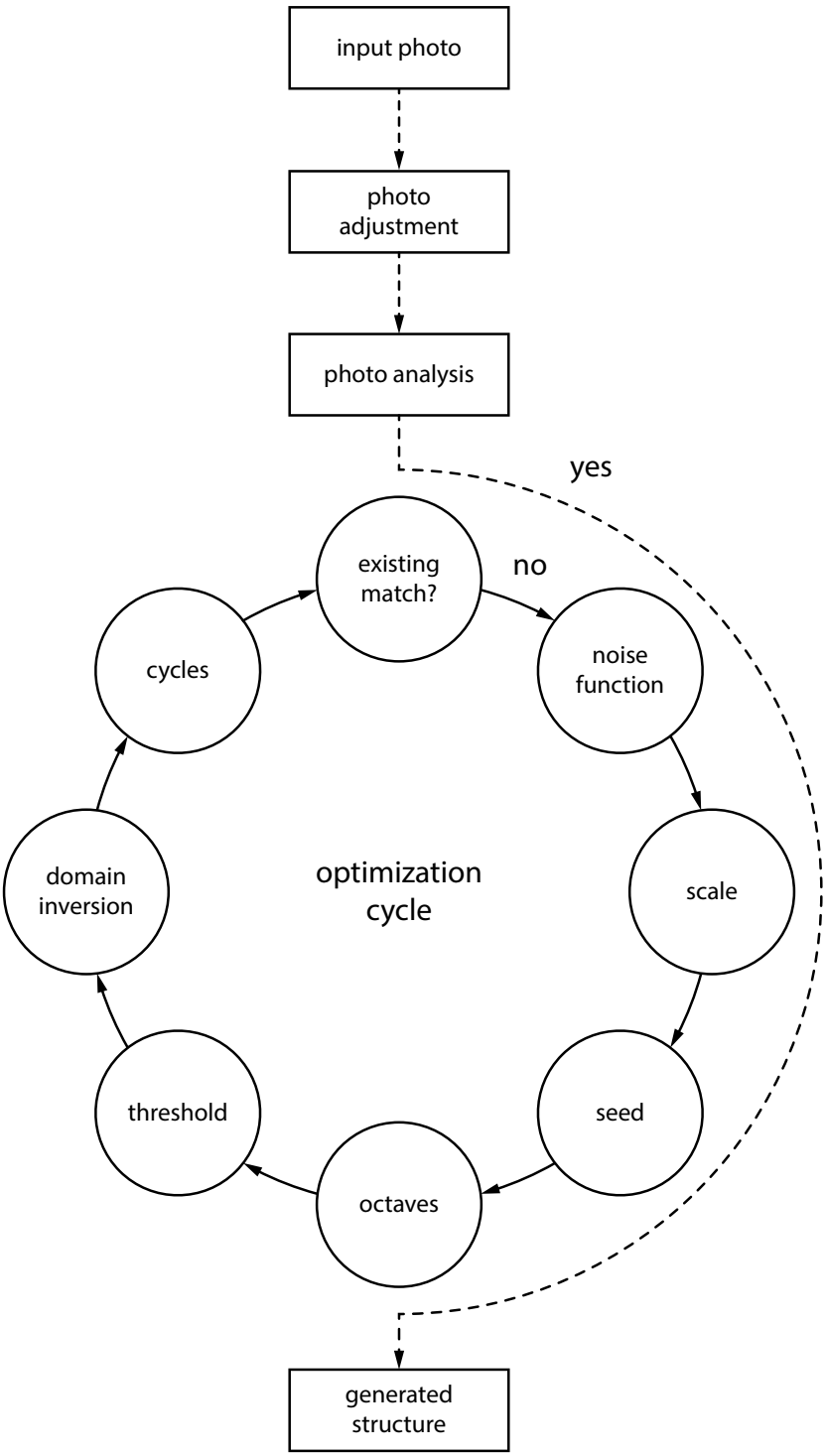

Fig. 7.8. Algorithm for concrete structure generation.

The algorithm was first published by the author in [231] in which its pure form and the SPH application in simulations was tested. The extended version which includes the heterogeneity amplification was proposed in [232]. It was found that the algorithm is stable and can be implemented as a subroutine in the SPH framework.

7.3.1 Input Photo

The idea of having an input photo as a source of information is convenient, yet the extraction of data can be difficult. Since a noise function should recreate domains of aggregate and mortar-matrix, it must be possible to get their distribution, shapes, sizes, and others from the photo. As shown in Fig. 7.9 for sharp aggregate, the process can be following. First, the input photo is read in and its colour spectrum is analysed. In the next step, the histogram of the photo is adjusted in such a way that black regions are clearly distinguishable from the other colours. Since mortar-matrix regions are mostly represented by light-grey tones and aggregate rather by dark-grey tones, the original photo can be converted to black and white. And since colours can be represented by numbers (function), it can be assumed that black has value of 1 and white value of 0.

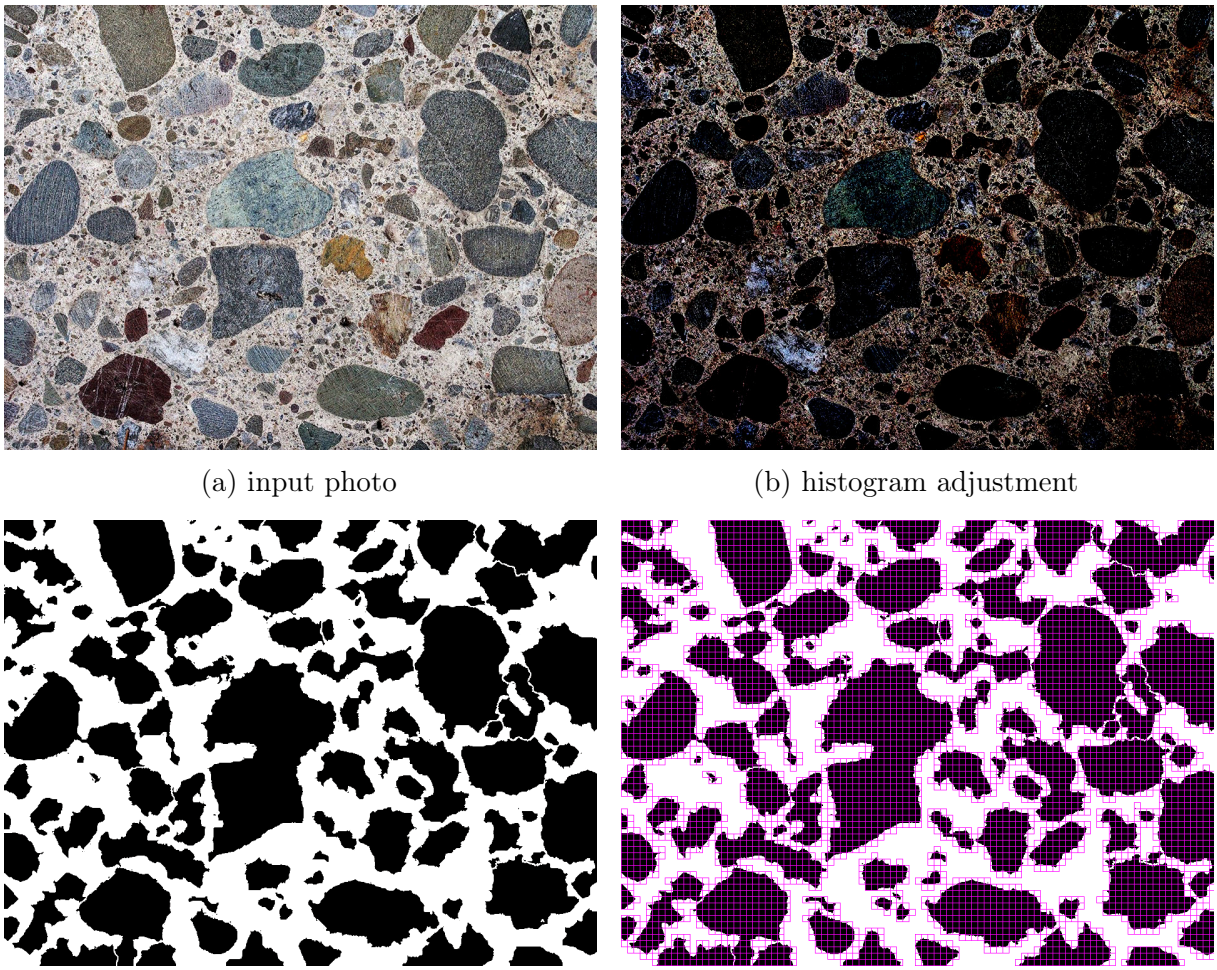

(a) input photo (b) histogram adjustment

(c) BW conversion (d) analysis

Fig. 7.9. Preparation of the input photo with sharp aggregate for concrete structure generation.

When the modified photo is prepared, it can be further analysed. There are some important responses which should be considered. Each grain of aggregate, in black in Fig. 7.9 (c), has a certain shape, size, and level of complexity on its boundary. Furthermore, the overall aggregate filling is yet another important response – lacunarity [233, 234, 235, 236]. All the responses can be extracted and processed with tools used in fractal analyses [237, 238]. Without going into detail, the stored information can be subsequently used in the noise function optimization process as shown in Fig. 7.8. For the concrete with rounded aggregate as shown in Fig. 7.10, the process is the same. First, the colour spectrum is adjusted with the histogram threshold so the aggregate is clearly distinguishable from the mortar-matrix. Following by the conversion to the black and white function. And when the analysis of the input photo is finished, the noise optimization can start.

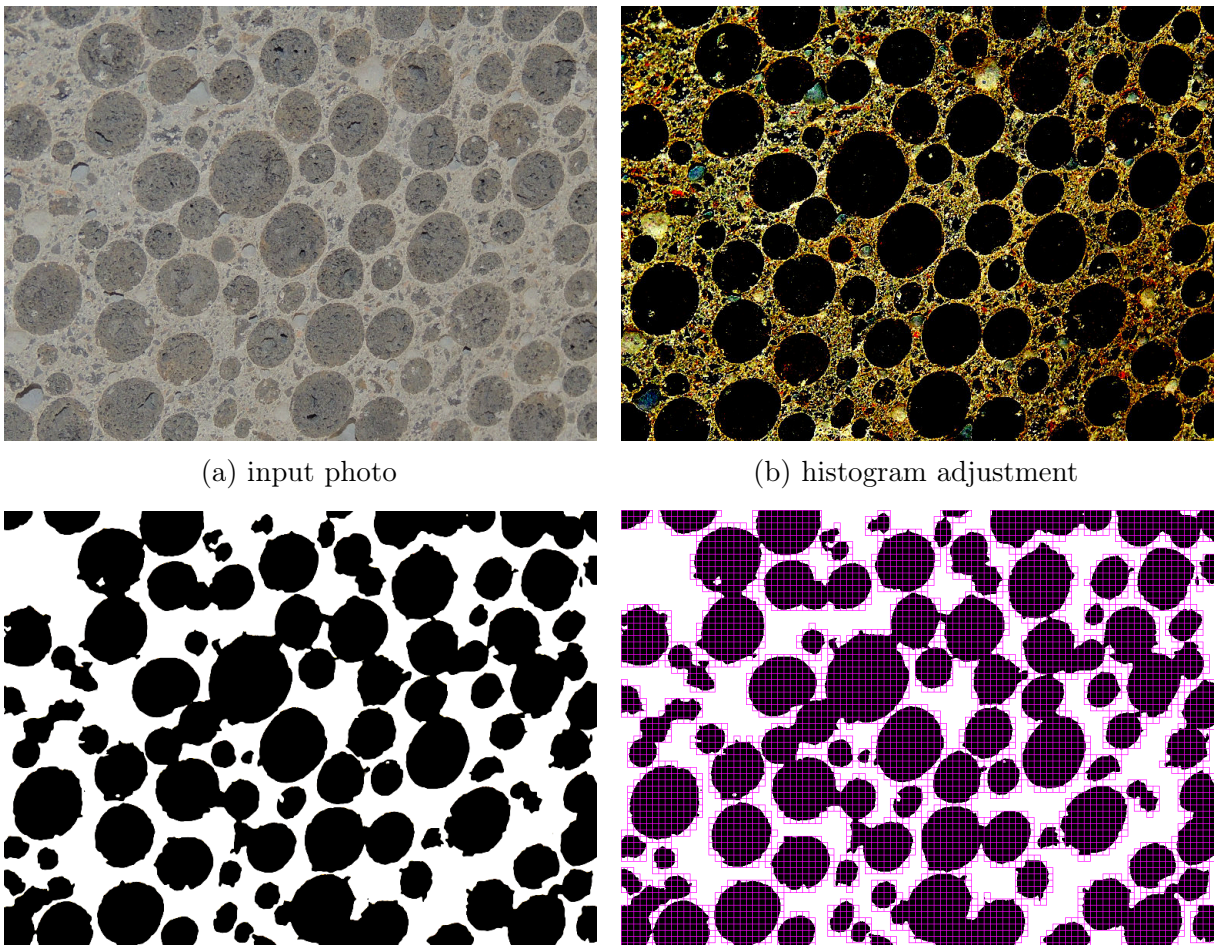

(a) input photo (b) histogram adjustment

(c) BW conversion (d) analysis

Fig. 7.10. Preparation of the input photo with rounded aggregate for concrete structure generation.

7.3.2 Noise Optimization

The noise optimization process follows a certain logic. In the first step, the noise function itself must be selected. In the majority of cases the Perlin noise [227, 228, 230] is a good starting point. If it is not possible to achieve a good match with the input photo, the

algorithm can select another family of functions, e.g. Worley, Simplex, or Cellular noise functions. It is important to understand that during the noise function optimization, the process similar to the input photo analysis as shown in Fig. 7.9 is executed every iteration.

For the sharp aggregate concrete this is shown in Fig. 7.11 (a). The scale optimization is the second step. Since the size of the aggregate is known from the input photo analysis, scaling the noise to have a comparable result is not difficult, see Fig. 7.11 (b). In the next step, the seed value of the pseudorandom noise is adjusted. This results in a modified pattern in the 2D cut, i.e. the shape distribution and overall lacunarity, see Fig. 7.11 (c). Since the noise functions are rather smooth, the number of octaves is important when sharp aggregate is used. As shown in Fig. 7.5, the number of accumulated octaves does not change the overall look of the function but the complexity at the boundary. For this reason, the local lacunarity (per each shape) is stored during the input phase of the algorithm. The number of octaves can be constrained since the level of detail in the subsequent SPH approximation might not be used anyway, see Fig. 7.11 (d).

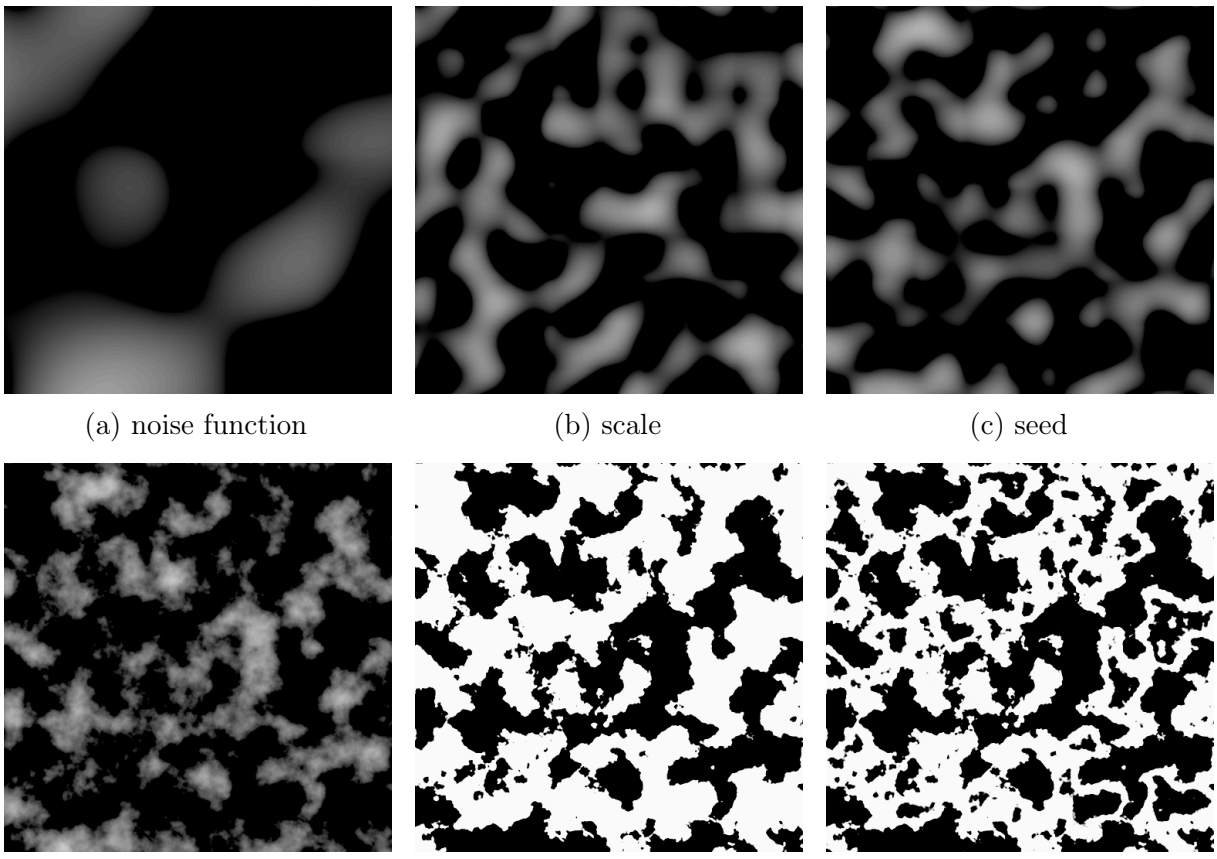

(a) noise function (b) scale (c) seed

(d) octaves (e) threshold + inversion (f) cycles

Fig. 7.11. Noise optimization with sharp aggregate.

At this point, the generated image already shows similarities to the input photo. So far the algorithm was working only with shapes, yet not directly with ‘aggregate’ and ‘mortar-matrix’ regions. In other words, the algorithm still does not know where is the aggregate and where is the mortar-matrix. Therefore, the grey tones of the noise function are again reduced to a subdomain of black and white, and tested for the domain inversion, see Fig. 7.11 (e). If the inverted domain satisfies the overall lacunarity and shape distribution

better, it is taken instead of the original one. The image reconstruction is almost complete. The resulting matrix-mortar domain might be over-estimated in terms of the size. For that reason, the number of cycles might be increased. The cycles, sometimes termed iterations, specify how many times is the noise function projected into itself. With every cycle, a new noise layer is created and blended (multiplied) with the previous one. For that reason, the noise values can only increase. For instance, as shown in Fig. 7.11 (f), the number of cycles was increased, therefore, the aggregate domain occupies more space. After the optimization cycle is finished, the image analysis takes place once again. In the next step, the responses extracted from the input photo are compared to those from the generated image. If the responses are within specified range, the image generation process is finished and the noise function is optimized. If the differences are not within the acceptable range, another optimization cycle follows, perhaps with a different noise function.

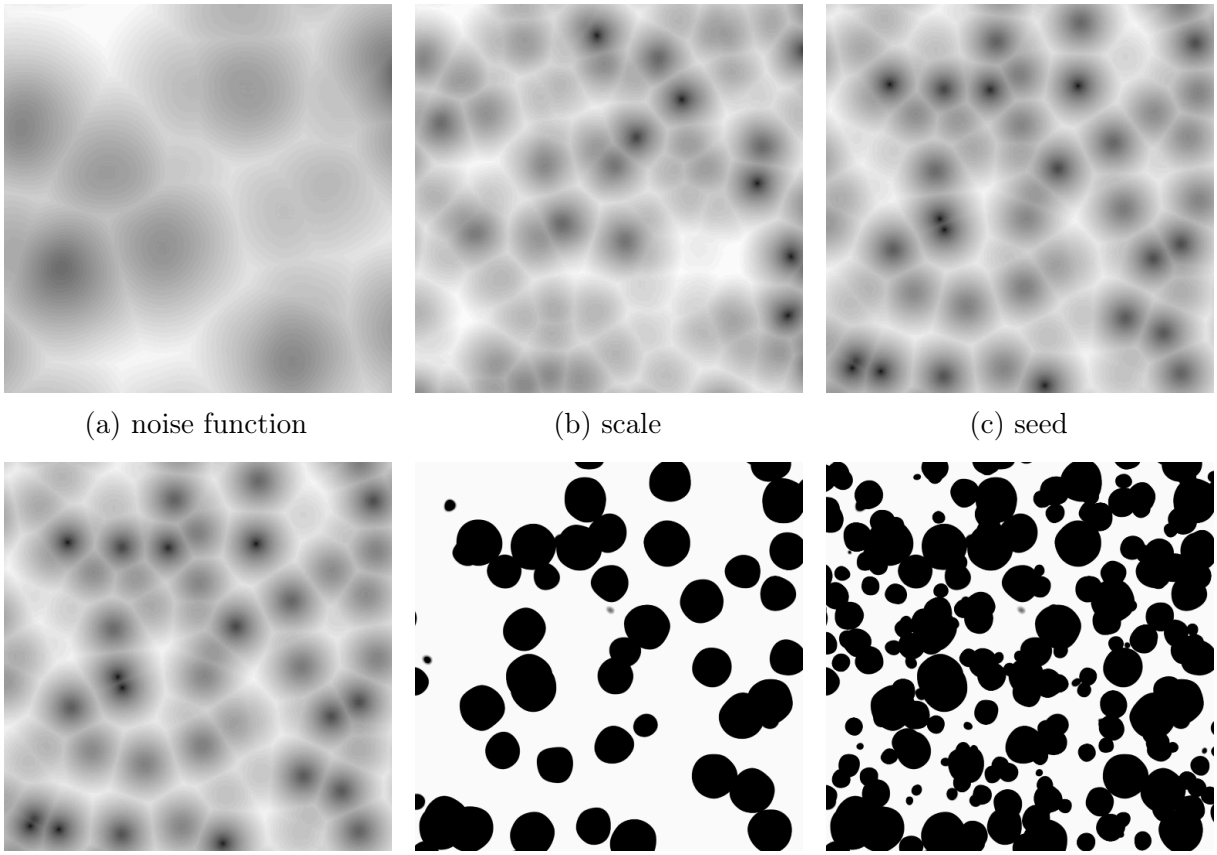

(a) noise function (b) scale (c) seed

(d) octaves (e) threshold + inversion (f) cycles

Fig. 7.12. Noise optimization with rounded aggregate.

The noise function optimization for the rounded aggregate is shown in Fig. 7.12. The process is identical to the previous one with one difference, the Worley noise was used instead. Again, after the appropriate scale and seed are found, the roughness of the aggregate is optimized. Interestingly enough, as shown in Fig. 7.12 (c) and (d) there was no change between the two steps, since the aggregate is rounded and no additional octaves are needed. After the conversion to black and white it was found that no domain inversion is necessary. Due to the overall lacunarity value, however, the number of cycles was increased. The noise optimization resulted in the final form as shown in Fig. 7.12 (f).

7.3.3 Input Photo vs. Generated Image

The outcome of Fig. 7.8 is a generated image of a noise. It is important to keep in mind that there is no mathematical proof that a noise function can reproduce an input photo completely. However, since the generated structure is used as a subdomain for the SPH approximation, differences are acceptable.

In case of the sharp aggregate, when the input photo is compared to the generated image in Fig. 7.13, the subjective understanding is that both are very similar. The domains of aggregate and matrix-mortar are well distributed, the level of detail and roughness of the aggregate is captured quite well. The scale of the noise is comparable, and the number of cycles seems to be right as well. From the detail view in Fig. 7.13 it seems that some similarities in the noise pattern are achieved above expectations.

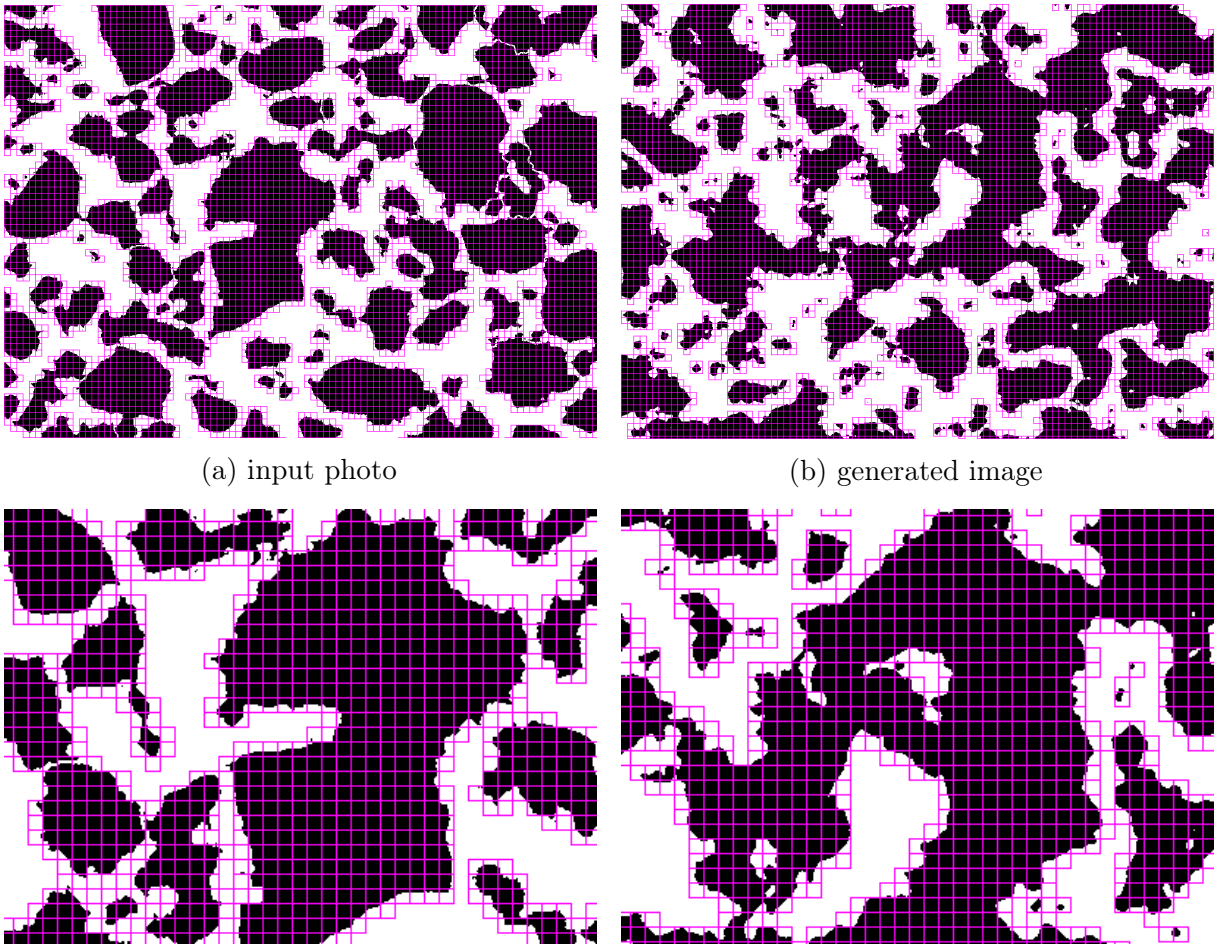

(a) input photo (b) generated image

(c) input photo in detail (d) generated image in detail

Fig. 7.13. Comparison of the photo with sharp aggregate and the generated image.

The outcome of the rounded aggregate optimization is compared with the input photo in Fig. 7.14. Overall, the result is again within an acceptable range. The shape and size of the generated aggregate is similar to the one shown in the input photo, yet is seems that the overall lacunarity could have been improved. The reason why is the generated

domain of the mortar-matrix over-estimated is related to the part of the algorithm in which the number of cycles is being tested. As shown in Fig. 7.12 (f), after the cycles have been increased, the aggregate domain indeed covers more space. Yet instead of forming independent grains of aggregate, merged 'chunks' are formed instead. However, the overall image is acceptable and can be used in SPH simulations.

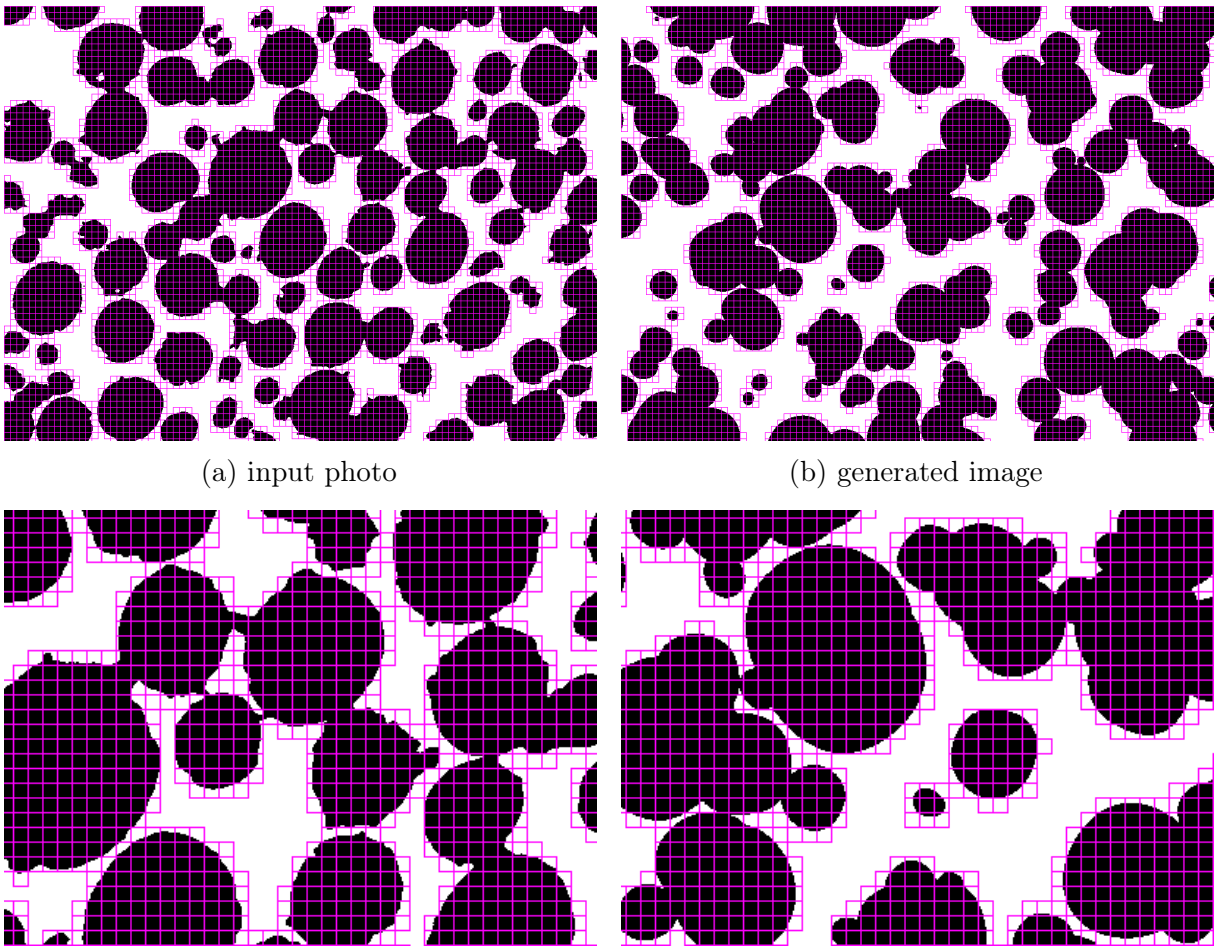

(a) input photo (b) generated image

(c) input photo in detail (d) generated image in detail

Fig. 7.14. Comparison of the photo with rounded aggregate and the generated image.

7.3.4 Generated Structure

The beauty of the process is that the noise functions are spatial, although only 2D slices were optimized. In the background, spatial structures of concrete were generated. Yet it is quite difficult to imagine a spatial structure from a 2D image. Therefore, the same technique as in Fig. 7.6 can be used again. In the first step, an initial geometry (a domain) must be specified to which the sculpting is applied. A very well known specimen from civil engineering can be used; a cylindrical specimen with height of 300 mm and diameter of 150 mm. Since the assumptions of the mesolevel modelling were considered, domains of aggregate, mortar-matrix, and ITZ are shown in Fig. 7.15 and Fig. 7.16 for the sharp and rounded aggregate, respectively.

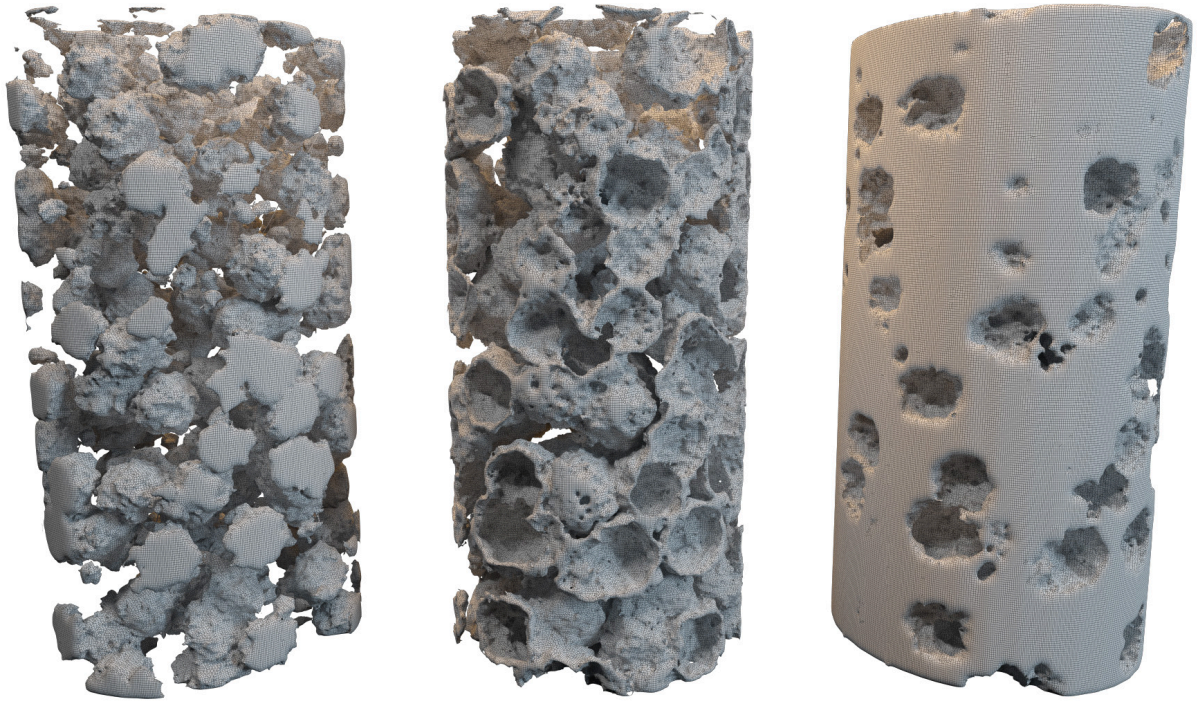

(a) aggregate (b) ITZ (c) mortar-matrix

Fig. 7.15. Generated structure of the concrete with sharp aggregate.

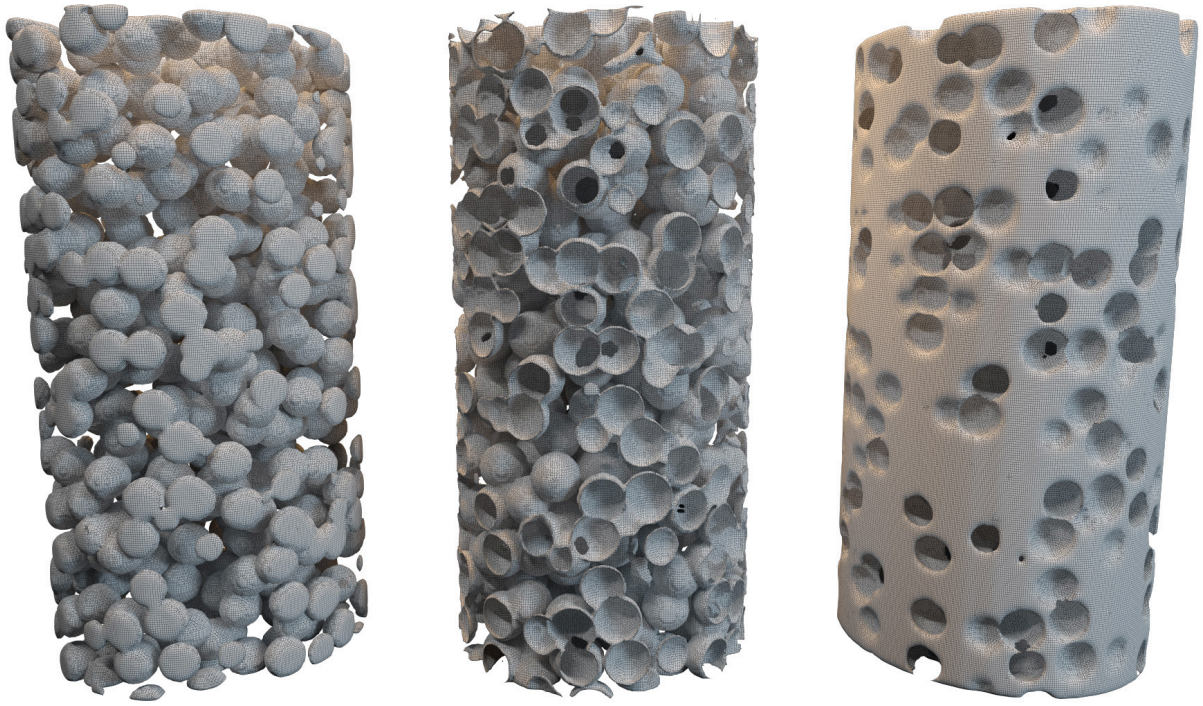

(a) aggregate (b) ITZ (c) mortar-matrix

Fig. 7.16. Generated structure of the concrete with rounded aggregate.

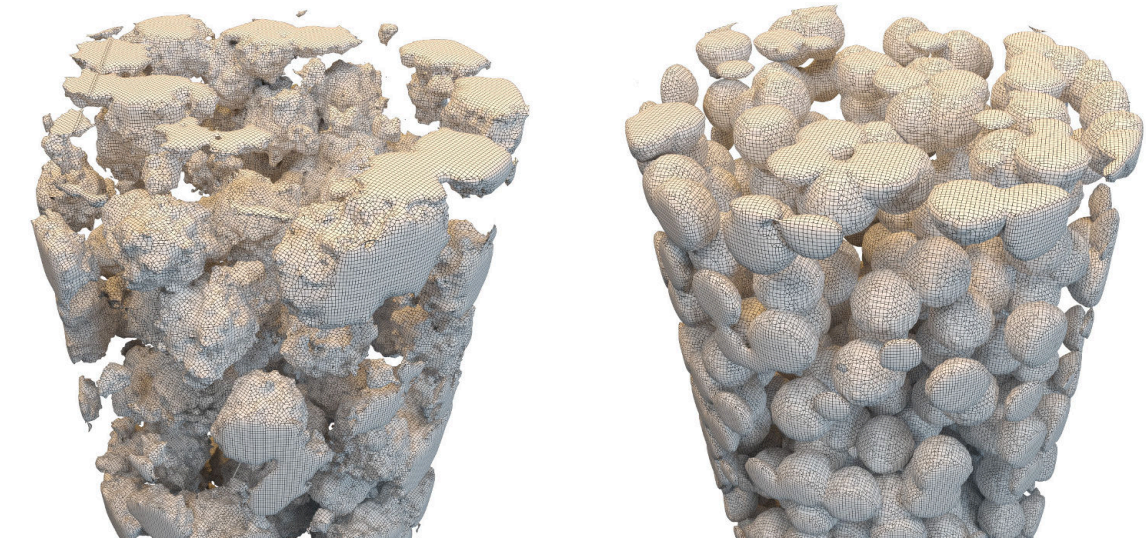

(a) aggregate

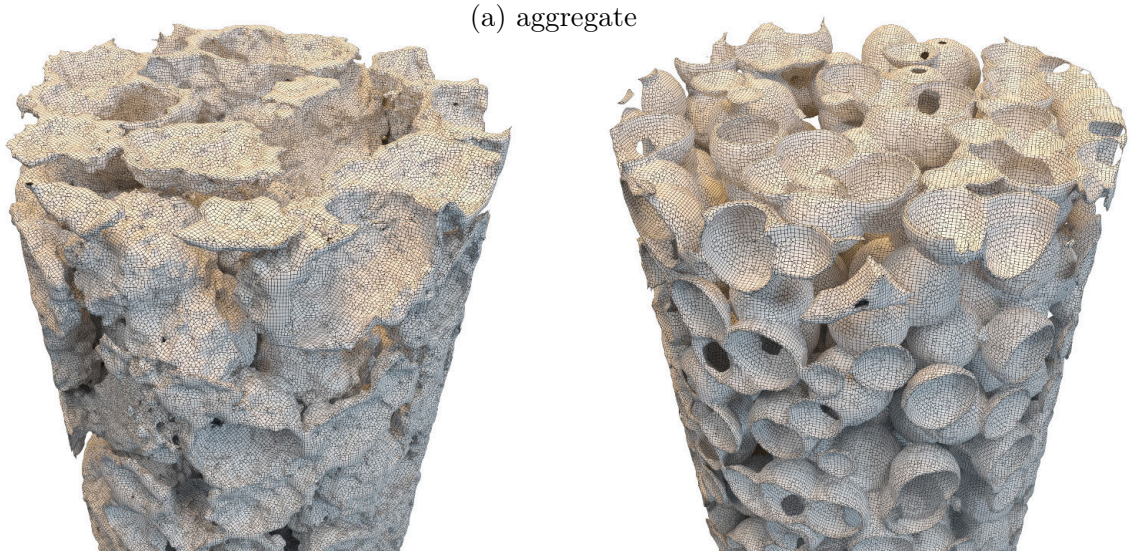

(b) ITZ

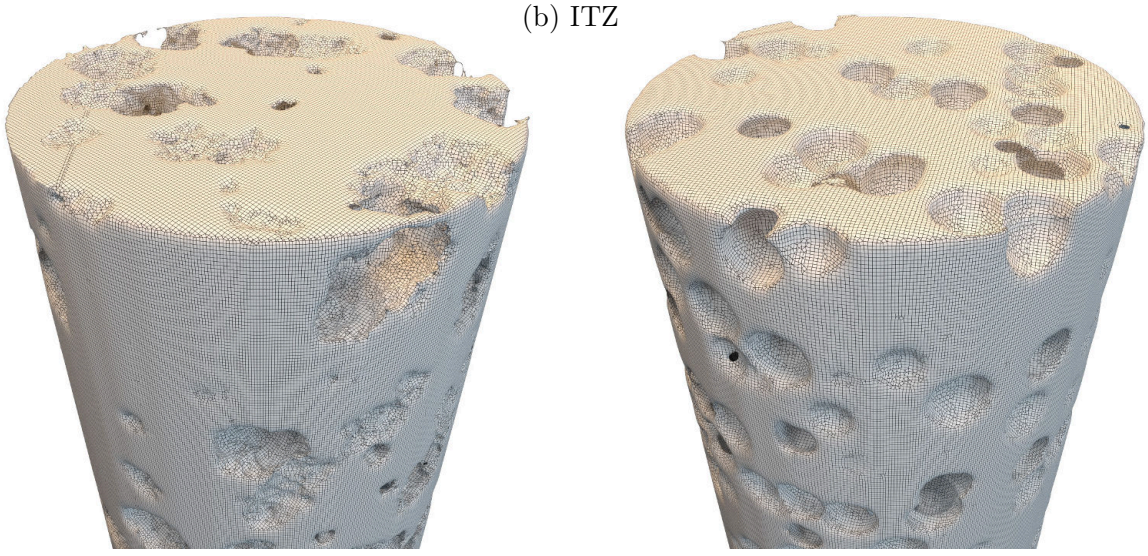

(c) mortar-matrix

Fig. 7.17. Detail of the generated structure of the concrete with sharp aggregate (left) and rounded aggregate (right).

Both generated concrete structures make a very realistic and convincing impression. From the detailed comparison as shown in Fig. 7.17 it is clear that the noise functions are able to represent the complexity of concrete which is 'superior' to standard mathematical functions for generating random fields. Since only the creation of the aggregate and mortar-matrix domains were discussed, the idea behind the creation of the ITZ follows.

In this particular case the ITZ is a 'side' product. As shown in Fig. 7.13 and Fig. 7.14, only black and white domains were created during the optimization process. However, the ITZ corresponds to the boundary between them. Therefore, it is quite simple to create the third domain. Put simply, the domains of the aggregate and mortar-matrix can be offset inside themselves so there is a gap between them. The gap is again a volumetric domain, representing the ITZ.

7.4 Putting it all Together

With the algorithm for concrete structure generation, see Fig. 7.8, 'random' fields can be generated in few seconds. Within these fields, SPH particles can have different properties. If the properties are identical in all domains, the model is again homogenized (macrolevel). If the properties differ, the model is with the numerical heterogeneity (mesolevel). The properties do not have to vary in all domains, however. It could be that CSCM is used as a base material, yet in the ITZ domain the UCS or density varies.

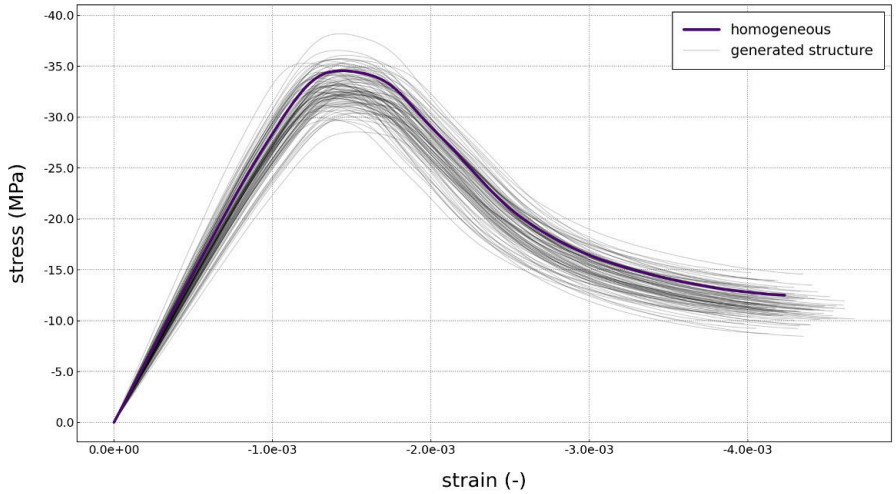

Fig. 7.18. Comparison of uniaxial compressive strengths of the homogenous model and those with generated structure.

The approach of the strength variation within the ITZ domain was used in UCS simulations on cylindrical concrete specimens. The discussed generated specimen with height of 300 mm and diameter of 150 mm as shown in Fig. 7.15 was used. To show the impact of the variation within the ITZ domain, 100 samples were generated in total, subsequently approximated with SPH particles, and initially assigned with a base CSCM. The UCS of the base CSCM was 35 MPa, yet in the ITZ domain the strength was defined with the Gaussian (normal)

distribution with the mean value $\mu = 35\,\text{MPa}$ and the standard deviation $\sigma = 10\%$ of the base UCS.

The stress-strain diagrams are collected in Fig. 7.18 for the initial homogenous model and the generated 100 samples. Since the simulations were purely structural, the sign convention from structural engineering is used. That is, compressive stress and strain are negative. Clearly, the responses are not identical. The majority of UCS values are lower than the one defined in the base material model. This points to the fact, that any introduced numerical heterogeneity decreases the integrity of a model. Yet the responses are not completely random, which was the intention. It might be that the similarity between the individual samples is pronounced due to the introduced artificial viscosity. The full study can be found in the author's [231, 232].

The outlined approach for the numerical heterogeneity implementation was proposed to bypass perhaps the biggest difficulty in applied engineering, i.e. the need for many material parameters. As shown in **Chapter 5** *Quasi-Brittle Materials*, more than 40 parameters is necessary to fully define CSCM. Yet, with the *algorithm for concrete structure generation* perhaps only two simple material models with different properties are needed, e.g. Mohr-Coulomb as shown in Fig. 3.2. Then one model would be assigned to the domain of aggregate, the second to the domain of mortar-matrix. As a result, responses would be nonlinear, heterogeneous-like. This is how can be complex material models with many input parameters bypassed. More can be found in the author's [231, 232].

Chapter 8

Experiment – High Velocity Impact

In this chapter, all the learning from the presented theory and discussed examples is applied in a numerical simulation of a high velocity impact (HVI) experiment which was performed by the author and his colleagues. The chapter serves as a proof that Smoothed Particle Hydrodynamics (SPH) is indeed a proper tool when it comes to structural dynamic simulations in which concrete is employed. Since SPH is validated from the mathematical point of view in many papers, studies, and books, an experimental validation is offered here. At the beginning of the chapter, the experiment is discussed, described in detail. The numerical concept and implementation of SPH follow. Conclusions and findings are discussed at the end of the chapter.

8.1 Experiment Description

The experiment can be described as an impact test in which the focus is on the impacted specimen rather than on the impactor. In this particular case, the specimen was a reinforced concrete beam and the impactor was a steel battering ram. Now the question, why is the experiment referred to as HVI if it is just a simple impact test? As in any other scientific field, also in civil engineering, load rate has its limits. For example, the velocity of a moving vehicle impacting a bridge pillar is not likely to exceed the sound speed. Therefore, an impact test would be considered HVI in civil engineering. Of course, under such conditions, a material with structural strength does not behave like a fluid yet. However, this is yet another benefit stemming from the experiment. Since the load rate is not quasi-static either, both stress state (represented by constitutive models) and momentum (represented by conservation laws) play significant role. If SPH can reproduce the experimental measurements, it is indeed a proof that the method is perspective in civil engineering.

The reinforced concrete beam of length 1.7 m with a rectangular cross-section of 120 mm × 250 mm was specially designed for the experiment. The size was limited by the operating tower where the battering ram was mounted. A schema of the experiment can be seen in Fig. 8.1, and as obvious, special supports were designed as well. The supports were made of wood, reinforced with steel brackets and fasteners. There were two reasons

for such a construction. First, the supports had to be fairly robust and stable, yet light when it comes to transportation. Second, the supports should behave like dampers, since the battering ram was 500 kg. That said, it should be kept in mind the beam was not simply supported.

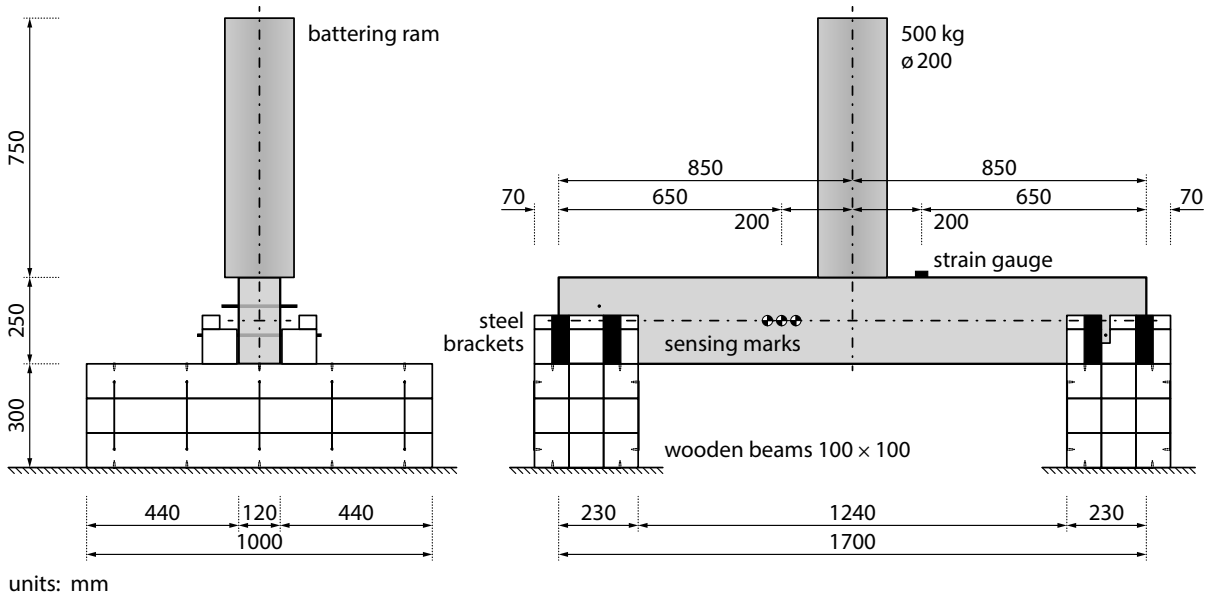

Fig. 8.1. Schema of the HVI experiment.

The concrete *ordered* for the experiment was of class C30/37 [209] together with steel class B500B [209], yet the emphasis on 'ordered'. Both are discussed in the following section in more detail. The reinforcement ratio, thickness of the cover layer, creation process, and others were all in agreement with Eurocode 2 [209]. Therefore, the reinforced beam can be understood as a representative of standard concrete specimens. A schema of the reinforcement is shown in detail in Fig. 8.2.

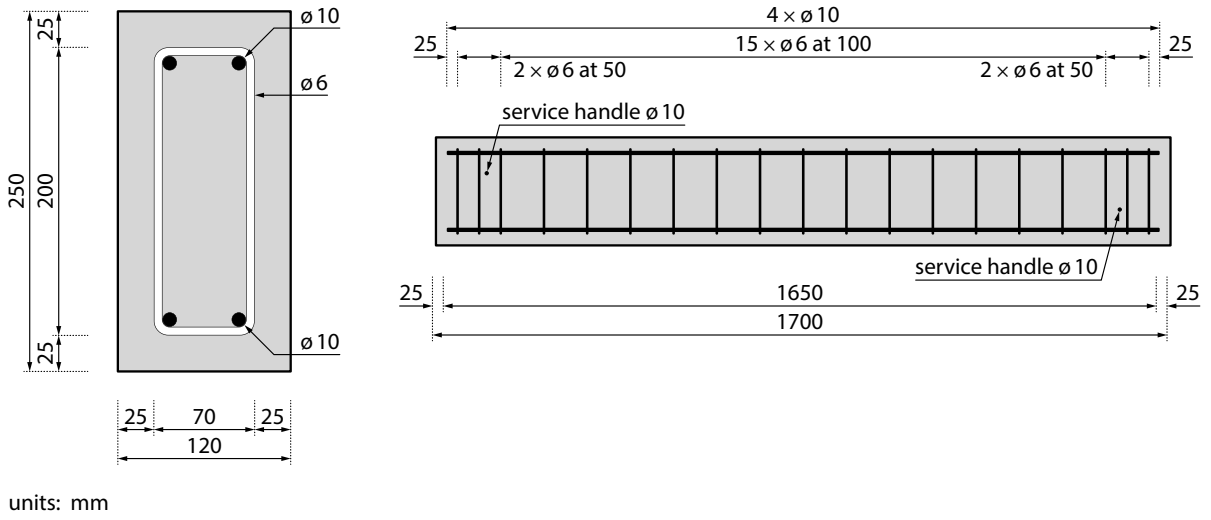

Fig. 8.2. Reinforcement of the concrete beam used in the HVI experiment.

Three responses were studied in detail – longitudinal strain at the top surface of the beam during the impact, vertical displacement in the middle of the height of the beam during the impact, and damage of the beam after the impact. For the strain measurements, a strain gauge was glued to the top surface of the beam. The gauge was placed with an eccentricity of 200 mm from the symmetry axis. The displacement was not directly measured, but recorded with a slow motion camera with rate of 1000 frames per second. The camera was placed 1 m in front of the beam, focused on sensing marks. The marks were placed with an eccentricity of 200 mm from the symmetry axis, yet in the middle of the height of the beam. After the impact, a damaged zone of the beam was documented as well. Therefore, the size, number of cracks, crack pattern, and crack openings were known.

(a) operating tower (b) beam placement

Fig. 8.3. Photos of the HVI experiment setup.

Photos from the experiment are shown in Fig. 8.3. As can be seen, the operating tower is quite high, allowing drops from up to 8 m. However, in the experiment, the drop height of 0.95 m was tested. The reason for 0.95 m 'only' was that the beam was exposed to two drops in total. The first drop was meant for a damage initiation, the second drop for a post-critical behaviour analysis. Only the first drop is discussed in the thesis, however.

8.2 Measurements

Seven specimens were tested in total, all with the same drop height of 0.95 m. The first two measurements were used for in-situ calibration purposes, therefore, they are not included in the result overview and were not considered for the material calibration. Each specimen had its own identification code starting with '7IX' and a number (3 to 7). In Fig. 8.4 and Fig. 8.5, strains and displacements over time are shown, respectively. Negative strains stand for compression in the longitudinal direction of the beam, and negative displacements stand for a movement downwards. For convenience, all diagrams start at time 0 s, which is also considered the time of the impact. Simulation results follow the same convention.

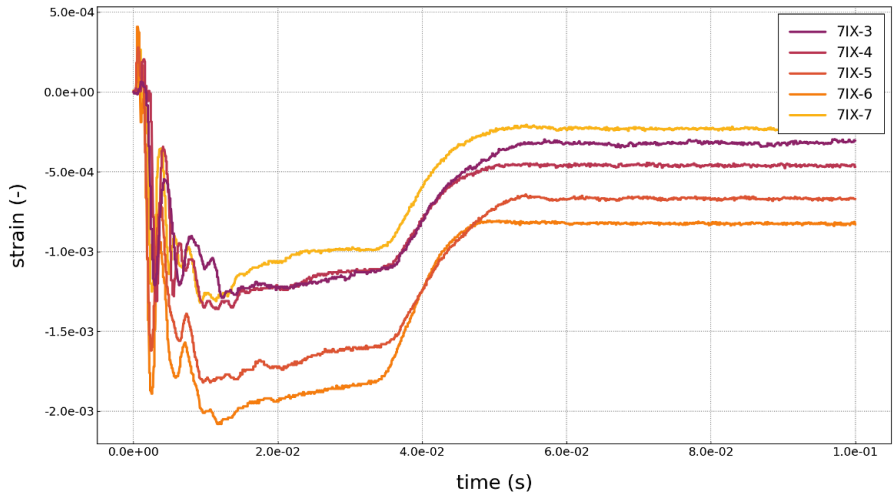

Fig. 8.4. Strain at the top surface of the beam over time (experiment only).

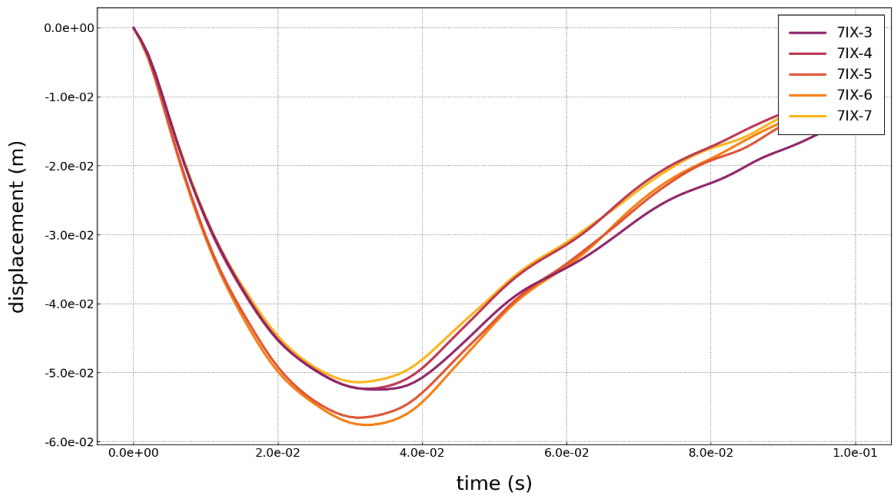

Fig. 8.5. Displacement at mid-span of the beam over time (experiment only).

(a) 7IX-3

(b) 7IX-5

(c) 7IX-6

(d) 7IX-7

(e) 7IX-4

Fig. 8.6. Damaged specimens after the impact.

As can be seen in Fig. 8.4, just right after the impact strains grow to tension, yet drop immediately to compression. The same trend can be seen in the measurements of all specimens. It is not a measurement error though. During the first milliseconds of the impact, a zone in the proximity of the battering ram is deformed locally. In other words,

just before the beam bends as a whole and its top part is put into compression, a local zone in the proximity of the contact is in tension. It did not take too long for the beam to bend, however. After the beam is set in motion, the strains are only in compression. The important finding is that the region where the strain gauge was placed is in compression even after the impact. In other words, after the peak in displacement is reached and the beam starts to move upwards Fig. 8.5, strains are still in compression Fig. 8.4.

What does it mean? From the slow motion camera footage it is clear that after the impact the beam moves up and down, oscillates. Yet, strains in the proximity of the strain gauge are kept in compression. The reason for that is, that the beam was broken during the impact. Its ultimate load-carrying capacity was exceeded, therefore, the beam was irreversibly damaged. This can be seen in Fig. 8.6 in which, e.g. specimen 7IX-4 was already taken down from the supports yet remained deformed since the reinforcement exceeded its yield strength. The state in which specimen 7IX-4 was, however, is perfect for the post-critical analysis.

Fig. 8.7. Damaged specimen 7IX-4 after the second impact (post-critical damage).

Since all the tested specimens ended in the same damage state as shown in Fig. 8.6, i.e. the failure mode, crack pattern, and size of the damaged region, the following comment can be understood in general. Three types of failure can be distinguished in the damaged region. The contact region where the battering ram impacted the beam shows clearly concrete spalling. It is not a failure in compression or tension but rather a separation of a matter in the proximity of the contact, i.e. pieces of concrete (debris) flew away. In contrast, the bottom part of the beam shows flexural cracks which point toward the impacted region. Although the failure is said to be in bending, it is in fact a tensile failure. Given the size of the cracks openings, it is without a question that the reinforcement failure is also included. The cracking in the middle of the height of the beam is a shear failure. Very

often referred to as a cone cracking or conical failure (shape of the curly-wedge symbol ⅄), sometimes followed by a plug failure. These are secondary formed cracks after the load-carrying capacity in bending was reached. Put simply, the battering ram was pushing a conical volume of a concrete out, therefore, the shear failure. In addition, the damage is also noticeable in vicinity of the supports where the contact regions between the beam and supports were formed.

Although it is not the scope of the discussion here, a post-critical damage is shown in Fig. 8.7. The post-critical damage is a result of the second impact. It is a very nice example of a sudden snap of the reinforcement in tension. The author believes that understanding of a structure behaviour after its ultimate load-carrying capacity was reached is an important aspect in a design. In a common civil engineering praxis, such a construction would be taken down immediately. Yet, in some cases, e.g. military objects, it might be beneficial to keep the construction in its post-critical state and just remediate it for the time being.

specimen	drop height (m)	displacement (m)	strain (-)
7IX-3	0.950	-5.245×10^{-2}	-1.290×10^{-3}
7IX-4	0.950	-5.235×10^{-2}	-1.360×10^{-3}
7IX-5	0.950	-5.653×10^{-2}	-1.820×10^{-3}
7IX-6	0.950	-5.759×10^{-2}	-2.080×10^{-3}
7IX-7	0.950	-5.139×10^{-2}	-1.320×10^{-3}

Tab. 8.1. Overview of the HVI experiment measurements.

In addition to Fig. 8.4 and Fig. 8.5, the measurements are also collected in Tab. 8.1. Since the drop height was constant, also the impact velocity was. Taking into account the drop height $h = 0.95\,\mathrm{m}$ and the standard acceleration due to gravity $g = 9.80665\,\mathrm{m/s^2}$, then the impact velocity can be calculated as

$$v = \sqrt{2gh}, \tag{8.2.1}$$

which is roughly $4.317\,\mathrm{m/s}$. Since the negative displacement values in Tab. 8.1 stand for movement downwards, the impact velocity should be also negative, $v = -4.317\,\mathrm{m/s}$. The strains in Tab. 8.1 are raw data from the measurements, therefore, the negative values mean compressive strains. The same sign convention is used in the results section.

8.3 Numerical Model

The numerical model was not a pure SPH model but a coupled with the Finite Element Method (FEM). The main reason for using the coupled model was computational requirements. It would be possible to build a pure SPH model, however, since SPH can be quite expensive in terms of computational requirements, it would be impractical to use

SPH in regions of a lower importance. For that reason, FEM was used mainly for the supports.

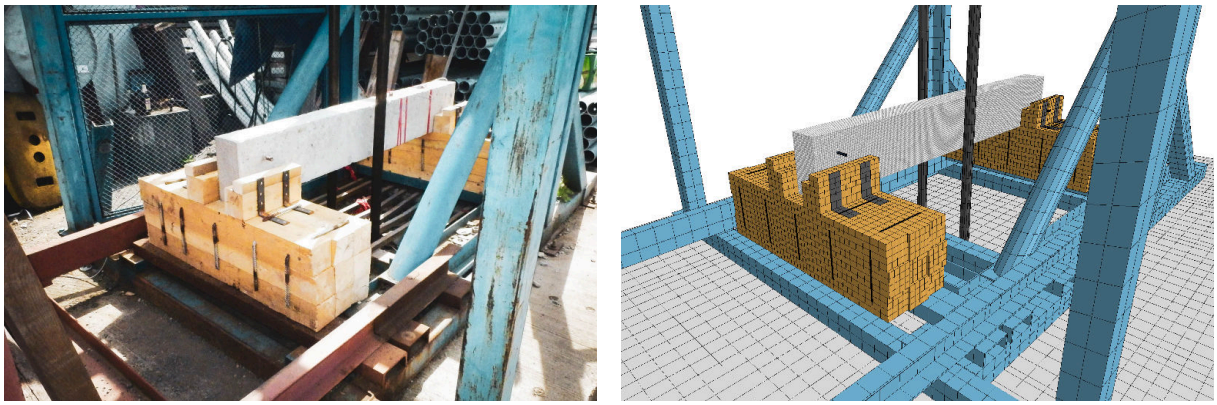

(a) experiment (b) numerical model

Fig. 8.8. Comparison of the real experiment and numerical model.

Since the focus of the study was not only to examine perfectly vertical impacts but also cases in which the battering ram impacts under an angle, the operating tower was built as a parametric model in which the rails of the battering ram can be arbitrarily rotated. A photo of the tower with prepared beam on the supports can be seen in Fig. 8.8 in comparison to the numerical model. For the SPH functionality demonstration in the thesis however, the rails were kept vertical, therefore, the tower is not further shown in the results section. The functional parts of the model can be seen in Fig. 8.9 in which the reinforced concrete beam, wooden supports, and battering ram are the main parts. As can be seen, all details including the service handles, steel brackets, and fasteners were also modelled, however.

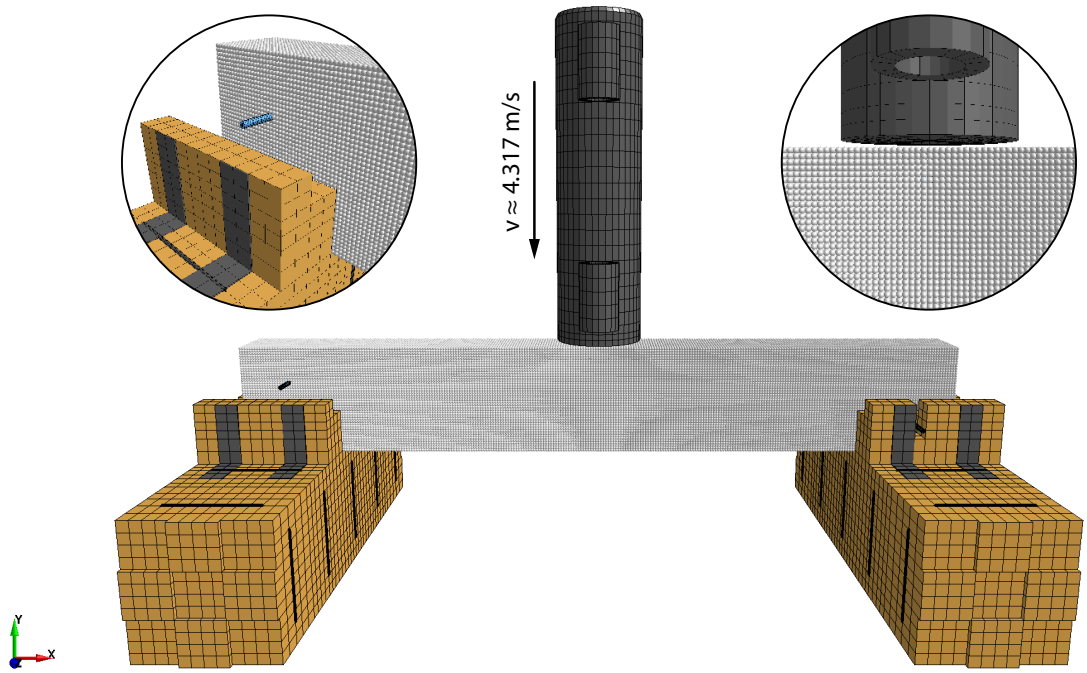

Fig. 8.9. Numerical model of the HVI experiment.

The FEM components of the model used solid, shell, and beam elements. The 8-node solid elements with only translational degrees of freedom (DOF) and with reduced number of the integration points (constant stress) proved to be enough in this particular case. The shell and beam elements had combined translational and rotational DOFs, however, both with a constant cross-section. As can be seen in Fig. 8.10, the numerical model captured the essence of the real experiment quite well.

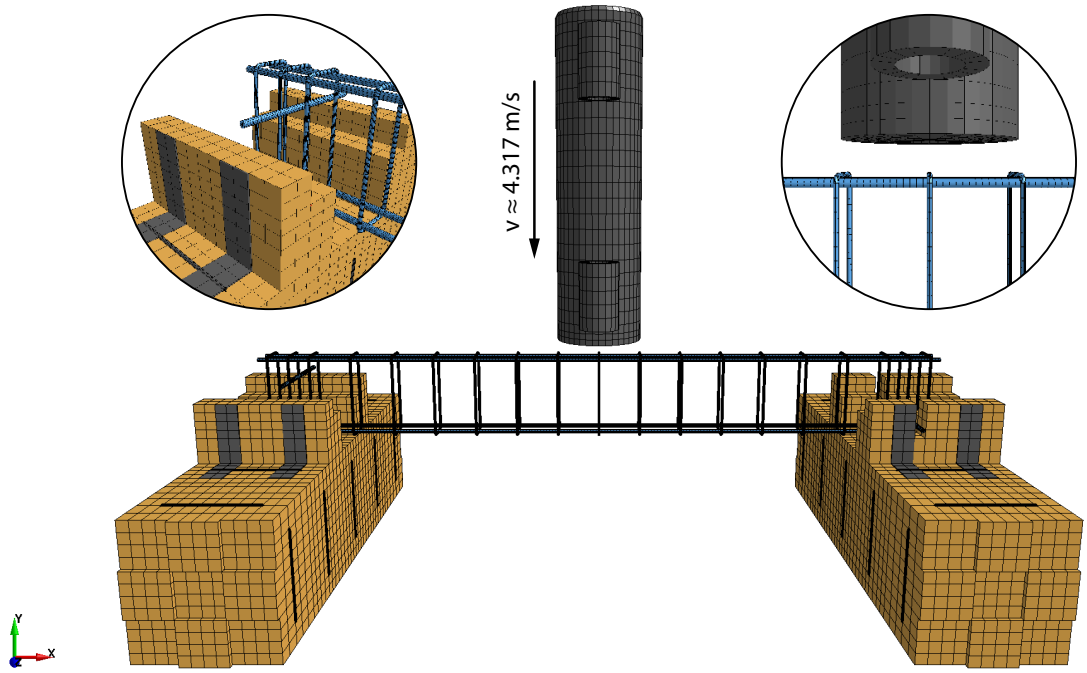

Fig. 8.10. Numerical model of the HVI experiment with uncovered reinforcement (no SPH particles shown).

The reinforcement was modelled with the proposed coupled SPH-FEM sublayer approach. As previously discussed in **Chapter 4** *Coupling SPH and FEM* and section *Sublayer Coupling with FEM*, the coupling is valid as long as a proper ratio of nodal and particle masses is defined, see Fig. 6.8. With respect to these chapters, equal mass distribution was used. That is, FEM nodes and SPH particles had the same mass, and when combined, the real mass of the reinforcement was captured. However, the same cannot be used for the Young's modulus since SPH masses directly influence the lumped volumes, therefore, have an impact on the resulting stiffness. For that reason, the Young's modulus of numerical zero was used for SPH as also previously discussed in section *Sublayer Coupling with FEM*. Since the FEM reinforcement and SPH sublayer shared the same nodes/particles, the coupling with the SPH concrete was done in natural way with overlapping support domains. The logic of the reinforcement composition is shown in Fig. 8.11.

Regardless of the coupling with shared nodes, which was used only for the reinforcement, the concrete beam interacted with the supports and battering ram through the penalty-based contact. The logic of the contact implementation can be found in [185], therefore, there is no need to discuss it here further. Interestingly enough, the contact was also used between the individual pieces of the reinforcement, i.e. between the stirrups and longitudinal reinforcing bars. Functionality of the contact is discussed in the results section in detail.

The battering ram was modelled as a rigid entity, yet with contact parameters corresponding to a construction steel. Its shape was simplified to one cylindrical body, which is in contrast to reality where additional masses are attached to the battering ram on its sides as shown in Fig. 8.3. However, since the battering ram with the additional masses is symmetric as a whole, it can be that only the main part is modelled with increased density, therefore, its total mass is equal to the real one of 500 kg. Interestingly, since the battering ram have been through a lot over the years, its contact surface is no longer perfectly flat, but slightly convex, oval-like. For that reason, the battering ram was modelled with rounded contact surface with radius of 2 m. Note, that a sensitivity study was performed in which uncertain parameters were varied (including the radius of the contact surface). The study is being published separately to the thesis, however.

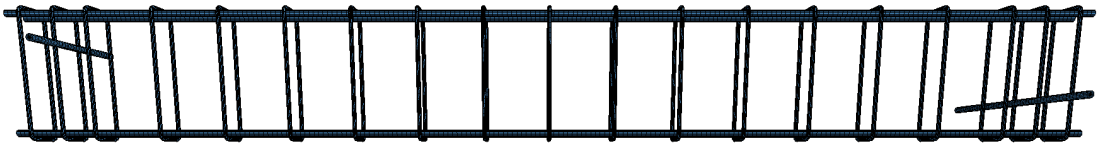

(a) FEM reinforcement

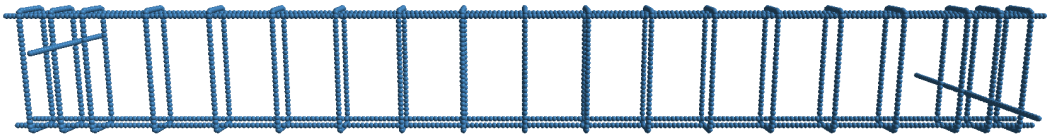

(b) SPH sublayer for the concrete and reinforcement coupling

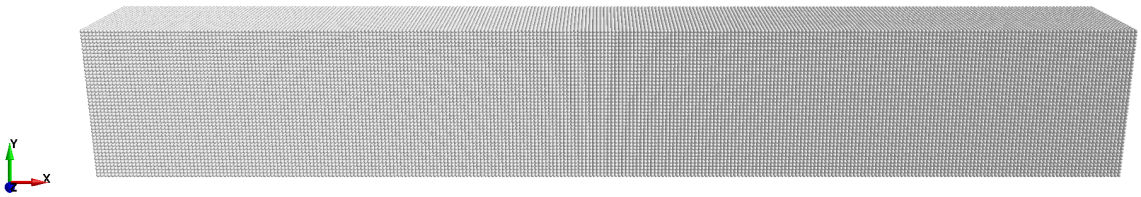

(c) SPH concrete

Fig. 8.11. Implementation of the FEM reinforcement into the SPH model.

The SPH part of the model (the concrete) was generated into a cubic lattice with a particle spacing $\Delta x = 6 \pm 0.05$ mm in all three directions. This resulted in more than 255,000 SPH particles in total, including those in the reinforcement sublayer for the FEM coupling. As discussed in section *Variable Smoothing Length*, it is important that the particle spacing of all SPH parts is more or less similar, therefore, the FEM beam elements of the reinforcement were approximately 6 ± 0.5 mm long. And since the SPH coupling sublayer used shared nodes, this resulted in a particle spacing $\Delta x = 6 \pm 0.5$ mm.

All the SPH components used the same isotropic Eulerian kernel Fig. 2.36 together with the cubic spline Fig. 2.8 with $h = 1.2\,\Delta x$ and $\kappa = 2$. The support domains were not constant but dynamic in time and space, driven by (2.4.36). Furthermore, the conservation laws in the SPH framework defined in (2.10.15), (2.10.16), and (2.10.17) were used for the continuity, momentum, and energy equation, respectively.

ρ	mass density (kg/m^3)	2124.0
E	Young's modulus (GPa)	25.28
G	shear modulus (GPa)	11.0
K	bulk modulus (GPa)	12.04
ν	Poisson's ratio (-)	0.15
f_c	compressive strength (MPa)	26.5
f_t	tensile strength (MPa)	2.1
α	TXC surface constant term (Pa)	1.3990×10^{7}
θ	TXC surface linear term (-)	2.8570×10^{-1}
λ	TXC surface nonlinear term (Pa)	1.0510×10^{7}
β	TXC surface exponent (Pa^{-1})	1.9290×10^{-8}
α_1	TOR surface constant term (-)	7.4730×10^{-1}
θ_1	TOR surface linear term (Pa^{-1})	1.2370×10^{-9}
λ_1	TOR surface nonlinear term (-)	1.7000×10^{-1}
β_1	TOR surface exponent (Pa^{-1})	7.3730×10^{-8}
α_2	TXE surface constant term (-)	6.6000×10^{-1}
θ_2	TXE surface linear term (Pa^{-1})	1.4900×10^{-9}
λ_2	TXE surface nonlinear term (-)	1.6000×10^{-1}
β_2	TXE surface exponent (Pa^{-1})	7.3730×10^{-8}
N_h	hardening initiation (-)	1.0000
C_h	hardening rate (-)	0.0000
R	cap surface aspect ratio (-)	5.0000
X_0	cap pressure axis intercept (Pa)	8.9070×10^{7}
W	hardening law maximum compaction (-)	5.0000×10^{-2}
D_1	hardening law linear exponent (Pa)	2.5000×10^{-10}
D_2	hardening law nonlinear exponent (Pa^2)	3.4920×10^{-19}
B	compressive softening parameter (-)	1.0000×10^{2}
G_{fc}	compressive fracture energy (J/m^2)	5.9320×10^{3}
D	tensile/shear softening parameter (-)	1.0000×10^{-1}
G_{ft}	tensile fracture energy (J/m^2)	5.9320×10^{1}
G_{fs}	shear fracture energy (J/m^2)	5.9320×10^{1}
μ	compressive damage transition power (-)	5.0000
υ	tensile damage transition power (-)	1.0000
ξ	moderate pressure adjustment parameter (-)	0.0000
η_{c_0}	compressive fluidity parameter (-)	1.0110×10^{-4}
$\bar{\eta}_c$	compressive fluidity power (-)	7.8000×10^{-1}
η_{t_0}	tensile fluidity parameter (-)	5.8900×10^{-5}
$\bar{\eta}_t$	tensile fluidity power (-)	4.8000×10^{-1}
ψ	ratio of shear to tensile fluidity parameter (-)	1.0000
ω	power applied to fracture energies (-)	1.0000

Tab. 8.2. Material parameters of CSCM used in the HVI experiment simulations.

Shock fronts were smoothed out with the Monaghan type artificial viscosity (2.9.3) with parameters $\alpha_l = 1$ and $\beta_q = 1$. The renormalization proposed in [35] was used to improve stress profiles at the boundaries of SPH domains, yet no special treatment was applied to alleviate the tensile instability.

The complete list of the Continuous Surface Cap Model (CSCM) material parameters can be found in Tab. 8.2. The table is divided into two parts – commonly used concrete parameters for the class identification and the numerical parameters of CSCM in the base International System of Units (SI) for convenience. Interestingly, concrete class C30/37 was ordered, yet independent tests of the unconfined or uniaxial compressive strength (UCS) showed that the class is rather C20/25. At the end of the calibration process, however, the UCS value in CSCM was 26.5 MPa. Apparently, the truth is somewhere between; C25/30 perhaps?

ρ	mass density (kg/m^3)	7830.0
E	Young's modulus (GPa)	200.0
E_{tan}	tangent modulus (GPa)	1.0
ν	Poisson's ratio (-)	0.29
f_y	yield strength (MPa)	500.0

Tab. 8.3. Material parameters of the steel used in the HVI experiment simulations.

For the reinforcement, yet also for the rest of the steel parts, a simplified elastoplastic material model was used (bilinear). As previously mentioned, steel class B500B was used for the reinforcement which translated to numbers is summarized in Tab. 8.3. The tangent modulus was estimated to be only 0.5% of the initial stiffness. In retrospect, this was an underestimation.

ρ	mass density (kg/m^3)	612.0
E	Young's modulus (GPa)	12.7
E_{tan}	tangent modulus (GPa)	0.127
ν	Poisson's ratio (-)	0.374
f_y	yield strength (MPa)	50.8

Tab. 8.4. Material parameters of the wood used in the HVI experiment simulations.

For the supports, again the simplified elastoplastic material model was used but with parameters of a hardwood, see Tab. 8.4. Although it might seem the supports are oversimplified, it was found that responses of the reinforced beam are not sensitive when it comes to the material properties of the supports.

The question was, however, if it makes sense to include the constitutive model strain-rate effects or not. The impact velocity of 4.317 m/s is surely not quasi-static, yet still far from

the velocity which delivers enough energy to set the concrete in a flow-like motion. The common practice is to test both models, i.e. with and without the constitutive model strain-rate effects. Of course, the rate effects related to structural inertia were always considered, see section *Materials with Softening*. To improve readability, the constitutive model strain-rate effects are shortened in the following sections to just with/without the rate effects or even simpler, rate effects/no rate effects.

8.4 Results

Since the goal of the thesis is to provide a proof of the SPH functionality when used in structural dynamics, it is crucial to present a calibrated model which is able to represent all the measured responses. In this particular case the model was able to represent the strains over time, displacements over time, and damage state after the impact. Needless to say that 5 measurements give a range into which the numerical model should fit. This is especially useful when a change of one parameter has an impact on all responses. Note that the calibration of the material parameters is not discussed here as it is not the goal of the thesis.

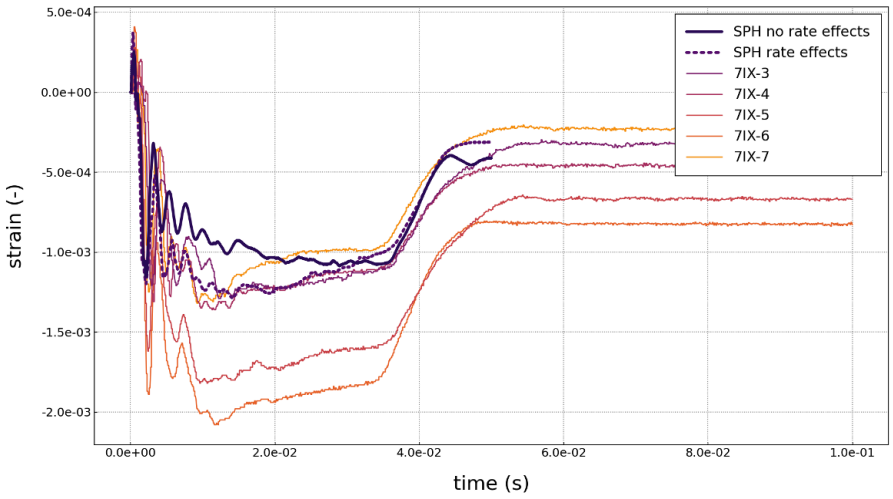

Fig. 8.12. Strain at the top surface of the beam over time (experiment vs. simulation).

Starting with the strains over time in Fig. 8.12, both models (with and without the constitutive model strain-rate effects) reproduce the measurements quite well. The model with the strain-rate effects predicts strain responses slightly better, as it seems that all the gradients fit quite nicely. Both models represent rather a lower bound of the measurements, not the mean, however. Yet with the given number of uncertainties, the overall picture is acceptable.

In more detail, just right after the impact, tensile strains develop at the top surface of the beam. As the beam starts to move, the strains change into compressive. It is nice to see that even this unpredictable 'initial tensile jump' has been captured by both models. As the beam further bends, compressive strains at the top surface reach peak values, the

time approximately 0.01 s. As the battering ram starts to slow down, the strains keep at a constant value, the time window between 0.01 and 0.03 s, again with a good correlation with the measurements. At time 0.04 s the battering ram starts to move upwards which results in a sudden relaxation in the strains. Yet, the values are not going to zero but are kept at a certain level of compression. The reason for this is that the ultimate load-carrying capacity was reached and the beam, in both models, has been 'broken'.

Displacements in Fig. 8.13 are also quite nicely represented by both models. Yet, only down to the peak, the unloading branches show some differences. The initial loading branches (movement downwards) show almost identical rate (stiffness) and peak values as in the experiment. As it was the case for the strains, also the displacements represent rather a lower bound of the measurements. As previously mentioned, the ultimate load-carrying capacity was reached in both models, therefore, the unloading branches show slower unloading rate (lower stiffness). In practice, it means that the numerical model was damaged more than in the experiment. In retrospect, this behaviour is due to the underestimated tangent modulus of the steel. However, post-critical responses were not the main objectives of the study. For that reason, the responses are acceptable. Interestingly enough, displacements of both models are almost identical. Which means, that the global behaviour of the beam is not driven by the constitutive model strain-rate effects.

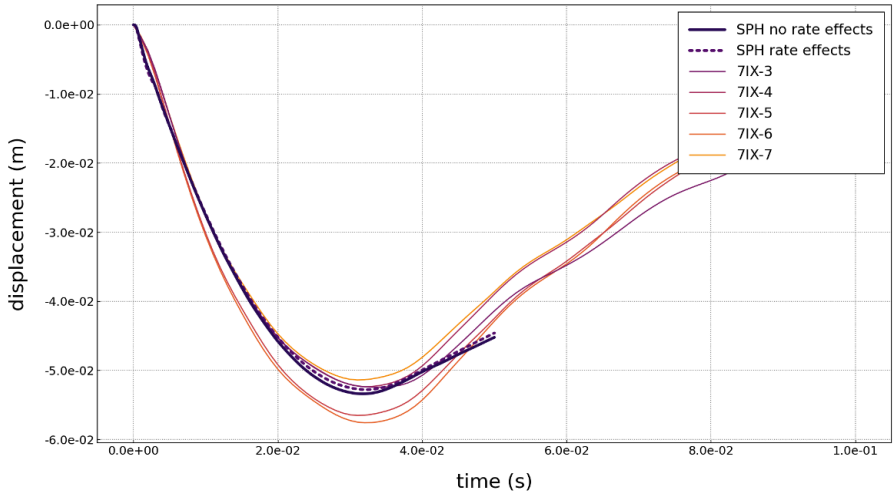

Fig. 8.13. Displacement at mid-span of the beam over time (experiment vs. simulation).

The damage of the concrete at the end of the simulation is shown for both models in Fig. 8.14. When compared to the photos in Fig. 8.6, it is without a doubt that both models represent the crack pattern quite well. Some important observations can be made at this point. Both models show concrete crushing in the contact region with the battering ram, both models show a flexural and shear cracking as in the experiment. Yet it is clear that the model without the strain-rate effects shows multiple cracks, which is in contrast to the model with the rate effects in which only few main cracks form the damaged region. More importantly, the overall damage shape, therefore, the failure mode, is different. The model without the rate effects shows cracks in the expected conical slope; shape of the curly-wedge 人. However, the model with the rate effects shows rather an arch shape ∩ of the crack pattern. The difference might not be that pronounced, yet the model without

the rate effects shows better correlation with the experiment. In addition, the model with the rate effects shows cracks growing along the longitudinal reinforcement which is not observed for any specimen in Fig. 8.6.

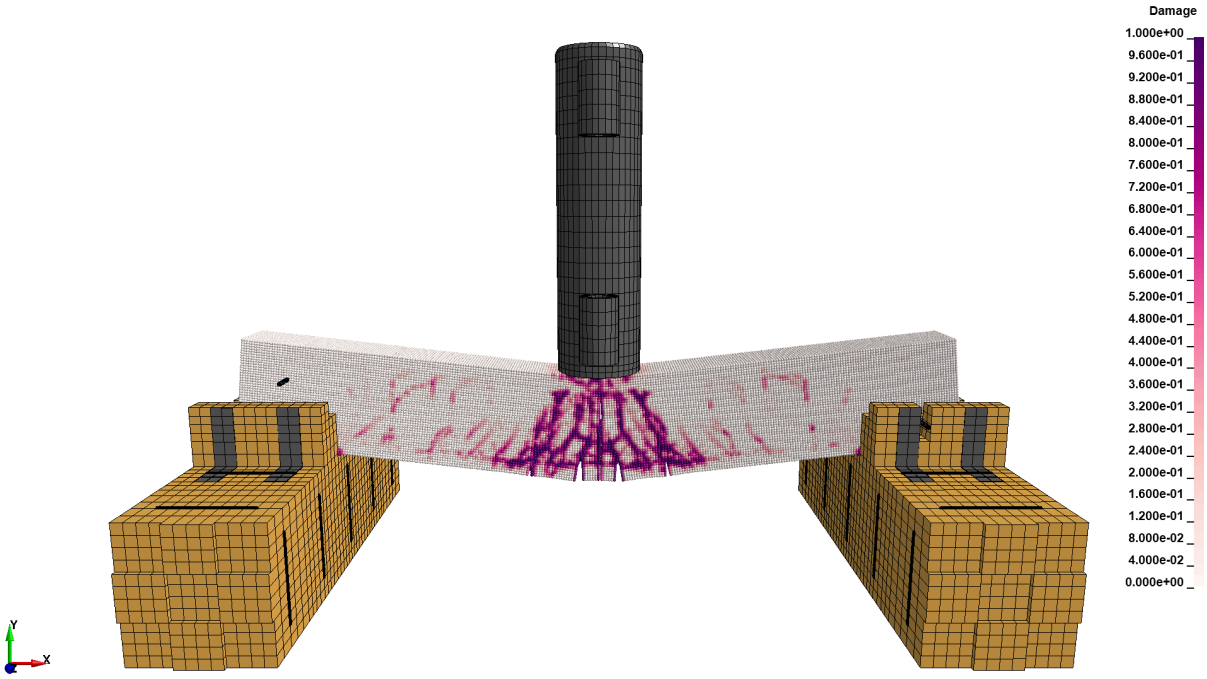

(a) no rate effects

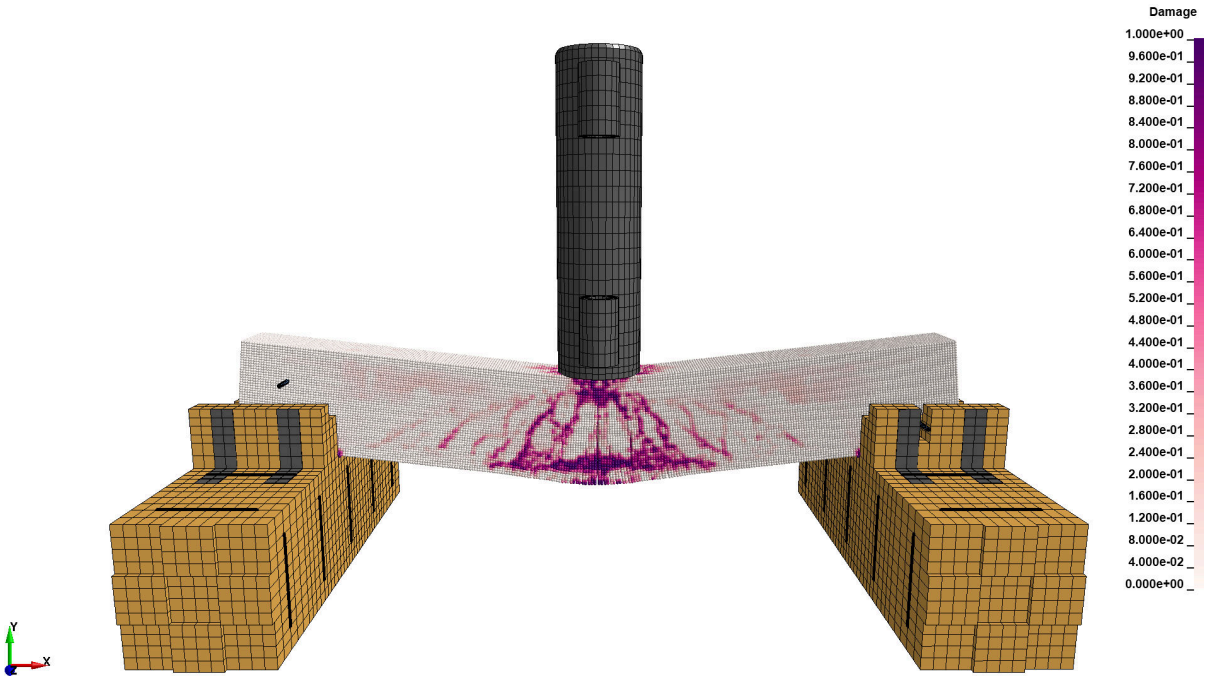

(b) rate effects

Fig. 8.14. Damage comparison of the model with and without the constitutive model strain-rate effects.

From a closer look it might seem that the model without the rate effects is burdened with the tensile instability at the bottom part of the model. However, it is not the case. The opening is truly material opening and can be confirmed by the fact the particles in the proximity of the opened cracks reached the damage value of 1 over time. Interestingly enough, from Fig. 8.6 it is clear that some cracks are opened enough to be $\Delta x = 6 \pm 0.05\,\text{mm}$, which leads to the particles separation and the visible crack propagation.

The reinforcement can be discussed next. The comparison of the effective stresses (von Mises) of both models is shown in Fig. 8.15. The comparison shows the maximum reached stress over time. The stress distribution is as expected, clearly showing that the sublayer coupling approach works quite well. Furthermore, the contact between the individual parts of the reinforcement works as well. This is supported by the fact that the reinforcement skeleton kept its shape. One difference between the models is quite obvious – the buckling of the stirrups in the model with the rate effects. This is indeed quite surprising response which comes along with the ∩ shaped concrete cracks. The explanation for the behaviour is that due to the distribution of the arch forces in the model, the stirrups are loaded also in the longitudinal direction of the concrete beam.

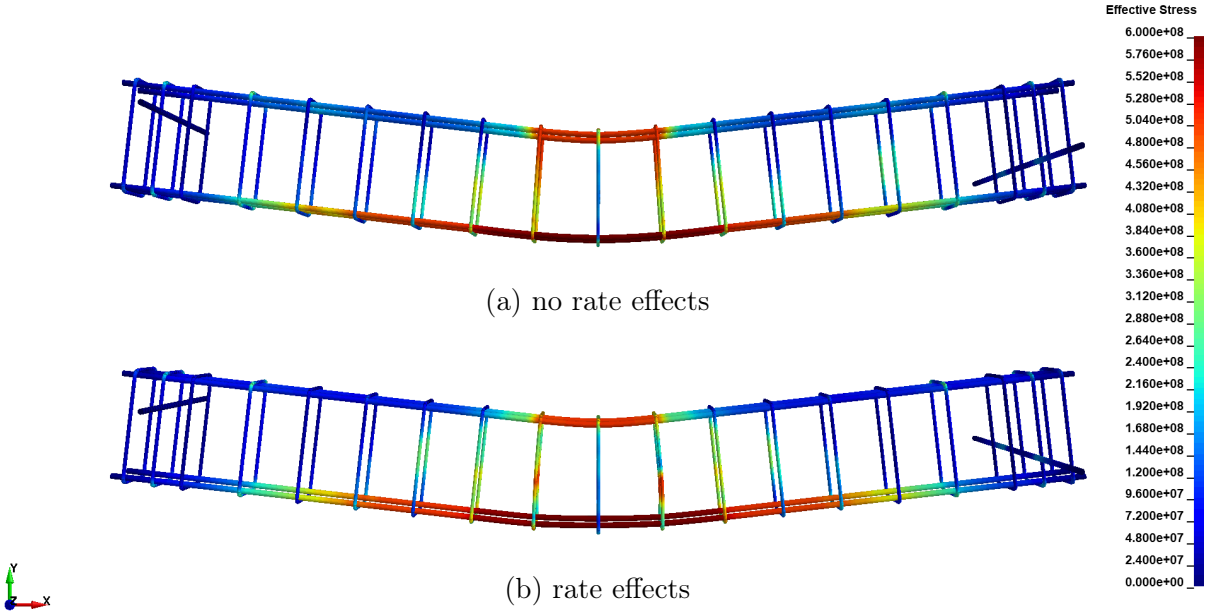

(a) no rate effects

(b) rate effects

Fig. 8.15. Effective stress comparison in the reinforcement of the model with and without the constitutive model strain-rate effects.

In both models, however, the yield strength was exceeded which further supports the fact that the beam was broken just after the impact. A better understanding of the damaged region is shown in Fig. 8.16 in which plastic strains of the reinforcement are shown. Results are again as expected, only the two bottom longitudinal reinforcing bars exceeded the elastic state and are in plastic mode. Since the tangent modulus of the steel was underestimated, plastic strains are in the case of the model without the rate effects up to 12.5%, and approximately 9% in the case of the model with the rate effects. By the definition of Eurocode 2 [209], steel class B500B should withstand plastic strains $\geq 5\%$. However, 12.5% is perhaps too much. By increasing the tangent modulus of the steel, both 'problems' the unloading rate and plastic deformations would better correspond

to the measurements. Of course, it is not expected that the results prior the ultimate load-carrying capacity would change with adjusted tangent modulus. Therefore, the model is considered calibrated for the purpose of the SPH functionality demonstration.

Considering everything, the optimal model would be somewhere in between the model with and without the constitutive model strain-rate effects. Of course, more complex material models of the steel and wood might further improve the calibration results. Strictly speaking of the SPH part of the model, no stability issues or other numerical problems were observed. The cubic spline together with the isotropic Eulerian kernel proved to be a good choice, fully capable to simulate complex responses of the reinforced quasi-brittle material. The tensile instability was not observed in any of the models. The next step of the experiment evaluation is to analyse the post-peak behaviour of the pre-damaged beam. And since SPH allows carrying state variables during the model initialization, e.g. damage values, it can be used again. This is yet another highlight of the Lagrangian meshfree method.

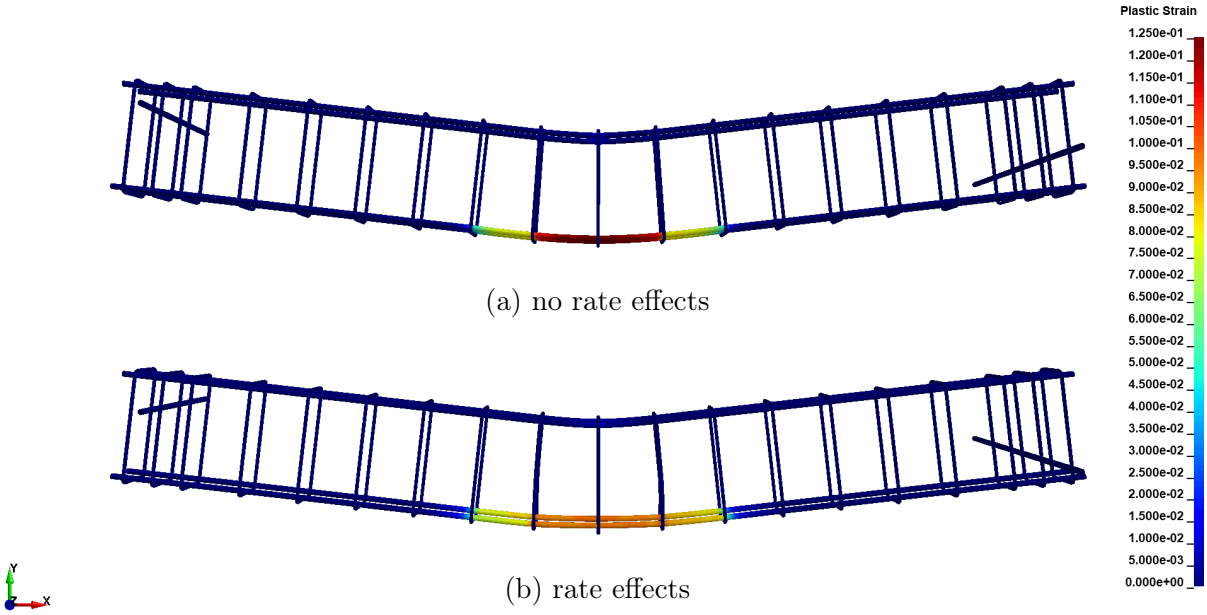

(a) no rate effects

(b) rate effects

Fig. 8.16. Plastic strain comparison in the reinforcement of the model with and without the constitutive model strain-rate effects.

The fact that the coupled SPH model was able to capture all the responses of the experiment is not only a proof that SPH is fully functional and can be used in civil engineering applications, but also that the proposed *sublayer coupling* approach works. Since the coupling can be fully automized, it means, it can be also directly implemented into the SPH framework and further developed as a direct reinforcement method. And since the algorithm for the numerical heterogeneity is automized as well, it can be that together might offer a very powerful tool in Computer-Aided Engineering (CAE) with a minimal user input.

Chapter 9

Experiment – Explosion

In this chapter, capabilities of Smoothed Particle Hydrodynamics (SPH) are tested again, perhaps even more. As in the previous chapter, a coupled SPH model with the Finite Element Method (FEM) is used to simulate what was observed in an explosion experiment. This time, however, SPH simulates both structural parts and fluids. The experiment was performed by the author's colleagues, who also provided the measurements, for which the author is grateful. The goal of the experiment was to analyse the behaviour of a reinforced concrete slab exposed to a close-in explosion with a stand-off distance only few centimetres. Although the simulation results show a good agreement with the experimental measurements, some differences were found. To understand the differences better, a sensitivity study of uncertain parameters was performed.

9.1 Experiment Description

It is not a surprise that a civil engineer might be asked to design a construction or building to withstand an explosion. An explosion might be a result of unexpected events, e.g. an accident in a factory due to a wrong manipulation with explosives or just a failure of a storage unit. Of course, it could be that an explosion is a result of a terrorist attack or military intention. However, it is not the goal here to discussed what can cause an explosion but how can it be simulated with SPH.

For this purpose, a simple experiment was designed to study a close-in explosion, i.e. when a charge (an explosive) is placed and detonated relatively close to the examined specimen. The specimen was a reinforced concrete slab of standard concrete class C30/37 defined by Eurocode 2 [209] and a steel reinforcement of class B500B [209]; both discussed in the following section in detail. Since all the design parameters of the concrete slab were with agreement with Eurocode 2 [209], it can be assumed, that the reinforced slab is again representative of standard concrete specimens.

A schema of the experiment is shown in Fig. 9.1. The idea was that the concrete slab of $500\,\text{mm} \times 500\,\text{mm} \times 60\,\text{mm}$ is placed on a rigid support which would minimize the number of unknown parameters in the numerical simulation. However, it was not possible to find a

proper 'support' for this particular purpose, therefore, a prefabricated concrete column base was used. Unfortunately, the inner hole of the base was 550 mm × 550 mm which leaves 25 mm space between the concrete slab and base. To create a sufficient rigid support for the slab, a steel frame made of L-profiles was built and used between the slab and base. To minimize rigid contacts (concrete-steel-concrete), a layer of a hard rubber was placed between the frame and base. Additionally, four bolts were used to stabilize or reduce a possible motion of the frame. In retrospect, it is the author's opinion that the construction was not rigid enough, perhaps unnecessarily complex, and it unfortunately introduced many unknown and uncertain variables into the numerical simulation. For instance, the pre-stress force in the bolts was not defined, yet it has a great impact on displacement of the concrete slab during the explosion. Furthermore, mechanical properties of the rubber were not measured, which again gives a great unknown when material parameters of the concrete slab should be calibrated.

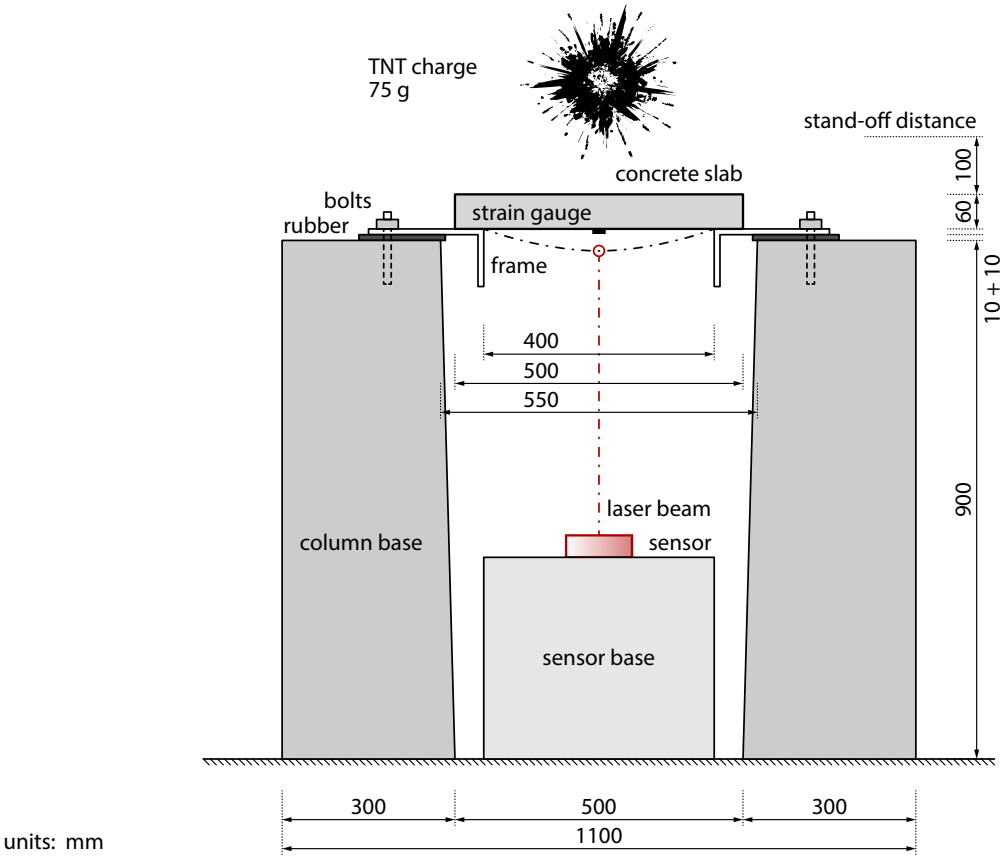

Fig. 9.1. Schema of the explosion experiment.

The explosive was a standard military 75 g Trinitrotoluene (TNT) charge of a cylindrical shape with a diameter of 30 mm and height of 70 mm. The charge was placed above the concrete slab with a stand-off distance of 100 mm, i.e. the clear distance not the detonation point distance. The orientation of the charge was such that the axial axis of the cylinder was perpendicular to the concrete slab. However, as shown in section *Uncertainty in the Charge Placement*, after reviewing the available photo documentation, the orientation of the charge was not always as intended.

The reinforcement was standardized 6 mm diameter reinforcing wire mesh with 100 mm spacing. In other words, five reinforcing bars in each direction. A schema of the reinforcement can be seen in Fig. 9.2. The reinforcement was placed in the middle of the height of the slab, i.e. 30 mm from the bottom and top surface of the slab. All the tested specimens were freely placed on the steel frame which was mounted to the column base.

Two responses of the concrete slab were measured over time – displacement and strain at its bottom surface. The displacement was measured over time with optoNCDT 2300 laser sensor with scanning frequency of 49 kHz. The sensor was placed inside the column base, and since scabbing and spalling of the concrete was expected it was protected with a protective shield made from plexiglass. In principle, this was a great idea, yet in some cases concrete debris blocked the view of the laser. The strain was also measured over time with a strain gauge which was glued to the bottom surface of the slab. Due to the concrete scabbing it was not always possible to get the response, however.

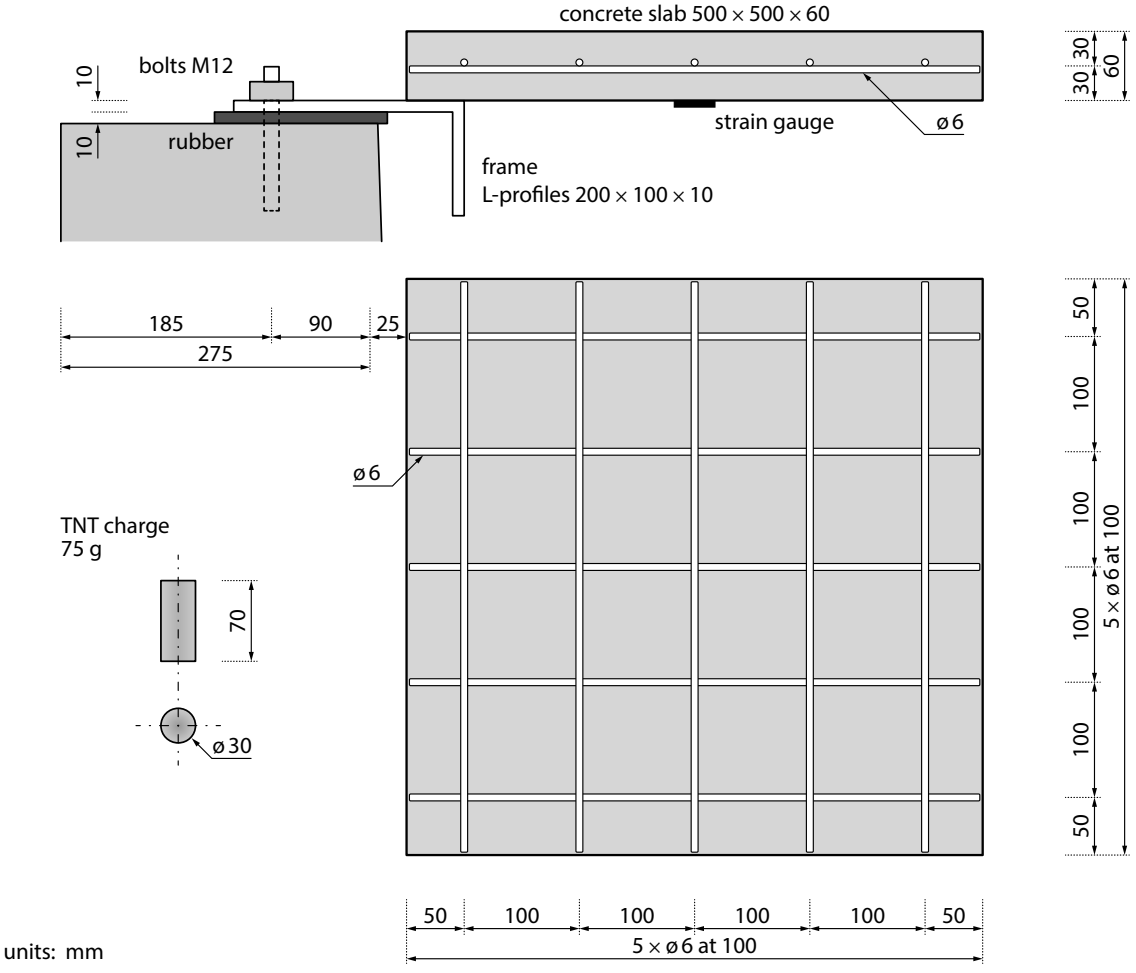

Fig. 9.2. Reinforcement of the concrete slab used in the explosion experiment.

An overview of the experiment configuration can be seen in Fig. 9.3, where in (a) a wooden tripod is shown. The tripod was used for the charge placement. Put simply, the charge was wired to the tripod, leaving the charge 'freely' in the air as shown in (b). The strain gauge can be seen in (c), and as obvious, strain was measured along one of the sides of

the slab, not in the diagonal direction. The laser sensor inside the column base after the so-called detonation calibration is shown in (d).

In addition to the laser sensor and strain gauge, three cameras were used for a documentation over time. The first slow motion camera with rate of 39,000 frames per second was focused on the detonation point. The second slow motion camera with rate of 10,000 frames per second was focused on the concrete slab from a distance, i.e. a bit zoomed out compared to the first camera. And the third camera was a standard one with rate of 30 frames per second for an overview monitoring. When all the measurements and recordings are put together, a completely new perspective on the blast loading can be seen.

(a) experiment setup

(b) placed charge before detonation

(c) strain gauge

(d) laser sensor protected with plexiglass

Fig. 9.3. Photo documentation of the explosion experiment.

9.2 Measurements

Different stand-off distances were tested in the experiment, however, the focus here is on the stand-off distance of 0.1 m for which six specimens were tested in total. Yet, one of the specimens was damaged in a rather non-standard way, therefore, it is not shown in the result overview and was not considered for the material calibration. Each specimen had its own identification code starting with '4X' and a number (1 to 6, number 4 skipped). In Fig. 9.4 and Fig. 9.5, strains and displacements over time are shown, respectively. As in the

previous experiment, positive strains stand for tensile strain and negative displacements stand for a movement downwards. For convenience, all diagrams start at time 0 s, which is also considered the time of the detonation. Simulation results follow the same convention.

It must be noted, however, the strain measurements were not successful as expected. Only one measurement of specimen 4X-6 was retrieved due to the complexity of the experiment. The measurement in Fig. 9.4 (a) shows tensile strain at the bottom surface of the specimen as theoretically expected. The sudden increase in strain up to 4.713×10^{-3} clearly points to the bending of the slab, followed by oscillations as shown in (b) in detail. From the recordings it is clear that every specimen was set in motion upwards after the maximum displacement in the downwards direction was reached. Put simply, every specimen was thrown in the air since the steel frame together with the rubber acted as a spring. Interestingly enough, the subsequent drop is also visible in Fig. 9.4 (a), at approximately 0.2 s.

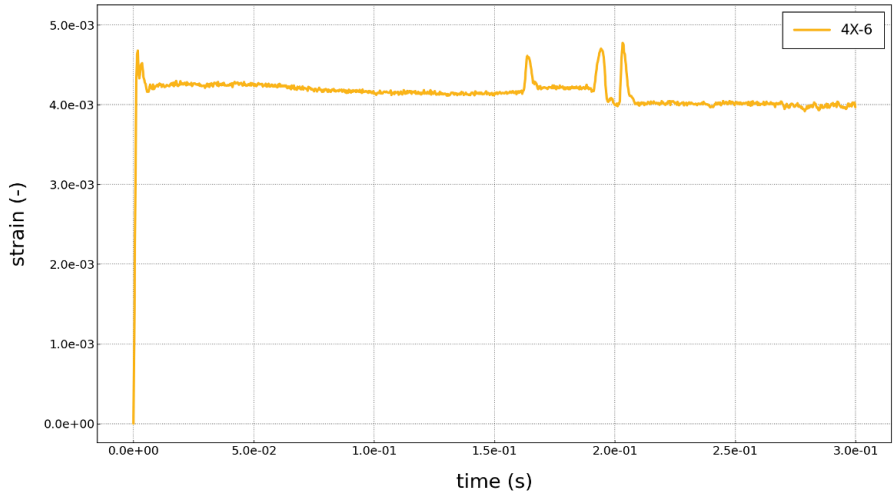

(a) overall

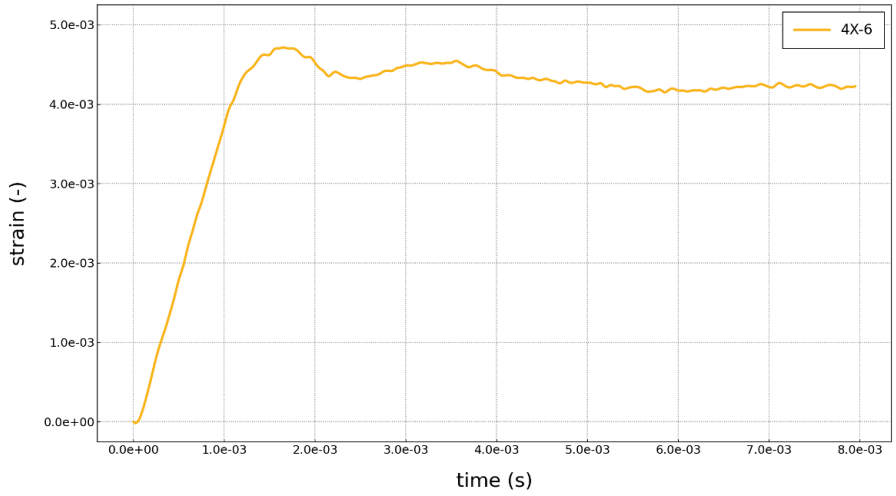

(b) after detonation

Fig. 9.4. Strain at the bottom surface of the slab over time (experiment only).

In contrast, it was possible to use all five displacement measurements for the calibration purposes. In Fig. 9.5 (a), displacements over time are shown, where clearly, after the specimens reached their maximum downwards displacement they were thrown into the air. In the connection to the strain graph, at approximately 0.2 s, the specimens dropped back down. Since it makes no sense to calibrate the behaviour of the specimens after the downwards peak was reached, the time window in Fig. 9.5 (b) was adjusted to better show the region of interest. The overall diagrams are shown as points over time since it was not possible to create continuous diagrams. The reason for that is quite simple, due to debris falling and dust in the air the laser sensor was not able to see the specimen the whole time.

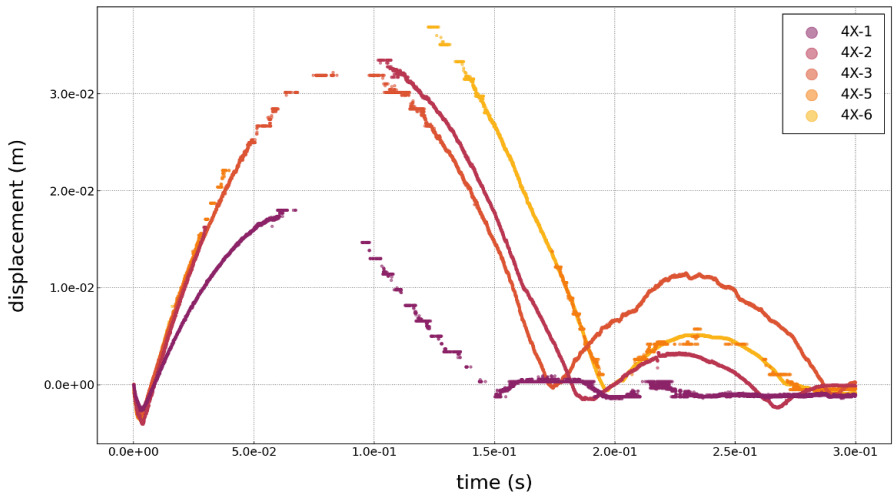

(a) overall

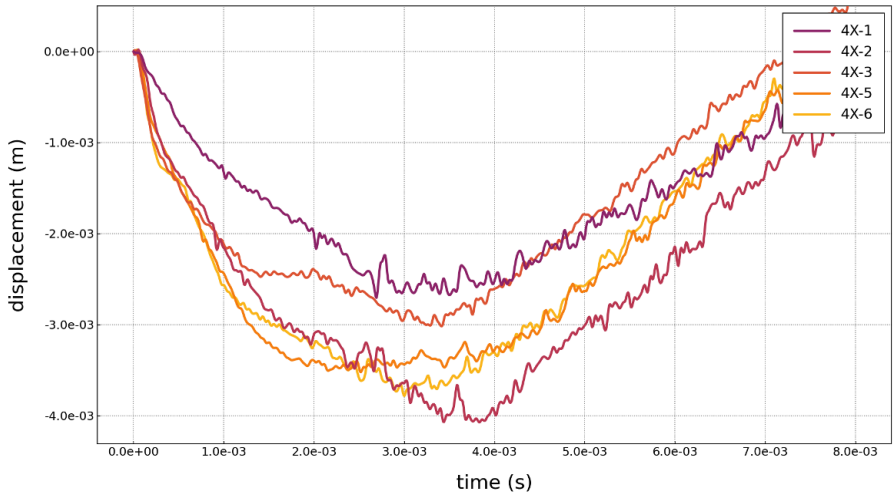

(b) after detonation

Fig. 9.5. Displacement at mid-span of the slab over time (experiment only).

In addition to Fig. 9.4 and Fig. 9.5, the measurements are also collected in Tab. 9.1. Looking at the displacements at mid-span of the slabs, it is found interesting that such a relatively small charge was able to 'bend' such rather rigid slabs down to 4 mm. Of

course, it is important to keep in mind that the values are displacements as a whole, i.e. a rigid motion of the slabs plus their relative deflections. Therefore, the values are strongly influenced by the steel frame, rubber, and bolts (their location and pre-stress force), since together they create a highly nonlinear system.

As already mentioned, it was not possible to retrieve all the strain measurements, therefore, only one value can be found in Tab. 9.1. The strain is again a raw data from the measurement, therefore, positive values stand for tensile strain. The same sign convention is used in the results section. Since a calibration window was missing for the strains, i.e. there was no range in which numerical solutions might vary, it was rather difficult to calibrate to both displacements and the strain measurement. However, when a multi-objective calibration is being done, it is a good practice to find the best parameters for each objective and then compare to the best multi-objective parameter set as well. Usually, the solutions are not far from each other.

specimen	stand-off distance (m)	displacement (m)	strain (-)
4X-1	0.100	-2.705×10^{-3}	-
4X-2	0.100	-4.073×10^{-3}	-
4X-3	0.100	-3.017×10^{-3}	-
4X-5	0.100	-3.520×10^{-3}	-
4X-6	0.100	-3.781×10^{-3}	4.713×10^{-3}

Tab. 9.1. Overview of the explosion experiment measurements.

Strains and displacements are not the only responses to focus on. Very often it is the damage state which has the highest priority. Since strengths of SPH are being examined, all three responses are considered to be the same priority objectives. Only if all three responses of the numerical simulations are within acceptable agreement with the experiment, i.e. the trend of the damage together with displacements and strains are similar to those from the measurements, it can be said, the numerical model is calibrated.

An overview of the damaged slabs after the explosion is shown in Fig. 9.6. As can be seen, the crack patterns are usually the same, except for the specimen 4X-4 which as previously mentioned was damaged in rather different way, therefore, not considered for the calibration.

Based on the photo documentation it can be said that the top surfaces of the specimens show little to no damage but rather blackened patterns caused by the imperfect combustion of the charge. Some products of the explosion were simply imprinted on the surface, the same way the smoke from a fire blacken a white wall. However, the true damage is found at the bottom surface. Except specimen 4X-4, the crack patterns show again a similar trend. That is, from the centre of the slab several cracks propagate in parallel and diagonal directions all the way through the specimen. Micro-cracks are not promoted, only main cracks are opened.

(a) 4X-3 top

(b) 4X-3 bottom

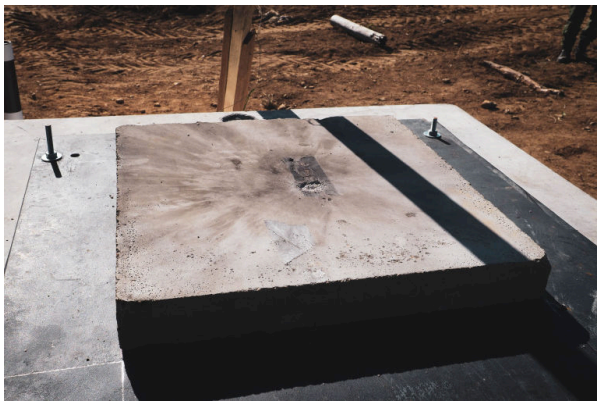

(c) 4X-4 top

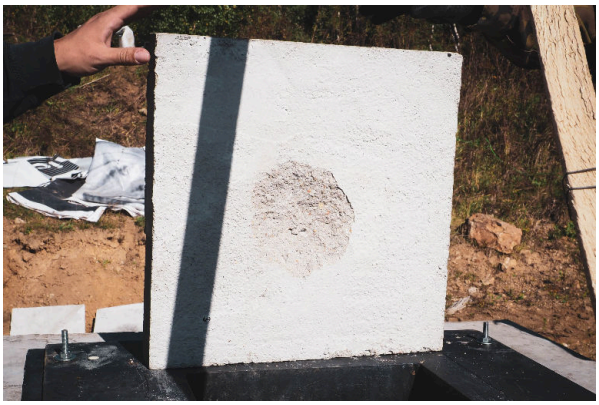

(d) 4X-4 bottom

(e) 4X-5 top

(f) 4X-5 bottom

(g) 4X-6 top

(h) 4X-6 bottom

Fig. 9.6. Damaged specimens after the explosion.

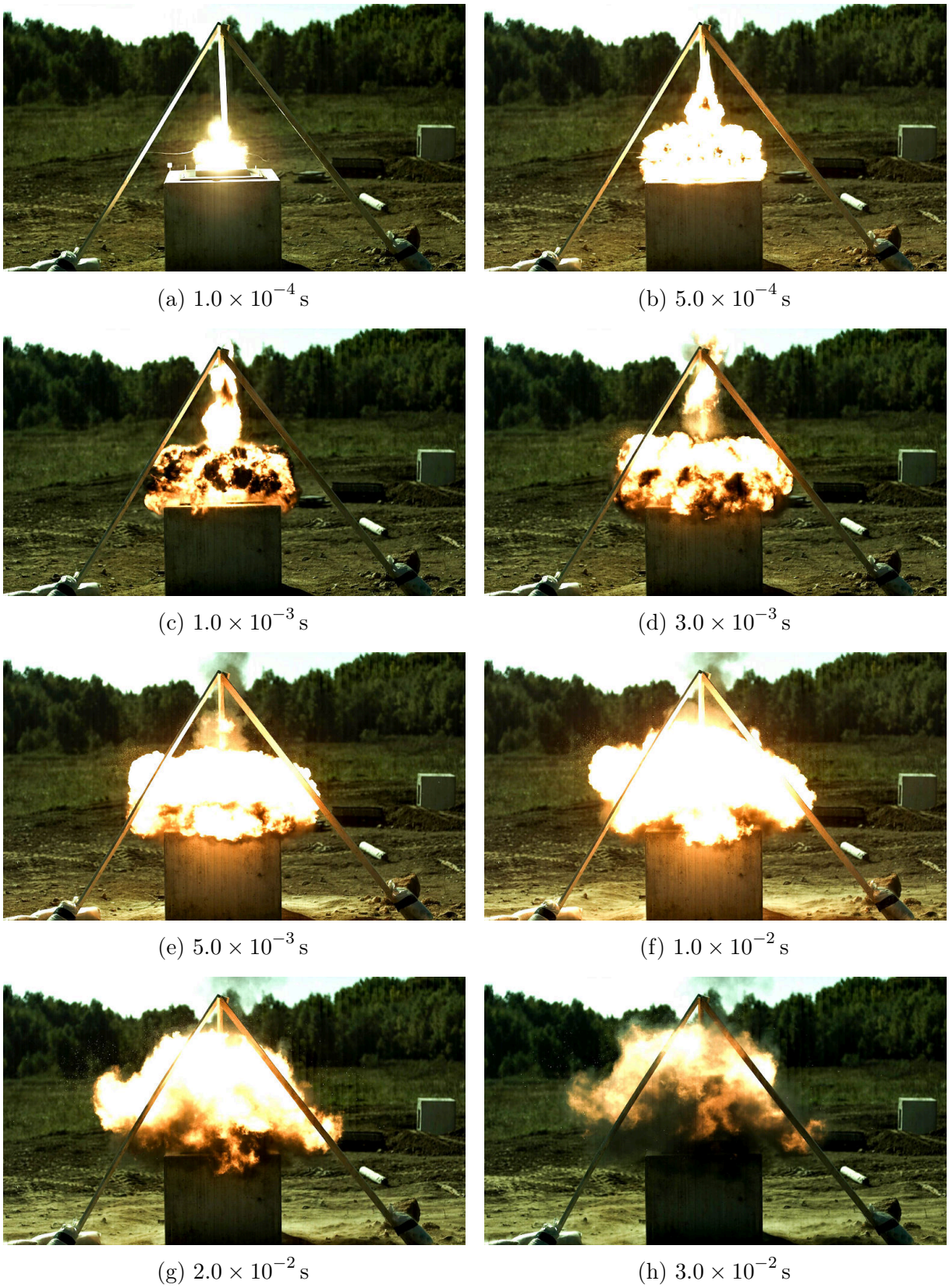

(a) 1.0×10^{-4} s (b) 5.0×10^{-4} s

(c) 1.0×10^{-3} s (d) 3.0×10^{-3} s

(e) 5.0×10^{-3} s (f) 1.0×10^{-2} s

(g) 2.0×10^{-2} s (h) 3.0×10^{-2} s

Fig. 9.7. Time-lapse of the explosion.

It is interesting to see that cracks propagate in parallel and diagonal directions at the same time. Usually only cracks in the diagonal direction are the result of a blast load

(simply supported slabs). When damages as such were found, the author's first question was regarding the supports. In retrospect, it is without a doubt that the 'support system' (the column base, rubber, frame, and bolts) strongly influenced responses of the slabs. This makes the calibration of the concrete parameters even more difficult, since the calibration of the supports must be somehow included.

As previously mentioned, slow motion cameras can provide a completely different perspective into blast simulations. In Fig. 9.7, a time-lapse of the explosion with the stand-off distance of 0.1 m is shown. For convenience, the detonation time was adjusted to time 0 s, therefore, the sequence in Fig. 9.7 corresponds to the strain and displacement diagrams in Fig. 9.4 and Fig. 9.5, respectively.

What should be highlighted first is the shape of the detonation products (the fire ball) just after the detonation in Fig. 9.7 (a). It is important to understand that the charge was cylindrical, therefore, the shape of the detonation products is not spherical. As a result, the formed pressure field in the close distance of the detonation point is not spherical either. This is a common mistake in close-in explosion simulations with simplified methods in which the charge is assumed to be spherical. The experiment discussed here is exactly the case in which the assumption of a spherical charge would lead to errors.

Furthermore, in Fig. 9.7 (b) another important aspect of the explosion can be seen. The shape of the detonation products is i) symmetric and ii) perpendicular to the plane of the concrete slab. It is quite obvious there is a formed 'spear' pointing directly up to the zenith. In fact, this is the core of the discussion in section *Uncertainty in the Charge Placement*.

The following sequence, Fig. 9.7 (c) and (d), shows a formation of dark regions which are nothing else than the product of the imperfect combustion of the charge. Furthermore, at the time of (e) and (f) the temperature of the gasses is much higher than the temperature of the air, therefore, they start to rise while the surroundings are illuminated. However, at this point the blast wave is already dissipated in space, hundreds meters from the detonation point. The time-lapse is quite spectacular.

9.3 Numerical Model

As in previous **Chapter 8** *Experiment – High Velocity Impact*, the numerical model was coupled with FEM, yet the load itself (the explosion) was simulated with pure SPH. The structural parts of the model are discussed first, the charge follows.

For the same reasons as in the previous experiment, the support system was modelled with FEM. Without going into details, strictly hexagonal solid elements with reduced integration points (constant stress) were used. The model is shown in Fig. 9.8 and as it is clear from the details, different element sizes were used. This is usually not a problem if treated correctly in the contact definition. The rubber and steel frame had to fulfil another requirement however – at least three elements over the thickness since the brick elements had only translational degrees of freedom (DOF). For instance, the rubber had assigned a hyper-elastic material which could result in volumetric errors if only one or two elements over the thickness were used in corner details. The FEM part of the reinforcement is shown

in Fig. 9.9 in a cross-section while SPH particles are hidden. When compared to Fig. 9.2, it is clear that both layers of the reinforcement are in the same layer, sharing the node in their crossing. This is in contrast to reality where the reinforcing wire mesh is also welded but in two layers. The error resulting from such a simplification is usually minimal.

The column base was placed on a rigid ground. The idea of a deformable ground was also considered, however. Preliminary simulations with a variable ground stiffnesses were calculated, showing almost no effect. With the given mass of the column base of 2040 kg it was found that the 75 g charge is not able to give sufficient momentum to the base to have an impact on the slab deformation. In other words, before the concrete base starts to move, the concrete slab is already deformed. However, bigger charges or explosives with a better performance than TNT might deliver enough energy to deform the base itself. Therefore, the idea of a deformable ground should be tested when possible.

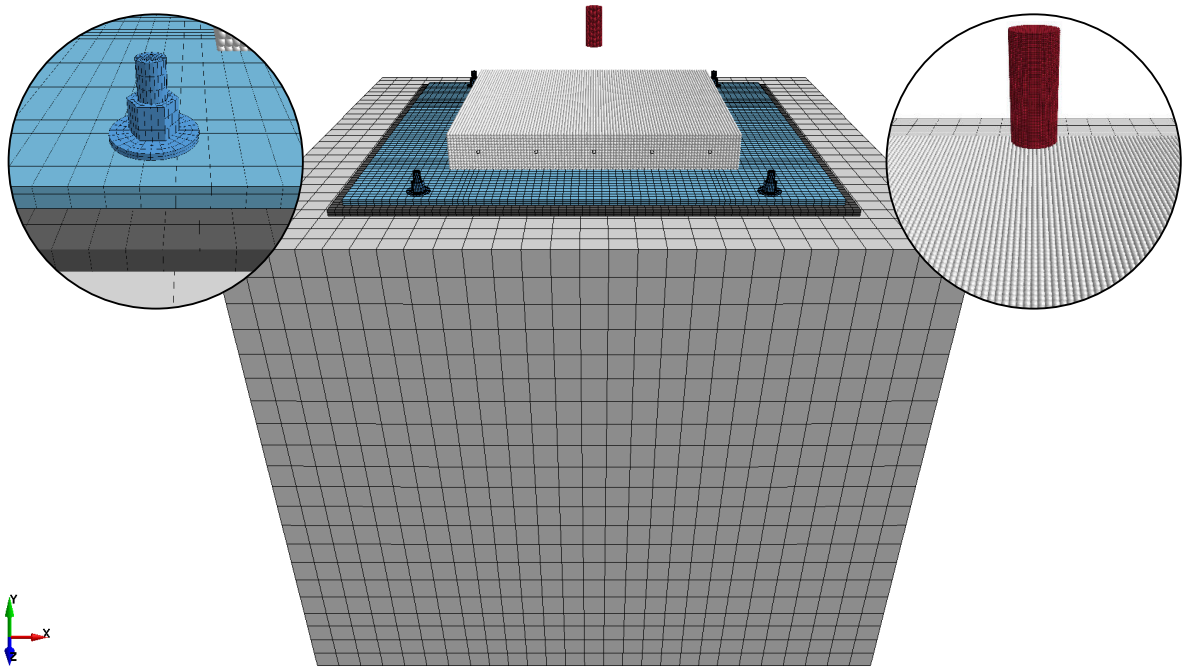

Fig. 9.8. Numerical model of the explosion experiment.

As in the previous experiment, the concrete portion of the reinforced slab was modelled with SPH and the reinforcement with the proposed coupled SPH-FEM sublayer approach. As previously discussed in **Chapter 4** *Coupling SPH and FEM* and section *Sublayer Coupling with FEM*, the coupling is valid as long as a proper ratio of nodal and particle masses is defined, see Fig. 6.8. With respect to these chapters, equal mass distribution was used. That is, FEM nodes and SPH particles had the same mass, and when combined, the real mass of the reinforcement was captured. However, the same cannot be used for the Young's modulus since SPH masses directly influence the lumped volumes, therefore, have an impact on the resulting stiffness. For that reason, the Young's modulus of numerical zero was used for SPH as also previously discussed in section *Sublayer Coupling with FEM*. Since the FEM reinforcement and SPH sublayer shared the same nodes/particles, the coupling with the SPH concrete was done in natural way with overlapping support domains. The logic of the reinforcement composition is shown in Fig. 9.10.

Regardless of the coupling with shared nodes, which was used only for the reinforcement, the concrete slab interacted with the support system through the penalty-based contact. The logic of the contact implementation can be found in [185], therefore, there is no need to discuss it here further. The same contact algorithm was used for the interaction between the rest of the FEM parts but with one difference. The penetration detection was not nodal-based but segment-based. Put simply, when FEM elements start to warp during their deformation, the nodal-based detection might not be enough to prevent edge-to-face penetrations. In more detail in [185].

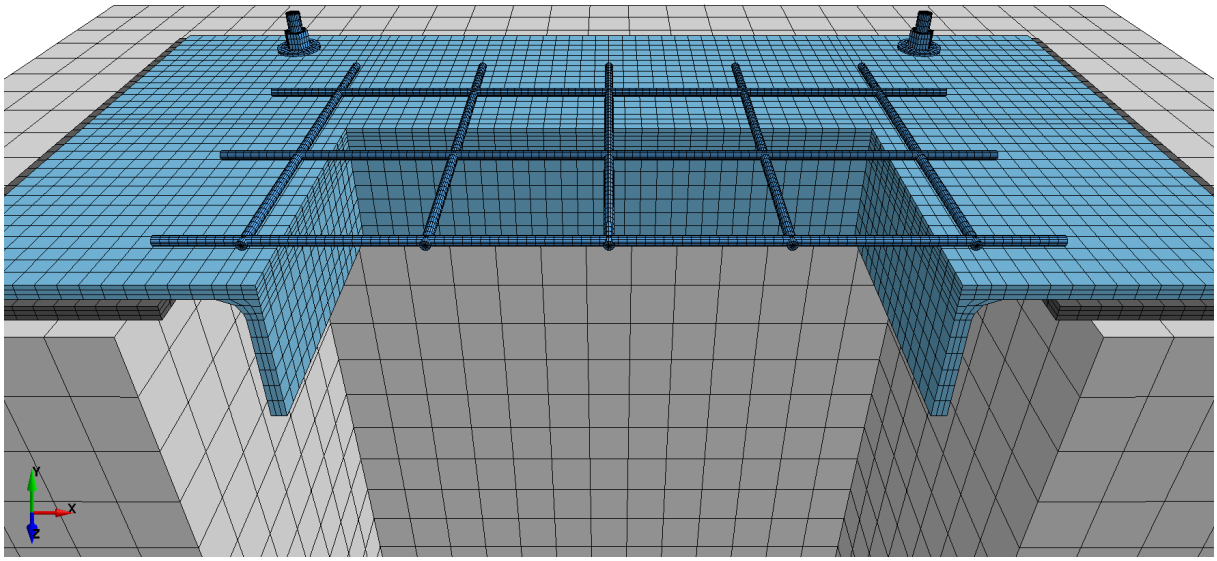

Fig. 9.9. Numerical model of the explosion experiment in a cross-section with uncovered reinforcement (no SPH particles shown).

The SPH part of the reinforced slab (the concrete) was generated into a cubic lattice with a particle spacing $\Delta x = 5\,\text{mm}$ in all three directions. This resulted in more than 135,000 SPH particles in total, including those in the reinforcement sublayer for the FEM coupling. As discussed in section *Variable Smoothing Length*, it is important that the particle spacing of all SPH parts is relatively similar, therefore, the FEM beam elements of the reinforcement were 5 mm long. And since the SPH coupling sublayer used shared nodes, this resulted in a particle spacing $\Delta x = 5\,\text{mm}$.

The coupling forces in this particular case were relatively low, however. This can be explained as a result of the reinforcement location in the middle of the height which is also the neutral axis of the slab. Therefore, the coupling would work quite well even for different particle spacings. As long as the support domains of the separate SPH parts are relatively similar and not, e.g. 100 times different, there should be no issue.

The material parameters for all structural parts are collected in Tab. 9.2 for the concrete slab, in Tab. 9.4 for the steel reinforcement, in Tab. 9.5 for the construction steel which was used for the frame and bolts, in Tab. 9.6 for the rubber, and in Tab. 9.3 for the concrete column base.

ρ	mass density (kg/m^3)	2124.0
E	Young's modulus (GPa)	26.36
G	shear modulus (GPa)	11.46
K	bulk modulus (GPa)	12.55
ν	Poisson's ratio (-)	0.15
f_c	compressive strength (MPa)	30.0
f_t	tensile strength (MPa)	2.4
α	TXC surface constant term (Pa)	1.4500×10^{7}
θ	TXC surface linear term (-)	2.9650×10^{-1}
λ	TXC surface nonlinear term (Pa)	1.0510×10^{7}
β	TXC surface exponent (Pa^{-1})	1.9290×10^{-8}
α_1	TOR surface constant term (-)	7.4730×10^{-1}
θ_1	TOR surface linear term (Pa^{-1})	1.1510×10^{-9}
λ_1	TOR surface nonlinear term (-)	1.7000×10^{-1}
β_1	TOR surface exponent (Pa^{-1})	7.0570×10^{-8}
α_2	TXE surface constant term (-)	6.6000×10^{-1}
θ_2	TXE surface linear term (Pa^{-1})	1.3870×10^{-9}
λ_2	TXE surface nonlinear term (-)	1.6000×10^{-1}
β_2	TXE surface exponent (Pa^{-1})	7.0570×10^{-8}
N_h	hardening initiation (-)	1.0000
C_h	hardening rate (-)	0.0000
R	cap surface aspect ratio (-)	5.0000
X_0	cap pressure axis intercept (Pa)	9.0540×10^{7}
W	hardening law maximum compaction (-)	5.0000×10^{-2}
D_1	hardening law linear exponent (Pa)	2.5000×10^{-10}
D_2	hardening law nonlinear exponent (Pa^2)	3.4920×10^{-19}
B	compressive softening parameter (-)	1.0000×10^{2}
G_{fc}	compressive fracture energy (J/m^2)	6.8380×10^{3}
D	tensile/shear softening parameter (-)	1.0000×10^{-1}
G_{ft}	tensile fracture energy (J/m^2)	6.8380×10^{1}
G_{fs}	shear fracture energy (J/m^2)	6.8380×10^{1}
μ	compressive damage transition power (-)	5.0000
υ	tensile damage transition power (-)	1.0000
ξ	moderate pressure adjustment parameter (-)	0.0000
η_{c_0}	compressive fluidity parameter (-)	1.0030×10^{-4}
$\bar{\eta}_c$	compressive fluidity power (-)	7.8000×10^{-1}
η_{t_0}	tensile fluidity parameter (-)	6.1760×10^{-5}
$\bar{\eta}_t$	tensile fluidity power (-)	4.8000×10^{-1}
ψ	ratio of shear to tensile fluidity parameter (-)	1.0000
ω	power applied to fracture energies (-)	0.0000

Tab. 9.2. Material parameters of CSCM for the slabs used in the explosion experiment simulations.

Both concrete parts the slab and base used the Continuous Surface Cap Model (CSCM) but with different concrete classes. The concrete for the slabs was calibrated to class C30/37, i.e. the unconfined or uniaxial compressive strength (UCS) value of 30 MPa, and class C45/55 for the column base, i.e. the UCS of 45 MPa. Note that the base was prefabricated and the concrete class was guaranteed by the manufacturer, therefore, not 'calibrated'. Also in this experiment, the question was if it makes sense to include the constitutive model strain-rate effects or not. The speed of the blast wave is incomparable to the previous experiment, yet it is not a structure-to-structure interaction but fluid-to-structure. For calibration purposes, however, both variants were tested.

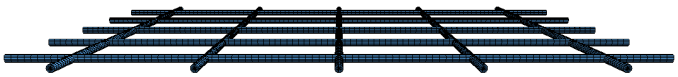

(a) FEM reinforcement

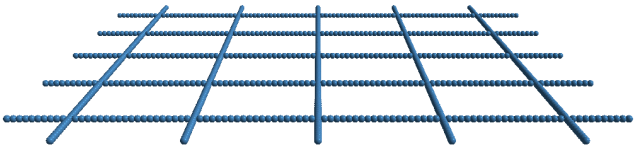

(b) SPH sublayer for the concrete and reinforcement coupling

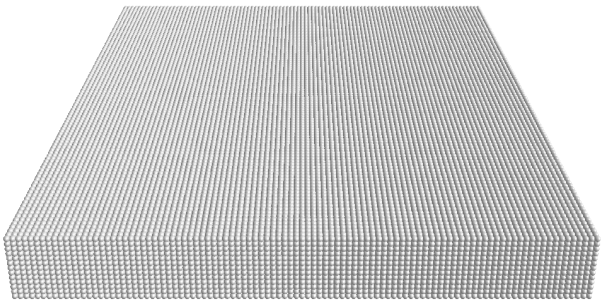

(c) SPH concrete

Fig. 9.10. Implementation of the FEM reinforcement into the SPH model.

Steel class B500B was used for the reinforcement as it was the case in **Chapter 8** *Experiment – High Velocity Impact*. Unfortunately, there was too little information available about the reinforcing wire mesh used in the experiment. Therefore, the best estimate with respect to [209] was the yield strength of 500 MPa. The material model was again the simplified elastoplastic (bilinear) with the tangent modulus of 0.5% of the initial stiffness. Since the yield strength was not reached, the tangent modulus is rather not important.

The structural steel used for the frame was estimated to class S355 [239], which translated to numbers for profiles with thickness ≤ 40 mm gives the yield strength of 355 MPa. The material model was again the simplified elastoplastic (bilinear). Although the yield strength and tangent modulus were defined, the maximum stress reached was still far from the yielding. The same applies for the bolts, which were simulated without pre-stress, therefore, they were in the elastic state throughout the simulation. Note that a sensitivity study was performed in which uncertain parameters were varied (including the pre-stress value applied to the bolts). In the study, the axial stress in bolts often reached the yielding point.

However, the study is being published separately to the thesis, therefore, not discussed here where the focus is on the SPH performance.

ρ	mass density (kg/m^3)	2425.0
E	Young's modulus (GPa)	30.38
ν	Poisson's ratio (-)	0.15
f_c	compressive strength (MPa)	45.0
f_t	tensile strength (MPa)	3.1
G_f	fracture energy (J/m^2)	92.3

Tab. 9.3. Material parameters of CSCM for the base used in the explosion experiment simulations.

Regarding the rubber, initial studies were performed, pointing to the fact that deformation of the concrete slab is strongly influenced by the mechanical properties of the rubber layer. Without going into details, the Mooney-Rivlin material was used for the rubber [240, 241]. The stiffness related material parameters C_{10} and C_{01} are very often available for various rubber types. Based on [242], the stiffness parameters were adjusted to the Young's modulus of 5 GPa, which corresponds to a moderate/hard rubber. Other combinations of C_{10} and C_{01} can be found in [243, 244, 245, 246].

ρ	mass density (kg/m^3)	7830.0
E	Young's modulus (GPa)	200.0
E_{tan}	tangent modulus (GPa)	1.0
ν	Poisson's ratio (-)	0.29
f_y	yield strength (MPa)	500.0

Tab. 9.4. Material parameters of the steel reinforcement used the in explosion experiment simulations.

There are several approaches which can be used to simulate a blast load. The very first choice because of its simplicity is usually the empirical approach termed ConWep [247] or just simply the 'pressure projection' method [248, 249, 250]. As the name suggests, the empirically calculated pressure is directly mapped onto the outer surface of the loaded specimen. The pressure is a function of time, and since the pressure applied to the model corresponds to a directly given value it is possible to capture the positive phase of the blast wave (overpressure), as well as the negative phase (suction). Unfortunately, information about shape of a charge is not taken into account and it is not possible to simulate potential reflections and interferences of the blast wave (even though a direct reflection from the loaded surface can be included as a multiplier of the incident pressure).

The most versatile approach for blast simulations is without a question the combined Lagrangian/Eulerian FEM method. Today simple termed Multi-Material Arbitrary Lagrangian-Eulerian (MM-ALE) [249, 250, 251, 252, 253]. Detonation products, air, and

other fluids are simulated within the Eulerian domain where material flows through the computational mesh. The structural parts of the model are simulated with the Lagrangian elements where the material deforms with the mesh. The interaction between both domains is handled with coupling algorithms, e.g. penalty or constraint-based interface methods. These are very often referred to as fluid-structure interaction (FSI) algorithms. Blast wave reflections, interferences, shape of the charge, and overall complex behaviour can be captured.

ρ	mass density (kg/m^3)	7850.0
E	Young's modulus (GPa)	200.0
E_{tan}	tangent modulus (GPa)	2.0
ν	Poisson's ratio (-)	0.27
f_y	yield strength (MPa)	355.0

Tab. 9.5. Material parameters of the construction steel used in the explosion experiment simulations.

Since the ConWep and MM-ALE can be coupled with the Lagrangian elements, it would be possible to use both approaches for the blast wave generation together with SPH. However, particle methods can be used directly to simulate an explosion. Interestingly enough, many standard methods can be used for exactly this purpose; the already *mentioned* SPH, but also the Discrete Element Method (DEM), the Corpuscular Particle Method (CPM), and the CPM-based Particle Blast Method (PBM). When particles discretize explosive materials and subsequently approximate detonation products, the fact that the material can be tracked very easily and therefore provide a great amount of information can be advantage. However, one should realize how is the blast wave delivered to the structure.

ρ	mass density (kg/m^3)	1100.0
E	Young's modulus (MPa)	5.0
ν	Poisson's ratio (-)	0.4997
C_{10}	Mooney-Rivlin constant (MPa)	0.7785
C_{01}	Mooney-Rivlin constant (MPa)	0.0550

Tab. 9.6. Material parameters of the rubber used in the explosion experiment simulations.

In case of an air burst, a charge is detonated in the air, touching nothing but the air, yet surroundings are hit by a blast wave. How is it possible? The transport mechanism is mediated by the air itself. After the detonation, the charge is instantly converted to a superheated gas (a part of detonation products), i.e. trying to occupy a space 10,000 to 20,000 times its original volume (based on the explosive). As the detonation products start to expand, the surrounding air is compressed and the blast wave (pressure) is formed. If there are no obstacles, the wave propagates through the air in the direction from the detonation point. It does not mean the air travels, but the pressure, the air simply moves

back and forth. In a vacuum, however, the transport mechanism is quite different since there is no air, no medium. Assuming the explosive is already detonated, fully converted into an expanding gas, the only transport mechanism is the moving gas itself, i.e. when the detonation products *touch* surroundings. However, such a 'blast wave' will only continue until its material, the medium, is spread out too far to interact.

In numerical simulations, it is up to the user to decide if the air domain should be modelled or not. However, it is a good standard to include the air domain if possible [250]. There are cases in which the air domain can be completely omitted, e.g. buried charges [254, 255, 256, 257, 258] or should not influence the solution significantly, e.g. close-in explosions [259, 260]. If however the air domain or other surrounding medium is omitted, the negative phase cannot be captured. For close-in explosions, however, the suction phase is not so important, especially when smaller charges are used. Both variants with and without the air domain were initially tested. Since differences between both were minimal, the air domain was neglected.

The charge was modelled with pure SPH. To capture the true potential of the detonation products the Jones-Wilkins-Lee (JWL) Equation of State (EOS) [261, 262, 263, 264, 265] was used in combination with the burn material model [266, 267]. The detonation process was based on the Chapman–Jouguet (CJ) theory [268, 269] and the Rankine-Hugoniot (RH) jump conditions [270, 271, 272]. In the JWL EOS, pressure is defined as

$$p_{\text{EOS}} = A\left(1 - \frac{\omega}{R_1 V}\right)e^{-R_1 V} + B\left(1 - \frac{\omega}{R_2 V}\right)e^{-R_2 V} + \frac{\omega E}{V}, \tag{9.3.1}$$

where parameters A, B, R_1, and R_2 are the constant fitting parameters associated with the JWL EOS, while the parameter ω is assumed the constant material parameter which can characterize the Grüneisen function Γ [265]. The form in (9.3.1) is incomplete since Γ was assumed constant as $\Gamma = \omega$ [265, 273], therefore, $p_{\text{EOS}} = p(E, V)$. Note that the parameters A and B have a dimension of pressure, while the other constants are dimensionless. The parameter E is the current detonation energy density or the so-called detonation energy per unit volume, and V is the volume relative to the undetonated state defined as

$$V = \frac{v}{v_0} = \frac{\rho_0}{\rho}, \tag{9.3.2}$$

where v is the volume of the detonation products, v_0 is the volume of the undetonated explosive, ρ is the density of the detonation products, and ρ_0 is the density of the undetonated explosive. Note that the JWL EOS symbols were taken as usually found in literature. For convenience, the full list is collected in *Symbols in JWL EOS*. From (9.3.1), the actual released pressure p from the detonated material is defined as

$$p = F p_{\text{EOS}}, \tag{9.3.3}$$

where F is the burn fraction of the explosive. Typically, the JWL parameters for detonation products are fit to data for the release isentrope from the CJ state [274] and (9.3.3) must satisfy the RH jump conditions for volume

$$V_{\mathrm{CJ}} = \frac{v_{\mathrm{CJ}}}{v_0} = 1 - \frac{p_{\mathrm{CJ}}}{\rho_0 D^2}, \tag{9.3.4}$$

and for energy

$$E_{\mathrm{CJ}} = E_0 + \frac{p_{\mathrm{CJ}}}{2}(1 - V_{\mathrm{CJ}}), \tag{9.3.5}$$

where again $v_{\mathrm{CJ}}, p_{\mathrm{CJ}}$, and E_{CJ} are the volume of detonation products, pressure, and current detonation energy density but for the release isentrope from the CJ state. The parameter D is the detonation velocity of the explosive and E_0 is the initial value of the previously defined detonation energy per unit volume E. Clearly $E = e\rho$ where e is the specific detonation energy or the so-called detonation energy per unit mass. More about the model implementation can be found in [201, 274]. Note that the unit of the detonation energy density (detonation energy per unit volume) is $\mathrm{J/m^3}$ which is again the unit of pressure since $\mathrm{J/m^3} = \mathrm{N/m^2}$.

The material and EOS parameters of the TNT are summarized in Tab. 9.7. The initial mass density of the charge was recalculated from available information, i.e. from the given volume (diameter of 30 mm and height of 70 mm) and the given mass (75 g). The density was indeed lower than normally used, yet still in range when compared to [275, 276, 277, 278] and [279]. To consider the density decrease, the initial detonation energy density was taken into account with respect to [275].

ρ_0	initial mass density ($\mathrm{kg/m^3}$)	1515.0
D	detonation velocity (m/s)	6930.0
p_{CJ}	Chapman–Jouguet pressure (GPa)	21.0
A	linear coefficient (GPa)	373.8
B	linear coefficient (GPa)	3.747
R_1	nonlinear coefficient (-)	4.15
R_2	nonlinear coefficient (-)	0.90
ω	nonlinear coefficient (-)	0.35
E_0	initial detonation energy density (GPa)	6.0
V_0	initial relative volume (-)	1.0

Tab. 9.7. Material parameters of the TNT charge used in the explosion experiment simulations.

Two variants of the SPH charge were generated for testing purposes, both with a particle spacing of approximately $\Delta x = 1\,\mathrm{mm}$ in all three directions, both with more than 50,000 SPH particles. The only difference was the initial particle distribution. As highlighted

many times in the thesis, it is a general recommendation to use a uniform particle distribution especially with brittle materials; see section *Variable Smoothing Length* and section *Influence of the Particle Discretization Density*. However, the SPH charge is meant to simulate detonation products rather than the solid state of the charge. The charge is in the solid state only at the beginning, after the detonation however, SPH particles represent the detonation products.

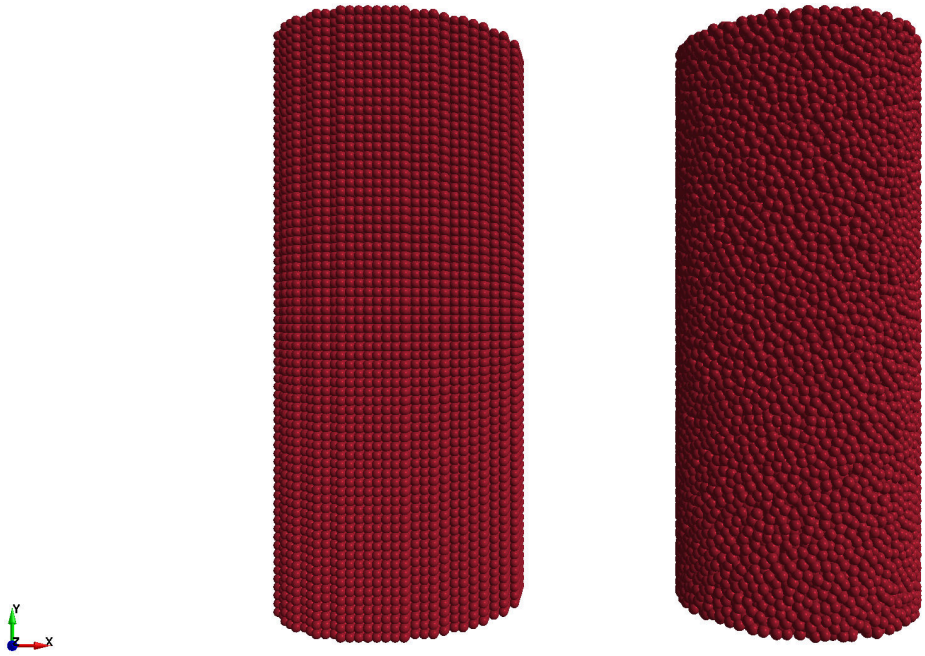

(a) uniform (b) Voronoi

Fig. 9.11. Initial discretization comparison of the charge (front view).

In Fig. 9.11 two particle distributions of the same charge are shown. The charge on the left is with a uniform distribution (a cubic lattice), the charge on the right is generated with the Voronoi tessellation, also known as Voronoi decomposition, or Voronoi partition. The number of particles is approximately the same in both charges, also the diameter and height. Yet, there is one visual difference. The uniform particle distribution can never approximate the cylinder smoothly. In contrast, the Voronoi tessellation places points directly on surfaces of the cylinder, therefore, the shape is quite smooth. This point was also discussed in section *Insights*. From the computational point of view there is no difference in the initial state. The smoothness of the initial geometry plays a significant role after the detonation, however.

To show the impact of the initial discretization, both charges were detonated at their centre of gravity (CG) while the air domain was neglected. In Fig. 9.12, top views of both particle distributions are shown at time 2.5×10^{-4} s after the detonation. The maximum axial distance (in a horizontal plane from the detonation vertical axis) in both cases is 1.5 m, yet differences in particle distributions are obvious. The charge with the uniform distribution shows 'spikes' pointing in the direction out from the detonation point. The

charge with the Voronoi distribution shows a rather smooth circular profile. It is important to understand that in case of the charge with the uniform distribution the spikes are not related to the Rayleigh-Taylor instability [280] since there was no air domain to interact with. Furthermore, the spikes are not an outcome of the burn model or the JWL EOS. They are formed due to presence of sharp corners in the initial particle distribution.

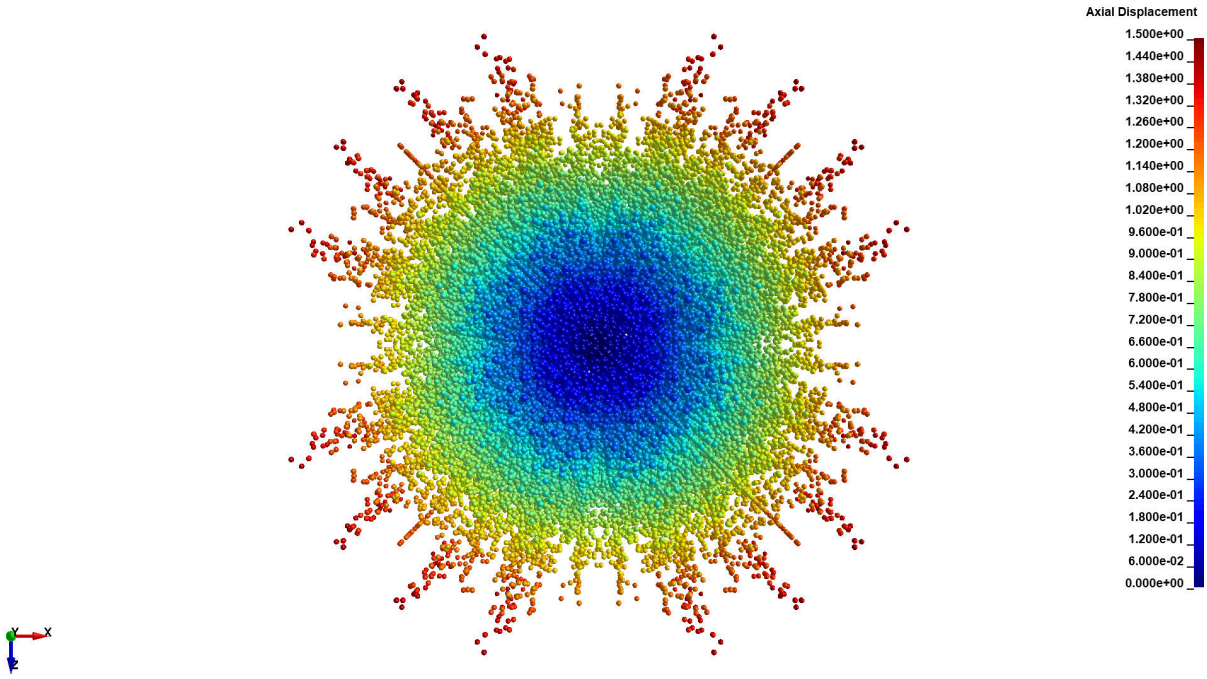

(a) uniform

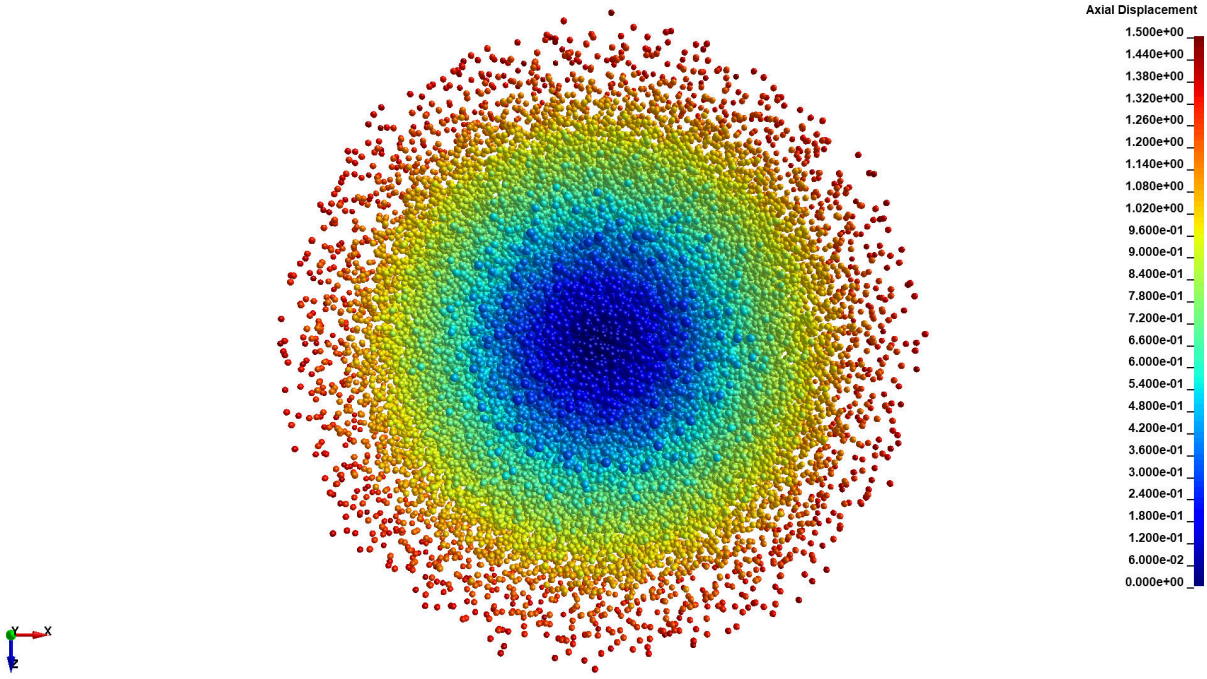

(b) Voronoi

Fig. 9.12. Particle distributions comparison after the detonation (top view).

Since the air domain was neglected, there is no answer which model is better. Furthermore, the spikes are noticeable only when their axial distance from the detonation point is more than 1.25 m. For axial distances smaller than 1 m, both models show a smooth circular profile. Since the concrete slab is only 0.5 m × 0.5 m from the top view, and the charge is only 0.1 m from the slab, both models can be used. That said, and due to the simplicity of the particle generation into a cubic lattice, the charge with the uniform distribution was used.

All SPH components used the same isotropic Eulerian kernel Fig. 2.36 together with the cubic spline Fig. 2.8 with $h = 1.2\,\Delta x$ and $\kappa = 2$. The support domains were not constant but dynamic in time and space, driven by (2.4.36). Furthermore, the conservation laws in the SPH framework defined in (2.10.15), (2.10.16), and (2.10.17) were used for the continuity, momentum, and energy equation, respectively. Shock fronts were smoothed out with the Monaghan type artificial viscosity (2.9.3) with parameters $\alpha_l = 1$ and $\beta_q = 1$. The renormalization proposed in [35] was used to improve stress profiles at the boundaries of the SPH domains, yet no special treatment was applied to alleviate the tensile instability.

Since SPH particles were used not only for the structural parts but the fluid part as well (detonation products), it was necessary to ensure that the developing pressure field after the detonation is sufficiently smooth. For that reason, yet another SPH correction was employed. As discussed in section *Density Correction*, the Shepard filter defined in (2.12.3) and (2.12.4) smooths out the density field and as a consequence the pressure field as well. Using both the renormalization and Shepard filter, the simulations exhibited the expected behaviour.

9.4 Results

As it is particularly important to show a sufficient proof of the SPH functionality in structural dynamics, it is crucial to present a calibrated model which is able to represent all the measured responses. Therefore, the focus should be on displacements over time, strains over time, and damage of the specimens after the explosion. In this case, however, the experimental measurements of strains are limited to only one signal. Yet, for the displacements and damage a sufficient number of measurements is available. Note that the calibration of the material parameters is not discussed here as it is not the goal of the thesis.

As previously mentioned, the detonation time was set/adjusted to 0 s for the experimental measurements and simulations. Thanks to that, the results can be conveniently compared as shown in Fig. 9.13 for the strains and in Fig. 9.14 for the displacements.

Starting with the strain diagrams; it can be said that the overall trend was captured quite well by both models with and without the rate effects (constitutive model strain-rate effects shortened as in the previous chapter). The peak value in tension of both models is comparable with the peak measured in the experiment, i.e. 4.713×10^{-3}. Both models show a rather brittle behaviour, however. This is especially pronounced in the model without the rate effects considered. In contrast, the model with the rate effects shows initial 'rigidity', yet sort of softening or a change in the failure mode over time. Therefore,

the model with the rate effects gives a better approximation in strains compared to the second model. However, it could very well be that the strain behaviour of specimen 4X-6 was quite unique. Without having another measurements for comparison, the statement that the model with the rate effects is better might be misleading.

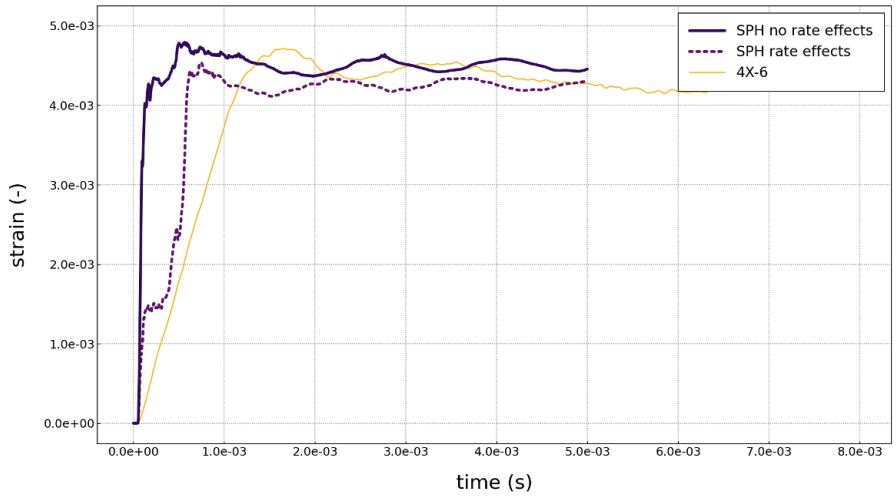

Fig. 9.13. Strain at the bottom surface of the slab over time (experiment vs. simulation).

The comparison of displacements in Fig. 9.14 shows again a good agreement between both simulations and the experimental measurements. The gradient of the initial motion downwards is quite well captured for four out of the five specimens. The reason for this is that the initial part shows only the displacement or rather the deflection of the concrete slab itself, yet not the deformation of the support system. After the time of 1×10^{-3} s however, very strong oscillations appear. This behaviour is evident not only in the simulations but in the measurements as well, e.g. specimen 4X-3 (red curve). In the measurements, however, the frequency seems to be lower, reduced, or damped even. The only damping in the numerical simulations was the artificial viscosity.

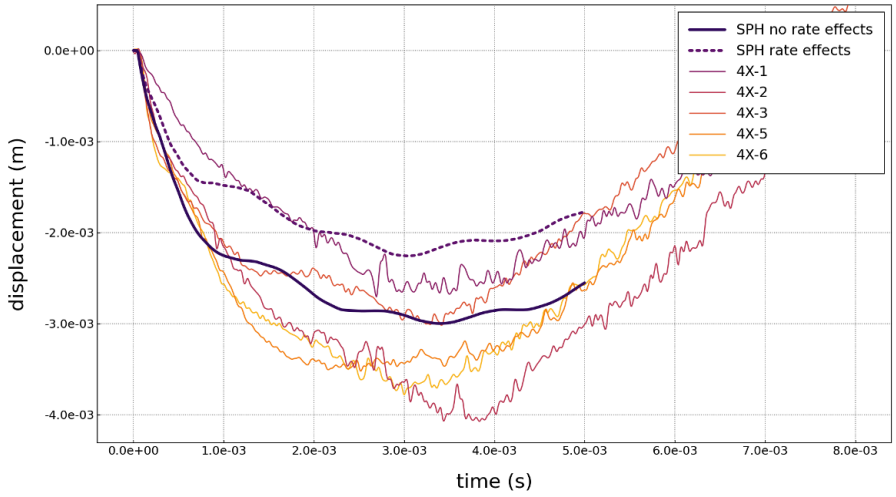

Fig. 9.14. Displacement at mid-span of the slab over time (experiment vs. simulation).

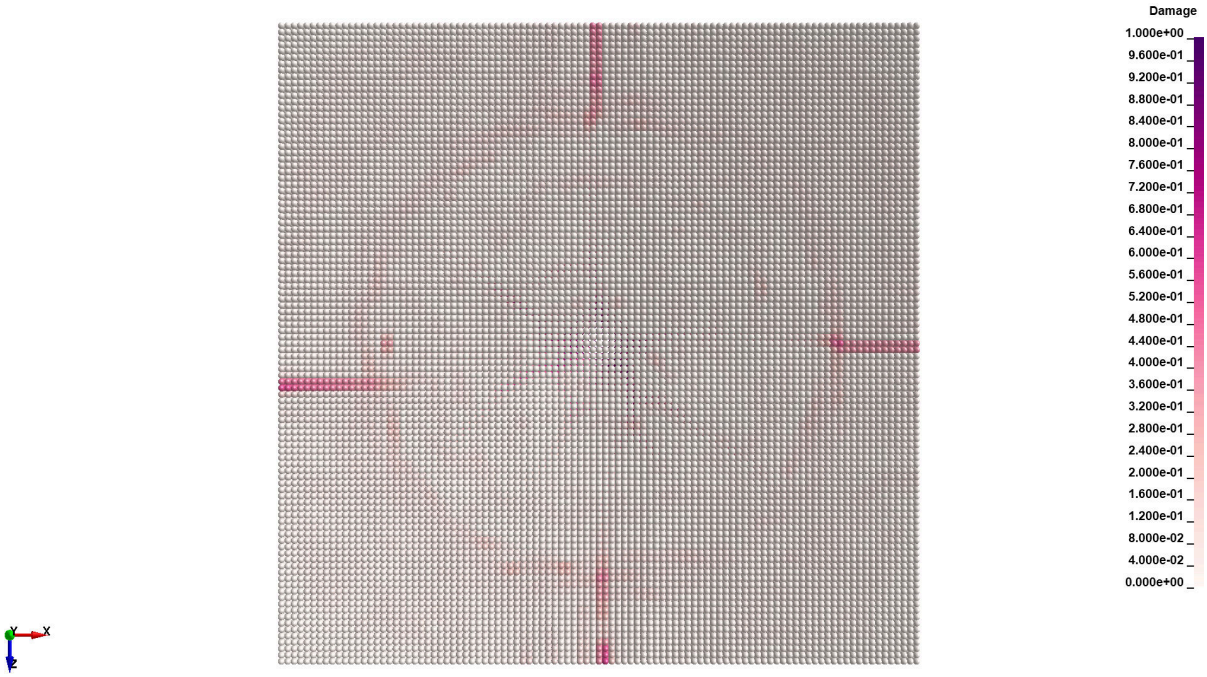

(a) no rate effects

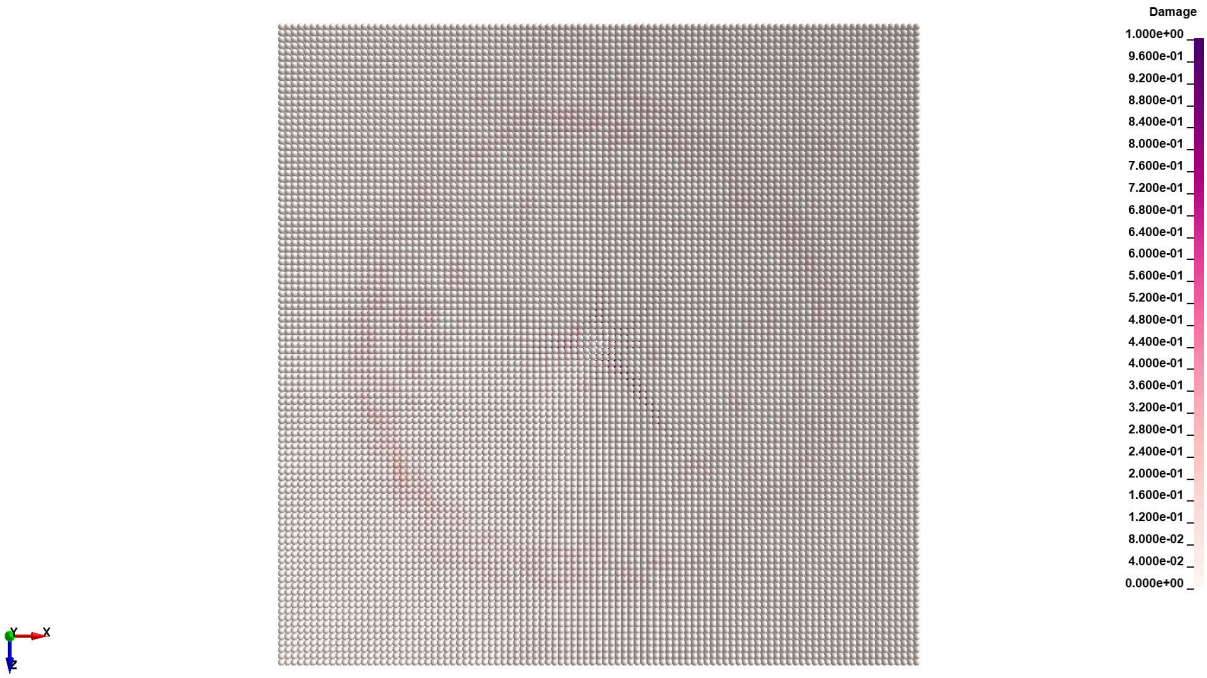

(b) rate effects

Fig. 9.15. Damage comparison of the model with and without the constitutive model strain-rate effects (top view).

Since the maximum displacements at mid-span of the slabs are given by their rigid motion and their actual deflection, it can be said that the calibration was successful. Clearly, a better response is given by the model without the rate effects with the maximum displacement of 3 mm. The value fits nicely to the average of all the measurements in Tab. 9.1. In contrast, the model with the rate effects gives only 2.3 mm with is rather a

lower bound of the measurements. Both models however show maximum displacement at the correct time, i.e. between 3×10^{-3} and 4×10^{-3} s. Since the upwards motion was not part of the calibration, the simulation end time was at 5×10^{-3} s.

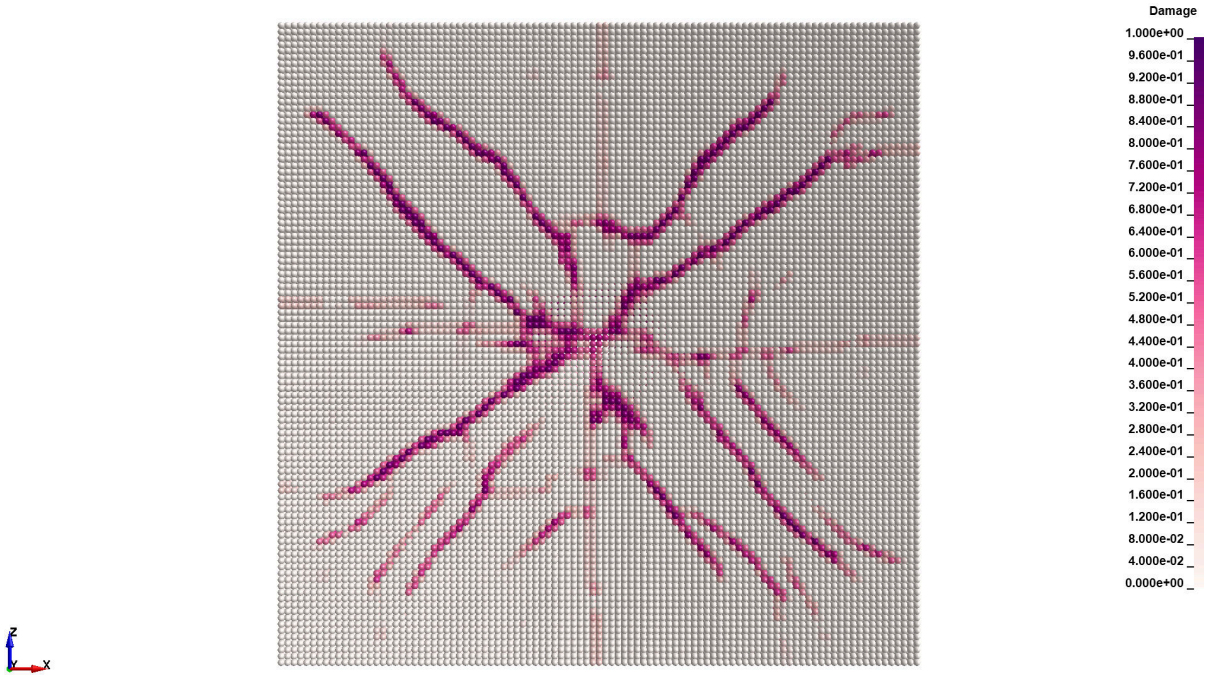

(a) no rate effects

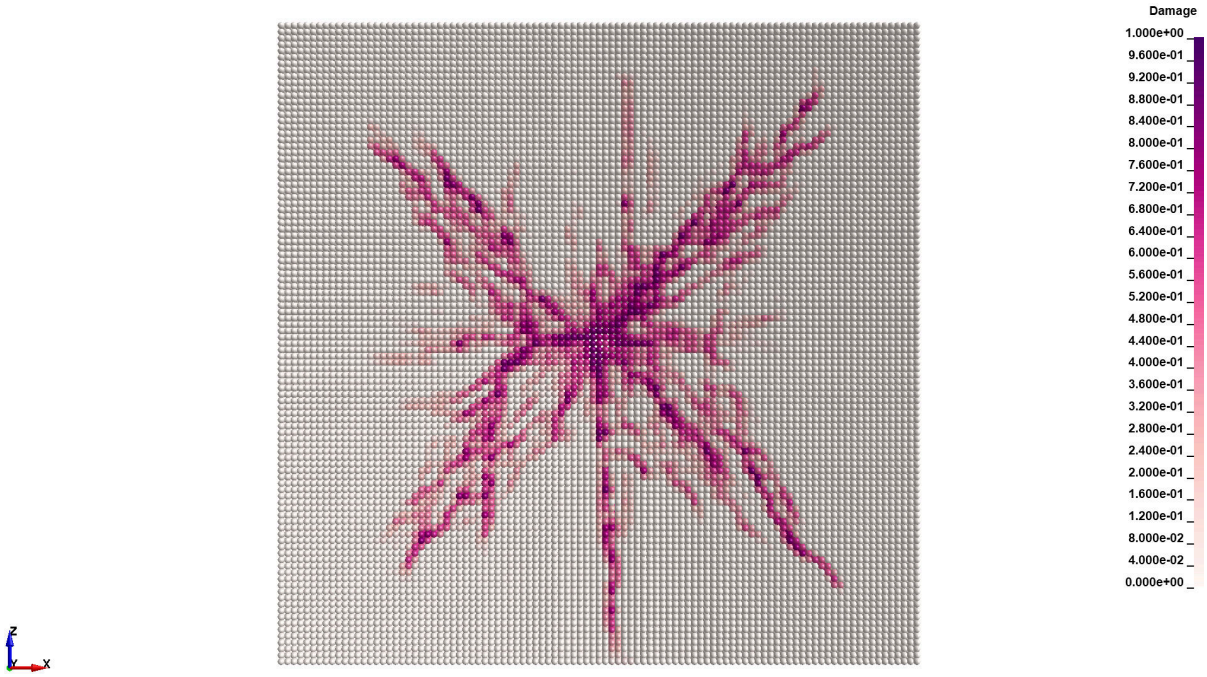

(b) rate effects

Fig. 9.16. Damage comparison of the model with and without the constitutive model strain-rate effects (bottom view).

The next compared are the damage states of the concrete slabs. As previously shown in Fig. 9.6, the top surface of the slabs were relatively undamaged. The only obvious change

compared to the specimens prior the detonation were the blackened patterns caused by the imperfect combustion of the charge. As shown in Fig. 9.15, there is almost no damage visible on the top surface of the slabs. Only the model without the rate effects shows an initialization of a cracking in the middle of the sides. The damage values are only 10 to 15%, however.

The bottom surfaces reveal far more interesting results. As shown in Fig. 9.16, both models show crack patterns, yet with some noticeable differences. From a visual comparison to Fig. 9.6, both models yield more individual cracks oriented in the diagonal direction rather than in the direction perpendicular/parallel to the sides of the slab. However, it must be pointed out that what is shown in Fig. 9.16 is the so-called *accumulated damage*. Very often can be seen that a brittle crack closes after the applied load is removed. This could be due to a reinforcement or stress state. Since the cracks highlighted in Fig. 9.6 are only those visually detectable, i.e. they were still opened during the examination, it might be that closed brittle cracks are not highlighted. In other words, the crack pattern of the model without the rate effects seems to be correlated to the crack patterns seen in the experiment. The model with the rate effects, however, is not.

The crack pattern of the model with the rate effects clearly shows a propagation of micro-cracks. That is, a region with many small cracks dominates and main cracks are barely distinguishable. This could point to the fact, that the fluidity parameters η_t, η_c, and η_s were not calibrated properly. As obvious from Tab. 9.2, an attempt to increase the brittleness of the concrete by setting $\omega = 0$ was not enough. As discussed in section *CSCM Material Model*, when $\omega = 0$ fracture energies are not increased with the strain rate but kept at the initial values, therefore, the softening branch of the stress-strain diagram is steeper.

Yet it seems the model without the rate effects fits far more better. The question is why. The strain rate developed in the concrete by the impulse of the explosion should be somewhere between $\log \dot{\varepsilon} = 2$ and $\log \dot{\varepsilon} = 4$, see Fig. 5.3. Again, based on Fig. 5.3 that would mean an increase in the compressive strength by at least 100% and in the tensile strength by at least 700%. Of course, this effect is highly localized. However, if the compressive and tensile strengths without the strain-rate increase reflect reality better, it could be that i) the fluidity parameters are to blame, or and most likely ii) the boundary conditions of the slab were not defined correctly. For instance, the stiffness of the support system was not calibrated correctly and the charge was never truly vertical but rotated as discussed in section *Uncertainty in the Charge Placement*.

The reinforcement shows the expected behaviour in both models. As shown in Fig. 9.17, the maximum reached effective stress (von Mises) over time is not more than 300 MPa. Since the yield strength of the reinforcement was 500 MPa as defined in Tab. 9.4, there is no need to discuss plastic strains in this case. Since displacements of the model without the rate effects were larger than those of the model with the rate effects, the stresses are again increased in the reinforcement of the model without the rate effects. The stress distribution of both models follows the same trend and is meaningful, which again points to the fact that the SPH-FEM sublayer coupling worked as expected.

Last to discuss is the charge itself. Just after the detonation, a shock front starts to propagate with the detonation velocity through the explosive and SPH particles starts to

move from the detonation point. The particles reach the velocity close to the detonation velocity (due to the given artificial viscosity) and release the energy specified in Tab. 9.7, i.e. approximately 0.3 MJ with respect to the volume of the charge. The pressure and energy releases were driven by (9.3.1) in time. As shown in Fig. 9.18, the initial shape of the charge has a great impact on the shape of the detonation products, therefore, on the profile of the blast wave as well.

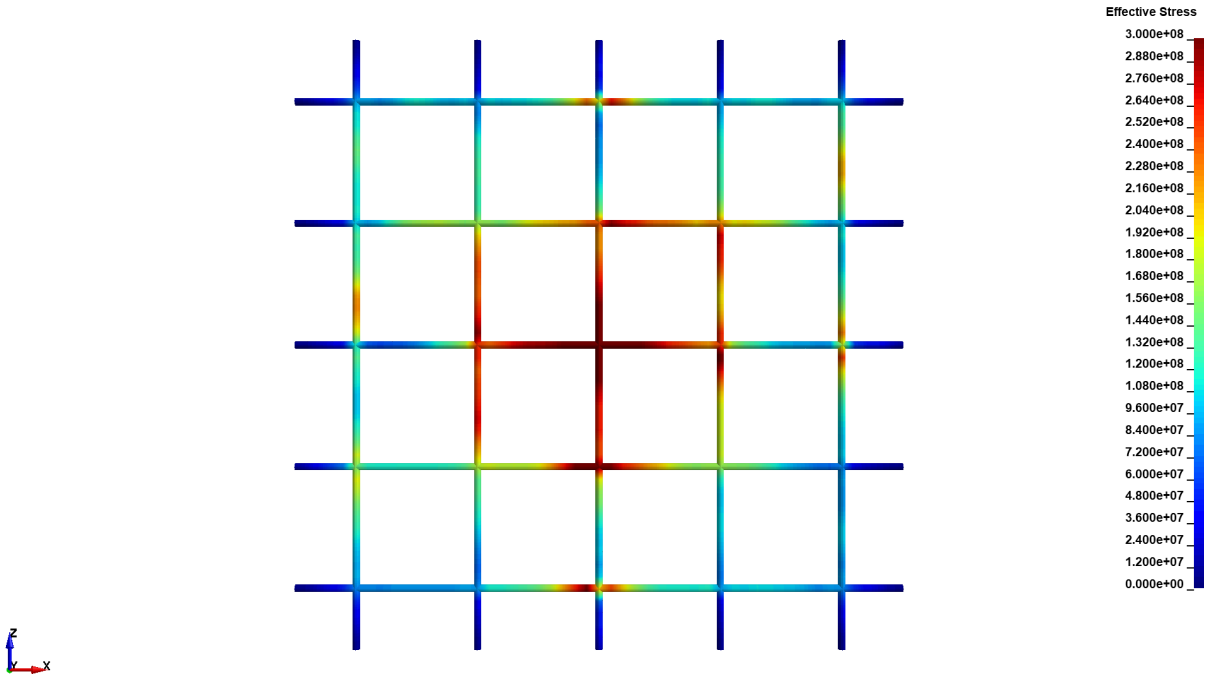

(a) no rate effects

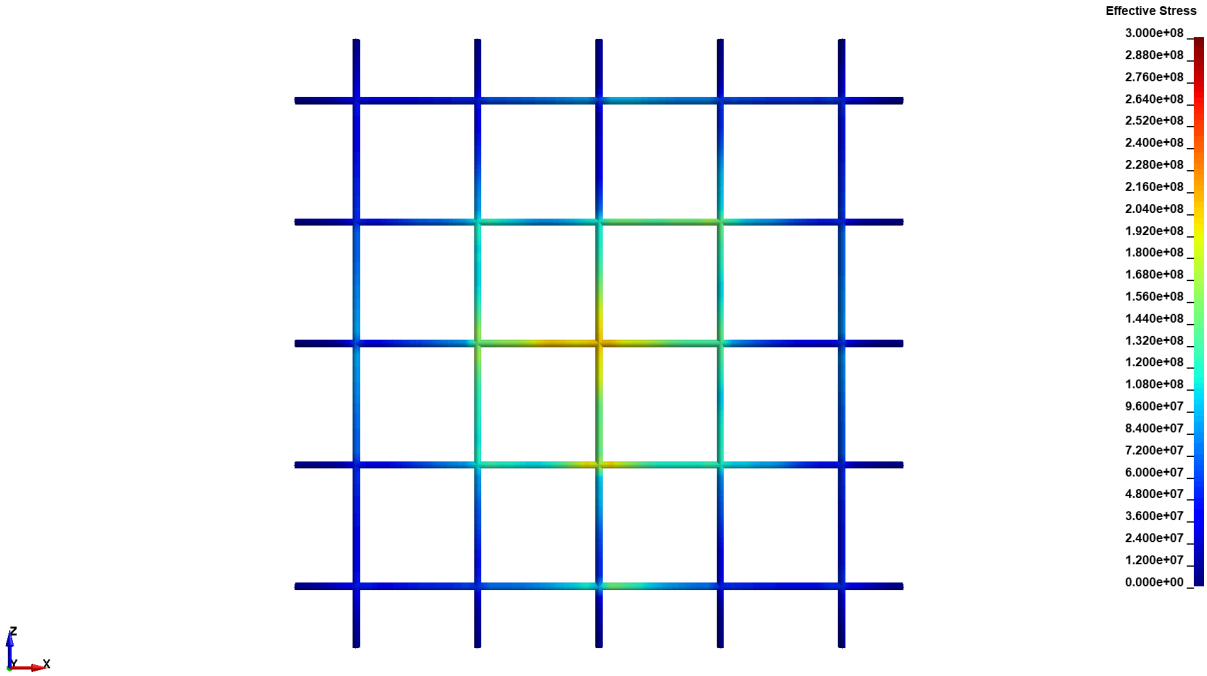

(b) rate effects

Fig. 9.17. Effective stress comparison in the reinforcement of the model with and without the constitutive model strain-rate effects (bottom view).

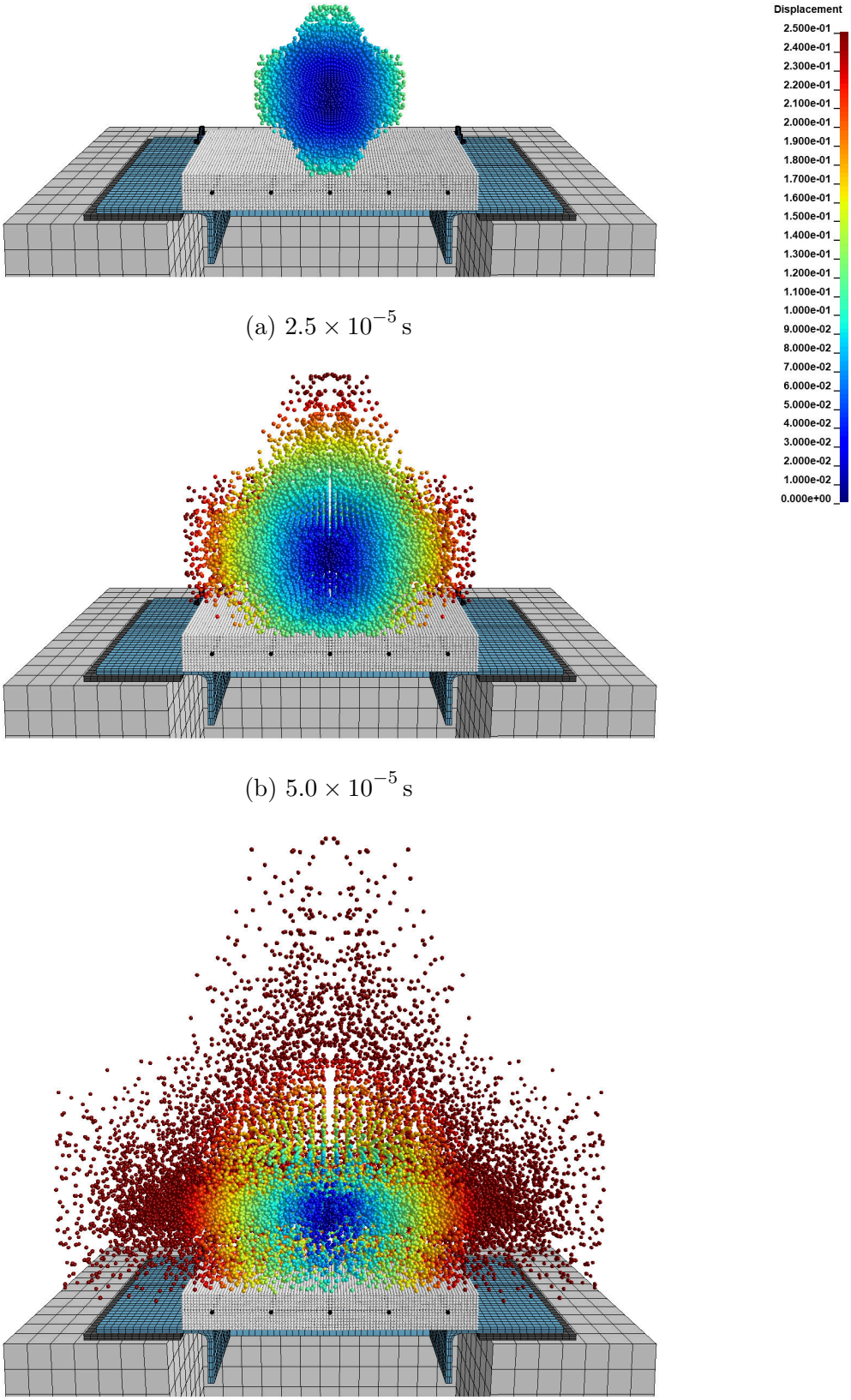

(a) $2.5 \times 10^{-5}\,\mathrm{s}$

(b) $5.0 \times 10^{-5}\,\mathrm{s}$

(c) $1.0 \times 10^{-4}\,\mathrm{s}$

Fig. 9.18. Detonation of the TNT charge simulated with SPH (cross-section).

The contour plot in Fig. 9.18 is shown only for the charge since the deformations of the structural parts are almost 1000 times smaller. Although the view is in the cross-section as previously shown in Fig. 9.9, the profile of the detonation products can be still seen well. When the SPH particles development in time is compared to Fig. 9.7, it is quite impressive how are the detonation products profiles similar. It is just another indicator that SPH can simulate FSI quite well. It should be no surprise though, since strengths of SPH are in fluid simulations. The slightly increased size of the SPH profile with respect to time compared to the footage can be addressed to the neglected air domain.

9.5 Uncertainty in the Charge Placement

As previously mentioned, the behaviour of the support system was highly nonlinear. This was a problem when the material parameters of the concrete were calibrated. Despite that, a set of parameters was found for which the examined responses of the concrete slab exhibited similarities with the experimental measurements. It must be pointed out, that the concrete class was expected lower than the calibrated C30/37. If a lower grade was used, the applied force would completely destroy the slab in the simulations, however. But if the lower grade concrete was taken as a fact, what would reduce the applied force?

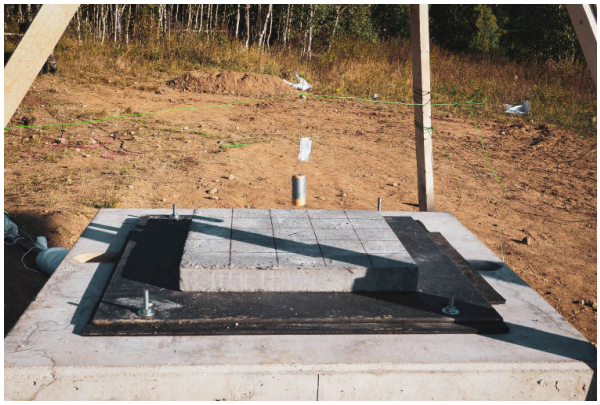

(a) correctly placed charge

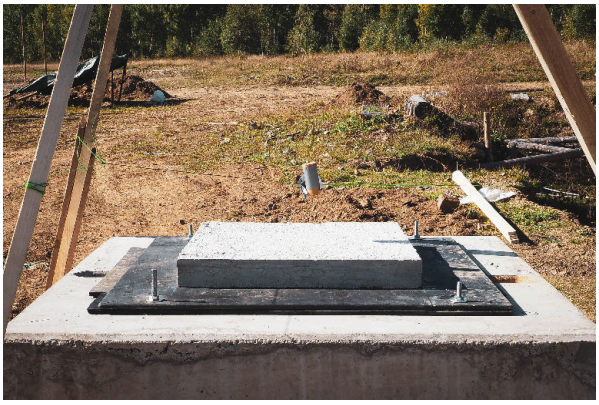

(b) incorrectly placed charge

(c) blackened pattern of the correctly placed charge

(d) blackened pattern of the incorrectly placed charge

Fig. 9.19. Comparison of the correctly placed charge (left) and incorrectly placed charge (right) before and after the explosion (increased contrast).

Since only one type of the charge was used for all the specimens, the assumption was that the applied load was constant (in terms of magnitude). Therefore, the only variable should have been the concrete itself, since structure of concrete is always variable. Responses of some specimens, however, pointed to the fact that the assumption of the constant load is not necessary valid. From detailed study of the available photo documentation it was clear that not all the concrete slabs were blackened in the same way. In fact, it seemed that the blackened patterns and initial rotations of the charges were correlated. As shown in Fig. 9.19 it is obvious that the charge in (a) points directly to the zenith (up) as was intended, yet the charge in (b) is rotated. From the distance it might seem there is no difference. After the explosion, however, when both blackened patterns are compared, differences are more obvious. Since the charge in Fig. 9.19 (a) is the one placed as intended, it is further referred to as the *correctly placed*. In contrast, the charge shown in Fig. 9.19 (b) is rotated (the axial axis of the charge is not perpendicular to the concrete slab), therefore, is referred to as the *incorrectly placed*.

The observations led to the formulation of the following theory. When a cylindrical charge detonates, a pressure field is formed and propagates through the air from the detonation point. Given to the shape of the charge, the pressure field is not spherical. When the detonation point is in the centre of the cylinder, the peak value of the formed pressure field is expected either on the axial axis of the cylinder or in the middle of the lateral surface of the cylinder, this can be seen in Fig. 9.7 (a). When the axial axis of the cylinder is not perpendicular to the concrete slab surface, three things happen. First, the applied load is not symmetric which results in additional force moments applied to the slab. Second, the pressure peak on the slab is smaller since the blast wave is not reflected from the surface in the exactly opposite direction but rather under a certain angle. Third, the boundary conditions (supports) are more important since the resulting force is moving from the centre to the boundaries.

In the ideal case, the base of the cylindrical charge is parallel to the concrete slab surface. After the explosion, the applied pressure field is radially symmetric and centred on the axis of symmetry of the concrete slab. The resultant force of the pressure field is therefore located at the centre of the concrete slab and is normal to the surface. Furthermore, the sum of the force moments at the centre point of the slab is zero since the applied forces are symmetric. The blackened pattern should correspond to the aforementioned characteristics, i.e. is symmetric and centred at the slab centre. The correct charge placement and the proper (expected) blackened pattern are shown in Fig. 9.19 (a) and (c), respectively. It is obvious that the blackened pattern is more or less centred and fades out from the centre smoothly. This supports the fact that the charge was centred and the axial axis of the charge was perpendicular to the concrete slab.

When the charge is placed incorrectly, i.e. rotated or shifted from the centre of the slab, an asymmetric pressure distribution, smaller peak pressure, and more or less random damage of the slab can be expected. Such a placement is shown in Fig. 9.19 (b). It is obvious that the axial axis of the charge is not perpendicular to the concrete slab surface. The incorrect charge placement might result in an asymmetric blackened pattern as shown in Fig. 9.19 (d). Several points can be made regarding the pattern in this case. The imaginary centre of the pattern is not aligned at the centre of the concrete slab. Furthermore, the imaginary principal axes of the pattern distribution tend to rotate. This means that the rotation of the charge was spatial, i.e. around two imaginary principal axes.

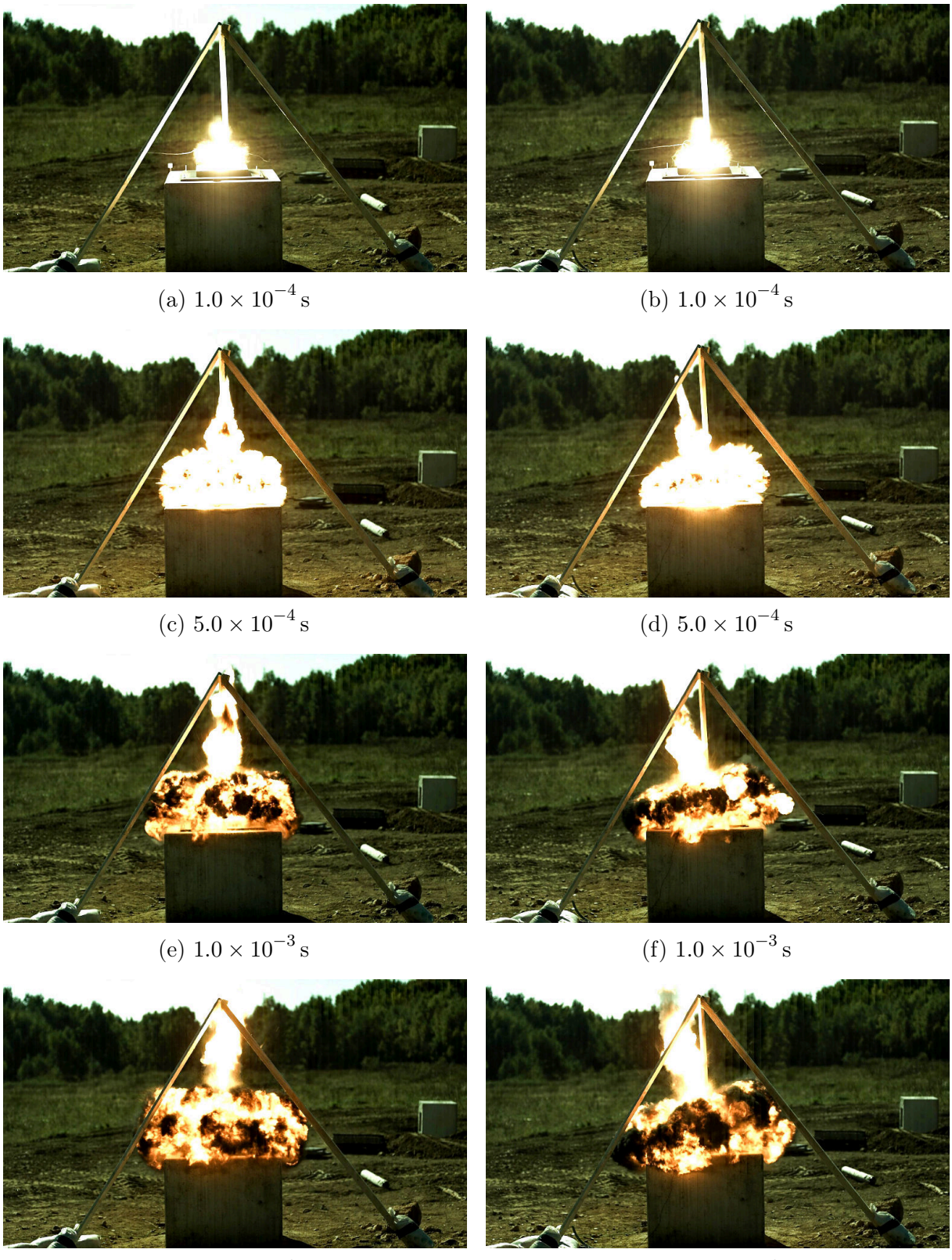

(a) 1.0×10^{-4} s (b) 1.0×10^{-4} s

(c) 5.0×10^{-4} s (d) 5.0×10^{-4} s

(e) 1.0×10^{-3} s (f) 1.0×10^{-3} s

(g) 2.0×10^{-3} s (h) 2.0×10^{-3} s

Fig. 9.20. Explosion time-lapse comparison of the correctly placed charge (left) and incorrectly placed charge (right).

The photo documentation in Fig. 9.19 can be supported with time-lapses of both explosions of the correctly and incorrectly placed charges. As shown in Fig. 9.20 when the same time frames are compared, it is clear that from the beginning the detonation products have the exactly same shape. Yet, the detonation products of the incorrectly placed charge are spatially rotated. Maybe the most obvious difference is at time 5×10^{-4} s when the charges are detonated and the detonation products are fully developed (yet not expanded). The formed 'spear' in the case of the correctly placed charge points to the zenith. In the case of the incorrectly placed charge, the spear is rotated roughly by 20°.

The question is, how different is the acting force on the concrete slab when the charge is initially rotated? A comprehensive study was performed by the author in [281] in which a detailed explanation was given. For the completeness of the thesis however, the most important findings of [281] are discussed here as well.

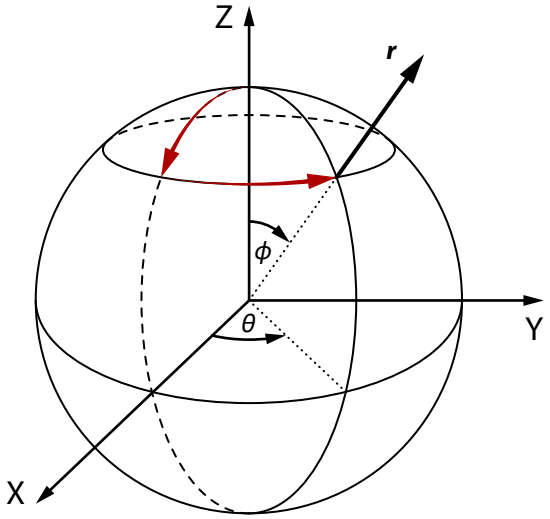

Fig. 9.21. Definition of the zenith ϕ and azimuth θ.

To quantify the influence of the initial rotation deviation, a variation window with rotations must be specified first. Since the charge could have been rotated spatially in the experiment, two independent angles of rotation must be considered. The angle between the vertical axis and axial axis of the charge, the so-called *zenith* angle ϕ, and the angle of the rotation around the vertical axis, the so-called *azimuth* angle θ.

Both angles are defined in Fig. 9.21 in which the axis Z represents the zenith axis. For convenience the angles are further referred to as the zenith and azimuth. The spatial rotation cannot be simply represented by vectors since $\phi + \theta \neq \theta + \phi$, therefore, it is important in which order the rotation angles are applied to the initial (perfectly vertically aligned) charge. In [281] the assumption was that the zenith is applied first and the azimuth follows; also indicated in Fig. 9.21 with the red arrows. When the origin of the rotation axes is placed at the CG of the charge, a direction vector $\boldsymbol{r}$ can be found, which is in fact the orientation of the charge after the rotation. The larger the zenith and azimuth are, the greater the deviation from the intended experiment.

Both parameters and their ranges are listed in Tab. 9.8. The ranges were established based on the photo documentation from the experiment. The zenith of 0° corresponds to the perfectly vertically aligned charge. The maximum zenith was set to 45° as it was found that the rotational deviation was never greater. The range of the azimuth was only 0 to 90° due to the symmetry of the experiment. Yet it is clear from Fig. 9.21 that when the zenith is 0°, the value of the azimuth has no influence on the direction vector $\boldsymbol{r}$.

ϕ	zenith (deg)	0 – 45
θ	azimuth (deg)	0 – 90

Tab. 9.8. Variation window of the zenith angle and azimuth angle.

However, when the origin of the rotation axes is placed at the CG of the charge and the charge is spatially rotated, the minimum vertical distance (the stand-off distance) between the top surface of the concrete slab and the charge is no longer 0.1 m. To keep the distance constant, the charge must move up or down after it is rotated. And since the detonation point is also at the CG of the charge, it must move as well. The minimum vertical distance between the top surface of the slab and the charge δ_{min} was constant 0.1 m, therefore, the vertical distance between the top surface of the slab and the detonation point can be found as

$$\delta_{det} = \delta_{min} + \alpha + \beta, \tag{9.5.1}$$

where α and β are the correction distances based on the length, diameter, and zenith of the charge. They are defined as

$$\alpha = \frac{1}{2} l \cos\phi, \tag{9.5.2}$$

and

$$\beta = \frac{1}{2} d \sin\phi, \tag{9.5.3}$$

where l and d are the length and diameter of the charge. From (9.5.2) and (9.5.3) it is clear that when the zenith is 0°, the detonation point distance is δ_{min} plus half of the length. And when the zenith is 90°, the detonation point distance is δ_{min} plus half of the diameter. The azimuth plays no role in the detonation point vertical offset since it only defines the rotation in the horizontal plane. Therefore, no matter what the value of the azimuth is, the vertical distance of any point of the charge from the concrete slab is controlled by the zenith only. Furthermore, no offset in the horizontal plane was considered in [281]. In other words, CG of the charge was still located directly above the centre of the slab even after the rotation.

One way to understand the effect of the initial rotational deviation is to calculate and evaluate several simulations. In statistics, each individual simulation (set of parameters) is usually called a *design*. Every design is generated with respect to the given ranges of variables. Together, all designs create what is termed a *space of designs*. Since the number of designs might be quite high, it would be very expensive to calculate the full model. And since the question is only how the applied load varies with the initial rotation of the charge, a simplified model was used in [281].

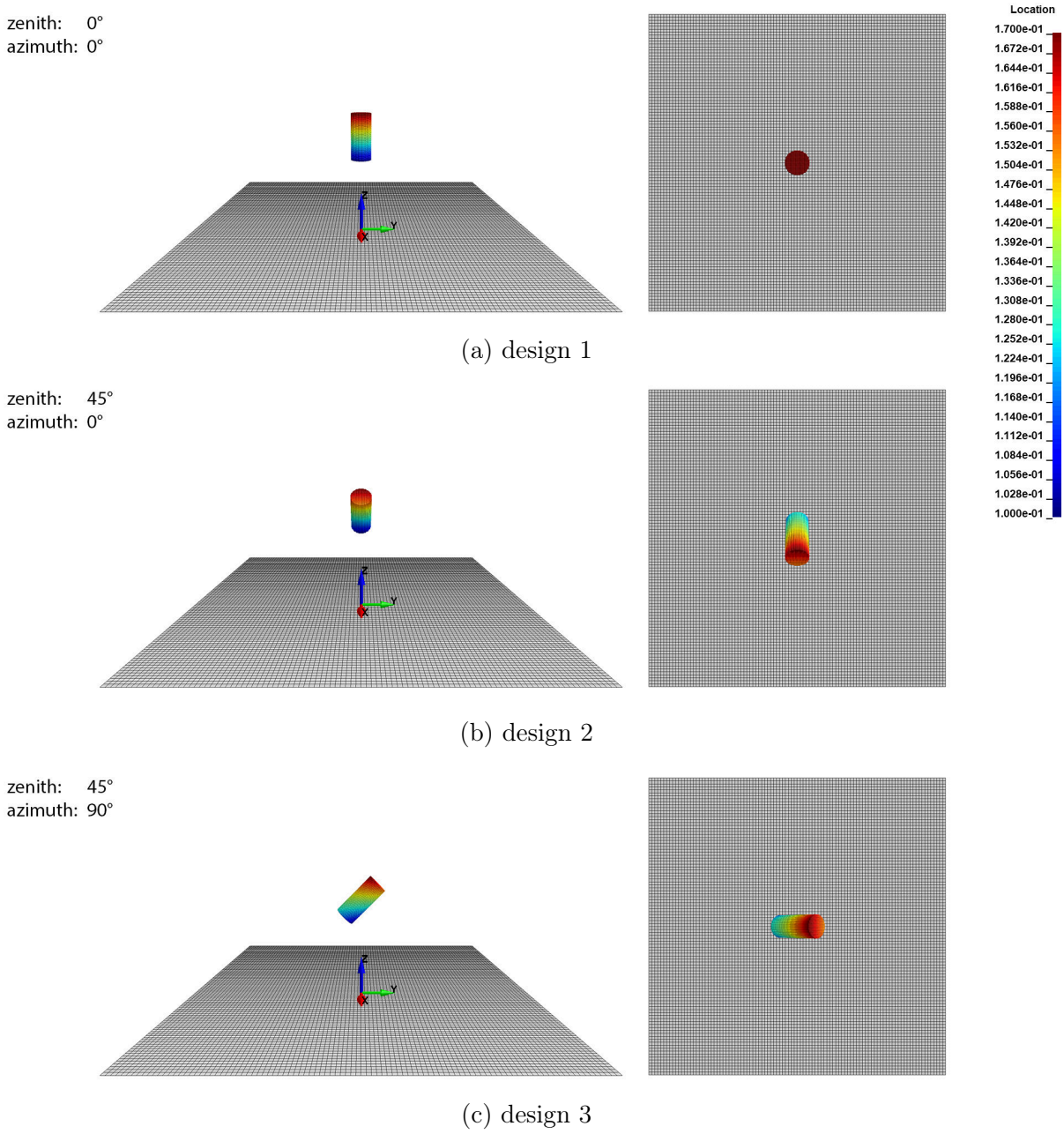

(a) design 1

(b) design 2

(c) design 3

Fig. 9.22. Three designs comparison with different zenith and azimuth, iso view (left) and top view (right).

Instead of the detailed model of the reinforced concrete slab as shown in Fig. 9.8, only its top surface was constructed using the FEM shell elements. The sole purpose of this layer

of elements was to measure the applied pressure from explosions, i.e. to act as a sensor recording pressure distribution over time. The behaviour of the sensor was, therefore, rigid. The interaction between SPH and FEM was done with the penalty-based contact. The easiest way to evaluate the overall loading effect is to calculate a sum of all applied forces. This was done with a predefined boundary condition. Given the rigid behaviour of the sensor, only one constrained node can be defined. In this particular case, the centre node corresponding to the CG of the sensor was constrained. In other words, all translational and rotational DOFs were fixed. With this approach, not only the total reaction force can be measured, but also its components, the force moment components, and the total force moment as well. When all the six reaction components are available, a very good picture of the asymmetric pressure distribution can be drawn. To capture the peak pressure, a very fine mesh of 10,000 elements was used. An example of three so-called boundary designs, those with combinations of the extreme values of variables, are shown in Fig. 9.22. As can be seen from the contour plot, the minimum distance between the sensor and the charge was always 0.1 m even when the charge was rotated.

The question is, what is the most efficient way to generate a design space so as to have evenly distributed values and cover all the given ranges? Many sampling algorithms have been developed for exactly this purpose. Yet it is not that simple in this case, since the input parameters are angles but designs are defined by their product, the direction vector $\boldsymbol{r}$ as shown in Fig. 9.21. To better understand how are the individual designs generated and what is the orientation of the charge, a point can be projected onto a unit sphere. The point itself is nothing else than an intersection of the direction vector $\boldsymbol{r}$ and unit sphere as shown in Fig. 9.21. The coordinates of the point in Cartesian system can be calculated from the given angles as

$$\begin{aligned} x &= r \sin\phi \cos\theta, \\ y &= r \sin\phi \sin\theta, \\ z &= r \cos\phi, \end{aligned} \tag{9.5.4}$$

where r is the radius of the unit sphere, which is 1. The relative coordinates x, y, and z can then provide a better understanding of how the charge is oriented in simulations. For example, when 125 designs are generated with the Monte Carlo (MC) sampling method [282], the design space may be filled quite well. Yet when the coordinates are visualized, as shown in Fig. 9.23 (a), it is obvious that the design space of the direction vector $\boldsymbol{r}$ is not filled well. A great quantity of designs are located close to the top of the sphere, while there are very few anywhere else. One could say it is a problem with the MC method, and that a more advanced sampling method should be used, e.g. the Latin Hypercube Sampling (LHS) method [282]. However, when LHS is used, the result is more or less the same as shown in Fig. 9.23 (b). The question is, what is the root of the problem?

The problem is that the sampling algorithms have no information that the design space should be evenly filled with the product of the input parameters and not the input parameters themselves. For example, many designs were generated on the top of the unit sphere, as it is obvious from Fig. 9.23 (a) and (b). This means that the zenith as the input parameter was more or less constant, and that the azimuth was evenly filled in within the specified range. Unfortunately, in this particular case it also means that their product,

the direction vector $\boldsymbol{r}$, is almost identical for every design. Thus, the orientation of the charge is identical as well. There is no meaningful reason why hundreds of almost identical designs should be calculated.

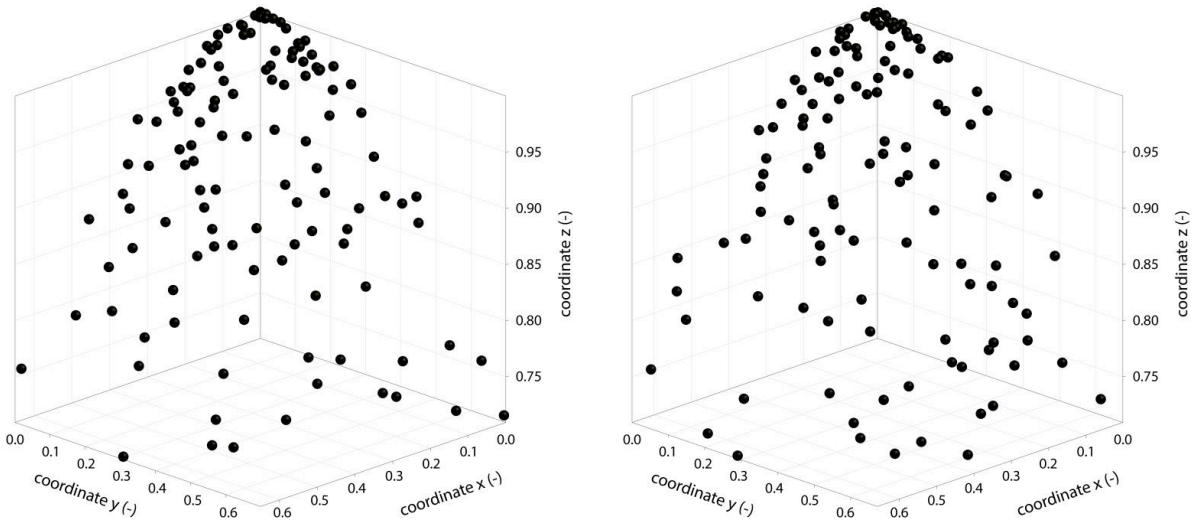

(a) Monte Carlo (b) Latin Hypercube

Fig. 9.23. Design space generated with standard sampling methods.

To correct the problem, a unique sampling method was tailored. It is a very difficult problem to evenly distribute points onto the surface of a sphere. The Fibonacci sphere algorithm, also known as Fibonacci lattice, can be useful, however [283].

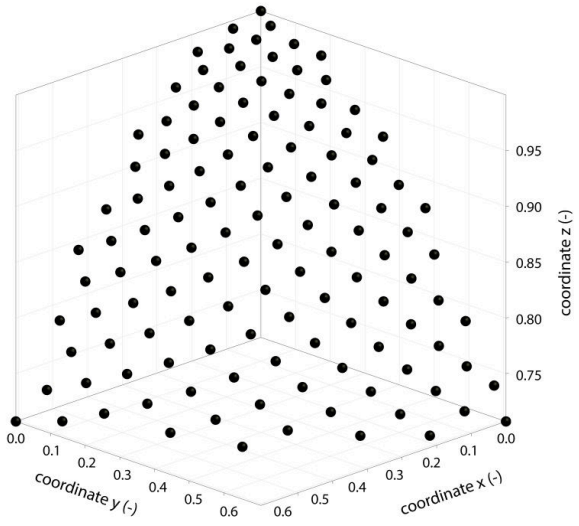

Fig. 9.24. Design space generated with the Fibonacci sphere sampling.

Since optiSLang [282, 284] was used in the study, it was possible to directly implement the Fibonacci sphere algorithm to the optiSLang framework and use it for the design space generation. The generated points (designs) are shown in Fig. 9.24, and as can be seen the points are distributed evenly and not repeated. Additionally, the aforementioned boundary

designs were generated, see Fig. 9.22. These designs correspond to the extreme values of the specified ranges (it is not possible to generate them directly with the Fibonacci sphere algorithm). To achieve a good design space coverage, 125 designs were calculated in total.

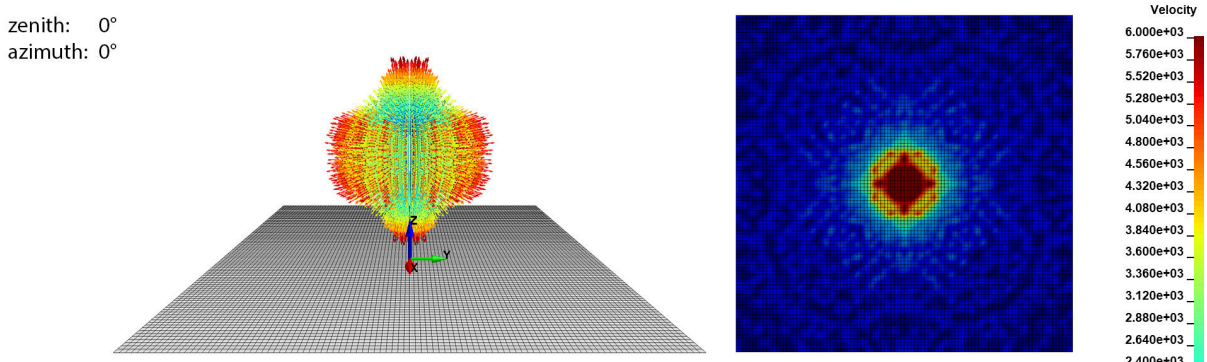

(a) design 1

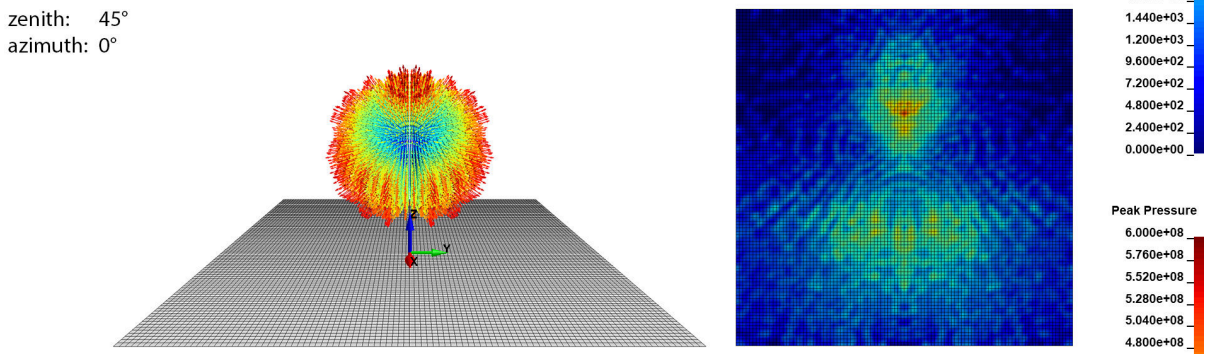

(b) design 2

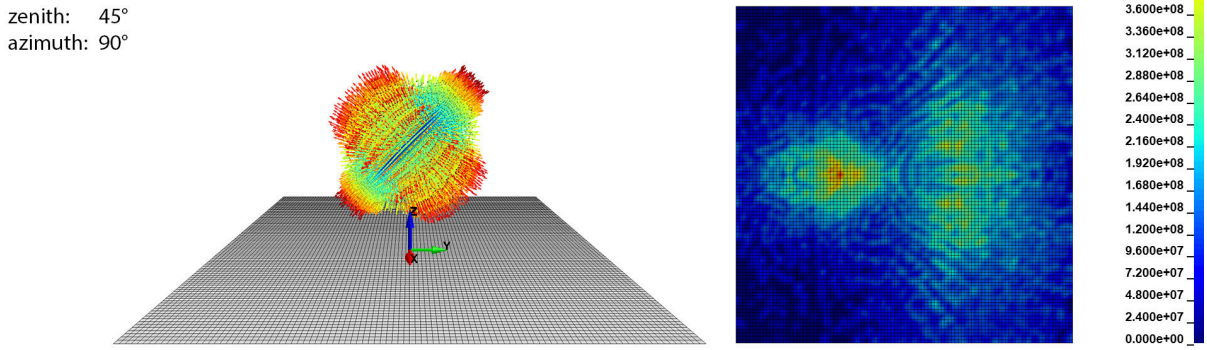

(c) design 3

Fig. 9.25. Three designs comparison with different zenith and azimuth, velocity vector (left) and peak pressure over time (right).

To understand the effect of the initial rotation deviation, metamodels [282] for several responses were generated. The discussed responses in [281] were the force and moment reactions including all their components, and peak pressure over time. When all the responses are evaluated together with pressure distribution plots, quite interesting deductions can be made.

For instance, in Fig. 9.25 the three boundary designs are shown again. In the left portion of the figure, velocity vector fields of all detonated charges are shown at time 2×10^{-5} s. Since the red vectors of the maximum velocity point in different directions, the pressure field of each is also different as shown in the right portion of the figure from the top view. It makes sense that design 2 and 3 are identical yet mirrored, since only the value of the azimuth is different.

Interestingly enough, the peak pressure plots show the maximum measured pressure over time, therefore, the contours represent a heat map (colours can get only warmer). And since the charge was identical for all the three designs, it is in fact quite interesting to see that the heat maps are that different. It is clear that the extreme case is reached when the zenith is 0°, yet it is not a surprise. The pressure plots in Fig. 9.25 have yet another meaning. As a consequence of the imperfect combustion of the charge, the concrete slab is blackened in the direction in which the detonation products propagate. Since SPH particles represent the detonation products, the pressure imprint should more or less correspond to the blackened pattern from the real experiments.

By a definition, a metamodel represents a response surface, an approximation of a model. In terms of the optiSLang, however, a metamodel is an optimized response surface to provide not only the best approximability but also predictability of a model. For that reason, the metamodel is termed a Metamodel of Optimal Prognosis (MOP) and is quantified by a Coefficient of Prognosis (CoP) [282].

R	Moving Least Squares	97%
M	Isotropic Kriging	95%
M_x	Isotropic Kriging	97%
M_y	Isotropic Kriging	98%
P	Linear Regression	83%

Tab. 9.9. MOPs with corresponding CoPs with respect to the responses.

The CoP is based on the summation of squared prediction errors. These errors are estimated based on cross validations [282]. The CoP is defined in a range from 0 to 100%, where 100% is the best MOP quality possible. The CoP is influenced by the approximation method. Since it is not the goal of the thesis to explain individual methods, Tab. 9.9 simply provides an overview of the MOPs with respect to the approximation method and the corresponding CoPs. Yet, there are only four reaction responses in Tab. 9.9 instead of eight (two total and six components). The reason for that is quite simple. Since there is no friction between the detonation products and sensor, the components X and Y of the force reaction together with the component of the moment reaction Z are zero. Therefore, the total force reaction R can be calculated as

$$R = R_z, \tag{9.5.5}$$

where R_z is the component of the force reaction along the Z axis, and the total moment reaction M as

$$M = \sqrt{M_x^2 + M_y^2}, \tag{9.5.6}$$

where M_x and M_y are the components of the total moment reaction around the X and Y axes, respectively. The last response in Tab. 9.9 is the already discussed peak pressure P over time. Note that maximum values of the responses were used for the MOPs constructions. This is important to keep in mind when two different responses or designs are compared because both could correspond to a different time in the simulation. All the CoPs have high value which means that the corresponding MOPs have a good explainability of the studied responses. In other words, observations based on the MOPs should correlate to reality quite well. Additional comments can be found in [281].

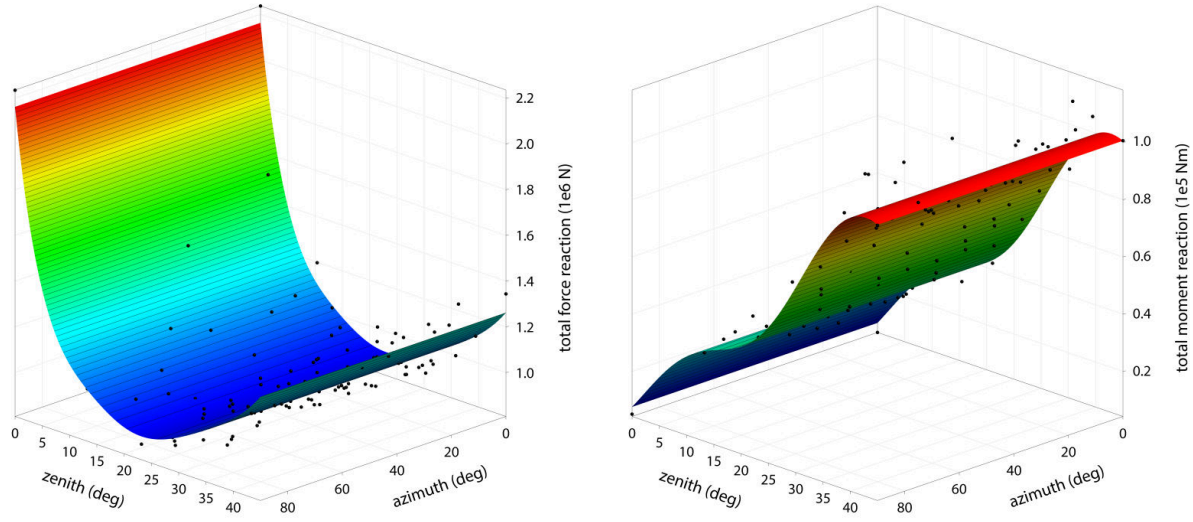

(a) total force reaction (b) total moment reaction

Fig. 9.26. MOP of the total force reaction and total moment reaction.

The MOP of the total force reaction R in Fig. 9.26 (a) shows quite a shocking picture. When the zenith is 0°, R is almost 2235 kN. When the zenith increases and the axial axis of the charge is no longer perpendicular to the sensor, R drastically drops. When the zenith is approximately 22°, R is only 808 kN, which is only 36% of the maximum reachable force. From the available photo documentation from the experiment it seems the zenith was around 15° in most cases. Zenith of 15° corresponds to 924 kN, which is only 41% of the reachable force. In retrospect, the applied load during the calibration of the material parameters in the simulations could have been twice as much as in the experiment, therefore, overestimated.

Another significant finding is that the azimuth is almost insignificant when R is evaluated. It is understandable that for the zenith of 0° the azimuth plays no role. But when the zenith increases, the effect of the azimuth should be evident. However, R is the sum of all the applied forces on the sensor. It could very well be that in close-in explosions, and

in this particular case, the number of particles which impact the sensor is more or less constant no matter what the azimuth is. This could possibly cause the almost total lack of obvious influence of the azimuth on R. The MOP is only an approximation, though. When a detailed comparison is made, design by design, small differences due to changes in the azimuth are evident.

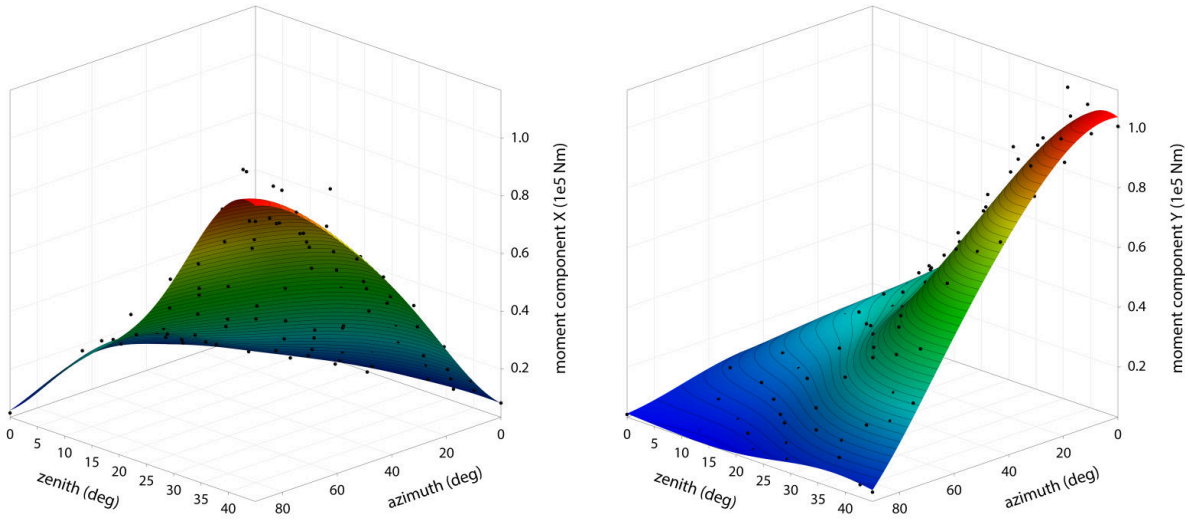

(a) moment component X (b) moment component Y

Fig. 9.27. MOP of the moment reaction components X and Y.

While looking at the MOP of the total moment reaction M in Fig. 9.26 (b), it can be seen that the trend is reversed compared to the MOP of the total reaction force. When the zenith increases, so does M. This makes sense, of course, since the centre of the pressure distribution over time is no longer aligned with the centre of the sensor. It is interesting that M is also not influenced by the azimuth. The reason for this can be found in Fig. 9.27 (a) and (b) in which MOPs of the moment reaction components are shown. It might not be obvious but the MOPs of the moment components M_x and M_y are, in fact, mirrored. This was already outlined in Fig. 9.25, in which design 2 and 3 are mirrored as well.

ϕ (deg)	θ (deg)	M (kN m)	M_x (kN m)	M_y (kN m)
0	0	0	0	0
45	0	100	0	100
45	90	100	100	0

Tab. 9.10. Comparison of force moments of the three boundary designs.

The symmetry is also obvious from the results collected in Tab. 9.10 in which the total moment reaction and its components are compared for the three boundary designs. It should be noted that absolute values of M_y were used. This was due to the orientation of the coordinate system. Yet it does not change the value of M since the calculation is based on the Euclidean norm in (9.5.6). The main outcome of the moment MOPs is how

the asymmetricity of the loading increases, therefore, how the stress distribution and most likely the damage of the concrete slabs changes with the zenith. This is indeed a problem since the strain gauges were placed at the centre (mid-span) of the slabs, yet the maximum deflection and strain could have been somewhere else.

The trend of the pressure MOP in Fig. 9.28 makes perfect sense even though the corresponding CoP was lower compared to the rest of the metamodels. When the zenith increases, the peak pressure drops. This happens because the SPH particles impact the sensor under a smaller angle. The smaller the angle, the smaller the normal force from the particle impact. When the zenith is 45°, the particles with the highest velocity, as shown in Fig. 9.25, impact the sensor under the angle of 45°. When the zenith is more than 45°, the particles initially located on the lateral surface of the cylinder impact the sensor under higher angle (getting closer to the perpendicular) and again cause an increase in pressure. Since the range of the zenith was only up to 45°, the mentioned increasing part of the MOP is not visible, however. Note that the actual (absolute) values of the pressure are irrelevant since the SPH particles impact a rigid sensor. Furthermore, the peak is correlated to a dispersion of SPH particles which is more pronounced with increasing zenith. Put simply, when the zenith is 0° and the charge is perfectly vertically aligned, all the particles located at the base of the cylinder impact the sensor at approximately the same time, therefore, the pressure values are amplified as the contributions from all particles are summed up.

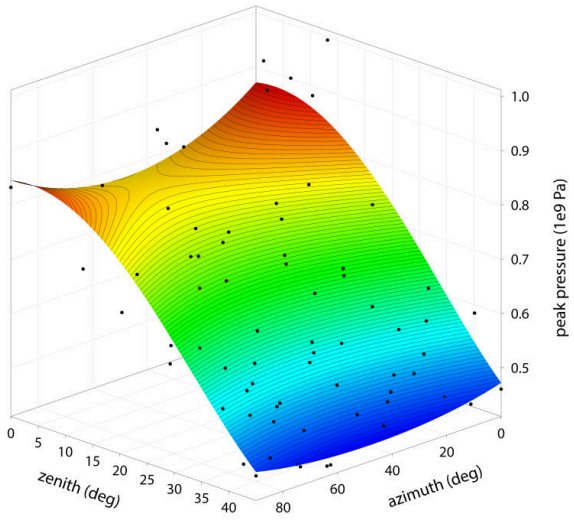

Fig. 9.28. MOP of the maximum pressure.

The MOPs together with the pressure imprints provide a great deal of information. Not only the initial rotation of the charge can be identified for individual specimens, but the acting forces and moments can be found as well. How to find the initial rotation (deviation angles) of the charge? As already outlined, from the blackened patterns on the top surfaces of the specimens. The idea is following. When an explosive detonates, detonation products expand through the air. As discussed, the direction of the expansion is determined by the shape of the charge. Since TNT is a non-ideal explosive, its combustion is not complete. It is for this reason that the blackened pattern can be observed at the location through which the blast wave (together with the detonation products) would expand if there was no obstacle (the concrete slab in this case). Therefore, the idea of similarity between the

experiment and the simulation is based on a visual comparison of the blackened patterns and the pressure imprints on the sensor.

(a) blackened pattern of the incorrectly placed charge

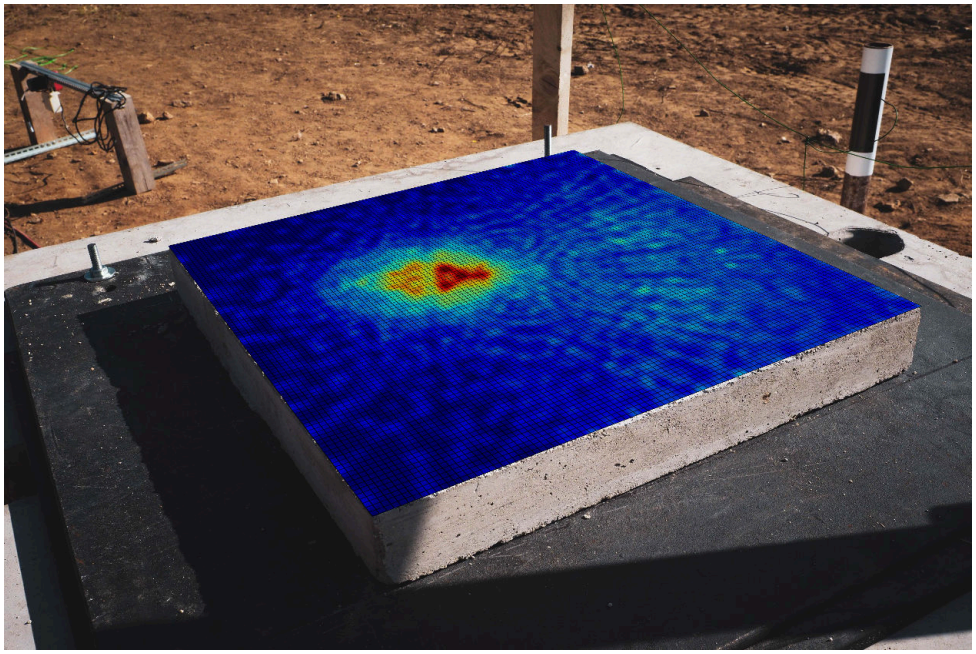

(b) corresponding SPH peak pressure heat map

Fig. 9.29. Comparison of the blackened pattern from the experiment and the estimate of the pressure imprint from the simulation.

For instance, the charge shown in Fig. 9.19 (b) was clearly rotated. The photo cannot give both rotation angles, however. The azimuth was roughly 20° as observed in Fig. 9.20. To identify both rotations more precisely, the same technique as in [232] can be used. Since the idea of the identification is based on the visual comparison of the blackened pattern

and the available (simulated) pressure imprints, the best matching design can be found. That would be design 76, with the rotation angles and responses collected in Tab. 9.11.

The total reaction force of design 76 is only 44% of the maximum force reachable (when the zenith is 0°). Of course, this value corresponds to an increase in the additional (unbalanced) force moment. It is important to keep in mind that the sensor acted as a rigid body. That means the peak pressure is i) highly localized, ii) strongly correlated to the contact stiffness, and iii) amplified when the dispersion of SPH particles is minimal (when the zenith $\longrightarrow 0°$). Therefore, the peak pressure rather represents a bi-component of the force reaction.

The comparison of the blackened pattern of the incorrectly placed charge from the experiment and the calculated design 76 is shown in Fig. 9.29. The pressure distribution shows the maximum pressure reached on the sensor over the simulated time. In real life, the surface of the concrete slab was white and could only have become darker after the explosion. It is exactly the same in the case of the simulation, but with contours of the heat map. The comparison of both patterns in Fig. 9.29 looks more than believable.

ϕ	zenith (deg)	27.0
θ	azimuth (deg)	64.2
R	total force reaction (kN)	977.0
M	total moment reaction (kN m)	51.8
M_x	moment component X (kN m)	46.5
M_y	moment component Y (kN m)	22.8
P	peak pressure (MPa)	549.0

Tab. 9.11. Deviation angles and responses of design 76.

The study presented in [232] brought quite an uncertainty to the set of the already calibrated material parameters. Furthermore, taking into account the highly nonlinear support system, the calibrated material parameters of the concrete might be indeed questionable. However, the goal of the thesis is to show the functionality of SPH and demonstrate its strengths. The numerical simulation of the explosion experiment together with the study of possible uncertainties clearly show advantages of SPH over others numerical methods. The discussed non-standard combination of SPH simulations, metamodels, and image reconstructions show the state of the art in applied mechanics and reverse engineering.

Chapter 10

Conclusion

The main goal of the thesis was to provide a sufficient mathematical and application proof of the Smoothed Particle Hydrodynamics (SPH) utilization in fields of structural dynamics with an emphasis on quasi-brittle materials. It is always ambitious to use numerical methods in fields for which they were never developed, never intended. It cannot be left without saying that in case of SPH the subject of the thesis went a long way from the original application intention. Since SPH was originally developed for astrophysical problems, it is quite extraordinary to say that now it can be used to simulate responses of concrete or even reinforced concrete under extreme conditions. As far as the mathematical and application proof goes, the thesis offered not only one but many verifications and validations supported with experiments and benchmarks. That said, the main goal of the thesis was fulfilled. SPH can be used with quasi-brittle materials in fields of structural dynamics with many advantages compared to standard (mesh-based) numerical methods. Furthermore, with the proposed improvements in the thesis, it can be said that SPH has become a generic tool for civil engineering problems.

In detail, the first chapters of the thesis provided a comprehensive overview of the SPH history, theory, mathematical implementation, modifications, and state-of-the-art corrections with respect to structural dynamics. Therefore, the introduction part can be considered a handbook for all students, researchers, and engineers who are interested in the SPH application in structural dynamics. The theoretical part was supplemented by a number of examples which show how to use the method, what to expect, where to be cautious, and what are the strengths and weaknesses of SPH. All the examples provided necessary collection of parameters, therefore, it is possible to simply reproduce what was presented.

Since the author is aware of the considerable popularity of the Finite Element Method (FEM), a chapter was dedicated to coupled SPH-FEM models. Three different coupling approaches were discussed in detail. Since there is no general answer to which approach is better, a study in which a coupled beam was subjected to large deformations was performed. The results clearly point to the fact that both methods are interchangeable and combinable. The studied responses were almost identical for all three approaches and correlated quite well to the pure FEM model. However, the stress field might oscillate in the proximity of the SPH-FEM interface when hybrid elements are not used. Furthermore,

it was found that each of the tested interfaces introduces an energy dissipative term into the model. The effect was pronounced the most in case of the hybrid elements. Such findings might seem to be negligible, yet it is crucial to consider this fact especially in high velocity impact (HVI) simulations if coupled models are employed.

Since it was found there is a significant gap in the research on quasi-brittle materials within the SPH framework, the author decided to improve that and provide as many answers as possible in the thesis. There are many material models which can be used with SPH and represent behaviour of concrete. Yet there are only few material models which can represent behaviour of concrete under all load rates. For that reason, the Continuous Surface Cap Model (CSCM) was chosen and discussed in detail. The assumptions of the model together with its mathematical background were outlined. Again, the theory was supported with examples, therefore, the thesis can be used as a handbook for interested readers. To prove the functionality of SPH with CSCM, two very well known experiments were simulated. Despite the fact that plain concrete was used in both experiments, SPH was tested to the full. In the first experiment, the L-shaped structural members were subjected to deformation often resulting into singularities in mesh-based numerical models. It was proved that SPH is able to reproduce the behaviour observed in the experiment, it is not dependent on the discretization density, and the normalization of the fracture energy is stable within the SPH framework. To push the boundaries even further, irregular subdomains of clustered SPH particles were nested into the otherwise uniform models. It was found that SPH is able to bypass such a numerical difficulty, yet the size of the support domain must be calibrated first. In the second experiment, an initially pure FEM model was assigned with CSCM while allowing the element erosion. To conserve mass and energy, the eroded FEM elements were adaptively transformed to SPH. From the simulated experiments it was proved that the models with the standard element erosion cannot reproduce experimental measurements. The element erosion must be either calibrated for every case individually, therefore, not applicable for predictive engineering or must be improved with SPH to conserve mass and energy. The finding is very important as it is the case that the element erosion is quite popular and often used without knowing the consequences. It was proved that SPH is superior to standard mesh-based methods in HVI simulations, and can be used either in pure SPH models or coupled with other mesh-based methods.

Since it is not likely that concrete would be used without any reinforcement, a chapter dedicated to the numerical modelling of reinforced concrete with SPH was also included. It is a well known fact that SPH suffers from a numerical instability, the so-called *tensile instability*. This is a very important aspect of a numerical modelling, since in case of reinforced concrete it causes openings of numerical (artificial) cracks and yielding of the reinforcement before the yielding stress is reached. There are several solutions to bypass the problem. As shown in the thesis, the total Lagrangian kernel can be used. Yet it is so that while using the total Lagrangian kernel, the adaptivity of SPH is lost. For that reason, it is better to use the Eulerian kernel, however, with FEM for the reinforcement since it is free of the instability. Since the reinforcement in case of FEM usually consists of beam elements, which cannot be simply coupled with meshfree methods, a new *sublayer coupling* approach was proposed. The idea of using the SPH sublayer proved to work well for no-slip conditions. Given that the concept employs FEM elements for the SPH sublayer generation while the actual connection between the concrete and reinforcement is done with the natural adaptivity of SPH, the idea is not only simple to use but also transparent.

The results presented in the chapter are therefore significant findings with a high potential for a real application and development.

Concrete structure is very complex which leads to a variability in experimental measurements although the tested specimens might be visually identical. In contrast, numerical simulations can and do return identical responses if there is no variability in input parameters. To get closer to reality, the author proposed the *algorithm for concrete structure generation*. The idea is based on utilization of spatial noise functions. This rather abstract technique proved to be robust, stable, and able to provide a generated spatial geometry of concrete which can be further used with SPH models. The concept consists of several rather complex steps, yet easy to implement in a high level programming language. At the beginning, a noise function is chosen to represent a concrete structure on the mesolevel resolution. To capture the size, shape, and distribution of aggregate in concrete, an input photo of a concrete can be used. When the noise function is optimized in the way that there is a visual correlation between the input photo and a cross-section of the noise function, the structure is generated. The result is a spatial geometry of three domains – aggregate, mortar-matrix, and the interfacial transition zone (ITZ). Since it is quite easy to generate SPH particles into rather complex spatial geometries, all three generated domains can be discretized with SPH and have assigned completely different material models or the same material model but with different properties to capture randomness in behaviour. Combining the algorithm for concrete structure generation with material parameters oscillations, the so-called *numerical heterogeneity* can be implemented. The algorithm was developed by the author and is unique across material structure generation systems.

As it is necessary to test the functionality of the proposed approaches, two experiments were performed by the author and his colleagues. The first experiment focused on HVI in which a reinforced concrete beam was the subject of the study. The beam was impacted by a battering ram of 500 kg from a drop height of approximately 1 m. Given that, the impact energy was quite high. The concrete beam was modelled with SPH while the reinforcement with FEM beam elements. For the SPH-FEM coupling, the proposed approach with the SPH sublayer was used. To see how is the model affected by rate effects resulting from the constitutive model, a variant with and without CSCM strain-rate effects were compared. Both models showed comparable responses, both with a sufficient correlation with the experimental measurements. The simulations provided many answers. The most important ones would be i) the proposed SPH-FEM coupling approach works well and shows no influence of the tensile instability, ii) SPH in combination with CSCM is robust, stable, accurate, and well performing, and iii) the constitutive model strain-rate effects have an influence on the model responses, especially in terms of damage, with respect to the set of the calibrated material parameters.

The second experiment focused on a blast load in which the subject of the study was a reinforced concrete slab and the charge itself. The concrete slab was again modelled with the coupled SPH-FEM in which the reinforcement was introduced with the proposed approach with the SPH sublayer. The charge was modelled with pure SPH while employing the Shepard filter for the pressure field smoothing. Also in this case, two models with and without the constitutive model strain-rate effects were considered. Except of the concrete damage, responses of both models were sufficiently close to the experimental measurements. This among the others proved again that the proposed approach for the

SPH-FEM coupling works well and is stable despite the load rate. The experimental damage of the concrete was captured only by the model in which the constitutive model strain-rate effects were not considered. In other words, the formation of several main cracks propagating from the centre of the concrete slab as in the experiment were represented only by the model without the rate-effects. In contrast, the model with the rate-effects showed a region rather damaged with micro-cracks which was not observed in the experiment. The explanation for the failure mode was not established yet, as it was found that the charge in the experiment was not always placed as intended which could cause the different responses of the concrete. The behaviour of the SPH charge was in correlation with observations from the experiment. The charge performed as intended and due to the natural adaptivity of SPH it was quite easy to establish the interaction between the concrete and detonation products. For that reason, it can be said, SPH is able to represent structural and fluid parts within the same problem domain without any special treatment. This proved again that SPH can be superior to the other standard (mesh-based) numerical methods. Furthermore, the uncertain charge placement was analysed in a sensitivity study. Among the others, the study revealed that the concrete slabs could have been loaded by only 50% of the intended force yet with additional moments. The finding is in a correlation with the available documentation of the experiment, i.e. the damage of the concrete slabs was not always as expected, sometimes asymmetric. With the techniques for a visual resemblance as described in the material structure optimization it was possible to predict deviation angles of the charge for a selected specimen. The findings have a high potential in applied mechanics.

With respect to the summary of the outcomes and findings written in this chapter, the thesis met the expected results and all the goals defined in section *Goals of the Thesis* were fulfilled.

References

[1] Lucy, L. B., "A Numerical Approach to the Testing of the Fission Hypothesis," *The Astronomical Journal*, vol. 82, no. 12, pp. 1013–1024, Dec. 1977. DOI: 10.1086/112164.

[2] Gingold, R. A. and Monaghan, J. J., "Smoothed Particle Hydrodynamics: Theory and Application to Non-Spherical Stars," *Monthly Notices of the Royal Astronomical Society*, vol. 181, no. 3, pp. 375–389, 1977. DOI: 10.1093/mnras/181.3.375.

[3] Gingold, R. A. and Monaghan, J. J., "Kernel Estimates as a Basis for General Particle Methods in Hydrodynamics," *Journal of Computational Physics*, vol. 46, no. 3, pp. 429–453, 1982. DOI: 10.1016/0021-9991(82)90025-0.

[4] Monaghan, J. J., "Why Particle Methods Work," *Journal on Scientific Computing*, vol. 3, no. 4, pp. 422–433, 1982. DOI: 10.1137/0903027.

[5] Zukas, J. A., Nicholas, T., Swift, H. F., Greszczuk, L. B., and Curran, D. R., *Impact Dynamics*, First Edition. New York: John Wiley and Sons, Inc., Jan. 1982, ISBN: 978-0471086772.

[6] Monaghan, J. J. and Gingold, R. A., "Shock Simulation by the Particle Method SPH," *Journal of Computational Physics*, vol. 52, no. 2, pp. 374–389, 1983. DOI: 10.1016/0021-9991(83)90036-0.

[7] Monaghan, J. J., "Particle Methods for Hydrodynamics," *Computer Physics Reports*, vol. 3, pp. 71–124, 1985. DOI: 10.1016/0167-7977(85)90010-3.

[8] Monaghan, J. J., "Extrapolating B Splines for Interpolation," *Journal of Computational Physics*, vol. 60, no. 2, pp. 253–262, 1985. DOI: 10.1016/0021-9991(85)90006-3.

[9] Monaghan, J. J. and Lattanzio, J. C., "A Refined Particle Method for Astrophysical Problems," *Astronomy and Astrophysics*, vol. 149, no. 1, pp. 135–143, 1985. [Online]. Available: https://ui.adsabs.harvard.edu/abs/1985A&A...149..135M.

[10] Monaghan, J. J. and Pongracic, H., "Artificial Viscosity for Particle Methods," *Applied Numerical Mathematics*, vol. 1, no. 3, pp. 187–194, 1985. DOI: 10.1016/0168-9274(85)90015-7.

[11] Benz, W., "Applications of Smooth Particle Hydrodynamics (SPH) to Astrophysical Problems," *Computer Physics Communications*, vol. 48, no. 1, pp. 97–105, 1988. DOI: 10.1016/0010-4655(88)90027-6.

[12] Monaghan, J. J., "An Introduction to SPH," *Computer Physics Communications*, vol. 48, pp. 89–96, 1988. DOI: 10.1016/0010-4655(88)90026-4.

[13] Monaghan, J. J., "On the Problem of Penetration in Particle Methods," *Journal of Computational Physics*, vol. 82, pp. 1–15, 1989. DOI: 10.1016/0021-9991(89)90032-6.

[14] Benz, W., *Smoothed Particle Hydrodynamics: A Review*, NATO workshop, Les, Arcs, France, 1989.

[15] Benz, W., "Smoothed Particle Hydrodynamics: A Review," in *The Numerical Modeling of Non-Linear Stellar Pulsation: Problems and Prospects*, J. R. Buchler, Ed., Boston: Kluwer Academic Publishers, 1990, pp. 269–288. DOI: 10.1007/978-94-009-0519-1_16.

[16] Monaghan, J. J., "Modelling the Universe," *Proceedings of the Astronomical Society of Australia*, vol. 8, no. 3, pp. 233–237, 1990. [Online]. Available: https://ui.adsabs.harvard.edu/abs/1990PASAu...8..233M.

[17] Libersky, L. D. and Petscheck, A. G., "Smooth Particle Hydrodynamics with Strength of Materials," in *Proceedings of the Next Free Lagrange Conference*, H. Trease, J. Fritts, and W. Crowley, Eds., ser. Proceedings of The Next Free Lagrange Conference, vol. 395, Springer-Verlag, NY, United States, Jun. 1990, pp. 248–257. DOI: 10.1007/3-540-54960-9_58.

[18] Zukas, J. A., *High Velocity Impact Dynamics*, First Edition. New York: John Wiley and Sons, Inc., Jun. 1990, ISBN: 978-0471514442.

[19] Monaghan, J. J. and Lattanzio, J. C., "A Simulation of the Collapse and Fragmentation of Cooling Molecular Clouds," *The Astrophysical Journal*, vol. 375, pp. 177–189, 1991. DOI: 10.1086/170179.

[20] Monaghan, J. J., "Smoothed Particle Hydrodynamics," *Annual Review of Astronomical and Astrophysics*, vol. 30, pp. 543–574, 1992. DOI: 10.1146/annurev.aa.30.090192.002551.

[21] Libersky, L. D., Petschek, A. G., Carney, T. C., Hipp, J. R., and Allahdadi, F. A., "High Strain Lagrangian Hydrodynamics: A Three-Dimensional SPH Code for Dynamic Material Response," *Journal of Computational Physics*, vol. 109, no. 1, pp. 67–75, 1993. DOI: 10.1006/jcph.1993.1199.

[22] Allahdadi, F. A., Carney, T. C., Hipp, J. R., Libersky, L. D., and Petschek, A. G., "High Strain Lagrangian Hydrodynamics: A Three-Dimensional SPH Code for Dynamic Material Response," Phillips Laboratory Kirtland AFB, NM 87117-5776, Albuquerque, NM, United States, Technical Report PL-TR–92-1054, Mar. 1993. [Online]. Available: https://apps.dtic.mil/dtic/tr/fulltext/u2/a262798.pdf.

[23] Benz, W. and Asphaug, E., "Explicit 3D Continuum Fracture Modeling with Smooth Particle Hydrodynamics," in *Proceedings of the Lunar and Planetary Science Conference*, ser. Lunar and Planetary Science Conference, Mar. 1993, p. 99. [Online]. Available: https://ui.adsabs.harvard.edu/abs/1993LPI....24...99B.

[24] Stellingwerf, R. F. and Wingate, C. A., "Impact Modeling with Smooth Particle Hydrodynamics," *International Journal of Impact Engineering*, vol. 14, no. 1–4, pp. 707–718, 1993. DOI: 10.1016/0734-743X(93)90065-F.

[25] Monaghan, J. J., "Simulating Free Surface Flows with SPH," *Journal of Computational Physics*, vol. 110, no. 2, pp. 399–406, 1994. DOI: 10.1006/jcph.1994.1034.

[26] Swegle, J. W., Attaway, S. W., Heinstein, M. W., Mello, F. J., and Hicks, D. L., "An Analysis of Smoothed Particle Hydrodynamics," Sandia National Laboratories, Albuquerque, NM, United States, Technical Report SAND-93-2513, Mar. 1994. DOI: 10.2172/10159839.

[27] Benz, W. and Asphaug, E., "Impact Simulations with Fracture. I. Method and Tests," *ICARUS*, vol. 107, no. 1, pp. 98–116, 1994. DOI: 10.1006/icar.1994.1009.

[28] Benz, W. and Asphaug, E., "Simulations of Brittle Solids Using Smooth Particle Hydrodynamics," *Computer Physics Communications*, vol. 87, no. 1–2, pp. 253–265, 1995. DOI: 10.1016/0010-4655(94)00176-3.

[29] Swegle, J. W., Hicks, D. L., and Attaway, S. W., "Smoothed Particle Hydrodynamics Stability Analysis," *Journal of Computational Physics*, vol. 116, no. 1, pp. 123–134, 1995. DOI: 10.1006/jcph.1995.1010.

[30] Dyka, C. T. and Ingel, R. P., "An Approach for Tension Instability in Smoothed Particle Hydrodynamics (SPH)," *Computers & Structures*, vol. 57, no. 4, pp. 573–580, 1995. DOI: 10.1016/0045-7949(95)00059-P.

[31] Libersky, L. D., Randies, P. W., and Carney, T. C., "SPH Calculations of Fragmentation," in *Proceedings of the 3rd U. S. Congress on Computational Mechanics*, ser. 3rd U. S. Congress on Computational Mechanics, Dallas, TX, United States, Jun. 1995.

[32] Wendland, H., "Piecewise Polynomial, Positive Definite and Compactly Supported Radial Functions of Minimal Degree," *Advances in Computational Mathematics*, vol. 4, pp. 389–396, 1995. DOI: 10.1007/BF02123482.

[33] Fulbright, M. S., Benz, W., and Davies, M. B., "A Method of Smoothed Particle Hydrodynamics Using Spheroidal Kernels," *The Astrophysical Journal*, vol. 440, pp. 254–262, 1995. DOI: 10.1086/175266.

[34] Monaghan, J. J. and Kocharyan, A., "SPH Simulation of Multi-Phase Flow," *Computer Physics Communications*, vol. 87, no. 1–2, pp. 225–235, 1995. DOI: 10.1016/0010-4655(94)00174-Z.

[35] Randles, P. W. and Libersky, L. D., "Smoothed Particle Hydrodynamics: Some Recent Improvements and Applications," *Computer Methods in Applied Mechanics and Engineering*, vol. 139, no. 1–4, pp. 375–408, 1996. DOI: 10.1016/S0045-7825(96)01090-0.

[36] Morris, J. P., "A Study of the Stability Properties of Smooth Particle Hydrodynamics," *Publications of the Astronomical Society of Australia*, vol. 13, no. 1, pp. 97–102, 1996. DOI: 10.1017/S1323358000020610.

[37] Morris, J. P., "Analysis of Smoothed Particle Hydrodynamics with Applications," Ph.D. dissertation, Monash University, 1996.

[38] Liu, W. K., Chen, Y., Jun, S., Chen, J. S., Belytschko, T., Pan, C., Uras, R. A., and Chang, C. T., "Overview and Applications of the Reproducing Kernel Particle Methods," *Archives of Computational Methods in Engineering*, vol. 3, pp. 3–80, 1996. DOI: 10.1007/BF02736130.

[39] Chen, J. S., Pan, C., Wu, C. T., and Liu, W. K., "Reproducing Kernel Particle Methods for Large Deformation Analysis of Non-Linear Structures," *Computer Methods in Applied Mechanics and Engineering*, vol. 139, no. 1–4, pp. 195–227, 1996. DOI: 10.1016/S0045-7825(96)01083-3.

[40] Belytschko, T., Krongauz, Y., Organ, D., Fleming, M., and Krys, P., "Meshless Methods: An Overview and Recent Developments," *Computer Methods in Applied Mechanics and Engineering*, vol. 139, no. 1–4, pp. 3–47, 1996. DOI: 10.1016/S0045-7825(96)01078-X.

[41] Johnson, G. R., "Artificial Viscosity Effects for SPH Impact Computations," *International Journal of Impact Engineering*, vol. 18, no. 5, pp. 477–488, 1996. DOI: 10.1016/0734-743X(95)00051-B.

[42] Johnson, G. R. and Beissel, S. R., "Normalized Smoothing Functions for SPH Impact Computations," *International Journal for Numerical Methods in Engineering*, vol. 39, no. 16, pp. 2725–2741, 1996. DOI: 10.1002/(SICI)1097-0207(19960830)39:16<2725::AID-NME973>3.0.CO;2-9.

[43] Johnson, G. R., Stryk, R. A., and Beissel, S. R., "SPH for High Velocity Impact Computations," *Computer Methods in Applied Mechanics and Engineering*, vol. 139, no. 1–4, pp. 347–373, 1996. DOI: 10.1016/S0045-7825(96)01089-4.

[44] Fulk, D. A. and Quinn, D. W., "An Analysis of 1-D Smoothed Particle Hydrodynamics Kernels," *Journal of Computational Physics*, vol. 126, no. 1, pp. 165–180, 1996. DOI: 10.1006/jcph.1996.0128.

[45] Dyka, C. T., Randles, P. W., and Ingel, R. P., "Stress Points for Tension Instability in SPH," *International Journal for Numerical Methods in Engineering*, vol. 40, no. 13, pp. 2325–2341, 1997. DOI: 10.1002/(SICI)1097-0207(19970715)40:13<2325::AID-NME161>3.0.CO;2-8.

[46] Morris, J. P. and Monaghan, J. J., "A Switch to Reduce SPH Viscosity," *Journal of Computational Physics*, vol. 136, no. 1, pp. 41–50, 1997. DOI: 10.1006/jcph.1997.5690.

[47] Morris, J. P., Fox, P. J., and Zhu, Y., "Modeling Low Reynolds Number Incompressible Flows Using SPH," *Journal of Computational Physics*, 1997. DOI: 10.1006/jcph.1997.5776.

[48] Monaghan, J. J., "SPH and Riemann Solvers," *Journal of Computational Physics*, vol. 136, no. 2, pp. 298–307, 1997. DOI: 10.1006/jcph.1997.5732.

[49] Belytschko, T., Krongauz, Y., Dolbow, J., and Gerlach, C., "On the Completeness of Meshfree Particle Methods," *International Journal for Numerical Methods in Engineering*, vol. 43, no. 5, pp. 785–819, 1998. DOI: 10.1002/(SICI)1097-0207(19981115)43:5<785::AID-NME420>3.0.CO;2-9.

[50] Moussa, B. B., Lanson, N., and Vila, J. P., "Convergence of Meshless Methods for Conservation Laws Applications to Euler equations," in *Hyperbolic Problems: Theory, Numerics, Applications*, M. Fey and R. Jeltsch, Eds., ser. International Series of Numerical Mathematics, vol. 129, Birkhäuser, Basel, 1999, pp. 31–40. DOI: 10.1007/978-3-0348-8720-5_4.

[51] Dilts, G. A., "Moving-Least-Squares-Particle Hydrodynamics—I: Consistency and Stability," *International Journal for Numerical Methods in Engineering*, vol. 44, no. 8, pp. 1115–1155, 1999. DOI: 10.1002/(SICI)1097-0207(19990320)44:8<1115::AID-NME547>3.0.CO;2-L.

[52] Chen, J. K., Beraun, J. E., and Carney, T. C., "A Corrective Smoothed Particle Method for Boundary Value Problems in Heat Conduction," *International Journal for Numerical Methods in Engineering*, vol. 46, no. 2, pp. 231–252, 1999. DOI: 10.1002/(SICI)1097-0207(19990920)46:2<231::AID-NME672>3.0.CO;2-K.

[53] Vila, J. P., "On Particle Weighted Methods and Smooth Particle Hydrodynamics," *Mathematical Models and Methods in Applied Sciences*, vol. 9, no. 2, pp. 161–209, 1999. DOI: 10.1142/S0218202599000117.

[54] Hicks, D. L. and Liebrock, L. M., "SPH Hydrocodes can be Stabilized with Shape-shifting," *Computers & Mathematics with Applications*, vol. 38, no. 5–6, pp. 1–16, 1999. DOI: 10.1016/S0898-1221(99)00210-2.

[55] Morris, J. P., Zhu, Y., and Fox, P. J., "Parallel Simulations of Pore-Scale Flow Through Porous Media," *Computers and Geotechnics*, vol. 25, no. 4, pp. 227–246, 1999. DOI: 10.1016/S0266-352X(99)00026-9.

[56] Rasio, F. A. and Lombardi, J. C., "Smoothed Particle Hydrodynamics Calculations of Stellar Interactions," *Journal of Computational and Applied Mathematics*, vol. 109, pp. 213–230, 1999. DOI: 10.1016/S0377-0427(99)00159-4.

[57] Lee, W. H. and Kluzniak, W., "Newtonian Hydrodynamics of the Coalescence of Black Holes with Neutron Stars — II. Tidally Locked Binaries with a Soft Equation of State," *Monthly Notices of the Royal Astronomical Society*, vol. 308, no. 3, pp. 780–794, 1999. DOI: 10.1046/j.1365-8711.1999.02734.x.

[58] Hultman, J. and Pharasyn, A., "Hierarchical, Dissipative Formation of Elliptical Galaxies: Is Thermal Instability the Key Mechanism? Hydrodynamical Simulations Including Supernova Feedback, Multi-Phase Gas and Metal Enrichment in CDM: Structure and Dynamics of Elliptical Galaxies," *Astronomy and Astrophysics*, vol. 347, pp. 769–798, 1999. [Online]. Available: https://ui.adsabs.harvard.edu/abs/1999A&A...347..769H.

[59] García-Senz, D., Bravo, E., and Woosley, S. E., "Single and Multiple Detonations in White Dwarfs," *Astronomy and Astrophysics*, vol. 349, pp. 177–188, 1999. [Online]. Available: https://ui.adsabs.harvard.edu/abs/1999A&A...349..177G.

[60] Bonet, J. and Lok, T. S. L., "Variational and Momentum Preservation Aspects of Smooth Particle Hydrodynamic Formulations," *Computer Methods in Applied Mechanics and Engineering*, vol. 180, no. 1–2, pp. 97–115, 1999. DOI: 10.1016/S0045-7825(99)00051-1.

[61] Monaghan, J. J. and Kos, A., "Solitary Waves on a Cretan Beach," *Journal of Waterway, Port, Coastal and Ocean Engineering*, vol. 125, no. 3, pp. 145–155, 1999. DOI: 10.1061/(ASCE)0733-950X(1999)125:3(145).

[62] Cummins, S. J. and Rudman, M., "An SPH Projection Method," *Journal of Computational Physics*, vol. 152, no. 2, pp. 584–607, 1999. DOI: 10.1006/jcph.1999.6246.

[63] Moussa, B. B. and Vila, J. P., "Convergence of SPH Method for Scalar Nonlinear Conservation Laws," *SIAM Journal on Numerical Analysis*, vol. 37, no. 3, pp. 863–887, 2000. DOI: 10.1137/S0036142996307119.

[64] Dilts, G. A., "Moving Least-Squares Particle Hydrodynamics II: Conservation and Boundaries," *International Journal for Numerical Methods in Engineering*, vol. 48, no. 10, pp. 1503–1524, 2000. DOI: 10.1002/1097-0207(20000810)48:10<1503::AID-NME832>3.0.CO;2-D.

[65] Monaghan, J. J., "SPH Without a Tensile Instability," *Journal of Computational Physics*, vol. 159, no. 2, pp. 290–311, 2000. DOI: 10.1006/jcph.2000.6439.

[66] Randles, P. W. and Libersky, L. D., "Normalized SPH with Stress Points," *International Journal for Numerical Methods in Engineering*, vol. 48, no. 10, pp. 1445–1462, 2000. DOI: 10.1002/1097-0207(20000810)48:10<1445::AID-NME831>3.0.CO;2-9.

[67] Belytschko, T., Guo, Y., Liu, W. K., and Xiao, S. P., "A Unified Stability Analysis of Meshless Particle Methods," *International Journal for Numerical Methods in Engineering*, vol. 48, no. 9, pp. 1359–1400, 2000. DOI: 10.1002/1097-0207(20000730)48:9<1359::AID-NME829>3.0.CO;2-U.

[68] Vignjevic, R., Campbell, J., and Libersky, L., "A Treatment of Zero-Energy Modes in the Smoothed Particle Hydrodynamics Method," *Computer Methods in Applied Mechanics and Engineering*, vol. 184, no. 1, pp. 67–85, 2000. DOI: 10.1016/S0045-7825(99)00441-7.

[69] Bonet, J. and Kulasegaram, S., "Correction and Stabilization of Smooth Particle Hydrodynamics Methods with Applications in Metal Forming Simulations," *International Journal for Numerical Methods in Engineering*, vol. 47, no. 6, pp. 1189–1214, 2000. DOI: 10.1002/(SICI)1097-0207(20000228)47:6<1189::AID-NME830>3.0.CO;2-I.

[70] Chen, J. K. and Beraun, J. E., "A Generalized Smoothed Particle Hydrodynamics Method for Nonlinear Dynamic Problems," *Computer Methods in Applied Mechanics and Engineering*, vol. 190, no. 1–2, pp. 225–239, 2000. DOI: 10.1016/S0045-7825(99)00422-3.

[71] Berczik, P., "Modeling the Star Formation in Galaxies Using the Chemo-Dynamical SPH Code," *Astrophysics and Space Science*, vol. 271, no. 2, pp. 103–126, 2000. DOI: 10.1023/A:1002485702347.

[72] Morris, J. P., "Simulating Surface Tension with Smoothed Particle Hydrodynamics," *International Journal for Numerical Methods in Fluids*, vol. 33, no. 3, pp. 333–353, 2000. DOI: 10.1002/1097-0363(20000615)33:3<333::AID-FLD11>3.0.CO;2-7.

[73] Lee, W. H., "Newtonian Hydrodynamics of the Coalescence of Black Holes with Neutron Stars — III. Irrotational Binaries with a Stiff Equation of State," *Monthly Notices of the Royal Astronomical Society*, vol. 318, no. 2, pp. 606–624, 2000. DOI: 10.1046/j.1365-8711.2000.03870.x.

[74] Bonet, J. and Kulasegaram, S., "Remarks on Tension Instability of Eulerian and Lagrangian Corrected Smooth Particle Hydrodynamics (CSPH) Methods," *International Journal for Numerical Methods in Engineering*, vol. 52, no. 11, pp. 1203–1220, 2001. DOI: 10.1002/nme.242.

[75] Lanson, N. and Vila, J. P., "Meshless Methods for Conservation Laws," *Mathematics and Computers in Simulation*, vol. 55, no. 4–6, pp. 493–501, 2001. DOI: 10.1016/S0378-4754(00)00285-8.

[76] Gray, J. P., Monaghan, J. J., and Swift, R. P., "SPH Elastic Dynamics," *Computer Methods in Applied Mechanics and Engineering*, vol. 190, no. 49–50, pp. 6641–6662, 2001. DOI: 10.1016/S0045-7825(01)00254-7.

[77] Thacker, R. J. and Couchman, H. M. P., "Star Formation, Supernova Feedback, and the Angular Momentum Problem in Numerical Cold Dark Matter Cosmogony: Halfway There?" *The Astrophysical Journal*, vol. 555, no. 1, pp. 17–20, 2001. DOI: 10.1086/321739.

[78] Belytschko, T. and Xiao, S., "Stability Analysis of Particle Methods with Corrected Derivatives," *Computers & Mathematics with Applications*, vol. 43, no. 3–5, pp. 329–350, 2002. DOI: 10.1016/S0898-1221(01)00290-5.

[79] Li, S. and Liu, W. K., "Meshfree and Particle Methods and Their Applications," *Applied Mechanics Reviews*, vol. 55, no. 1, pp. 1–34, 2002. DOI: 10.1115/1.1431547.

[80] Inutsuka, S., "Reformulation of Smoothed Particle Hydrodynamics with Riemann Solver," *Journal of Computational Physics*, vol. 179, no. 1, pp. 238–267, 2002. DOI: 10.1006/jcph.2002.7053.

[81] Randles, P. W., Petschek, A. G., Libersky, L. D., and Dyka, C. T., "Stability of DPD and SPH," in *Meshfree Methods for Partial Differential Equations*, ser. Lecture Notes in Computational Science and Engineering, M. Griebel and M. A. Schweitzer, Eds., vol. 26, Springer, Berlin, Heidelberg, 2003. DOI: 10.1007/978-3-642-56103-0_24.

[82] Liu, M. B., Liu, G. R., and Lam, K. Y., "Constructing Smoothing Functions in Smoothed Particle Hydrodynamics with Applications," *Journal of Computational and Applied Mathematics*, vol. 155, no. 2, pp. 263–284, 2003. DOI: 10.1016/S0377-0427(02)00869-5.

[83] Liu, M. B., Liu, G. R., and Lam, K. Y., "A One-Dimensional Meshfree Particle Formulation for Simulating Shock Waves," *Shock Waves*, vol. 13, pp. 201–211, 2003. DOI: 10.1007/s00193-003-0207-0.

[84] Rabczuk, T., Eibl, J., and Stempniewski, L., "The SPH/MLSPH Method for the Simulation of High Velocity Concrete Fragmentation," in *Proceedings of the Meshfree Methods for Partial Differential Equations*, M. Griebel and M. A. Schweitzer, Eds., vol. 26, Berlin, Heidelberg, Germany: Springer, 2003, ch. Lecture Notes in Computational Science and Engineering, pp. 327–338, ISBN: 978-3-642-56103-0. DOI: 10.1007/978-3-642-56103-0_23.

[85] Liu, G. R. and Liu, M. B., *Smoothed Particle Hydrodynamics: A Meshfree Particle Method*, First Edition. Singapore: World Scientific Publishing Co. Pte. Ltd., Oct. 2003, ISBN: 981-238-456-1. DOI: 10.1142/5340.

[86] Rabczuk, T., Belytschko, T., and Xiao, S. P., "Stable Particle Methods Based on Lagrangian Kernels," *Computer Methods in Applied Mechanics and Engineering*, vol. 193, no. 12–14, pp. 1035–1063, 2004. DOI: 10.1016/j.cma.2003.12.005.

[87] Li, S. and Liu, W. K., *Meshfree Particle Methods*, First Edition. New York: Springer, Jan. 2004, ISBN: 978-3-540-22256-9. DOI: 10.1007/978-3-540-71471-2.

[88] Monaghan, J. J., "Smoothed Particle Hydrodynamics," *Reports on Progress in Physics*, vol. 608, pp. 1703–1759, 2005. DOI: 10.1088/0034-4885/68/8/R01.

[89] Vila, J. P., "SPH Renormalized Hybrid Methods for Conservation Laws: Applications to Free Surface Flows," in *Meshfree Methods for Partial Differential Equations II.*, M. Griebel and M. A. Schweitzer, Eds., ser. Lecture Notes in Computational Science and Engineering, vol. 43, Springer, Berlin, Heidelberg, 2005, pp. 207–229. DOI: 10.1007/3-540-27099-X_12.

[90] Randles, P. W. and Libersky, L. D., "Boundary Conditions for a Dual Particle Method," *Computers & Structures*, vol. 83, no. 17–18, pp. 1476–1486, 2005. DOI: 10.1016/j.compstruc.2004.11.027.

[91] Liu, M. B. and Liu, G. R., "Restoring Particle Consistency in Smoothed Particle Hydrodynamics," *Applied Numerical Mathematics*, vol. 56, no. 1, pp. 19–36, 2006. DOI: 10.1016/j.apnum.2005.02.012.

[92] Moussa, B. B., "On the Convergence of SPH Method for Scalar Conservation Laws with Boundary Conditions," *Methods and Applications of Analysis*, vol. 13, no. 1, pp. 29–62, 2006. DOI: 10.4310/MAA.2006.v13.n1.a3.

[93] Hu, X. Y. and Adams, N. A., "Angular-Momentum Conservative Smoothed Particle Dynamics for Incompressible Viscous Flows," *Physics of Fluids*, vol. 18, no. 101702, pp. 1–4, 2006. DOI: 10.1063/1.2359741.

[94] Sigalotti, L. D. G., López, H., Donoso, A., Sira, E., and Klapp, J., "A Shock-Capturing SPH Scheme Based on Adaptive Kernel Estimation," *Journal of Computational Physics*, vol. 212, no. 1, pp. 124–149, 2006. DOI: 10.1016/j.jcp.2005.06.016.

[95] Cleary, P. W., Prakash, M., Ha, J., Stokes, N., and Scott, C., "Smooth Particle Hydrodynamics: Status and Future Potential," *Progress in Computational Fluid Dynamics, An International Journal*, vol. 7, no. 2–4, pp. 70–90, 2007. DOI: 10.1504/PCFD.2007.013000.

[96] Cabezón, R. M., García-Senz, D., and Relaño, A., "A One-Parameter Family of Interpolating Kernels for Smoothed Particle Hydrodynamics Studies," *Journal of Computational Physics*, vol. 227, no. 19, pp. 8523–8540, 2008. DOI: 10.1016/j.jcp.2008.06.014.

[97] Lacome, J. L., Limido, J., and Espinosa, C., *SPH Formulation with Lagrangian Eulerian Adaptive Kernel*, 4th international SPHERIC workshop, Nantes, France, May 2009.

[98] Vignjevic, R. and Campbell, J., "Review of Development of the Smooth Particle Hydrodynamics (SPH) Method," in *Predictive Modelling of Dynamic Processes*, S. Hiermaier, Ed., Springer, 2009, pp. 1–25. DOI: 10.1007/978-1-4419-0727-1_20.

[99] Lastiwka, M., Basa, M., and Quinlan, N. J., "Permeable and Non Reflecting Boundary Conditions in SPH," *International Journal for Numerical Methods in Fluids*, vol. 61, no. 7, pp. 709–724, 2009. DOI: 10.1002/fld.1971.

[100] Xu, R., Stansby, P., and Laurence, D., "Accuracy and Stability in Incompressible SPH (ISPH) Based on the Projection Method and a New Approach," *Journal of Computational Physics*, vol. 228, no. 18, pp. 6703–6725, 2009. DOI: 10.1016/j.jcp.2009.05.032.

[101] Xu, F., Zhao, Y., Li, Y., and Kikuchi, M., "Study of Numerical and Physical Fracture with SPH Method," *Acta Mechanica Solida Sinica*, vol. 23, no. 1, pp. 49–56, 2010. DOI: 10.1016/S0894-9166(10)60006-7.

[102] Price, D. J., "Smoothed Particle Hydrodynamics and Magnetohydrodynamics," *Journal of Computational Physics*, vol. 231, no. 3, pp. 759–794, 2010. DOI: 10.1016/j.jcp.2010.12.011.

[103] Liu, M. B. and Liu, G. R., "Smoothed Particle Hydrodynamics (SPH): An Overview and Recent Developments," *Archives of Computational Methods in Engineering*, vol. 17, no. 1, pp. 25–76, 2010. DOI: 10.1007/s11831-010-9040-7.

[104] Antuono, M., Colagrossi, A., Marrone, S., and Molteni, D., "Free-Surface Flows Solved by Means of SPH Schemes with Numerical Diffusive Terms," *Computer Physics Communications*, vol. 181, no. 3, pp. 532–549, 2010. DOI: 10.1016/j.cpc.2009.11.002.

[105] Adami, S., Hu, X. Y., and Adams, N. A., "A New Surface-Tension Formulation for Multi-Phase SPH Using a Reproducing Divergence Approximation," *Journal of Computational Physics*, vol. 229, no. 13, pp. 5011–5021, 2010. DOI: 10.1016/j.jcp.2010.03.022.

[106] Hughes, J. P. and Graham, D. I., "Comparison of Incompressible and Weakly-Compressible SPH Models for Free-Surface Water Flows," *Journal of Hydraulic Research*, vol. 48, no. 1, pp. 105–117, 2010. DOI: 10.1080/00221686.2010.9641251.

[107] Liu, G. R., *Meshfree Methods: Moving Beyond the Finite Element Method*, Second Edition. New York: CRC Press, Oct. 2010, ISBN: 978-1-4200-8209-8.

[108] Jiang, T., Ouyang, J., Li, Q., Ren, J. L., and Yang, B. X., "A Corrected Smoothed Particle Hydrodynamics Method for Solving Transient Viscoelastic Fluid Flows," *Applied Mathematical Modelling*, vol. 35, no. 8, pp. 3833–3853, 2011. DOI: 10.1016/j.apm.2011.02.014.

[109] Jiang, T., Ouyang, J., Li, X. J., Zhang, L., and Ren, J. L., "The First Order Symmetric SPH Method for Transient Heat Conduction Problems," *Acta Physica Sinica*, vol. 60, no. 9, pp. 1–10, 2011.

[110] Ren, J., Ouyang, J., Yang, B., Jiang, T., and Mai, H., "Simulation of Container Filling Process with Two Inlets by Improved Smoothed Particle Hydrodynamics (SPH) Method," *International Journal of Computational Fluid Dynamics*, vol. 25, no. 7, pp. 365–386, 2011. DOI: 10.1080/10618562.2011.603308.

[111] Marrone, S., Antuono, M., Colagrossi, A., Colicchio, G., Le Touzé, D., and Graziani, G., "δ-SPH Model for Simulating Violent Impact Flows," *Computer Methods in Applied Mechanics and Engineering*, vol. 200, no. 13, pp. 1526–1542, 2011. DOI: 10.1016/j.cma.2010.12.016.

[112] Monaghan, J. J., "Smoothed Particle Hydrodynamics and Its Diverse Applications," *Annual Review of Fluid Mechanics*, vol. 44, pp. 323–346, 2012. DOI: 10.1146/annurev-fluid-120710-101220.

[113] Adami, S., Hu, X. Y., and Adams, N. A., "A Generalized Wall Boundary Condition for Smoothed Particle Hydrodynamics," *Journal of Computational Physics*, vol. 231, no. 21, pp. 7057–7075, 2012. DOI: 10.1016/j.jcp.2012.05.005.

[114] Akinci, N., Ihmsen, M., Akinci, G., Solenthaler, B., and Teschner, M., "Versatile Rigid-Fluid Coupling for Incompressible SPH," *ACM Transactions on Graphics*, vol. 31, no. 4, pp. 1–8, 2012. DOI: 10.1145/2185520.2185558.

[115] Federico, I., Marrone, S., Colagrossi, A., Aristodemo, F., and Antuono, M., "Simulating 2D Open-Channel Flows Through an SPH Model," *European Journal of Mechanics - B/Fluids*, vol. 34, pp. 35–46, 2012. DOI: 10.1016/j.euromechflu.2012.02.002.

[116] Xu, X. Y., Ouyang, J., Yang, B. X., and Liu, Z. J., "SPH Simulations of Three-Dimensional Non-Newtonian Free Surface Flows," *Computer Methods in Applied Mechanics and Engineering*, vol. 256, pp. 101–116, 2013. DOI: 10.1016/j.cma.2012.12.017.

[117] Prayogo, R. D. and Naa, C. F., "Three-Dimensional Smoothed Particle Hydrodynamics Method for Simulating Free Surface Flows," in *International Symposium on Computational Science*, ser. Recent development in computational science, Kanazawa University, Japan, Feb. 2013, pp. 125–133. arXiv: 1309.4074 [physics.flu-dyn].

[118] Adami, S., Hu, X. Y., and Adams, N. A., "A Transport-Velocity Formulation for Smoothed Particle Hydrodynamics," *Journal of Computational Physics*, vol. 241, pp. 292–307, 2013. DOI: 10.1016/j.jcp.2013.01.043.

[119] Skillen, A., Lind, S., Stansby, P. K., and Rogers, B. D., "Incompressible Smoothed Particle Hydrodynamics (SPH) with Reduced Temporal Noise and Generalised Fickian Smoothing Applied to Body–Water Slam and Efficient Wave–Body Interaction," *Computer Methods in Applied Mechanics and Engineering*, vol. 265, pp. 163–173, 2013. DOI: 10.1016/j.cma.2013.05.017.

[120] Yang, X. F., Peng, S. L., and Liu, M. B., "A New Kernel Function for SPH with Applications to Free Surface Flows," *Applied Mathematical Modelling*, vol. 38, no. 15–16, pp. 3822–3833, 2014. DOI: 10.1016/j.apm.2013.12.001.

[121] Ihmsen, M., Cornelis, J., Solenthaler, B., Horvath, C., and Teschner, M., "Implicit Incompressible SPH," *IEEE Transactions on Visualization and Computer Graphics*, vol. 20, no. 3, pp. 426–435, 2014. DOI: 10.1109/TVCG.2013.105.

[122] Puri, K. and Ramachandran, P., "Approximate Riemann solvers for the Godunov SPH (GSPH)," *Journal of Computational Physics*, vol. 270, pp. 432–458, 2014. DOI: 10.1016/j.jcp.2014.03.055.

[123] Rosswog, S., "Boosting the Accuracy of SPH Techniques Newtonian and Special-Relativistic Tests," *Monthly Notices of the Royal Astronomical Societ*, vol. 448, no. 4, pp. 3628–3664, 2015. DOI: 10.1093/mnras/stv225.

[124] Rosswog, S., "SPH Methods in the Modelling of Compact Objects," *Living Reviews in Computational Astrophysics*, vol. 1, pp. 1–109, 2015. DOI: 10.1007/lrca-2015-1.

[125] Liu, M. B. and Liu, G. R., *Particle Methods for Multi-Scale and Multi-Physics*, First Edition. Singapore: World Scientific Publishing Co. Pte. Ltd., Feb. 2016, ISBN: 978-981-4571-69-2. DOI: 10.1142/9017.

[126] Bankole, A. O., Dumbser, M., Iske, A., and Rung, T., "A Meshfree Semi-Implicit Smoothed Particle Hydrodynamics Method for Free Surface Flow," in *Meshfree Methods for Partial Differential Equations VIII*, M. Griebel and M. A. Schweitzer, Eds., ser. Lecture Notes in Computational Science and Engineering, vol. 115, 2017, pp. 35–52. DOI: 10.1007/978-3-319-51954-8_3.

[127] Frontiere, N., Raskin, C. D., and Owen, J. M., "CRKSPH – A Conservative Reproducing Kernel Smoothed Particle Hydrodynamics Scheme," *Journal of Computational Physics*, vol. 332, pp. 160–209, 2017. DOI: 10.1016/j.jcp.2016.12.004.

[128] Zhang, C., Hu, X. Y., and Adams, N. A., "A Generalized Transport-Velocity Formulation for Smoothed Particle Hydrodynamics," *Journal of Computational Physics*, vol. 337, pp. 216–232, 2017. DOI: 10.1016/j.jcp.2017.02.016.

[129] Collé, A., Limido, J., and Vila, J. P., "An Accurate SPH Scheme for Dynamic Fragmentation Modelling," in *DYMAT 2018 – 12th International Conference on the Mechanical and Physical Behaviour of Materials under Dynamic Loading*, ser. Modelling and Numerical Simulation, vol. 183, EPJ Web of Conferences, Sep. 2018, pp. 1–6. DOI: 10.1051/epjconf/201818301030.

[130] Röthlin, M., Klippel, H., and Wegener, K., "Meshless Methods for Large Deformation Elastodynamics," *Computational Physics*, pp. 1–40, 2018. arXiv: 1807.01117 [physics.comp-ph].

[131] Tafuni, A., Domínguez, J., Vacondio, R., and Crespo, A. J. C., "A Versatile Algorithm for the Treatment of Open Boundary Conditions in Smoothed Particle Hydrodynamics GPU Models," *Computer Methods in Applied Mechanics and Engineering*, vol. 342, pp. 604–624, 2018. DOI: 10.1016/j.cma.2018.08.004.

[132] Filho, C. A. D. F., *Smoothed Particle Hydrodynamics: Fundamentals and Basic Applications in Continuum Mechanics*, First Edition. Cham: Springer, Jan. 2019, ISBN: 978-3-030-00772-0. DOI: 10.1007/978-3-030-00773-7.

[133] Ramachandran, P., Muta, A., and Mokkapati, R., "Dual-Time Smoothed Particle Hydrodynamics for Incompressible Fluid Simulation," *Computational Physics*, 2019. arXiv: 1904.00861 [physics.comp-ph].

[134] Ramachandran, P. and Puri, K., "Entropically Damped Artificial Compressibility for SPH," *Computers & Fluids*, vol. 179, pp. 579–594, 2019. DOI: 10.1016/j.compfluid.2018.11.023.

[135] Negi, P., Ramachandran, P., and Haftu, A., "An Improved Non-Reflecting Outlet Boundary Condition for Weakly-Compressible SPH," *Computational Physics*, pp. 1–39, 2020. arXiv: 1907.04034 [physics.comp-ph].

[136] Muta, A., Ramachandran, P., and Negi, P., "An Efficient, Open Source, Iterative ISPH Scheme," *Computer Physics Communications*, 2020. DOI: 10.1016/j.cpc.2020.107283.

[137] Fugelso, E. and Taylor, J. W., "Evaluation of Combined Obliquity and Yaw for U-0.75% Ti Penetrators," Los Alamos National Laboratory, Los Alamos, NM, United States, Technical Report LA-7402-MS, 1978.

[138] Courant, R., Friedrichs, K., and Lewy, H., "Über die partiellen Differenzengleichungen der mathematischen Physik," *Mathematische Annalen*, vol. 100, pp. 32–74, 1928. DOI: 10.1007/BF01448839.

[139] Liu, G. R. and Gu, Y. T., *An Introduction to Meshfree Methods and Their Programming*, First Edition. Netherlands: Springer, Jan. 2005, ISBN: 978-1-4020-3228-8. DOI: 10.1007/1-4020-3468-7.

[140] Fulk, D. A., "A Numerical Analysis of Smoothed Particle Hydrodynamics," Ph.D. dissertation, Air Force Institute of Technology, 1994.

[141] Hernquist, L. and Katz, N., "TREESPH: A Unification of SPH with the Hierarchical Tree Method," *Astrophysical Journal Supplement Series*, vol. 70, pp. 419–446, 1989. DOI: 10.1086/191344.

[142] Schoenberg, I. J., "Contributions to the Problem of Approximation of Equidistant Data by Analytic Functions," *Quarterly of Applied Mathematics*, vol. 4, pp. 45–99, 1946. DOI: 10.1090/qam/15914.

[143] Schoenberg, I. J., *Cardinal Spline Interpolation*, First Edition, ser. CBMS-NSF Regional Conference Series in Applied Mathematics. Philadelphia: Society for Industrial and Applied Mathematics, Jan. 1973, ISBN: 978-0898710090. DOI: 10.1137/1.9781611970555.

[144] Hockney, R. W. and Eastwood, J. W., *Computer Simulation Using Particles*, First Edition. Bristol: Taylor & Francis, Inc., Jan. 1988, ISBN: 978-0852743928. [Online]. Available: http://cds.cern.ch/record/205864.

[145] Schaback, R. and Wendland, H., "Kernel Techniques: From Machine Learning to Meshless Methods," *Acta Numerica*, vol. 15, pp. 543–639, 2006. DOI: 10.1017/S0962492906270016.

[146] Dehnen, W. and Aly, H., "Improving Convergence in Smoothed Particle Hydrodynamics Simulations without Pairing Instability," *Monthly Notices of the Royal Astronomical Society*, vol. 425, no. 2, pp. 1068–1082, 2012. DOI: 10.1111/j.1365-2966.2012.21439.x.

[147] Valcke, S., De Rijcke, S., Rödiger, E., and Dejonghe, H., "Kelvin-Helmholtz Instabilities in Smoothed Particle Hydrodynamics," *Monthly Notices of the Royal Astronomical Society*, vol. 408, pp. 71–86, 2010. DOI: 10.1111/j.1365-2966.2010.17127.x.

[148] Shapiro, P. R., Martel, H., Villumsen, J. V., and Owen, J. M., "Adaptive Smoothed Particle Hydrodynamics, with Application to Cosmology: Methodology," *Astrophysical Journal Supplement Series*, vol. 103, pp. 269–330, 1996. DOI: 10.1086/192279.

[149] Nelson, R. P. and Papaloizou, J. C. B., "Variable Smoothing Lengths and Energy Conservation in Smoothed Particle Hydrodynamics," *Monthly Notices of the Royal Astronomical Society*, vol. 270, pp. 1–20, 1994. DOI: 10.1093/mnras/270.1.1.

[150] Steinmetz, M. and Müller, E., "On the Capabilities and Limits of Smoothed Particle Hydrodynamics," *Astronomy and Astrophysics*, vol. 268, no. 1, pp. 391–410, 1993. [Online]. Available: https://ui.adsabs.harvard.edu/abs/1993A&A...268..391S.

[151] Owen, J. M., Villumsen, J. V., Shapiro, P. R., and Martel, H., "Adaptive Smoothed Particle Hydrodynamics: Methodology. II.," *Astrophysical Journal Supplement Series*, vol. 116, no. 2, pp. 155–209, 1998. DOI: 10.1086/313100.

[152] LSTC, *LS-DYNA Keyword User's Manual Volume I*, R12.0, Livermore Software Technology Corporation (LSTC), Livermore, CA, United States, 2020.

[153] Zhu, Q., Hernquist, L., and Li, Y., "Numerical Convergence in Smoothed Particle Hydrodynamics," *The Astrophysical Journal*, vol. 800, no. 1, pp. 1–13, 2015. DOI: 10.1088/0004-637X/800/1/6.

[154] Sigalotti, L. D. G., Klapp, J., Rendón, O., Vargas, C. A., and Peña-Polo, F., "On the Kernel and Particle Consistency in Smoothed Particle Hydrodynamics," *Applied Numerical Mathematics*, vol. 108, pp. 242–255, 2016. DOI: 10.1016/j.apnum.2016.05.007.

[155] Von Neumann, J. and Richtmyer, R. D., "A Method for the Numerical Calculation of Hydrodynamic Shocks," *Journal of Applied Physics*, vol. 21, no. 3, pp. 232–237, 1950. DOI: 10.1063/1.1699639.

[156] Lattanzio, J. C., Monaghan, J. J., Pongracic, H., and Schwarz, M. P., "Controlling Penetration," *SIAM Journal on Scientific and Statistical Computing*, vol. 7, no. 2, pp. 591–598, 1986. DOI: 10.1137/0907039.

[157] Heuzé, O., "Complete Forms of Mie–Grüneisen Equation of State," in *AIP Conference Proceedings*, vol. 1793, Jan. 2017, p. 50 001. DOI: 10.1063/1.4971535.

[158] Menikoff, R. and Plohr, B. J., "The Riemann Problem for Fluid Flow of Real Materials," *Reviews of Modern Physics*, vol. 61, no. 1, pp. 75–130, 1989. DOI: 10.1103/RevModPhys.61.75.

[159] Balsara, D. S., "Von Neumann Stability Analysis of Smoothed Particle Hydrodynamics—Suggestions for Optimal Algorithms," *Journal of Computational Physics*, vol. 121, no. 2, pp. 357–372, 1995. DOI: 10.1016/S0021-9991(95)90221-X.

[160] Lanson, N. and Vila, J. P., "Renormalized Meshfree Schemes I: Consistency, Stability, and Hybrid Methods for Conservation Laws," *SIAM Journal on Numerical Analysis*, vol. 46, no. 4, pp. 1912–1934, 2007. DOI: 10.1137/S0036142903427718.

[161] Sigalotti, L. D. G. and Lopez, H., "Adaptive Kernel Estimation and SPH Tensile Instability," *Computers & Mathematics with Applications*, vol. 55, no. 1, pp. 23–50, 2008. DOI: 10.1016/j.camwa.2007.03.007.

[162] O'Brien, G. G., Hyman, M. A., and Kaplan, S., "A Study of the Numerical Solution of Partial Differential Equations," *Journal of Mathematics and Physics*, vol. 29, no. 1–4, pp. 223–251, 1950. DOI: 10.1002/sapm1950291223.

[163] Shepard, D., "A Two-Dimensional Interpolation Function for Irregularly-Spaced Data," in *Proceedings of the 1968 23rd ACM National Conference*, ser. ACM '68, Association for Computing Machinery, New York, NY, United States, Jan. 1968, pp. 517–524. DOI: 10.1145/800186.810616.

[164] Gomez-Gesteira, M., Rogers, B. D., A., D. R., and Crespo, A. J. C., "State-of-the-art of Classical SPH for Free-Surface Flows," *Journal of Hydraulic Research*, vol. 48, pp. 6–27, 2010. DOI: 10.1080/00221686.2010.9641242.

[165] Liu, W. K., Jun, S., Li, S., Adee, J., and Belytschko, T., "Reproducing Kernel Particle Methods for Structural Dynamics," *International Journal for Numerical Methods in Engineering*, vol. 38, no. 10, pp. 1655–1679, 1995. DOI: 10.1002/nme.1620381005.

[166] Krongauz, Y. and Belytschko, T., "Enforcement of Essential Boundary Conditions in Meshless Approximations Using Finite Elements," *Computer Methods in Applied Mechanics and Engineering*, vol. 131, no. 1–2, pp. 133–145, 1996. DOI: 10.1016/0045-7825(95)00954-X.

[167] Colagrossi, A. and Landrini, M., "Numerical Simulation of Interfacial Flows by Smoothed Particle Hydrodynamics," *Journal of Computational Physics*, vol. 191, no. 2, pp. 448–475, 2003. DOI: 10.1016/S0021-9991(03)00324-3.

[168] Bilotta, G., Russo, G., Hérault, A., and Negro, C. D., "Moving Least-Squares Corrections for Smoothed Particle Hydrodynamics," *Annals of Geophysics*, vol. 54, no. 5, pp. 622–633, 2011. DOI: 10.4401/ag-5344.

[169] Li, S. and Liu, W. K., "Moving Least-Square Reproducing Kernel Method Part II: Fourier Analysis," *Computer Methods in Applied Mechanics and Engineering*, vol. 139, no. 1–4, pp. 159–193, 1996. DOI: 10.1016/S0045-7825(96)01082-1.

[170] Liu, W. K., Li, S., and Belytschko, T., "Moving Least-Square Reproducing Kernel Methods (I) Methodology and Convergence," *Computer Methods in Applied Mechanics and Engineering*, vol. 143, no. 1–2, pp. 113–154, 1997. DOI: 10.1016/S0045-7825(96)01132-2.

[171] Bicknell, G. V. and Gingold, R. A., "On Tidal Detonation of Stars by Massive Black Holes," *Astrophysical Journal*, vol. 273, pp. 749–760, 1983. DOI: 10.1086/161410.

[172] Lancaster, P. and Salkauskas, K., "Surfaces Generated by Moving Least Squares Methods," *Mathematics of Computation*, vol. 37, pp. 141–158, 1981. DOI: 10.1090/S0025-5718-1981-0616367-1.

[173] Nayroles, B., Touzot, G., and Villon, P., "Generalizing the Finite Element Method: Diffuse Approximation and Diffuse Elements," *Computational Mechanics*, vol. 10, pp. 307–318, 1992. DOI: 10.1007/BF00364252.

[174] Belytschko, T., Lu, Y. Y., and Gu, L., "Element-Free Galerkin Methods," *International Journal for Numerical Methods in Engineering*, vol. 37, no. 2, pp. 229–256, 1994. DOI: 10.1002/nme.1620370205.

[175] Hillman, M. and Chen, J. S., "An Accelerated, Convergent, and Stable Nodal Integration in Galerkin Meshfree Methods for Linear and Nonlinear Mechanics," *International Journal for Numerical Methods in Engineering*, vol. 107, no. 7, pp. 603–630, 2015. DOI: 10.1002/nme.5183.

[176] Yreux, E. and Chen, J. S., "A Quasi-Linear Reproducing Kernel Particle Method," *International Journal for Numerical Methods in Engineering*, vol. 109, no. 7, pp. 1045–1064, 2016. DOI: 10.1002/nme.5319.

[177] Yreux, E., "MLS-Based SPH in LS-DYNA for Increased Accuracy and Tensile Stability," in *Proceedings of the 15th International LS-DYNA Users Conference*, LSTC, Detroit, Michigan, United States, Jun. 2018, pp. 1–10. [Online]. Available: https://www.dynalook.com/conferences/15th-international-ls-dyna-conference/sph/mls-based-sph-in-ls-dyna-r-for-increased-accuracy-and-tensile-stability.

[178] Monaghan, J. J., "SPH Compressible Turbulence," *Monthly Notices of the Royal Astronomical Society*, vol. 335, no. 3, pp. 843–852, 2002. DOI: 10.1046/j.1365-8711.2002.05678.x.

[179] Li, D. and Wong, L. N. Y., "The Brazilian Disc Test for Rock Mechanics Applications: Review and New Insights," *Rock Mechanics and Rock Engineering*, vol. 46, pp. 269–287, 2013. DOI: 10.1007/s00603-012-0257-7.

[180] Carmona, S. and Aguado, A., "New Model for the Indirect Determination of the Tensile Stress–Strain Curve of Concrete by Means of the Brazilian Test," *Materials and Structures*, vol. 45, pages1473–1485, 2012. DOI: 10.1617/s11527-012-9851-0.

[181] Swegle, J. W., "SPH in Tension," Sandia National Laboratories, Albuquerque, NM, United States, Technical Report, 1992.

[182] Sulsky, D., Zhou, S. J., and Schreyer, H. L., "Application of a Particle-in-Cell Method to Solid Mechanics," *Computer Physics Communications*, vol. 87, no. 1–2, pp. 236–252, 1995. DOI: 10.1016/0010-4655(94)00170-7.

[183] Parshikov, A. N. and Medin, S. A., "Smoothed Particle Hydrodynamics Using Interparticle Contact Algorithms," *Journal of Computational Physics*, vol. 180, no. 1, pp. 358–382, 2002. DOI: 10.1006/jcph.2002.7099.

[184] Vidal, Y., Bonet, J., and Huerta, A., "Stabilized Updated Lagrangian Corrected SPH for Explicit Dynamic Problems," *International Journal for Numerical Methods in Engineering*, vol. 69, no. 13, pp. 2687–2710, 2006. DOI: 10.1002/nme.1859.

[185] LSTC, *LS-DYNA Theory Manual*, R12.0, Livermore Software Technology Corporation (LSTC), Livermore, CA, United States, 2020.

[186] Murray, Y. D., "Users Manual for LS-DYNA Concrete Material Model 159," APTEK, Inc., 1257 Lake Plaza Drive, Colorado Springs, United States, Technical Report FHWA-HRT-05-062, May 2007. [Online]. Available: https://www.fhwa.dot.gov/publications/research/infrastructure/pavements/05062/index.cfm.

[187] Ožbolt, J., Bede, N., Sharma, A., and Mayer, U., "Dynamic Fracture of Concrete L-Specimen: Experimental and Numerical Study," *Engineering Fracture Mechanics*, vol. 148, pp. 27–41, 2015. DOI: 10.1016/j.engfracmech.2015.09.002.

[188] Ožbolt, J., Sharma, A., and Reinhardt, H. W., "Dynamic Fracture of Concrete – Compact Tension Specimen," *International Journal of Solids and Structures*, vol. 48, no. 10, pp. 1534–1543, 2011. DOI: 10.1016/j.ijsolstr.2011.01.033.

[189] Ožbolt, J., Bošnjak, J., and Sola, E., "Dynamic Fracture of Concrete Compact Tension Specimen: Experimental and Numerical Study," *International Journal of Solids and Structures*, vol. 50, no. 25–26, pp. 4270–4278, 2013. DOI: 10.1016/j.ijsolstr.2013.08.030.

[190] Ožbolt, J., Sharma, A., Irhan, B., and Sola, E., "Tensile Behavior of Concrete under High Loading Rates," *International Journal of Impact Engineering*, vol. 69, pp. 55–68, 2014. DOI: 10.1016/j.ijimpeng.2014.02.005.

[191] Irhan, B., Ožbolt, J., and Ruta, D., "3D Finite Element Simulations of High Velocity Projectile Impact," *International Journal of Solids and Structures*, vol. 72, pp. 38–49, 2015. DOI: 10.1016/j.ijsolstr.2015.07.010.

[192] Murray, Y. D. and Lewis, B. A., "Numerical Simulation of Damage in Concrete," APTEK, Inc., 1257 Lake Plaza Drive, Colorado Springs, United States, Technical Report DNA-TR-94-190, Nov. 1995. [Online]. Available: https://apps.dtic.mil/sti/citations/ADA301935.

[193] Schwer, L. E., "Strain Rate Induced Strength Enhancement in Concrete: Much ado about Nothing?" In *Proceedings of the 7th European LS-DYNA Conference*, LSTC, Salzburg, Austria, May 2009, pp. 1–15. [Online]. Available: https://www.dynalook.com/conferences/european-conf-2009/M-I-04.pdf.

[194] Li, Q. M. and Meng, H., "About the Dynamic Strength Enhancement of Concrete-Like Materials in a Split Hopkinson Pressure Bar Test," *International Journal of Solids and Structures*, vol. 40, no. 2, pp. 343–360, 2003. DOI: 10.1016/S0020-7683(02)00526-7.

[195] Zhou, X. Q. and Hao, H., "Modelling of Compressive Behaviour of Concrete-Like Materials at High Strain Rate," *International Journal of Solids and Structures*, vol. 45, no. 17, pp. 4648–4661, 2008. DOI: 10.1016/j.ijsolstr.2008.04.002.

[196] Ross, C. A., Tedesco, J. W., and Kuennen, S. T., "Effects of Strain Rate on Concrete Strength," *Materials Journal*, vol. 92, no. 1, pp. 37–47, 1995. DOI: 10.14359/1175.

[197] Bischoff, P. H. and Perry, S. H., "Impact Behavior of Plain Concrete Loaded in Uniaxial Compression," *Journal of Engineering Mechanics*, vol. 121, no. 6, pp. 685–693, 1995. DOI: 10.1061/(ASCE)0733-9399(1995)121:6(685).

[198] Willam, K. J. and Warnke, E. P., "Constitutive Models for the Triaxial Behavior of Concrete," in *Proceedings of the International Association for Bridge and Structural Engineering*, ser. Concrete Structures Subjected to Triaxial Stresses, IABSE, vol. 19, IABSE, May 1974, pp. 1–30. DOI: 10.5169/seals-17526.

[199] Schwer, L. E. and Murray, Y. D., "A Three-Invariant Smooth Cap Model with Mixed Hardening," *International Journal for Numerical and Analytical Methods in Geomechanics*, vol. 18, no. 10, pp. 657–688, 1994. DOI: 10.1002/nag.1610181002.

[200] Schwer, L. E., "Viscoplastic Augmentation of the Smooth Cap Model," *Nuclear Engineering and Design*, vol. 150, no. 2–3, pp. 215–223, 1994. DOI: 10.1016/0029-5493(94)90138-4.

[201] LSTC, *LS-DYNA Keyword User's Manual Volume II*, R12.0, Livermore Software Technology Corporation (LSTC), Livermore, CA, United States, 2020.

[202] Schwer, L. E. and Murray, Y. D., "Continuous Surface Cap Model for Geomaterial Modeling: A New LS-DYNA Material Type," in *Proceedings of the 7th International LS-DYNA Users Conference*, LSTC, Detroit, Michigan, United States, May 2002, pp. 16–35. [Online]. Available: https://www.dynalook.com/conferences/international-conf-2002/Session_16-3.pdf.

[203] Murray, Y. D., Abu-Odeh, A., and Bligh, R., "Evaluation of LS-DYNA Concrete Material Model 159," APTEK, Inc., 1257 Lake Plaza Drive, Colorado Springs, United States, Technical Report FHWA-HRT-05-063, May 2007. [Online]. Available: https://www.fhwa.dot.gov/publications/research/infrastructure/structures/05063/index.cfm.

[204] Rubin, M. B., "Simple, Convenient Isotropic Failure Surface," *Journal of Engineering Mechanics*, vol. 117, no. 2, pp. 348–369, 1991. DOI: 10.1061/(ASCE)0733-9399(1991)117:2(348).

[205] Simo, J. C. and Ju, J. W., "Strain- and Stress-Based Continuum Damage Models—I. Formulation," *International Journal of Solids and Structures*, vol. 23, no. 7, pp. 821–840, 1987. DOI: 10.1016/0020-7683(87)90083-7.

[206] Simo, J. C. and Ju, J. W., "Strain- and Stress-Based Continuum Damage Models—II. Computational Aspects," *International Journal of Solids and Structures*, vol. 23, no. 7, pp. 841–869, 1987. DOI: 10.1016/0020-7683(87)90084-9.

[207] Simo, J. C., Kennedy, J. G., and Govindjee, S., "Non-Smooth Multisurface Plasticity and Viscoplasticity. Loading/Unloading Conditions and Numerical Algorithms," *International Journal for Numerical Methods in Engineering*, vol. 26, no. 10, pp. 2161–2185, 1988. DOI: 10.1002/nme.1620261003.

[208] Sandler, I., Di Maggio, F. L., and Barron, M. L., "An Extension of the Cap Model with Inclusion of Pore Pressure Effects and Kinematic Hardening to Represent an Anisotropic Wet Clay," in *Mechanics of Engineering Materials*, ser. Wiley series in numerical methods in engineering, C. S. Desai and R. H. Gallagher, Eds., First Edition, New York: John Wiley and Sons, Inc., 1984, ch. Chapeter 28, p. 691, ISBN: 978-0471902768.

[209] CEN, "EN 1992-1-1 Eurocode 2: Design of Concrete Structures – Part 1-1: General Ruels and Rules for Buildings," European Committee for Standardization, Brussels, Belgium, Standard EN 1992-1-1, Jul. 2018.

[210] Winkler, B., Hofstetter, G., and Niederwanger, G., "Experimental Verification of a Constitutive Model for Concrete Cracking," *Proceedings of the Institution of Mechanical Engineers, Part L: Journal of Materials: Design and Applications*, vol. 215, no. 2, pp. 75–86, 2001. DOI: 10.1177/146442070121500202.

[211] Ožbolt, J. and Sharma, A., "Numerical Simulation of Dynamic Fracture of Concrete through Uniaxial Tension and L-Specimen," *Engineering Fracture Mechanics*, vol. 85, pp. 88–102, 2012. DOI: 10.1016/j.engfracmech.2012.02.013.

[212] Hušek, M., Kala, J., Hokeš, F., and Král, P., "How to Handle Irregular Distribution of SPH Particles in Dynamic Fracture Analysis," *International Journal of Theoretical and Applied Mechanics*, vol. 1, pp. 212–217, 2016. [Online]. Available: http://www.iaras.org/iaras/filedownloads/ijtam/2016/009-0032.pdf.

[213] Hušek, M., Kala, J., Král, P., and Hokeš, F., "Effect of the Support Domain Size in SPH Fracture Simulations," *International Journal of Mechanics*, vol. 10, pp. 396–402, 2016. [Online]. Available: http://www.naun.org/main/NAUN/mechanics/2016/b162003-208.pdf.

[214] Kala, J. and Hušek, M., "Improved Element Erosion Function for Concrete-Like Materials with the SPH Method," *Shock and Vibration*, vol. 2016, pp. 1–13, 2016, IF: 1.158 (2016), JCR: Q3 (Mechanics), JCR: Q3 (Acoustics), JCR: Q4 (Engineering, Mechanical). DOI: 10.1155/2016/4593749.

[215] Kala, J. and Hušek, M., "High Speed Loading of Concrete Constructions with Transformation of Eroded Mass into the SPH," *International Journal of Mechanics*, vol. 10, pp. 145–150, 2016. [Online]. Available: http://www.naun.org/main/NAUN/mechanics/2016/a442003-194.pdf.

[216] Buchar, J., Krejčí, J., and Forejt, M., "Response of Concrete to the Impact of Fragments Simulating Projectiles," *Engineering Mechanics*, vol. 8, no. 1, pp. 63–69, 2001, ISSN: 1805-4633.

[217] Buchar, J. and Voldřich, J., *Terminální balistika*, First Edition. Praha, Czech Republic: Academia, Jan. 2003, ISBN: 80-200-1222-2.

[218] NSA, "STANAG 2920 PPS – Ballistic Test Method for Personal Armour Materials and Combat Clothing," NATO Standardization Agency, Brussels, Belgium, Standard STANAG 2920, Jul. 2003, Edition 2.

[219] Johnson, G. R. and Cook, W. H., "Fracture Characteristics of Three Metals Subjected to Various Strains, Strain Rates, Temperatures and Pressures," *Engineering Fracture Mechanics*, vol. 21, no. 1, pp. 31–48, 1985. DOI: 10.1016/0013-7944(85)90052-9.

[220] Steinberg, D. J., "Equation of State and Strength Properties of Selected Materials," Lawrence Livermore National Laboratory, Livermore, CA, United States, Technical Report UCRL-MA-106439, Feb. 1996, Change 1.

[221] Grüneisen, E., "Theorie des festen Zustandes einatomiger Elemente," *Annalen der Physik*, vol. 344, no. 12, pp. 257–306, 1912. DOI: 10.1002/andp.19123441202.

[222] Eckardt, S., "Adaptive Heterogeneous Multiscale Models for The Nonlinear Simulation of Concrete," Ph.D. dissertation, Bauhaus-Universität Weimar, 2009.

[223] Zaitsev, Y. B. and Wittmann, F. H., "Simulation of Crack Propagation and Failureof Concrete," *Materials and Structures*, vol. 14, no. 5, pp. 357–365, 1981. DOI: 10.1007/BF02478729.

[224] Hušek, M., Hokeš, F., Kala, J., and Král, P., "A Simple Solution for Randomized Failure Modeling with the SPH Method," *International Journal of Theoretical and Applied Mechanics*, vol. 1, pp. 253–258, 2016. [Online]. Available: http://www.iaras.org/iaras/filedownloads/ijtam/2016/009-0038.pdf.

[225] Hušek, M., Hokeš, F., Kala, J., and Král, P., "Inclusion of Randomness into SPH Simulations," *WSEAS Transactions on Heat and Mass Transfer*, vol. 12, pp. 1–10, 2017. [Online]. Available: http://www.wseas.org/multimedia/journals/heat/2017/a025812-166.pdf.

[226] Hušek, M., Král, P., Kala, J., Hradil, P., and Maňas, P., "Concrete Targets with Heterogeneities under Impact Loading," *Advances in Military Technology*, vol. 13, no. 1, pp. 107–118, 2018. DOI: 10.3849/aimt.01216.

[227] Perlin, K., "An Image Synthesizer," *SIGGRAPH Computer Graphics*, vol. 19, no. 3, pp. 287–296, 1985. DOI: 10.1145/325165.325247.

[228] Bevins, J. "libnoise." (2020), [Online]. Available: http://libnoise.sourceforge.net (visited on 11/11/2020).

[229] Kessenich, J., Sellers, G., and Shreiner, D., *OpenGL Programming Guide: The Official Guide to Learning OpenGL, Version 4.5 with SPIR-V*, Ninth Edition. Crawfordsville: Addison-Wesley Professional, Jul. 2016, ISBN: 978-0-13-449549-1.

[230] Vivo, P. G. and Lowe, J. "The Book of Shaders." (2015), [Online]. Available: https://thebookofshaders.com (visited on 11/11/2020).

[231] Hušek, M. and Kala, J., "How to Get Closer to Reality in Pressure Test Simulations with the SPH Method," *International Journal of Mechanics*, vol. 11, pp. 226–233, 2017. [Online]. Available: http://www.naun.org/main/NAUN/mechanics/2017/a642003-aan.pdf.

[232] Hušek, M. and Kala, J., "Material Structure Generation of Concrete and Its Further Usage in Numerical Simulations," *Structural Engineering and Mechanics, An International Journal*, vol. 68, no. 3, pp. 335–344, 2018, IF: 3.017 (2018), JCR: Q1 (Engineering, Civil), JCR: Q2 (Engineering, Mechanical). DOI: 10.12989/sem.2018.68.3.335.

[233] Plotnick, R. E., Gardner, R. H., and O'Neill, R. V., "Lacunarity Indices as Measures of Landscape Texture," *Landscape Ecology*, vol. 8, no. 3, pp. 201–211, 1993. DOI: 10.1007/BF00125351.

[234] Plotnick, R. E., Gardner, R. H., Hargrove, W. W., Prestegaard, K., and Perlmutter, M., "Lacunarity Analysis: A General Technique for the Analysis of Spatial Patterns," *Physical Review E*, vol. 53, no. 5, pp. 5461–5468, 1996. DOI: 10.1103/PhysRevE.53.5461.

[235] Smith, T. G., Lange, G. D., and Marks, W. B., "Fractal Methods and Results in Cellular Morphology – Dimensions, Lacunarity and Multifractals," *Journal of Neuroscience Methods*, vol. 69, no. 2, pp. 123–136, 1996. DOI: 10.1016/S0165-0270(96)00080-5.

[236] McIntyre, N. E. and Wiens, J. A., "A Novel Use of the Lacunarity Index to Discern Landscape Function," *Landscape Ecology*, vol. 15, pp. 313–321, 2000. DOI: 10.1023/A:1008148514268.

[237] Karperien, A. B., "Defining Microglial Morphology: Form, Function, and Fractal Dimension," Ph.D. dissertation, Charles Sturt University, 2004. [Online]. Available: https://researchoutput.csu.edu.au/files/9307966/31797.

[238] Karperien, A. B., *FracLac for ImageJ*, 2013. [Online]. Available: https://imagej.nih.gov/ij/plugins/fraclac/FLHelp/Introduction.htm.

[239] CEN, "EN 1993-1-1 Eurocode 3: Design of Steel Structures – Part 1-1: General Ruels and Rules for Buildings," European Committee for Standardization, Brussels, Belgium, Standard EN 1993-1-1, Mar. 2015.

[240] Mooney, M., "A Theory of Large Elastic Deformation," *Journal of Applied Physics*, vol. 11, pp. 582–592, 1940. DOI: 10.1063/1.1712836.

[241] Rivlin, R. S., "Large Elastic Deformations of Isotropic Materials. I. Fundamental Concepts," *Philosophical Transactions of the Royal Society of London*, vol. 240, no. 822, pp. 459–490, 1948. DOI: 10.1098/rsta.1948.0002.

[242] Jerrams, S. J. and Bowen, J., "Modelling the Behaviour of Rubber-Like Materials to Obtain Correlation with Rigidity Modulus Tests," *Transactions on Modelling and Simulation*, vol. 12, pp. 1–8, 1995. DOI: 10.2495/CMEM950561. [Online]. Available: https://www.witpress.com/Secure/elibrary/papers/CMEM95/CMEM95056FU.pdf.

[243] Yeoh, O. H., "Some Forms of the Strain Energy Function for Rubber," *Rubber Chemistry and Technology*, vol. 66, no. 5, pp. 754–771, 1993. DOI: 10.5254/1.3538343.

[244] Marckmann, G. and Verron, E., "Comparison of Hyperelastic Models for Rubber-Like Materials," *Rubber Chemistry and Technology*, vol. 79, no. 5, pp. 835–858, 2006. DOI: 10.5254/1.3547969.

[245] Shahzad, M., Kamran, A., Siddiqui, M. Z., and Farhan, M., "Mechanical Characterization and FE Modelling of a Hyperelastic Material," *Materials Research*, vol. 18, no. 5, pp. 918–924, 2015. DOI: 10.1590/1516-1439.320414.

[246] Jaramillo, H. E., "Evaluation of the Use of the Yeoh and Mooney-Rivlin Functions as Strain Energy Density Functions for the Ground Substance Material of the Annulus Fibrosus," *Mathematical Problems in Engineering*, vol. 2018, pp. 1–10, 2018. DOI: 10.1155/2018/1570142.

[247] US Army, *Structures to Resist the Effects of Accidental Explosions*, Technical Manual TM 5-1300, Departments of the Army, the Navy, and the Air Force, United States, Nov. 1990. [Online]. Available: https://www.wbdg.org/FFC/ARMYCOE/COETM/ARCHIVES/tm_5_1300_1990.pdf.

[248] Le Blanc, G., Adoum, M., and Lapoujade, V., "External Blast Load on Structures – Empirical Approach," in *Proceedings of the 5th European LS-DYNA Users Conference*, LSTC, Birmingham, UK, May 2005, pp. 1–12. [Online]. Available: https://www.dynalook.com/conferences/european-conf-2005/Leblanc.pdf.

[249] Schwer, L. E., "A Brief Introduction to Coupling Load Blast Enhanced with Multi-Material ALE: The Best of Both Worlds for Air Blast Simulation," in *Proceedings of the 9th LS-DYNA Forum*, LSTC, Bamberg, Germany, Oct. 2010, pp. 1–12. [Online]. Available: https://www.dynamore.it/de/download/papers/forum10/papers/J-I-01.pdf.

[250] Schwer, L. E., Teng, H., and Souli, M., "LS-DYNA Air Blast Techniques: Comparison with Experiments for Close-in Charges," in *Proceedings of the 10th European LS-DYNA Conference*, LSTC, Würzburg, Germany, Jun. 2015, pp. 1–20. [Online]. Available: https://www.dynalook.com/conferences/10th-european-ls-dyna-conference/7%20Simulation%20III%20-%20Blast-Penetration/03-Schwer-SchwerEngineering-P.pdf.

[251] Slavik, T. P., "A Coupling of Empirical Explosive Blast Loads to ALE Air Domains in LS-DYNA," in *Proceedings of the 7th European LS-DYNA Conference*, LSTC, Salzburg, Austria, May 2009, pp. 1–10. [Online]. Available: https://www.dynalook.com/conferences/european-conf-2009/J-I-03.pdf.

[252] Tabatabaei, Z. S. and Volz, J. S., "A Comparison between Three Different Blast Methods in LS-DYNA: LBE, MM-ALE, Coupling of LBE and MM-ALE," in *Proceedings of the 12th International LS-DYNA Users Conference*, LSTC, Detroit, Michigan, United States, Jun. 2012, pp. 1–10. [Online]. Available: https://www.dynalook.com/conferences/12th-international-ls-dyna-conference/blast-impact20-d.pdf.

[253] Trajkovski, J., "Comparison of MM-ALE and SPH Methods for Modelling Blast Wave Reflections of Flat and Shaped Surfaces," in *Proceedings of the 11th European LS-DYNA Conference*, LSTC, Salzburg, Austria, May 2017, pp. 1–14. [Online]. Available: https://www.dynalook.com/conferences/11th-european-ls-dyna-conference/air-blast/comparison-of-mm-ale-and-sph-methods-for-modelling-blast-wave-reflections-of-flat-and-shaped-surfaces.

[254] Toussaint, G. and Bouamoul, A., "Comparison of ALE and SPH Methods for Simulating Mine Blast Effects on Structures," Defence Research and Development Canada, Valcartier, Canada, Technical Report TR 2010-326, Dec. 2010. [Online]. Available: https://apps.dtic.mil/dtic/tr/fulltext/u2/a595432.pdf.

[255] Barsotti, M. A., Puryear, J. M. H., Stevens, D. J., Alberson, R. M., and McMahon, P., "Modeling Mine Blast with SPH," in *Proceedings of the 12th International LS-DYNA Users Conference*, LSTC, Detroit, Michigan, United States, Jun. 2012, pp. 1–12. [Online]. Available: https://www.dynalook.com/conferences/12th-international-ls-dyna-conference/blast-impact06-a.pdf.

[256] Barsotti, M. A., Sammarco, E., and Stevens, D., "Comparison of Strategies for Landmine Modeling in LS-DYNA with Sandy Soil Material Model Development," in *Proceedings of the 14th International LS-DYNA Users Conference*, LSTC, Detroit, Michigan, United States, Jun. 2016, pp. 1–16. [Online]. Available: https://www.dynalook.com/conferences/14th-international-ls-dyna-conference/blast/comparison-of-strategies-for-landmine-modeling-in-ls-dyna-with-sandy-soil-material-model-development.

[257] Chen, J. Y. and Lien, F. S., "Simulations for Soil Explosion and Its Effects on Structures Using SPH Method," *International Journal of Impact Engineering*, vol. 112, pp. 41–51, 2018. DOI: 10.1016/j.ijimpeng.2017.10.008.

[258] Kurtoglu, I., Salihoglu, B., Tasan, Y. C., and Tekin, G., "Validation of Mine Blast Simulations with Field Tests," in *Proceedings of the 9th LS-DYNA Conference*, LSTC, Manchester, UK, Jun. 2013, pp. 1–10. [Online]. Available: https://www.dynalook.com/conferences/9th-european-ls-dyna-conference/validation-of-mine-blast-simulations-with-field-tests.

[259] Toussaint, G. and Durocher, R., "Finite Element Simulation Using SPH Particles as Loading on Typical Light Armoured Vehicles," in *Proceedings of the 10th International LS-DYNA Users Conference*, LSTC, Detroit, Michigan, United States, Jun. 2008, pp. 1–8. [Online]. Available: https://www.dynalook.com/conferences/international-conf-2008/PenetrationBlast-2.pdf.

[260] Hilding, D., "Methods for Modelling Air Blast on Structures in LS-DYNA," in *Proceedings of the Nordic LS-DYNA Users' Conference*, LSTC, Gothenburg, Sweden, Jun. 2016, pp. 1–65.

[261] Wilkins, M. L., Squier, B., and Halperin, B., "The Equation of State for Detonation Products of PBX 9404 and LX04-01," University of California Radiation Laboratory at Livermore, Livermore, CA, United States, Technical Report UCRL-7797, Apr. 1964, Other Information: From 10th International Symposium in Combustion, Cambridge, Eng., Aug. 1964. Orig. Receipt Date: 31-DEC-64. [Online]. Available: https://www.osti.gov/biblio/4041362.

[262] Kury, J. W., Hornig, H. C., Lee, E. L., McDonnel, J. L., Ornellas, D. L., Finger, M., Strange, F. M., and Wilkins, M. L., "Metal Acceleration by Chemical Explosives," in *Proceedings of the 4th Symposium (International) on Detonation*, US Navy, Office of Naval Research, Washington, DC, United States, Oct. 1965, pp. 1–13. [Online]. Available: https://apps.dtic.mil/dtic/tr/fulltext/u2/656036.pdf.

[263] Lee, E. L., Hornig, H. C., and Kury, J. W., "Adiabatic Expansion of High Explosive Detonation Products," University of California Radiation Laboratory at Livermore, Livermore, CA, United States, Technical Report UCRL-50422, May 1968. [Online]. Available: https://www.osti.gov/biblio/4783904-adiabatic-expansion-high-explosive-detonation-products.

[264] Baker, E. L., "An Explosives Products Thermodynamic Equation of State Appropriate for Material Acceleration and Overdriven Detonation: Theoretical Background and Formulation," Armament Engineering Directorate, Picatinny Arsenal, New Jersey, United States, Technical Report ARAED-TR-91013, Jul. 1991. [Online]. Available: https://apps.dtic.mil/sti/pdfs/ADA238948.pdf.

[265] Segletes, S. B., "An Examination of the JWL Equation of State," Weapons and Materials Research Directorate, US Army Research Laboratory, Aberdeen Proving Ground, Baltimore, Maryland, United States, Technical Report ARL-TR-8403, Jul. 2018. [Online]. Available: https://apps.dtic.mil/sti/pdfs/AD1055483.pdf.

[266] Wilkins, M. L., "Fundamental Methods in Hydrodynamics," in *Methods in Computational Physics*, B. Alder, S. Fernbach, and M. Rotenberg, Eds., vol. 3, NY, United States: Academic Press, Jan. 1964, pp. 211–263, ISBN: 978-0124608030.

[267] Giroux, E. D., "HEMP User's Manual," Lawrence Livermore National Laboratory, Livermore, CA, United States, Technical Report UCRL-51079, Dec. 1973. DOI: 10.2172/4304397. [Online]. Available: https://www.osti.gov/servlets/purl/4304397.

[268] Chapman, D. L., "On the Rate of Explosion in Gases," *The London, Edinburgh, and Dublin Philosophical Magazine and Journal of Science*, vol. 47, no. 284, pp. 90–104, 1899. DOI: 10.1080/14786449908621243.

[269] Jouguet, E., "Sur la Propagation des Réactions Chimiques dans les Gaz," *Journal de Mathématiques Pures et Appliquées*, vol. 1, pp. 347–425, 1905, On the propagation of chemical reactions in gases. [Online]. Available: https://gallica.bnf.fr/ark:/12148/bpt6k107470r/f353.

[270] Rankine, W. J. M., "On the Thermodynamic Theory of Waves of Finite Longitudinal Disturbance," *Philosophical Transactions of the Royal Society of London*, vol. 160, pp. 277–288, 1870. DOI: 10.1098/rstl.1870.0015.

[271] Hugoniot, H., "Mémoire sur la Propagation des Mouvements dans les Corps et Spécialement dans les Gaz Parfaits (Première Partie)," *Journal de l'École Polytechnique*, vol. 57, pp. 3–97, 1887. [Online]. Available: https://books.google.com/books?id=wccAAAAAYAAJ&pg=PA3.

[272] Hugoniot, H., "Mémoire sur la Propagation des Mouvements dans les Corps et Spécialement dans les Gaz Parfaits (Deuxième Partie)," *Journal de l'École Polytechnique*, vol. 58, pp. 1–125, 1889. [Online]. Available: http://gallica.bnf.fr/ark:/12148/bpt6k4337130/f5.

[273] Davis, W. C., "Explosive Effects and Applications," in J. A. Zukas and W. P. Walters, Eds., First Edition. New York, United States: Springer, New York, NY, 1998, ch. Chapter 3 Shock Waves; Rarefaction Waves; Equations of State, p. 440, ISBN: 978-0-387-95558-2. DOI: 10.1007/978-1-4612-0589-0.

[274] Bois, P. D. and Schwer, L. E., *Explosives Modeling for Engineers*, LS-DYNA training class, Koblenz, Germany, Apr. 2019.

[275] Dobratz, B. M., "Properties of Chemical Explosives and Explosive Simulants," Lawrence Livermore National Laboratory, Livermore, CA, United States, Technical Report UCRL-51319, Dec. 1972. DOI: 10.2172/4285272. [Online]. Available: https://www.osti.gov/servlets/purl/4285272.

[276] Lee, E., Finger, M., and Collins, W., "JWL Equation of State Coefficients for High Explosives," Lawrence Livermore National Laboratory, Livermore, CA, United States, Technical Report UCID-16189, Jan. 1973. DOI: 10.2172/4479737. [Online]. Available: https://www.osti.gov/servlets/purl/4479737.

[277] Dobratz, B. M., "LLNL Explosives Handbook: Properties of Chemical Explosives and Explosives and Explosive Simulants," Lawrence Livermore National Laboratory, Livermore, CA, United States, Technical Report UCRL-52997, Mar. 1981. [Online]. Available: https://ntrl.ntis.gov/NTRL/dashboard/searchResults/titleDetail/UCRL52997.xhtml.

[278] Dobratz, B. M. and Crawford, P. C., "LLNL Explosives Handbook: Properties of Chemical Explosives and Explosives and Explosive Simulants. Change 2," Lawrence Livermore National Laboratory, Livermore, CA, United States, Technical Report UCRL-52997, Jan. 1985. [Online]. Available: https://ntrl.ntis.gov/NTRL/dashboard/searchResults/titleDetail/DE91006884.xhtml.

[279] Menikoff, R., "JWL Equation of State," Los Alamos National Laboratory, Los Alamos, NM, United States, Technical Report LA-UR-15-29536, Dec. 2015. DOI: 10.2172/1229709. [Online]. Available: https://permalink.lanl.gov/object/tr?what=info:lanl-repo/lareport/LA-UR-15-29536.

[280] Sharp, D. H., "An Overview of Rayleigh-Taylor Instability," *Physica D: Nonlinear Phenomena*, vol. 12, no. 1–3, pp. 3–10, 1984. DOI: 10.1016/0167-2789(84)90510-4.

[281] Hušek, M. and Kala, J., "Uncertainties in Blast Simulations Evaluated with Smoothed Particle Hydrodynamics Method," *Structural Engineering and Mechanics, An International Journal*, vol. 74, no. 6, pp. 771–787, 2020, IF: 3.101 (2019), JCR: Q1 (Engineering, Civil), JCR: Q2 (Engineering, Mechanical). DOI: 10.12989/sem.2020.74.6.771.

[282] Dynardo, *Methods for Multi-Disciplinary Optimization and Robustness Analysis*, Dynardo GmbH, Weimar, Germany, May 2020.

[283] González, Á., "Measurement of Areas on a Sphere Using Fibonacci and Latitude–Longitude Lattices," *Mathematical Geosciences*, vol. 42, pp. 49–64, 2010. DOI: 10.1007/s11004-009-9257-x.

[284] Ansys, *ANSYS Help*, 2020 R2, Ansys, Inc., Canonsburg, Pennsylvania, United States, 2020.

Acronyms

ADKE	adaptive density kernel estimation
AGSPH	approximate Riemann solver with Godunov Smoothed Particle Hydrodynamics
ALE	Arbitrary Lagrangian-Eulerian
ASPH	adaptive Smoothed Particle Hydrodynamics
BEM	Boundary Element Method
CAE	Computer-Aided Engineering
CD-SPH	Chemo-Dynamical Smoothed Particle Hydrodynamics
CFL	Courant-Friedrichs-Lewy
CG	centre of gravity
CJ	Chapman–Jouguet
CoP	Coefficient of Prognosis
CPM	Corpuscular Particle Method
CRKSPH	Conservative Reproducing Kernel Smoothed Particle Hydrodynamics
CSCM	Continuous Surface Cap Model
CSPH	Corrected Smoothed Particle Hydrodynamics
CSPM	Corrective Smoothed Particle Method
DEM	Discrete Element Method
DOF	degree of freedom
DPM	Dual Particle Method
DSPH	Discontinuous Smoothed Particle Hydrodynamics
DTSPH	Dual Time Smoothed Particle Hydrodynamics
EDAC	Entropically Damped Artificial Compressibility
EFG	Element Free Galerkin
EOS	Equation of State
EPEC	Evaluate-Predict-Evaluate-Correct
FDM	Finite Difference Method
FEM	Finite Element Method
FLIP	Fluid Implicit Particle
FO-SSPH	first order symmetric Smoothed Particle Hydrodynamics
FPM	Finite Particle Method
FSI	fluid-structure interaction
FVM	Finite Volume Method
GFDM	General Finite Difference Method
GFEM	Generalized Finite Element Method
GKR	General Kernel Reproduction
GSPH	Godunov Smoothed Particle Hydrodynamics

GTVF	generalized transport velocity formulation
HPC	high-performance computing
HVI	high velocity impact
IISPH	implicit incompressible Smoothed Particle Hydrodynamics
ISPH	incompressible Smoothed Particle Hydrodynamics
ITZ	interfacial transition zone
JHC	Johnson-Holmquist concrete
JWL	Jones-Wilkins-Lee
LDPM	Large Deformation Particle Method
LHS	Latin Hypercube Sampling
MC	Monte Carlo
MHD	magnetohydrodynamics
MLPG	Meshless Local Petrov-Galerkin
MLS	Moving Least Squares
MLSPH	Moving Least Square Particle Hydrodynamics
MM-ALE	Multi-Material Arbitrary Lagrangian-Eulerian
MOP	Metamodel of Optimal Prognosis
ODE	ordinary differential equation
PBM	Particle Blast Method
PCISPH	predictive-corrective incompressible Smoothed Particle Hydrodynamics
PDE	partial differential equation
PE	Poisson equation
PEC	Predict-Evaluate-Correct
PIC	Particle in Cell
PIM	Point Interpolation Method
RH	Rankine-Hugoniot
RKPM	Reproducing Kernel Particle Method
SI	International System of Units
SIISPH	simple itrative incompressible Smoothed Particle Hydrodynamics
SPG	Smoothed Particle Galerkin
SPH	Smoothed Particle Hydrodynamics
SPMHD	Smoothed Particle Magnetohydrodynamics
TNT	Trinitrotoluene
TOR	torsion
TVF	transport velocity formulation
TXC	triaxial compression
TXE	triaxial extension
UCS	unconfined or uniaxial compressive strength
UTS	unconfined or uniaxial tensile strength
WCSPH	weakly compressible Smoothed Particle Hydrodynamics
XFEM	Extended Finite Element Method
XSPH	X Smoothed Particle Hydrodynamics

Symbols

a	local variable
A	MLS and MLSPH correction matrix, area
B	renormalization correction tensor
c	adiabatic sound speed, cohesion
C_{CFL}	constant of Courant-Friedrichs-Lewy condition
C^n	order of smoothness, consistency
C_p	heat capacity at constant pressure
C_v	heat capacity at constant volume
d	dimension, number of spatial dimensions, diameter
d/dt	total time derivative, substantial derivative, material derivative, global derivative
dt	time step, time increment
e	specific internal energy
E	Young's modulus
f	force per unit mass, specific force
F	force
f_c	unconfined or uniaxial compressive strength
F_p	penalty force
f_t	unconfined or uniaxial tensile strength
g	standard acceleration due to gravity
G	shear modulus
h	smoothing length, radius of influence
H	smoothing length tensor
I	identity matrix
I_1, I_2, I_3	first, second, and third stress invariant
J_1, J_2, J_3	first, second, and third deviatoric stress invariant
K	bulk modulus
k_s	spring stiffness
l	length
L	gradient correction matrix
m	mass
M_n	Schoenberg's spline of nth degree
n	normal
N	number of neighbouring particles, particles within support domain
p	pressure
$\hat{p}$	monomial basis functions
p_{H}	Hugoniot polynomial

q	relative distance
r	distance, direction, radius
S	surface of integration domain in 3D, perimeter in 2D
t	time, thickness
u	displacement
v	velocity
V	volume
w	kernel prior the normalization
W	kernel, smoothing function, smoothing kernel function, smoothing kernel, kernel function
x	position, spatial coordinate
α	kernel correction parameter, correction distance
α_l	non-dimensional constant of linear bulk artificial viscosity
β	kernel and MLS correction vector, correction distance
β_q	non-dimensional constant of quadratic von Neumann-Richtmyer artificial viscosity
δ	Dirac delta
$\delta^{\alpha\beta}$	Kronecker delta
δ_{det}	detonation distance
δ_{ini}	initial penetration depth, initial gap
δ_{min}	minimum clear distance
δ_{pen}	penetration depth, gap
Δ	difference operator
ΔV	associated volume, volume of particle, lumped volume, volume difference
Δx	particle spacing, typical length
ϵ	clipping function factor in Monaghan type artificial viscosity
$\tilde{\epsilon}$	XSPH stepping factor
ε	total strain tensor
$\dot{\varepsilon}$	total strain-rate tensor
ε_v	volumetric strain
η	local variable
γ	adiabatic index, heat capacity ratio
Γ	Grüneisen parameter (function)
κ	smoothing function scaling factor
μ	first estimate of velocity divergence
μ_n	nth moment of a function
∇	grad, gradient, differential operator, nabla operator
$\nabla\cdot$	div, divergence
ν	Poisson's ratio
$\mathcal{O}$	residual estimate, residuum, remainder, error
ω	rotation (spin) tensor
$\dot{\omega}$	rotation-rate (spin-rate) tensor
Ω	support domain, integration domain, volume of integral
∂	partial derivative
ϕ	MLS based kernel, zenith angle
φ	inner friction angle

Π	artificial viscosity
Π_l	linear bulk artificial viscosity
Π_q	quadratic von Neumann-Richtmyer artificial viscosity
ρ	volumetric mass density
σ	Cauchy stress tensor
$\sigma_{\kappa h}$	normalization constant
σ_n	normal stress
τ	shear (deviatoric) stress
θ	azimuth angle
$\langle\ \rangle$	kernel approximation operator
$\langle\ \rangle^{\mathbf{MLS}}$	MLS kernel approximation operator

Symbols in CSCM

A	ductile (compressive) shape softening parameter
B	ductile (compressive) shape softening parameter
C	brittle (tensile/shear) shape softening parameter
C_h	hardening rate
d	damage scalar parameter
d_{max}	maximum value of damage scalar parameter
D	brittle (tensile/shear) shape softening parameter
D_1	linear shape parameter of pressure-volumetric strain curve, hardening law linear exponent
D_2	quadratic shape parameter of pressure-volumetric strain curve, hardening law nonlinear exponent
E	Young's modulus
f	yield surface
f_c	unconfined or uniaxial compressive strength
F_c	hardening cap failure surface
$f_{ck,cube}$	characteristic compressive cube strength at 28 days
$f_{ck,cyl}$	characteristic compressive cylinder strength at 28 days
f_d	dynamic strength general
f_{dc}	dynamic compressive strength
f_{dt}	dynamic tensile strength
F_f	shear failure surface
f_s	quasi-static strength general
f_t	unconfined or uniaxial tensile strength
G	shear modulus
G_b	limiting function for incremental back stress
G_f	fracture energy general
G_f^{vp}	fracture energy general with rate effects
G_{fb}	fracture energy for brittle damage
G_{fc}	fracture energy in unconfined or uniaxial compressive stress
G_{fd}	fracture energy for ductile damage
G_{fs}	fracture energy in pure shear stress
G_{ft}	fracture energy in unconfined or uniaxial tensile stress
I_1	first stress invariant
J_2, J_3	second and third deviatoric stress invariant
$\hat{J}_3$	normalized third deviatoric stress invariant
K	bulk modulus
k_b	non-dimensional stress invariant ratio in brittle mode of failure

k_d	non-dimensional stress invariant ratio in ductile mode of failure
L	intersection of the cap and shear surface
N_h	hardening initiation, fraction of the final yield surface
p	pressure
Q_1	scaling factor of pressure function of TOR strength
Q_2	scaling factor of pressure function of TXE strength
$\mathcal{R}$	Rubin strength three-invariant reduction factor (function)
R	ellipticity of the cap surface, the cap surface aspec ratio of its major and minor axes
r_b	brittle damage accumulation
r_{b_0}	brittle damage accumulation threshold
r_d	ductile damage accumulation
r_{d_0}	ductile damage accumulation threshold
r_0^{vp}	damage accumulation threshold with rate effects
W	maximum plastic volumetric strain, hardening law maximum compaction
X	intersection of the cap and pressure axis
α	triaxial compression surface constant term
α_1	torsion surface constant term
α_2	triaxial extension surface constant term
β	triaxial compression surface exponent
β_1	torsion surface exponent
β_2	triaxial extension surface exponent
$\hat{\beta}$	normalized angle as a function of Lode angle
Δ	difference operator
δ_c	overstress limit in compression
δ_t	overstress limit in tension
ε	total strain tensor
$\dot{\varepsilon}$	total strain-rate tensor
ε_{max}	maximum principal strain
ε_v	volumetric strain
ε_v^p	plastic volumetric strain
η	fluidity parameter
η_c	fluidity parameter for uniaxial compressive stress
η_{c_0}	base of fluidity parameter for uniaxial compressive stress
$\bar{\eta}_c$	power of fluidity parameter for uniaxial compressive stress
η_s	fluidity parameter for pure shear stress
η_t	fluidity parameter for uniaxial tensile stress
η_{t_0}	base of fluidity parameter for uniaxial tensile stress
$\bar{\eta}_t$	power of fluidity parameter for uniaxial tensile stress
γ	viscoplastic interpolation parameter, trial elastic and inviscid stress interpolation function
κ	cap hardening parameter
λ	triaxial compression surface nonlinear term
λ_1	torsion surface nonlinear term
λ_2	triaxial extension surface nonlinear term
μ	shear to compressive damage transition power

ν	Poisson's ratio
ω	power applied to fracture energies with rate effects
ψ	ratio of shear to tensile fluidity parameter
σ	stress general
$\sigma_1, \sigma_2, \sigma_3$	first, second, and third principal stress
σ_b	back stress
σ_d	stress with damage
σ_h	initial yield stress of hardening initiation
σ_p	inviscid plastic stress (without rate effects, without damage)
σ_r	radial stress
σ_t	trial elastic stress
σ_{vp}	viscoplastic stress (with rate effects, without damage)
σ_x	axial stress
τ	shear (deviatoric) stress
θ	triaxial compression surface linear term
θ_1	torsion surface linear term
θ_2	triaxial extension surface linear term
υ	shear to tensile damage transition power
ξ	moderate pressure adjustment parameter

Symbols in JWL EOS

A	linear coefficient of JWL EOS
B	linear coefficient of JWL EOS
D	detonation velocity
e	specific detonation energy, detonation energy per unit mass
E	detonation energy density, detonation energy per unit volume
E_{CJ}	Chapman–Jouguet energy
F	burn fraction
p	pressure
p_{CJ}	Chapman–Jouguet pressure
p_{EOS}	EOS pressure
R_1	nonlinear coefficient of JWL EOS
R_2	nonlinear coefficient of JWL EOS
v	volume of detonation products
V	volume relative to undetonated state
v_0	volume of undetonated explosive
V_{CJ}	Chapman–Jouguet volume
Γ	Grüneisen parameter (function)
ω	nonlinear coefficient of JWL EOS, fractional part of the adiabatic explonent
ρ	volumetric mass density of detonation products
ρ_0	volumetric mass density of undetonated explosive